(51)

HIGH ENERGY PHENOMENA

ON THE SUN

A symposium held at

GODDARD SPACE FLIGHT CENTER

Greenbelt, Maryland

September 28–30, 1972

NATIONAL AERONAUTICS AND SPACE ADMINISTRATION

HIGH ENERGY PHENOMENA

ON THE SUN

A symposium sponsored by the
National Aeronautics and Space Administration
and held at NASA's Goddard Space Fligh.. ..nter,
Greenbelt, Maryland, September 28–30, 1972

Edited by
R. RAMATY AND R. G. STONE

PREFACE

This volume contains the papers presented at a symposium on high energy phenomena on the sun held at the Goddard Space Flight Center in September 1972. This symposium was held nine years after a previous Goddard symposium on solar flares. The purpose of the 1963 symposium was to bring together specialists from several disciplines to discuss new observations and theories of the solar flare phenomenon, which had seen a very rapid development up to that time. Since that time, this development has continued and accelerated. We felt, therefore, that in 1972 a similar symposium at Goddard could serve a useful purpose in discussing and analyzing new data and theories pertinent to high energy phenomena on the sun.

The organizing committee for the 1972 symposium consisted of R. Ramaty (Chairman), L. A. Fisk, K. Frost, and R. G. Stone. The symposium was attended by 184 participants from the U.S., Australia, Great Britain, France, Japan, and the Netherlands. It consisted of both invited and contributed papers which were organized into six sessions chaired by T. Chubb, F. Haddock, D. Wentzel, J. Lockwood, T. Takakura, and A. Maxwell. A program of the meeting is contained in Appendix A and a list of participants is given in Appendix B.

We have decided to publish these proceedings even though several scientific journals publish papers on solar physics. This decision was reached not only because of the enthusiastic endorsement of the speakers for such a book, but also because there is a need for an up-to-date specialized volume dealing with high energy phenomena on the sun. We have ordered the 50 papers into 8 chapters according to the following topics: flare theories and optical observations, microwave and hard X-ray observations and theories, ultraviolet and soft X-ray emissions, nuclear reactions in flares, energetic particles from flares, magnetic fields and particle storage, and radio emissions in the corona and interplanetary space. Chapter 9 contains a summary and outlook paper. This arrangement differs slightly from the original program organization, but we hope this will still convey, as accurately as possible, all of the ideas and results presented at the conference. Obviously, some papers could have been placed in different chapters since their content spans a number of subjects. In some cases, new results obtained by the authors after the symposium have been included.

We are indebted to the other members of the organizing committee for their help in putting together a successful scientific program, to F. B. McDonald for providing support at all phases of the program's organization, to Pat Resch for outstanding secretarial help, and to the various support facilities at the Goddard Space Flight Center who were very helpful in the organizational aspect of the Symposium. We also wish to thank Peggy Wilson for her excellent secretarial help and assistance in handling the manuscripts.

R. Ramaty

R. G. Stone

CONTENTS

CONTENTS (continued)

CONTENTS (continued)

CONTENTS (continued)

IX: SUMMARY AND OUTLOOK

I: FLARE THEORIES
AND OPTICAL OBSERVATIONS

MASS MOTION IN SOLAR FLARES

P. A. Sturrock
Stanford University

ABSTRACT

Mass motions in solar flares are here considered in terms of a previously proposed model. Particle acceleration occurs during reconnection of a current sheet located at coronal heights. The downward component of the particle flux produces an impulsive hard X-ray burst and heats the upper layers of the chromosphere sufficiently to lead to explosive evaporation. Some of the evaporated gas remains trapped in newly closed magnetic field lines and is responsible for the soft thermal component of X-ray emission. Gas which flows along open magnetic field lines subsequently forms a plasmoid which is ejected by magnetic stresses into interplanetary space and may subsequently cause a geomagnetic storm. Analysis of a highly simplified model leads to formulas for the density, temperature, and other parameters of the flare-produced plasma in terms of a length scale and mean magnetic field strength for the flare.

INTRODUCTION

Our knowledge of solar flares, and our ideas concerning solar flares, have both developed considerably since a symposium on this subject was first held at the Goddard Space Flight Center in 1963 (Hess, 1964). At that symposium, there was considerable discussion concerning the basic energy release mechanism responsible for solar flares. The consensus, at that time, was that the preflare energy is magnetic, and this energy is released by some plasma process or processes.

This view has, if anything, been further endorsed in recent years (Sweet, 1969). My own view is that the preflare energy must be the "free energy" associated with currents in the sun's atmosphere and that, in order to explain the rapidity of solar flares, the current must be in the form of current sheets. Possible configurations, including those suggested by Sweet (1958) and Carmichael (1964) have been classified in a recent article (Sturrock, 1972a).

There are many indications that mass motions play an important role in solar flares, and these topics have recently been discussed and compiled during a symposium organized by Professor Öhman (1968). Most magnetic theories of solar flares make little reference to these mass motions. On the other hand, Hyder (1968) has given a detailed discussion of the flow of gas from coronal heights into the chromosphere during solar flares but does not fit this process into a specific model for the total flare phenomenon.

The aim of this contribution is to show how some of the gross characteristics of mass

motions in solar flares may be understood in terms of a magnetic theory which has been presented previously (Sturrock, 1968). For the purpose of discussing mass motions, a highly simplified model of solar flares will be given and analysed. Properties of this model and further work necessary to improve understanding of the model are also considered.

The basic ideas concerning mass motion in solar flares as described in this article were first reported at the Solar Wind Conference held at Asilomar, California, in March 1971 (Sturrock, 1972b).

MODEL

Perhaps the simplest model for a magnetic-field configuration associated with solar flares is the simple bipolar open-field configuration (Sturrock, 1968), which is closely related to that proposed by Carmichael (1964). This configuration, and the evolution of a flare according to this model, are shown in Figure 1.
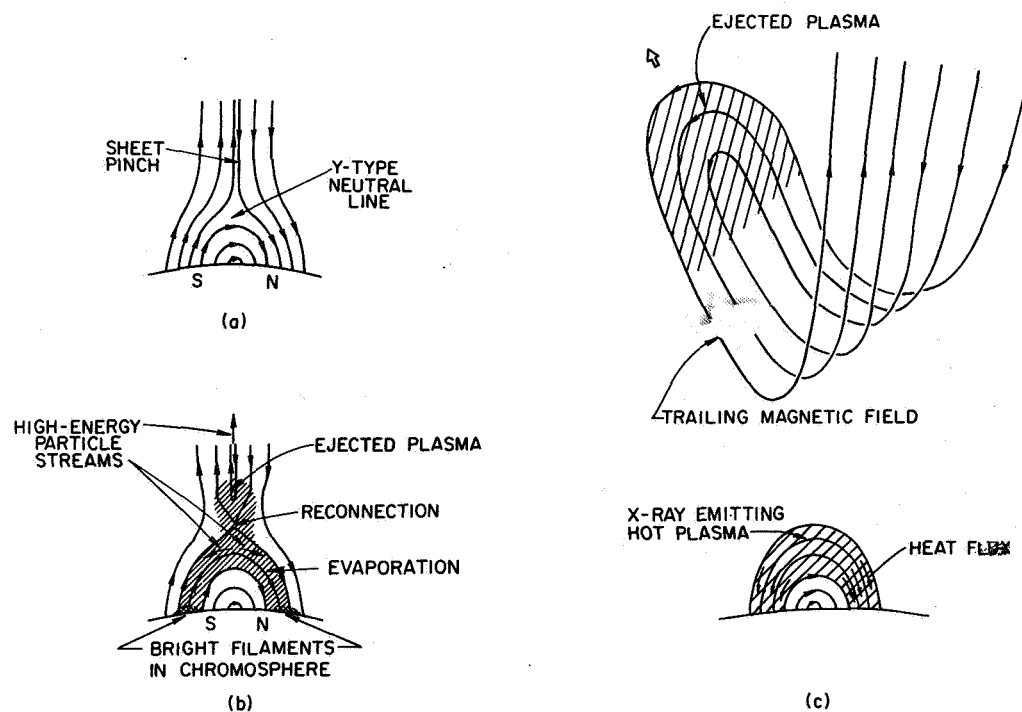
Figure 1. (a) Example of "open" current-sheet configuration above a bipolar magnetic region. (b) Reconnection results in particle acceleration which in turn leads to evaporation. (c) Following reconnection, magnetic field near sun's surface is in current-free state, and a mass of plasma – trailing magnetic-field lines – is ejected from the corona.

The length scale L of this configuration may vary over a wide range; if L is sufficiently small, the Y-type neutral point might be located in the chromosphere but, more generally, it will be located at coronal heights. When reconnection begins, the speed v_R at which magnetic-field lines move into the reconnection region is given by Petschek's analysis (Petschek, 1964), which gives the approximate formula

$$v_R \approx 10^{-1} v_A \tag{1}$$

where v_A is the Alfven velocity. For a fully ionized plasma with electron density n (and proton density n) in a magnetic field of strength B, this is given by

$$v_A \approx 10^{11.3} Bn^{-1/2} \tag{2}$$

It is well known that solar flares typically involve a rapid phase (variously termed the "impulsive phase," "flash phase," or "explosive phase") and a slow phase (sometimes termed the "main phase," "decay phase," or "thermal phase") (Syrovatskii, 1972). It has sometimes been proposed that the stored magnetic energy is released completely during the rapid phase and that the slow phase represents the slow decay of the result of this rapid energy conversion. However, this interpretation runs into difficulties.

It is not easy to understand how the reconnection mechanism can proceed so rapidly as to reconnect the entire magnetic flux involved in a large flare in a time of order 10^2 seconds. If the slow phase were really a decay phase, the shape of a flare should not change during this period; the only change should be a gradual reduction in intensity. Instead one observes that, for a large disk flare, the flare filaments gradually move apart during the slow phase. This is compatible with the model shown in Figure 1, if reconnection is proceeding throughout the slow phase.

Consideration of mass motion in flares also indicates that reconnection must be proceeding during the slow phase. Loop prominence systems (Kleczek, 1964) and rising-mound flares (Bruzek, 1964) indicate that large masses of gas are raised into the corona in some invisible form during a flare and appear at progressively greater heights as the flare proceeds. It is proposed that this gas is "evaporated" from the chromosphere. The reconnection process gives rise to streams of high-energy particles, some of which impinge upon the chromosphere, heating the upper layers to temperatures of the order of 10^7 K. Gas which is heated to such high temperatures will expand rapidly into the corona (Figure 1(b)). Some of this gas will cool quite rapidly to form "knots" of gas of temperature about 10^4 K which is then visible in Hα light. Cool gas at coronal heights will tend to stream down toward the chromosphere. This simple picture seems to be in accord with observations of loop prominence systems and rising-mound prominences. Indeed, this picture of the progressive reconnection of magnetic field lines is strongly suggested by Bruzek's (1964) careful analysis of rising-mound flares.

The existence of a large mass of gas of temperature of order 10^7 K at coronal heights is also indicated by the soft, thermal X-ray emission from flares (see, for instance, Drake, 1971). The view that gas responsible for soft X-ray emission has been evaporated from the chromosphere has also been proposed by Hudson and Ohki (1972). The impulsive X-ray burst may then be interpreted as bremsstrahlung produced by the high-energy particle streams impinging upon the chromosphere (Hudson, 1972).

In addition to explaining loop prominence systems, rising-mound flares, and the soft X-ray emission, the evaporation hypothesis offers explanations of certain other peculiarities of flares. For instance, it helps one to understand how large masses of gas can be ejected from the flare into interplanetary space. These masses are known to be as high as 10^{16} g on some occasions (Hundhausen, 1972). It has been hard to understand how such a large mass could be ejected either from the chromosphere or from the corona; if it came from the chromosphere, the flare process would have to occur in this region, but there is normally insufficient magnetic energy in this very thin region to account for the energy released during a large flare; if the gas came from the corona, the density in the corona would have to be much higher than is normally observed even in active regions. The evaporation hypothesis allows one to understand ejection as being produced by a two-stage process. As the reconnection proceeds, gas is evaporated from the chromosphere into the corona, so that the density of gas in the corona is much higher, during most of the flare, than it is at the very beginning of the flare. After a particular group of field lines has been reconnected, some of the newly evaporated gas is caught on field lines which are connected only to interplanetary space; this gas is therefore ejected from the sun as shown in Figure 1(c). The evaporation hypothesis also enables one to understand the difference between the rapid phase and the slow phase of a solar flare. We may interpret the rapid phase as comprising magnetic-field reconnection which occurs so early in the flare that the plasma density in the reconnection region is substantially the same as the preflare coronal density. During this stage the density is low, so that the Alfven speed is high and the reconnection rate is high. The slow phase, on the other hand, is to be identified with magnetic-field reconnection which proceeds after evaporation has begun so that reconnection is occurring with an enhanced plasma density in the reconnection region. This means that the Alfven velocity is reduced so that the reconnection rate also is reduced.

A highly simplified form of this flare model will be presented and analysed in the next section.

MASS MOTIONS IN FLARE MODEL

In order to simplify calculations, we approximate the model shown in Figure 1 to the highly schematic form shown in Figure 2. The width is characterized by the length L, and it is assumed also that the depth of the model is L. We assume that, at any instant in the evolu-

w = αL v_R v_R

←w→   ←w→

L
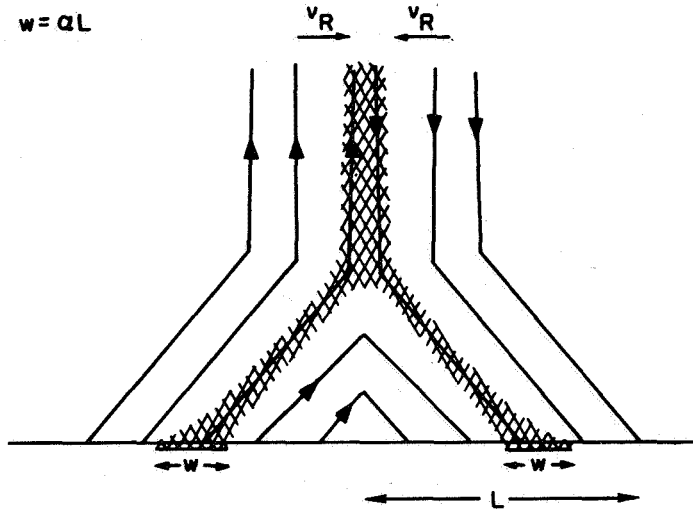
Figure 2. Schematic model of flare.

tion of the flare, energy conversion is occurring over a width w, and we introduce the parameter α, where

$$w = \alpha L \qquad (3)$$

Hence the model will be characterized by the length scale L (cm), the mean magnetic-field strength B (gauss) and the dimensionless parameter α, where $\alpha \leq 1$. The width of flare filaments indicates that, typically, $\alpha \approx 1/4$.

We suppose that magnetic-field reconnection leads to particle acceleration which, in turn, leads to evaporation of chromospheric gas into the reconnection region as indicated by the hatched area of Figure 2. If we assume that one-half of the total magnetic energy $B^2/8\pi$ in the reconnection region is "free energy" associated with currents which can be released by field-line connection, of which half goes into mass motion and half into particle acceleration; and if we further assume that, during acceleration, one-half of the high-energy particles bombard the chromosphere, the other half streaming out into interplanetary space, we obtain the relation

$$3nkT = \left(\frac{1}{2}\right)^3 \frac{B^2}{8\pi} \qquad (4)$$

by equating the rate of increase of thermal energy to the rate of decrease of magnetic energy. This may be rewritten as

$$nT = 10^{13.1} B^2 \qquad (5)$$

The temperature T of the flare plasma in the reconnection region will be set by a balance between the heating rate and the cooling rate. Without going into details of the time dependent process, we estimate the temperature by equating these two rates. The time scale of the rate of heating is estimated as

$$\tau_H = \frac{W}{v_R} \tag{6}$$

The time scale for cooling is given by

$$\tau_C = \frac{u_{TH}}{q} \tag{7}$$

where u_{TH} is the thermal energy per unit area and q is the downward heat flux per unit area. In the present simple model, u_{TH} is estimated to be

$$u_{TH} = 3nkT \cdot L \tag{8}$$

and q is estimated to be

$$q = \kappa T L^{-1} \tag{9}$$

where κ is the thermal conduction coefficient which, for fully ionized plasma, is given approximately (Spitzer, 1962) by

$$\kappa = 10^{-6} T^{5/2} \tag{10}$$

On equating the heating time scale τ_H and the cooling time scale τ_C, we obtain

$$n^{-1} T^5 = 10^{1.8} \alpha^{-2} B^2 L^2 \tag{11}$$

Equations (5) and (11) may now be solved to yield estimates of the density and temperature of the flare plasma:

$$n = 10^{10.6} \alpha^{1/3} B^{4/3} L^{-1/3} \tag{12}$$

$$T = 10^{2.5} \alpha^{-1/3} B^{2/3} L^{1/3} \tag{13}$$

The total energy released by the flare may be estimated as

$$W = \frac{1}{2} \cdot \frac{1}{8\pi} B^2 L^3 \approx 10^{-1.9} B^2 L^3 \tag{14}$$

on taking the total volume to be L^3 and assuming that one-half of the initial magnetic energy is "free energy."

8

We assume that the total mass of gas evaporated from the chromosphere is 2M and that, after the flare, a mass M is confined to the closed-field region and a mass M is attached to the reconnected open-field lines; the latter mass of gas will then be ejected into interplanetary space by magnetic stresses. The approximate relationship

$$2M = L^3 n m_p \tag{15}$$

where m_p is the proton mass, then leads to the estimate

$$M = 10^{-13.5} \alpha^{1/3} B^{4/3} L^{3/8} \tag{16}$$

The soft X-ray emission of the slow phase is produced by the mass of hot gas trapped in the closed-field region. Hence the emission measure H (cm^{-3}) of the postflare plasma may be estimated as

$$H = nMm_p^{-1} = 10^{20.9} \alpha^{2/3} B^{8/3} L^{7/3} \tag{17}$$

It was assumed earlier in this section that one-half of the energy released in the flare goes into particle acceleration and one-half into mass motion. The part which goes into mass motion will accelerate the ejected mass of plasma to a velocity V. Hence the ejection velocity is given by the equation

$$\frac{1}{2}W = \frac{1}{2}MV^2 \tag{18}$$

which leads to the formula

$$V = 10^{5.8} \alpha^{-1/6} B^{1/3} L^{1/6} \tag{19}$$

DISCUSSION

Formulas derived in the preceding section have been evaluated for three possible choices of the primary flare parameters L and B, and results are shown in Table 1. The first example is a small (L = 30,000 km) but intense flare (W = 10^{30} erg). The second example is of a small (L = 30,000 km) weak flare (W = 10^{28} erg). The third example is of an extended (L = 100,000 km) intense flare with total energy exceeding 10^{32} erg.

We see from Table 1 that certain derived parameters for the flare are sensitive to the primary parameters, whereas others are not. The total mass varies from 10^{12} to 10^{16} g, the emission measure H from $\sim 10^{46} cm^{-3}$ to $\sim 10^{50}$ cm^{-3}, and the number density from $\sim 10^{10}$ cm^{-3} to $\sim 10^{12}$ cm^{-3}. On the other hand, the plasma temperature varies by less than

an order of magnitude, and the ejection velocity by only a factor of two. The model and the calculations have been simplified to such an extent that one should not expect more than approximate agreement between theory and data. However, the ranges of values for the derived parameters shown in Table 1 seem to be in reasonable agreement with values yielded by observational data.

The gross agreement between the results shown in Table 1 and the typical properties of solar flare suggests that the primary assumption of the model is probably correct; that is, evaporation is an important mechanism leading to mass motion in solar flares. In order to pursue this topic, it will be necessary to make the model more realistic in various ways. In the first place, a self-consistent model for the magnetic field should be adopted. Second, the dynamic response of the chromosphere to a flux of high-energy electrons and protons should be calculated in detail. Third, one would need to follow a flare as it evolves in time, rather than regard the flare as a steady process. Fourth, it would be necessary to examine more carefully the relationship between quantities which can be calculated and quantities which can be measured. For instance, the ejection velocity yielded by this theory may or may not be directly comparable with time-of-flight measurements of solar flare ejecta, since a plasmoid ejected from the sun at high velocity may suffer substantial deceleration in traveling through the solar wind.

It is hoped that a more detailed study of this model may be reported at a later date.

Table 1

Calculated Results for Three Sets of Flare Primary Parameters.

Derived Parameters	Length (cm) and Magnetic Field Strength (gauss)		
	$L = 10^{8.5}, B = 10^3$	$L = 10^{8.5}, B = 10^2$	$L = 10^{10}, B = 10^2$
W (ergs)	$10^{29.8}$	$10^{27.8}$	$10^{32.3}$
T (K)	$10^{7.5}$	$10^{6.8}$	$10^{7.3}$
n (cm^{-3})	$10^{11.9}$	$10^{10.6}$	$10^{10.1}$
M (g)	$10^{13.3}$	$10^{12.0}$	$10^{16.0}$
H (cm^{-3})	$10^{49.0}$	$10^{46.3}$	$10^{49.8}$
V (cm·s^{-1})	$10^{8.3}$	$10^{8.0}$	$10^{8.2}$

REFERENCES

Bruzek, A., 1964, *Ap. J.*, **140**, 746.

Carmichael, H., 1964: Hess (1964, loc. cit.), 451.

Drake, J.F., 1971, *Solar Phys.*, **16**, 152.

Hess, W.N., (ed.), 1964, *Proc. AAS-NASA Symposium on the Physics of Solar Flares* (NASA SP-50, Washington, D.C.).

Hudson, H.S., 1972, *Solar Phys.*, **24**, 414.

Hudson, H.S., and Ohki, K., 1972, *Solar Phys.*, **23**, 155.

Hundhausen, A.J., 1972, *Solar Wind* (eds. C.P. Sonett, P.J. Coleman, Jr., and J.M. Wilcox, NASA SP-308), 393.

Hyder, C.L., 1968: Öhman (1968, loc. cit.), 57.

Kleczek, J., 1964: Hess (1964, loc. cit.), 77.

Öhman, Y., (ed.), 1968, *Mass Motions in Solar Flares and Related Phenomena* (New York: Wiley).

Petschek, H.E., 1964: Hess (1964, loc. cit.), 425.

Spitzer, L., 1962, *Physics of Fully Ionized Gases* (2nd ed., New York: Interscience), 143.

Sturrock: P.A., 1968, IAU Symp. 35 (Holland: Reidel), 471.

Sturrock, P.A., 1972a, *Solar Phys.*, **23**, 438.

Sturrock, P.A., 1972b, *Solar Wind* (eds. C.P. Sonett, P.J. Coleman, Jr., and J.M. Wilcox, NASA SP-308), 419.

Sweet, P.A., 1958, *Electromagnetic Phenomena in Cosmical Physics* (ed. B. Lehnert: Cambridge University Press), 123.

Sweet, P.A., 1969, *Ann. Rev. Astron. Astrophys.*, **7**, 149.

Syrovatskii, S.I., 1972, *Comments Astrophys. Space Phys.*, **4**, 65.

ENERGETIC PARTICLES AS A SOURCE OF FLARE ENERGY

H. Elliot

Imperial College of Science and Technology

INTRODUCTION

There is rather general support for the view that sunspot magnetic fields provide the reservoir of energy from which is drawn the $10^{31} - 10^{32}$ ergs required to produce a solar flare. In consequence, many of the flare models discussed in the literature are devices for the rapid conversion of the magnetic field energy $B^2/8\pi$ into the various forms of electromagnetic radiation and particle energy required to explain the flare phenomenon. As yet, however, we are far from having a satisfactory overall account of the flare process and in these circumstances it is desirable that we should not be too constrained in our basic approach to the problem.

Some time ago I suggested (Elliot, 1964) that high-energy protons stored in the sunspot fields might be an alternative source of energy that should be considered. In short, the proposition was that high-energy protons cause flares rather than vice versa, and a few years later I elaborated on this theme at the COSPAR Symposium in Tokyo (Elliot, 1969). It seems quite plausible that such particles could acquire their energy relatively slowly from the wave field associated with the active region in a manner analogous to the heating of the corona. Because of the constraining effect of the magnetic field, the maximum energy that the trapped particles can acquire is far in excess of that of coronal particles generally, where the field is weak and the particles leave with a relatively low energy as the solar wind. The two situations may be compared to a high-pressure boiler on the one hand and a saucepan with a lid on the other. The acceleration time for the protons could be as long as a day and the total energy density of the stored particles within an order of magnitude of the magnetic energy density. Schatzman (1967) has discussed a flare model with some similarities, in which particles are slowly accelerated in a magnetic bottle and then further accelerated during the flare itself.

I would now like to look at some of the aspects of this model in a semiquantitative way. The total energy release in a large flare is in the region of 10^{44} eV, which includes all electromagnetic and energetic particle emission together with the interplanetary blast wave. As far as the energy alone is concerned, it could of course be stored either as a large number of low-energy particles or as a much smaller number of high-energy particles. There are however a number of constraints that have to be met, and to examine these, I propose to use the model illustrated in Figure 1. The trapping region is taken as a cube of side 7×10^9 cm at a height of 14×10^9 cm above the solar surface in which the field strength due to a

bipolar sunspot is 300 gauss. The photospheric field is 3000 gauss and the ambient number density of protons and electrons in the trapping region is 10^7 cm^{-3}.
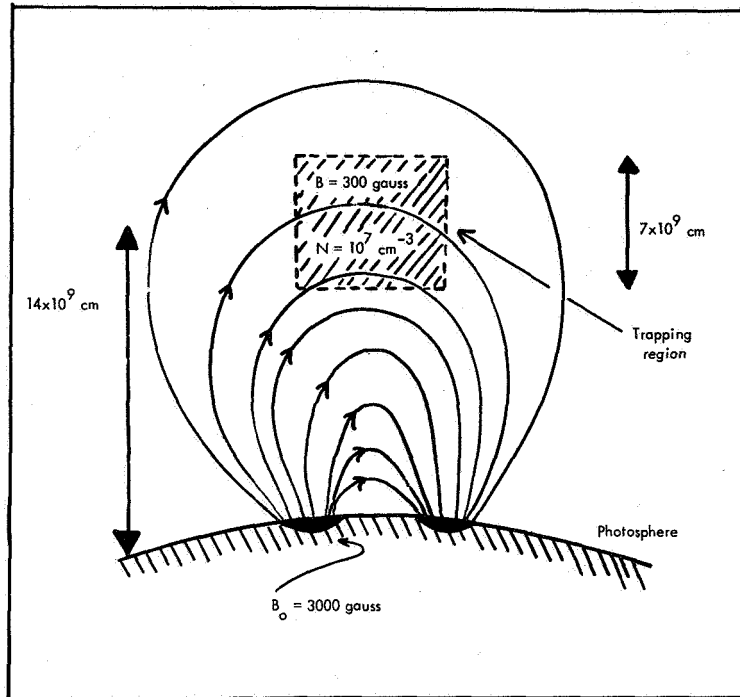
Figure 1. Model for trapping region in solar atmosphere.

PARTICLE STORAGE TIME IN THE MAGNETIC FIELD

In principle the power, P, available for the acceleration process could be used to set a lower limit to the storage time T_s since the total flare energy $W = \epsilon\, PAT_s$, where ϵ is the efficiency for converting wave energy into particle energy and A is the area presented by the storage region to energy flux. Unfortunately, we do not know what value to ascribe to ϵ, and P is known only between very wide limits. A lower limit to PA is given by the solar wind energy input at the sun of $\sim 10^{35}$ eV $\cdot$ s^{-1} for an average spot and a corresponding upper limit by the "missing energy flux" through the photosphere, which amounts to about 10^{41} eV $\cdot$ s^{-1}.

The constraints of particle motion in the magnetic field and of energy loss through coulomb collision in the solar atmosphere do however set firm upper limits to the storage time. Figure 2 shows how these limits depend on particle energy and it can be seen that for a coronal density of 10^7 cm^{-3} trapping lifetimes of $\sim 10^5$ second are possible for protons in the energy range 10^7 to 10^9 eV.
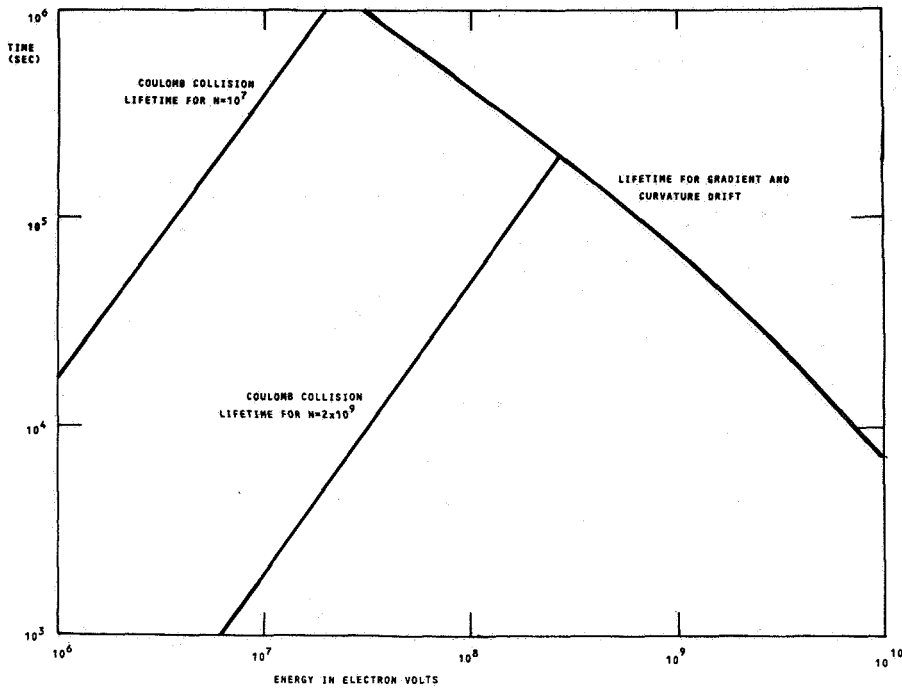
Figure 2. Particle lifetimes as functions of energy.

The energy spectrum of solar particles observed at 1 AU varies widely from event to event and from time to time within an event, but the spectrum for February 25, 1969, which is typical of a large flare, was of the general form $dN/dE = K/(E + 10)^3$ where E is in MeV. If we assume that the spectrum of the particles trapped in the corona was of the same form as that observed at 1 AU and take the total energy of the particle population to be

$$E_t = K_s \int_0^\infty \frac{E \, dE}{(E + 10)^3} = 10^{44} \text{ eV}$$

we obtain for the integral spectrum in the trapping region

$$N(>E) = \frac{10^{39}}{(E + 10)^2}$$

where E is in MeV. For a spectrum of this form more than 90 percent of the total energy content of the particles lies in the region between 3 and 300 MeV, where the trapping lifetime is longest. Nevertheless, if we take the average coronal energy input of 3×10^{17} $\text{eV} \cdot \text{s}^{-1} \text{ cm}^{-2}$ as the correct measure of the power of the accelerator, then for a storage time of 10^5 second, this falls short of the required value by a factor of ~ 100. Consequently, if

14

we take this to be the source of the particle energy we have to make the further assumption that the energy input to the corona is concentrated so as to flow through $\sim$ 1 percent of the solar surface. The "missing energy flux" is, of course, more than adequate to provide the necessary power.

The total amount of matter traversed by trapped particles in 10^5 seconds is less than 2×10^{-2} g $\cdot$ cm^{-2} so that there is negligible production of Li, Be, and B through spallation of heavier nuclei, which are expected to be present along with the protons.

RELEASE OF THE STORED ENERGY

Evidently it is possible to store the required amount of energy in the form of fast protons trapped in the sunspot magnetic field. How can it be suddenly released and what is the nature of the trigger mechanism? It seems inevitable that there will in general be a slow leakage of particles into the solar atmosphere through scattering into the loss cone, and I have pointed out (Elliot, 1969) that if the loss of particles into the chromosphere can, on occasion, rise above the required threshold, a jet of upward moving plasma can be produced which will traverse the magnetic field arch from end to end. The introduction of this plasma results in a catastrophic loss of high energy particles from the trapping region through violation of the "stable trapping limit" (Kennel and Petschek, 1966) which will be discussed below. The condition for such a jet to be produced is that the amount of energy deposited should be sufficient to raise the temperature of approximately one cubic scale height of the solar atmosphere to such a value that the velocity of sound exceeds the gravitational escape velocity (this is analogous to the case discussed by Colgate (1965) for a nuclear explosion in the terrestrial atmosphere). Impulsive losses of particles on a smaller scale will produce nothing more than a local brightening of the chromosphere without the jet.

The second stage of the trigger process depends on the inherent instability of the trapped particle population. Kennel and Petschek (1966) have shown that there is an upper limit to the flux of particles that can be stably trapped in a magnetic field when the individual energy, E, of particles (either protons or electrons) exceeds the average magnetic energy per particle $E_c = B^2/8\pi N$. Introduction of the plasma jet into the trapping region lowers E_c with the result that the trapping limit extends downwards to lower energies and many of the particles that were previously stably trapped are now scattered into the loss cone by ion cyclotron noise. Brice (1971) has emphasized the importance of this process in relation to the dumping of magnetosphere particles.

Protons in the MeV energy range precipitated from the trapping region are absorbed in the lower chromosphere where $N = 3 \times 10^{16}$ cm^{-3} and the scale height is in the region of 200 to 300 km. Under these conditions a cubic scale height of atmosphere contains $\sim 8 \times 10^{38}$ protons, and in order to meet the condition for hydrodynamic instability each must be given an energy of $\sim$ 400 eV, so that the total deposition of energy required to produce a jet is 3×10^{41}, which is less than 1 percent of total stored energy. Spread throughout this trapping volume, the 8×10^{38} protons produce a number density of 2×10^9 cm^{-3}

compared with 10^7 cm^{-3} prior to the flare, and there is a corresponding drop in E_c from 2.5 $\times$ 10^8 eV to 10^6 eV, with the consequence that most of the trapped particles will be dumped.

The range of a 10-MeV proton is $\sim 10^{-1}$ g $\cdot$ cm^{-2}, so that much of the 10^{44} eV is dissipated in the chromosphere in a sheet of area

$$49 \times 10^{18} \, \frac{B}{B_0} \sim 5 \times 10^{18} \text{ cm}^2$$

ELECTRON PRODUCTION

Electrons play an important role in the flare process since they are certainly the agents responsible for the X-ray and radio emission, and furthermore, high energy electrons are frequently observed in interplanetary space in association with flares.

It seems likely that some high-energy electrons must be accelerated along with the protons in the sunspot trapping region but they are unlikely to contribute more than a small fraction of the total proton energy for several reasons:

- Coulomb scattering is much more effective in dumping electrons into the loss cone than for protons

- Energy loss by bremsstrahlung and synchrotron radiation represents a serious additional drain on electron energy compared with protons

- The stable trapping limit for protons and electrons occur at same *flux* values so that the number density of protons in the trapping region can be much greater than for electrons of the same energy

For these reasons it seems likely that most of the electrons of energy up to a few MeV are produced by coulomb collision between the high-energy protons and thermal electrons as the protons are dumped into the chromosphere. The high-energy tail of the proton spectrum ($E > 200$ MeV) can generate electrons of higher energy (~ 50 MeV) by pion production in proton-proton collision and the subsequent $\pi \rightarrow \mu \rightarrow e$ decay process. The probability for a proton with velocity βc to produce a knock-on electron in the energy range E' to $E' + dE'$ is

$$p(E'\beta) = \frac{0.15}{\beta^2} \, \frac{dE'}{(E')^2} \left[1 - \beta^2 \, \frac{E'}{E'_m} \right] \text{ gm}^{-1} \text{ cm}^2$$

where E_m', the maximum energy transferable to the electron, is given by $\beta^2/(1 - \beta^2)$ MeV with E' measured in MeV. The proton population with the spectrum $dN/dE = 2 \times 10^{39}/(E + 10)^3$ has 10^{33} protons with $E > 10^9$ eV, and the number of electrons produced with energy between 1 and 2 MeV is therefore

$$N_e \sim 6 \times 10^{31} \text{ g}^{-1} \text{ cm}^2$$

16

The range of protons of this energy is several hundred g · cm^{-2}, so that the number of 1 to 2 MeV electrons produced is in the region of 10^{34}, which is comparable with Ramaty and Lingenfelter's (1968) estimate of the number required to produce a type IV solar radio burst. The number of electrons in the 10 to 100 keV range is estimated to be in the region 10^{39}, which appears to be adequate to account for the X-ray emission in this energy region.

SUMMARY

It seems feasible to store the 10^{32} ergs or so of energy required for a large flare in the form of protons trapped in sunspot magnetic fields. The particles are taken to have a power spectrum in kinetic energy with an average energy per particle of ~ 10 MeV. A trigger mechanism has been described whereby the particles can be rapidly dumped into the chromosphere when fast electrons are produced by coulomb collisions and probably also through pion production by the highest energy protons. The number of electrons produced seems to be adequate to account for the radio and X-ray emission observed from flares.

A model of this kind provides a natural explanation of a number of flare characteristics:

- Flares often start as one or more bright spots which on the present picture would correspond to the initial dumping of particles.

- Production of the plasma jet corresponds to the familiar surge which is often observed in association with flares.

- Flares frequently have two parallel bright regions which presumably correspond to the magnetically conjugate dumping areas.

- The flare loops seen in association with limb flares would appear to correspond to material which is left behind in the trapping regio   .d which eventually falls back into the chromosphere.

- The occurrence of the so-called homologous flares finds a natural explanation in this model, successive members of the series representing successive population and depopulation of favourable accelerating and trapping fields. The magnetic field configurations are not permanently disturbed by the flare, and in this respect the model described here differs radically from those that rely on conversion of magnetic field energy resulting in major changes in the field.

- On this model the apparently very high efficiency of the flare as an accelerator of energetic particles, which is hard to understand, is seen to be illusory in that the 2 or 3 percent of the total energy carried by the particles is just that part of the total population which escapes into interplanetary space, the remainder being either adiabatically decelerated or absorbed into the sun.

- The release time for the stored energy is very short, depending essentially on the particle velocities, which are high. It is therefore easy on this model to account for the very rapid flash phase of the flare.

REFERENCES

Elliot, H., 1964, *Planet. Space Sci.* **12**, 657.

Elliot, H., 1969, *Solar Flares Space Res.* (N. Holland), 356.

Schatzman, E., 1967, *Solar Phys.* **1**, 411.

Kennel, C.F., and Petschek, H.E., 1966, *J.G.R.* **71**, 1.

Colgate, S.A., 1965, *J.G.R.* **70**, 3161.

Brice, N., 1971, *J.G.R.* **76**, 4698.

Ramaty, R., and Lingenfelter, R.E., 1968, *Solar Phys.* **5**, 531.

SOLAR FLARE OBSERVATIONS
AND
SOLAR FLARE MODELS

Charles L. Hyder
Goddard Space Flight Center

ABSTRACT

Solar flare models must eventually be based on specific and detailed observations of solar flares. A good presentation of solar flare observations, some of which are in agreement with current thinking but some of which are not, should help us move toward flare models that are more realistic. On the other hand, detailed physical analyses of the consequences of our proposed models will lead to useful results. Then we will be able to determine the validity of our various models. I will show here how this process relegates the infall-impact model for flares to a secondary role in high energy solar events. The strictly thermal infall-impact model cannot lead to temperatures greater than 5×10^6 K. Thus we need at least one more process to explain the high energy aspects of solar flares; that is, temperatures equal to or greater than 10^7 K, nonthermal X-ray and radio emissions, white light flares, high energy particles far from the sun, and gamma-ray-producing particles in the sun.

INTRODUCTION

To date we have had the habit of evaluating solar flare models according to their theoretical elegance, their popularity, and their ability to draw large ~ .tities of research support money. One of the main reasons that this has been the case is that there has not been a good way to relate atmospheric structure to detailed spectral characteristics (line profiles, intensities, Doppler shifts, and so on). That is no longer the case. Various investigators have related detailed solar atmospheric structures to detailed observations of solar line profiles, by use of self-consistent quantitative analytic methods (see Athay, 1972).

It is now time for the authors of flare models and their colleagues to do the necessary follow-up physics to convert their proposed flare mechanisms into predicted atmospheric structure including density, temperature, and velocity distribution as functions of height in the sun. Then these model flare atmospheres can be used in the line profiles synthesis programs to predict the spectra that would result from the given model flare atmospheres. This would give us a powerful discriminant to determine when a given flare model would or would not be capable of leading to observed flare spectra. To date, the synthesis programs have been used exclusively in the low temperature regions of the sun. However, there is nothing intrinsic in the programs that would exclude analysis of high temperature and low density atmospheres, which characterize the high energy phenomena in the solar atmosphere.

INFALL-IMPACT FLARE OBSERVATIONS AND MODEL RESULTS

I have been studying infall-impact flares from both observational and theoretical aspects. Figure 1 shows a typical disparitiones brusques (DB) followed by a class II flare (flarelike brightening — FB) far from sunspot groups and other features usually associated with larger flares.
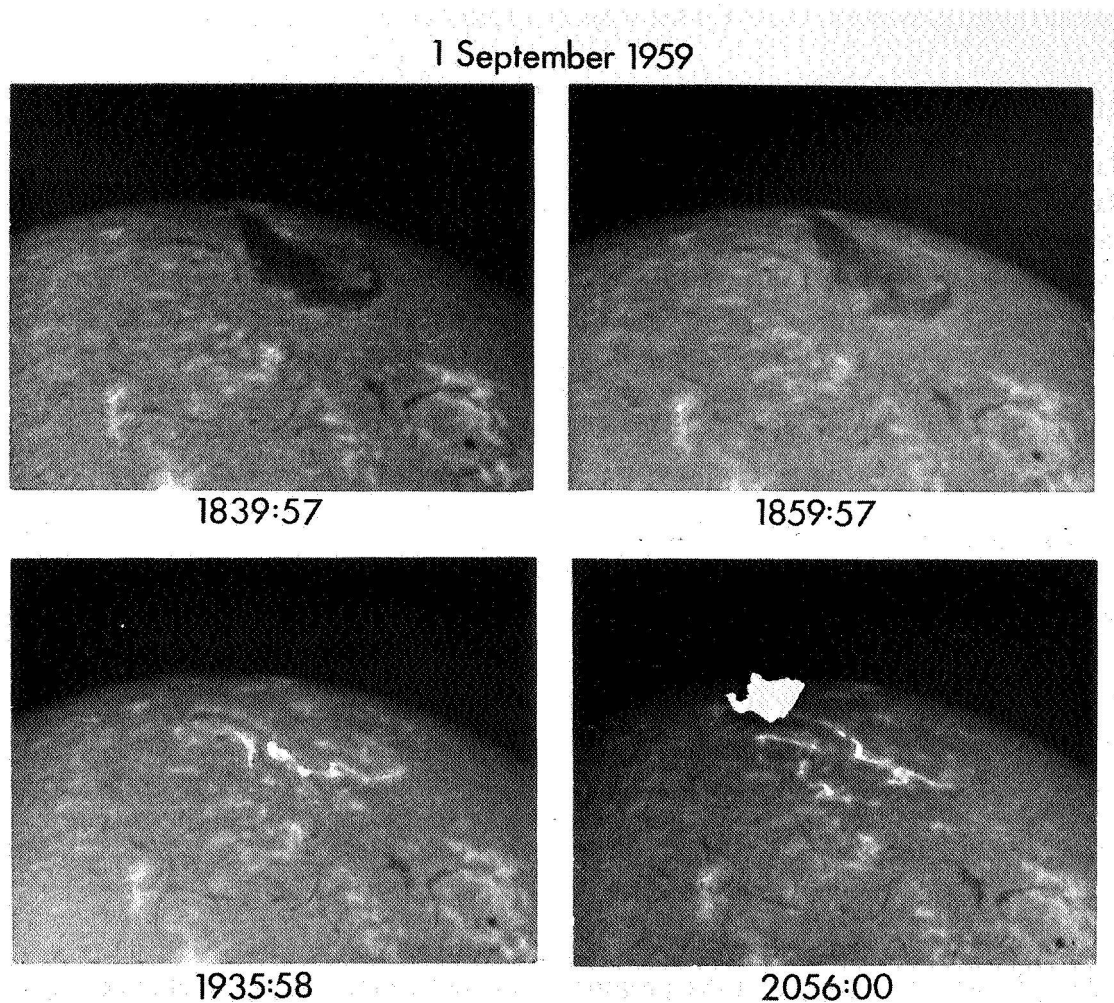
Figure 1. A large flare associated with a DB far from active regions
(September 1, 1969).

Svestka (1972) and Dodson-Prince (1972 — discussion during this symposium), have pointed out that it would require all of the magnetic energy of a region to produce a class II flare in a region devoid of sunspots. Observations of magnetic fields around filaments before a flare

(FB) and in the late phases of, or after such a flare, should be crucial to the validity of magnetic field annihilation models for the direct energy supply for those solar flares. The direct-field annihilation models have no substantial observational support after 14 years of looking in the photosphere. It appears that we need to look higher in the atmosphere, or to other mechanisms of energy conversion.

Nakagawa and I completed detailed theoretical studies of the corona-transition-chromospheric shocks by the densest ($n = 10^{12}$ cm^{-3}) and highest speed ($v = 300$ km $\cdot$ s^{-1}) falling streams conceivable. They never led to temperatures in infall-impact flares in excess of 5×10^{6} K. Therefore, it is obvious that the infall-impact mechanism must be relegated to a secondary role in flares exhibiting high-energy aspects characterized by effective temperatures of 10^{7} K or more.

On the other hand the infall-impact mechanism appears adequate to explain all of the chromospheric aspects of DB flares. This explanation does not preclude high energy processes occurring in the corona above an infall-impact flare in the chromosphere.

If DB flares are indeed explained primarily through the infall-impact mechanism (see Figures 2 and 3), then we need to explain how the rapid limb event* of March 1, 1969 (Figure 4) could be associated with hard and soft X-ray emissions (see Frost, 1969) associated with
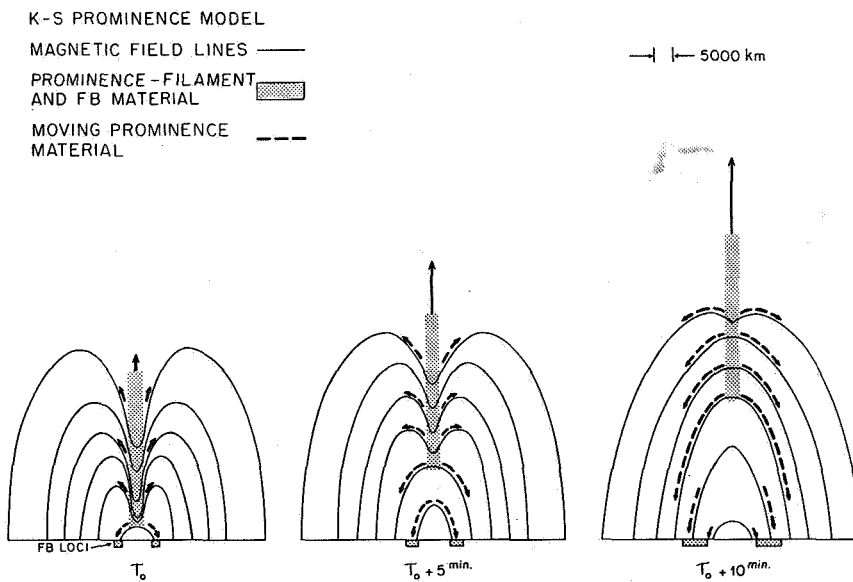
Figure 2. How the DB sheds its dense material to impact on the chromosphere and give separating two-ribbon flares.

---

*This limb event looked much like a spray, or an extremely fast DB.
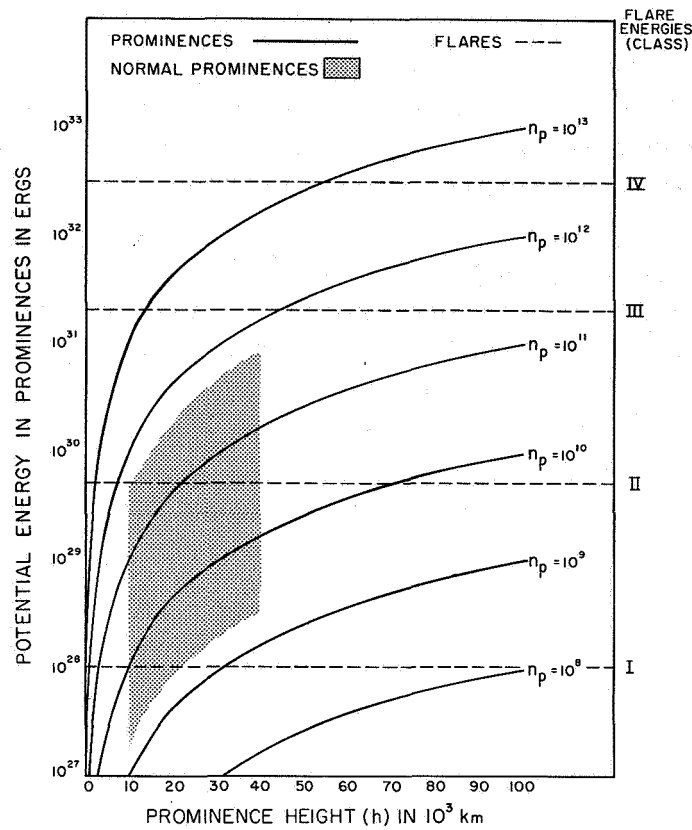
Figure 3. The amount of gravitational energy available in prominences of various densities (n_p) and heights. These energies are lower limits for flares associated w̶ ̶ ̶ ̶ B's.

that event, as shown in Figure 5. There was no chromospheric or photospheric disturbance or flare observed within 5 minutes of the X-ray event; therefore, all of the high energy radiations must have originated high in the corona.

Teske (private communication, 1969) has searched all of his data for X-ray events that were not associated with chromospheric flares. I examined Sacramento Peak Observatory prominence data and found four eruptive prominences (EPLs) that appeared above the limb within one minute of the onset of the associated X-ray burst. These bursts exhibited no short-lived structures. There were no other X-ray bursts observed by Teske while the Sacramento Peak limb patrol was operating. I found two other eruptive prominences that were not associated with X-ray emission (R. Teske, private communication, 1968). The only differences that I could find were that the four EPLs associated with X-rays exhibited projected outward speeds in excess of 100 km $\cdot$ s^{-1}, while the two that were not associated with X-rays did not exceed 70 km $\cdot$ s^{-1}. Since the speed of sound in the corona is about 150 km $\cdot$ s^{-1}, we appear to have been observing shock-associated X-rays. Mach 4 shocks in the
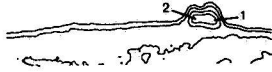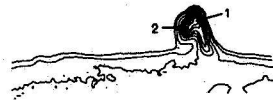
21:38:20   21:41:00   21:42:20
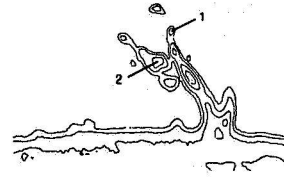
1 MARCH 1969

Figure 4. The rapid limb event (DB) of March 1, 1969.

OSO-Ⅴ
GSFC WHEEL EXP. IMP 3 E.P.L. + SPRAY 1 MARCH 1969

NATIONAL AERONAUTICS AND SPACE ADMINISTRATION
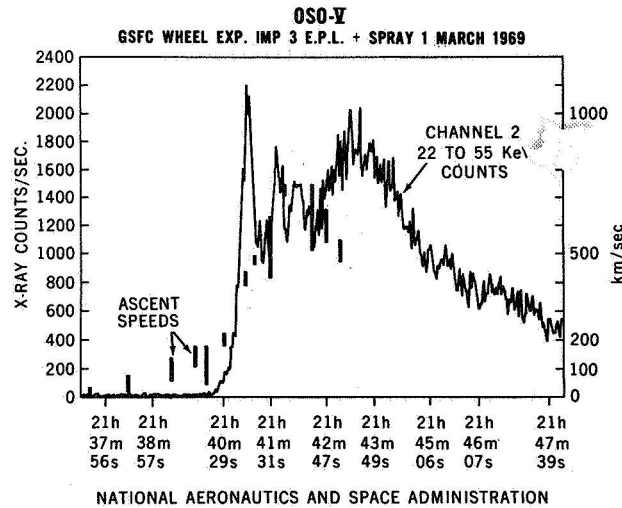
Figure 5. DB speeds and X-ray fluxes associated with the March 1, 1969 event. The short-lived X-ray bursts during the early phases of this event exhibited a hard power-law spectrum ($E^{-3.2}$) while the broad peak occurring later exhibited a softer power-law spectrum (E^{-5}). These X-ray data from OSO-5 were provided by K. Frost.

corona are capable of heating the corona to temperatures of between 10^7 and 2×10^7 K, and they also lead to emission measures between 3.8×10^{47} and 3.8×10^{48} cm^{-3}. These predictions agree well with large samples of X-ray data analyzed by Drake (1971).

OTHER PROCESSES IN FLARES

Thus, at least part of the hard and soft X-ray emissions associated with flares may come from the corona far from the chromospheric flare. This result is not incompatible with flare models in which at least part of the chromospheric and photospheric emissions are due to the precipitation of MeV protons and keV electrons from the corona (see Svestka, 1970; Najita and Orrall, 1970; and Hudson, 1972). These kinds of models would exhibit X-rays and gamma rays that were spatially in intimate association with the $H\alpha$ and white light aspects of the flare.

Ahluwalia (1971) has shown that 3 to 100 MeV protons in the corona could not last longer than 100 to 1000 seconds if they interacted with gas densities between 10^{10} and 10^{12} cm^{-3}. His results are shown in Figure 6. Such high gas densities are characteristic of the mid-to-upper chromosphere. These densities could possibly exist in the corona during a flare, but 10^{12} cm^{-3} is a little high, and its existence has no good observational support.
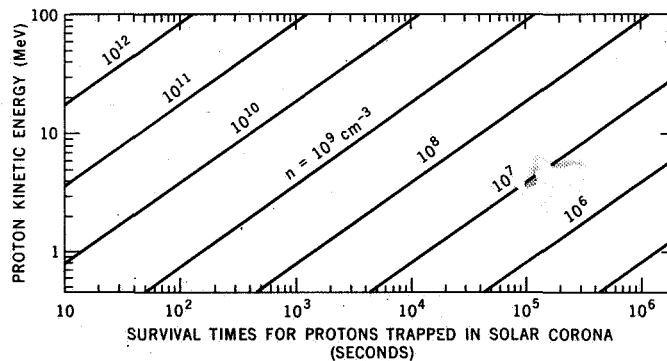
Figure 6. Lifetimes of protons trapped in the corona as functions of their energies (1 to 100 MeV) and the target densities. This figure is a high-density extension of Ahluwalia's work (1971).

Although magnetic field annihilation does not appear to be the direct source of flare energy, we still hold to the idea that magnetic field rearrangements accelerate protons and electrons, release high density trapped gasses outward (EPLs, type II and type III bursts, and so on) and inward (infall-impact and particle precipitation) and guide these direct energy sources to the observed flare sites.

REFERENCES

Ahluwalia, H.S., 1971, *12th Int. Conf. on Cosmic Rays,* Hobart, Australia.

Athay, R.G., 1972, *Line Formation,* in press.

Drake, J.F., 1971, *Solar Phys.* **16**, 152.

Frost, K., 1969, *Ap. J.* **158**, L159.

Hudson, H., 1972, *Solar Phys.* **24**, 414.

Najita, K., and Orrall, F.Q., 1970, *Solar Phys.* **15**, 176.

Svestka, Z., 1970, *Solar Phys.* **13**, 472.

OPTICAL OBSERVATIONS OF THE AUGUST 1972 FLARES

Katsuo Tanaka and Harold Zirin
Big Bear Solar Observatory, Hale Observatories
Carnegie Institution of Washington
California Institute of Technology

ABSTRACT

We describe the optical appearance of the flares in McMath 11976. The region showed complex, twisted magnetic fields from its birth on July 11, 1972. The flares occurred because of high field gradients and sheared field lines, which made transitions to lower energy field configurations possible. The Hα emission comes mainly from intense kernels about 10,000 km across in each magnetic polarity. Good Hα spectra enable us to measure the total Hα flux as 2.5×10^{30} ergs, much less than previous estimates. In the 3835-Å band, we can measure fast flashes of emission at the time of the impulsive flares, presumably due to dumping of energetic electrons in the chromosphere. The flashes last 5 or 10 seconds and have the same energy as the 50 keV electrons. In slower flares, the dumping is more gradual and occurs at the advancing front of the flare. The peak of emission in Hα from the kernels and the peak 3835-Å flashes agree very well with the hard X-ray peak.

The spectra show Hα emission 12 Å wide in the flash phase of the August 7 flare. There is red asymmetry but no evidence of deuterium. Outside the kernels, the emission is red shifted. The observations agree well with a model in which the energy is released in a kernel with volume 2×10^{27} cm^3, diffuses outward to form a coronal cloud which gradually cools, and heats the chromosphere to produce the extended Hα area. A sharp velocity discontinuity across the neutral line indicated motion of 5 km/s during and after the flare.

INTRODUCTION

The active region McMath 11976, which produced the great flares of August 1972, resulted in an unparalleled opportunity for the study of solar activity. We present optical observations made at the Big Bear Solar Observatory and its station at Tel Aviv University and comparisons with data made available by various colleagues.

Data from Big Bear Lake were obtained with a battery of telescopes on a single mount. Two 10-inch refractors produced large scale cinematographic data in various wavelengths, mostly Hα and Hα +1/2 Å, but also with a Chapman filter (Chapman, 1970) 15 Å wide, centered on 3835 Å. Observations of the full disk in Hα were made with an 8.6-inch vacuum refractor, and white-light full disk observations were made with a 6-inch refractor. Magnetograms were made with the Leighton-Smithson magnetograph, time sharing in one of the 10-inch refractors, and spectrograms were made with a 5-meter Coude spectrograph fed by a third 10-inch refractor. At Tel Aviv, observations were made with a 5-inch photoheliograph used

in the center of Hα. We were fortunate in that not only was the birth of the region observed in July, but all of the large flares as well were picked up on either the Big Bear or Tel Aviv photoheliographs. The principal large flares occurred at 0330, 1838, and 2005 August 2; 0620 August 4; and 1526 August 7, 1972.

Highlights of the observations are the following: The region showed inverted polarity from its inception on July 11; the great activity was due to extremely high shears and gradients in the magnetic field, as well as constant invasion of one polarity into the opposite polarity. Observations at 3835 Å show remarkable fast flashes in the impulsive flare of 1838 August 2 with lifetimes of 5 seconds, which may be due to dumping of particles into the upper photosphere. Spectroscopic observations show red asymmetry of the Hα emission in the flash phase of the August 7 flare, as well as substantial velocity shear in the photosphere during the flare, somewhat like earthquake movement along a fault. Finally, the total Hα emission of the August 7 flare could be measured accurately as about 2.5×10^{30} ergs, considerably less than coarser previous estimates for great flares.

DEVELOPMENT OF THE REGION, JULY 10 TO 15

McMath 11957, the predecessor of McMath 11976, first appeared on Big Bear Solar Observatory (BBSO) films on July 11, growing in a quiet region. Figure 1 shows an Hα picture of development on July 12, and Figure 2 shows the corresponding videomagnetograms. (All illustrations show south at top, west at left.) Contrary to usual belief, such regions do not emerge from the elements of the network but in the perfectly quiet regions in between—note the black dot (p polarity) in the July 10 magnetogram. The magnetic polarity was inverted from the start, the arched filaments being rotated 120° from the normal direction. In addition to the first set of flux loops, other systems arose, so that on July 12 there were two sets of f spots, both connected to the same p area. Between July 12 and July 13 there was rapid growth of the p spot, and the magnetogram for the 13th ws the strong field gradients thus produced. A number of small flares were observed in this region, and spectra were obtained of intense small surges at the limb on the 15th. The limb activity on the 15th was almost continuous, consisting of many small surges. It is clear that the great magnetic complexity of this region was inherent in its structure from its first emergence from below and was not a consequence of interaction with existing regions. McMath 11947, the region just ahead of it, died out on the back side and was not seen the next time around.

DEVELOPMENT OF JULY 30 TO AUGUST 12

McMath 11976* appeared at the east limb on July 29, with high resolution observations at Big Bear beginning on the 30th. Although the official prediction was that "solar activity will remain at a low to moderate level," close inspection of the small region showed a tightly twisted magnetic configuration with steep field gradients and f polarity directly south of the main spot. Figures 3, 4, and 5 show the disk transit of the region from July 30 to August 10,

---

*Dale Vrabec has informed us that the polarities in McMath 11976 were completely reversed; thus the spots p_1, p_2, p_3, etc. are all normally following polarity, and vice versa.
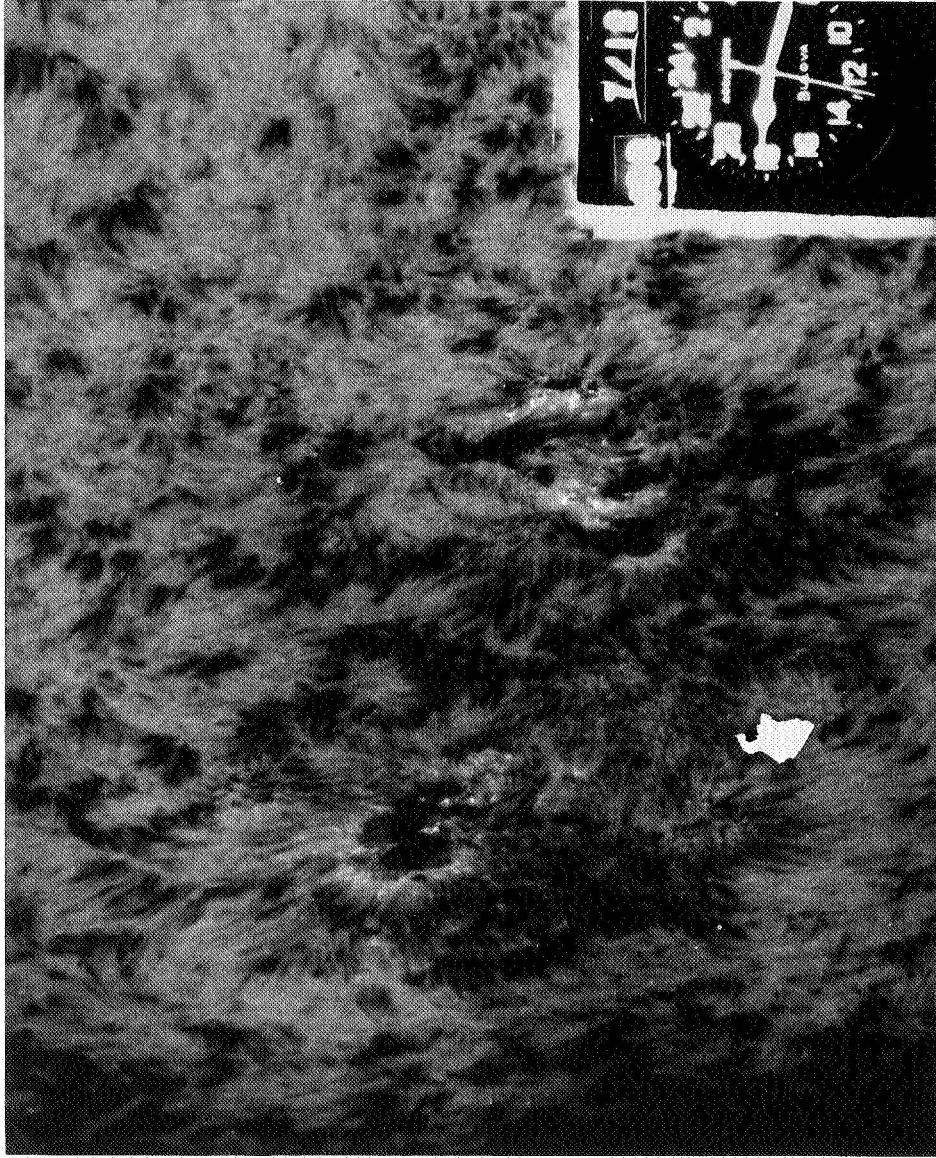
Figure 1. Early stage of McMath 11976 (as McMath 11957) at $18^h17^m23^s$, July 12, Hα +0.5 Å. It is in the center of the frame, a typical complex emerging flux region (EFR). The dark fibrils probably parallel new flux loops, and would normally run east-west in a simple region. Comparison with Figure 2 shows that the sunspot in the upper part of the group is p (preceding), or south polarity, and the regions below and sur- rounding are f (following) or north. The spots at left disappeared on the back side of the sun.
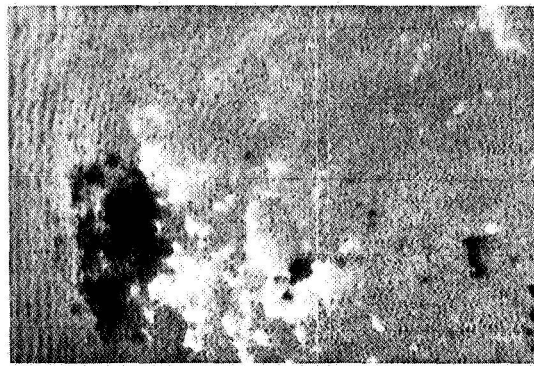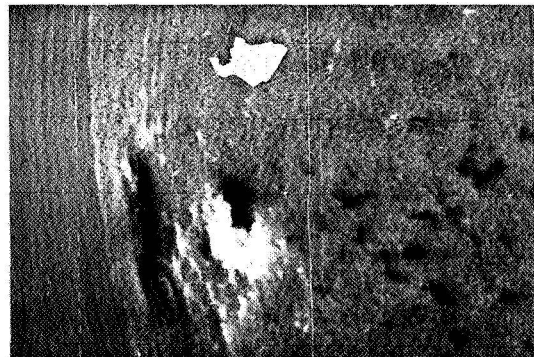
Figure 2. Birth of August, 1972 reversed polarity region. A series of videomagnetograms of the birth of McMath 11957 made by James Mosher. Dark is p (preceding), or south polarity in the northern hemisphere this cycle; white is f (following). Note the contrast of the complex new region with the larger old region at left, where dark (p) polarity leads, as it normally should.

29
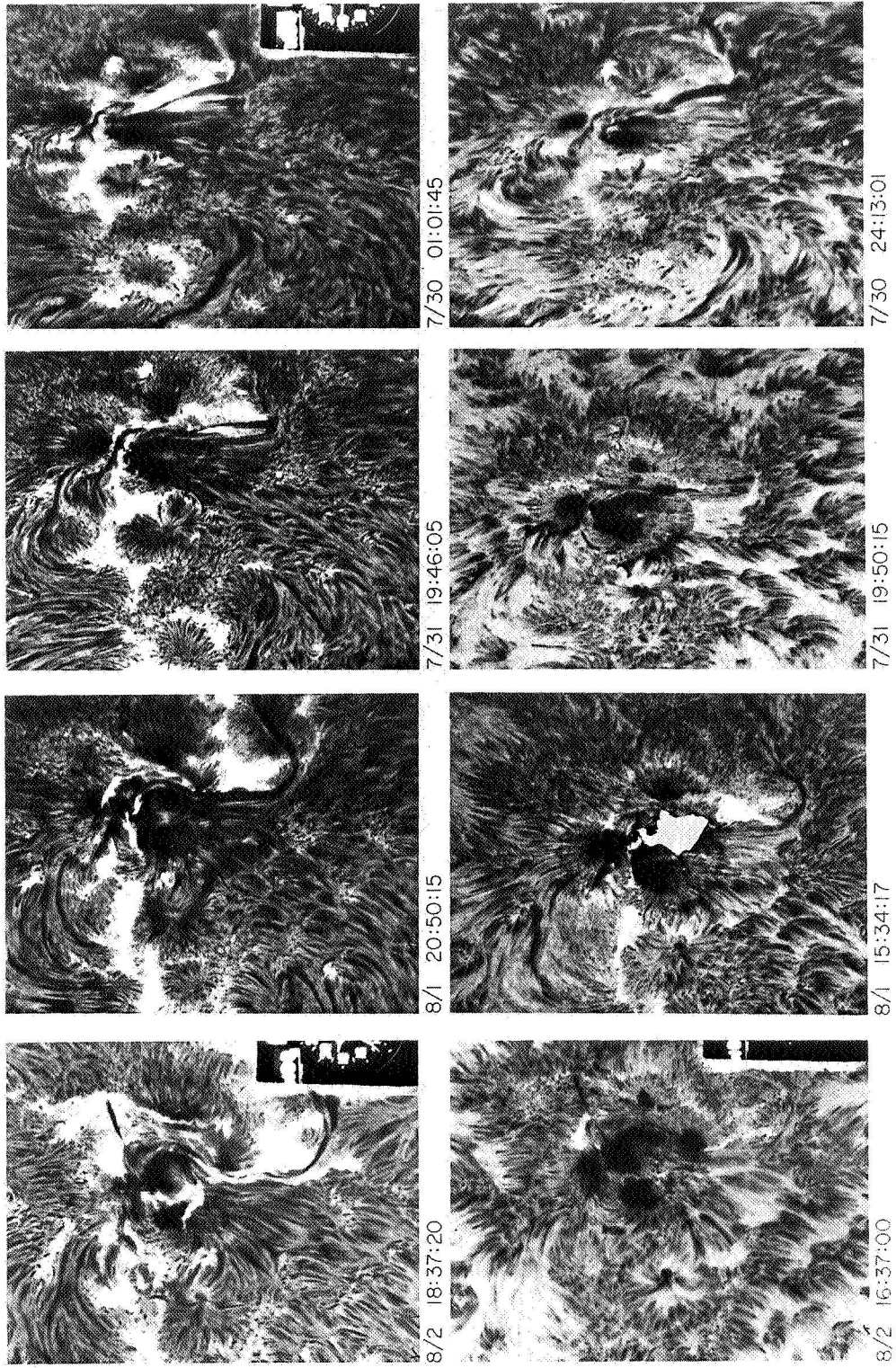
Figure 3. Synoptic series of active region development July 30 to August 2. Photos in Hα centerline, best for plages and filaments, in top row; and Hα +0.6 Å, best for sunspots, motions, and spicules, below. Note rapid growth of the lower spot, designated f_1.

30
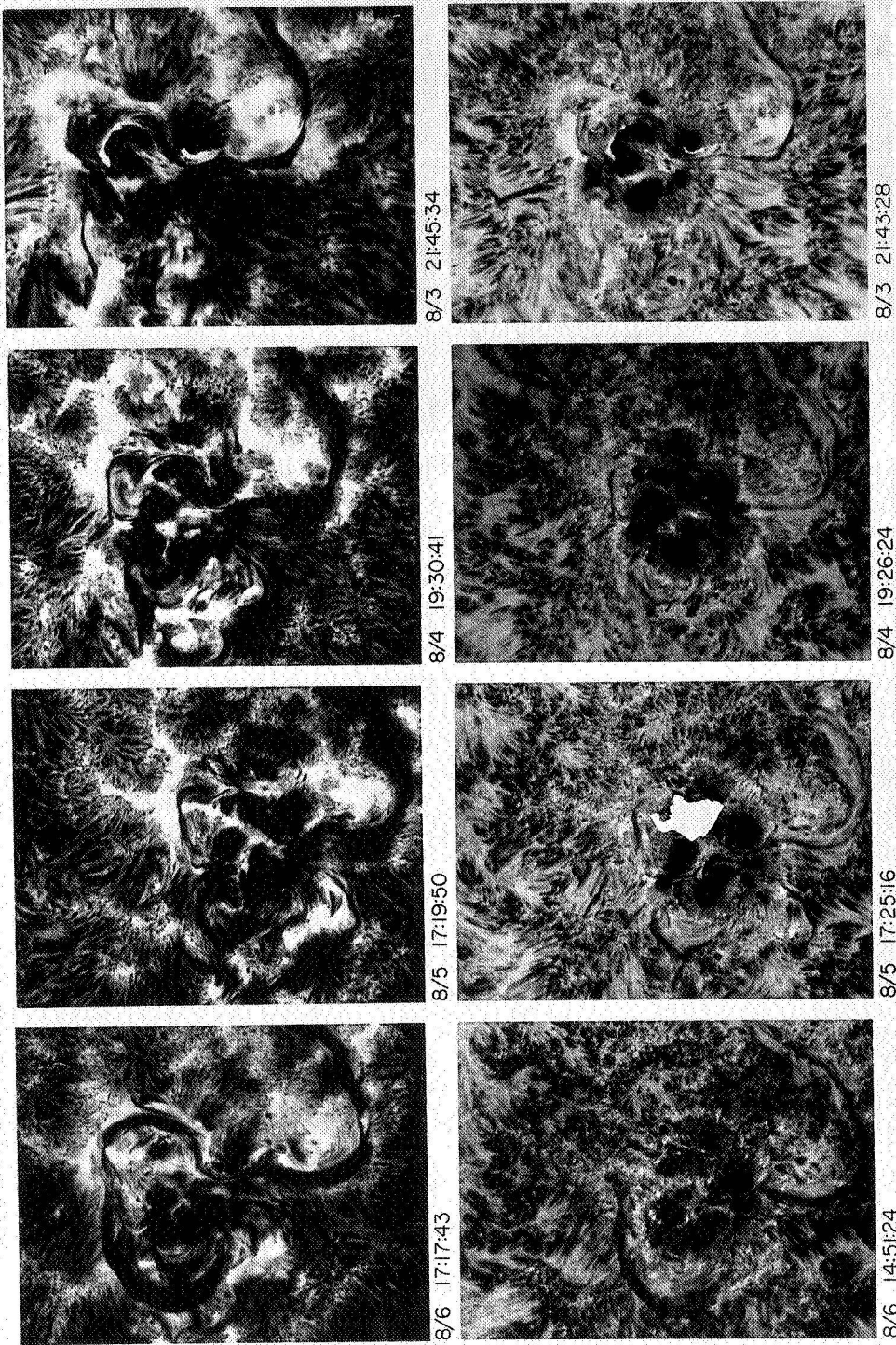
Figure 4. Further development, August 3 to 6. Note the filament development and the east-west separation of the *p* spots. On August 3 a bipolar flare is in progress. On August 6 a complex double ring exists around f_2 in the main flare area.

31

ACTIVE REGION DEVELOPMENT 8/7 - 8/10/72

8/7 14:58:30

8/7 14:28:37

8/8 15:11:37

8/8 15:35:29

8/9 19:48:09

8/9 18:14:17

8/10 16:21:11

8/10 17:36:14
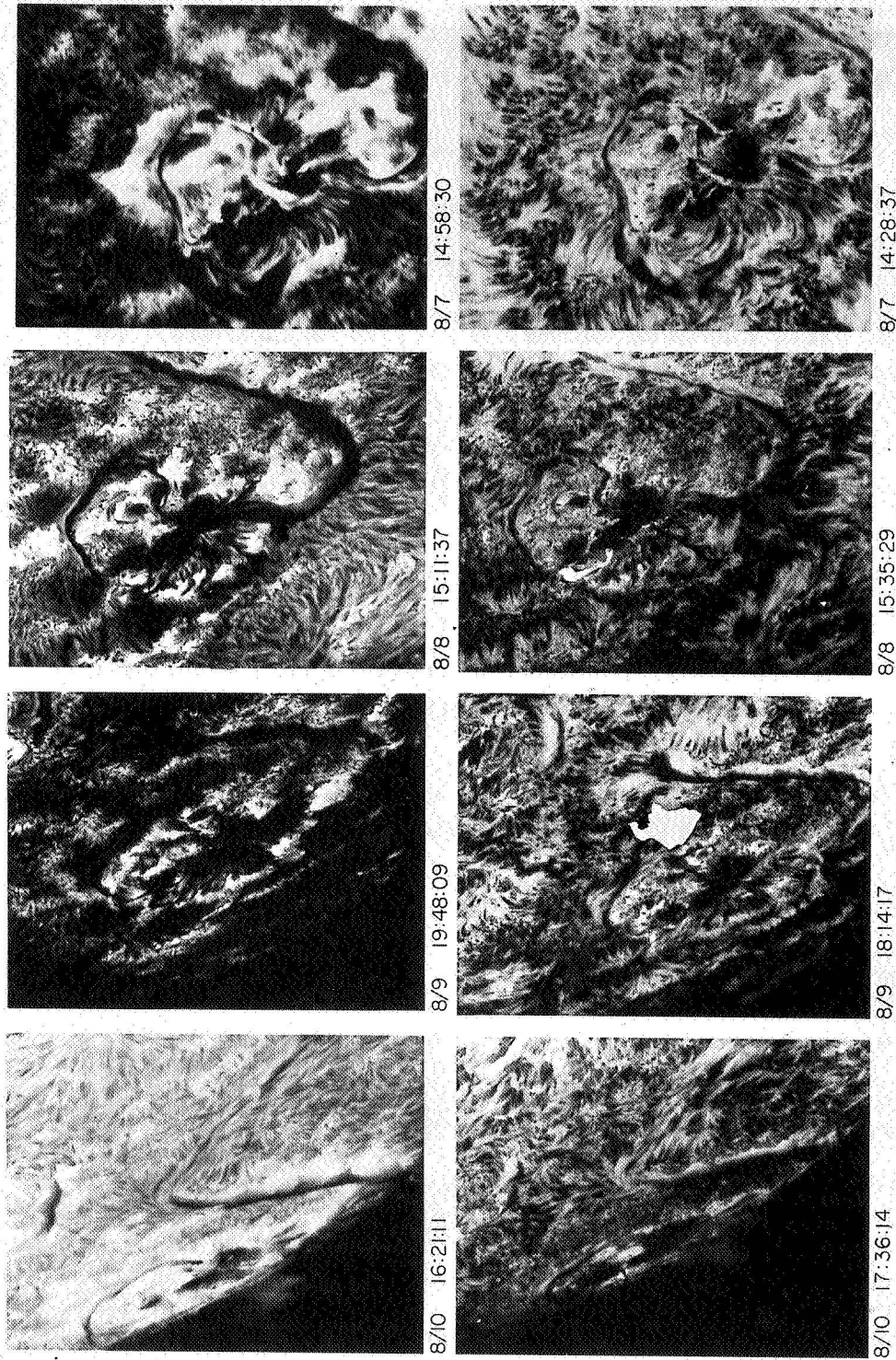
Figure 5. Development August 7 to 10. The region was simplified after the August 7 flare. The August 10 frames show how shallow is the vertical structure.

32

and Figure 6 shows the daily magnetograms. The region was only moderately active on July 30 and 31; there were a number of small flares along the neutral line, all fast and impulsive. This neutral line was the dominant feature of the group during its disk passage. It is best seen in Figure 7, which shows an enlarged view of the spot on August 3 in Hα-0.5 Å, on which we have marked various features. A ragged north-south line of field transition arches (FTA) and longer dark fibrils separates the f and p polarities. We distinguish these because the FTA in the upper part are short fibrils connecting nearby fields and running more or less perpendicular to the neutral line; whereas the fibrils in the lower (north) half, while physically similar, run, like filaments, parallel to the boundary line and are considerably longer. These long fibrils show the great shear that existed along the neutral line. Eventually the FTA were sheared into filaments, and filament 1 extended, with a few breaks, all the way through the group.

The spot f_1, in particular, which seems to have produced most of the activity, was connected to p_3, whereas a much shorter, lower energy connection to the near part of p_2 was possible. The large f plage pl_1, enclosed by the filament fil 1, which did not form completely until August 1, was sharply bounded on the left (west) by the filament, with horizontal polarity only a few thousand kilometers away. Note that the neutral line was almost north-south on August 1 and became sharply kinked afterwards.

The spot f_1 was indeed remarkable, and more so as it grew. It shows normal longitudinal spot polarity in the magnetogram, but the overlying Hα fibrils show a transverse field a few thousand kilometers above, so the field makes a sharp turn. Because the spot grew so rapidly it must be half of an emerging flux region (Zirin, 1972); but where is its sibling p polarity? The sibling appears to be the growing spot p_3. This spot and f_1 are seen to be connected by dark fibrils which are bright and active at both ends. Several flares (such as Figure 3 on August 3) are bright at both points. But these fibrils, in contrast to normal arched filament systems, are strongly twisted and not prominent in pictures off the center of Hα. The spots separated as in normal emerging flux, but opposite the normal direction—the p polarity moved east and the f polarity west.

On August 1 there were continual bright flashes along the neutral line, and by the end of the day, two areas at opposite ends of the neutral line, near p_3 and f_1, were growing steadily brighter. The spot f_1 was completely covered by horizontal fibril structure. These fibrils extend south from f_1, and crossing above f_1 are fibrils extending north from p_2. Since the fibrils must lie along the field lines, there were at least two polarity reversals above f_1, which of course must have longitudinal polarity. Fibril crossings of this type are common before flares.

FLARES OF AUGUST 2

On August 2, major activity began in the region with a remarkable series of complex flares. The first great flare (excluding the possible backside events) was reported at 0316 UT by Teheran; the later phases are visible on our Tel Aviv photograph at 0547 UT (Figure 8), which
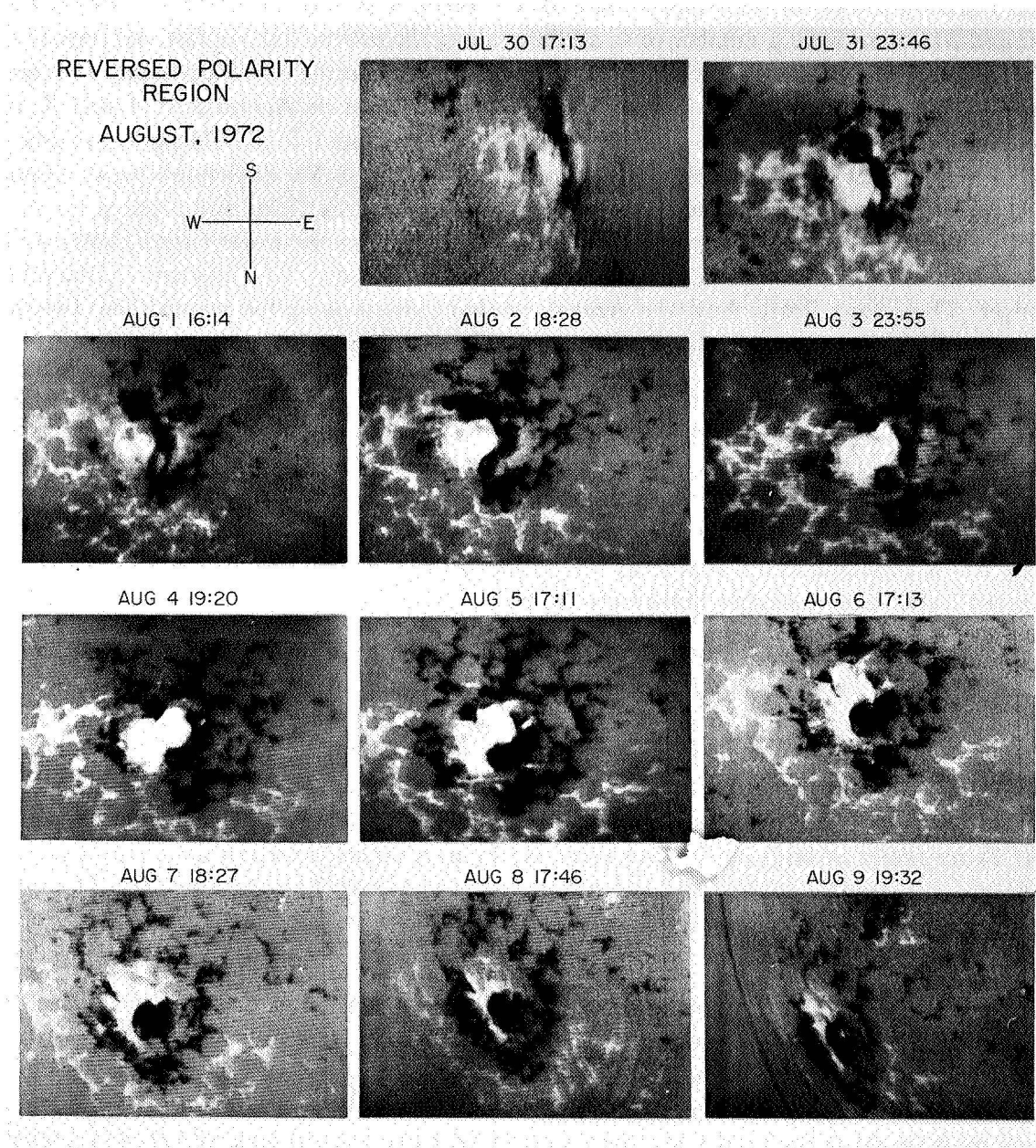
Figure 6. Videomagnetograms of reversed polarity region July 30 to August 9. In this series white is preceding (south polarity), dark is following; the intensity of light or dark shading is proportional to the longitudinal field strength. The growth of spot f_1 is clearly seen as intense dark polarity below, and the eastward spread of p_3 is seen as rightward spread of white polarity. Very rarely do such strong gradients appear.

34
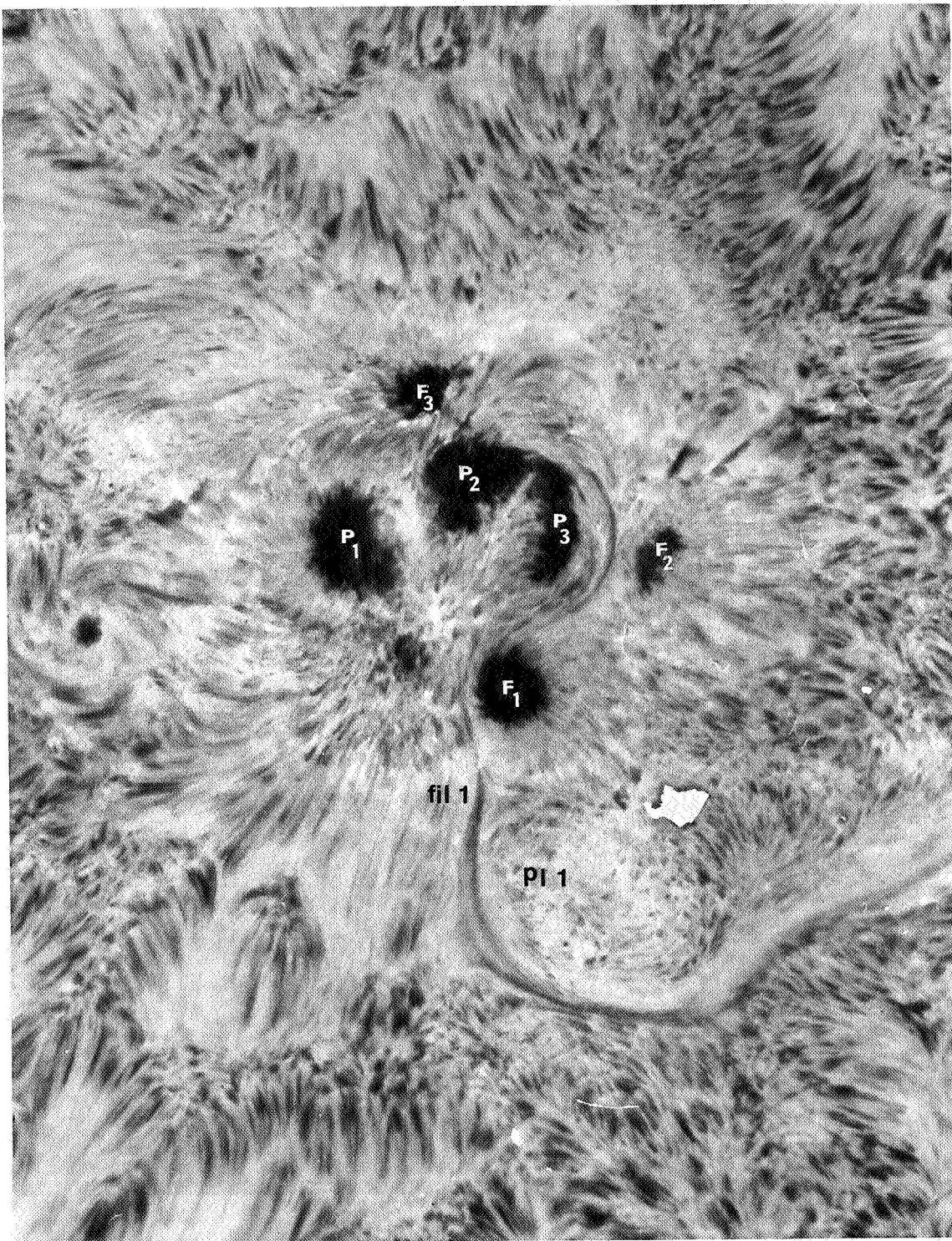
Figure 7. An enlarged frame for August 3 at Hα-0.5 Å, with various sunspots and areas marked to facilitate reference in the text.
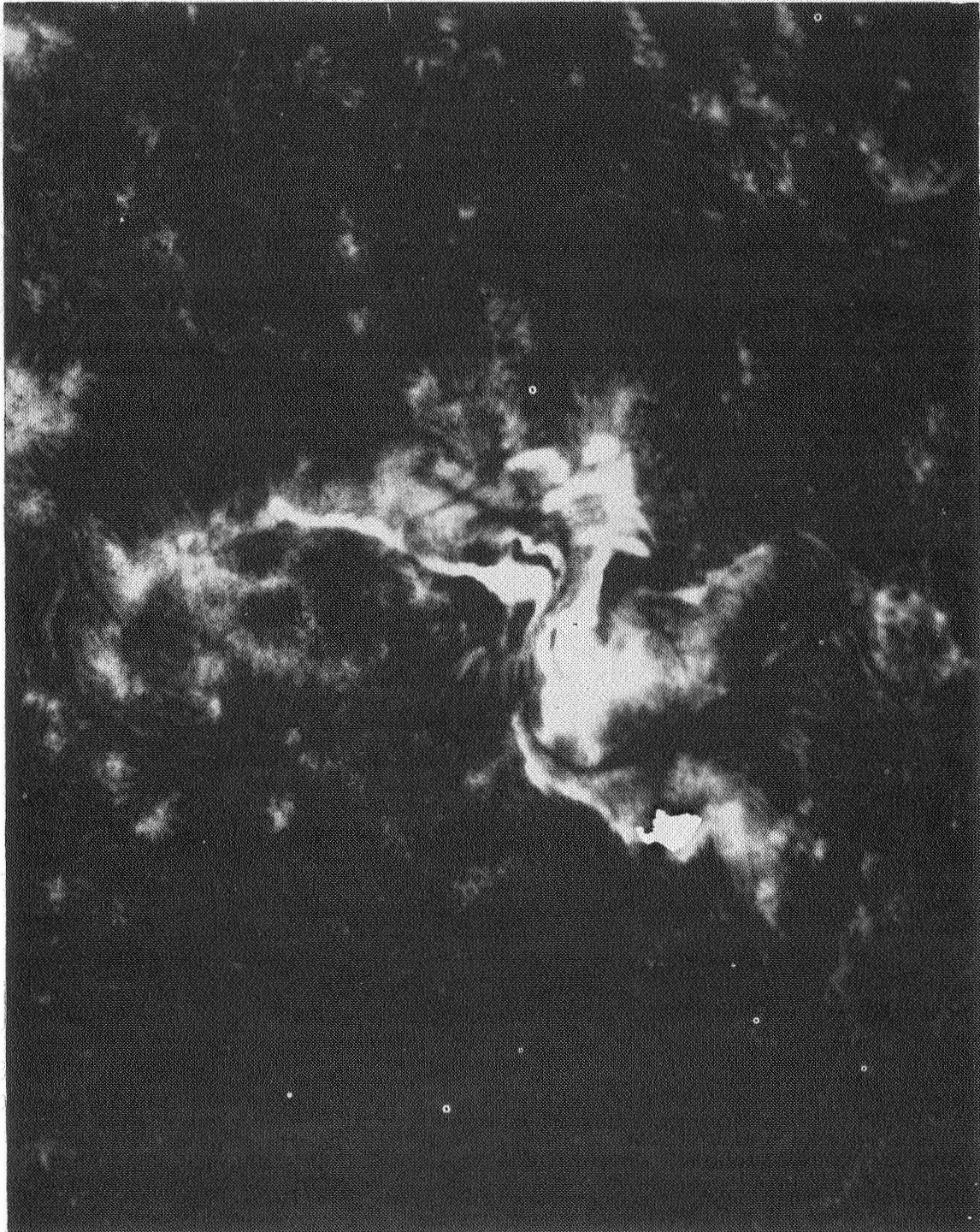
Figure 8. First flare, August 2, photographed at Tel Aviv, dawn, by Shlomo Hoory in Hα center-line. This photo at $05^h43^m38^s$, more than two hours after the flare began, shows that it was similar to the later great flare.

shows a large flare. Bright strands are shown covering p_1 and p_2 on one side and f_1 and f_2 on the other, the brightest portion being over f_2. The long, dark filament following the group had disappeared, blown away by the flare. It reformed in bits and pieces, was blown away again by the later flares, and was whole again on August 3. By contrast, the great flares of August 4 and 7 only made it wave about. Whether or not the flare was associated with changes in the magnetic field structure, there were definite changes during this period: the spot f_1 grew, and the spots f_2 and f_3 shrank, so that at 1600 August 2, f_1 was bigger than the other two (eventually f_1 became the largest spot in the group). Spot f_1 also pushed ahead relative to the other spots, as can readily be seen from the illustration; by August 2nd, the neutral line marked by the filament was directly beneath (north) of the p spots.

A remarkable change also occurred in the fibril structure preceding the spot f_3. On July 31, this was directly above (south) of p_1 and very close to f_3, connecting f_3 to the plage s preceding it; on August 2, the line had moved considerably ahead (west) of f_3 and a new fibril system connected f_3 to p_1, with f_3 rapidly decaying. We have noted before that a sheared neutral line can be replaced by shorter lines going directly across the neutral line to the nearest opposite polarity; this appears to occur here. The flux in f_3 can disappear by shortening and eventual subsidence below the surface of the flux loops. The energy released in flares would presumably be the difference between the elongated sheared lines and the shorter field lines of the final configuration. If there is a further contraction involved in the subsidence of field lines below the surface, this energy as well is available for the flare.

On August 2, Big Bear observations were made in Hα centerline and 3835 Å. After a small flare along the neutral line at 1601 hours, a brilliant impulsive flare began at 1838. Its development is shown in dark prints in Figure 9 and in normal print in Figures 10(a) and 10(b). The flare occurred along the neutral line between f_1 and p_3 and spread rapidly along that line; there was a fast increase at $18^h 39^m 02^s$ and another rise to a peak at $18^h 39^m 36^s$; these coincide with an early hard X-ray peak at $18^h 39^m 00\text{-}10^s$ and a main peak at $18^h 39^m 30\text{-}40^s$. (The X-ray time resolution is only 10 seconds.) The dark prints, Figures 9(d) and 9(e), and the negative print, Figure 9(f), show the structure of the kernel. (Figure 9(f) was dodged — selectively exposed in printing — to suppress the central kernel.) This was the most brilliant flare we have yet seen in Hα, although its limited area kept down the total flux.

Figure 10 shows how a brilliant sequence of fast flashes along the neutral line occurred in 3835 Å. They occurred precisely at the western edge of umbra f_1 and the eastern edge of umbra p_3, showing how close to the edge of the umbrae the field became horizontal; flashes over either umbra or penumbra would have been visible, but were not seen. The average lifetime of the points was 5 to 10 seconds (frame rate was 5 seconds) and their size can be seen to be around 1 arcsec. The double bright strand (1) in Figure 10(a) marks the Hα center, and presumably corresponds to the usual p and f polarity strands, but these are much closer. The strands (1) and point (2) rose with the first X-ray pulse, then broke up into faint points; a new bright point appeared at $18^h 39^m 24^s$, as the flux rose. It faded in 10 seconds, and a
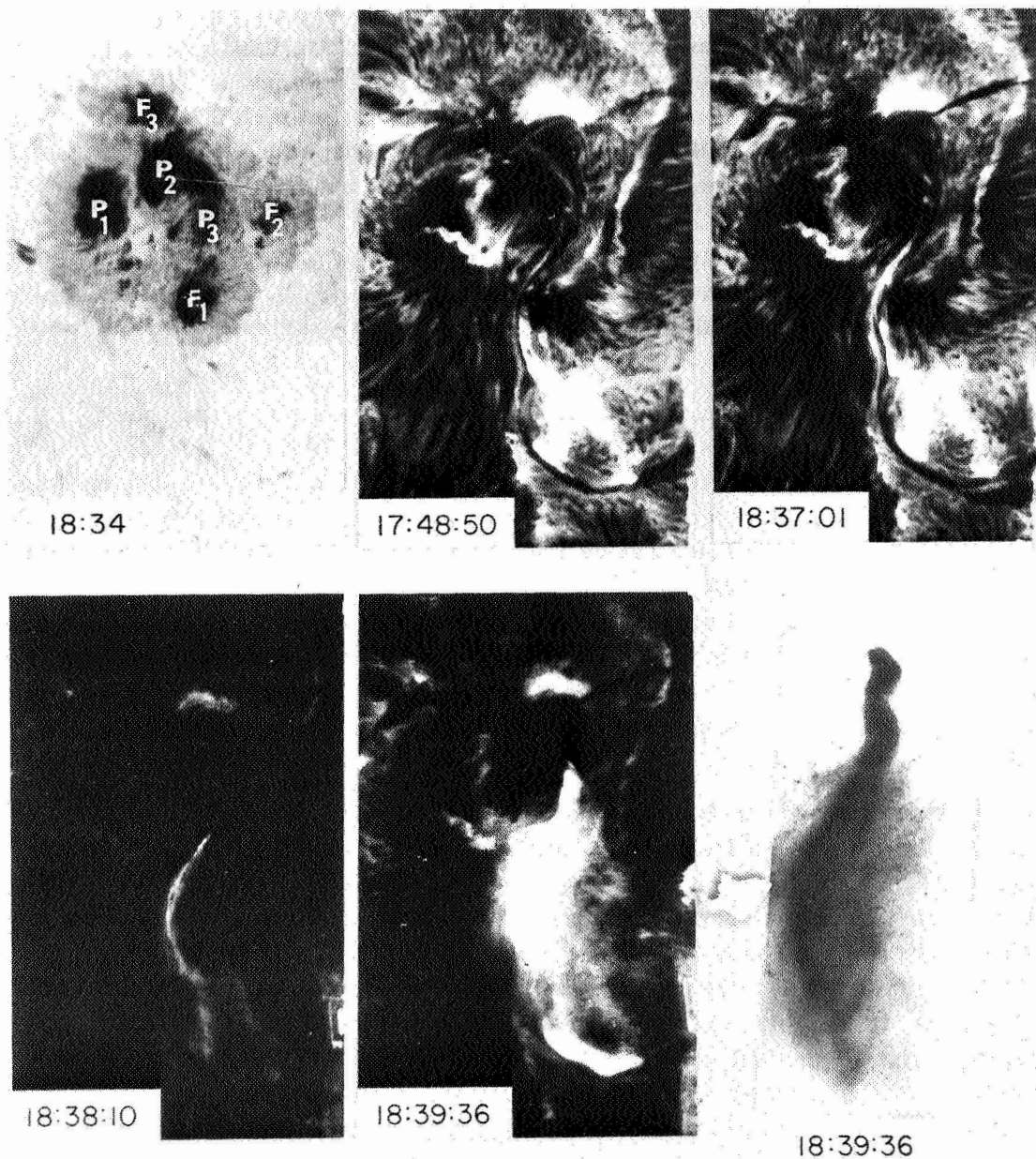
Figure 9. Various aspects of the August 2 flare. At 18^h34^m, Hα +1 Å with spot structure marked. Note that all the spots lie in one penumbra, and the umbrae and penumbrae of f_1 and p_3 are twisted to follow the horizontal lines of force, rather than the normally radial structure. At $17^h48^m50^s$ — Hα before the flare. At $18^h37^m01^s$ — the filament begins to brighten. At $18^h38^m10^s$ — dark print of flare beginning. At $18^h39^m36^s$ — brilliant halo around the flare, probably Hα scattered by surrounding chromosphere. At 18^h 39^m36^s — light negative print, heavily dodged to show structure of the flare kernel.
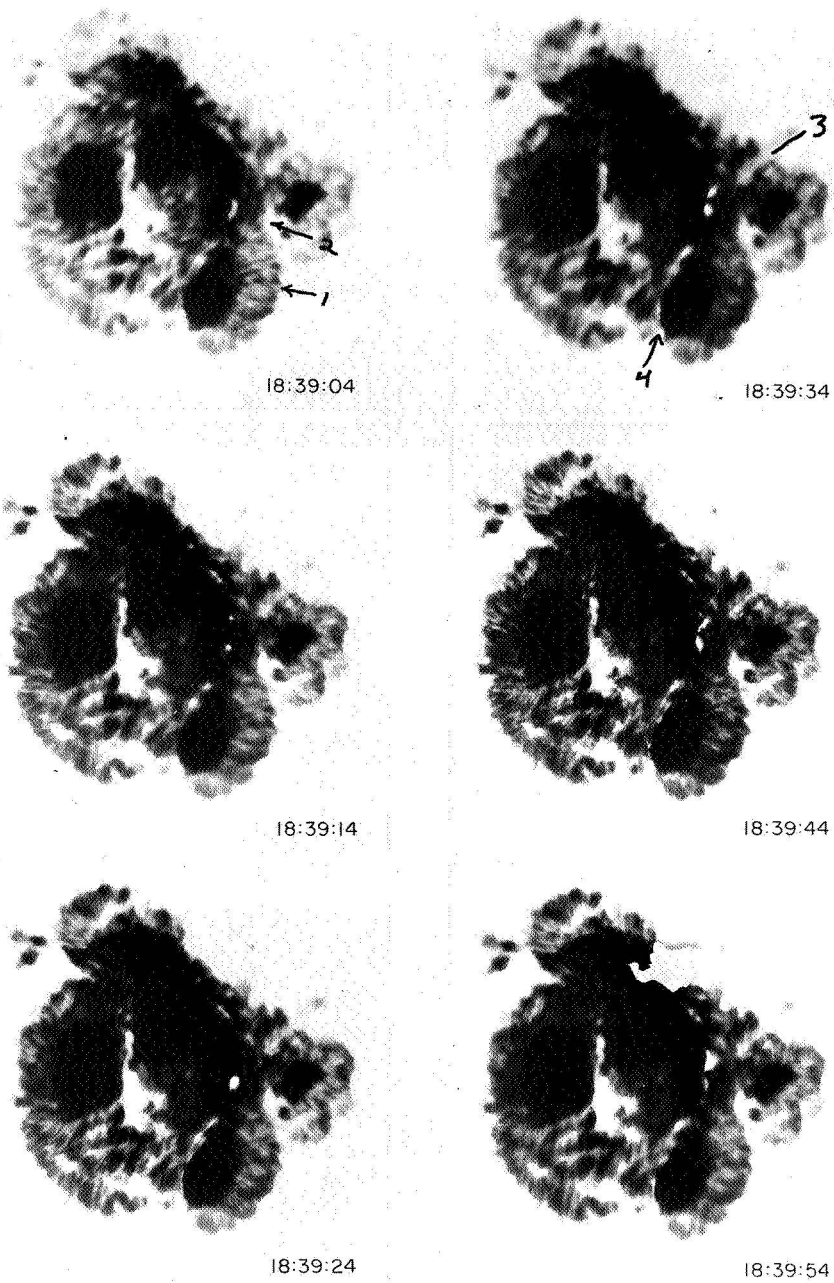
Figure 10. Dark prints showing the flashes in 15 Å band centered at 3835 Å. Point (1) at 18^h39^m 09^s is meant to point at the two bright fibrils on the left edge of the spot which coincide with the Hα maximum. Note that with the exception of point (1), the flashes occur precisely at the edge of the umbras, where the field lines turn and intersect the surface.
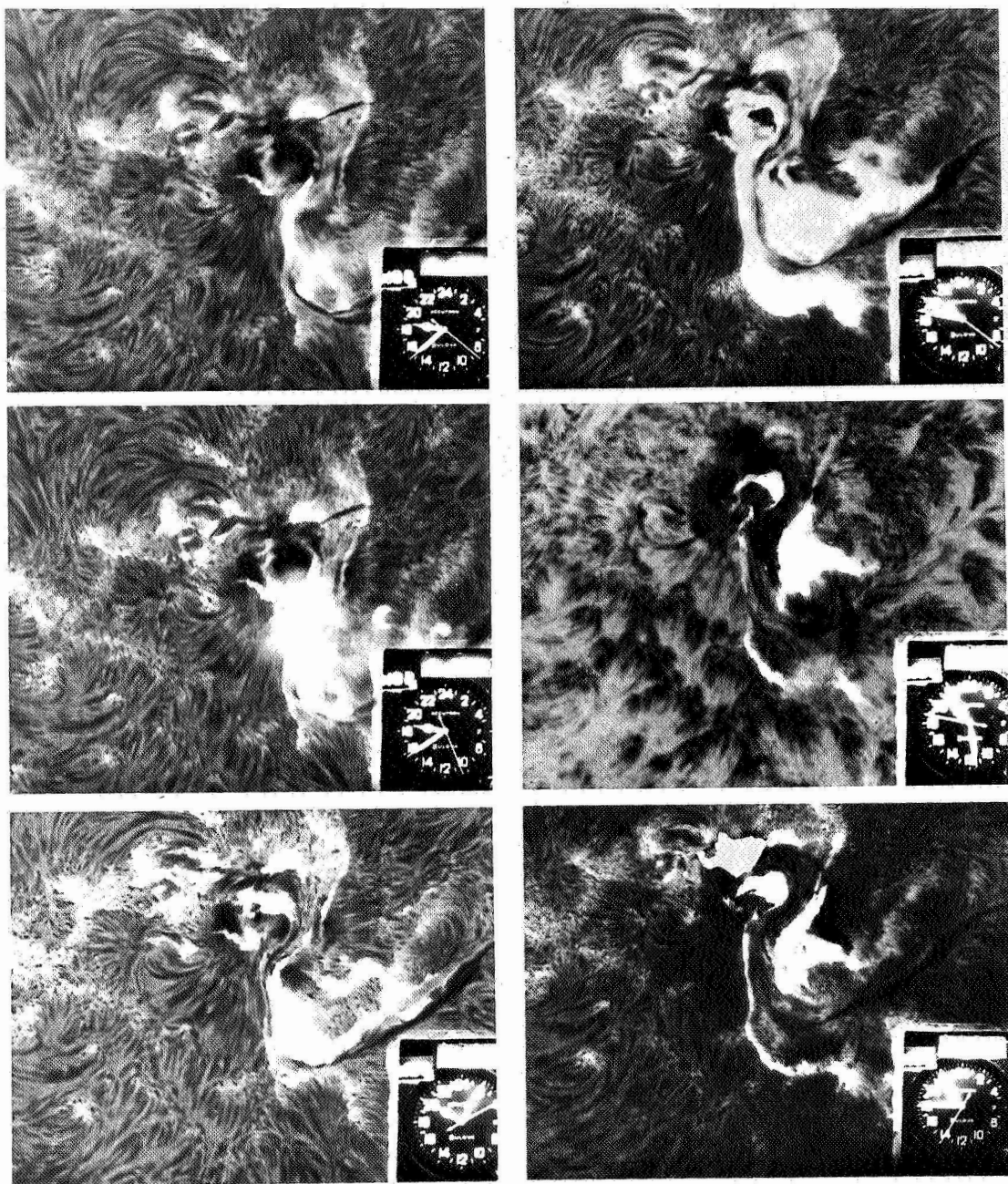
Figure 11. An Hα centerline sequence of the flares after 18^h38^m. The fifth frame (21^h28^m) shows an Hα +0.5 Å picture which reveals the loops raining down after the flare; the last frame (21^h45^m) shows the peak of the radio burst. Note that the emission has shifted to an entirely different location from the fourth frame (20^h47^m) and both f_1 and p_2-p_3 are covered by emission.

40

whole strand of points flashed into view at the X-ray maximum, $18^h 39^m 34^s$. The points appeared in symmetric pairs such as points 3 and 4; the lower points are less visible; by $18^h 40^m 00^s$, no more flashes were seen except for the lingering of point (4), which was under a long-lived Hα flare knot.

We interpret the 3835-Å flashes as occurring at the intersection of flux loops with the surface, except for the two strands (1) which are in the flare itself; the emission must be due to the heating of the chromosphere by energetic electrons as they are accelerated in individual flux tubes. We believe the emission is principally due to the Balmer H9 line which is formed at a height accessible to electrons above fifty kilovolts (Hudson, 1972; Brown, 1972). The observed intensity was equal to the undisturbed photosphere and can be explained by the emission from $n_e^2 H = 4 \times 10^{33}$ (H is the thickness of the emitting layer). This value is compatible with the column density the 50 keV electrons can penetrate, which is $n_e H = 2.5 \times 10^{20}$; we have $n_e = 1.6 \times 10^{13}$ cm^{-3} and H = 1.6×10^7 cm for the emitting layer. We may estimate total emissions from this layer by considering emissions from lines and continua of hydrogen. If we have a mean area of the flashes 6×10^{16} cm^2, the emission is 2.6×10^{27} ergs · s^{-1}, which is equal to the total energy in the electrons above 50 keV. Actually we see that time profiles of X-ray bursts above 50 keV were quite similar to the light curve of the 3835 flashes, while in the 20 keV range the burst lasted longer after the 3835 flashes ended. It is likely that the hardest electrons accelerated in individual flux tube dumped at the surface instantaneously and emitted X-rays by the thick target process (Hudson, 1972). Also the appearance of the 3835 flashes would suggest that the acceleration continued for 5 to 10 seconds at one place and that the place of acceleration moved from tube to tube with the same time scale.

In keeping with its fast rise time and great Hα brilliance, this was the hottest of the August flares. Although there was a dip at 15.7 GHz, the microwave . was still increasing at 35 GHz; in fact, the flux at 35 GHz was nearly as great as for the much larger event at 2145 hours. This was also the only event for which a sudden frequency deviation (SFD) was reported. The X-rays were very hard, the group at the University of California, San Diego (UCSD) having measured a spectrum proportional to $\nu^{-3.1}$ below 100 keV and $\nu^{-3.95}$ above 100 keV. This flare is a classic case of an impulsive, low-lying flare; it would be most interesting to know if there was any proton production involved, but entirely possible that the protons produced could not escape from the tight field configuration.

The activity of August 2 was not yet over; more flares were to come. Although filament 1 was disrupted, it reformed; bright areas resulting from the flare remained, particularly of the f edge of filament 1. At 1957 hours, the area below spot f_1 brightened slowly, then more rapidly after 2001. A weak brightening in 3835 Å appeared at the most intense portion of the Hα flare. This flare reached maximum at about 2005 hours and remained stable; it produced a modest hard X-ray burst, but little radio emission; at 2020 a new increase in area and brightness began on both sides of filament 1; and at 2030 another wave of brightening spread south from filament 1; this was matched by a bright region in 3835 (of twice the photospheric intensity) just at the edge of the advancing bright Hα front. At the

Figure 12. Maximum of the August 4 flare, at $06^h34^m19^s$, photographed at Tel Aviv. This is a classic two-strand flare, leaving two faint thin rims at the extreme edges for many hours.

same time the entire p side of filament 1 brightened as well. The 3835 emission in this flare was not impulsive at all, lasting more than 15 minutes, although the lifetime at any point on the surface was only a few minutes. Again it appears to mark the footpoints of flux loops containing the energetic material. The hard X-ray flux increased again and a large 6000-sfu (solar flux unit), 8800-MHz burst occurred. The $H\alpha$ front spread steadily on to a maximum at 2050 hours; the 3835-Å emission moved south and could be followed until 2105, but by now the $H\alpha$ emission near the filament was dying out and the whole flare faded, accompanied by fine dark loops. But the last bright parts of this flare, spreading over p_2 and f_1, produced at 2140 the greatest peaks of radio and X-ray flux. Weak 3835-Å emission appeared at this time over the penumbra of p_2. Note that this is different from the decay of other flares, which leave two widely separated strands on the flare perimeter; the emission actually shifted to a different place, and was strong off-band, indicating broad $H\alpha$ profile, and showed 3835-Å emission. There was a real flare resurgence, particularly over the main umbra. The UCSD X-ray data show a small resurgence of X-ray emission above 10 keV but much less than the peak of 2050. There were no more hard electrons, just a stronger magnetic field.

The varied aspects of the August 2 flares present an excellent opportunity to compare different flares in the same region. The comparison between the impulsive 1838 hours flare — small, violent, short-lived — with the large, long-lived, slowly rising flares at 0310 and 2000 is most instructive. The first was physically low in the atmosphere, confined to the neutral line in a small region, and by far the most brilliant and concentrated. It also produced the most intense hard X-ray burst. The 3835-Å observations show the impulsive nature very well. Radio emission was low below 2700 MHz, indicating a low source height. The 0310 and 2000 flares were by contrast complex and slow, with longer rise times both for $H\alpha$ and energetic electrons; furthermore, radio emission appeared at low frequencies as well, showing that the event reached high into the atmosphere. Since radio $f_{..}$ $_{j}$ proportional to electron density and magnetic field (NB), and X-rays to N^2, we can see how the large volume involved produced the huge radio bursts. At the highest frequencies the hardness of spectrum is more important, and thus at 35 GHz the 2140 hours peak is only slightly higher than the 1839 peak, although it is 20 times higher than 8.8 GHz. We may conclude that slow events may accelerate particles quite well, but that impulsive, low-lying flares produce the hardest spectra. Finally, we have the peculiar effect of the greatest radio burst occurring late in the event without an accompanying large change in the optical flare; apparently once the hard electrons are produced, phenomena over the greatest spots can produce great fluxes of radio emission.

Huancayo polarization data published by Lincoln and Leighton (1972) show a sharp variation from left to right hand circular (rhc) polarization, then back to left, in the 1838 flare, whereas the 2100 flare shows only right hand polarization. This corresponds to the fact that the later flare occurred primarily in the following (north polarity, rhc polarization) part of the group, while the impulsive flare was on the neutral line where changes in the polarity balance could easily occur. The August 7 flare was also found by Huancayo data to show

such a L-R-L shift in the impulsive phase. In both cases, the largest sunspot in the flare region was f_1, so that following polarity would dominate the radio propagation.

DEVELOPMENTS OF AUGUST 3 AND 4

After the great events of August 2, the region changed rapidly: The spot f_1 continued to grow and plow into the p region; p_2 and p_3 split apart; and a small emerging flux region (EFR) appeared between p_1 and f_1, eventually producing some new p spots. A series of small flares occurred during August 3, the largest being at 2210 hours, with arms around f_1 and the area between p_2 and f_3, where f_3 was approaching ever closer to p_2.

When the sun rose at Tel Aviv, a great flare was beginning; observations began at 0624, showing the flare rising to a peak brightness at 0635. But the most rapid rise occurred between 0624 and 0627, coinciding with a steep rise and peak in the radio burst. As on August 2 at 2145, the greatest peak in the radio emission came with brilliant emission covering the f spot. Figure 12 shows the peak of the flare photographed at Tel Aviv. It was a classic two-strand flare, with most of the area in the f polarity, and it did not have the irregular growth of the August 2 and 7 flares, nor was it so impulsive as the much smaller event of 1838 August 2, although a rise in radio flux of 26,000 sfu in three minutes must certainly be considered impulsive. Thus its radio spectrum fell off somewhat above 8.8 GHz. The radio flux reported by Slough Observatory dropped off after the flare passed maximum. At 0642, a group of bright loops passed across from the p to f side, filling the space between the two strands; these became dark 10 minutes later. Again, although the field lines on the surface ran tightly parallel to the neutral line, the loops high above were perpendicular. The bright strands faded and separated, leaving two thin strands at the farthest points from the neutral line, lasting many hours. This, and the slow decline of thermal X-ray emission, shows how the coronal cloud produced by the flare cools from the sun   , outward, leaving only the outermost loops at the end. These loops presumably produce the Hα strands by thermal conduction.

No Moreton wave appears on the film; although the observations are in Hα centerline, a Moreton wave should be visible. However, a section 0.6 $R_\odot$ from the spot of the long filament stretching eastward of the spot (filament 1) disappeared at 0626; and an emerging flux region of 0.7 $R_\odot$ from the flare brightened at about the same time. These distances imply a wave moving 1000 km·s^{-1} from a source at 0618 hours — it would be unlikely that the wave started earlier — but moving above the chromosphere so that it is seen only indirectly. More interesting, a bright wave or spray moved out from a point in the filament about 0.6 $R_\odot$ from the flare at 0624, with a velocity of 250 km·s^{-1}. This wave, which moved irregularly north-south from the filament, looks like a slow Moreton wave. If it was triggered by an invisible wave from the flare, we again estimate 1000 km·s^{-1} for the velocity. This is the first case we know of where such a surge was produced by a wave. The filament waved about continually until 0800.

Uchida (1972) has shown that the Moreton wave may be considered as a magnetohydrodynamic (MHD) wave which only touches the surface when it reaches a region where the

44

Alfven velocity is low, and consequently a steep shock develops. It may be that the wave in question did not touch the surface, but was able to affect the chromospheric features it passed by perturbing the field structures. The apparent triggering of a slower wave from the prominence is obviously a more complicated problem, involving either energy stored in the prominence or refocusing of the wave energy.

DEVELOPMENT OF AUGUST 4 TO 7

In photographs for August 4, we can recognize several changes which may be connected with the August 4 flare. F_1 and f_2 had grown, and the spot f_3 moved in ahead of p_2, almost touching it. A tight filament twisted in between them, and the field gradient was very large. Although f_3 did not take obvious part in the flares, its motion was as remarkable as that of f_1 — in fact, on August 6 the filament passed around it and it was an island of f polarity inside the p penumbra. Although the group gave the appearance of an extremely active one, there was little activity outside the very large flares. Most of the smaller flares were two-strand or two-point flares, which may be used to determine the ends of flux loops; for example, one at 0102 August 5 connecting p_1 and f_3 and several flares connecting p_3 and f_1.

Probably the most important change in sunspot structure was the rapid separation of p_3 from p_2. As can be seen in the off-band pictures of Figure 4, p_3 appeared separate from p_2 at dawn on August 3 and steadily drew apart. There were no more flares with footpoints in p_2. There was considerable small surge activity in the area just following p_3 on the f side of the neutral line. Such activity is characteristic of emerging flux, and the magnetograms for August 4, 5, and 6 show p polarity which was part of the emerging dipole imbedded in the f polarity region. Dark fibrils connected this flux to f_1. Eventually on August 7 the p flux broke through and filled this region. Small flares at 0137 and 1653 on August 5 extended along the dark fibrils from the EFR to f_1 and p_3, wh''~'''he flare at 0100 had just two bright points at p_1 and f_3. There was also rapid growth o₁ new p spots following p_1 and just across the neutral line from f_1.

On August 6, the dark filament 1 now stretched all the way through the region and around to the p side. It was not an ordinary filament, a complex of twisted dark fibrils along the neutral line. During the 6th, dark loops were visible on the red wing of Hα, pouring down into f_1.

THE GREAT FLARE OF AUGUST 7

Observations at Tel Aviv showed high plage brightness in the early hours of the 7th; when observations began at Big Bear at 1350, there was a flare in progress following f_1. Data from OSO-7 showed a steady increase in soft X-rays, beginning at 1000. The filament winding east of p_3 was continually active, and a small flare encircled p_3 at 1442. A wavelength scan at 1500 hours showed strong λ shifts. At 1503, the filament was more strongly activated, the entire length appearing very dark at Hα +0.5 Å, but also dark on the blue wing in its center. This was followed immediately by the beginning of the flare at 1505. The BBSO observa-

tions were simultaneous at ± 0.5 Å with 7-second intervals between frames. The first bright points appeared simultaneously over the f_1 umbra, directly across the neutral line in the new spots following p_1, along filament 1 north of f_1, and just preceding p_3. At 1512 a bright streak flowed north from spot f_1 along filament 1 into the northernmost bright element; at the same time the bright p points connected. This phase is seen in the first frame of Figure 13.

Now the main growth took place in the p region, first (at 1515) preceding p_3, then (at 1518) on the arc from p_1 to p_3. This brightening flowed along to p_2, then bounced back at $15^h 21^m 00^s$, and when it hit the neutral line at 1522 there was an enormous brightening all over, particularly in the p polarity, including, for the first time, the f polarity area directly across from p_3. This was the peak of the flash phase and appears to agree with the peak of the radio burst. However, spectra and dark prints show that this area was much fainter than the two flare kernels. The flare continued to grow, although more slowly, spreading over all the p spots except p_1 and forming an elegant sea-horse shape. On the 37-GHz records from Slough there are peaks at 1516, 1518, and 1521.5 hours, which appear to correspond to the stages enumerated above; this confirms our feeling that "quasiperiodic" microwave and X-ray pulsations, noted by Frost (1969) are just successive energy releases in different areas, the time spacing being the time it takes an MHD wave to cross the region. Where such velocities are seen as the advance of distinct bright fronts, we measure about 600 km·s⁻¹. However, if we look at the flare on a dark print, we find only two areas that over f and the curved branch on the p side are very bright — the rest of the Hα flare is much weaker and only appears as bright because of the saturation of the print.

At 1528 the first bright loops appeared crossing the center of the flare, connecting the two bright strands. As time passed, the angle between these loop and the neutral line rapidly increased. This change may be interpreted in two different ways: one picture is that the low field runs along the neutral line, strongly sheared in the direction of the dark fibrils, while the upper field is a potential field connecting p and f polarity with the minimum energy. As the flare plasma cools, condensation takes place in successively higher loops. Another picture is that the loops are not so much different in height, and indicate the reestablishment of potential-type field lines after reconnection during the flare. In any event, we can say that much of the flare energy is due to successive stripping away of long, highly sheared low field lines, and their replacement by potential fields.

SPECTRA OF THE AUGUST 7 FLARE

James Dominy was observing with the Coudé spectrograph, and spectra were taken beginning at 1500 hours at 10-second intervals in Hα. Until 1516, spectra were taken of the bright area north (below) f_1; at 1516, the spectrograph slit was shifted to the main bright p kernel and its development followed. Slit-jaw Hα pictures show the exact placement of the slit on the flare. The spectra (Figure 14) have been measured on the microdensitometer; they show two intense kernels of emission with full width half-maximum 12 Å wide. Although the peak emission is centered on Hα, there is always an asymmetry of 3 to 10 percent, centered

46
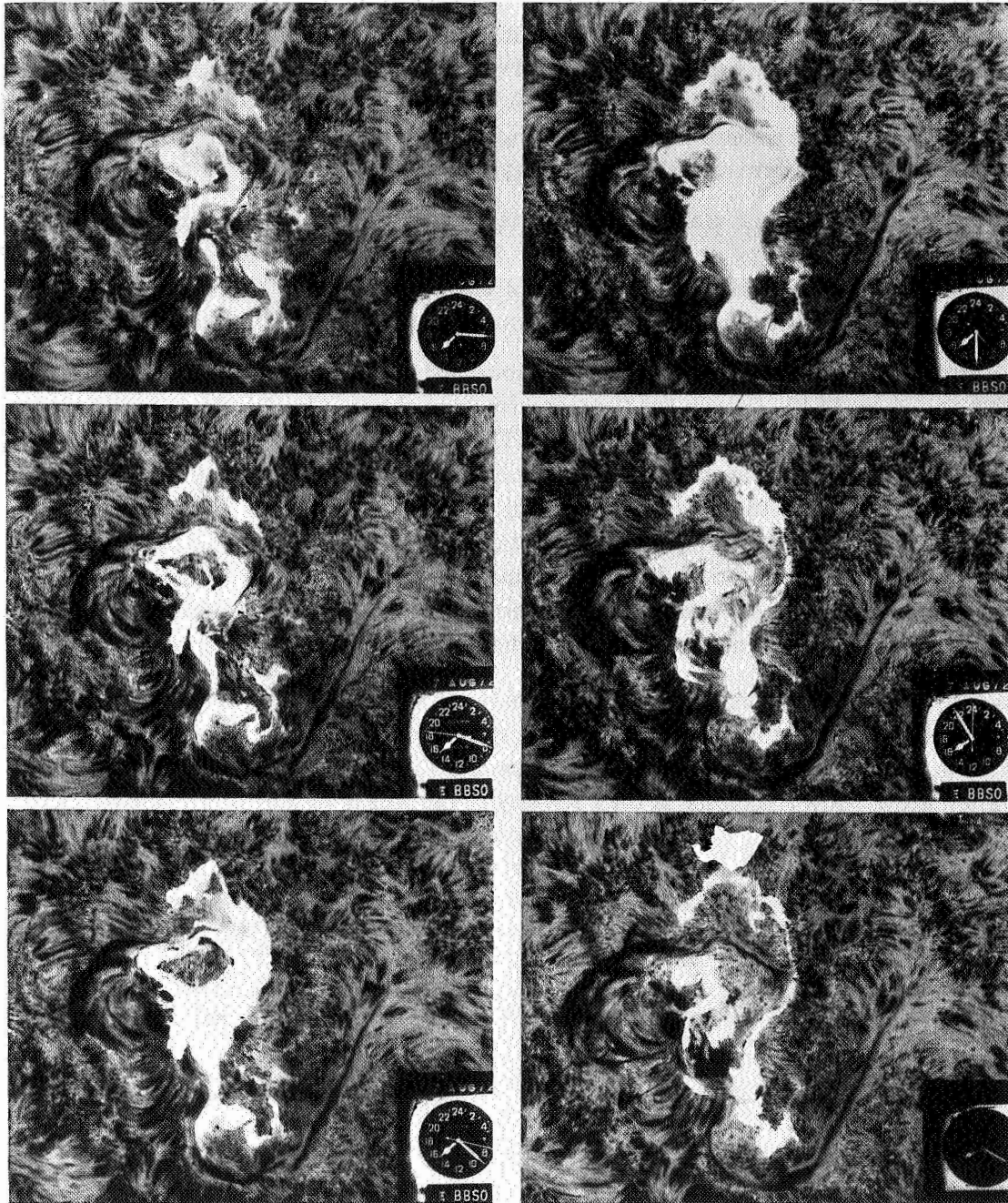
Figure 13. Development of the August 7 flare, Hα -1/2 Å. The intense kernels are located at f_1 and the lower half of the area curling just above the neutral line. Note the bright strands in the late phase of the flare.

2 Å toward red. This shift corresponds to the velocity imparted to protons by collisions with electrons moving near the speed of light. Aside from the flare kernels, the rest of the Hα flare is narrow. The first emission outside the kernels was strongly red-shifted, the peak emission occurring at least 2 Å red. This is also apparent in the filtergrams, which show much more extensive emission on the red wing. After 5 minutes the general emission moved to the center of Hα, narrow, with some red asymmetry.

We can conclude that the main energetic flare occurs in the kernels, and the outer areas are lit up as the flare energy spreads to higher flux loops, and hot red-shifted material rains down on the surface. The small amount of red asymmetry in the kernel may be due to superposition of the downward falling bright material which covers the flare area.

The Hα width dropped sharply after 1523 hours from 12 to 8 Å and continually afterward down to 1 Å by 1530. Late in the flare, spectra were obtained by Tanaka in various spectral regions, scanning over the whole flare area. They show a remarkable velocity discontinuity along the neutral line between f_1 and f_2, in a region which shows penumbra but no sunspot. The shear is seen in the spectrum to occur in all spectrum lines, amounting to 4 to 5 km $\cdot$ s^{-1}, or a little over 6 km $\cdot$ s^{-1} if the motion is in the surface plane of the sun. The motion was seen in spectra up to 1900 hours and is verified by proper motions measured on our pictures. Judging by proper motions on the Hα pictures, the motion was across the neutral line, pushing it S(up) from f_1; it may have resulted from the motion of f_2 toward f_1.

Study of before/after pairs shows some change in the spot group after the flare. A few small spots under the p kernel changed, but such spots are always changing. The most notable effect is the continued motion of spot f_2 toward f_1, which it joined on August 10. The magnetograms show a decrease in the f polarity in the area it vacates, and a general southeast expansion of the p polarity around p_3. The large filament $\measuredangle$ west of the p spots, which was active all day on August 7 on the blue wing, disappeared. Further evolution of the group to its limb passage is shown in Figure 5. It gradually simplified and was uninteresting except for the limb flare of the 11th.
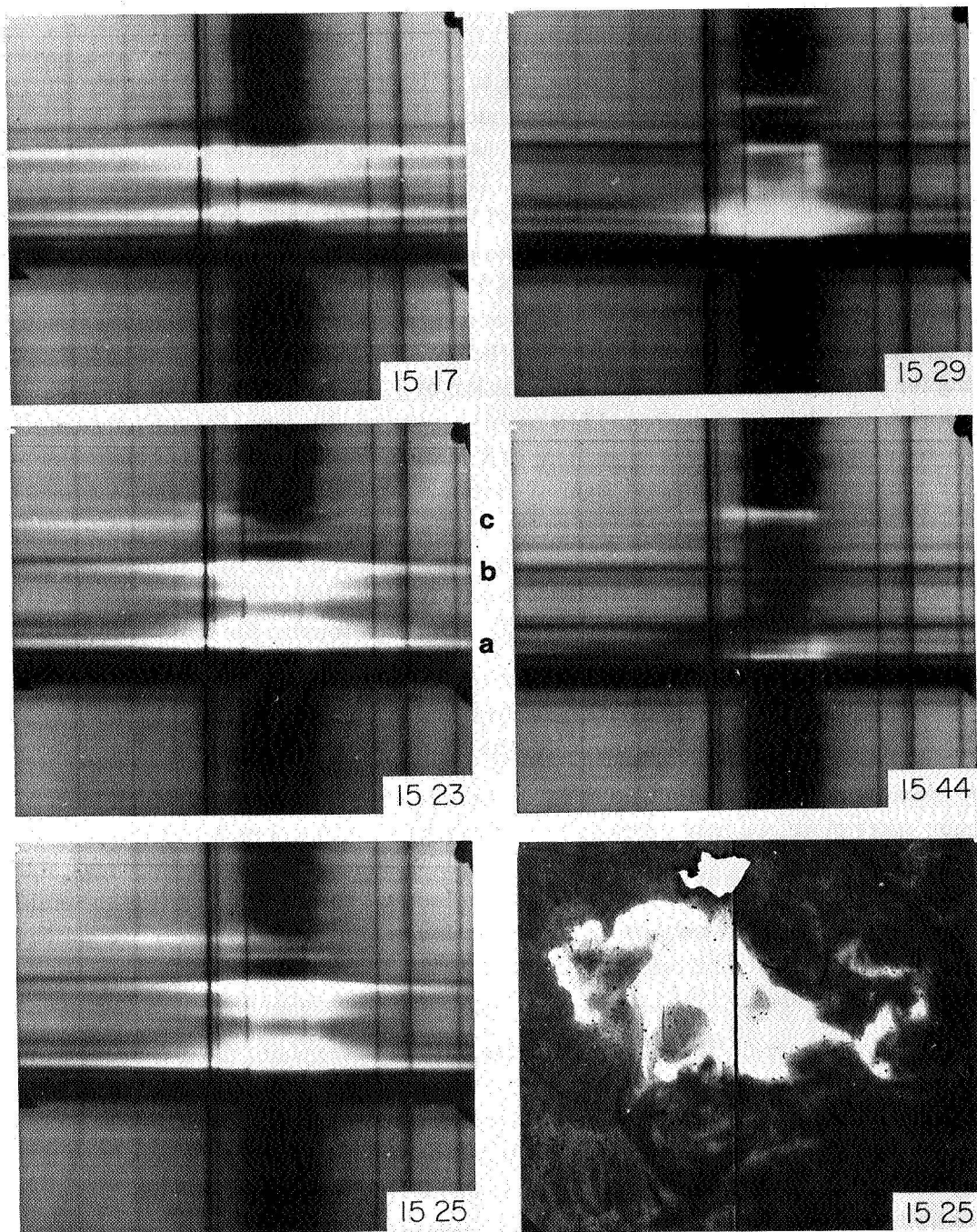
Figure 14. Sequence of Hα spectra of the August 7 flare. The bottom right picture shows slit-jaw Hα photograph, showing slit orientation for spectrum. Spectrum covering 10 Å, with red to the left. The upper part (c) of the flare appears as fainter, strongly red-shifted emission. Only the kernels (a) and (b) are really broad. Point (a) was observed as a white-light flare by Sacramento Peak (Rust, 1972). The dark streak is a sunspot.

Hα FLUX

There has been much attention paid to the total Hα flux from great flares in comparison with the total energy. In this case, with continuous Hα spectra and filtergrams on both wings of Hα, we can measure this in a more definitive way. We planimetered dark prints showing two intense kernels at 1520, 1527 and 1610 UT (the end of Hα spectra). At 1520 UT, this area was 3.4×10^{18} cm^2, with a bandwidth of 9.2 eq. Å. At 1527, the area had increased to 2.7×10^{19} cm^2, with 6.2 eq. Å bandwidth; and at 1610, the emission was a factor of 10 less. The total flare area in Hα centerline was 4.3×10^{19} cm^2, but the line width over most of the area was only about 1 eq. Å in the regions outside the kernel. Applying a filling factor of 0.74 for the fraction of the kernel that gives the broad emission on the spectrograms and correcting for projection, we find a total Hα emission of 1.2×10^{27} ergs $\cdot$ s^{-1} at the peak. Integrating over the flare lifetime from 1510 to 1610, with an allowance for the later tailoff, we find a total Hα energy in this huge flare of 2.5×10^{30} ergs. Why is this number so much smaller than previously published figures? Because the previous calculations assumed that the broad emission was characteristic of the entire flare area during its entire lifetime. In this case, comprehensive data enable us to make a better estimate, accurate within a factor of 2. We have no spectra for the August 4 event, but we planimetered it and assumed the same spectrum as for August 7. The result is 2×10^{30} ergs, roughly the same as for August 4.

If we compare this value with the total proton energy estimated by Ramaty and Lingenfelter (private communication, 1973) as 10^{35} protons above 10 MeV, or about 2×10^{30} ergs, we see that the Hα energy is comparable to the energy of the protons and hard electrons.

If we consider that energetic phenomena are limited to the kernel from which most of the emission takes place, we may estimate the volume involved by considering it as a loop connecting the two branches of the kernel. Each branch has about 1.7×10^{18} cm^2 and the separation is 25,000 km; hence for a semicircular loop we get 2×10^{27} cm^3. If the emission measure was $10^{48.3}$ for X-rays above 10 keV (same as the August 4 flare), we get $N_e N_i = 10^{21}$, or 3×10^{10} hard electrons/cm^3 above 10 keV. It appears that in this huge event all particles are accelerated in the kernel.

Finally, the dominance of Hα emission from the flare kernel explains the discrepancy usually found between the time of Hα maximum, which refers to the maximum area, and X-ray and radio bursts. A plot of the total Hα energy from the August 7 flare would peak at around 1522, the time of the peaks of radio and X-ray emission. The same time would be derived from peak kernel brightness or peak Hα line width. It would be a considerable improvement if such data were reported.

CONCLUSIONS

Based on the observations, we conclude that:

- The region exhibited twisted magnetic flux and high gradients from its birth.

- The flares occurred because of high field gradients and sheared field lines.

- The Hα flux of the large flares comes mainly from kernels whose emission peaks with radio and X-rays. The total Hα emissions from the great flares of August 4 and August 7 were 2.0×10^{30} and 2.5×10^{30} ergs, respectively.

- In the 3835-Å band we detect emission flashes due to the dumping of electrons in the chromosphere. The emission is on the edge of the flare and has a lifetime of 5 or 10 seconds.

- The Hα emission is 12 Å wide in the flare kernel and only 1 to 2 Å wide in the rest of the flare. This flare halo makes up most of the area and thus determines the assigned importance, but it produces only one-fourth of the Hα emission.

ACKNOWLEDGMENTS

REFERENCES

Brown, J., 1972, *Solar Phys.* 26, 441.

Chapman, G., 1970, *Solar Phys.* 13, 78.

Frost, K.J., 1969, *Ap. J.* 158, L159.

Hudson, H.S., 1972, *Solar Phys.* 24, 414.

Lincoln, J.V., and Leighton, H., 1972, Report UAG-21, World Data Center A, 80.

Ramaty, R., and Lingenfelter, R.E., 1973 (These Proceedings).

Rust, D., 1972, *Sky and Telescope,* 44, 3.

Uchida, Y., 1972 (These Proceedings).

Zirin, H., 1972, *Solar Phys.* 22, 34.

II: MICROWAVE AND HARD X-RAY OBSERVATIONS

CHARACTERISTICS OF NONTHERMAL ELECTRONS ACCELERATED DURING THE FLASH PHASE OF SMALL SOLAR FLARES

S.R. Kane

Space Sciences Laboratory
University of California, Berkeley

ABSTRACT

Observations of impulsive hard X-rays and other flash phase emissions from small solar flares are analyzed in order to determine the characteristics of energetic electrons accelerated during the flash phase. The electron spectrum and its time variation are deduced from a model of the X-ray source in which the electron injection is continuous, and the electron energy loss is primarily due to collisions with the ambient plasma and escape into the corona. The instantaneous electron spectrum in the X-ray source, as well as the acceleration spectrum, are found to be nonthermal. The observations are consistent with a flare model having the following properties: a) The acceleration region is located in the lower corona where the ion density is $\lesssim 10^9$ cm^{-3}. b) The total kinetic energy of the nonthermal electrons is ~ 10 percent of the total flare energy, so that the efficiency of the acceleration process is very high. c) The nonthermal electrons (and protons) provide energy for all flash phase emissions. d) The acceleration is a continuous process with a time constant $\lesssim 1$ second, or a continuous series of impulses each lasting $\lesssim 1$ second and a total duration of ~ 100 seconds. e) The electron spectrum continuously hardens during the increasing phase of the X-ray burst and softens during the decreasing phase. f) more energetic flares do not necessarily produce a harder electron spectrum.

INTRODUCTION

An important problem in the solar flare studies is the acceleration of electrons, protons and heavier nuclei. In order to understand the acceleration mechanism for these particles, we need to know their energy spectrum, total kinetic energy content, and other characteristics inside the flare region. As compared to energetic protons and heavier nuclei, it is easier to study the properties of energetic electrons in the flare region because of the relatively large X-ray and radio emission produced by these electrons, as they interact with the solar plasma and magnetic fields. The hard X-ray emission ($\gtrsim 10$ keV) is particularly well suited for this purpose, because the hard X-ray measurements at 1 AU can be more or less directly related to the energetic electrons in the flare region. Although the exact relationship between the spectra of X-rays $\gtrsim 10$ keV and electrons $\gtrsim 10$ keV depends on the assumed model of the X-ray source, the uncertainties involved are much smaller than those, for example, involved in deducing the electron spectrum from the microwave observations. Therefore hard X-rays are, at present, the best source of information about the energetic electrons in the flare region.

A number of properties of the energetic electrons and the flare process can be deduced from the observed hard X-ray and other related emissions. For example, by measuring the hard X-ray spectrum and its time variation we can deduce the energy spectrum of the accelerated electrons, and the physical processes responsible for their energy loss in the flare region. From an examination of a large number of bursts we can deduce the probability that an electron spectrum of a particular hardness will be produced in a flare. By comparing the X-ray observations with other simultaneous measurements such as EUV, Hα, microwave, type III radio, and interplanetary solar electrons, we can deduce the most probable location of the acceleration region, and how the electrons propagate in the solar atmosphere. Finally, by comparing the total kinetic energy of the energetic electrons with the total flare energy, we can estimate the efficiency of the acceleration process. Thus, by studying the hard X-rays and other related observations, we can deduce many important parameters of the flare process. These parameters can then be used as an input for constructing a model of solar flares.

OBSERVATIONS

In this paper we will be primarily concerned with the hard X-ray measurements made with the Orbiting Geophysical Observatory-1 (OGO-1), OGO-3, and OGO-5 satellites, and their implications regarding the acceleration of electrons in small solar flares (Hα-importance ≲ 1). We will also consider the implications of the simultaneous EUV (10 to 1030 Å), microwave, and type III radio observations made with ground based detectors, and the interplanetary solar electron measurements made with the Explorer-35 and Explorer-41 (IMP-5) spacecraft.

When examined on a time scale of ~ 2.3 seconds, about 10 percent of all X-ray bursts observed by the OGO-5 satellite show one or more prom.... intensity spikes during the increasing phase of the burst. An example is shown in Figure 1. Events like this suggest that the solar flare X-rays > 10 keV consist of two components – impulsive and slow – the impulsive component being associated with the flash phase (Kane, 1969). The most distinguishing characteristic of the impulsive component is its relatively rapid rise and decay times. Figure 2 shows the time variation of the X-ray rates during the increasing and decreasing phases of three impulsive bursts. It can be seen that for ~ 40 keV X-rays the rise time is ~ 3 seconds and the decay time is ~ 6 seconds, both time constants decreasing with increase in X-ray energy. Thus at least in the 10 to 60 keV range, the X-ray spectrum continuously hardens during the increasing phase and softens during the decay phase, the spectrum being hardest at the X-ray maximum.

Figure 3 shows the X-ray spectrum at the maxima of three impulsive bursts. In most events the X-ray spectrum is consistent with the form

$$\frac{dJ}{dE} = KE^{-\gamma} \text{ photons} \cdot \text{cm}^{-2}\text{s}^{-1}\text{keV}^{-1} \tag{1}$$
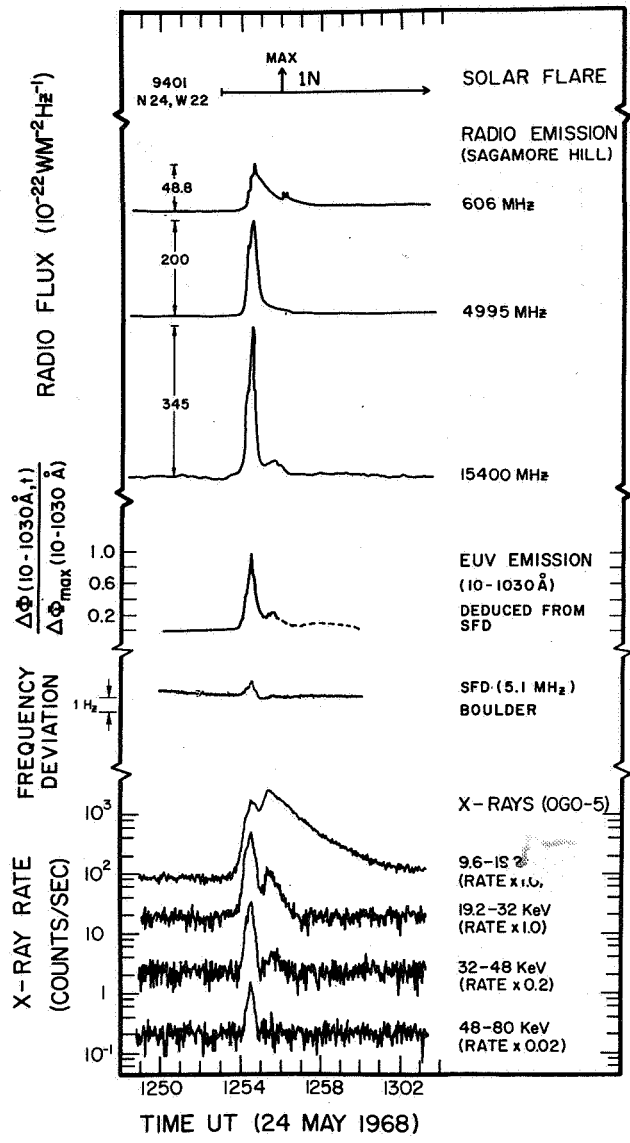
Figure 1. An example of two component structures (impulsive and slow) in hard X-ray, EUV, and microwave emission from solar flares.
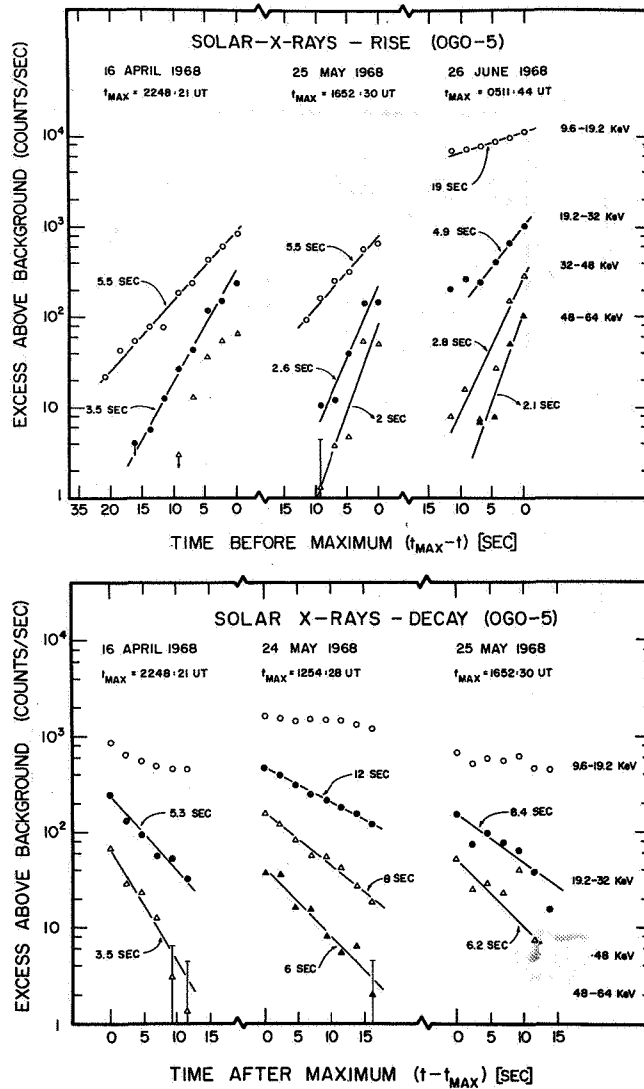
Figure 2. Rise and decay characteristics of
impulsive X-ray bursts.

for $10 \leqslant E \leqslant E_c$, and much steeper (larger γ) at energies $E > E_c$. The critical energy E_c usually lies in the range 80 to 100 keV, although in some events it can be as low as $\sim$ 60 keV (see Figure 3). Impulsive X-ray spectra of larger flares also show a critical energy $E_c \sim 100$ keV (Frost, 1969). Moreover, in some flares the impulsive X-ray emission may extend down to $\sim$ 3 keV (Kahler and Kreplin, 1971).

An important problem in the study of flare X-rays is the variation of the X-ray spectrum from one flare to another. Figure 4 shows the number distribution of the observed X-ray bursts as a function of the spectral exponent γ at the X-ray maximum. It can be seen that
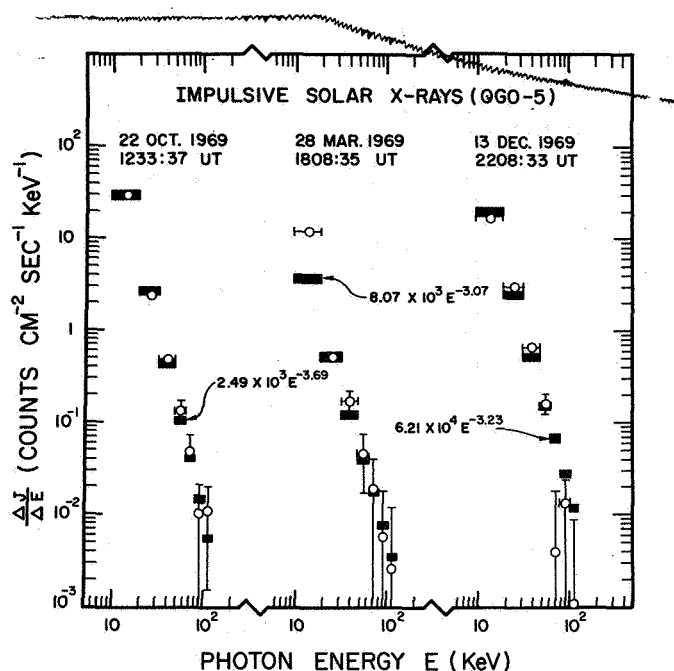
Figure 3. X-ray spectra at the maxima of three impulsive bursts. Open circles are observations and dark rectangles are computed response of the OGO-5 detector to a power law X-ray spectrum.

for $\gamma \lesssim 4$ the number of bursts rapidly decreases with the decrease in the value of γ. Furthermore, the probability of occurrence of a burst with $\gamma \lesssim$ is extremely small.

Figure 5 shows a regression plot of the energy flux ξ (20 — 100) of 20 to 100 keV X-rays and the spectral exponent γ observed at the maxima of different X-ray bursts. There is no apparent correlation between the magnitude of an X-ray burst and the hardness of the X-ray spectrum. Thus, more energetic X-ray bursts do not necessarily have a harder X-ray spectrum.

In addition to the impulsive X-rays, there are four other impulsive flare emissions which are known to have comparable rise times. These are impulsive EUV, Hα, microwave, and type III radio emissions. An example of the relationship between X-ray, EUV, and microwave emission is shown in Figure 1. The EUV emission is deduced from the ionospheric effect called sudden frequency deviation (SFD). The procedure has been described by Donnelly (1969). Relationship between X-ray and type III radio emission is illustrated in Figure 6. More examples of these relationships are given elsewhere (Arnoldy et al., 1968; Kane and Anderson, 1970; Kane and Donnelly, 1971; Wood and Noyes, 1972; Kane, 1972). The relationship between impulsive X-rays and Hα emission has been discussed in the literature (for example, see Vorpahl, 1972). Figure 7, taken from Kane and Donnelly (1971), shows a regression plot between the energy fluxes of impulsive X-rays and the 10 to 1030 Å EUV
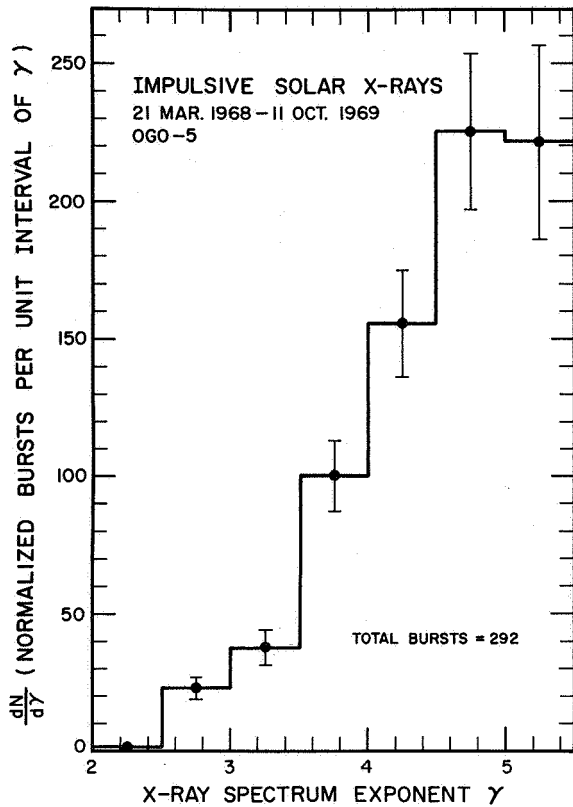
Figure 4. Number distribution of the observed impulsive X-ray bursts as a function of the X-ray spectrum exponent γ at the burst maximum. The distribution is normalized to the dynamic range of the detector for γ = 4.
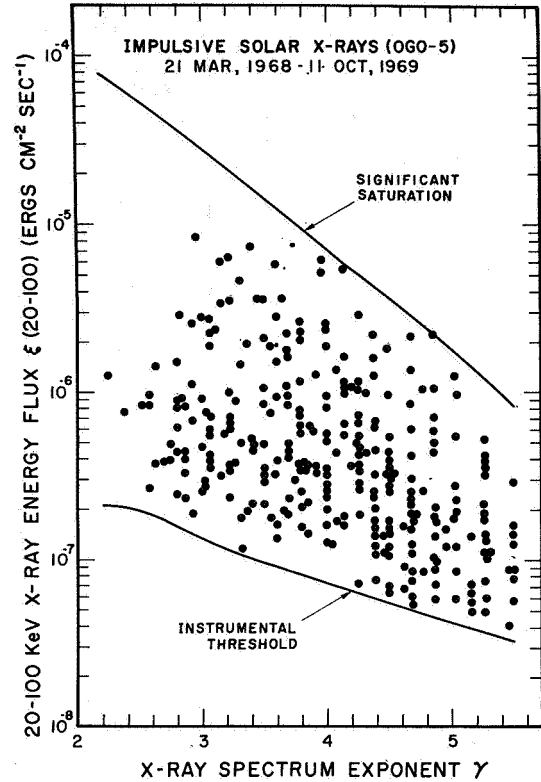
Figure 5. Regression plot of 20- to 100-keV X-ray energy flux against the X-ray spectrum exponent at the burst maximum. The region between the two solid lines represents the X-ray spectra which the detector can measure.

emission observed at the maxima of a wide range of X-ray bursts. The energy flux estimates for both emissions are believed to be accurate within a factor of ~ 4. Figure 7 shows that the peak EUV energy flux is approximately proportional to the peak X-ray energy flux, the ratio R_{xe} being given by

$$R_{xe} = \frac{\xi(\gtrsim 10 \text{ keV})}{\xi(10-1030 \text{ Å})} \sim 10^{-5} \tag{2}$$

This value of R_{xe} is applicable specifically to flares located near the central meridian. For flares located near the solar limb, the value of R_{xe} is much larger, indicating an absorption of EUV by the solar matter between the EUV source and the detector.

60
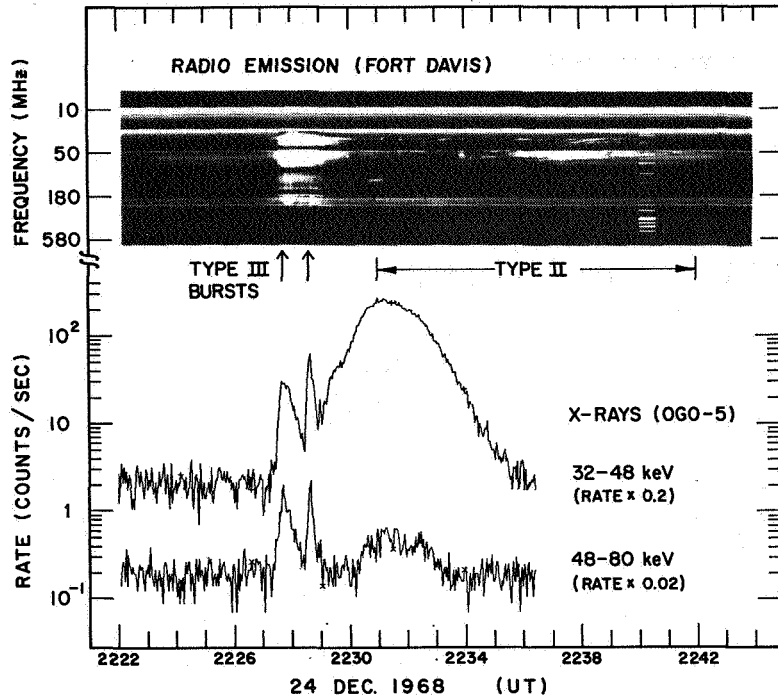
Figure 6. An example of the good time correlation between impulsive
X-ray bursts and type III radio bursts.

Figure 8, which is a more complete version of the data published earlier (Kane and Winckler, 1969), shows a regression plot of the impulsive X-ray energy flux and microwave energy flux observed at the maxima of a large number of X-ray bursts. Again we find that the peak microwave flux is approximately proportional to the peak X-ray flux, the ratio of the two peak fluxes being given by

$$R_{xm} = \frac{\xi(\geqslant 20 \text{ keV})}{\xi(\sim 3 \text{ cm})} \sim 10^2 \tag{3}$$

Here we have taken $\Delta f \sim 10^4$ MHz as the effective bandwidth of the microwave emission. The variation of R_{xm} with the central meridian distance (CMD) of the flare is not well known at this time. If such a dependence exists, it is believed to be small.

It is evident that the impulsive X-ray, EUV, Hα, microwave emissions, and the type III (flare associated) radio emissions are well correlated in time and are to be identified with the flash phase of solar flares. In the case of X-ray, EUV, and microwave emissions, the peak energy fluxes are approximately·proportional.
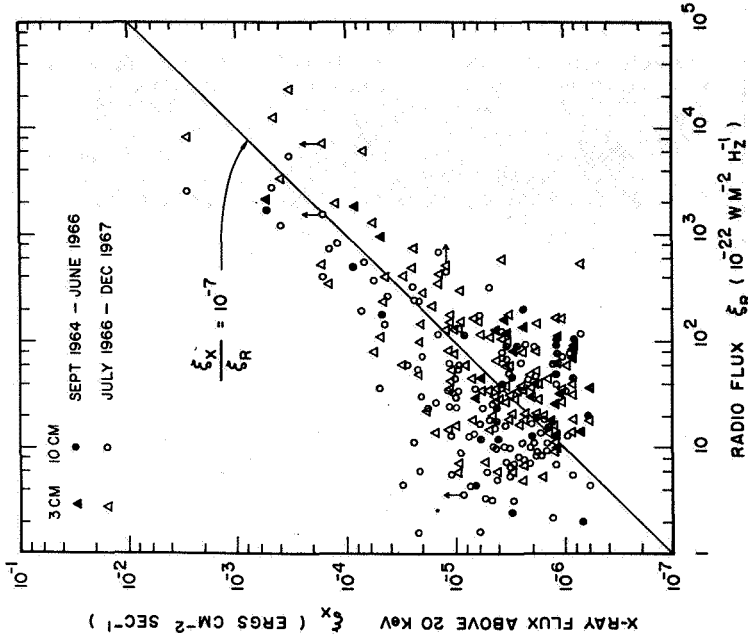
Figure 8. Regression plot of the microwave radio flux and ⩾ 20-keV X-ray flux observed at the maxima of impulsive flare events.
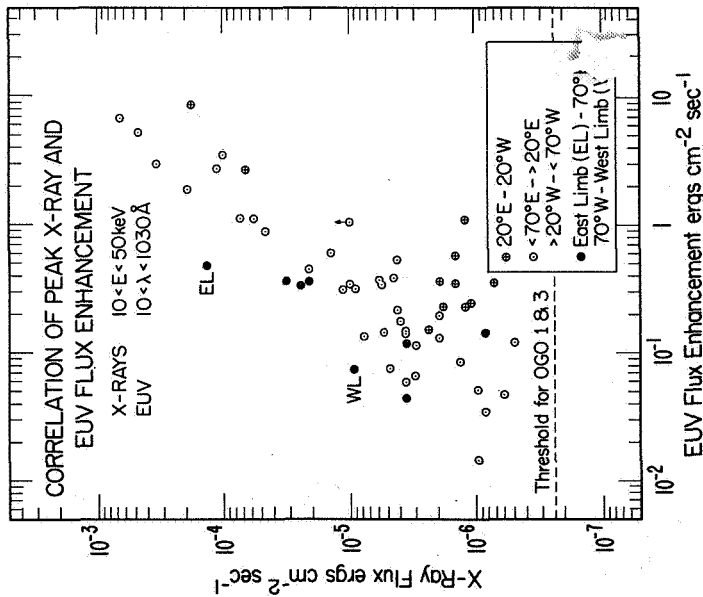
Figure 7. Regression plot of 10- to 1030-Å EUV flux and 10- to 50-keV X-ray flux observed at the maxima of impulsive flare events (Kane and Donnelly, 1971).

EMISSION MECHANISMS AND RELATIVE LOCATIONS OF HARD X-RAY, EUV, AND MICROWAVE SOURCES

In order to determine directly the relative locations of the hard X-ray, EUV, and microwave emission sources, we need observations of these flare emissions with high spatial (a few arcsec) and temporal ($\leqslant 1$ second) resolution. Since such observations are not available at present, we must deduce the relative locations of these emission sources indirectly, from observations of flares behind the solar limb and from the physical processes which are most likely to produce these emissions.

The mechanisms for the hard X-ray and microwave emission have been widely discussed in the literature (Peterson and Winckler, 1959; Kundu, 1965; Korchak, 1967; Arnoldy et al., 1968; Acton, 1968; Holt and Cline, 1968; Ramaty and Petrosian, 1972; Takakura, 1972). It is generally believed that the hard X-ray emission and the microwave emission are, respectively, the bremsstrahlung, and gyrosynchrotron radiation from energetic ($\gtrsim 10$ keV) electrons in the flare region.

There are two principal controversies in the interpretation of the impulsive hard X-ray emission: whether the spectrum of the radiating electrons is thermal or nonthermal, and whether the X-ray bremsstrahlung is a thin-target or thick-target process. The nonthermal nature of the electron spectrum has been stressed by Peterson and Winckler (1959), Anderson and Winckler (1962), De Jager (1964), Arnoldy et al. (1968), Kane (1969), and others. The thermal interpretation is primarily due to Chubb et al. (1966) and Chubb (1972). Hudson et al. (1969) found the electron spectrum to be thermal at the X-ray maximum and during the decay. They also reported a constancy of the emission measure during the X-ray burst. However, this was later found to be an instrumental effect (Kane and Hudson, 1970). The power law nature of the X-ray spectrum indicates a power law spectrum for the electrons. If such an X-ray spectrum is to produced by a thermal electron spectrum, a combination of several thermal distributions with temperatures $\gtrsim 10^8$ K are required (Kane and Anderson, 1970). In view of the rapid rise times (~ 1 second), power law spectrum, and good correlation with other simultaneous nonthermal phenomena such as impulsive microwave and type III radio bursts, we believe that the X-ray emission is nonthermal. Additional support to such a conclusion can be found in the X-ray polarization measurements reported by Tindo et al. (1970).

Although the nature of the X-ray source (thin-target or thick-target) has not yet been clearly established, the available observations of a large number of disc flares and the behind-the-limb flare of March 30, 1969, (Kane and Donnelly, 1971; Frost and Dennis, 1971) are consistent with most of the hard X-ray emission being produced in a thin-target or intermediate-target source; that is, ion density in the X-ray source is $n_i \leqslant 10^{10}$ cm^{-3} Additional support for such a conclusion is found in a comparison of the electron spectra deduced from hard X-ray measurements with the measurements of solar flare electrons in the interplanetary space (Lin, 1970). Such a comparison of the number distribution of the electron spectral exponent ϕ observed in different flares is shown in Figure 9. It can be seen
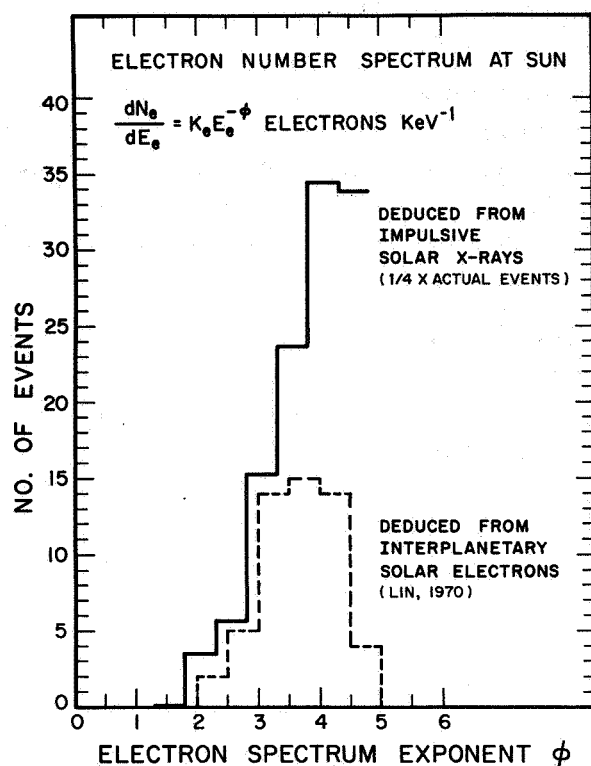
Figure 9. Comparison of the number distribution of the electron spectrum at the sun, deduced from the solar electron observations in the interplanetary space (Lin, 1970) and from the impulsive hard X-ray measurements (Figure 4).

that the two distributions are very similar for events with relatively hard electron spectra ($\phi \leqslant 4$). In case of softer spectra ($\phi > 4$), the difference in the two distributions could be attributed to the effect of propagation of these electrons from the acceleration region on the sun to the detectors at 1 AU. Theoretical models for the microwave emission suggest ion density $n_i \lesssim 10^{10}$ cm^{-3} in the microwave source (Ramaty and Petrosian, 1972; Takakura, 1972). Thus it seems very likely that spatially the hard X-ray source and the microwave source are essentially coincident.

The mechanisms for impulsive EUV emission have been discussed by Kane and Donnelly (1971). They found that the following explanation is consistent with observations: A significant fraction of the energetic charged particles continuously accelerated during the flash phase are stopped in a region where plasma density is $\gtrsim 10^{12}$ cm^{-3}, and the plasma is initially only partially ionized. The energetic charged particles further ionize the plasma and produce a large number of thermal electrons. These electrons subsequently produce 10 to

1030 Å radiation by free-free, free-bound, and bound-bound emission. It is important to note that the primary function of the energetic charged particles is to transport energy rapidly from the region of flare instability to the EUV source. Since the energy spectrum of these particles generally decreases with increasing energy, the lowest energy part of the spectrum is most important for the EUV emission. Hence the EUV emission will be essentially unchanged if, for example, the electrons with energy $\lesssim 10$ keV preferentially propagate to the EUV source while most of the higher energy ($\gtrsim 20$ keV) electrons remain in the hard X-ray source for a short time and then escape from the X-ray source into the corona. A physical process which could produce such an effect is the coulomb scattering of the energetic electrons inside the X-ray source.

The energetic electrons exciting the EUV emission will also produce X-rays by thick-target bremsstrahlung. Thus, at a given time the X-ray emission will be produced at a wide range of altitudes ($10^9 < n_i < 10^{12}$), the intensity of the emission at a given altitude depending on the local ion density n_i, and the instantaneous density of energetic electrons at that altitude. Thus we are led to a schematic model of the relative location of the hard X-ray, EUV, and microwave sources as shown in Figure 10.
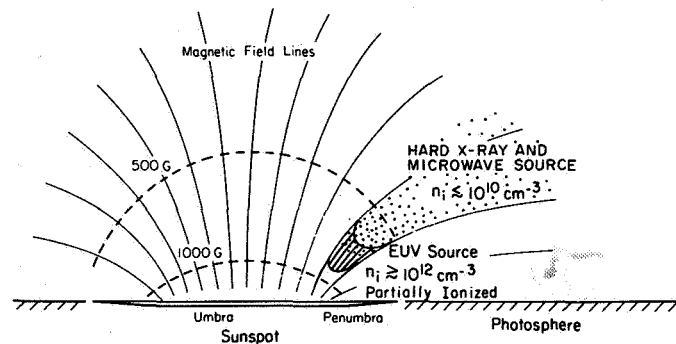
Figure 10. A model of the relative locations of the impulsive X-ray, microwave, and EUV emission sources in solar flares.

CHARACTERISTICS OF ENERGETIC ELECTRONS DEDUCED FROM HARD X-RAY MEASUREMENTS

Acceleration and Injection Process

As far as the time scale for the electron injection in the hard X-ray source is concerned, two types of models have been proposed in the past, namely, "impulsive" injection (Takakura and Kai, 1966; Brown, 1972) and "continuous" injection (Arnoldy et al., 1968; Kane and Anderson, 1970; Syrovatskii and Shmeleva, 1971; Hudson, 1972, 1973). In the impulsive

injection model, the electron injection begins at the onset of the X-ray burst and stops at the time of the X-ray maximum. The energetic electrons, which are assumed to be trapped in a magnetic bottle, emit X-rays by thin-target bremsstrahlung, and the decay of the X-ray burst is primarily determined by the collision loss of the electrons in the ambient plasma. On the other hand, the continuous injection model assumes that the electron acceleration process primarily determines the time intensity profile of the entire X-ray burst. The time constants for trapping and/or collision loss are assumed to be short compared to the characteristic time for acceleration. The X-ray radiation process could be thick-, intermediate-, or thin-target bremsstrahlung, depending on the assumed plasma density in the X-ray source.

The X-ray observations presented earlier show that during the increasing phase of an X-ray burst, the X-ray flux as well as the hardness of the X-ray spectrum continuously increases with time. This implies that the energetic electrons are continuously injected into the X-ray source V in such a way that the total number of energetic electrons in V, as well as their average energy, continuously increases with time until the X-ray emission reaches its maximum. Comparison of impulsive X-ray bursts and the associated type III radio emission shows that the maxima of the two emissions are essentially simultaneous and their total durations are comparable (Kane, 1972). This indicates that the acceleration process continues even after the X-ray maximum is reached. We may therefore conclude that the available observations for small flares favor a continuous injection model. In this model electrons are continuously accelerated and injected into the X-ray source in such a way that the electron spectrum continuously hardens from the onset to the maximum of the X-ray burst; it then softens during the decay of the X-ray burst. The characteristic time for acceleration process is $\sim$ 1 second and its duration is $\sim$ 100 seconds. Since the time resolution of the X-ray observations is $\sim$ 2 seconds, the observations are also consistent with an acceleration process which consists of a *continuous series* of impulsive accelerations, each lasting for $\leqslant$ 1 second.

We will assume, for simplicity, that the electron spectrum $s(E_e, t)$ (electrons $\cdot$ s^{-1} keV^{-1}) accelerated during the flash phase is injected into the X-ray source V without much modification. That is, the acceleration spectrum and the injection spectrum are essentially identical. After the electrons are injected into V, their spectrum will change subsequently because of energy loss inside V and escape of some electrons from V. Hence the instantaneous spectrum $\partial N_e(E_e,t)/\partial E_e$ (electrons $\cdot$ keV^{-1}) of the electrons inside V, is given by the equation of continuity in the phase space (Ginzburg and Syrovatskii, 1964; Lin and Hudson, 1971).

$$\frac{\partial}{\partial t}\left[\frac{\partial N_e(E_e,t)}{\partial E_e}\right] + \frac{\partial}{\partial E_e}\left[\frac{\partial N_e(E_e,t)}{\partial E_e}\frac{dE_e}{dt}\right]$$

$$= s(E_e,t) - \left[\frac{\partial}{\partial t}\frac{\partial N_e(E_e,t)}{\partial E_e}\right]_{escp} \quad \text{electrons} \cdot \text{s}^{-1}\text{keV}^{-1} \qquad (4)$$

66

Since the instantaneous electron spectrum can be deduced from the observed X-ray spectrum, and the rate of energy loss and life time against escape are known from the assumed model of the X-ray source, the acceleration spectrum $s(E_e, t)$ can, in principle, be determined as a function of time. The details of such a procedure will be given elsewhere (Kane, 1973). In what follows, we will present only an estimate of $s(E_e, t)$ based on a very simple model of the X-ray source.

Instantaneous Electron Spectrum in the X-Ray Source

The procedure for deducing the instantaneous electron spectrum in the X-ray source from the observed X-ray spectrum has been given by Kane and Anderson (1970), Brown (1971) and others. For nonrelativistic electrons ($E_e \leqslant 200$ keV) the relationship between the electron spectrum $\partial N_e(E_e, t)/\partial E_e$ in the X-ray source V, and the X-ray spectrum $\partial J(E, t)/\partial E$ observed at 1 AU is given by

$$\frac{\partial J(E,t)}{\partial E} \approx 1.1 \times 10^{-42} \frac{n_i}{E} \int_E^{200} \left[E_e^{-\frac{1}{2}} \frac{\partial N_e(E_e,t)}{\partial E_e} \ln \left\{ \left(\frac{E_e}{E}\right)^{\frac{1}{2}} \right. \right.$$

$$\left. \left. + \left(\frac{E_e}{E} - 1\right)^{\frac{1}{2}} \right\} \right] dE_e \quad \text{photons} \cdot \text{cm}^{-2}\text{s}^{-1}\text{keV}^{-1} \tag{5}$$

where n_i is the ion density in V. If the instantaneous electron spectrum in V is a power law in 10 to 100 keV range

$$\frac{\partial N_e(E_e,t)}{\partial E_e} = K_e(t)E_e^{-\phi(t)} \quad \text{electrons} \cdot \text{keV}^{-1} \tag{6}$$

and zero above 100 keV, then the X-ray spectrum obtained for $\phi = 2.5$ is shown in Figure 11. It can be seen that the X-ray spectrum also is approximately a power law of the form $\sim E^{-3.25}$ in 10 to 60 keV range and much steeper at higher energies. This spectrum is very similar to that observed at 22h08m33s UT on December 13, 1969 (see Figure 3), which shows that in this flare event the electron spectrum was of the form $\sim E_e^{-2.5}$ in the 10 to 100 keV range and extremely steep at energies > 100 keV.

The critical energy E_c above which the X-ray spectrum steepens rapidly is determined by the steepness of the electron spectrum above 100 keV as compared to its steepness below 100 keV. For most of the available X-ray observations, E_c lies in the range 80 to 100 keV. This indicates that the instantaneous electron spectrum is of the form of Equation (6) in the 10 to 100 keV range and much steeper (larger ϕ) above 100 keV.
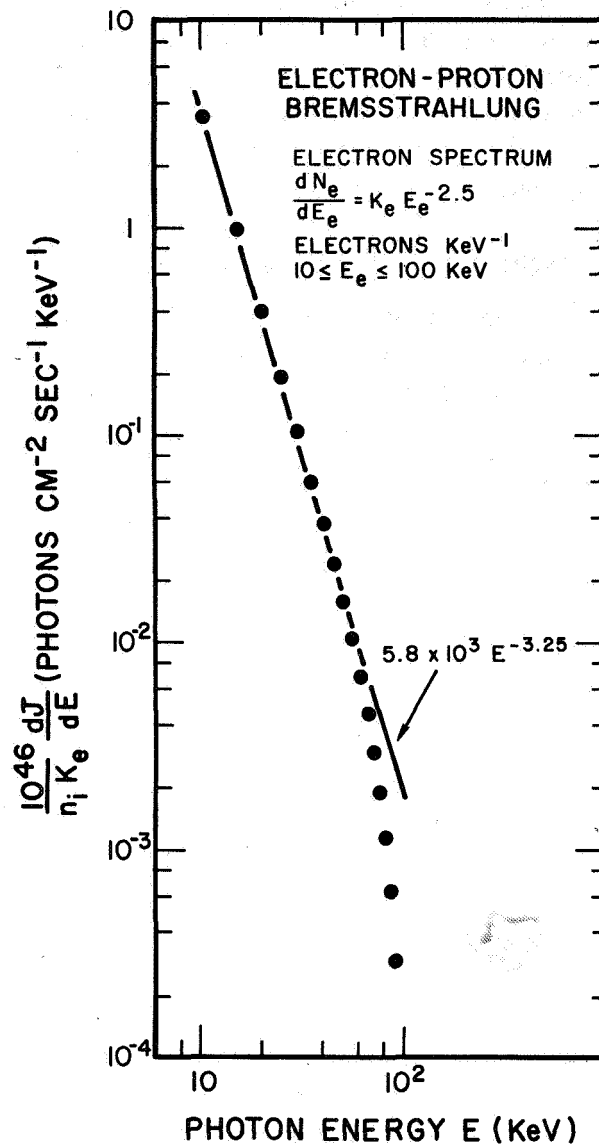
Figure 11. Electron-proton bremsstrahlung as computed for an electron spectrum of the form $K_e E_e^{-2.5}$ electrons keV^{-1} for $10 \leqslant E_e \leqslant 100$ keV and zero at higher energies; n_i is the ion density in the X-ray source.

68

Electron Loss Processes

The total kinetic energy of the 10 to 100 keV electrons inside the source V may decrease with time because of one or more of the following processes: collision loss, radiation loss (bremsstrahlung and gyrosynchrotron emission), plasma instabilities, and escape of electrons from V. The energy loss due to bremsstrahlung alone is less than the total collision loss by a factor of 10^3 to 10^4 (Berger and Seltzer, 1964), and may therefore be neglected. Also, since the instantaneous density of energetic electrons is expected to be small compared to the ambient plasma density, the effects of plasma instabilities can be neglected. We will therefore consider only three loss processes, namely, collision loss, gyrosynchrotron radiation loss, and electron escape.

For electrons of kinetic energy E_e, the rate of energy loss due to collisions and the e-folding collision loss time τ_{coll} (E_e) are given by (Trubnikov, 1965; Kane and Anderson, 1970)

$$\left(\frac{dE_e}{dt}\right)_{coll} \approx -4.9 \times 10^{-9} \, n_i \, E_e^{-\frac{1}{2}} \text{ keV} \cdot \text{s}^{-1} \tag{7}$$

$$\tau_{coll}(E_e) \approx \frac{10^8}{n_i} E_e^{3/2} \text{ seconds} \tag{8}$$

The energy loss due to gyrosynchrotron radiation is given by (Schwinger, 1949)

$$\left(\frac{dE_e}{dt}\right)_{synch} \approx -3.91 \times 10^{-9} \, B_\perp^2 \, E_e \quad \text{keV} \cdot \text{s}^{-1} \tag{9}$$

where B is the component of the magnetic field (in gauss) perpendicular to the electron velocity. The e-folding energy loss time is given by

$$\tau_{synch}(E_e) \approx \frac{2.56 \times 10^8}{B_\perp^2} \quad \text{seconds} \tag{10}$$

which is independent of the electron energy. In the X-ray source region we expect $n_i \gtrsim 10^9$ cm^{-3} and $B_\perp \lesssim 500$ gauss. Therefore for 10 to 100 keV electrons the ratio of collision loss time to the synchrotron loss time is $\lesssim 0.1$. Hence the energy loss due to gyrosynchrotron radiation can be neglected in comparison with the collision loss.

The loss of electrons due to escape can be important if n_i is $\lesssim 10^{10}$ ions$\cdot$cm^{-3}. This type of loss can be approximately estimated in the following manner. If we assume that the number

of escaping electrons at any given time t are proportional to the number of electrons present in V at that time, then

$$\left[\frac{\partial}{\partial t} \frac{\partial N_e(E_e,t)}{\partial E_e} \right]_{escp} \approx \frac{1}{\tau_{escp}(E_e)} \frac{\partial N_e(E_e,t)}{\partial E_e} \quad \text{electrons} \cdot s^{-1}keV^{-1} \tag{11}$$

where $\tau_{escp}(E_e)$ is the average lifetime of an electron of energy E_e (inside V) before it escapes from V. If $1(E_e)$ is the average distance (inside V) traveled by an electron of energy E_e and velocity v_e before it escapes, then $\tau_{escp} \sim 1(E_e)/v_e$. If we assume that most electrons travel essentially the same distance inside V, then $\tau_{escp}(E_e) \sim E_e^{-\frac{1}{2}}$. In order to determine the constant of proportionality we note that if L is the linear dimension of V, then $1 \geqslant L$. If we take $L \sim 10^9$ cm, the dimension of an Hα-flare, then we find $\tau_{escp}(E_e) > 0.1$ second for 20 to 100 keV electrons. An upper limit on τ_{escp} can be found from the decay of the X-ray burst. For X-rays $\geqslant 20$ keV, the decay time is $\leqslant 10$ seconds (Figure 2). Since the decay of the X-ray burst is believed to be due to the decrease in the acceleration spectrum, all other time constants must be much smaller than the decay time of the X-rays. Thus $0.1 \leqslant \tau_{escp}(E_e) \ll 10$ seconds, which shows that for 20 to 100 keV electrons $\tau_{escp} \sim 1$ second. Hence we can write

$$\tau_{escp}(E_e) \approx 5 \, E_e^{-\frac{1}{2}} \quad \text{seconds} \tag{12}$$

Acceleration Spectrum and Total Energy

Consider an X-ray source region V in which energetic electrons are continuously injected, the energy loss of the electrons being determined by collision loss and escape given by Equations (7) and (11) respectively. Let the instantaneous spectrum of 20 to 100 keV electrons inside V be given by the power law Equation (6). Then Equation (4) gives the instantaneous acceleration spectrum

$$s(E_e,t) \approx \frac{\partial}{\partial t} \left\{ K_e(t) E_e^{-\phi(t)} \right\} + 4.9 \times 10^{-9} \, n_i K_e(t)$$

$$[\phi(t) + 0.5] \, E_e^{-[\phi(t) + 1.5]} + 0.2 K_e(t) E_e^{-[\phi(t) - 0.5]}$$

$$\text{electrons} \cdot s^{-1}keV^{-1} \tag{13}$$

The total number S and total kinetic energy ξ of electrons E_e being accelerated at a given time can be computed by integrating s and E_es over the desired range of E_e.

The time variation of s, S, and ξ deduced in this manner from observations of several X-ray bursts will be discussed elsewhere (Kane, 1973). Here we are mainly concerned with an estimate of the time integrated values of S and ξ over the duration of the X-ray burst. If Δt

(seconds) is the full width at half maximum of the X-ray burst, then the total kinetic energy and total number of electrons $\geqslant E_e$ accelerated during the X-ray burst are approximately given by

$$\Delta S(\geqslant E_e) \approx S(\geqslant E_e, t_m) \Delta t \quad \text{electrons} \tag{14}$$

$$\Delta \xi(\geqslant E_e) \approx \xi(E_e, t_m) \Delta t \quad \text{ergs} \tag{15}$$

where t_m is the time of X-ray maximum.

ENERGY BALANCE OF A SMALL SOLAR FLARE

About 10 percent of all small flares (Hα-importance $\leqslant 1$) have been found to have a detectable impulsive X-ray burst. We will now consider the energy of nonthermal electrons in these flares and examine how it compares with the energy distribution in various flare emissions. A study of this kind has been reported earlier by Anderson et al. (1970) and Lin (1970).

From the distribution of impulsive X-ray bursts observed by the OGO-5 satellite (Kane, 1971), we find that for the burst most often observed, the X-ray spectrum at the burst maximum is given by $\sim 10^6$ $E^{-4.5}$ photons $\cdot$ cm^{-2} s^{-1} keV^{-1} at 1 AU. The peak energy flux of X-rays $\geqslant 10$ keV is $\sim 10^{-6}$ ergs $\cdot$ cm^{-2}s^{-1} and the full width at half maximum of the burst profile is ~ 10 seconds. If we assume that the ion density in the X-ray source is $n_i \sim 10^{10}$ cm^{-3}, the instantaneous spectrum of 10 to 100 keV electrons is found to be a power law, Equation (6), with $K_e(t_m) \approx 3 \times 10^{38}$ and $\phi(t_m) \approx 3.75$. From Equations (13), (16), and (17) we can get, respectively, the acceleration spectrum at X-ray maximum, the total number of electrons $\geqslant 20$ keV accelerated during the burst, and their total kinetic energy

$$s(E_e, t_m) \approx 6 \times 10^{37} (1 + 10^3 \, E_e^{-2}) \, E_e^{-3.25} \quad \text{electrons} \cdot \text{s}^{-1}\text{keV}^{-1} \tag{16}$$

$$\Delta S(\geqslant 20) \approx 7 \times 10^{35} \quad \text{electrons} \tag{17}$$

$$\Delta \xi(\geqslant 20) \approx 3 \times 10^{28} \quad \text{ergs} \tag{18}$$

In the 30 to 100 keV range, we find $s(E_e, t_m) \sim E_e^{-3.7}$.

Table 1 presents the energy distribution in other emissions associated with such a hard X-ray burst. The references given in the last column were used as basis for the estimated energy. In some cases extrapolation was necessary to arrive at the numbers given in the table. Shock waves as indicated by type II radio bursts are usually not associated with small solar flares. The energy content of such waves is therefore believed to be small. No estimates are available at present about the energy dissipated in bulk motions of the solar gas directly resulting from small flares. We will assume that Table 1 represents most of the energy in a small solar flare.

Table 1
Energy Balance of a Small Solar Flare

Quantity	Type	Peak flux at 1 AU (ergs · cm^{-2} s^{-1})	Total Energy at Sun (ergs)	Reference
Nonthermal emissions				
Hard X-rays ($\gtrsim 10$ keV)	Impulsive	4×10^{-6}	10^{23}	Kane (1971)
EUV (10 to 1030 Å)	Impulsive	4×10^{-1}	10^{28}	Kane & Donnelly (1971)
Hα	Impulsive	10^{-4}	5×10^{25}	Vorpahl (1972)
Microwave radio	Impulsive	10^{-8}	10^{20}	Kane & Winckler (1969)
Decimeter and meter radio	Type III	10^{-10}	5×10^{18}	Wild et al., (1963)
Electrons ($\gtrsim 20$ keV)	Accelerated	—	3×10^{28}	This paper
	Escaping	—	5×10^{24}	Kane & Lin (1972)
Thermal emissions				
Soft X-rays (1 to 12 Å)	Slow	5×10^{-3}	10^{28}	Thomas & Teske (1971) Horan (1970)
EUV (10 to 1030 Å)	Slow	5×10^{-3}	10^{28}	Wood et al., (1972)
Hα	Slow	5×10^{-3}	10^{28}	Thomas & Teske (1971)
Microwave	Slow	10^{-8}	10^{20}	Hudson & Ohki (1972)
Ions and electrons (T~10^7 K)	Plasma	—	10^{29}	Hudson & Ohki (1972)

Table 1 indicates two important characteristics of small solar flares: First, the observations are consistent with a model in which the energy necessary for various nonthermal (impulsive) emissions is supplied primarily by energetic electrons, protons, and heavier nuclei accelerated during the flash phase. Second, the energetic particles represent ~ 10 percent of the total flare energy (thermal and nonthermal) implying that the flare process is highly efficient in accelerating particles.

Because of the large energy content of the nonthermal electrons, several workers (Kahler et al., 1970; McKenzie et al., 1973) have considered the possibility that these electrons provide energy also for the thermal soft X-ray emission. However, in view of the fact that only ~ 10 percent of the soft X-ray emitting flares produce detectable nonthermal X-rays, it seems unlikely that the nonthermal electrons produced during the flash phase are the primary energy source for the soft X-ray emitting plasma.

LOCATION OF THE ACCELERATION REGION AND PROPAGATION OF ENERGETIC ELECTRONS IN THE SOLAR ATMOSPHERE

Since the total kinetic energy of the energetic electrons (and other particles) accelerated during the flash phase is a large fraction of the total flare energy, the acceleration is expected to occur inside the region where the flare instability takes place. It is therefore important to determine from observations the location of the acceleration region, so that the physical requirements for the onset of the instability may be identified. Here we will be concerned only with the acceleration of electrons $\lesssim 200$ keV associated with the flash phase. The acceleration of high energy electrons, protons, and heavier nuclei associated with large flares may occur in a second stage of acceleration following the flash phase (for example, see De Jager, 1969).

Recent attempts to determine the acceleration region have been based on comparison of the various flash phase emissions. For example, Zirin et al. (1971) and Vorpahl (1972), who have compared hard X-rays, Hα, and microwave emission, suggest that the acceleration process occurs in the lower chromosphere (altitude $\lesssim 5000$ km). On the other hand, from a study of hard X-rays, type III radio bursts, and interplanetary solar electrons, Kane and Lin (1972) and Kane (1972) have concluded that a more likely location of the acceleration region is in the lower corona (ion density $n_i \lesssim 10^9$ cm^{-3}). In fact, the observations described by Zirin et al. (1971) and Vorpahl (1972) are not inconsistent with electron acceleration in the lower corona. Additional support for acceleration in the corona can be found in the recent spectral measurements of the interplanetary solar electrons, which do not show a turn-over in the electron spectrum down to energies ~ 6 keV (Lin, 1972). The location of the acceleration region in the lower corona is also consistent with flare models such as those proposed by Alfven and Carlqvist (1967), Sturrock (1968), and Syrovatskii (1969).

The sources of hard X-rays, EUV, and microwave emissions are located at much lower altitudes ($n_i \gtrsim 10^9$ ions $\cdot$ cm^{-3}); the electrons, which produce type III radio bursts and escape into interplanetary space, must reach much higher altitudes ($n_i \lesssim 10^9$ ions $\cdot$ cm^{-3}). Therefore, the magnitudes of these emissions depend on the propagation of the energetic

electrons from the acceleration region to the various parts of the solar atmosphere. The magnetic field and density structure in the flare region, which determine the propagation and energy loss processes for the accelerated electrons, may vary from one flare to another. Also, the relative magnitudes of the various flash phase emissions may vary from one flare to another even if the same electron spectrum is produced in different flares. This explanation of the relationship between the various flash phase emissions is consistent with the schematic models of the flare region proposed earlier (Anderson et al., 1970; Kane and Donnelly, 1971), and is similar to those proposed, for example, by De Jager and Kundu (1963), Wild et al., (1963), Takakura (1968), and Svestka (1970).

ACKNOWLEDGMENTS

REFERENCES

Acton, L.W., 1968, *Ap. J.* 152, 305.

Alfven, H., and Carlqvist, P., 1967, *Solar Phys.* 1, 220.

Anderson, K.A., Kane, S.R., and Lin, R.P., 1970, International Seminar on the Problem of Cosmic Ray Generation on the Sun, Leningrad, U.S.S.R.

Anderson, K.A., and Winckler, J.R., 1962, *J.G.R.* 67, 4103.

Arnoldy, R.L., Kane, S.R., and Winckler, J.R., 1968, *Ap. J.* 151, 711.

Berger, M.J., and Seltzer, S.M., 1964, *Tables of Energy Losses and Ranges of Electrons and Positrons*, NASA SP-3012.

Brown, J.C., 1971, *Solar Phys.* 18, 489.

Brown, J.C., 1972, *Solar Phys.* 25, 158.

Chubb, T.A., 1972, *Solar-Terrestrial Physics/1970, Part I*, (ed. E.R. Dyer, Dordrecht, Holland: D. Reidel Publ. Co.), 99.

Chubb, T.A., Kreplin, R.W., and Friedman, H., 1966, *J.G.R.* 71, 3611.

De Jager, C., 1964, *Research in Geophysics*, Vol. 1 (ed. H. Odishaw, Cambridge, Mass., M.I.T. Press), Chapt. 1.

De Jager, C., 1969, *Solar Flares and Space Research* (ed. C. De Jager and Z. Svestka), 1.

De Jager, C., and Kundu, M.R., 1963, *Space Res.* 3 (ed by W. Priester, Amsterdam, North Holland Publ. Co.), 836.

Donnelly, R.F., 1969, *J.G.R.* 74, 1973.

Frost, K.J., 1969, *Ap. J. (Letters)* 158, L159.

Frost, K.J., and Dennis, B.R., 1971, *Ap. J.* 154, 1027.

Ginzburg, V.L., and Syrovatskii, S.I., 1964, *The Origin of Cosmic Rays*, (New York: Pergamon Press) Chapt. V.

Holt, S.S., and Cline, T.L., 1968, *Ap. J.* 154, 1027.

Horan, D., 1970, Ph.D. thesis, Catholic University of America.

Hudson, H.S., 1972, *Solar Phys.* 24, 414.

Hudson, H.S., 1973, These Proceedings.

Hudson, H.S., and Ohki, K., 1972, *Solar Phys.* 23, 155.

Hudson, H.S., Peterson, L.E., and Schwartz, D.A., 1969, *Ap. J.* 157, 389.

Kahler, S.W., and Kreplin, R.W., 1971, *Ap. J.* 168, 531.

Kahler, S.W., Meekins, J.F., Kreplin, R.W., and Boyer, L.S., 1970, *Ap. J.* 162, 293.

Kane, S.R., 1969, *Ap. J. (Letters)* 157, L139.

Kane, S.R., 1971, *Ap. J.* 170, 587.

Kane, S.R., 1972, *Solar Phys.* (in press).

Kane, S.R., 1973, Paper to be presented at 3rd Meeting of Solar Physics Division of AAS (Los Cruces, New Mexico, Jan. 4-6).

Kane, S.R., and Anderson, K.A., 1970, *Ap. J.* 162, 1003.

Kane, S.R., and Donnelly, R. F., 1971, *Ap. J.* 164, 151.

Kane, S.R., and Hudson, H.S., 1970, *Solar Phys.* 14, 414.

Kane, S.R., and Lin, R.P., 1972, *Solar Phys.* 23, 457.

Kane, S.R., and Winckler, J.R., 1969, *Solar Phys.* 6, 304.

Korchak, A.A., 1967, *Soviet Astron. – AJ* 11, 258.

Kundu, M.R., 1965, *Solar Radio Astronomy*, (New York: Interscience Publ.) Chap. 13.

Lin, R.P., 1970, Seminar on Acceleration of Particles in Near-earth and Interplanetary Space, Galaxy and Metagalaxy (Leningrad, U.S.S.R., July 13-15).

Lin, R.P., 1973, These Proceedings.

Lin, R.P., and Hudson, H.S., 1971, *Solar Phys.* 17, 412.

McKenzie, D.L., Datlowe, D., and Peterson, L.E., 1973, *Solar Phys.* (in press).

Peterson, S.E., and Winckler, J.R., 1959, *J.G.R.* 64, 697.

Ramaty, R., and Petrosian, V., 1972, *Ap. J.* 178, 241.

Schwinger, J., 1949, *Phys. Rev.* 75, 1912.

Sturrock, P.A., 1968, IAU Symp. 35, 471.

Svestka, Z., 1970, *Solar Phys.* 13, 471.

Syrovatskii, S.I., 1969, *Solar Physics and Space Research* (eds. C. De Jager and Z. Svestka, COSPAR Symp.), 346.

Syrovatskii, S.I., and Shmeleva, O.P., 1971, Lebedev Inst. Preprint 158.

Takakura, T., 1968, *Solar Phys.* 6, 133.

Takakura, T., 1972, *Solar Phys.* (in press).

Takakura, T., and Kai, K., 1966, *Publ. Astron. Soc. Japan* 18, 57.

Thomas, R.J., and Teske, R.G., 1971, *Solar Phys.* 16, 431.

Tindo, I.P., Ivanov, V.D., Mandelstam, S.L., and Shuryghin, A.I., 1970, *Solar Phys.* **14**, 204.

Trubnikov, B.A., 1965, *Rev. Plasma Phys.* **1**, 105.

Vorpahl, J.A., 1972, *Solar Phys.* (in press).

Wild, J.P., Smerd, S.F., and Weiss, A.A., 1963, *Ann. Rev. Astron. Astrophys.* **1**, 291.

Wood, A.T., Jr., and Noyes, R.W., 1972, *Solar Phys.* **24**, 180.

Wood, A.T., Jr., Noyes, R.W., Dupree, A.K., Huber, M.C.E., Parkinson, W.H., Reeves, E.M., and Withbroe, G.L., 1972, *Solar Phys.* **24**, 169.

Zirin, H., Pruss, G., and Vorpahl, J., 1971, *Solar Phys.* **19**, 463.

STRUCTURE OF PROTON CENTERS AND ASSOCIATED NONTHERMAL BURSTS AT MICROWAVE FREQUENCIES

Shinzo Énomé and Haruo Tanaka

The Research Institute of Atmospherics

Nagoya University

INTRODUCTION

A very broad band of electromagnetic radiation is emitted during solar flares, especially at the explosive phase. This implies that there is, in the flaring region, a large variety of plasmas with various densities and a wide range of temperatures or energies.

It is our ultimate aim to know how these plasmas are heated and accelerated to sub-relativistic and relativistic energies. We will give observational evidence on the characteristics of active regions which produced proton flares and on the structure of the associated nonthermal microwave bursts of the sun. We will also describe the behaviour of sub-relativistic electrons on the sun. Our data are based on observations made with the Toyo-kawa interferometers at 3 cm and 8 cm, which have the same spatial resolution of 1.1 arcmin. It takes 10 seconds and 160 seconds to complete a scan of the sun for 8 cm and 3 cm, respectively (Tanaka et al., 1967, 1969).

CHARACTERISTICS OF PROTON CENTERS

First we will summarize the microwave features of proton centers or active regions which produce proton flares. In the past several years we have carried out a short-term forecast of proton flares for the practical purpose of making balloon or rocket experiments of solar radiation, and coordinated studies of solar flares (Takakura et al., 1971; Simon and Svestka, 1969; Svestka and Simon, 1969). The study of forecasting is to know observational conditions for the occurrence of proton flares, which on the other hand, is the study of solar flares itself. According to the most recent results of our studies, the requirements for the occurrence of proton flares are as follows:

- The spectrum of S-component associated with the active region is flat between 3 cm and 8 cm, or more precisely, the ratio of 3-cm to 8-cm flux is equal to or greater than 0.8. This condition may be quantitatively the same as the high gradients of magnetic fields in active regions related to important flares, including proton flares, found by Severny (1960).

- The source of the S-component must have a peculiar circular polarization distribution, which we call the P-configuration.

The feature of this P-configuration, denoted P for proton, is shown in Figure 1. It shows

1969 MAR 20

9400MHz
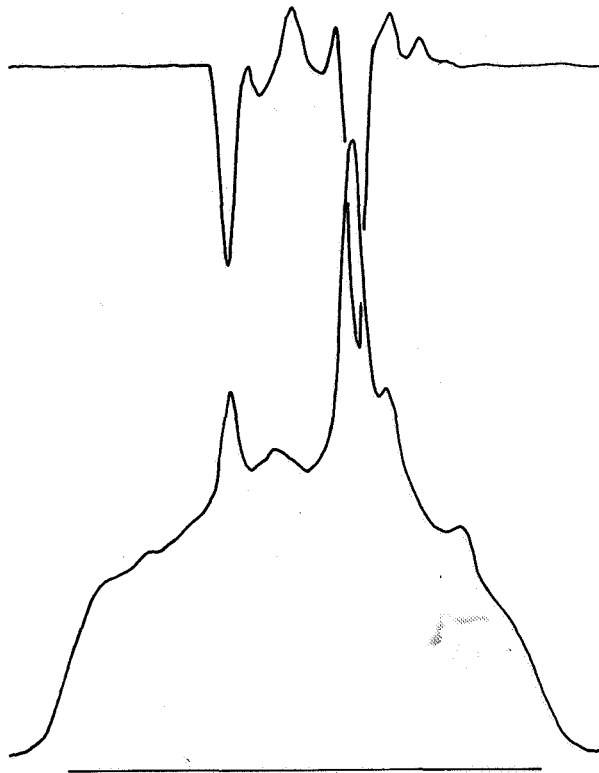
P—configuration

Figure 1. Strip-scan curves of the sun about 0300 UT on
March 20, 1969, taken with 1.1-arcmin beam at 3 cm. The
upper curve shows the polarization record or R − L, and
the lower curve the intensity or R + L. The gain of the
polarization channel is increased about four times com-
pared with the intensity channel. The east-west direction
is reversed from the ordinary sense.

3-cm drift curves of the sun on March 20, 1969. The upper and lower curves in the figure represent the difference and sum of the right- and left-hand circular polarizations, called the polarization and intensity curves respectively. The gain of the polarization record is increased about four times compared with the intensity record. The active region McMath 9994 with the P-configuration consists of a strongly polarized main peak and subpeaks on either side of it, which are polarized opposite to the main peak. At 3 cm we are looking in the active region, the upper chromosphere or lower corona, which is inferred from the fact that temperature of the S-component reaches as high as a few hundreds of thousands of kelvins. It is also well known that the right- and left-hand circular polarizations of S-components correspond to the north and south, or positive and negative, magnetic polarities of sunspot field. Thus it is possible to picture the magnetic configuration, though our resolution above the active region is very poor compared with optical maps.

In Figure 2, at the photospheric level we have the Mt. Wilson solar magnetogram and the sunspot sketch of March 20, 1969, the same day as in Figure 1, which shows that the active region McMath 9994 consisted of two closely separated bipolar spot groups, and that the central two adjacent spots were in a well-developed stage. It must be noted that if one looks only at this part of the region it appears as a reversed polarity region, as described by Smith and Howard (1968). When we look at a height of upper chromosphere or lower corona, the dominant polarization in the active region at 3 cm is left-handed, so it is inferred that nega-
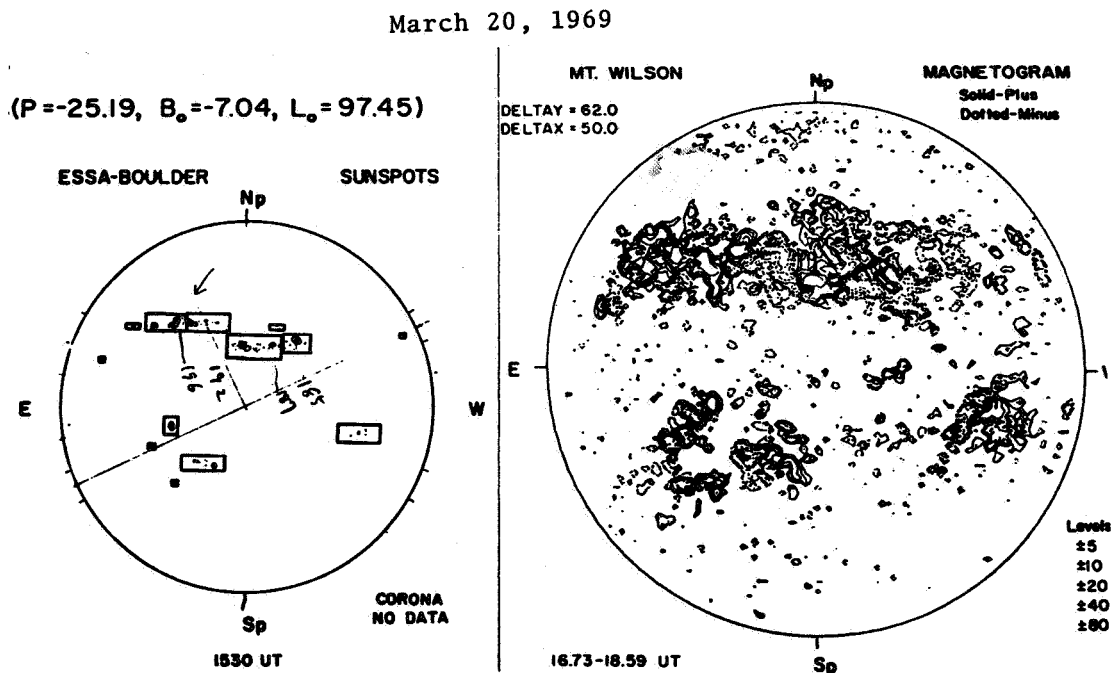
March 20, 1969

Figure 2. Sunspot sketch and Mt. Wilson magnetogram on March 20, 1969, after Solar Geophysical Data, NOAA. The active region McMath 9994 is indicated by an arrow.

80

tive magnetic polarity of the preceding spot in the eastern spot group was extending up into the corona. We have another example of the active region of this type, composed of two bipolar groups approaching each other. It is the active region McMath 9946, which produced proton flares. A similar configuration of sunspots in active regions associated with proton flares is mentioned by Fortini and Torelli (1968). Some of the so-called reversed polarity regions noticed by other people may belong to this class of active region (Sakurai, 1967, 1969, 1972; Zirin, 1970). These descriptions of the active region suggest the Sweet mechanism operating in the proton center to accelerate protons (Sweet, 1956). It is also suggested that the field configuration as large as the scale of an active region may govern the nature of the active region as to proton-productive or not.

STRUCTURE OF ASSOCIATED MICROWAVE BURSTS

Here we shall deal mainly with the bursts on February 26 and March 21, 1969, both of which were accompanied by minor proton events. In Figure 3, time profiles of the burst on February 26, 1969, at frequencies of 1000, 2000, 3750, and 9400 MHz show a rather
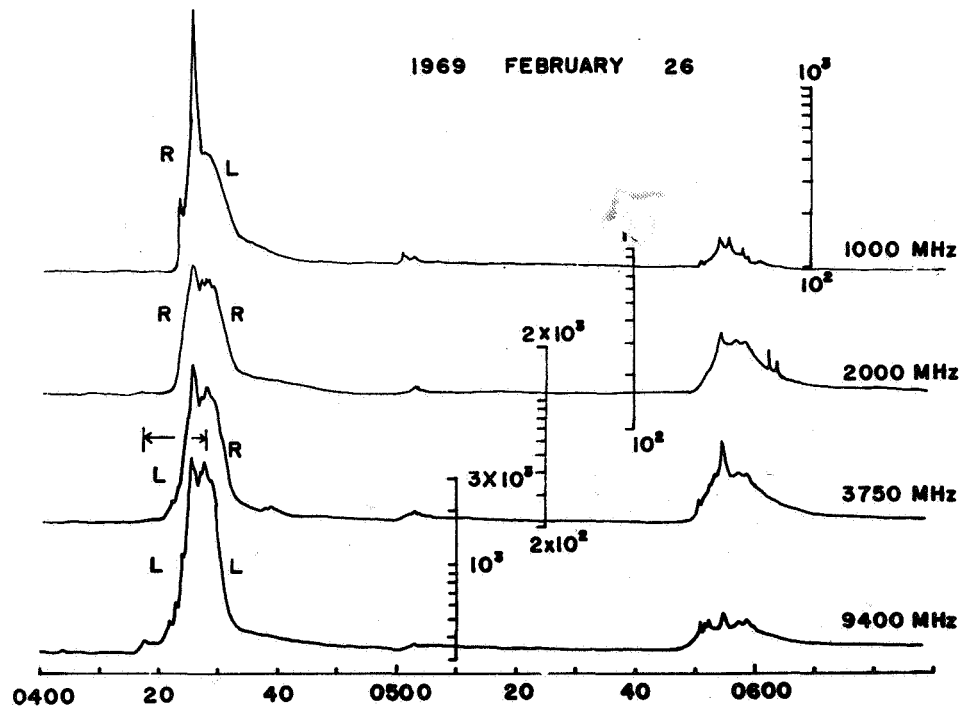
Figure 3. Intensity-time profiles at four frequencies are illustrated for the burst on February 26, 1969. Intensities are expressed in logarithmic scale in units of 10^{-22} $W.m^{-2}Hz^{-1}$. The sense of polarization is written beside the curves. R and L stand for the right- and left-hand circular polarization.

simple and broadband feature of activities around 0425, 0500, and 0555 UT. The sense of circular polarization is indicated by the curves of time profiles with symbol R or L, which denotes the right- or left-hand circular polarization. At 3750 MHz there is a sense reversal with respect to time around 0423 UT.

This sense reversal is also noted in Figure 4, a schematic drawing of time variations of the brightnesses in intensity and polarization, or R + L and R – L, observed through the quick-scan technique (Tanaka et al., 1969). Before the onset of the burst, the right-hand polarization was stronger in the source at 3750 MHz; but with the start of the burst at 0420, the left-hand polarized radiation became stronger. By careful examination of the quick-scan record it is found that the burst originated first in the western part of the source, which was left-hand polarized before the onset of the burst. At about 0423.5, however, another activity commenced in the eastern part of the active region. The radiation in this part was polarized in the right-hand with degrees stronger than those of the left-hand polarized radiation in the western part. Consequently, the right-hand radiation suppressed the left-hand in the course of time after 0424.
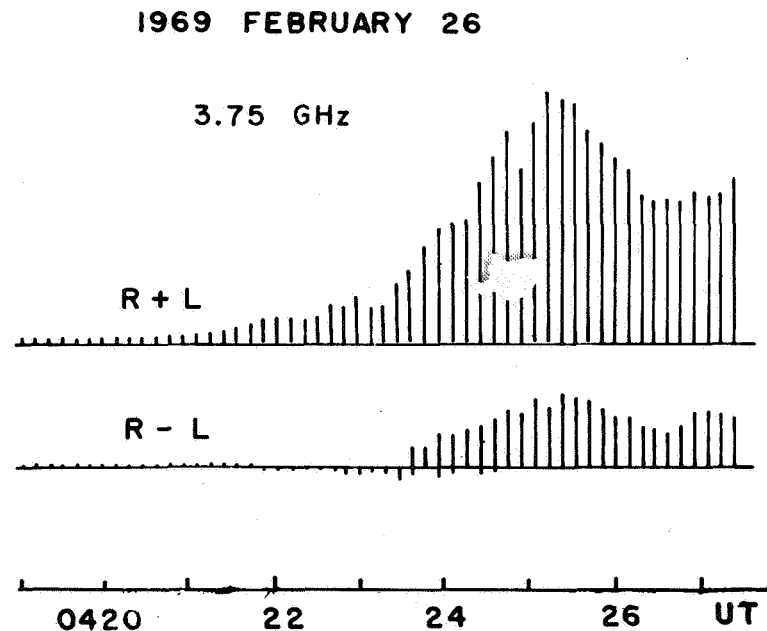
Figure 4. Schematic drawings of time history of the brightnesses in intensity and polarization channels taken with the 1.1-arcmin beam at 8 cm. A quick-scanning technique is employed. The interval covered in this figure is indicated by arrows in the 8-cm time history in Figure 3.

These situations are clearly seen in Figure 5, where quick-scan curves at 3750 MHz of the intensity channel are shown covering the time of polarization reversal mentioned previously.

82

The position of peaks in the polarization channel is expressed by lines in these strip-scan curves. With the appearance of the right-hand polarized radiation, an enhancement in the eastern part is remarkable in the strip-scan curves at 0423.7 and 0424.6 in Figure 5. Detailed calculations confirm that there was no apparent difference between the position of the S-component before the onset of the burst and that of the burst source. At 9400 MHz there was not such distinctive activity in the eastern part of the active region that no reversal of polarization occurred. An important point to be mentioned at this stage is that source of the burst is, for the first time, resolved into components at microwave frequencies.
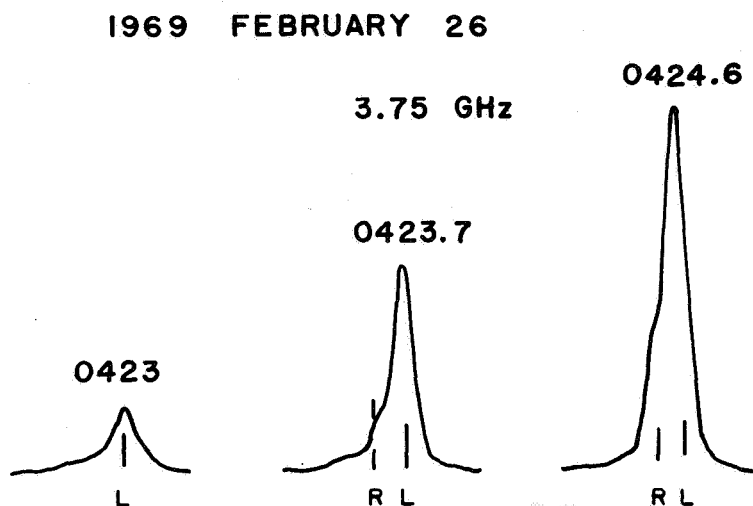
Figure 5. Quick-scan curves across the source of the burst on February 26, 1969. Polarized centers are indicated by lines. A small hump in the strip-scan curves at 0423.7 and 0424.6 corresponds to the right-hand polarized component of the source.

The position of the components is indicated in the sunspot sketch observed on the same day at Tokyo Astronomical Observatory, as shown in Figure 6. The western and eastern components of the source are found to correspond to the preceding spot of the western spot group and the following spot of the eastern spot group respectively. The right- and left-hand polarized radiations were associated with the north and south magnetic polarities, respectively, according to the data on sunspot magnetic fields published by the U.S.S.R. Academy of Sciences. This event was, therefore, another example which exhibited a sense reversal with respect to time and/or frequency, resulting from a superposition of different spectra and time histories of components of the burst source as suggested previously (Tanaka et al., 1967). As for the polarization state of the burst in the microwave range, radiation was right-hand polarized at 2000 MHz during the whole course of the burst activity. At 1000 MHz, however, there was a sense reversal between 0427 and 0429 UT. Therefore, it may be in-

ferred that the already-mentioned characteristics of the source structures at 3750 and 9400 MHz may be extended down to 2000 MHz, but not further, to explain the polarization features.

On the occasion of the burst on March 21, 1969, we observed a similar source structure. In this case we could identify five components in the source, which were also circularly polarized in the extraordinary sense as seen in Figure 7.
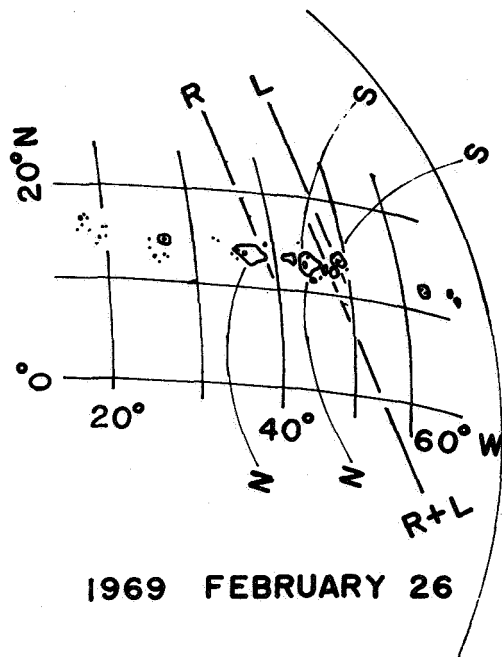
Figure 6. A sketch of the active region responsible for the burst on February 26, 1969. Positions of the source on the intensity channel or of polarized components are indicated by lines with symbols R + L, R, and L respectively. Polarities of sunspot magnetic fields are also indicated. Note that the R- and L-polarized components correspond to north and south magnetic polarity, respectively.
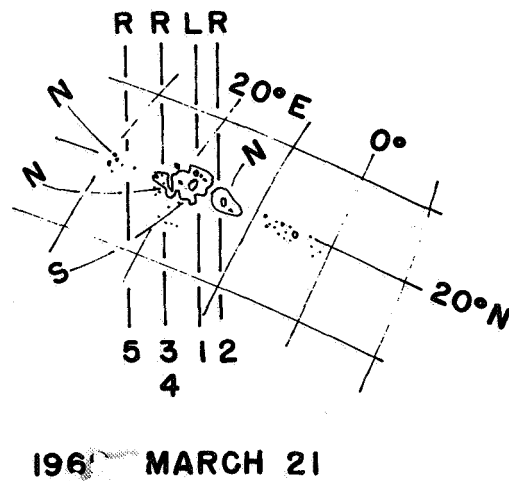
Figure 7. A sketch of the active region which produced the burst on March 21, 1969. Positions of five polarized components are denoted by lines. Sunspot polarities are also shown.

CONCLUSION

Summarizing these results, we have the following characteristics for the structure of microwave bursts associated with proton flares:

- In both cases the emission of the burst originated from the main peak and subpeaks of the S-component which existed before the burst. The bursts consisted of more than one component, that is, a main peak and subpeaks.

- The positions of these components coincided with individual sunspots in the active region.

- These components were circularly polarized in the extraordinary sense, at least at 3 cm and 8 cm.

- Each component showed its own individual evolution, which brought about a temporal reversal of polarization during the burst in the record of total flux measurements, which is remarkable at 8 cm.

- The size of components is about 1 to 0.5 arcmin or less.

- The brightness temperature, therefore, does not exceed 10^9 K.

- In the case of the limb event on March 30, 1969, the height of the source is estimated to have been higher than 10^4 km and showed an unusual expansion of the source at 3 cm (Énomé and Tanaka, 1971).

It is inferred from these characteristics that subrelativistic electrons are responsible for these bursts, and that the acceleration of electrons to subrelativistic energy may take place within well localized regions of an active region as small as 2 to 3 X 10^4 km or less, in the close neighborhood of sunspots. The fact of an individual evolution with respect to time for each component strongly suggests that trapping of electrons between any pair of these localized regions is excluded.

REFERENCES

Énomé, S. and Tanaka, H., 1971, *Proc. IAU Symp.* **43**, 413.

Fortini, T. and Torelli, M., 1968, *Proc. IAU Symp.* **35**, 50.

Sakurai, K., 1967, *Rpt. Ionosph. Space Res. (Japan)* **21**, 113.

Sakurai, K., 1969, *J. Geomag. Geoelec.* **21**, 463.

Sakurai, K., 1972, *Solar Phys.* **23**, 142.

Severny, A.B., 1960, *Izv. Krymsk. Astrofiz. Observ.* **22**, 12.

Simon, P. and Svestka, Z., 1969, *Annals IQSY* **3**, 463.

Smith, S.F. and Howard, R., 1968, *Proc. IAU Symp.* **35**, 33.

Svestka, A. and Simon, P., 1969, *Solar Phys.* **10**, 3.

Sweet, P.A., 1956, *Proc. IAU Symp.* **6**, 123.

Takakura, T., Ohki, K., Shibuya, N., Fujii, M., Matsuoka, M., Miyamoto, S., Nishimura, J., Oda, M., Ogawara, Y., and Ota, S., 1971, *Solar Phys.* **16**, 454.

Tanaka, H., Kakinuma, T., and Énomé, S., 1967, *Proc. Res. Inst. Atmospherics, Nagoya Univ.* **14**, 23.

Tanaka, H., Kakinuma, T., Énomé, S., Torii, C., Tsukiji, Y., and Kobayashi, S., 1969, *Proc. Res. Inst. Atmospherics, Nagoya Univ.* **16**, 113.

Zirin, H., 1970, *Solar Phys.* **14**, 328.

SPECTRAL CHARACTERISTICS OF MICROWAVE BURSTS

Donald A. Guidice and John P. Castelli
Air Force Cambridge Research Laboratories

ABSTRACT

Various statistical parameters of the peak flux-density spectra of solar microwave bursts have been examined for 1968 to 1971 based on spectra obtained from fixed-frequency observations at 245, 606, 1415, 2695, 4995, 8800, 15400, and 35000 MHz made at the Sagamore Hill Radio Observatory, Hamilton, Mass. For bursts having a centimeter-radiation component, the great majority were found to have type C spectra (single spectral maximum) in the L-band to K-band range. A small percentage had miscellaneous type spectra (more than one spectral maximum) and another small percentage had what might be taken as thermal spectra. Even for gradual rise-and-fall bursts, often thought to be of thermal origin, less than 20 percent were found to have spectra which could be classified as thermal. The relationship between the burst spectral maximum (f_{max}) and the photospheric magnetic field strength of the region associated with the burst was examined. A tendency for greater correlation at higher f_{max} for stronger magnetic fields is noted; however, this is overshadowed by the overall high correlations for those regions having strong photospheric magnetic fields. For bursts with cm components >50 solar flux units (sfu), the relation between the low-frequency cutoff f_{cut} and the spectral maximum f_{max} was studied. It was found statistically that f_{cut} is well correlated with f_{max}, with higher correlation for intensity 2 (50 to 500 sfu) bursts than for intensity 3 (>500 sfu). intensity 2 bursts, a good fit to the relation $f_{max} = A f_{cut}$ was found with $A = 3.4$.

INTRODUCTION

In the early 1960s, it was realized that a need existed for a consistent, well-calibrated, daily-operating solar radio patrol covering a wide range of frequencies to monitor the radio emission from the sun on a routine basis, to warn of solar events that might disturb the earth's ionosphere, and to gather data on emission characteristics that might be useful in investigating the physics of solar emission mechanisms. The observations were to be at fixed frequencies roughly an octave apart, extending (eventually) from meter to millimeter wavelengths, since the sun's emission is quite different at different wavelength ranges. They would be low resolution to maintain routine coverage of the whole sun, using beamwidths several times the sun's diameter to assure accurate flux density measurements. The patrol was to be capable of measurements of the nondisturbed sun (quiet sun and slowly varying component) and of the disturbed sun (radio bursts) over a wide dynamic range of intensities — from about 1 sfu to tens (even hundreds) of thousands of flux units. The initial operation was to begin at the Sagamore Hill Radio Observatory, Hamilton, Massachusetts,

which would serve as the standard for other Air Force observatories, with the eventual goal of worldwide coverage.

The implementation of these plans was begun under the technical direction of J. Castelli of AFCRL in 1965 at the Sagamore Hill Radio Observatory. The station is operated by military personnel of the Air Weather Service. The dates when the radiometric systems at various frequencies became operational at Sagamore Hill are listed below. Additional solar radio patrol stations patterned after the Sagamore Hill station were started at the Manila Observatory in 1967 and at the National Observatory of Athens in 1969, but they presently have somewhat less frequency coverage. (See Figure 1.) In 1973, the final station in the network will begin operation (initially with limited frequency coverage) at Palehua, Hawaii, thus completing the goal of worldwide coverage.

Dates When Systems at Various Frequencies Became
Operational at the Sagamore Hill Radio Observatory

245 MHz	February 1969
410 MHz	April 1971
606 MHz	January 1966
1415 MHz	January 1966
2695 MHz	January 1966
4995 MHz	January 1966
8800 MHz	January 1966
15,400 MHz	January 1968
35,000 MHz	November 1968

Because of the limitation in frequency coverage of the other sites, the data base used in the study of the statistical distribution of microwave spectral parameters has been limited to data from the Sagamore Hill Radio Observatory. In fact, since spectral coverage at the higher microwave frequencies (K-band) only came to Sagamore Hill in 1968, most of the investigations discussed in this paper are limited to the Sagamore Hill data of 1968 to 1971.
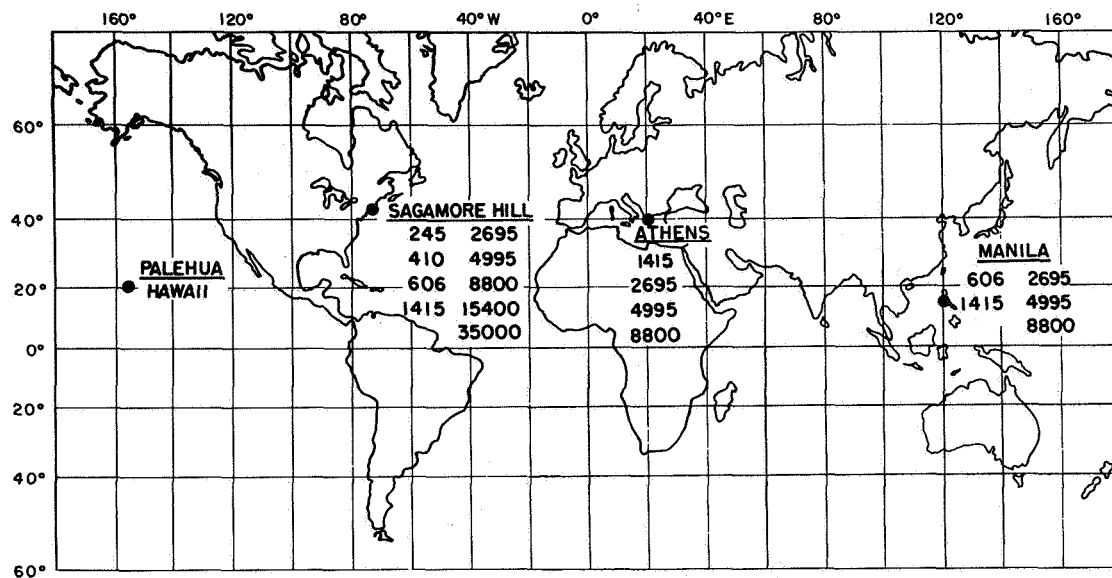
Figure 1. Stations and presently operating frequencies (MHz) of the Air Force solar radio patrol. Objective is to obtain worldwide coverage with stations roughly 90°apart in longitude.

CLASSIFICATION OF BURST AREA

The basic observations used in our studies are in the form of continuous time records of flux density at each of the Sagamore Hill patrol's fixed frequencies. The chief parameter used in our investigation of the statistical properties of radio bursts is the peak flux density at each patrol frequency. The peak flux density at any frequency usually (>90 percent of the time) occurs within one minute of the peak at the other frequencies. For a few bursts, this holds true only for the centimeter component and the decimeter component separately. For the very small number of bursts for which the times of flux density peaks are widely and irregularly separated, these bursts are simply not included in the statistical base used in our studies.

From the peak flux density values measured at each patrol frequency, we obtain a spectrum for each burst and classify the burst according to its intensity and spectral properties. Initially our emphasis was on centimeter-band characteristics, but later the patrol broadened its frequency coverage to include the decimeter band. The basic classification scheme is illustrated in Figure 2 (Castelli and Guidice, 1970). We have three basic spectral types: type G, flux density increasing with decreasing frequency; type C, flux density reaching a single spectral maximum in the centimeter range and decreasing on both sides of this spectral maximum; type A, flux density increasing with increasing frequency. Burst intensity is divided into three levels: intensity 1, flux density reaches a value less than 50 sfu; intensity 2, flux density reaches a value between 50 and 500 sfu; intensity 3, flux denisty reaches a value greater than 500 sfu at one of the patrol frequencies. (A solar flux unit is $10^{-22} \, W \cdot m^{-2} Hz^{-1}$.)

89
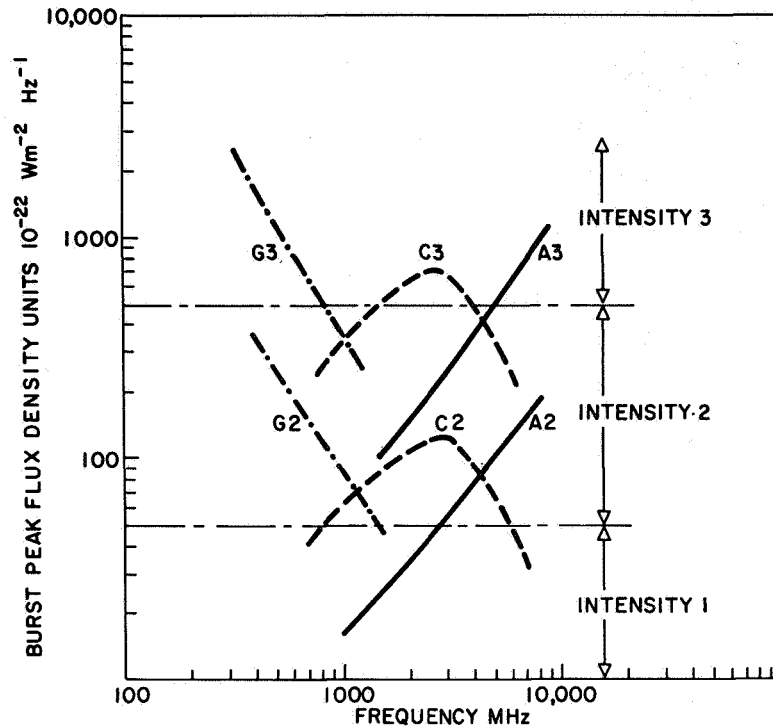
Figure 2. Idealized drawing showing principal burst spectral types and
intensity subgrouping.

For type C bursts, we have an additional classification c⸱ ⸱ory, the band in which the burst reaches its spectral maximum. For centimeter wavelengtns, the fixed patrol frequencies are associated with certain radar bands: 1415 MHz with L-band, 2695 MHz with S-band, 4995 MHz with C-band, 8800 MHz with X-band, 15400 MHz and 35000 MHz with K-band. When we say the spectral maximum occurs in one of these bands, it is the band corresponding to the patrol frequency at which the largest peak flux density value was measured (even though the actual spectral maximum obviously does not occur precisely at any patrol frequency).

In addition to the basic spectral types (G, C, and A), another centimeter-range type is related to the type C and called the miscellaneous, or type M. While its flux density decreases at high frequencies and at low frequencies when there is no decimeter tail (see later discussion in this section on composite, or GC, spectra), the type M spectrum has more than one (rarely more than two) spectral maxima in the centimeter band. About 5 percent of all bursts exhibit this miscellaneous type spectrum.

There are some centimeter-range spectra which show a sharp rise in intensity with increasing frequency (L- to S-band, S- to C-band, and so on) and then level out or decrease very slightly at the highest patrol frequencies (K-band). Since these typically fit within the type C classification (or even type A, if their sharp rise occurs at the upper frequency end and the pre-

90

sumed flat part is beyond the frequency range of our observations), they are assigned within the type C (or type A) category and are not given a separate classification. However, since this type of spectrum resembles that due to bremsstrahlung or thermal radiation, it has received some attention, especially with regard to those bursts thought to have emission of thermal origin. Based on our Sagamore Hill data, less than 5 percent of all bursts have spectra which are (or could possibly be) of the so-called thermal type.

Although the classification system adopted by AFCRL was primarily intended to characterize centimeter bursts, it became apparent that there were two distinct emission regimes to be considered: the centimeter and the decimeter. Many bursts having a clearly type C spectrum in the centimeter range also had a low frequency tail in the decimeter range which increased (often very steeply) with decreasing frequency. It was decided to introduce the concept of composite spectra. For example, a burst with a type C centimeter component with a spectral maximum of 25 sfu at 8800 MHz and a decimeter component reaching 100 sfu at 606 MHz (or lower frequency) would be classified as G2C1X. With the advent of the 245-MHz and 410-MHz systems at Sagamore Hill, the decimeter component was found in some cases to have its own spectral maximum within the frequency limit of our observations (>245 MHz and $\leqslant 600$ MHz). However, a complete classification scheme for the decimeter range has not yet evolved, so that decimeter components are all designated only by G and a number (1, 2, or 3) indicative of their intensity level.

The idealized case of a peak flux density spectrum is shown in Figure 3. The spectrum shown would be classified G2C3C. In addition to intensity level and frequency of spectral maximum (f_{max}), the values of several other useful parameters may be obtained. The slope (α) on the high-frequency side of the centimeter component is related to the slope of the energy spectrum of those electrons (believed to be barelativistic) responsible for the gyrosynchrotron emission observed in the centimeter range. The cutoff frequency (f_{cut}) in some cases may be related to electron density of the solar region in which the emission originates.

From early studies of the peak flux density spectra of large radio bursts came an important tool in the prediction of solar proton events: the U-shape signature (Castelli et al., 1967). The criteria for predicting a major proton event (i.e., one that will cause >2 dB polar cap absorption at 30 MHz) have been established as follows: (1) flux density rising in the centimeter range to values $\geqslant 1000$ flux units, (2) a dip or minimum (hence, the term U-shape) in the decimeter range (roughly between 500 and 2000 MHz), and (3) flux density rising in the low frequency direction to large values (>1000 sfu; often $>10,000$ sfu) in the meter wavelength range. The criteria associated with the U-shape signature have made possible a prediction accuracy of almost 100 percent for polar cap absorption (PCA) events with absorptions >2 dB at 30 MHz associated with visible-hemisphere events of the current sunspot cycle.
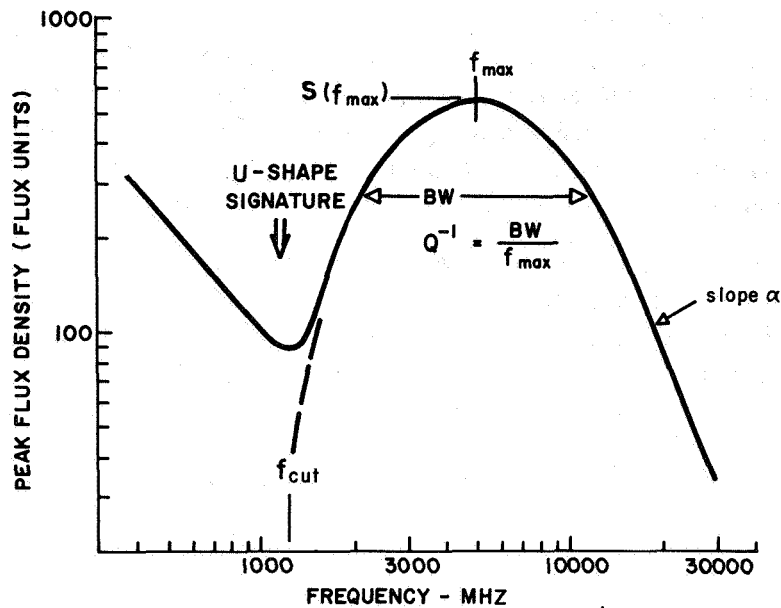
Figure 3. Idealized peak-flux-density spectrum of a radio burst (representative of actual burst spectra) used for burst classification, emission-region parameter estimation, and signature detection.

STATISTICAL DISTRIBUTIONS OF SPECTRAL PARAMETERS

To determine the distribution of the spectral types of radio bursts, we have considered the total number of bursts recorded without regard to intensity level or morphological class (impulsive, gradual rise-and-fall, complex, and so forth). Based on the 1968 to 1971 Sagamore Hill data, we obtain the data given below. The most significant finding to be gleaned from the spectral-type distribution data is that the type C spectrum, either alone (pure G) or with its decimeter tail (GC), accounts for about 75 percent of all radio bursts.

Percentage of Occurrence of Different Spectral Types

Pure type G	19
Pure type C	54
Type A	~1
Composite type (GC)	21
Miscellaneous type	5

To determine the intensity level distribution, we first considered all radio bursts without regard to morphological class or spectral type. Later we examined the intensity level distribution of the type G and type C components of the radio bursts. Based on the 1968 to 1971 Sagamore Hill data, we obtain the data listed. Only 8 percent of all bursts have peak flux densities at any frequency (centimeter or decimeter wavelengths) greater than 500 sfu. Only

92

3 percent of type C bursts or burst components have peak flux densities greater than 500 flux units. In general, the intensities of type G components are distributed more to the higher levels than for the type C components.

Intensity Level Distribution of Solar Radio Bursts

	Percentage Distribution		
	Int. 1	Int. 2	Int. 3
All bursts	66	26	8
Type G components	45	40	15
Type C components	80	17	3

Since such a large percentage of all radio bursts have a type C spectrum or spectral component, we decided to examine other statistical aspects of these bursts. Figure 4 shows the percentage distribution of the spectral maximum frequency (f_{max}) of type C burst spectra, based on 1968 to 1971 Sagamore Hill data. As measured by our widely-separated fixed-frequency radiometers, the greatest number of type C spectra have their observed f_{max} at 4995 MHz (C-band). However, the actual peak of the f_{max} distribution is probably around 6500 MHz. The percentage distribution for the observed f_{max} for the individual years, 1968 through 1971, is shown in Figure 5. While there are obvious statistical variations, the spectral distribution of f_{max} is fairly similar from year to year.

While the percentage distribution of f_{max} stays roughly the same, the actual number of bursts with type C spectra changes markedly from year to year through the course of the sunspot cycle. Figure 6 shows the yearly distribution of the total number of bursts with type C spectra or spectral component. For comparison purposes, the yearly mean flux density above that of the quiet sun at 4995 MHz is also plotted. To extend the comparison over a large portion of the sunspot cycle, burst data for the years 1966 and 1967 are also included, even though the K-band radiometric systems were not operational at Sagamore Hill during these years. With their absence, one could not distinguish between f_{max} occurring at X-band or K-band; however, since statistically only a small percentage (~12 percent) of type C spectra have f_{max} at K-band and most of these probably had some measured flux density at X-band (which was operational), very few bursts were lost and the burst count for 1966 and 1967 was probably not too adversely affected. The 4995 MHz (C-band) yearly mean flux density was chosen for comparison because C-band is the wavelength range in which the slowly varying component has its highest variation in flux density. Radio bursts originate in the active regions which rotate around the face of the sun; these "hot" regions are the source of the slowly varying component of solar radio emission. Thus, the similarity of the two distributions illustrated in Figure 6 is not altogether unexpected.

For gyrosynchrotron emission (magnetobremsstrahlung) from a given number and distribution of energetic electrons, in theory both the intensity and the spectral maximum frequency should increase with increasing magnetic field. Therefore, a logical continuation of this spec-
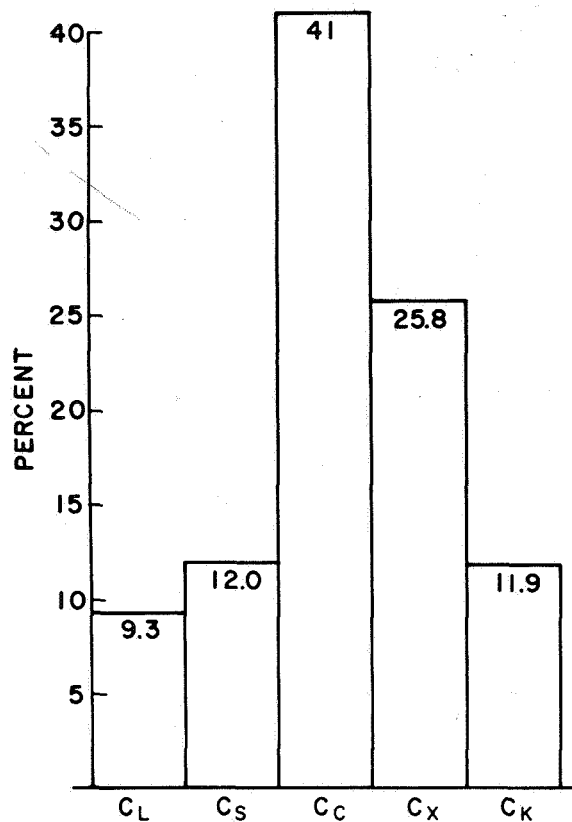
Figure 4. Percentage distribution of type C burst
spectra for 1968 to 1971, Sagamore. Subscripts
L, S, C, X, and K refer to wavelength ranges where
spectral maxima occurred.

tral study is the investigation of the variation in the distribution of f_{max} with intensity. Based on the 1968 to 1971 Sagamore Hill data, we obtain the spectral-band distribution of f_{max} of type C spectra for the three different intensity levels, as shown in Figure 7. The evidence for spectral hardening (the upward shift of the f_{max} distribution with increasing intensity) appears strongest for intensity 3 bursts, with not too much of a change indicated between the intensity 1 and intensity 2 distributions. We see that, when the peak flux density exceeds 500 sfu, the greatest percentage of type C spectra have their f_{max} at K-band (15 GHz or above). Very few of the most intense events (great bursts) have spectral maxima below 5 GHz.

While, in general, no regard was given to separation according to morphological class in tabulating the burst spectra, it was decided to look into the spectral character of one particular class: the gradual rise-and-fall burst. It was obvious that for all bursts taken together, the overall percentage having even a *possibly* thermal spectrum was rather small — less than 5 percent. Since the large majority of microwave bursts fall in the weak implusive class, ther-
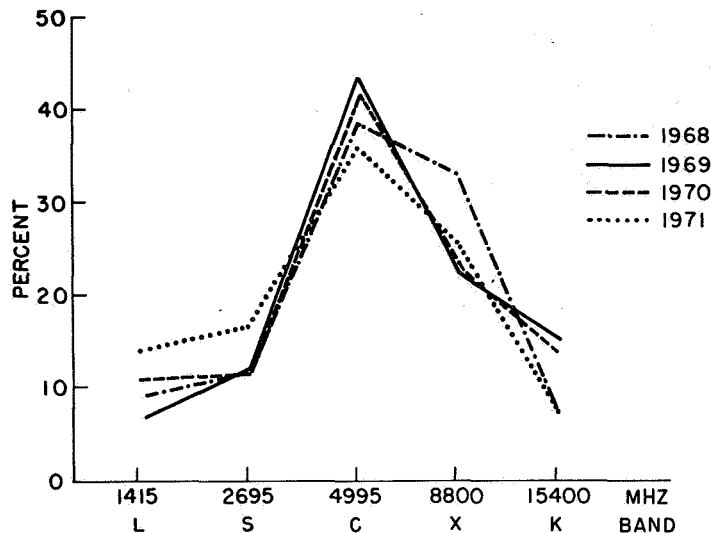
Figure 5. Distribution of percentage of type C spectra peaking
in different frequency bands as a function of year (Sagamore
Hill data).

mal radiation (bremsstrahlung) is clearly not the emiss̸ì̸ ̸ ̸ ̸ ̸ ̸ ̸ ̸ ̸ ̸ ̸ ̸ ̸ ̸ ̸ ̸ ̸ ̸ ̸ ̸echanism responsible for this class of microwave bursts. As for the great complex bursts, both observational and theoretical considerations rule out thermal radiation as the principal emission mechanism. However, in the past it had been suggested by some solar astronomers (Kundu, 1963) that gradual rise-and-fall centimeter bursts appear to have thermal origin.

We selected out and studied the peak flux density spectra of the gradual rise-and-fall bursts recorded at Sagamore Hill, 1968 to 1971. The following criteria were used for judging the presence of a possibly thermal spectra: (a) a sharp rise in peak flux density with increasing frequency to a value at least five times the lowest peak flux density recorded in the cm range (L-band or above), and (b) a relatively flat top at frequencies beyond the steep rise, so that for $f > f_{max}$ the observed peak flux densities are no more than 20 percent less than that at f_{max}. In the case of type A spectra, we assumed that they could be flat at frequencies beyond our patrol (>35 GHz) so that, if its rise was steep, a type A spectrum was considered *possibly* thermal. The results of our investigation are shown in Table 1. Overall, only about 20 percent of all gradual-rise-and-fall bursts were found to have *possibly* thermal spectra. Under more stringent criteria, the percentage could be far less. In conclusion, we
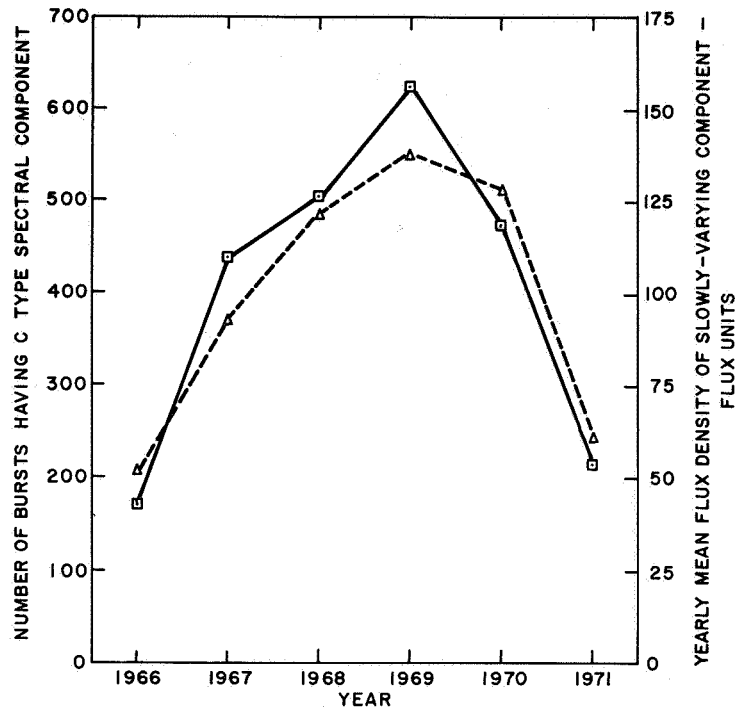
Figure 6. Comparison of the number of bursts with type C spectral component (solid line) with the yearly mean flux density above the quiet sun (taken as 96 sfu) at 4995 MHz (broken line). (Sagamore Hill data.)

96

find that it is doubtful that thermal emission is the principal mechanism even for the gradual rise-and-fall bursts.
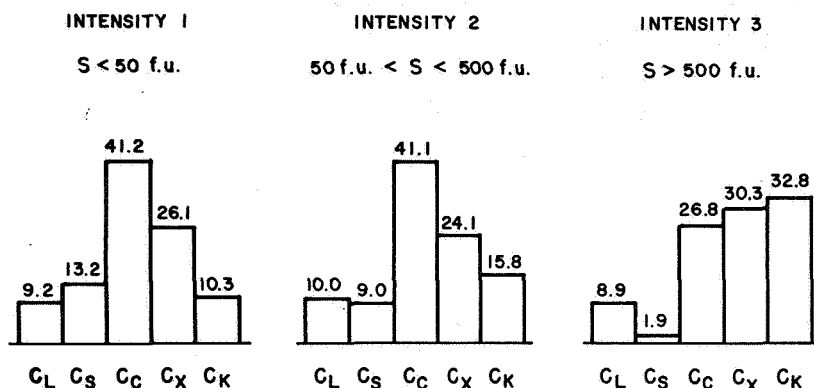
Figure 7. Percentage distribution of spectral maxima of type C spectra for the three intensity levels. The spectral hardening (upward shift of f_{max}) for intensity 3 bursts is quite noticeable.

Table 1
Spectral Classification of Gradual Rise-and-Fall Bursts.

	1968	1969	1970	1971	Total Four Years
Gradual rise-and-fall bursts considered	115	137	85	50	387
Miscellaneous type C spectra	94	114	62	40	310
Possible thermal spectra	21	23	23	10	77
Percent miscellaneous type C spectra	81.7	83.2	71.9	80.0	80.1
Percent possible thermal spectra	18.3	16.8	28.1	20.0	19.9

PHOTOSPHERIC MAGNETIC FIELD AND BURST SPECTRAL MAXIMUM

Since the dominant mechanism for microwave bursts is thought to be gyrosynchrotron emission, it would be expected that the f_{max} of type C bursts would be indicative of the magnetic field strength in the burst region. Unfortunately, magnetic field strength at burst heights (chromosphere) is not measurable directly. However, assuming that chromospheric

fields are somewhat related to photospheric fields (which are measurable by the Zeeman effect on optical emission lines), one might expect a general trend of correlation between f_{max} and photospheric magnetic field strength.

We have looked for experimental evidence of this correlation using the Sagamore Hill radio burst data and the Mt. Wilson magnetic field data. The photospheric magnetic field strength of the region associated with a radio burst is determined (when it can be) by finding the optical flare corresponding to the radio burst (mainly by time coincidence) and locating the region of flare occurrence on the sun, and then obtaining the Mt. Wilson magnetic field data on this region. For an appreciable number of bursts (more than half) no successful association with a flare region could be made for any of several reasons (no flare reported, no reasonable time coincidence with any flare reported, more than one flare reported in different areas of the sun at about the same time as the radio burst, or no Mt. Wilson observations on the days involved).

The results of our experimental investigation are presented in Figure 8. For *each* f_{max} band, the ratio (as a percentage) of the number of type C bursts identified with photospheric mag-
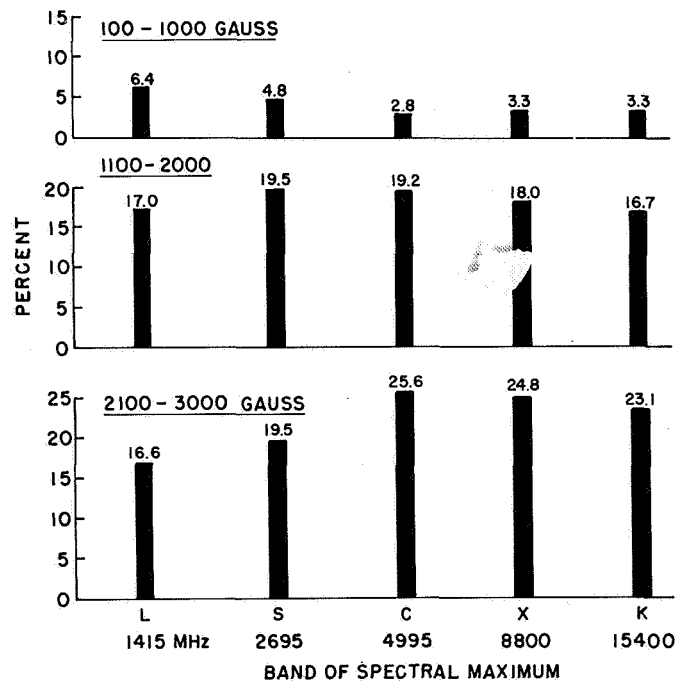
Figure 8. Ratio (for each f_{max} band) of type C bursts identi-
fied with photospheric magnetic field strengths of various levels
to all type C with f_{max} in that band (Sagamore Hill data).

netic fields of various levels (100 to 1000, 1100 to 2000, and 2100 to 3000 gauss) to the *total* number of type C bursts having their f_{max} in that band is shown. This normalized ratio is used to equalize the data base for each f_{max} band, since the distribution of f_{max} is not uniform (it is highly peaked at C-band; see Figure 4). For low fields (100 to 1000 gauss) we see a relatively greater correspondence with bursts having a low f_{max} (L-band), while for high fields (2100 to 3000 gauss) the greatest correspondence occurs for bursts having their f_{max} between C- and X-bands. We also see a greater *increase* in the percentage of bursts correlated with regions of high fields (2100 to 3000 gauss) for bursts with f_{max} at X-band or K-band than for bursts with f_{max} at L-band or S-band. Unfortunately, the f_{max}-associated tendencies are overshadowed by the overall higher correlation of bursts with regions of strong magnetic field for all type C bursts *irrespective* of their f_{max} band, caused principally by the low likelihood of burst occurrence in regions of low magnetic field strength.

We realize that the strength of the underlying photospheric magnetic field in a burst region is only one factor in determining the radio burst spectra. There are other correlative parameters such as sunspot configuration and area, magnetic configuration, and so on, which should have varying degrees of influence on the emission spectra produced. For example, akin to the greater burst occurrence associated with stronger magnetic fields, in a distribution of burst occurrence versus sunspot magnetic class there is a greater likelihood of burst occurrence for the more complex magnetic regions. Figure 9 (unfortunately, based only on 1970 data) shows the percentage of correlated type C spectra (all f_{max} bands) for various sunspot magnetic classes. The greatest correlation occurs for the δ class, which has the most complex configuration.
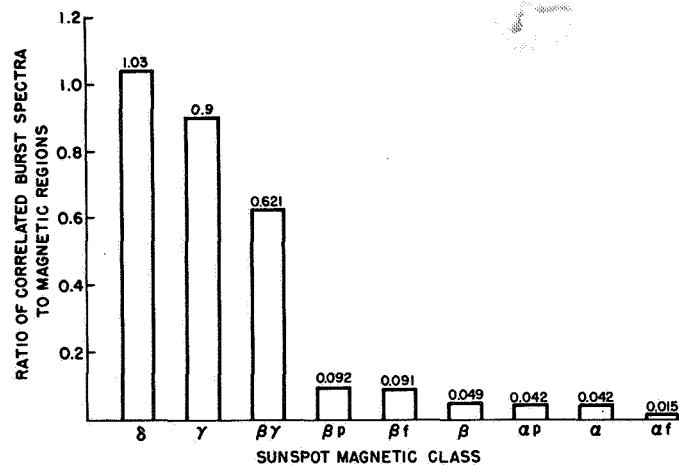
Figure 9. Centimeter burst productivity for different magnetic
regions according to Mt. Wilson classification for 1970 radio
burst data from Sagamore Hill.

It should be apparent that the statistical investigations reported here constitute only a small beginning into what may eventually prove to be a most enlightening study of the relationship between magnetic field parameters and radio-burst parameters.

RELATION BETWEEN f_{max} AND f_{cut} IN TYPE C COMPONENTS

For some peak flux-density spectra, the flux density on the low-frequency side of the spectral maximum (f_{max}) decreases rather abruptly, reaching an apparent cutoff within an octave or so below f_{max}. For other spectra, the peak flux density decreases less steeply, taking perhaps a decade below f_{max} before it decreases to a value one-tenth or less than that of f_{max}. When the spectrum has a decimeter tail (composite GC spectra), the flux density on the low-frequency side of f_{max} may not reach a value much less than one-third to one-fourth that at f_{max} before the decimeter tail causes it to start increasing with decreasing frequency. (In these cases, the decimeter type G component would have to be subtracted in order to obtain a meaningful estimate of the f_{cut} of the type C (centimeter) component.) From this casual overall look at type C spectral properties, the question arises on how does the so-called cutoff frequency (f_{cut}) on the low-frequency side relate to f_{max} on a statistical basis.

To hold the investigation to a modest effort, certain limitations and simplifications had to be made. Because of the difficulty in determining f_{cut} for low-intensity bursts, only bursts with a type C (centimeter) component of intensity 2 or 3 (peak flux density $\geq$ 50 sfu at f_{max}) were considered. This step limited the data base to ~350 bursts (compared to >2000, if intensity 1 bursts were included), thus permitting a scatterplot of f_{cut} versus f_{max} without overcrowding. Although certainly not the optimum definition, for simplicity f_{cut} was defined as the frequency below f_{max} at which the flux density of the high-frequency component (type C) was 10 dB below the flux density at f_{max}, using a best fit hand-drawn (as estimated by the data analyst) parabolic curve to the experimental (patrol frequency) data points. When a decimeter G component was present along with the type C (about 30 percent of the bursts), it was removed by extending its slope and subtracting its apparent contribution in the centimeter range. (Usually, the flux density at the lowest-intensity data point in the valley between the dm-G and cm-C components was divided into equal dm-G and cm-C values, which were then used to draw the estimated curves for the separated dm-G and cm-C components.)

By its definition, the location of f_{cut} was not restricted to patrol frequencies. In addition, because the parabolic fitting usually moved the maximum of the resulting curve somewhat away from the data-point frequency, the location of f_{max} was also freed from the restriction to patrol frequencies. Therefore, a scatterplot of f_{cut} versus f_{max} would not suffer from the problem of having all its data points stacked along a few horizontal and vertical lines corresponding to the patrol frequencies.

The results of our investigation based on 1968 to 1971 Sagamore Hill observations are presented in Figure 10, a scatterplot of f_{cut} versus f_{max} for the type C component of bursts

100
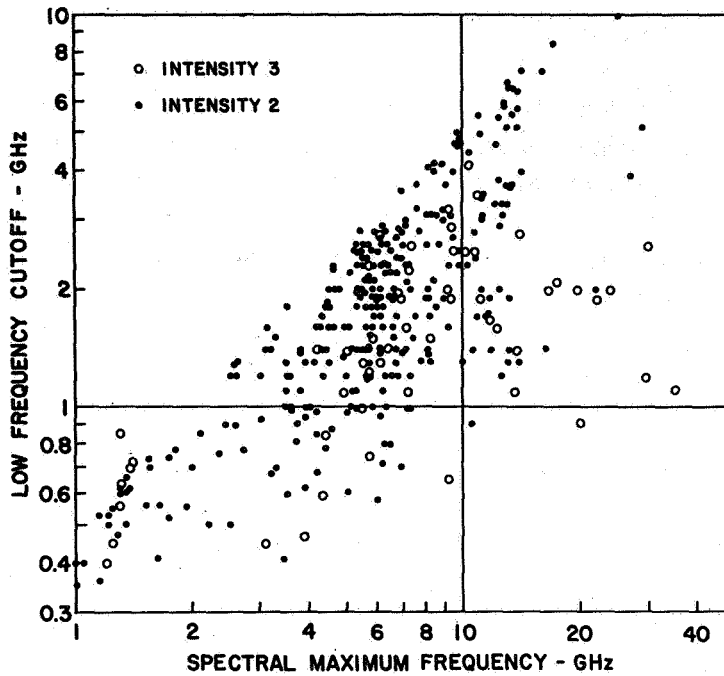
Figure 10. Scatter-plot of f_{cut} versus f_{max} for radio bursts with type
C component of intensity 2 (50-500 sfu) and intensity 3 (>500 sfu)
for 1968 to 1971 (Sagamore Hill data).

with peak flux densities greater than 50 flux units. We see that f_{cut} is well correlated with f_{max} for intensity 2 bursts (small closed circles), but not as well correlated for intensity 3 bursts (larger open circles). By computer, we found the lea~~ares best-fit straight lines on the log-log scale (Figure 10) for intensity 2 and 3 bursts taken together and separately. These lines correspond to the best-fit power-law curves of the form $f_{cut} = A(f_{max})^B$. The correlation coefficient R is given for each set listed.

Intensities 2 and 3	$f_{cut} = 0.48\,(f_{max})^{0.69}$	R = 0.72
Intensity 2	$f_{cut} = 0.41\,(f_{max})^{0.81}$	R = 0.78
Intensity 3	$f_{cut} = 0.60\,(f_{max})^{0.42}$	R = 0.62

Beside having the greater correlation coefficient, the best-fit line for intensity 2 bursts has a much steeper slope than that for the intensity 3 bursts (almost twice as steep, a power law of 0.81 compared to 0.42). In fact, the best-fit power law is not too different from unity. For intensity 2 bursts only, we computed the least-squares best-fit "straight line of 45° slope" on the log-log plot. This corresponds to the best-fit unity-power-law curve of the restricted form $f_{cut} = Kf_{max}$. We obtained: For intensity 2, then, $f_{cut} = 0.294\,f_{max}$, or expressed reciprocally, $f_{max} = 3.4\,f_{cut}$.

What information regarding solar burst mechanisms can we gain from the f_{cut} versus f_{max}

plot? Let us consider three hypothetical situations. If f_{cut} values were random and substantially independent of f_{max}, we should see the points distributed all over the graph and a low value of correlation coefficient. This situation would occur when f_{cut} had no close dependence on any parameter having a limited range of values or an association with f_{max}. If f_{cut} values were substantially independent of f_{max} but *not* randomly distributed (that is, concentrated around a relatively narrow range of f_{cut}, we should see a best-fit curve of the form $f_{cut} = A(f_{max})^B$ with $B \approx 0$ (that is, f_{cut} = constant) and a moderately high value of correlation coefficient. This situation could be caused by a dependence of f_{cut} on a parameter which itself has a limited range, but no association with f_{max}. For example, the plasma frequency f_p depends on the electron density N_e, but not on the magnetic field H (which we know influences f_{max}). The narrow-ranging of f_p (and consequently of f_{cut}) could be caused by the emission height of radio bursts being restricted to a narrow range of solar altitudes, thus restricting N_e and f_p. If f_{cut} values were substantially dependent on f_{max}, we should see a fairly high value of correlation coefficient and a best-fit curve of the form $f_{cut} = A(f_{max})^B$ with B in the broad neighborhood of unity (it could be ½ or 2, the particular value would depend upon the linking parameter's relationship with f_{cut} and f_{max}). This situation would occur when the mechanism determining f_{max} also determines f_{cut}. For example, if the emission spectrum is shaped by severe and *systematic* attenuation of the first few harmonics of the gyrofrequency f_H ($f_H \propto H$) so that $f_{max} = Kf_H$, where K is a number not dependent on f_H, then the location of the frequency (f_{cut}) where the flux density is 10-dB down will certainly depend on the location of the burst's f_{max}.

For intensity 3 bursts (mainly, the great complex bursts), the actual f_{cut} versus f_{max} distribution we obtained (Figure 10) does not clearly favor any of the three hypothetical situations cited above. It appears possibly to be a mixture of all three situations. Since these results for intensity 3 bursts are at present inconclusive, insight into the emission mechanisms of the great complex bursts can be gained from our statistical f_{cut} versus f_{max} studies at this time.

For intensity 2 bursts, however, we have a very different finding. The experimental results clearly favor the third situation hypothesized: f_{cut} highly correlated with f_{max} and a near-linear (unity power law) relationship between f_{cut} and f_{max}. The intensity 2 bursts are for the most part made up of moderate-size impulsive bursts, although no deliberate morphological separation was intended. Most great complex bursts were excluded (from intensity 2 level) by their being too intense. Most gradual rise-and-fall bursts were excluded by the choice of *peak* flux density (rather than some "time-duration-inclusive" measure such as *integrated* flux density) as the criterion of intensity. Comparatively few gradual-rise-and-fall bursts have a peak flux density greater than 50 flux units, although the integrated flux density of most gradual-rise-and-fall bursts would exceed that of most impulsive bursts. *Weak* impulsive bursts were also excluded by the 50-sfu peak flux density criterion, but there is no reason to believe that impulsive bursts of <50 sfu are significantly different in mechanism from impulsive bursts of >50 sfu. We will, therefore, apply our conclusions based on "moderate" impulsive bursts to all impulsive bursts.

102

For impulsive bursts (weak to moderate), we find that the statistical evidence supports the theory (Takakura, 1967; Takakura and Kai, 1966) that the centimeter radiation results from barely to mildly relativistic electrons in strong magnetic fields, with the spectra shaped by the severe attenuation of the lower-order harmonics of the gyrofrequency, causing the observed spectrum to be peaked at an $f_{max} \approx 3$ or 4 f_H. Since for intensity 2 bursts, we found f_{max} related to f_{cut} over a broad range of values (between 2 and 12) statistically centered at $f_{max} = 3.4$ f_{cut}, then f_{cut} (as we have defined it) appears to be on the order of the gyrofrequency f_H. Our results in no way distinguish between the various attenuation mechanisms postulated as being responsible for the low-frequency attenuation. These proposed mechanisms include ionized-medium suppression or gyroabsorption of the lower harmonics of f_H, thermal (free-free) absorption in the outer layers of the emitting region, and synchrotron self-absorption if the emitting-region angular size is very small (very high brightness temperature).

ACKNOWLEDGMENTS

REFERENCES

Castelli, J.P., Aarons, J., and Michael, G.A., 1967, *J.G.R.* 72, 5491.

Castelli, J.P., and Guidice, D.A., 1970, *Proc. IEEE G-AP Internat. Symp.* (Columbus, Ohio), 70C-36-AP, 88.

Kundu, M.R., 1963, *Proc. AAS-NASA Symp. on Physics of Solar Flares* (Greenbelt, Maryland), NASA SP-50, 335.

Takakura, T., 1967, *Solar Phys.* 1, 304.

Takakura, T., and Kai, K., 1966, *Publ. Astron. Soc. Japan* 18, 57.

MILLIMETER WAVELENGTH OBSERVATIONS OF SOLAR ACTIVE REGIONS

M.R. Kundu

Astronomy Program, University of Maryland

ABSTRACT

Polarization properties of active regions at 9 mm are discussed, and the observed degree of polarization is used to obtain an estimate of chromospheric magnetic fields. Also discussed is the polarization structure at 9 mm of an active region that produced a minor flare around 1900 UT on September 28, 1971. Total power observations indicate that new regions develop, or weak regions intensify at millimeter wavelengths as a result of bursts at distant sites. The spectra of the peak flux density of moderately strong bursts observed at 9 mm show a sharp drop toward the shorter millimeter wavelengths. The weak bursts at 3.5 mm are manifest mainly as heating phenomena.

INTRODUCTION

High resolution observations of the sun have been made at 9.5-mm and 3.5-mm wavelengths, using the 85-foot diameter telescope of the Naval Research Laboratory and the 36-foot diameter telescope of the National Radio Astronomy Observatory. The half-power beamwidth of the 85-foot telescope at 9.5 mm is 1.6 arcmin; the 36-foot telescope has half-power beamwidths of 1.2 and 3.5 arcmin at 3.5- and 9.5-mm wavelengths. Both telescopes are equipped with circular horns followed by a quarter-wave plate and a dual-mode transducer. In this arrangement, complete information can be obtained on the circular polarization of the source being investigated. In this paper we discuss the properties of the polarization structure of active regions at 9.5-mm wavelength, as well as the evolution of the total power structure of active regions leading to bursts at both 9.5- and 3.5-mm wavelengths.

POLARIZATION OF ACTIVE REGIONS AT 9.5-mm WAVELENGTH

Figure 1 shows an example of a polarization (R – L) map, along with the total intensity (R + L) map, Hα picture, and Mt. Wilson magnetogram for September 27, 1971. The essential features of the polarization structure of active regions at 9.5 mm can be described as follows (Kundu and McCullough, 1972):

Each prominent active region in the total power map is found to be bipolar in nature, and the line of zero polarity, the neutral line, often passes somewhere near the peak of the region. The R – L maps show an almost one-to-one correspondence with the Mt. Wilson magnetograms. All the significant magnetic features of the magnetograms appear on the 9.5-mm R – L maps; the millimeter and Mt. Wilson regions also appear to be identical in
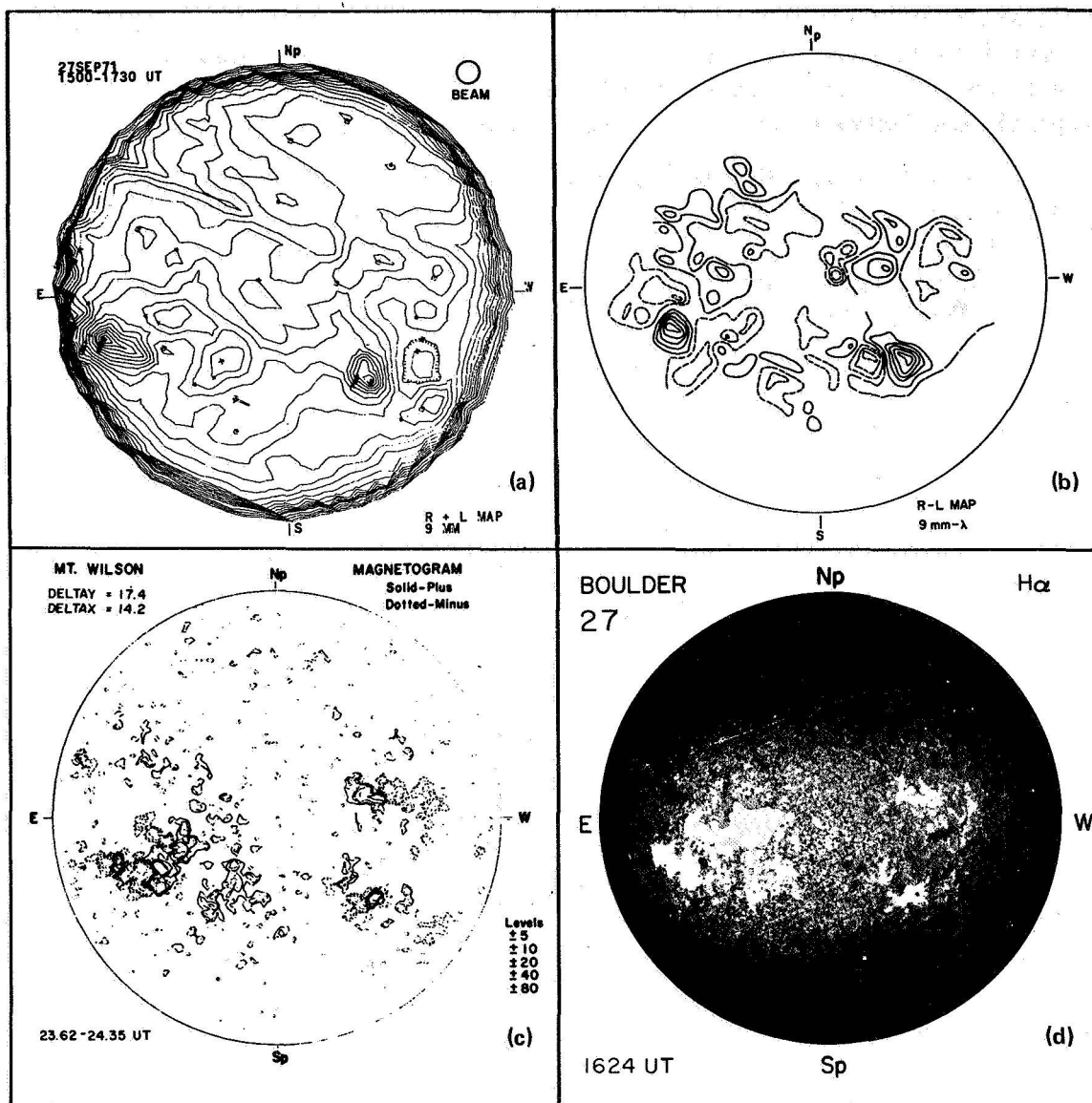
Figure 1. (a) Total intensity (R + L) map of the sun at 9.5 mm for September 27, 1971. The outermost contour has a temperature of 6900 K; the contours are plotted at intervals of 100 K. Regions marked by small dashes are temperature depressions. (b) Circular polarization (R - L) map. Solid and dashed lines correspond to plus (R) and minus (L) values of R - L signals respectively. Long dashed lines correspond to zero polarization. The L and R polarities of 9.5-mm maps correspond to minus (dashed) and plus (solid) polarities on magnetograms, respectively. Polarized intensity contours are plotted at intervals of ±3 K. (c) Mt. Wilson magnetogram. (d) Hα picture.

extent in most cases. The magnetogram features near the limb do not show up in the R − L maps, because of the difficulty of measuring polarization near the limb (see Kundu and McCullough, 1972). Because of the relatively poorer resolution at 9.5 mm (1.6 arcmin compared to 17 arcsec for magnetograms), many of the small magnetic features on magnetograms are seen as weak but large regions of one dominant polarity on the R − L maps. The polarization of 9.5-mm active region emission is in the extraordinary mode.

On September 28, 1971 a flare of importance -B occurred at 1857 UT (maximum at 1902 UT) in position S02 E32. (This region is the same as the prominent southeastern region on the R + L map of September 27, 1972.) Simultaneously there was a burst at 10.7-cm wavelength, which started at 1857 UT and ended at 1930 UT with maximum around 1900 UT. The burst was also observed at 9.5 mm. The active region where the flare occurred was observed on magnetograms as one of complex polarization structure. However, because of comparatively poor resolution, at 9.5-mm wavelength, the region showed up as a simple bipolar region. Both the R- and L-circular regions were 2 percent polarized. The neutral region, as is usually the case, passed near the intensity peak of the region. Near the flare maximum (1903 UT), the intensity at 9.5-mm wavelength increased by about 900 K from the preflare intensity; 24 minutes after the flare maximum, the intensity decreased below the preflare level to ⁻900 K. The Hα flare ended at 1920 UT. Approximately 30 minutes later the 9.5-mm peak intensity of the region decreased even further to 600 K. We believe that the excess brightness temperature of 1100 K observed at 1550 UT may have been due to preflare heating of the region. Consequently the decrease of intensity below the preflare level observed at 1927 and 1948 UT might imply that after the flare the region came to the level that existed before the heating occurred. The degree of circular polarization decreased from 2 percent before the flare to 1.5 percent immediately after the flare maximum. After the flare, the degree of polarization still remained high at least an hour after the flare maximum. The entire bipolar flare region could not be scanned during the flare maximum; however, after the flare maximum, the region could be mapped entirely. One observes considerable change in the polarization structure of the region, particularly in the right circularly polarized region (Figure 2). The latter region which was simple before the flare broke up into three distinct regions after the flare (1948 UT). There is definite suggestion of the L-component undergoing some structural change also.

| SE ACTIVE REGION | REGION DURING FLARE | REGION AFTER FLARE (1) | REGION AFTER FLARE (2) |
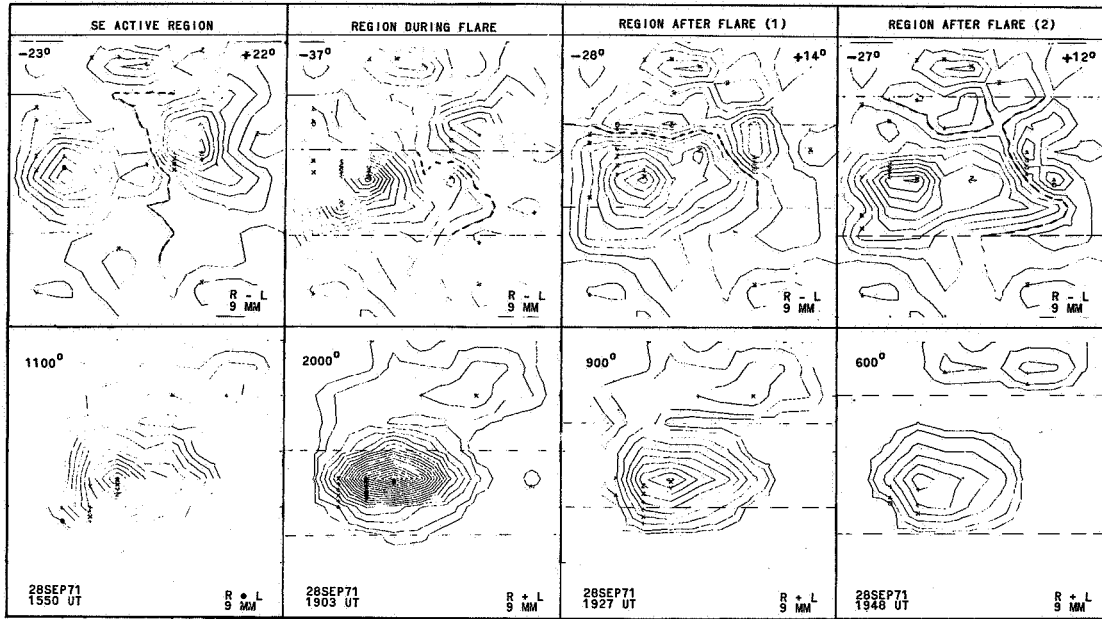
Figure 2. The (R + L) and (R − L) maps of the active region that produced a flare at 1857 UT September 28, 1971. Maps at 1550 UT correspond to the preflare region; those at 1903 UT were taken around the flare maximum; those at 1927 and 1948 UT were obtained after the flare maximum. Temperatures at the top of each R − L map give the peak polarized intensities of the R and L components; the temperature on the top of each R + L map gives the excess brightness temperature of the region.

ESTIMATE OF CHROMOSPHERIC MAGNETIC FIELDS

One important objective of the polarization measurements is to determine magnetic fields at chromospheric levels. For the active regions the exact computations of magnetic fields are complicated since the regions are optically thick. However, an estimate of magnetic fields in active regions can be obtained through the simplified calculations as follows:

$$p = \frac{T_{be} - T_{bo}}{T_{be} + T_{bo}} \tag{1}$$

where p is the observed degree of circular polarization; T_{be} and T_{bo} are the brightness temperatures for the extraordinary and ordinary waves. In the above relation, it is assumed that there is no coupling between the two waves. Now

$$T_{be} + T_{bo} \approx 2T_b \tag{2}$$

107

where T_b is the brightness temperature for the unpolarized wave. Therefore, combining Equations (1) and (2), we get

$$T_{bo} = T_b (1 - p)$$

and

$$T_{be} = T_b (1 + p)$$

Using the relation $T_{bo} = T_e (1 - e^{-\tau_o})$, where T_e is the electron temperature, we get τ_o, the optical thickness in the ordinary mode. Similarly, from the relation $T_{be} = T_e (1 - e^{-\tau_e})$, we get τ_e, the optical thickness in the extraordinary mode. τ_o and τ_e are related to τ_n, the optical thickness in the absence of magnetic field, and y_L by the relations (for example, see Kundu, 1965)

$$\tau_o = \frac{\tau_n}{(1 + y_L)^2} \quad \text{and} \quad \tau_e = \frac{\tau_n}{(1 - y_L)^2}$$

Therefore

$$\tau_o = \left(\frac{1 - y_L}{1 + y_L}\right)^2 \tau_e$$

We have used this relation to determine magnetic fields at the levels of the chromosphere where 9.5-mm radiation originates. We find typical values of 300 to 500 gauss in moderately active regions. These values of magnetic fields obtained in plage regions are quite consistent with the high photospheric fields of several hundred gauss obtained by Livingston and Harvey (1969).

As we know, the burst at centimeter wavelengths is optically thin during the postburst phase. Since our measurements were made during periods after the flare maximum, we can probably assume that the burst at 9.5-mm wavelength is also optically thin. Consequently, we can easily convert the excess polarization observed immediately after the burst maximum by the simple relation (for example, see Kundu, 1965)

$$p = \frac{2y_L}{1 + y_L^2}$$

where p is the observed degree of polarization, and y_L is related to the longitudinal component of the magnetic field H_L (in gauss) through the relation $y_L = 2.8 H_L / f$, where f is the frequency in megahertz. The resulting magnetic field immediately after the burst maximum is found to be about 100 gauss. This value is less than that derived from polarization observations of a single centimeter-wave burst (Gelfreikh, 1962).

108

PROPERTIES OF BURST REGIONS AT 9 AND 3.5 mm

The bursts observed at 9 mm are usually flare-associated. The burst of March 3, 1970, was an important one. During this burst, the active region was scanned repeatedly over a period of an hour; the resulting sets of scans are shown in Figure 3. It is clear that the active region at the west limb increased greatly in intensity around 2050 hours. The angular size of the burst region is 2.1 arcmin and the excess brightness temperature of the burst is about 2500 K. The flux density is about 5.8×10^{-22} W $\cdot$ m^{-2} Hz^{-1}. It is interesting to note that some regions situated quite far from the burst region were disturbed as a result of the flare. This is quite similar to distant activation often observed in Hα. A new region (a in Figure 3) seems to have developed near the center as a result of the burst. The region a was observed through the end of March 4.
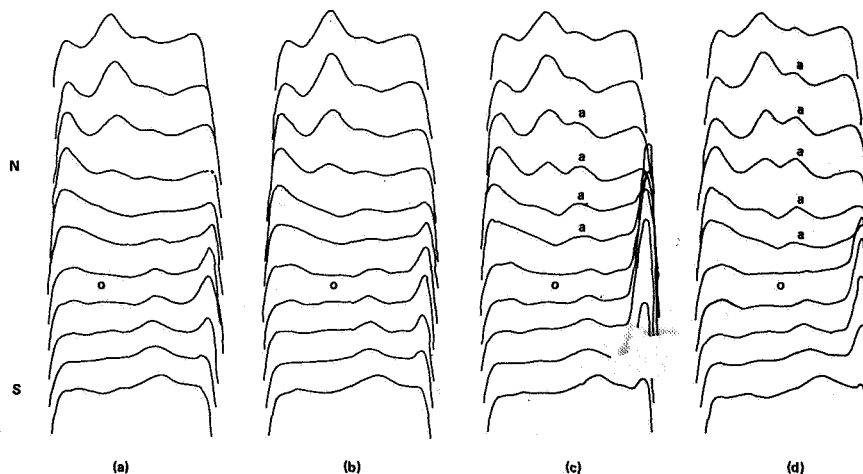
Figure 3. Four sets of scans illustrating the development of a burst at 9 mm on March 3, 1970. (a) Undisturbed sun scans at 1847 UT. (b) Scans near start of burst at 2001 UT. (c) Scans near burst maximum at 2033 UT. (d) Postmaximum scans at 2110 UT. The scan marked 0 is the scan through the center of the sun. The upper and lower scans in each set are successive northern and southern scans at intervals of 1 arcmin. Note the development of a new region marked a, caused by distant activation initiated by the burst at 9 mm.

For two other bursts observed on March 1 and 4 (Figure 4), the burst sizes are estimated to be 2.8 and 0.9 arcmin, respectively. The excess brightness temperatures of the bursts are 3500 K and 2800 K and the flux densities are 13.6×10^{-22} W $\cdot$ m^{-2} Hz^{-1} and 2.1×10^{-22} W $\cdot$ m^{-2} Hz^{-1}, respectively.
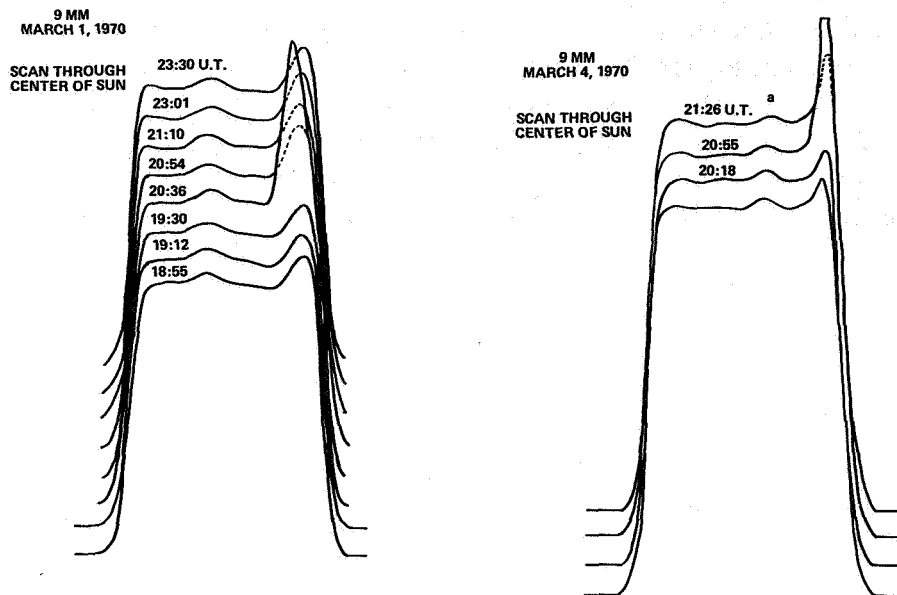
Figure 4. Scans at 9 mm through the sun's center at different times on March 1
(at left) and March 4, 1970. Note the development of bursts. The region a that
developed as a result of the burst on March 3 (Figure 3) persists on March 4 also.

The spectra of the two bursts observed at 9 mm on March 1 and 3, 1970, are shown in
Figure 5. The spectra show a sharp drop toward the shorter millimeter wavelengths. The
mechanism for these millimeter wavelength radiation from solar bursts is believed to be
gyrosynchrotron radiation.

To date, at 3.5 mm we have observed no burst in association with flares. However, often the
3.5-mm active regions have been observed to exhibit burstlike phenomena. An example is
shown in Figure 6. These transient features usually last from about 10 minutes to 2 hours.
They are similar to the gradual rise and fall types of bursts observed at centimeter
wavelengths, and are probably manifestations of local excitation and heating. Such events
are often not associated with any flare or subflare. Perhaps such phenomena are
manifestations of chromospheric instability which gives rise to detectable emission at 3.5
mm, but not enough to produce any visible effect in the Hα. The size of the burst region in
Figure 6 is about 2 arcmin and its excess brightness temperature is about 700 K. These
3.5-mm burst phenomena appear to be similar to the "thermal bursts" reported by
Shimabukuro (1972) at 3.3-mm wavelength.
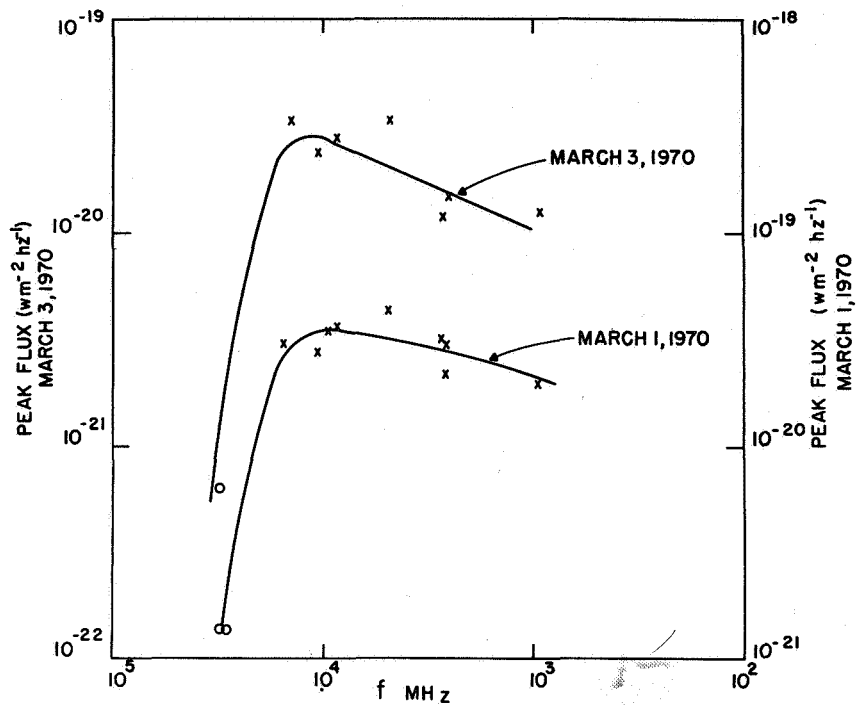
Figure 5. The flux density spectra of the bursts observed on March 1 and 3, 1970. The values at wavelengths other than 9 mm were taken from *Solar Geophysical Data*.
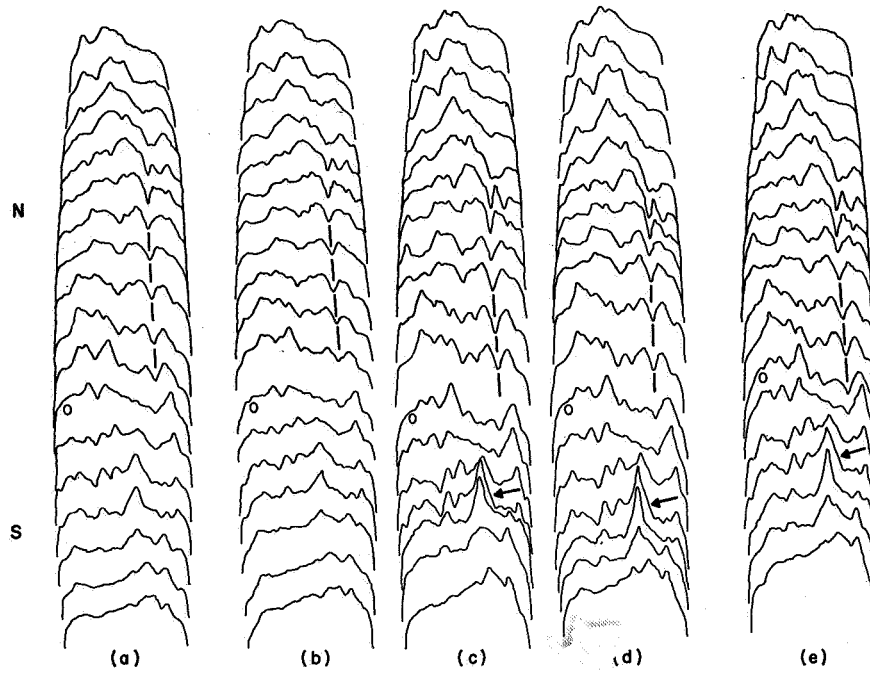
Figure 6. Five sets of active region scans at 3.5-mm wavelength. The scan marked 0 is the scan through the center of the sun. The upper and lower scans in each set are successive northern and southern scans at intervals of 1 arcmin. The short vertical lines indicate the depression areas. The arrows indicate burstlike features. (a) 2125 UT. (b) 2155 UT. (c) 2222 UT. (d) 2249 UT. (e) 2313 UT.

REFERENCES

Gelfreikh, G.B., 1962, *Solnechnye Donnye Biulleten* (Moscow) **5**, 67.

Kundu, M.R., 1965, *Solar Radio Astronomy* (New York: John Wiley—Interscience Publishers), 234.

Kundu, M.R., and McCullough, T.P., 1972, *Solar Phys.* **24**, 133.

Livingston, W., and Harvey, J., 1969, *Solar Phys.* **10**, 294.

Shimabukuro, F.I., 1972, *Solar Phys.* **23**, 169.

SOLAR MILLIMETER-WAVE BURSTS

David L. Croom
Science Research Council
Radio and Space Research Station
Slough, England

ABSTRACT

During the current solar cycle there has been a considerable increase in solar burst observations in the region above 10 GHz (wavelengths less than 3 cm). These observations have shown that many major solar events have large millimeter-wave components, and that the total burst radio energy is frequently concentrated in this part of the spectrum.

INTRODUCTION

Prior to the current solar cycle, almost all solar radio astronomy observations were made at wavelengths longer than 3 cm, with the main emphasis being placed on events at meter and decimeter wavelengths. However, as long ago as 1948, Piddington and Minnett (1949) carried out solar burst monitoring at a wavelength of 12.5 mm. Although this was close to sunspot maximum, in four months of observation they observed no events greater than about 60×10^{-22} W $\cdot$ m^{-2} Hz^{-1} peak increase. Later observations by Hagen and Hepburn (1952) at the still shorter wavelength of 8.5 mm did result in some records of events up to nearly 600×10^{-22} W $\cdot$ m^{-2} Hz^{-1}, but these were neverthe weaker in intensity than the corresponding events at longer wavelengths. It thus seemed that millimeter bursts were little more than the high frequency tails of what were essentially centimeter-, decimeter-, and meter-wavelength events. However, in 1959 Coates (1966) recorded three events at 4.3 mm, one of which was clearly more intense than the corresponding 3- and 9-cm events. Nevertheless, because of instrumental and atmospheric problems and the wider variety of activity at longer wavelengths, there were no further observations of large millimeter events in the 19th solar sunspot cycle.

RECENT OBSERVATIONS AT WAVELENGTHS LESS THAN 3 CM

However, early in the 20th cycle a few observatories (see Table 1) started to carry out long term observations of solar bursts at these very short wavelengths, by monitoring the integrated output of the whole solar disk. In addition, other observatories, notably Bonn (Germany) at 8.5 mm, Aerospace Corporation (United States) at 3.3 mm, and Queen Mary College (United Kingdom) at 1.2 mm, carried out less regular solar mapping observations using narrow-beam antennas, which enabled much weaker events to be detected. These observations have served to demonstrate quite clearly that millimeter bursts are not only not

114

Table 1
Observatories Operating Long-Term Programs of Solar Burst Monitoring at Frequencies Above 15 GHz

Frequency (GHz)	Wavelength (mm)	Observatory	Country
71	4.2	Slough	U.K.
37	8.1	Slough	U.K.
35	8.5	AFCRL*	U.S.A.
35	8.5	Tokyo	Japan
19	15.8	Slough	U.K.
17	17.6	Tokyo	Japan
15.4	19.5	AFCRL*	U.S.A.

*Air Force Cambridge Research Laboratories.

as rare as was previously believed, but that they can be extremely intense (Croom and Powell, 1969) and can represent an important and sometimes major part of the emitted radio energy (Croom, 1971a). Figure 1, for example, shows the spectrum of an event, which although having its peak power density increase in the conventional region below 10 GHz (3 cm), nevertheless has more than half of its energy in the short wavelength region (<3 cm).
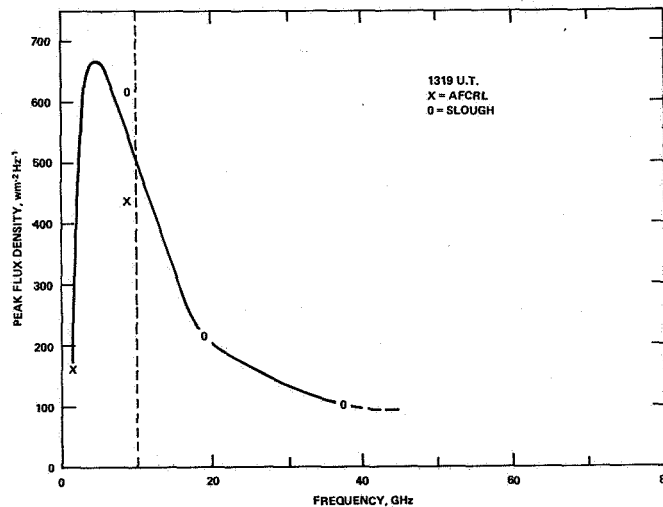
Figure 1. Peak flux density spectrum for the burst of June 15, 1970 (1319 UT).

Figure 2 illustrates an event which has almost all its energy, together with its peak power density, in the millimeter region. (Both these events are from the prolonged series of flares of mid-June 1970.)
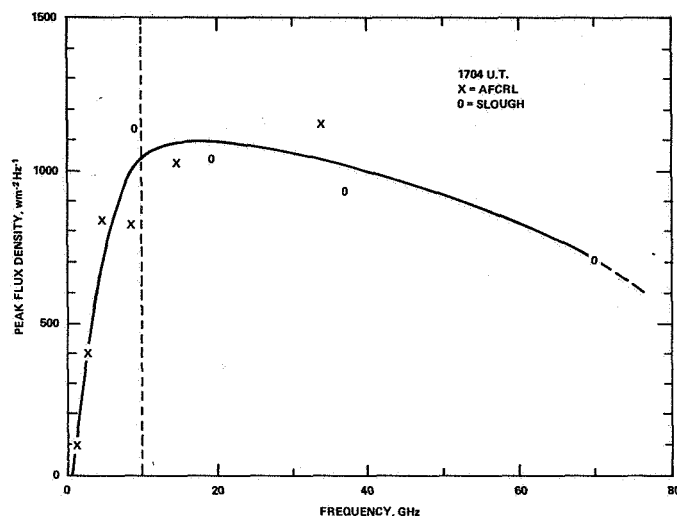
Figure 2. Peak flux density spectrum for the burst of
June 14, 1970 (1704 UT).

Figure 3, which is taken from Croom and Powell (1971), shows the degree of activity at 15.8 mm from mid-1967 to the end of 1969, a period covering the rise and peak of the current sunspot cycle. Although there was considerable activity, with several bursts of outstanding intensity, it can be seen that even in 1969 there was a period of 4 to 5 months with very little activity. This diagram is based on about 90 percent time coverage, so one can understand how Piddington and Minnet's 1948 observations came to suggest that activity was very low at these wavelengths.

Examples of events at 4.2 and 15.8 mm have been given in Croom (1970) and Croom and Powell (1971). More recent examples of events at 8.1 mm are shown in Figure 4 for the outstanding solar flares of August 1972. There is an appreciable decrease in the number of events observed as the wavelength decreases, this being due in part to the fact that most minor bursts peak at around 4- to 6-cm wavelength. However, it also results from the increased atmospheric and technical problems (particularly receiver sensitivity), coupled with the fact that a given burst intensity represents a decreasing fraction of the quiet-sun background as the wavelength decreases. For example, an event of 500×10^{-22} W $\cdot$ m^{-2} Hz^{-1} is generally recognized as a major event, and at 3 cm this represents an increase of
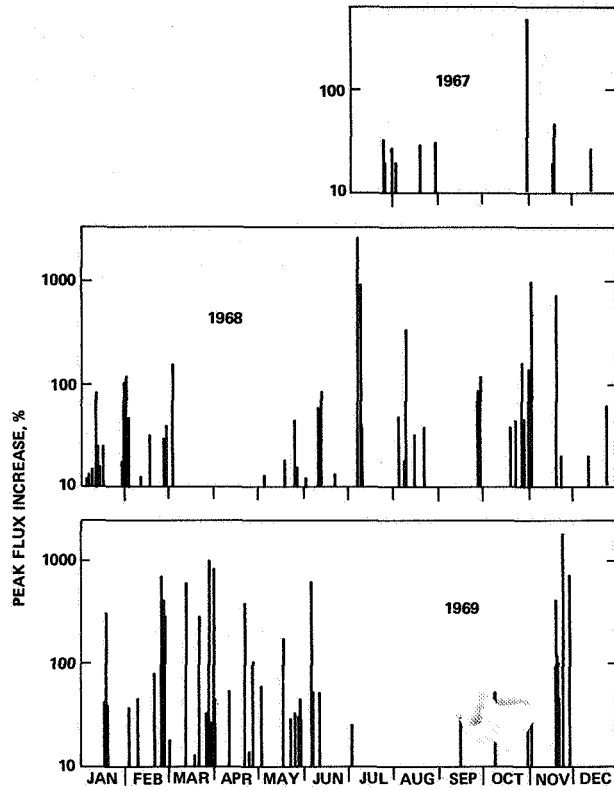
Figure 3. Solar burst activity at 19 GHz for the period July 1967 to December 1969, based on Slough 19-GHz data and on extrapolations from Tokyo Observatory 17-GHz and AFCRL, Massachusetts 15.4-GHz data (100 percent = preburst flux level $\sim 690 \times 10^{-22}$ W · m^{-2} Hz^{-1}). The diagram corresponds to about 90 percent time coverage of the solar activity.
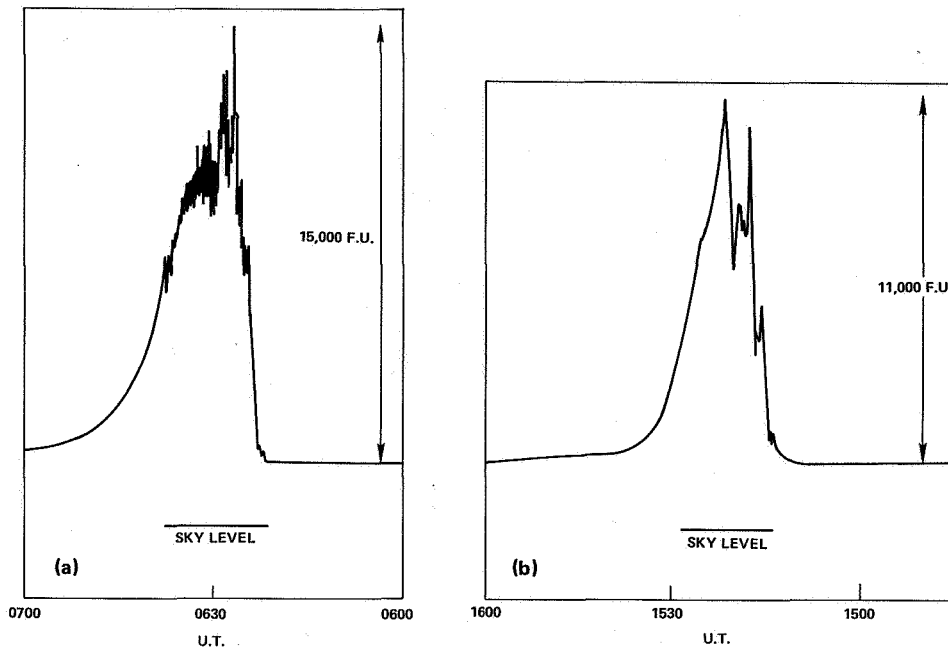
Figure 4. The 8.1-mm (37-GHz) outbursts of (a) August 4, 1972 and
(b) August 7, 1972, from Slough data.

about 150 percent relative to the undisturbed solar output. At 4.2 mm, however, such an event corresponds to only a 7 percent increase, which, taken in conjunction with the observational difficulties, means that it is not surprising that relatively few events have been recorded at the shortest wavelengths. Nevertheless, in the ᴸ᷉ solar cycle about eight events were recorded at $\lambda < 10$ mm, in the current cycle about 80 have been recorded, and allowing for both the increasing interest in this region and in likely improvements in techniques over the next few years, it is likely that several hundred will be recorded in the next cycle.

SPECTRAL TYPES

Figure 5 illustrates the main spectral forms observed in the mm to cm region. The diagram includes also the dm region, as sometimes microwave events are classified according to whether or not they are accompanied by a decimeter event. Basically one can get events which are isolated decimeter (D), centimeter (C) or millimeter (M) events, or any combination of the three, though triple peak (DCM) events, such as that of March 21, 1969 (at 1933 UT) are very rare. Also rare is an M event such as that of July 6, 1968, which was still rising at 71 GHz (42 mm), though others peaking between 30 and 70 GHz have been recorded.

118
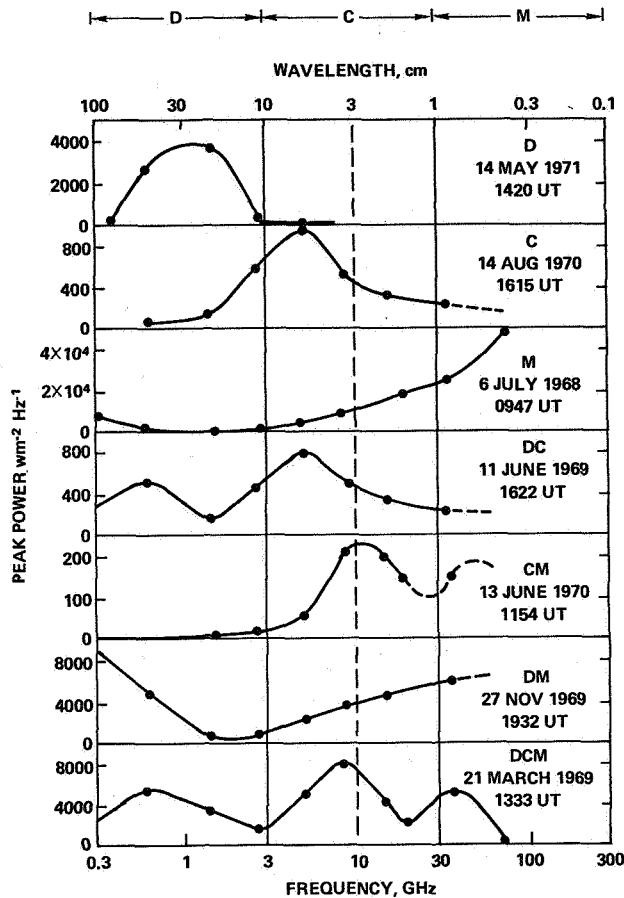
Figure 5. Examples of burst spectra (D = ̶̶̶̶meter component, C = centimeter component, ̶̶ = millimeter component). The broken vertical line at 10 GHz (3 cm) shows the approximate boundary between the well studied decimeter-centimeter region and the more novel centimeter-millimeter region.

RELATION TO PROTON EVENTS

The relation of solar events at $\lambda < 3$ cm to solar protons has been discussed by Croom (1971a, b, c). Basically, those events which peak at the shorter wavelengths tend to be closely associated with solar proton events. Furthermore, the averaged duration of individual bursts can be used as an indication of the peak proton flux for particle energies $E_p > 10$ MeV. As an extension to this, Figures 6 and 7 show the relation of mean burst duration T_M to higher energy protons, Figure 6 being for protons exceeding 60 MeV, and Figure 7 for the energy level for which the actual flux exceeds 10 particles $\cdot$ sr^{-1} cm^{-2} s^{-1}. The proton data came from the Johns Hopkins University — Goddard Space Flight Center
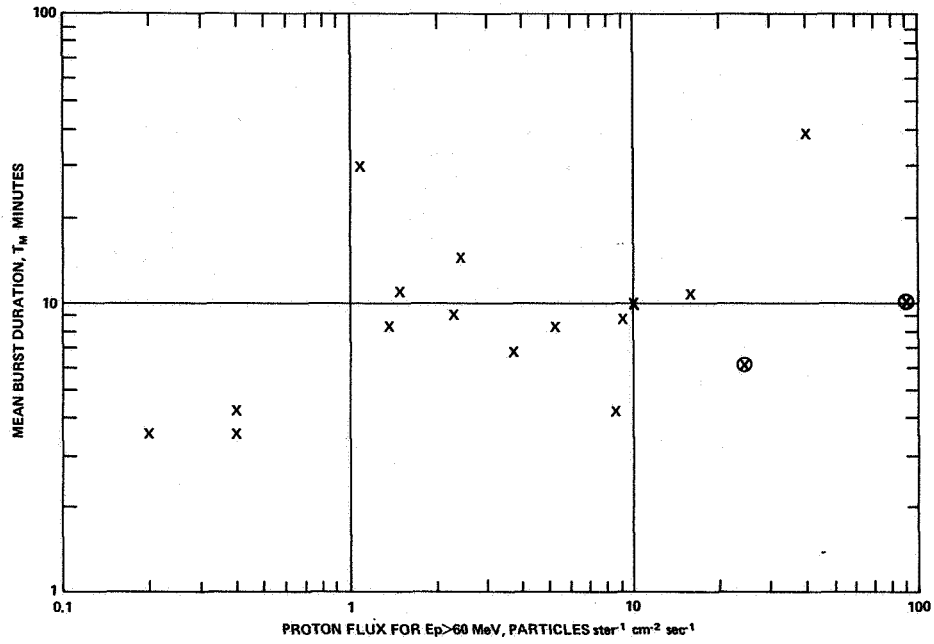
Figure 6. Microwave burst mean duration as a function of particle flux for energies exceeding 60 MeV.
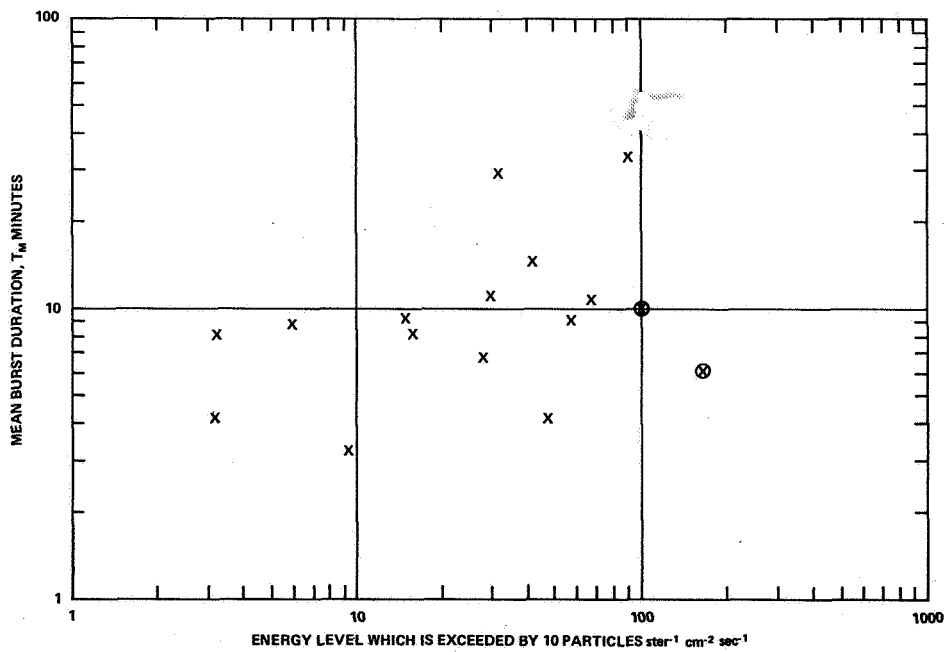
Figure 7. Microwave burst mean duration as a function of the particle energy exceeded by 10 particles • sr^{-1} cm^{-2} s^{-1}.

Explorer-34 and -41 satellites proton data for the period May, 1967 to December, 1969 (ESSA 1967-70), and the values of T_M from corresponding radio events, mainly in the 15 to 19 GHz band

$$T_M = \frac{1}{P_{max}} \int_0^T P(t)\, dt$$

where P_{max} is the peak flux density, $P(t)$ is the flux density at time t, and T is the overall burst duration. The level of 10 particles $\cdot$ sr^{-1} cm^{-2} s^{-1} was chosen as being one to which most of the available proton spectra could be readily interpolated or extrapolated. The spectra used are shown in Figures 8(a) and 8(b). Although Figures 6 and 7 do not show such a clear relationship as for the lower energies, there are fewer high-energy events available for study, and in any case, the vast majority of microwave bursts have mean durations of much less than 1 minute and are apparently nonproton events. That is, they correspond to points lying well to the left of, and below the lower left hand corners of the diagrams. Allowing for this, there would seem to be the same general tendency for the peak proton flux to increase as T_M increases, in contrast with the results of Sakurai (1970), who found that the rise-times of Hα and X-ray events actually decrease with increasing proton energy. However, Sakurai considered the period 1942 to 1963, for which direct proton data were not available. He divided his proton events into only two discrete classes: GeV (BeV) flares, defined by the occurrence of ground level particle events, and MeV flares, defined by the occurrence of sudden ionospheric disturbances (SIDs). Kahler (1970) has previously queried this inverse relationship between rise time and proton intensity, though he also used discrete classes, adding a third category, namely, nonproton events. Since microwave burst rise time and T_M are closely related (increasing rise time is also a good indicator of proton events, Croom, 1971b), there would seem to be a surprising difference between X-rays and microwave bursts in their relation to solar protons.

However, the lack of measurable proton emission is particularly noticeable for short-rise-time microwave bursts, even though very intense, as in the case of the August 8, 1968 event (2200×10^{-22} W $\cdot$ m^{-2} Hz^{-1}). This event had a rise time of about 1.5 minutes and a T_M of 1.8 minutes, as opposed to 3 to more than 30 minutes for both parameters for proton associated flares. This indicates that the proton rise time may be longer than the few tens of seconds suggested for electrons by the fine scale quasi-periodicities superimposed on many large microwave events, and by the short rise times of the nonproton bursts, even though it may not necessarily be as long as the full Hα, X-ray, or microwave rise times. However, the complexity of many events probably means that the rise time in fact covers two or more related and overlapping events in the same general region, and that such a staggered boost sequence is necessary in order to accelerate the protons to the higher energy ranges.
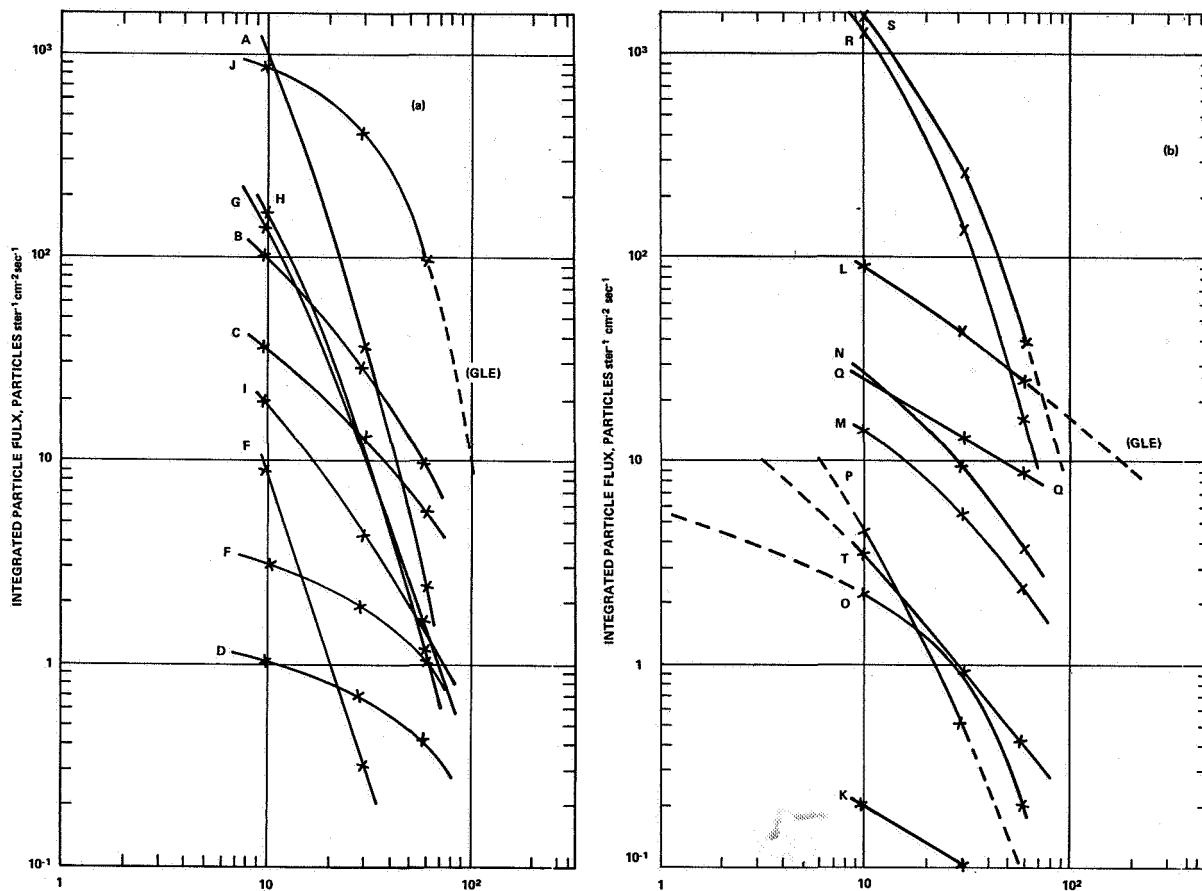
Figure 8. Integral energy spectra of major proton events from May 1967 to December 1969, for which microwave burst data are available (proton data recorded by the Johns Hopkins University-Goddard Space Flight Center Explorer-34 and -41 satellites):

A	May 23, 1967 (1947)	K	Dec 27, 1968 (1055)
B	May 28, 1967 (0542)	L	Feb 25, 1969 (0911)
C	June 9, 1968 (0850)	M	Feb 26, 1969 (0429)
D	July 6, 1968 (1712)	N	Feb 27, 1969 (1408)
E	Sept 26, 1968 (0030)	O	Mar 12, 1969 (1741)
F	Sept 29, 1968 (1621)	P	Mar 21, 1969 (1327)
G	Oct 31, 1968 (0010)	Q	Mar 30, 1969 (0249)
H	Nov 1, 1968 (0912)	R	Apr 10, 1969 (0400)
I	Nov 4, 1968 (0520)	S	Nov 2, 1969 (1041)
J	Nov 18, 1968 (1030)	T	Nov 24, 1969 (0919)

(The times in parentheses are those of the peaks of the associated microwave bursts.)

ACKNOWLEDGMENT

REFERENCES

Coates, R.J., 1966, *Proc. IEEE* **54**, 471.

Croom, D.L., 1970, *Solar Phys.* **15**, 414.

Croom, D.L., 1971a, *Nature* **229**, 142.

Croom, D.L., 1971b, *Solar Phys.* **19**, 152.

Croom, D.L., 1971c, *Solar Phys.* **19**, 171.

Croom, D.L., and Powell, R.J., 1969, *Nature* **221**, 945.

Croom, D.L., and Powell, R.J., 1971, *Solar Phys.* **20**, 136.

ESSA, 1967-70, *Solar Geophys. Data* (Boulder).

Hagen, J.P., and Hepburn, N., 1952, *Nature* **170**, 244-5.

Kahler, S., 1970, *J.G.R.* **75**, 5637.

Piddington, J.H., and Minnett, H.C., 1949, *Austral. J. Scientific Res., Series A (Phys. Sci.)* **2**, 539.

Sakurai, Kunitomo, 1970, *J.G.R.* **75**, 225 and 5642.

POSSIBLE LOW ENERGY (E < 10 keV) NONTHERMAL X-RAY EVENTS

S.W. Kahler

American Science and Engineering, Inc.

ABSTRACT

A search of the 3- to 30-keV data from the NRL proportional counter detector on the Orbiting Geophysical Observatory-5 (OGO-5) satellite has yielded several events which may be nearly completely nonthermal in the $3 < E < 10$ keV range. In each case an impulsive hard X-ray burst accompanied by an impulsive microwave burst was associated with a low energy X-ray burst whose profile was a simple rise and fall. The lack of a two-component nature in the low energy range argues that the low energy X-ray flux is due to a single physical mechanism, in this case nonthermal bremsstrahlung from accelerated electrons. However, the spectra and time profiles are quite consistent with a thermal interpretation. Polarization measurements are probably necessary to resolve the physical origin of such bursts.

INTRODUCTION

The properties of the impulsive, hard $(E > 10\,keV)$ X-ray events have been discussed at length by Kane and his collaborators (Kane and Anderson, 1970; Kane and Donnelly, 1971; Kane, 1971).

Recently, Kahler and Kreplin (1971) investigated the nature of the impulsive X-ray bursts in the $3 < E < 10$ keV energy range, using data from the Naval Research Laboratory proportional counter experiment in the OGO-5 satellite. Out of 12 impulsive events for which they had data they were able to separate the low energy impulsive component from the slowly varying thermal component in only two cases. Figure 1, taken from their paper, shows the counting rate profiles of the four lowest energy channels during an impulsive event on April 16, 1968. The profiles of the thermal component were estimated during the impulsive burst and are shown in dashed lines in the figure. Kahler and Kreplin concluded that the $3 < E < 10$ keV impulsive fluxes were probably nonthermal; however, they could not rule out a possible thermal interpretation.

It is clear from Figure 1 that the April 16 event was dominated in the $3 < E < 10$ keV region by the slowly varying thermal component. Such an event is shown schematically in Figure 2 as the event labeled A. It is reasonable to ask whether there might also be events of the kind labeled B. In such an event the low-energy $(E \sim 4\,keV)$ flux profile is due completely or nearly completely to the impulsive component. The slowly varying thermal component is of substantially smaller intensity.
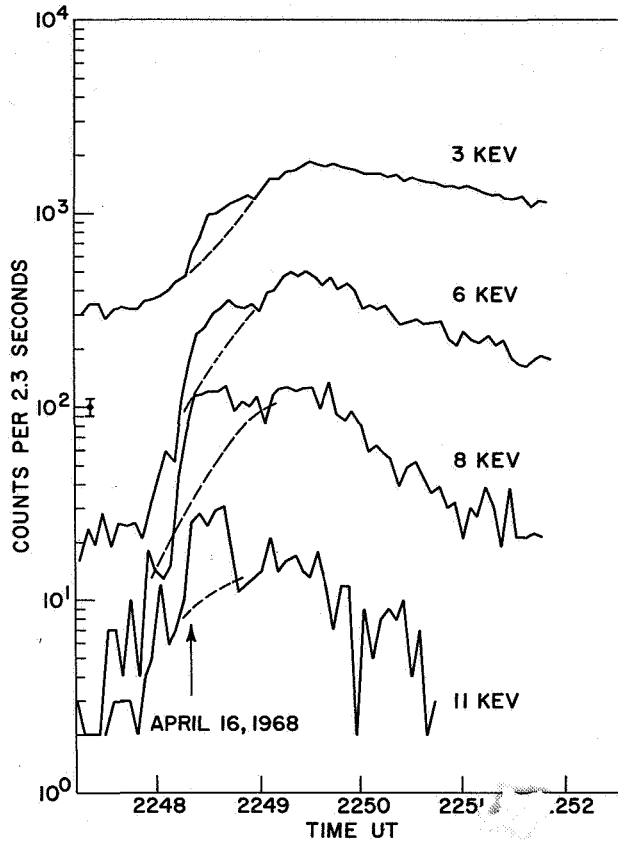
Figure 1. The impulsive event of April 16, 1968, from Kahler and Kreplin (1971). The arrow indicates the approximate time of the peak of the event reported by Kane and Anderson (1970). The flux of the slowly varying thermal component was estimated during the time of the impulsive burst and is shown by the dashed line of each profile. The profiles of the impulsive burst were obtained by subtracting the estimated thermal component fluxes from the total fluxes.
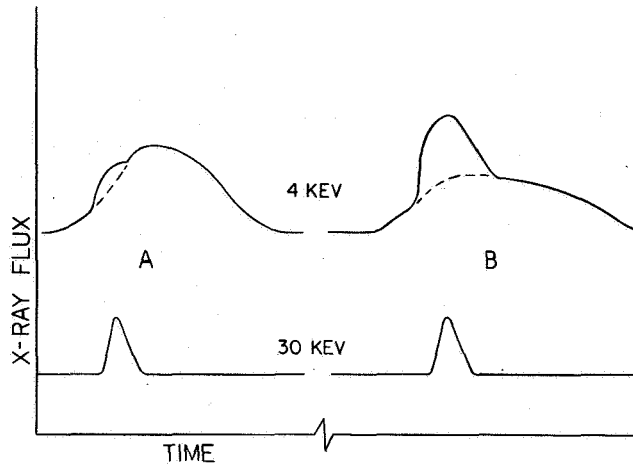
Figure 2. A schematic of two possible kinds of low energy impulsive X-ray bursts. In both cases an impulsive event is seen at 30 keV. In case A, the low energy fluxes are dominated by the slowly varying thermal component. In case B, the impulsive component dominates the thermal component.

OBSERVATIONS

In order to search for nearly completely impulsive X-ray events in the $3 < E < 10$ keV region, a list of impulsive microwave bursts was compileu (.AU, 1968) for times in 1968 during which OGO-5 data were available. The X-ray data were then examined to search for X-ray events which were well correlated in time with the impulsive radio events and which had simple rise-and-fall profiles; that is, they did not show a complex structure. It was further required that the ~ 10 keV flux peak should occur between the times of onset and maximum of an accompanying Hα flare. Finally, it was confirmed (Kane, private communication, 1972) that the three events presented here were observed as hard X-ray bursts in the University of California scintillator on OGO-5.

The first example is the event of October 18, 1968, shown in Figure 3. The bottom trace shows the impulsive flux profile of hard (~ 25 keV) X-rays. It can be seen that as one observes successively lower energy profiles the simple rise and fall is still apparent and is well correlated with the 25-keV flux profile. This argues that the physical mechanisms responsible for the 25-keV event are also responsible for the 5-keV event. This mechanism must be emission from impulsive nonthermal electrons.

126
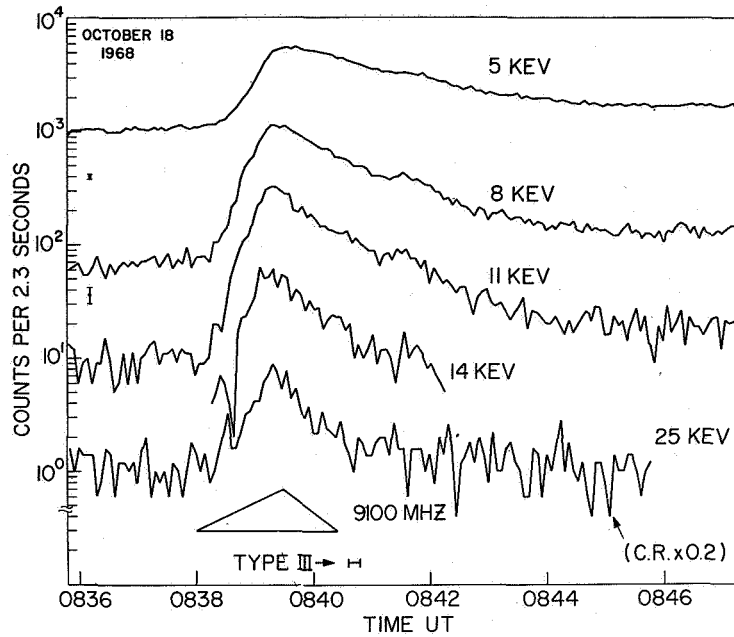
Figure 3. The impulsive X-ray event of October 18, 1968. The
9100-MHz event is shown on the bottom. The lower energy
flux profiles are shown to be well correlated with the 25-keV
profile.

Two further examples are shown in Figure 4 — those of April 15, 1968, and of August 21,
1968. Again, the profiles are simple rise and fall and show a smooth transition from one
energy profile to the next. Type III radio bursts were reported throughout the duration of
the August 21 event.
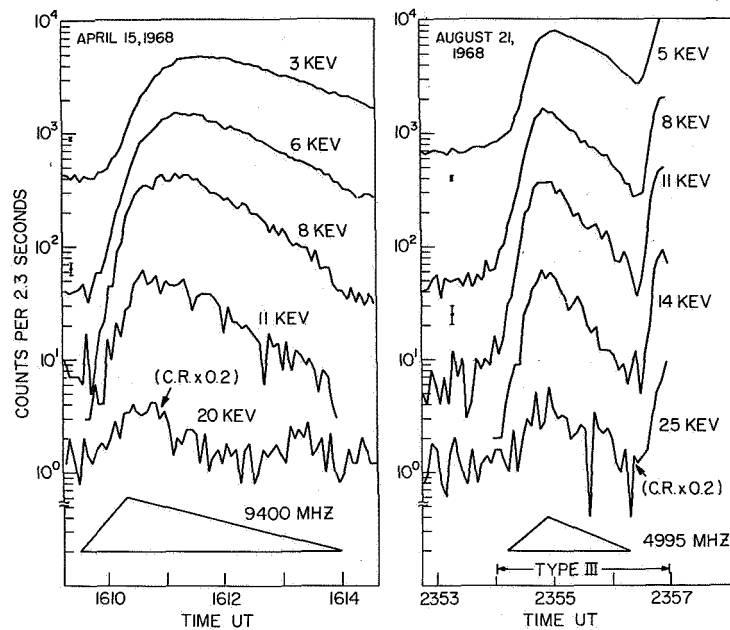
Figure 4. The impulsive events of April 15 and August 21, 1968. The profiles of the associated microwave bursts with the highest reported frequencies are shown for each event. Again, one can trace the gradual change of the X-ray flux profiles from the ~ 20-keV range down to the lowest observed energy.

INTERPRETATION AND CONCLUSIONS

There are three basically different interpretations that one can give to the low-energy flux profiles shown in Figures 3 and 4. First, one may argue that the nonthermal electron spectra producing the hard X-ray events have low-energy cutoffs at about 10 or 20 keV. The X-ray emission below 10 keV is then due mostly to accompanying thermal emission from heated coronal gas. The second interpretation is that the event is almost completely nonthermal because the accelerated electron spectrum extends down to 3 keV or lower. The third possibility is that both thermal and nonthermal contributions are substantial in the low-energy region. We now discuss each of these possibilities.

The thermal interpretation yields results that one would expect on the basis of other studies with thermal X-radiation (Horan, 1971). The inferred temperatures range from 10 to 30×10^6 K. The emission measures, $n_e^2 V$, where n_e is the electron density and V is the volume, range from 10^{46} to 10^{48} cm^{-3}. Since all three events are subflares, it is not surprising that these emission measures are smaller than those found by Horan (1971) for larger events. These events also show the typical signature of thermal X-ray events: The lower energy fluxes peak at later times and the flux profiles are very gradual, with no impulsive or short duration (time scale, $\tau < 10$ seconds) changes. Thus the three events are quite consistent with a thermal interpretation.

128

On the other hand, there are a number of reasons for thinking that the nonthermal interpretation is valid. First, there is the good correlation of the X-ray flux profiles with the microwave profiles mentioned earlier. It might be argued that the radio emission is thermal, but if we use the X-ray values of temperature and emission measure, then the expected thermal radio flux is less than one solar flux unit (10^{-22} W $\cdot$ Hz^{-1} m^{-2}). The radio profiles of Figures 3 and 4 are therefore most likely nonthermal.

Kane and Anderson (1970) found that in the impulsive, hard X-ray bursts the e-folding rise and decay times were longer for lower energies. An examination of the profiles of the three events presented here shows that this property also holds for the low-energy X-ray region. In addition, if we fit the three events to power law spectra of the form

$$\frac{dN}{dE} = AE^{-\gamma} \text{ photons} \cdot \text{cm}^{-2} \text{ s}^{-1} \text{ keV}^{-1}$$

where E is energy and A and γ are constants, we find that the range of values for γ is between 3 and 6, approximately the same range found for the high-energy events studied by Kane (1971).

As mentioned above, the lower energy flux profiles of the events in Figures 3 and 4 show peaks at successively later times. Since all the impulsive flux profiles in the E > 10 keV range appear to show simultaneous peaks, it might be argued that the dispersion of the low-energy peaks with time constitutes an argument against the nonthermal interpretation. Figure 5 presents X-ray flux profiles of two different events. The event of July 6, 1968 is an example of the case A event of Figure 2. In order to derive the profiles for the impulsive event of July 6, it was necessary to estimate the profiles for the slowly varying thermal component and subtract them from the profiles of the total flux as described in Kahler and Kreplin (1971). Although the July 6 event is more impulsive than the event of August 21, it can be seen that in both cases the lower energies peak at later times. The crude profiles of the two events of Figure 3 of Kahler and Kreplin (1971) also show the same general behavior. We conclude that the temporal dispersion of the low-energy flux peaks does not constitute an argument against the nonthermal interpretation.

The events of Figures 3 and 4 are unusually short-lived in comparison with other events observed by OGO-5. Although they have rather typical features associated with thermal events, their short-lived nature and good correlation with hard X-ray and microwave emission make them good possibilities for the nonthermal interpretation.

The third interpretation of the events presented here is that they result from substantial contributions of both thermal and nonthermal emission. The simple rise-and-fall profiles would then indicate that the thermal emission must vary in such a way that it closely matches the nonthermal emission in time. However, the thermal emission is a function of both the temperature and the emission measure, which vary widely throughout the flare (Horan, 1971). One would have to argue that the temperature and emission measure vary in
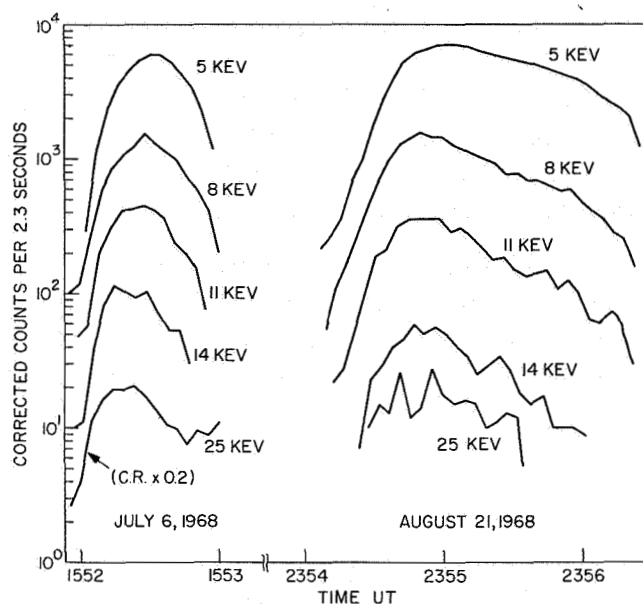
Figure 5. A comparison between the type A event of July 6, 1968 and the type B event of August 21, 1968. In both cases the background and slowly varying components were estimated and subtracted from the total flux to get these profiles. In both cases the lower energy peaks occur at later times.

such a way that the thermal emission profiles can match the nonthermal profiles in time. While this is possible, it seems unlikely to have happened in all three events presented here. Our conclusion is that the low-energy fluxes of Figures 3 and 4 are either completely thermal or completely nonthermal in nature.

The importance of distinguishing between the thermal and nonthermal interpretations can be seen by comparing the total energies of the two cases. In the thermal interpretation we can estimate the energy of the coronal gas, E_t, from the equation

$$E_t = 3 \times (n_e^2 V)^{1/2} V^{1/2} \text{ keV}$$

We have assumed a temperature of 12×10^6 K. Taking the emission measure as 10^{48} cm^{-3} and the electron density $n_e = 10^{10}$ cm^{-3}, the thermal energy for these events is $E_t \sim 3 \times 10^{29}$ ergs.

For the nonthermal interpretation we can use the thick-target theory as discussed by Brown (1971) and by Hudson (1972). By using Equations (A5) and (A7) of Hudson, the total number of nonthermal electrons can be calculated and their total energy estimated. For the

130

event of August 21, 1968, this total becomes $\sim 10^{32}$ ergs for electrons above 3.5 keV. Syrovatskii and Shmeleva (1972) have applied thick-target theory to five impulsive X-ray bursts discussed by Lin and Hudson (1971). They found that the total energy of electrons with $E > 22$ keV ranged from $\sim 3 \times 10^{29}$ to 3×10^{30} ergs. If we assume that the electron spectra extended down at least to 10 keV with the same power law exponent, then their energy estimates for the five events will be increased to the range $\sim 3 \times 10^{30}$ to 3×10^{31} ergs. Syrovatskii and Shmeleva pointed out that since the total energy of the flares they considered was taken to be 10^{29} ergs, they were finding more energy in the $E > 22$ keV nonthermal electrons than in the total flare energy. The extension of the nonthermal electron spectra down to 10 keV increases this difference by another order of magnitude. Thus, although our estimate of 10^{32} ergs for the nonthermal electron energy of the August 21 subflare seems quite high, it may be consistent with the derived values for other events in which the low-energy cutoffs of the nonthermal electron spectra are extended down to sufficiently low energies. Before we can rule out the nonthermal X-ray interpretation, it will be necessary to get good estimates of the total energy deposited in the Hα chromospheric region, taking into account all the various energy loss mechanisms.

It was pointed out in Kahler and Kreplin (1971) that there is an intrinsic difficulty in trying to resolve the physical nature of the origin of the $3 < E < 10$ keV X-ray emission. We have shown here that there are important physical consequences involved in the resolution of this problem. At the present time, it appears that only X-ray polarization measurements in the $3 < E < 10$ keV energy range will be capable of resolving the nature of these bursts.

REFERENCES

Brown, J.C., 1971, *Solar Phys.* **18**, 489.

Horan, D.M., 1971, *Solar Phys.* **21**, 188.

Hudson, H.S., 1972, *Solar Phys.* **24**, 414.

Kahler, S.W., and Kreplin, R.W., 1971, *Ap. J.* **168**, 531.

Kane, S.R., 1971, *Ap. J.* **170**, 587.

Kane, S.R., and Anderson, K.A., 1970, *Ap. J.* **162**, 1003.

Kane, S.R., and Donnelly, R.F., 1971, *Ap. J.* **164**, 151.

Lin, R.P., and Hudson, H.S., 1971, *Solar Phys.* **17**, 412.

Syrovatskii, S.I., and Shmeleva, O.P., 1972, *Soviet Astron.* **16**, 273.

IAU, *Quart. Bull. Solar Activity*, 1968 (Zurich).

THERMAL AND NONTHERMAL X-RAY BURSTS
OBSERVED FROM OSO-7

L. E. Peterson, D. W. Datlowe, and D. L. McKenzie*
University of California, San Diego

ABSTRACT

The UCSD solar X-ray experiment on the OSO-7 observes X-rays in the 2 to 15 keV range with a proportional counter and in the 10.6 to 300 keV range with a scintillation counter. The dynamic range and instrument parameters are chosen to separate X-ray emission due to a hot thermal plasma from that due to nonthermal electron populations for a large number of X-ray events associated with small flares. Many different morphological classes have been observed in the 200 or so principal events observed between October 1971 and June 1972. For events which have both a thermal and nonthermal component, we can perform an analysis which shows that in not all events is it possible for the nonthermal electrons to energize the thermal plasma. We observe many events which have no nonthermal component, at least one event which was purely power law on initiation, and several events which had a long, slow decay of the hard X-rays.

INTRODUCTION

We report here preliminary results obtained from the University of California/San Diego (UCSD) hard X-ray experiment on the OSO-7 satellite, which was designed to study the relationship between "thermal" (Culhane and Phillips, 1 ; Kahler et al., 1970), and "nonthermal" (Kane and Anderson, 1970; Kahler and Kreplin, 1971) impulsive X-ray emission in solar flares. Previous measurements have been of either the thermal component or the nonthermal component, or have been confused because of instrumental problems such as pulse pileup, channel resolution, and dynamic range (Kane and Hudson, 1970). Understanding the relationship between thermal and nonthermal X-rays and their associated electron populations is important for determining the energetics of solar flares and for separating the acceleration and heating processes from relaxation phenomena (de Jager, 1968).

INSTRUMENTATION

The UCSD experiment on the OSO-7, which was launched September 29, 1971, consists of a proportional counter and a scintillation counter (Harrington et al., 1972; Datlowe et al., 1972). The instruments are designed to avoid pulse pileup for steep spectra and to have a

*Presently at Aerospace Corporation, El Segundo, California.

132

large dynamic range. The proportional counter, which covers the 1.9 to 14.6 keV range, has a Xe/CO_2 fill and a 0.32 cm^2 Be window 115 mg · cm^{-2} thick. The data are accumulated in seven pulse-height channels, with approximately linear spacing. The scintillation counter covers the range from 10.6 to 323 keV and consists of a 1-cm thick, 9.6-cm^2 area NaI(Tl) detector with an active anticoincidence shield and a 41 mg · cm^{-2} Al window. The data from this instrument are read out in nine channels, which are logarithmically spaced with a channel ratio of approximately 1.4.

Both instruments are collimated to have an angular response of 20° × 90° full width with the long axis located in the rotating wheel plane of the OSO-7 satellite. As a result of this rotation, solar X-ray events are counted for approximately 0.5 seconds out of every nominal 2-second rotation and accumulated in registers which are read out every 10.24 seconds. In the usual mode of operation, this is the limiting time resolution. However, in another rarely used mode, time resolution up to 50 ms on one channel of hard X-ray data can be obtained.

The dynamic range between background to saturation is approximately from 10^2 to 3 × 10^4 photons · $cm^{-2}s^{-1}$ > 5 keV and from 0.1 to 3 × 10^2 photons · $cm^{-2}s^{-1}$ > 20 keV. Events larger than those usually associated with subflares will saturate the proportional counter at peak intensity, but only the largest flares produce enough hard X-rays to saturate the scintillation counter.

EVENT TYPES

Most of the events falling into the operating range of the OSO-7 instrument are associated with small flares or subflares. The objective of this experiment is to study a rather large number of medium-size bursts to obtain relationships between the various phenomena which occur in flares and to delineate different classes, rather than to study a few very large events.

In terms of the X-ray spectra observed on the OSO-7, events fall into the following general categories:

- Those with a pure thermal spectrum, usually associated with subflares

- Those with a thermal soft X-ray burst lasting typically 10 minutes accompanied by a nonthermal hard X-ray burst with a duration of less than 1 minute

- Those having a single power law extending over both the soft and hard X-ray energies at the start, followed by a soft thermal spectrum

- Those having a long, slowly decaying hard X-ray phase, usually associated with type IV radio emission

In the 9-month interval from launch to June 5, 1972, we have obtained about 40 percent observational coverage, and have seen ~200 events which contain a 5-keV flux >10^3 counts · $cm^{-2}s^{-1}$; of these approximately 40 percent had a significant nonthermal

component > 20 keV. In addition, there are hundreds of events which produced a significant increase in the lower energy channels but were too small to analyze into spectral type.

A typical event containing both thermal and nonthermal spectra is that of 0518 UT November 16, 1971, which has been described in detail elsewhere (McKenzie et al., 1972). Figure 1 shows the rates of various channels of the proportional and scintillation counters as a function of time during the burst, whose major features we review here. Clearly, at higher energies the hard X-ray event seems more and more impulsive on the 10.24-second time scale. A large increase in soft X-ray emission was associated with the hard X-ray burst. The soft X-ray emission, however, decayed with a much longer time constant until approximately 15 minutes later, when an additional event occurred.
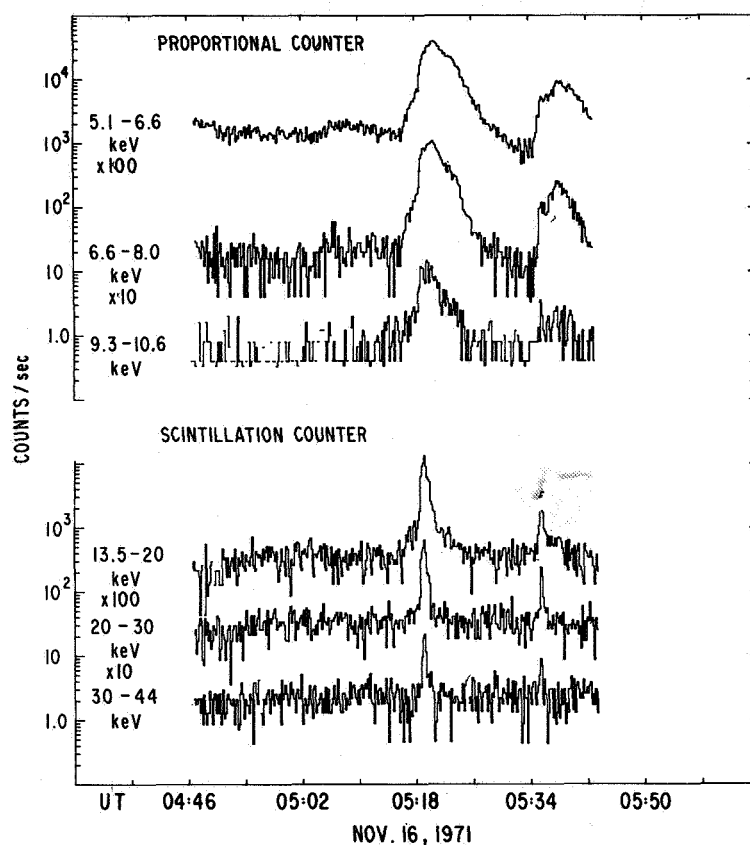
Figure 1. X-ray counting rates with a 10.24-second resolution as a function of time and energy observed by OSO-7 at 0518 UT November 16, 1972. Vertical locations of the various proportional and scintillation counter channels have been displaced by multiplying by the amount indicated. Higher energy X-rays are increasingly impulsive. Another event occurred at 0536 UT.

THERMAL AND NONTHERMAL ANALYSES

In this section we will briefly review the procedure used to determine parameters of the thermal plasma and of the nonthermal electron distribution, using the OSO-7 counting rate data. These procedures have been discussed in more detail elsewhere (McKenzie et al., 1972; Datlowe et al., 1972).

First, we determine the temperature (T) and emission measure ($N_e^2 V$, where N_e is electron density and V is volume) characterizing the thermal spectrum which, when folded through the proportional counter response including resolution spread, gives the best fit to the pulse height distribution. Then we assume that the spectrum above 10 keV consists of a power law $AE^{-\gamma}$ plus an extrapolation of the thermal spectrum using the temperature and emission measure already determined. (Here, E is energy and A and γ are constants.) Next we determine the values of A and γ which, when the spectrum is folded through the response of the sodium iodide detector, including resolution spreading and K-escape, gives the best fit to the pulse height distribution. The spectral fits resulting from this procedure for the November 16 event in Figure 1 are shown in Figure 2 as solid lines.
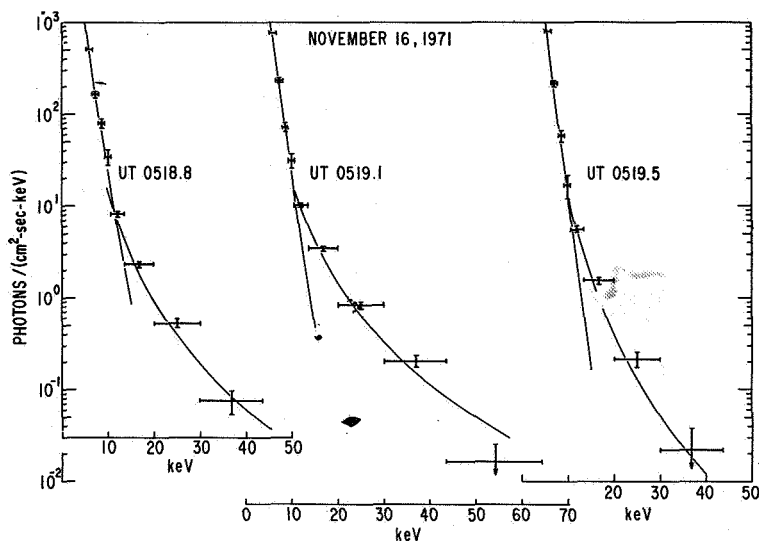
Figure 2. Corrected photon fluxes of the November 16 event compared with fitted photon thermal and nonthermal spectra for several times during development of the event. This illustrates the characteristic hardening, then softening, of the event. From the X-ray spectral parameters, characteristics and energy relations of the hot thermal plasma and the nonthermal electron population may be obtained.

135

From A and γ we can compute the number of nonthermal electrons and the power dissipated in collisions using the formulas of Brown (1971) for the thick target approximation and McKenzie (1972) for the thin target approximation. We can also compute the product of the thermal energy in the hot flare plasma and the ambient density, $(3NkT)n_i$, which is the product of the temperature, emission measure, and a constant. By doing this for successive spectra it is possible to compare the energy input by collisions of nonthermal electrons with the energy which appears in the hot flare plasma as a function of time.

The results of carrying out the complete analysis as a function of time for the event of 1520 UT January 30, 1972, shown in Figure 3, are indicated in Figure 4. The temperature reached a maximum near the peak of hard X-ray emission, while the emission measure and heat content product continued to increase even when a nonthermal X-ray spectrum could not be detected. We also show the power in nonthermal electrons above a 10-keV cutoff energy.
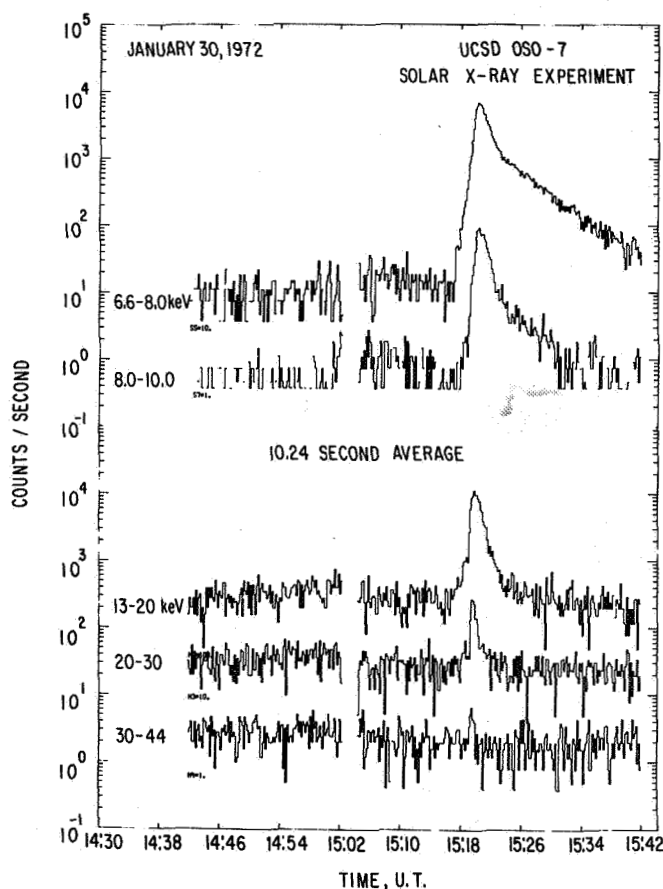
Figure 3. A soft and hard X-ray burst observed at 1520 UT January 30, 1972 which has been analyzed to show relations between the energetics of various electron populations during a solar flare.
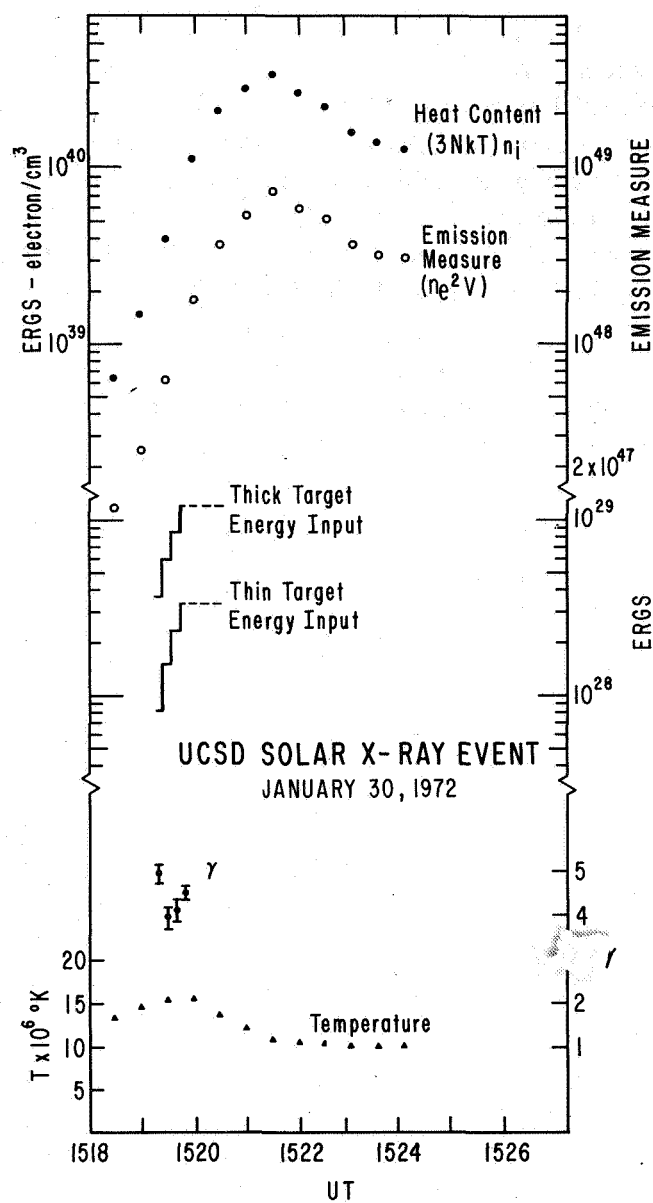
Figure 4. Analysis of thermal and nonthermal plasma parameters derived from fitting X-ray spectra to the data on January 30, 1972. The temperature, emission measure, and heat content product are derived from the soft X-ray spectrum. For the hard X-rays the exponent γ is shown, from which we compute the collisional energy lost by nonthermal electrons of energy greater than 10 keV, in either a thin or thick target approximation. Since the thermal plasma began to heat before the nonthermal X-ray burst and continued after it, we conclude that the main energy input to the plasma cannot be from collisions of nonthermal electrons.

137

The power injected into the flare region depends on an assumption regarding the electron lifetime (Arnoldy, Kane and Winckler, 1968). Figure 4 shows both the thin and thick target approximations. In the thick target case, all the energy is given to the plasma, whereas in the thin target case, a large fraction escapes to a low density region. Figure 4 shows the time integrated power and the energy available from the nonthermal electrons > 10 keV to heat the thermal region under the two assumptions. For the 1520 UT January 30, 1972 event, the thermal region must have a density of at least 10^{12} ions $\cdot$ cm^{-3} (thin target) or 3×10^{11} ions $\cdot$ cm^{-3} (thick target) for the heating to be energetically allowed. The actual input depends strongly on the low-energy electron cutoff. However, the product $(3NkT)n_i$ continues to increase even after appreciable nonthermal energy input has ceased. We conclude on the basis of this event, because of the time history, that the nonthermal electrons do not supply all of the heating of the thermal plasma, and that an additional source of heat input is required.

In the case of the 0518 UT November 16, 1971 event, it appears possible, at least in the thick target case, for the energetic electrons to heat the thermal plasma. In either case, we have assumed the thermal plasma to have a constant density during the flare development.

EVENT MORPHOLOGIES

As indicated earlier, there are several different types of events in addition to that described above. Most of the analysis so far, however, has been on events which show both thermal and nonthermal spectra, since these bear directly on the problem of flare energetics and heat input.

As an example of a pure thermal event, we show the burst in Figure 5 which occurred at 2158 UT February 23, 1972. One can clearly see from the counting rates that while the soft X-rays in the 5.1 to 6.6 keV region increased nearly two orders of magnitude, the flux in the 20 to 30 keV range remained undetectable. The analysis of this spectra shown in Figure 6 indicates emission measure increasing during the event from 10^{47} to 3×10^{48} cm^3, while the temperature decreased from approximately 12 to 8×10^6 K. Below 8×10^6 K, the flux is insufficient to provide a definitive temperature measurement.
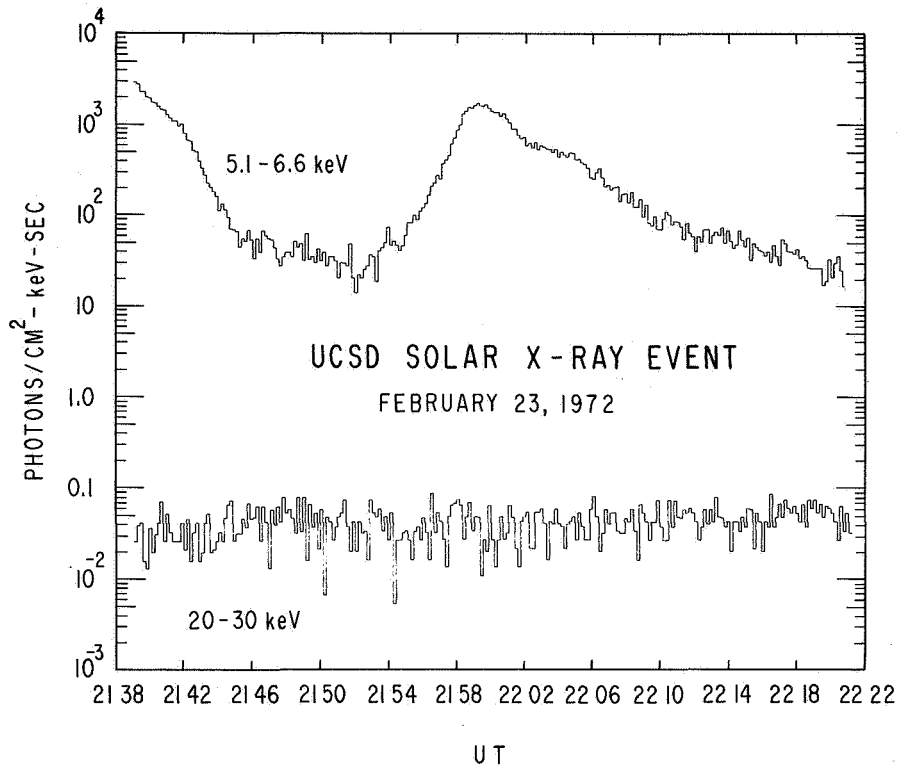
Figure 5. A large thermal event in soft X-rays, unaccompanied by an impulsive phase or a hard X-ray burst, observed at 2158 UT February 23, 1972. Small to medium size events such as these comprise the majority observed by the OSO-7.

One event, March 3, 1972, exhibited a pure power law during its initial phase, and is shown in Figure 7. The impulsive hard X-ray burst almost entirely preceded the soft X-ray burst, which continued for some ten to fifteen minutes after the impulsive high energy component had vanished. Analysis of the spectrum during the peak of the hard X-ray event is shown in Figure 8. The data extending from 6 to 100 keV fit a power law spectrum with a number index of 3.7. There was apparently no important thermal component at the lower energies during the early phases of this event. Note the close similarity of the thermal components, both in magnitude and duration, between this event and that of 2158 UT February 23, 1972 (Figure 5).
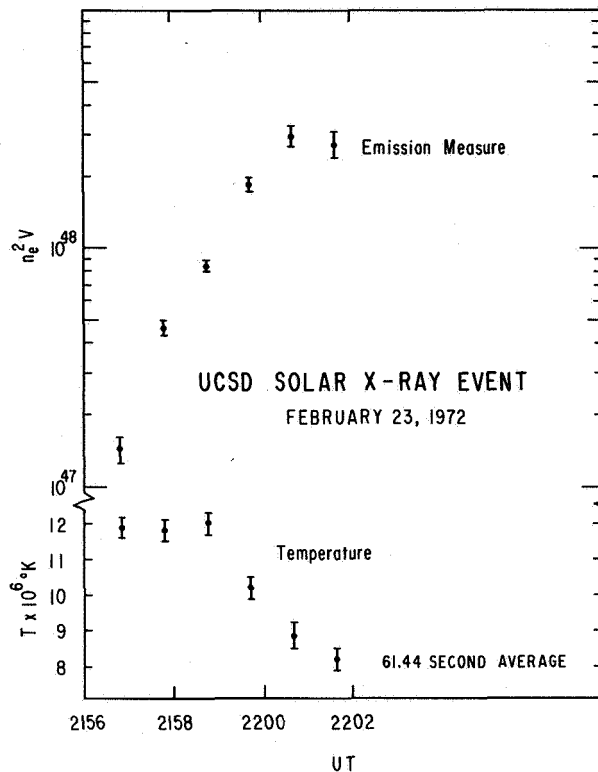
Figure 6. The temperature and emission measure derived from the analysis of the proportional counter rates for the event of 2158 UT February 23, 1972. Because of the steepness of the spectrum and the location of the instrument threshold, it is not possible to measure temperatures less than about $8 \times 10^6 \text{K}$.

Occasionally, we observe hard X-ray events which have very different morphologies, such as events with very long decay times. The e-folding decay time at 20 keV for such a burst is on the order of 20 minutes, and they apparently are similar to the events described by Frost (1969). Examples of this type occurred on November 22, 1971 and February 8, 1972. The latter, at 0720 UT, is shown in Figure 9. The event of interest occurred near the beginning of the time profile in Figure 9. In addition to the long-decay event, which occurred between 0700 and 0800, a different event, apparently much larger, occurred during a period of missing data. This produced a soft X-ray event which lasted many hours with a very slow decay, also recognizably present after another hard and soft X-ray burst at around 1940
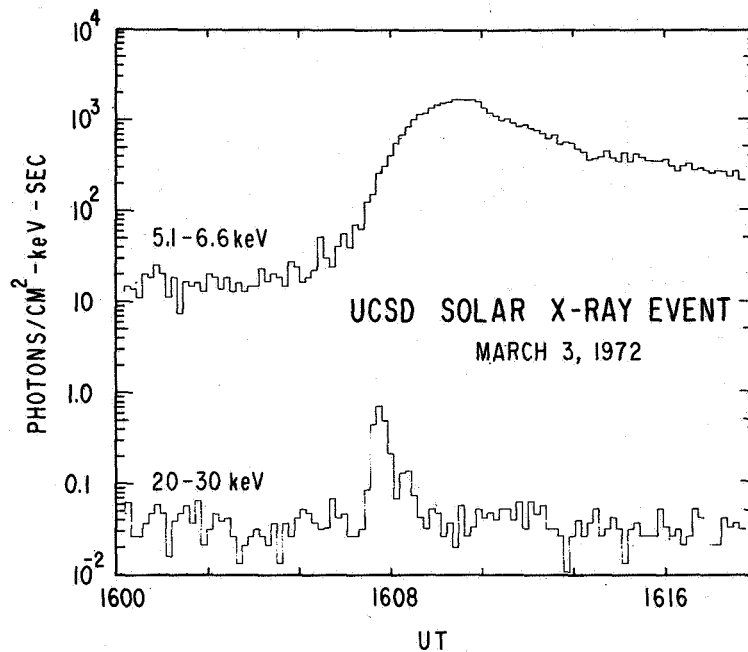
Figure 7. The burst of 1608 UT March 3, 1972, showing an impulsive hard X-ray component near the start of the event, followed by a thermal component with a long decay phase. Note that the hard X-ray burst clearly precedes the increase in soft X-rays.

Figure 10 shows the analysis of the 0720 UT event b̆ on the thermal and nonthermal interpretation of the spectra. The temperature remained relatively high, $> 10^7 K$, for nearly an hour, and the heat content product reached a maximum while detectable energy input from nonthermal electrons continued. In this case, the requirements on the electron density range from only 10^9 cm^{-3} in the thick target case to about 6×10^9 cm^{-3} in the thin target assumption. We conclude that in these events it is possible, both from density and time morphology arguments, that the thermal plasma can be heated by nonthermal electrons. Furthermore, these events are accompanied with type IV radio emission, which is usually attributed to nonthermal electrons. The longer time constants of the event also require nonthermal electron residence in a lower density region.
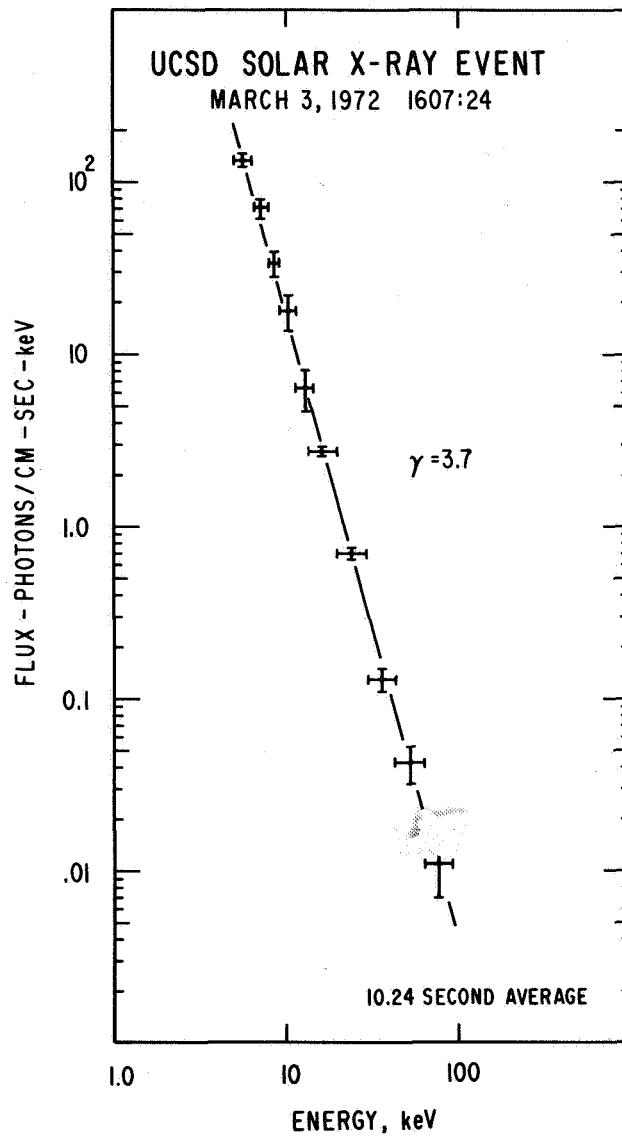
Figure 8. The spectrum at the hard X-ray maximum of the burst in Figure 6 fits a power law from 5 to 100 keV, with no recognizable thermal component, although a thermal plasma developed later in the event. One can trace the power law component to a lower energy in this flare than in any other yet discoverd in the OSO-7 data.

142
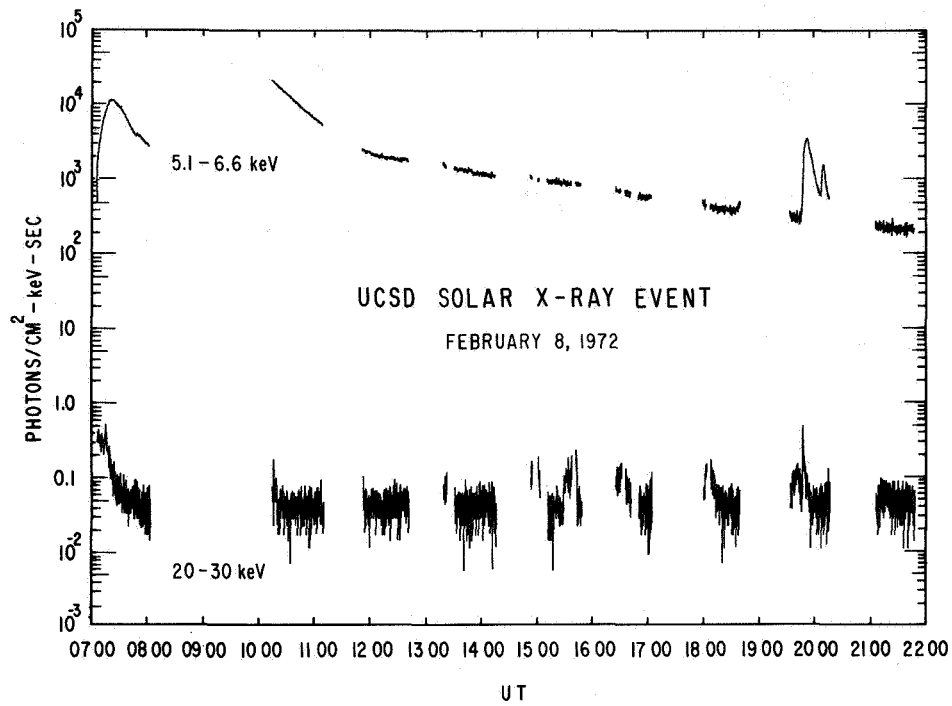
Figure 9. A hard X-ray event with a 10- to 20-minute decay time occurred at 0720 UT, near the beginning of the plot. Another large event apparently occurred about 1000, during a period of no data coverage, and produced a hot plasma which persisted for nearly 12 hours.
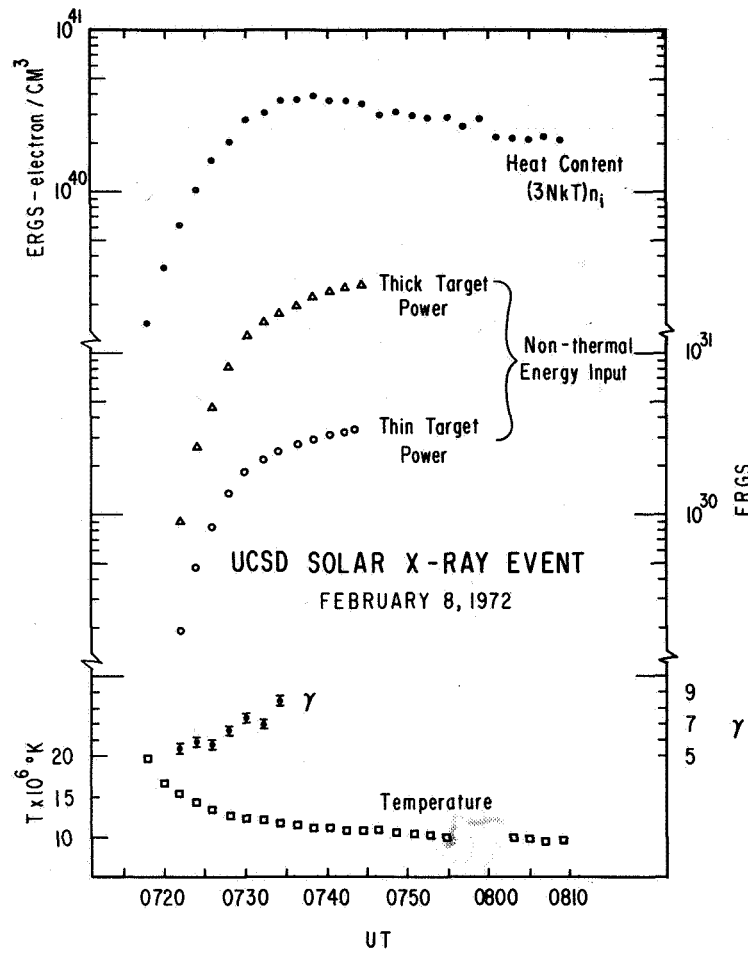
Figure 10. Parameters of the event 0720 UT February 8, 1972 derived from the data. The heat content began to decrease when the nonthermal energy input ceased, and the minimum density requirement to heat the thermal plasma from the nonthermal electrons is in the range 10^9 to $6 \times 10^9 \cdot cm^{-3}$. We conclude that in this event it is possible to heat the plasma with the nonthermal electrons.

144

SUMMARY AND CONCLUSION

In this brief paper, we have indicated typical results being obtained from the UCSD instrument on the OSO-7 satellite, which is designed to measure hard and soft X-ray bursts in the 2 to 300 keV range. The dynamic range of the instrument permits separation of thermal from nonthermal continuum emission for a large number of medium sized events in the range of 10^{30} to 10^{31} ergs total energy. We measure the temperature of the hottest portion of the plasma with $T \gtrsim 8 \times 10^6$ K to about 20×10^6 K, depending on the event. The nonthermal photon index, $dN/dE \sim E^{-\gamma}$, is typically in the range $\gamma = 3$ to 8. We do not see indexes flatter than $\gamma \cong 3$ for events which do not saturate the instrument.

We have divided events into a number of different classes, based on the relative intensity and morphology of the thermal and nonthermal components. For a large class of events containing both spectral types, we conclude that it is not possible for the nonthermal electrons to provide the heat input to the thermal plasma, because of energy requirements and the time history, and that there must be additional sources of energy input, such as ohmic heating, to the hot flare plasma. The exact amount of added energy depends on the event and on assumptions regarding the density of the region in which the nonthermal electrons interact; that is, a thin or a thick target case.

In addition to these extensively analyzed events, we note additional event signatures, which include those with purely thermal spectra, at least one event with pure power law X-ray spectra at initiation which relaxed to thermal spectra, and several events with long-lived, hard X-ray emission.

ACKNOWLEDGMENTS

REFERENCES

Arnoldy, R.L., Kane, S.R., and Winckler, J.R., 1968, *Ap. J.* 151, 711.

Brown, J.C., 1971, *Solar Phys.* 18, 489.

Culhane, J.L., and Phillips, K.J.H., 1970, *Solar Phys.* 11, 117.

Datlowe, D.W., McKenzie, D.L., and Peterson, L.E., 1972, Univ. California, San Diego SP-72-06.

De Jager, C., 1968, *Proc. XIth COSPAR Symp. Solar Flares and Space Research*, 1.

Frost, K.J., 1969, *Ap. J.* **158**, L159.

Harrington, T.M., Maloy, J.O., McKenzie, D.L., and Peterson, L.E., 1972, *IEEE Trans. Nuc. Sci.* **NS-19**, 596.

Kahler, S.W., and Kreplin, R.W., 1971, *Ap. J.* **168**, 531.

Kahler, S.W., Meekins, J.F., Kreplin, R.W., and Bowyer, C.S., 1970, *Ap. J.* **162**, 293.

Kane, S.R., and Anderson, K.A., 1970, *Ap. J.* **162**, 1003.

Kane, S.R., and Hudson, H.S., 1970, *Solar Phys.* **14**, 414.

McKenzie, D.L., 1972, *Ap. J.* **175**, 481.

McKenzie, D.L., Datlowe, D.W., and Peterson, L.E. 1973, *Solar Phys.* **28**, 175.

OBSERVATION OF MeV GAMMA-RAY EVENTS
DURING MAY 1967 FROM ERS-18*

D.E. Gruber, L.E. Peterson
University of California, San Diego

J.I. Vette
Goddard Space Flight Center

ABSTRACT

Gamma-ray fluxes between 25 keV and 6 MeV were observed by instruments aboard the Environmental Research Satellite-18 (ERS-18) during the great solar flares of May 21 and May 23, 1967. Measurements were made with a 6.35-cm-diameter by 7.65-cm-long NaI scintillation counter with five differential channels between 0.25 and 6.0 MeV. Data obtained during the event at 1945 UT on May 23, 1967, can be fitted by a two-part, power-law, differential-number spectrum. One part is of spectral index 3.2 between 8 keV and 0.6 MeV, and the other is of spectral index 1.2 above 0.6 MeV. An upper limit of 0.52 photons $\cdot$ $cm^{-2}s^{-1}$ is set for 2.23 MeV line strength for this event. In all three bursts, tentatively associated with white light flares, the MeV-range fluxes declined more slowly than the 25-keV fluxes.

INTRODUCTION

In this paper we report observations of solar gamma-ray bursts with spectra extending to at least 3.7 MeV during the outstanding solar flares of May 1967. These observations were made with a scintillation counter on ERS-18. Fluxes in this range have been predicted due to thermonuclear processes during solar flares, bremsstrahlung of energetic electrons, and nuclear reactions of solar protons (Lingenfelter and Ramaty, 1967). Although considerable effort has been expended searching for such fluxes using balloon and satellite instruments (Chupp, 1971), and hard X-ray bursts have been observed extending to many hundred keV (Holt and Cline, 1968), this is the earliest reported observation of an event with detectable fluxes extending well into the MeV range.

INSTRUMENTATION

ERS-18, launched April 28, 1967, into an elliptical orbit with apogee 18 R_e and perigee 2.7 R_e, carried a variety of detectors sensitive to X-rays, gamma rays, and charged particles. The principal instrument, a 6.35-cm-diameter by 7.65-cm-long NaI(Tℓ) scintillator, measured an energy loss spectrum in seven channels: an integral channel above 25 keV, five logarithmically spaced channels between 250 keV and 6 MeV, and an integral channel above 6 MeV. The 7.8 Kg satellite presented an average shielding of about 8 g $\cdot$ cm^{-2} to the

detector. Charged particle events in this detector were rejected by an anticoincidence shield consisting of 1-cm-thick plastic scintillator surrounding the detector on all sides except for the face joined to the photomultiplier tube. The anticoincidence system was periodically cycled off to determine the energy loss spectrum of charged particles. Events due to MeV-range charged particles penetrating through the photomultiplier tube were possible, and in fact were observed during the once-per-orbit transit of the outer trapped radiation belt, and during solar charged-particle events. But such occasions were clearly marked by their time history and their correlation with counting rates in the satellite's Geiger counters, two solid-state detectors, and two other scintillation detectors.

Data transmission was limited to 4.7-second sequential live-time samplings of a single detector channel. The Geiger tubes and charged-particle monitors were sampled once every 74 seconds, as were the > 25-keV and > 6-MeV channels of the scintillation counter. The five channels covering the 0.25- to 6.0-MeV range were sampled approximately once every 10 minutes. The minimum background duty cycle of these channels was reduced by a factor of two by the on-off-cycle of the plastic anticoincidence shield, for the purpose of measuring cosmic-ray effects. The on-off cycle had a period of ~ 30 minutes. The low data rate, while adequate for measurement of diffuse cosmic background, severely limited measurements of these transient solar events.

In late May 1967, only one of the three Geiger counters included the sun in its field of view, which swept across the sky during the 6-second satellite rotation. Its peak response to 1- to 10-keV solar X-rays was, however, strongly modulated by a 5-minute precession of the satellite spin axis. Correction of the Geiger counter peak response to zero aspect angle was not attempted in this work, due to uncertainties in the Geiger counter angular response and in the aspect solution. Therefore, only 5-minute time solution is possible with these data. The data of Van Allen (1968) covering the May 23, 1967 flare in this energy band are properly corrected for instrument aspect. Data at 25-keV and greater are not affected by aspect problems since the detector is nearly omnidirectional in its response.

OBSERVATIONS

The ERS-18 was moving toward perigee, as shown in Figure 1, during both large solar flares of 1919 UT May 21 and 1800 to 1950 UT May 23, 1967. Steady and low background counting rates prevailed until 2100 UT May 21 and 2040 UT May 23, after which the counter responded to geomagnetically trapped particles.

148

5/21-22/67   5/23-24/67

ERS-18

ORBIT PROJECTION ON ECLIPTIC PLANE
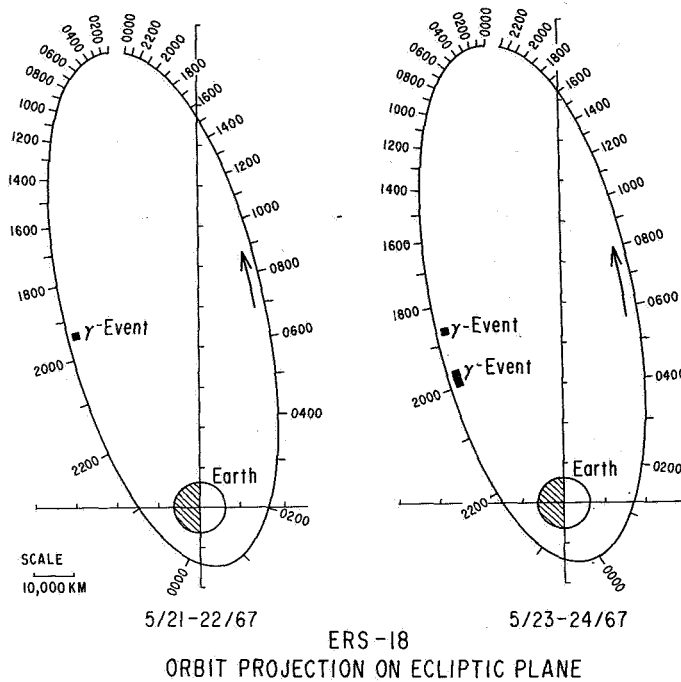
Figure 1. Projection of ERS-18 orbit on the ecliptic plane for periods of May 21-22 (on left) and May 23-24, 1967. Solar direction is to the right and the sunset meridian is toward the vertical, with Universal time marked along the orbit. The satellite was at a distance of 8 to 10 earth radii at the time of the solar gamma-ray bursts on May 21 and.

May 21 Event

Table 1 and Figure 2 show the chronology of the May 21 event. The Hα emission commenced at 1919 UT, peaked at 1926, and continued until 2012. White light emission started at about 1922 and peaked at 1926. Microwave emission also commenced at about 1922, peaked between 1924 and 1926, and declined to less than 10 percent of peak by 1930. The 2 to 12 Å X-ray flux observed by the Geiger counters rose significantly above background by 1923.5, peaked at 1928, and decayed to background levels by 2040. The 25-keV X-ray emission closely followed the microwave emission, starting between 1923 and 1924.2, peaking between 1924.2 and 1925.5, and returning to the background level at 1929. The three MeV-range channels, sampled between 1925 and 1928, show rates statistically significant above background: the 1 to 2 MeV channel at the 2.9σ confidence level, the 2 to 3.7 MeV channel at 2.0σ, and the 3.7 to 6 MeV channel at 1.2σ. The 0.6 to 1 MeV channel, sampled at 1923.6 during the rising phase of the event, showed no increase above background.

149

Table 1
Highlights of Solar Flare of 1919 UT May 21, 1967.

Frequency or Energy	Start (UT)	Peak (UT)	End (UT)	Peak Flux
606 MHz	1922	1923.2	2017	$1842 \times 10^{-22} \text{W} \cdot \text{m}^{-2} \text{ Hz}^{-1}$
1415 MHz	1921	1924.8	2024.6	736.9
2695 MHz	1922.5	1924.0	1948.0	1048
4995 MHz	1922.2	1925.2	1948.0	1787
8800 MHz	1922.8	1925.7	1949.0	1966
10700 MHz	1922.7	1925.3	1930.3	1465
Hα	1919	1926	2024	2n Flare
White Light	1922±4	1926±2	—	
EUV	1920.8	1925.4	>1927	$3 \qquad , \cdot \text{cm}^{-2} \text{ s}^{-1}$
2-12Å	1923.5	1928	2040	0.50
25 keV	>1923.0	1924.2±1	1929	$610 \text{ photons} \cdot \text{cm}^{-2} \text{ s}^{-1}$
1-2 MeV	(1924.9)			$0.090 \pm 0.031 \text{ counts} \cdot \text{cm}^{-2} \text{ s}^{-1} \text{ MeV}^{-1}$
2-3.7 MeV	(1926.2)			0.028±0.014
3.7-6 MeV	(1927.4)			0.012±0.010
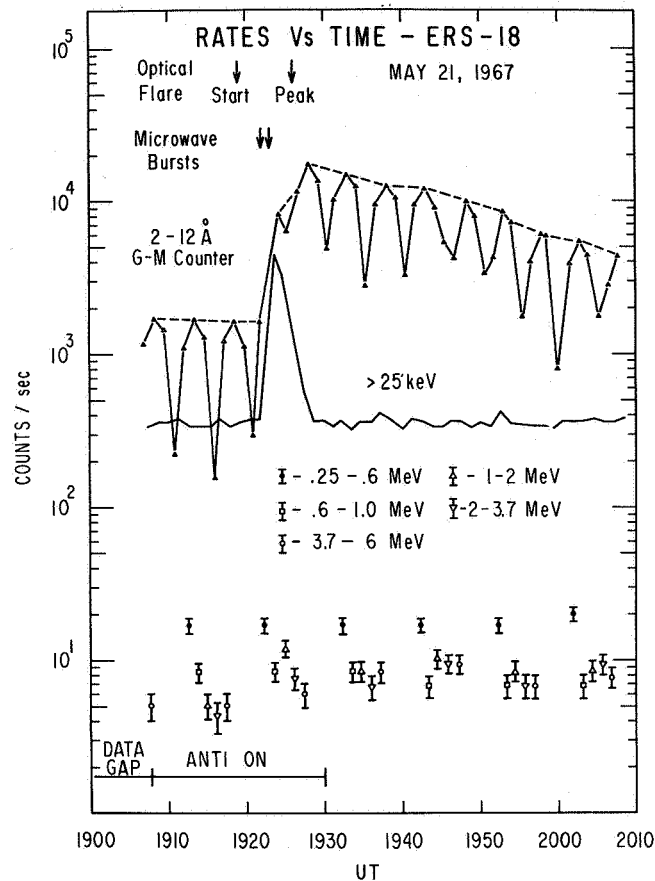
Figure 2. Uncorrected counting rat̶e̶s̶ ̶o̶f̶ the ERS-18 detectors during the event of 1919 ̶U̶T̶ on May 21, 1967. Modulation of the Geiger counter rates is due to precession of satellite spin axis. Only the readout of the 1 to 2 MeV channel at 1924 is significantly above background.

May 23 Event

The extended flare of 1804 to 2100 UT May 23, 1967, peaked three times in Hα at 1814, 1845, and 1955. Figure 3 shows the event chronology along with ERS-18 counting rates. The flare has been described by Dodson (1969) in terms of three phases, each associated with an optical maximum, and a peak in the 2 to 12 Å X-ray emission.

Phase I was marked by modest 2695-MHz emission peaking at 1810, and 2 to 12 Å emission which increased to a level of 0.03 ergs $\cdot$ cm^{-2}s^{-1} at 1817 (Van Allen, 1968).

151
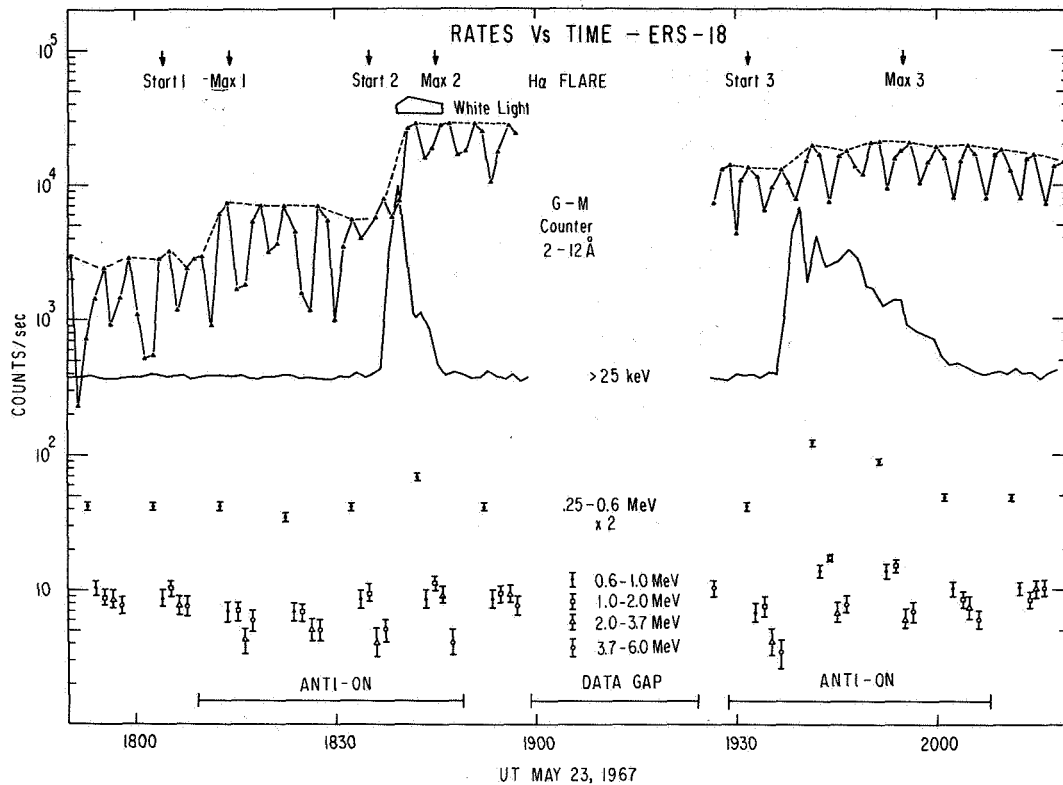
Figure 3. Counting rates of ERS-18 instruments during events of 1804 and 1932 UT on May 23, 1967. Rates of the 0.25- to 6-MeV channel are multipled by a factor of two.

Phase 2, whose main features are shown in Table 2, commenced at about 1835 with another Hα emission increase. The 25-keV emission start and peak times coincide with those of the microwave emission. Unlike the May 21 event, however, the 25-keV flux failed to follow the microwave emission after maximum. The 25-keV flux decayed 9 minutes after peaking at 1839 UT, while microwave emission continued at a high level until the beginning of phase 3.

One full cycle of MeV-range channels was read out by ERS-18 during the decay of phase 2. Table 3 shows the observed rates and statistical significances. Three of the five channels show statistically significant fluxes; these were sampled when the 25-keV flux had declined to between 10 and 1 percent of its peak value at 1839. Further gamma-ray data during phase 2 were not obtained until 1927, at which time the 25-keV channel and the MeV-range channel were counting at background levels.

Table 2

May 23, 1967 Flare — Phase 2 Highlights.

Frequency or Energy	Start (UT)	Peak (UT)	End (UT)	Peak Flux
184 MHz	1835	~1836	1848	—
606 MHz	1835.6	1839.5	—	$534 \times 10^{-22} W \cdot m^{-2} Hz^{-1}$
2695 MHz	1835.5	1839.1	—	2500
8800 MHz	1835	1839.7	—	8100
Hα	1835	1845	—	3b Flare
White Light	1838	1840	1846	14 percent of continuum
EUV	1835.5	~1841	—	$>8 \text{ ergs} \cdot cm^{-2} s^{-1}$
2-12Å (Explorer-33)	1834	1846	—	0.65
10 keV (OGO-III)	1836	1841	—	3×10^{-3}
>25 keV (ERS-18)	1836	1839	1848	$>900 \text{ photons} \cdot cm^{-2} s^{-1}$
>35 keV (ERS-27)	1836	1839	1848	420
0.25-6 MeV (ERS-18)	<1842	—	1846	$0.37 \text{ counts} \cdot cm^{-2} s^{-1}$

Phase 3 began at 1932 with the appearance of new Hα flare segments. The main features of this phase are given in Table 4. Microwave activity greatly increased at 1936, peaked at about 1950, then declined exponentially with an e-folding time of about 8 minutes. The 25-keV emission also started at about 1937, reached a peak at 1940, declined slowly with some evidence of time structure until 1950, £ ⁻ eturned rapidly to the background level by 2006. Three full cycles of the five MeV-range readouts indicated fluxes above background between 1942 and 2006. These observations, shown in Table 3, reached a high level of statistical significance during the first readout cycle, with measurable fluxes still present 20 minutes later. White-light emission, noted during the May 21 and May 23 phase 2 bursts, may have also accompanied the phase 3 event (McIntosh and Donnelly, 1972).

Table 3
Net Counting Rate of Gamma-Ray Channels, 1842-2006 UT May 23, 1967.

Channel	Energy Loss (MeV)	UT hr/min/s	Counts	Net Rate (c/s)	σ (c/s)	Net Rate/σ
8-3	0.25-0.6	184212	144	11.26	2.80	4.03
8-4	0.6-1	184326	40	1.73	1.50	1.15
8-5	1-2	184440	52	4.12	1.68	2.45
8-6	2-3.7	184554	44	5.51	1.51	3.65
8-7	3.7-6	184708	20	-0.43	1.10	-0.39
8-3	0.25-0.6	194122	288	42.4	3.8	11.1
8-4	0.6-1	194236	64	6.92	1.83	3.78
8-5	1-2	194350	80	10.18	2.04	4.99
8-6	2-3.7	194504	32	2.92	1.30	2.24
8-7	3.7-6	194618	36	3.03	1.40	2.17
8-3	0.25-0.6	195114	224	28.6	3.4	8.4
8-4	0.6-1	195228	64	6.92	1.83	3.78
8-5	1-2	195341	72	8.44	1.94	4.35
8-6	2-3.7	195455	00	2.05	1.23	1.67
8-7	3.7-6	195609	52	2.17	1.32	1.64
8-3	0.25-0.6	200109	112	5.05	2.51	2.01
8-4	0.6-1	200221	48	3.46	1.62	2.13
8-5	1-2	200335	40	1.52	1.50	1.01
8-6	2-3.7	200449	36	3.78	1.38	2.74
8-7	3.7-6	200603	28	1.30	1.25	1.04

Table 4

May 23, 1967 Flare — Phase 3 Highlights.

Frequency or Energy	Start (UT)	Peak (UT)	End (UT)	Peak Flux
184 MHz	—	—	—	$>6480 \times 10^{-22}\,W \cdot m^{-2}\,Hz^{-1}$
606 MHz	1930	1948.5	2124	19,200
2695 MHz	1936	1951.8	2023	54,000
8800 MHz	1936	1947	2025	23,000
Hα	1932	1955	2100	3b Flare
White Light (possible)	—	~1937	—	
EUV	1936	~1942	—	$3\ ergs \cdot cm^{-2}\ s^{-1}$
2-12Å (Explorer-33)	1936	1953	>2400	0.28
10 keV (OGO-III)	1934	1942	2030	4×10^{-4}
>25 keV (ERS-18)	1936	1940	2006	$450\ photons \cdot cm^{-2}\ s^{-1}$
>35 keV (ERS-27)	1936	1937.5	2008	280
0.25-6 MeV (ERS-18)	<1941	—	2000	$1.1\ counts \cdot cm^{-2}\ s^{-1}$

DISCUSSION

The X- and gamma-ray fluxes measured by the ERS-18 during the three events are shown in Figure 4. One cannot directly interpret the data in Figure 4 as a set of energy spectra, because individual channels were sampled sequentially, and there may have been time evolution. However, we believe that the MeV-range data of 1940 to 1950 UT May 23 approximate a true energy-loss spectrum since the 25-keV fluxes were nearly constant during this interval. Comparison of rates during decay of the May 23 phase 3 event indicates that fluxes at the MeV energies are more persistent than at 25 keV; a factor of 100 decay in 25-keV X-rays between 1940 and 2005 is accompanied by a decrease in the gamma-ray rates of a factor of only 2 to 5. This relatively long lifetime must have been true in the earlier bursts, for if one assumes the gamma-radiation at higher energies followed the 25-keV time variation, a correction of these observations to a common time would give a spectrum increasing with energy between 0.25 and 6 MeV. We consider such a peculiar instantaneous spectrum highly unlikely.
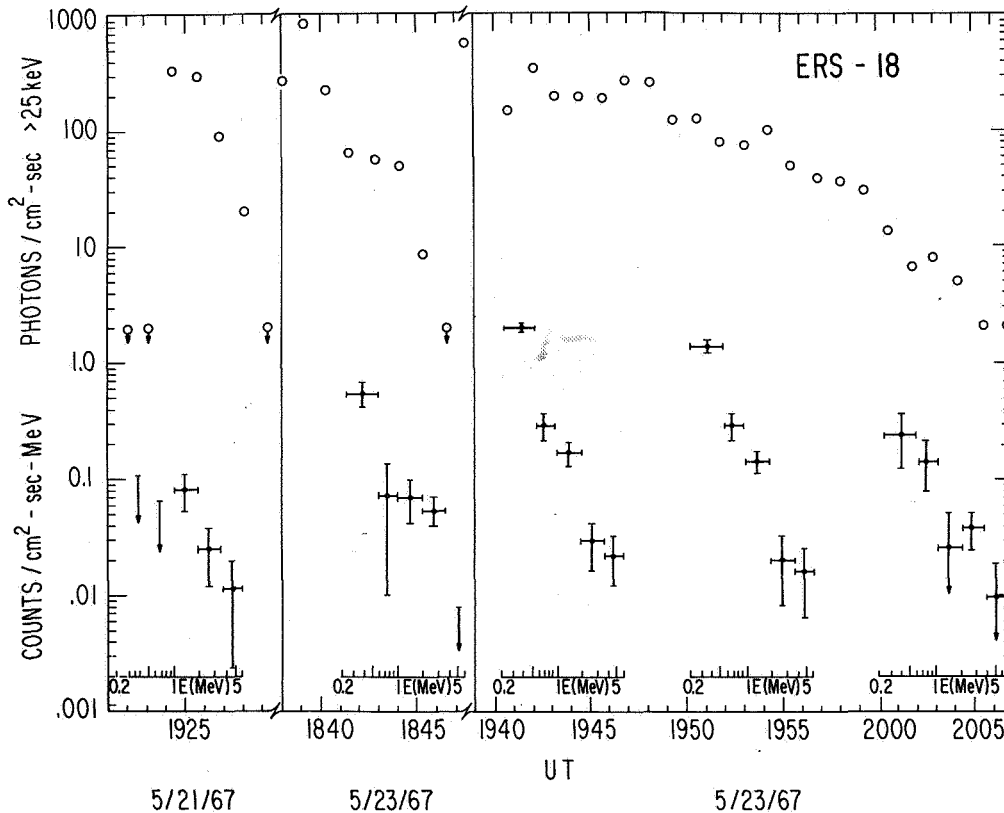
Figure 4. Counting rates of ERS-18 gamma-ray channels during the solar flares of May 21 and 23, 1967. Open circles are measured integral photon fluxes above 25 keV. Crosses represent differential counting rates in the energy range 0.25 to 6 MeV, as indicated by the superimposed energy scale. Only the samples between 1940 and 1946 UT may be read directly as a spectrum; for other data the integral flux above 25 keV changes rapidly during the readout cycle.

156

Model Spectra

A unique determination of photon spectra from energy loss counting rates is not possible, since assumptions must be made about the photon flux above 6 MeV. Absorption in satellite structure introduces a large correction to the 25-keV rates; this is also spectrum dependent. Above ~ 500 keV, the observed energy loss has a complicated statistical relationship to the photon energy, because of the detector response. Taking these various factors into account, we can interpret the observed counting rates during the 1940 to 1950 UT period of the phase 3 flare on May 23 in terms of simple but physically interesting model spectra which are adjusted to fit the data.

A power law photon spectrum of index 3.2 is consistent with results from Orbiting Geophysical Observatory-III (OGO-III) (Kane and Winckler, 1969), and from ERS-18 and ERS-27 (Gardner et al., 1968) in the region 7 keV $\leqslant$ E $\leqslant$ 40 keV, as shown in Figure 5. An extension of this spectrum to the higher energies is clearly a poor fit to the data. Several models have been used to fit the 0.25 to 6-MeV observations: 1) a single power law, 2) a power law with an excess in the 0.25- to 0.6-MeV channel, and 3) a power law with excesses in both the 0.25- to 0.6-MeV and 1- to 2-MeV channels. The values of the parameters obtained for each of these cases are given in Table 5. Monte Carlo calculations for this detector (Peterson et al., 1970) have shown that for power-law spectra, the input photon spectrum may be obtained from the observed energy-loss spectrum by multiplying by a factor of $2.0\,E^{.45}$. In addition, the calculations show that the 0.51-MeV positron annihilation line will be detected with an efficiency of 0.8 in the 0.25- to 0.6-MeV channel. The 2.23-MeV line from deuteron formation will produce energy losses in the crystal mainly in the 1- to 2-MeV channel, with an efficiency of 0.24.

Model 1 produced only a poor fit to the data, but model 2 resulted in an acceptable fit. The good fit was improved only slightly in going from model 2 to model 3, and the 2.23-MeV line strength inferred is not statistically significant. Due to the recent Orbiting Solar Observatory-7 (OSO-7) observation of this line (Chupp et al., 1973) in the August 4, 1972 flare, we determined the maximum 2.23-MeV line strength consistent with the data (model 4 in Table 5). The resulting 95 percent confidence level upper limit of 0.52 photons $\cdot$ cm^{-2}s^{-1} is 1.6 times the OSO-7 measurement. Another model is one in which all the MeV-range radiations which are not a part of the $E^{-3.2}$ power law are attributed to the four nuclear lines at 1.6, 2.23, 4.43, and 6.13 MeV, observed by OSO-7 on August 4, 1972. The fit requires that these lines be present in the ratios 0.4 : 1 : 1 : 1. These ratios are in conflict with the ratios of 0.11 : 1 : 0.12 : 0.12 observed by OSO-7 and also with the calculations of Lingenfelter and Ramaty (1967). Further, the model conflicts with the OSO-7 observation of strong continuum emission accompanying the line emission.
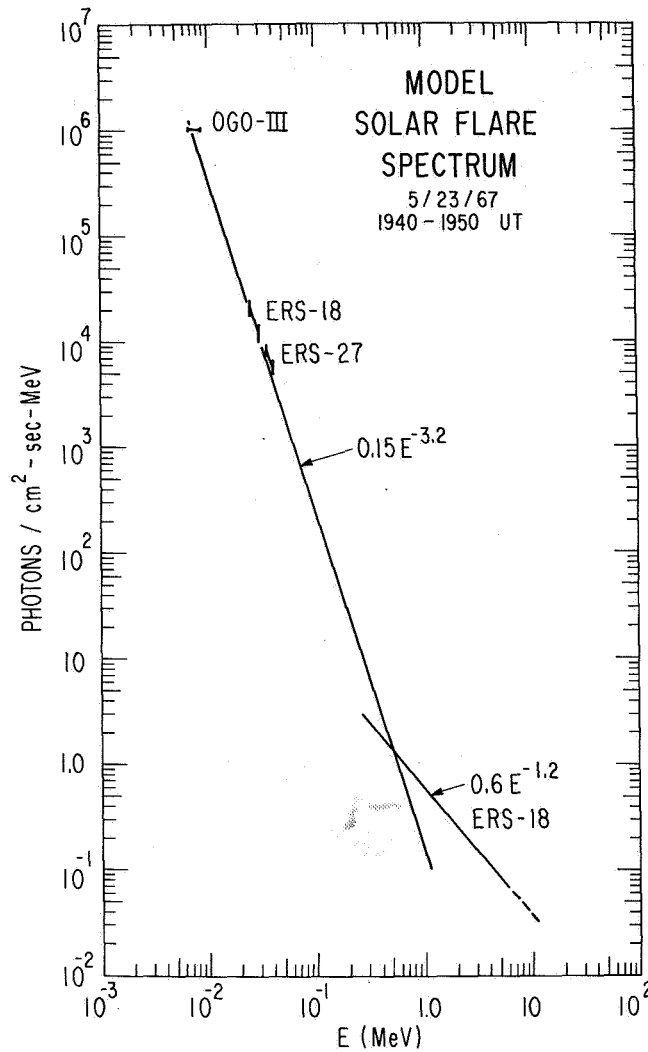
Figure 5. Model photon spectrum between 8 keV
and 10 MeV for the peak of the 1942 UT May 23
event. The $E^{-1.2}$ power law best fitted the data
between 0.25 and 6 MeV. The $E^{-3.2}$ slope represents
a best fit to the X-ray data and to the excess above
the $E^{-1.2}$ spectrum between 0.25 to 0.6 MeV. The
extension of the $E^{-3.2}$ spectrum to such high energies
is uncertain, since the 0.25- to 0.6-MeV excess may be
due to line emission.

Table 5

Best-Fit Model Spectra for May 23 Phase 3 Gamma-Ray Flare

A. Count Rate Spectra

Model	Power law C_0 $(E/0.6\ MeV)^{-I}$		0.25-0.6 MeV excess	1 – 2 MeV excess	Chi-square probability
	C_0 (counts $\cdot$ $cm^{-2}\ s^{-1}\ MeV^{-1}$)	I	(counts $\cdot$ $cm^{-2}\ s^{-1}$)	(counts $\cdot$ $cm^{-2}\ s^{-1}$)	
1	0.88±0.07	2.25±0.12	—	—	0.042
2	0.54±0.04	1.67±0.12	0.37±0.13	—	0.23
3	0.46±0.03	1.65±0.10	0.43±0.14	0.057±0.040	0.37
4	0.30±0.03	1.50±0.10	0.56±0.16	0.125*	0.05

B. Photon Spectra

Model	Power law N_0 $(E/0.6\ MeV)^{-I}$		0.511 MeV line	2.23 MeV line	Chi-square probability
	N_0 (photons $\cdot$ $cm^{-2}\ s^{-1}\ MeV^{-1}$)	I	(photons $\cdot$ $cm^{-2}\ s^{-1}$)	(photons $\cdot$ $cm^{-2}\ s^{-1}$)	
1	1.76±0.14	1.80±0.12	—	—	0.042
2	1.08±0.08	1.22±0.12	0.46±0.16	—	0.23
3	0.92±0.06	1.20±0.10	0.54±0.17	0.24±0.17	0.37
4	0.60±0.06	1.05±0.10	0.70±0.20	0.52*	0.05

*95 percent confidence upper limit

EMISSION MODELS

The two power laws shown in Figure 5 result from using model 2 and attributing the excess in the 0.25- to 0.6-MeV channel to the 3.2 index spectrum which fits the data at lower energy. If this excess were due, instead, to 0.51-MeV radiation, the observation requires a line strength of 0.46 photons $\cdot$ $cm^{-2} s^{-1}$, which is five times the line strength at 0.51 MeV observed by OSO-7 on August 4, 1972. The association of all or most of the 0.25- to 0.6-MeV excess with the 3.2 index spectrum is indicated by a) the excellent fit to the extrapolated 3.2 index power law; b) the above inconsistency with the OSO-7 results; and c) results of fitting model 2 to later data of phase 3, which indicate that the excess declines in time with the $\sim$ 10 minute decay time of the 25-keV results, rather than the $\sim$ 20-minute decay time of the higher energy data.

A power law photon spectrum results, most likely, from bremsstrahlung from a nonthermal power law electron spectrum

$$n(\gamma) = K(\gamma-1)^{-I}$$

and an apparent power law photon spectrum over a decade or less in energy results if the electrons are distributed as an exponential law in rigidity

$$n(\gamma) = K\gamma(\gamma^2-1)^{-\frac{1}{2}} \exp \frac{-0.51\sqrt{\gamma^2-1}}{R_o}$$

where I represents spectral index, R_o is characteristic rigidity, γ is the kinematical $(1-v^2/c^2)^{\frac{1}{2}}$ and K has the dimensions of number density. This terminology and the numbers below follow the calculations of Cheng (1969).

The $E^{-3.2}$ photon spectrum observed over two decades in energy cannot be explained by the rigidity distribution. The observations imply a power-law electron spectrum with spectral index 3.2 and "emission measure" $\int_V n_i K\, dV$ of 1.1×10^{42}. Further, the observed decay time of ~ 10 minutes implies a rather low ambient density, n_i, of about $10^8 \mathrm{cm}^{-3}$ in the radiating region. With this value of n_i we calculate the total number of electrons above 25 keV to be 1.9×10^{36}, with total kinetic energy 2.7×10^{29} ergs.

The $E^{-1.2}$ photon spectrum can result from either a power law or rigidity law electron distribution. The electron power law is characterized by spectral index 1.2 and emission measure 3×10^{42}, while the best-fit rigidity distribution results when R_o is 100 MV and the emission measure is 0.25×10^{40} The ~ 2 minute decay time determines an ambient density, n_i, of $3 \times 10^{(9\pm.5)}\mathrm{cm}^{-3}$. Using $n_i = 3 \times 10^9$ cm^{-3}, we calculate the total number of electrons with energy between 1 and 100 MeV to be 2.6×10^{32} and total energy for these of 0.7×10^{28} ergs. Likewise, for a rigidity spectrum, we obtain 3×10^{32} for the total number of electrons and 5×10^{28} ergs for their total energy. In either case, the failure of a synchrotron radiation cutoff to develop in the 20 minutes between 1945 and 2005 limits the ambient magnetic field to about 100 gauss or less.

On the other hand, if we choose to consider line emission, the upper limit to 2.23-MeV line emission implies an upper limit to the total number of flare-accelerated protons of 4×10^{32} assuming a characteristic rigidity for the protons of 200 MV and a density of 10^{16} cm^{-3} in the radiating region. This corresponds to 1.3×10^{28} ergs in protons, which certainly represents a small portion of the energetics of such events.

It is clear from these results that photons in the MeV range are emitted from the sun in certain flares, and that detailed observations of such events in this region of the spectrum can yield valuable information about the particle acceleration characteristics, and quite possibly about the nuclear reactions which may follow.

ACKNOWLEDGMENTS

REFERENCES

Cheng, Chung-Chieh, 1969, Unpublished thesis, Harvard Univ.

Chupp, E.L., 1971, *Space Sci. Rev.* **12**, 486.

Chupp, E.L., Forrest, D.J., Higbie, P.R., Suri, A.N., Tsai, C., and Dunphy, P.D., 1973, *Nature* **241**, 333.

Dodson, Helen, W., 1969, *World Data Center A*, Report AUG-5, Environmental Science Services Administration, U.S. Dept. of Commerce.

Gardner, J.B., Chapman, M.C., and Vette, J.I., 1968, *Trans. Am. Geophys. Union* **49**, Abstract GA75, 139.

Holt, S.S., and Cline, T.L., 1968, *Ap. J.* **154**, 1027.

Kane, S.R., and Winckler, J.R., 1969, *Solar Phys.* **6**, 304.

Lingenfelter, R.E., and Ramaty, R., 1967, in *High Energy Nuclear Reactions in Astrophysics* (New York, W.A. Benjamin, Inc.)

McIntosh, P.S., and Donnelly, R.F., 1972, *Solar Phys.* **23**, 444.

Peterson, L.E., Gruber, D., Matteson, J.L., Vette, J.I., 1970, Univ. California, San Diego SP-70-03.

Van Allen, 1968, *Ap. J.* **152**, L85.

HIGH-ENERGY SOLAR X-RAY POLARIMETRY

R.S. Wolff

Columbia Astrophysics Laboratory
Departments of Astronomy and Physics
Columbia University

ABSTRACT

This paper reviews the evidence, obtained by many workers, for the existence of a highly energetic nonthermal electron distribution in the solar atmosphere during energetic flares. Relationships are discussed between the proposed X-ray emission processes, electron distribution, and possible X-ray polarization. A description of various techniques of measuring X-ray polarization is given, and the applicability of these methods to the problem of solar X-ray measurements is considered. An idealized polarimeter capable of obtaining the most useful data related to the energetics of solar flares is proposed, and current and projected polarization experiments are discussed.

INTRODUCTION

Evidence for the existence of a highly energetic population of nonthermal electrons in the solar atmosphere during large flares has been obtained through numerous observations of the temporal and wavelength dependences of hard X-ray bursts. Correlation of the X-ray and microwave emissions indicates that high energy electrons may be responsible for both phenomena. To explain the observations, models have been proposed in which nonthermal electrons trapped by magnetic field lines simultaneously emit microwaves by synchrotron radiation and X-rays by linear bremsstrahlung in collisions with the ambient gas. Further support for the fundamental role of high-energy electrons in flares is given by comparisons of X-ray and optical flares. The comparisons indicate that the onset of the hard X-ray flares generally precedes the maxima in Hα. The gradual rise in low-energy X-ray and optical emission following the initial impulsive hard X-ray phase suggests the heating of ambient plasma through thermalization of the energetic electrons. Thus the high-energy electron population may play a central role in the diverse aspects of solar flares. Measurements of the properties of these electrons would then be of great importance in understanding the energetics and mechanisms of flares.

Additional information concerning the nature of the nonthermal electron population and its origin can be obtained by measuring the polarization of the hard X-ray bursts. Linearly polarized X-rays will be produced through collisions by an anisotropic electron flux. The degree of polarization, angle of orientation, and wavelength dependence are all functions of the properties of the electron population and the conditions in the emitting region.

Observations of polarized bursts of hard X-rays during large flares have been reported by Tindo et al. (1972), confirming the proposed emission mechanism. Thorough analysis and quantitative inferences await more detailed measurements of the energy and time variations of the polarization.

In subsequent sections of this paper we will review the evidence for high-energy electrons and their role in flare phenomena; discuss the theory of polarized X-ray emission and its application to solar conditions; and describe methods of detecting solar X-ray polarization. We then summarize the experimental situation to date and the outlook for future measurements.

HIGH-ENERGY X-RAY BURSTS

Observations of high-energy X-rays ($E > 10$ keV) emitted during flares were first made by Peterson and Winckler (1959) and have subsequently been performed with numerous balloon-, sounding-rocket-, and satellite-borne instruments. Detailed studies of these X-ray bursts have revealed high temporal variations, spectra, and correlations with related flare phenomena. The time development of the X-ray flux of a large number of flares has been examined by Kane and Anderson (1970). Using data obtained from the Orbiting Geophysical Observatory-5 (OGO-5) satellite, they found that the impulsive, hard X-ray bursts are characterized by very short rise times, 2 to 5 seconds at 40 keV, and rapid decay times, 3 to 10 seconds at 40 keV. These impulsive bursts are often superimposed, particularly at lower energies, on a more gradually rising component of the X-ray flux, which reaches its maximum after the decline of the impulsive phase. Frost (1969) has measured the time behavior of X-rays over the 14- to 250-keV range with the OGO-5 satellite. His results show very rapid growth and decay as well as the appearance of repetitive peaks, several seconds in duration and separated by about 30 to 40 seconds. These pulses are most readily seen in the short wavelength region, where the gradually rising component of the X-ray flux is least apparent.

An important aspect of the temporal structure of the hard X-ray flux, first pointed out by Kundu (1961), is its close association with microwave bursts. First, there is a similarity in the time development of the X-ray and radio fluxes; second, the detailed features are well correlated in the two phenomena, as shown in Figure 1 (Frost, 1969). X-ray bursts observed by OGO-5 (Kane and Anderson, 1970) also exhibit good correlation with radio emission at frequencies ranging from 1400 MHz to 15,400 MHz. More than a year of data obtained by the Orbiting Solar Observatory-3 (OSO-3) satellite were studied by McKenzie (1972), who found that 94 percent of the hard X-ray bursts could be associated with micro-wave events. The degree of correlation increased with the intensity of the impulsive component of the X-ray flare.
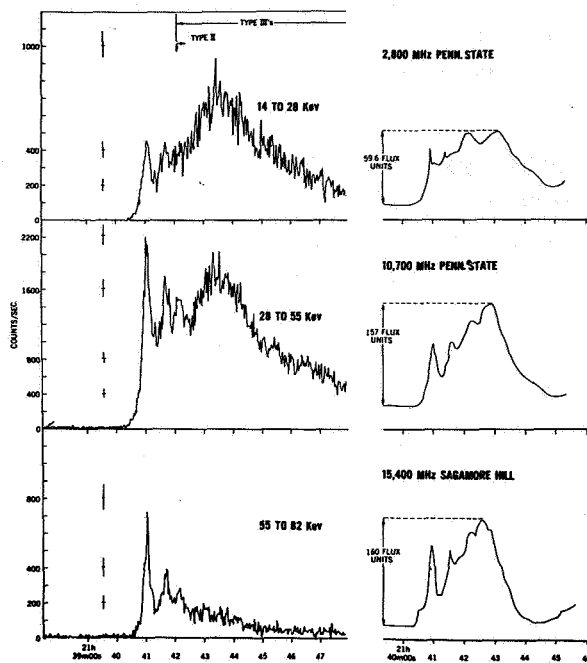
Figure 1. Comparison of hard X-ray and radio bursts
of March 1, 1969, measured by OSO-5 (Frost, 1969).

Spectral measurements of impulsive X-ray 〱 ⁓⁓⁓s have been carried out by instruments on OSO-3, OSO-5, and OGO-5. Kane and Anderson (1970) find that the photon flux is consistent with a power-law spectral distribution

$$N(E) = KE^{-\gamma} \text{ photons} \cdot \text{cm}^{-2} \text{ s}^{-1} \text{ keV}^{-1} \tag{1}$$

where γ ranges between 2.7 and 4.5 for $10 \leqslant E \leqslant 70$ keV. Of 129 X-ray events recorded by OGO-5, all could be characterized by spectra with $\gamma > 2.4$ (Kane, 1971). The shape of the spectrum varies with time. Frost (1969) has shown that the flux at the peak of an X-ray burst could be characterized by a power-law spectrum with $\gamma = 3/2$, but later in the event the spectrum had steepened and could be fitted by $\gamma = 5$. This later measurement was interpreted as the mixture of thermal and nonthermal components of the X-ray flux. Similar changes in the shape of the spectrum have been reported for OGO-5 data.

The properties of the hard X-ray bursts are generally ascribed to the existence of a population of nonthermal, highly energetic electrons in the solar atmosphere. Synchrotron, inverse-Compton scattering, or bremsstrahlung can be invoked as possible X-ray production mechanisms, but bremsstrahlung seems to be the most plausible (Korchak, 1971). The

164

impulsive behavior and correlation with microwaves argue strongly in favor of linear bremsstrahlung from electrons with a power-law distribution

$$N_e(E) = K_e E^{-\delta} \text{ electrons} \cdot \text{cm}^{-2} \text{ s}^{-1} \text{ keV}^{-1} \qquad (2)$$

where the index δ is related to the photon distribution exponent by

$$\gamma = \delta + 1.2$$

for thin target bremsstrahlung (Kane, 1971). This inference is supported by both the time behavior of the X-ray flux and the simultaneous measurements of microwave emission. As the incident electron flux collides with the ambient gas, energy is lost, and the high-energy electron population is depleted. The electron spectrum, and consequently the photon spectrum, steepens, as is evidenced by the increases in γ during the decay phase of the X-ray burst. The growth of the slow-rising X-ray component of the flare further supports this argument, as the second phase of X-ray emission is interpreted as thermal bremsstrahlung from a high-temperature plasma, heated by thermalization of the electron flux. Finally, the microwaves are generated by synchrotron emission from the same electron population. As the electrons travel into the chromosphere, they are trapped on the magnetic field lines and subsequently lose some of their energy by the synchrotron process. The time required for 10- to 100-keV electrons to lose their energy by synchrotron emission in a magnetic field of 1000 gauss or less is approximately 200 seconds. This implies that the microwave emission is consistent with the X-ray production, but does not constitute a controlling factor in the energetics of the electron distribution (Holt and Cline, 1968).

Direct measurements of electrons in the interplanetary medium correlated with nonthermal X-ray emission have been reported by Lin and Hudson (1971). They find that the electron flux can be interpreted as a fraction of the nonthermal atmospheric electron flux responsible for the flare X-ray bursts which have escaped to the interplanetary medium. The efficiency that is required for escape is between 0.1 percent and 1 percent. These direct measurements, in conjunction with the interpretations of the hard X-ray bursts, are conclusive evidence for the existence of a nonthermal electron distribution. Further properties of these electrons can be ascertained by examining the polarization of the X-rays.

X-RAY POLARIZATION

The polarization of X-rays produced by electron bremsstrahlung can be readily calculated. Using the geometry shown in Figure 2, we find that in the nonrelativistic limit of the Born-Coulomb approximation for electron collisional bremsstrahlung, the differential cross sections are given by (Elwert and Haug, 1970)

$$\sigma_{\perp} = CA \qquad (3a)$$

$$\sigma_{\parallel} = C(A + B \sin^2 \theta) \qquad (3b)$$
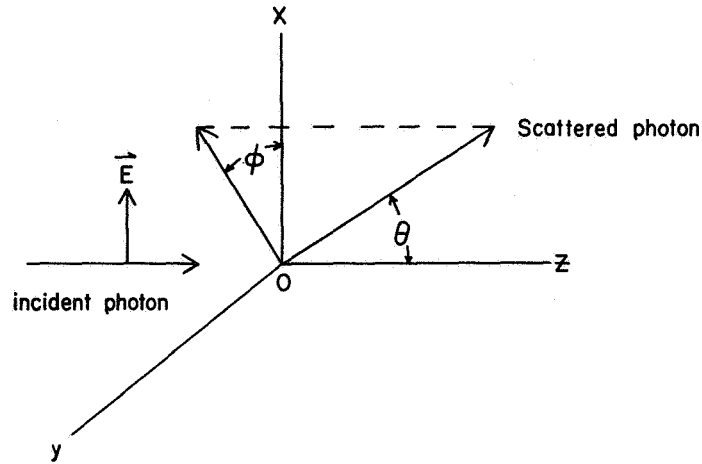
Figure 2. Coordinate system for Thomson scattering. The electric field of the incident photon is taken parallel to the X axis.

where A, B, and C are functions of the initial and final electron momenta, photon energy, and target nucleus mass. The two cross sections refer to emission of photons with electric vectors perpendicular and parallel to the plane of emission, and θ is the angle between the initial electron momentum and the line of sight. The degree of polarization of the radiation is defined by

$$P = \frac{\sigma_\perp - \sigma_\parallel}{\sigma_\perp + \sigma_\parallel} \tag{4}$$

which, when combined with Equations (3a) and (3b), yields

$$P = -\frac{B \sin^2 \theta}{2A + B \sin^2 \theta} \tag{5}$$

For $\theta = \pi/2$, the polarization will be a maximum and will vanish for $\theta = 0$.

Applications of Equations (3), (4), and (5) to the X-ray bursts associated with solar flares require a knowledge of the electron energy and velocity distributions as well as the density and composition of the target material. Elwert (1968), Korchak (1967), and Elwert and Haug (1970) have considered possible conditions in which electron bremsstrahlung would give rise to polarized hard X-ray bursts. For a beam of monoenergetic, unidirectional electrons incident on hydrogen gas, the amount of polarization and its sign depend on

166

photon energy and viewing angle as shown in Figure 3(a) (Korchak, 1967). When the viewing angle is 90 degrees, the degree of polarization reaches 100 percent for maximum photon energy E_γ. The negative sign indicates that the electric vector lies in the plane of emission. The polarization passes through zero and becomes positive for $E_\gamma = 0.12\ E_0$, where E_0 is the incident electron energy, independent of the viewing angle. This energy dependence is an important aspect of linear bremsstrahlung polarization, as photons produced by the synchrotron process are polarized negatively, independent of energy. Thus measurement of the energy dependence of X-ray polarization serves to distinguish the two production mechanisms.
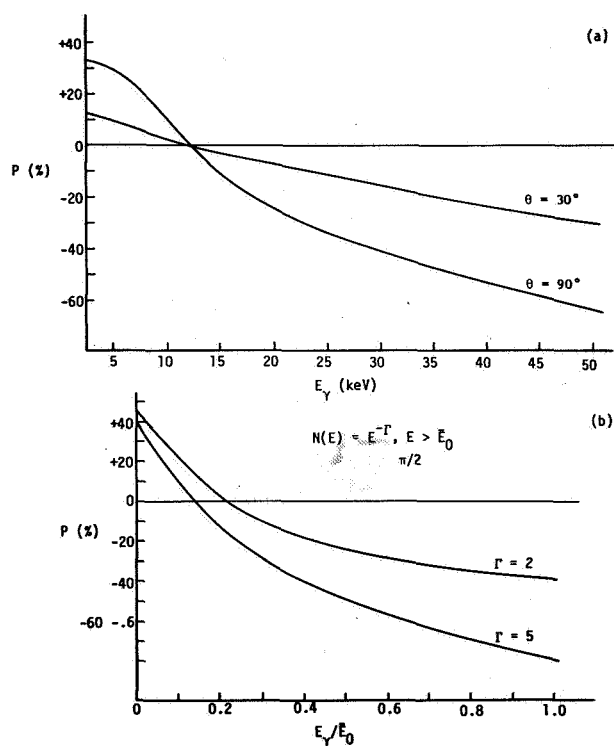
Figure 3. (a) Polarization of bremsstrahlung as a function of the photon energy E_γ for two viewing angles θ relative to the direction of the electron flux. Electron energy $E_0 = 100$ keV (Korchak, 1967). (b) X-ray polarization as a function of energy for bremsstrahlung from a power-law distribution of electrons N(E). Viewing angle is $90°$ (Korchak, 1967).

Under more realistic conditions, the electrons have an energy distribution, and, as suggested by the photon spectral measurements, a power law is expected. If Equations (3) are integrated over electron energy E_e where

$$N_e(E_e) = KE_e^{-\delta}, \quad E_e \geqslant E_0 \tag{6}$$

the resultant polarization becomes a function of δ. For a viewing angle of $\pi/2$, the results are shown in Figure 3(b) (Korchak, 1967). The basic shape of the energy dependence of the polarization is preserved, but the maximum polarization and energy of zero polarization vary with δ. For values of $\delta \leqslant 1$, the polarization is always positive, but as discussed in the previous section, such a shallow electron spectrum is not expected.

The assumption that the electron beam is parallel can also be relaxed, resulting in further modifications of the shape of the polarization curve. Elwert and Haug (1970) have considered the case in which the electrons are trapped on magnetic-field lines and are gyrating with a pitch angle α measured relative to the direction of the field. If the nonthermal electron distribution is given by (Elwert and Haug, 1970)

$$N_e(E_e) = a - b (E_e - c)^2 \tag{7}$$

the subsequent polarization, obtained by integrating over electron energy and direction, is as shown in Figure 4 for various viewing angles. These curves are specific to photons observed at 3 keV. The more general case, where the electrons are distributed in pitch angle in accordance with

$$F(\alpha) = \sin^n \alpha \tag{8}$$

where n is an integer, has been considered by Korchak (1967). He finds that the greatest polarization is obtained for the high values of n. If we average over both a power-law energy distribution and a sinusoidal angle distribution for the electron flux, the polarization of the photon flux is still maintained. At a viewing angle of $\pi/2$ relative to the magnetic field, the polarization will reach a maximum of 37 percent for an electron energy spectrum characterized by $\delta = 6$ and a direction distribution given by Equation (8) with n = 1. The important point is that anisotropy in the nonthermal electron distribution will result in the production of polarized photons.

Measurement of X-ray polarization provides a means of determining conditions in the emitting region. If the electrons are streaming radially into the solar atmosphere, as suggested by De Jager and Kundu (1963), the polarization will be a minimum in flares at the center of the disk and a maximum at the limb. The angle of polarization for limb flares should vary with latitude, reflecting the radial orientation of the magnetic field. If the electrons are gyrating about the field lines, their projected motion is tangential to the limb,
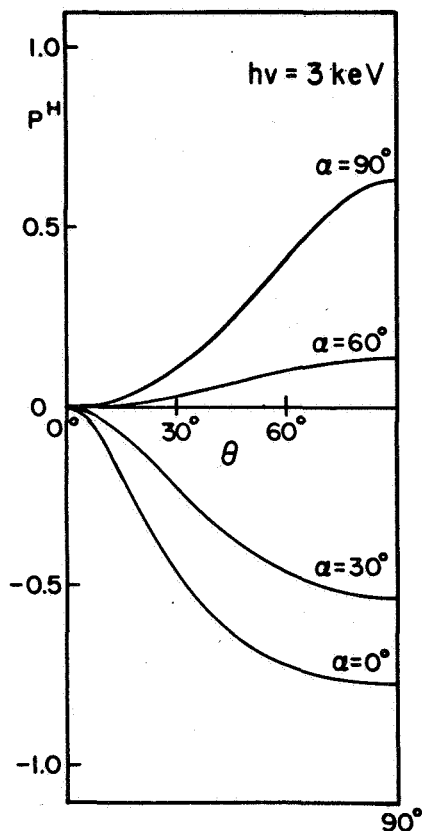
Figure 4. X-ray polarization as a function of viewing angle θ for bremsstrahlung from electrons spiraling around a magnetic field with pitch angle α (Elwert and Haug, 1970).

and the polarization at high energies should be similarly directed. In the alternative case, suggested by Takakura and Kai (1966), the electron motion is approximately horizontal in the emitting region. The polarization of disk flares will be large, but limb flares will be unpolarized if the magnetic field is equatorial.

MEASUREMENT OF X-RAY POLARIZATION

Several techniques are available for detecting X-ray polarization: anomalous transmission (Borrmann effect), incoherent (Thomson) scattering, and coherent (Bragg) reflection. The efficiency and wavelength range of each method must be considered to determine its applicability to solar X-ray polarization measurements. Detection of X-ray polarization is rendered particularly difficult by photoelectric absorption of the incident photons by the analyzing materials. Unlike photons at optical wavelengths, which scatter from atoms as a whole, X-rays are energetic enough to interact with individual atomic electrons causing ionization as well as scattering. Competition between photoelectric and scattering processes deems all polarization-sensitive effects for X-rays extremely inefficient, relative to the methods available in the visible part of the spectrum.

The Borrmann effect (Cole et al., 1961) occurs when X-rays incident on a perfect crystal set up standing waves in the lattice. If the wavelength, lattice parameters, and angle of incidence are properly chosen, the minima of the standing-wave pattern will occur at the atomic sites, reducing the probability of photoelectric absorption. The standing-wave effect is most pronounced for photons polarized perpendicular to the plane of incidence, and only the component of the incident beam bearing this polarization is transmitted. The polarization of the flux can be measured by rotating the analyzing crystal around the axis of the incident X-ray beam. The efficiency of Borrmann transmission is extremely low — typically 0.01 percent of the photons satisfying the wavelength criterion will reach the detector (Cole et al., 1961). An added disadvantage of this method is that the analyzer is monochromatic. Since knowledge of the energy dependence of the polarization is important in distinguishing the emission process, anomalous transmission is unsuitable for solar X-ray polarization measurements.

169

Coherent scattering, or Bragg reflection, using crystal lattices is a well-known technique for measuring X-ray polarization. If the Bragg condition for a wavelength λ is satisfied in a particular crystal at $2\theta = 90°$, the crystal will reflect only those X-rays with electric vectors perpendicular to the plane of incidence. As shown in Figure 5(a), a polarimeter can be constructed by detecting the scattered photons and rotating the analyzer and detector about the axis of the incident beam (Angel and Weisskopf, 1970). Since the Bragg condition is satisfied at only one photon energy for a given crystal lattice and orientation, polarization can be measured at a single wavelength. This limitation can be partially circumvented by constructing a curved panel of mosaic crystals. In a crystal polarimeter used for a stellar X-ray polarization measurement (Weisskopf et al., 1972), a curved crystal panel was employed to yield a response between 2 and 3.3 keV. In addition to photons lost due to the wavelength criteria, photoelectric absorption poses an additional limitation. The efficiency of the analyzer is improved by using low-Z materials with a high density of electrons in the lattice planes, such as graphite. With this technique, up to 0.15 percent of the flux from a continuum which satisfies the Bragg condition at 2.3 keV would reach the X-ray detector (Angel and Weisskopf, 1970).

Broad-band X-ray polarimetry can best be accomplished by using incoherent electron scattering, as was first demonstrated by Barkla in 1912 (Compton and Allison, 1935). At photon energies below the electron rest mass energy, the atomic incoherent scattering cross section closely resembles the Thomson cross section for a free electron and is polarization dependent (Heitler, 1954):

$$\frac{d\sigma}{d\Omega} = \left(\frac{e^2}{mc^2}\right)^2 (1 - \sin^2 \theta \cos^2 \phi) \tag{9}$$

where θ is the scattering angle and ϕ is the angle between the initial electric vector and a projection of the scattered momentum in a plane perpendicular to the initial momentum. The polarization of the incident flux can be inferred from the azimuthal dependence ϕ of the scattered flux perpendicular to the incident beam ($\theta = 90°$). As shown in Figure 5(b), a polarimeter utilizing this technique is readily constructed with a scattering block and detectors; polarization is manifested either as a modulation in the detected photon counting rate in each detector as the instrument is rotated, or as a difference in the rates for detectors on adjacent faces of the block. The advantages of incoherent scattering are that photoelectric losses can be minimized by choosing a low-Z scattering material, and that the Thomson cross section is independent of energy over a broad wavelength band.

Incoherent scattering polarimeters have been built and used for stellar X-ray polarimetry (Novick et al., 1972; Wolff et al., 1970). A similar instrument has been prepared for a solar X-ray flare polarization measurement. Satellite-borne solar X-ray polarimeters have been used on the Russian Intercosmos spacecraft (Tindo et al., 1972) and most recently on the OSO-7 satellite. The solar X-ray polarimeter built at this laboratory consists of a matrix of

170
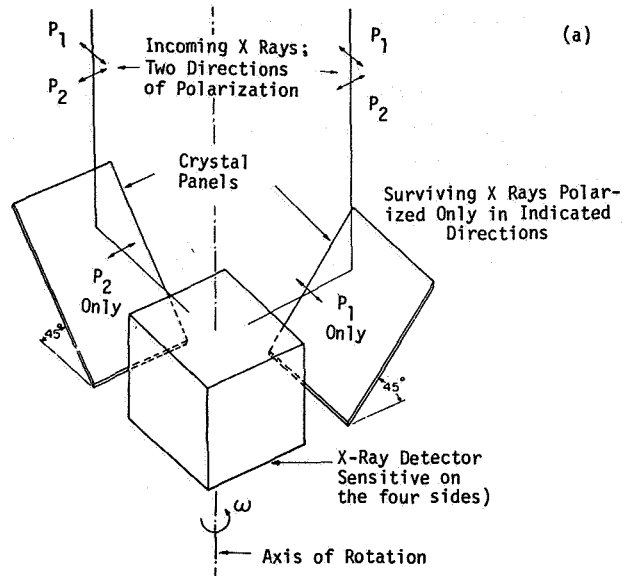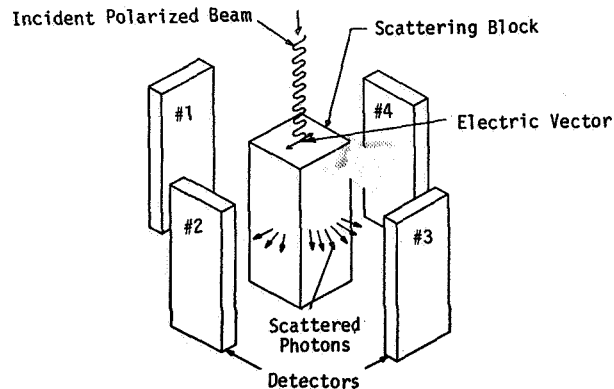
Figure 5. (a) Principle of operation of a coherent scattering polarimeter. Only those X-rays satisfying the Bragg condition and whose electric vectors are normal to the plane of scattering will be reflected into the detectors. (b) Principle of operation of an incoherent scattering polarimeter. Photons scattered at 90° obey a $\sin^2 \phi$ azimuthal dependence. The finite solid angle of the detectors results in a 30 percent modulation in the detected signal for a completely polarized incident X-ray flux.

twelve 2 X 2 X 5 inch lithium scattering blocks and sixteen proportional counters. The bandwidth of the instrument is determined by the high photoelectric absorption in the lithium below 5 keV and by the efficiency of the detectors and steeply declining X-ray flux at high energies. Using the X-ray data reported for a flare observed by OSO-3 (Hudson et al., 1969), we have calculated the minimum detectable polarization in energy bands up to 90 keV, as shown in the following list:

Minimum Detectable Polarization from 5 to 90 keV in 100-second
Observation Time at 99 percent Confidence Level

Energy Range (keV)	Polarization (percent)
5 to 9	<1
10 to 20	1
20 to 30	1.6
30 to 40	1.8
40 to 50	1.8
50 to 60	3.0
60 to 70	5
70 to 80	8.7
80 to 90	18.7

The response of this polarimeter is maximum between 10 and 25 keV, the region in which the hard X-ray flux observed in bursts is greatest. The time resolution of the polarimeter is determined by the telemetry capacity and the rotation rate. Measurements of polarization on a time scale of one second are achieva⁕ ⅃t the longer wavelengths where the flux is greatest. The instrument was prepared for use in a sounding rocket experiment, but due to the abnormally low level of solar activity between 1970 and 1972, the necessary conditions for a launch were not achieved.

OBSERVATIONS OF SOLAR X-RAY POLARIZATION

The observational situation of solar X-ray polarimetry is still rudimentary, primarily due to the difficulties inherent in making these measurements. Although the importance of examining flare X-ray bursts for polarization has long been appreciated, it is only most recently that sufficiently sophisticated X-ray polarimeters have been constructed and spacecraft made available. It is first worth noting the properties which a polarimeter must have to detect the degree of polarization which we can anticipate based on the probable X-ray burst emission mechanisms. We can then discuss the outlook for polarization measurements in progress and instruments planned for the future.

The broad energy range and rapid time variations of hard X-ray bursts immediately suggest parameters which should be incorporated in an X-ray polarimeter. The impulsive flux extends from 5 or 10 keV upwards to 100 keV or more, making a broadband instrument

172

highly desirable. Since measurement of polarization with energy can help to determine the production process, the polarimeter should be capable of obtaining spectral data. A single, broad energy channel has the further disadvantage that changes in the spectral shape of the incident flux will result in changes in the detected signal, which could be confused with changes due to X-ray polarization. Well-calibrated detectors, with pulse-height analysis, are strongly recommended. The rapid time variations in the flux dictate that a high data readout rate be utilized. Polarization could be varying with intensity, and the effect of long integration periods will be to average the measurements. The time structure of the bursts suggests that each data channel be sampled at least once per second.

The merits of using a stationary or rotating polarimeter are related to the need for a high data readout rate. A stationary polarimeter has the inherent disadvantage of relying on the comparison of data from different detectors to determine polarization. Such comparisons can be made only if the relative sensitivities of the individual detectors are well known or periodically measured by a calibration X-ray source. If the instrument is rotated, each detector serves as a separate polarimeter: Polarization is measured by analyzing the counting rate for modulation in phase with the rotation period. In this approach, the data from each detector are statistically independent. Comparisons of results from different detectors can be used as a check on the measurement but are not necessary to obtain a result. However, the rotation technique is applicable only if the polarization of the incident flux remains constant for at least a quarter of a rotation period. A rotation rate of 15 rpm would therefore be desirable.

The field of view of solar X-ray polarimeters can be wide enough to accept the whole sun, unless detailed examination of the emitting region is planned. Provided the energy range of the instrument is above 5 keV, the X-ray flu.* m the quiescent solar atmosphere will be negligible compared to the flare-associated X-ray burst. The size of the active region responsible for hard X-ray emission is likely to be quite small: Study of the spatial distribution of the polarized X-ray flux would require arc-second pointing accuracy and field of view. Such measurements would prove interesting in correlating the magnetic field configuration with the X-ray emission, but would put severe demands on the capabilities of the polarimeter spacecraft.

Although the incident flux due to hard X-ray bursts is substantial, the requirement of rapid temporal measurements combined with the relatively low efficiencies of polarimeters makes it necessary to utilize large-area instruments. As shown in the list preceding, high-precision measurements can be achieved if the polarimeter's effective area is large enough. The sounding-rocket polarimeter constructed by Columbia has an effective area of 300 cm^2. Since polarizations of 5 to 20 percent are expected, the sensitivity of instruments with smaller effective areas would be seriously limited by finite counting statistics.

Positive solar X-ray polarization measurements have been made with polarimeters on the Intercosmos 1 and 4 satellites (Tindo et al., 1972). These polarimeters consist of a stack of beryllium scattering plates surrounded by six proportional counters. Although the satellites

rotate, the rate is only 0.3° s^{-1}, and polarization is detected by comparison of the counting rates in different detectors. The data readout rate of 16 seconds per sample precludes the study of rapid time variations. The results for three impulsive flares are given for measurements made over a broad energy band centered at 15 keV. Polarization is seen to last for 5 to 10 minutes, being greatest at the beginning of the X-ray burst and again during secondary maxima. The maximum degree of polarization observed ranged between 12 and 21 percent. Data from a large number of events are required to establish correlations between the X-ray polarization, position of the flare on the disk, microwave emission, and other associated phenomena.

A small, beryllium block polarimeter has been included among the experiments on the OSO-7 satellite launched in 1971 (Neupert, private communication, 1972). Due to the relatively low level of solar activity in the past year and the limited area of the instrument, no results have been reported as yet. A small incoherent scattering X-ray polarimeter is planned for the Solrad-11 satellite (Doschek, private communication, 1972). To be launched in 1974, the instrument will consist of a lithium scattering block with 6 cm^2 effective area, surrounded by proportional counters. A readout rate of eight samples per revolution (15 rpm) is expected. Finally, recommendations have been made to place a large-area incoherent scattering polarimeter on the OSO-K satellite. Still in the planning phase, this spacecraft may be devoted entirely to the study of solar flares, as its 1978 launch date coincides well with the next solar maximum. The polarimeter suggested would incorporate all the features previously discussed that are required to measure the energy and time dependence of solar X-ray polarization.

ACKNOWLEDGMENT

REFERENCES

Angel, J.R.P., and Weisskopf, M.C., 1970, *Astron. J.* 75 231.

Cole, H., Chambers, F.W., and Wood, C.G.J., 1961, *J. Appl. Phys.* 32, 1942.

Compton, A.H., and Allison, S.K., 1935, *X-Rays in Theory and Experiment* (New York, D. Van Nostrand Co.).

De Jager, C., and Kundu, M.R., 1963, *Space Res.* III, 836.

Elwert, G., 1968, in *Structure and Development of Solar Active Regions* IAU Symp. 35, (Dordrecht, Holland, D. Reidel Publishing Co.), 444.

Elwert, G., and Haug, E., 1970, *Solar Phys.* **15**, 234.

Frost, K.J., 1969, *Ap. J.* (Letters) **158**, L159.

Heitler, W., 1954, *The Quantum Theory of Radiation*, 3rd ed. (Oxford, Clarendon Press).

Holt, S.S., and Cline, T.L., 1968, *Ap. J.* **154**, 1027.

Hudson, H.S., Peterson, L.E., and Schwartz, D.A., 1969, *Ap. J.* **157**, 389.

Kane, S.R., 1971, *App. J.* **170**, 587.

Kane, S.R., and Anderson, K.A., 1970, *Ap. J.* **162**, 1003.

Korchak, A.A., 1967, *Soviet Phys. — Doklady* **12**, 192.

Korchak, A.A., 1971, *Solar Phys.* **18**, 284.

Kundu, M.R., 1961, *J.G.R.* **66**, 4308.

Lin, R.P., and Hudson, H.S., 1971, *Solar Phys.* **17**, 412.

McKenzie, D.L., 1972, *Ap. J.* **175**, 481.

Novick, R., Weisskopf, M.C., Berthelsdorf, R., Linke, R., and Wolff, R.S., 1972, *Ap. J.* (Letters) **174**, L1.

Peterson, L.E., and Winckler, J.R., 1959, *J.G.R.* **64**, 697.

Takakura, T., and Kai, K., 1966, *Publ. Astron. Soc. Japan* **18**, 57.

Tindo, I.P., Ivanov, U.D., Mandel'shtam, S.L., and Shuryghin, A.I., 1972, *Solar Phys.* **24**, 429.

Weisskopf, M.C., Berthelsdorf, R., Epstein, G., Linke, R., Mitchell, D., Novick, R., and Wolff, R.S., 1972, *Rev. Sci. Instr.* **43**, 967.

Wolff, R.S., Angel, J.R.P., Novick, R., and Vanden Bout, P., 1970, *Ap. J.* (Letters) **160**, L21.

III: MICROWAVE AND HARD
X-RAY THEORIES

THEORY OF MICROWAVE AND X-RAY EMISSION

Tatsuo Takakura
Department of Astronomy
University of Tokyo

INTRODUCTION

The behaviour of the nonthermal electrons created at the impulsive phase of flares has been deduced from the microwave impulsive bursts and hard X-ray bursts by many researchers. There is almost no doubt of the emission mechanisms that radio emissions are due to gyrosynchrotron emission and hard X-rays are collisional bremsstrahlung. However, there remain three controversial problems. One is whether the emission sources of the microwave impulsive burst and hard X-ray burst are common or not. Another is whether the injection of the nonthermal electrons into the source is impulsive or continuous. The other is the relation among the nonthermal electrons, soft X-rays, EUV flash, Hα kernels, and white light flares. These three problems are not independent of each other.

I would like to show that the interpretations and models proposed so far by many researchers, including myself, on the first problem, were partly right but partly wrong. Some remarks on the second and third problems will be given in the last section.

The first problem is mainly ascribed to a large discrepancy between the numbers of nonthermal electrons estimated from hard X-rays and radio waves. X-ray estimates give about a thousand times greater value in the same energy range above 50 keV or 100 keV. It will be shown that this discrepancy is solved if we take into account the following three factors, implying that the sources of the X-rays and radio waves could be almost *common in a broad sense*. The three factors, all of which tend to decrease the discrepancy, are

- The magnetic field in the source is nonuniform.

- The energy distribution of electrons has a steeper slope above 100 keV.

- There is self-absorption (reabsorption) of gyrosynchrotron emissions at low microwave frequencies.

It may be remarked here that the electrons below 100 keV give only negligible contribution to the microwave bursts at high microwave frequencies. In this respect, the electrons emitting hard X-rays below 100 keV and electrons emitting microwaves are *not common,* even if they belong to the same family and have common emission sources.

NONUNIFORM MAGNETIC FIELD

It is highly probable that the magnetic field is not uniform in the radio source. In this case, the effective radio source depends on the frequency (Takakura and Scalise, 1970). For example, 80 percent of emissions at 9.4 GHz originate from a region in which magnetic field is ranging from 900 to 150 gauss, while it is 300 to 100 gauss at 3.75 GHz. Therefore, the volume of the effective source *at any point frequency* is only 10 percent or less of the whole source in which nonthermal electrons are trapped. Accordingly, the previous discrepancy is reduced by more than one order due to the above effect.

ENERGY SPECTRUM OF ELECTRONS

The spectra of hard X-rays have been shown by Frost (1969), Kane and Anderson (1970), Frost and Dennis (1971) to have a steep slope above 80 to 100 keV. It shows that the exponent Γ of power law energy spectrum of the nonthermal electrons is 4 to 5 above 100 keV. On the other hand, Γ is very sensitive to the gyrosynchrotron emission at high microwave frequencies, say above 10 GHz. Under a given integrated number of electrons above 100 keV, the radio flux decreases remarkably with increasing Γ at high microwave frequencies, while the flux of X-rays at 100 keV is almost the same. Accordingly, the previous discrepancy is reduced by two orders due to the above effect. This effect is analogous to the high energy cutoff of electrons above 1.5 MeV proposed by Holt and Ramaty (1969) to solve the discrepancy.

SELF-ABSORPTION OF GYROSYNCHROTRON EMISSIONS

The suppression of radio flux at low microwave frequencies due to the self-absorption (reabsorption) of gyrosynchrotron emission has been proposed by Holt and Ramaty (1969). The importance of this effect depends critically on the source size and Γ. If Γ is large, electrons with lower energies are relatively abundant and make the self-absorption of gyrosynchrotron emission effective at low microwave frequencies. Furthermore, the observed size of radio sources is rather small (Enome, 1973), typically 30 arcsec or less; this makes the required number density of nonthermal electrons higher. Accordingly, self-absorption must be taken into account. This effect is to limit the intensity at low microwave frequencies.

THEORETICAL RADIO SPECTRUM

Taking into account the above three factors, the radio spectrum of gyrosynchrotron emission from electrons trapped in part of a dipole magnetic field has been computed. The details will appear elsewhere (Takakura, 1972).

The model of the radio source is shown in Figure 1. The parameters for a standard model, denoted by subscript s, are

$$d_s = 1.11 \times 10^4 \text{ km}$$

$$B_s(0) = 2500 \text{ gauss}$$

$$B_s(2) = 60 \text{ gauss} \qquad (\chi = 1, \text{ see Figure 1})$$

where $\underline{B}(2)$ indicates the magnetic field at an upper boundary of radio source, Γ is 4, and the integrated number density of the electrons above 100 keV is set as

$$n_s(>0.2) = 10^6 \cdot {}^5 \text{cm}^{-3}$$
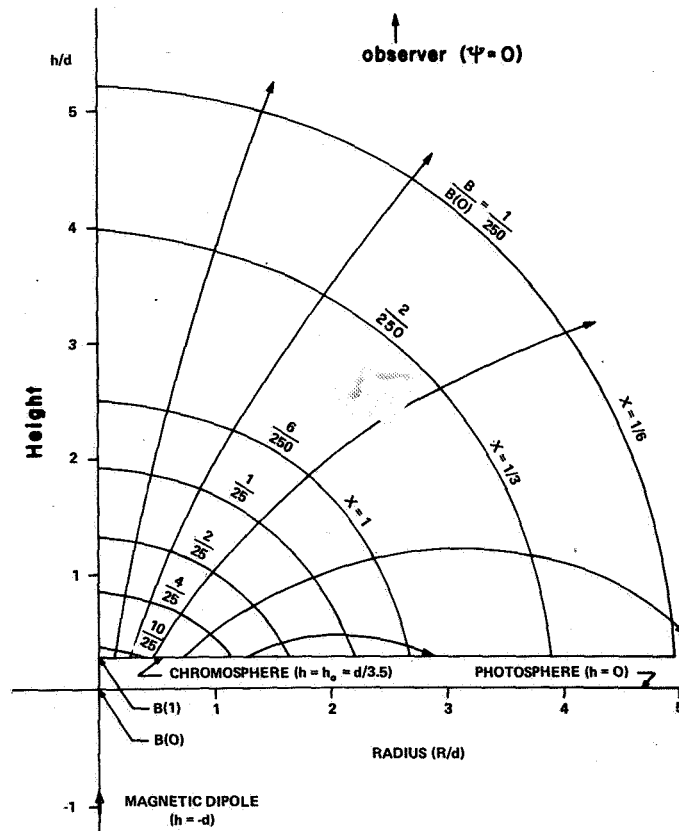
Figure 1. Model of magnetic field in the radio source showing a cross section in the ecliptic plane. The radio source is axially symmetric about the axis of the magnetic dipole in a limited range of the azimuthal angle ϕ. χ is a measure for the upper boundary of the radio source. The normalized value of the magnetic field strength is indicated on the curves.

The number density is assumed to be uniform in the source and the pitch-angle distribution is isotropic.

The theoretical spectra are shown in Figure 2, in which $\mathcal{L} = \underline{d/d}_s$ and $\mathcal{B} = \underline{B}(0)/\underline{B}_s(0)$ are dimensionless parameters proportional to the linear size of radio source and the magnetic field strength, respectively, and $\zeta\ (\equiv\eta\mathcal{L}/\mathcal{B})$ is proportional to the optical thickness for self-absorption, where $\eta = n(>0.2)/n_s(>0.2)$. These parameters are unity in the standard model. The flux at low frequencies depends on the outer boundary of the source. The decrease of flux at lower frequencies is ascribed to the saturation due to the self-absorption. This tendency is the same as in the uniform model given by Holt and Ramaty (1969). With increasing optical thickness ζ, the peak of the spectrum shifts towards higher frequencies, owing to the saturation at the lower frequencies.
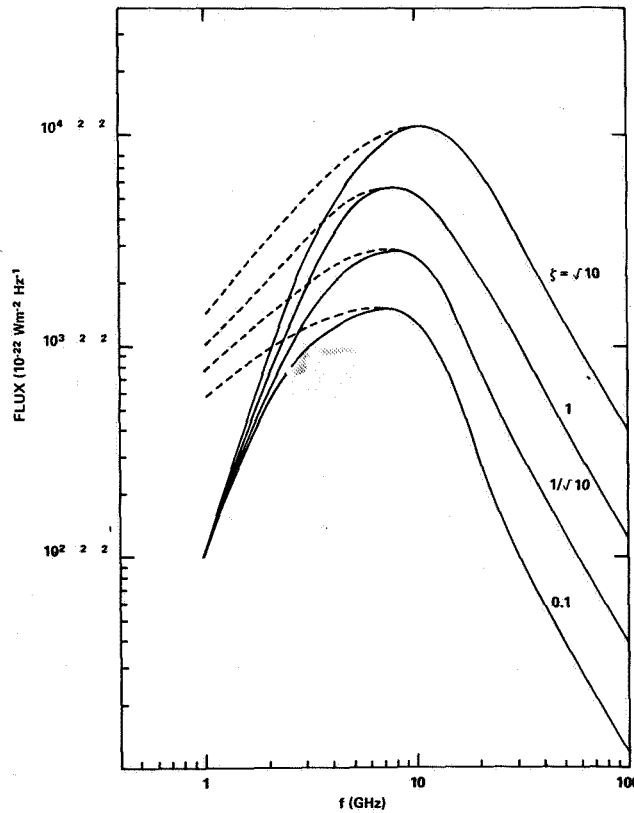
Figure 2. Theoretical radio spectra of the present model; azimuthal extension of the source is set as π. The solid curves are for $\chi = 1$, and dashed curves are for $\chi = 1/6$ (compare Figure 1). For the standard model, $\mathcal{B}$, $\mathcal{L}$, ζ, and χ are unity and ζ is proportional to the optical thickness of the source.

One example of observed radio spectrum and its time variation of burst on July 7, 1966, which has been well studied (Holt and Ramaty, 1969), is shown in Figure 3. Time is shown on the curves in minutes referring to the time at the peak intensity. It is remarkable that the frequency drift of the spectrum peak is comparatively small; this is a rather common characteristic of microwave bursts. It means that the time variation of the optical thickness ζ which is proportional to the number density of energetic electrons is small during the burst. This would imply that the acceleration region progressively moves *horizontally* (azimuthal direction in the present model (see caption to Figure 1). Movement from one azimuth, ϕ_1, to another ϕ_2, leaves the accelerated electrons behind during the increasing phase of the burst. Thereafter, the energetic electrons trapped in the magnetic tubes decay successively from ϕ_1 to ϕ_2, due to collisions and/or escape into the chromosphere.
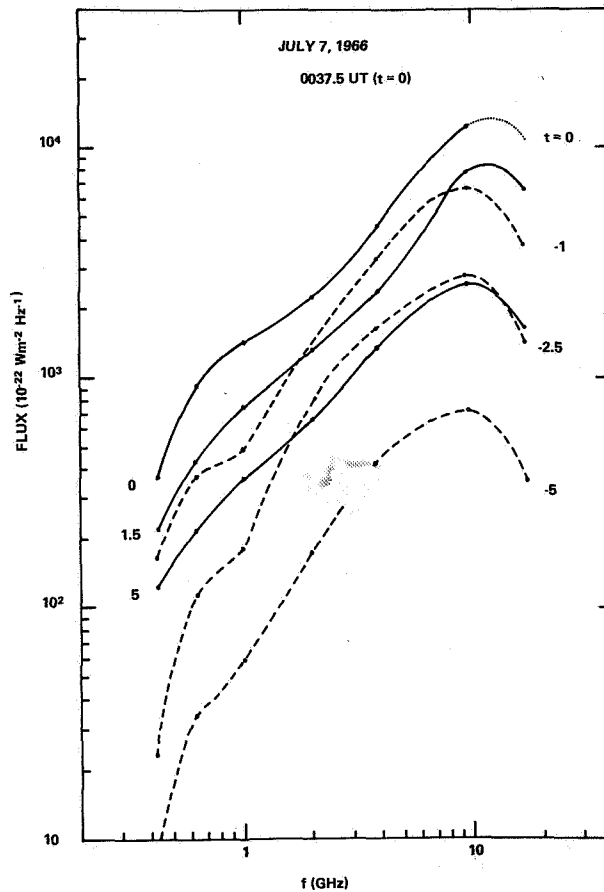
Figure 3. Time variation of spectrum of the radio burst on July 7, 1966. Time t on the curves indicates time difference in minutes measured from the time of peak flux, 0037.5 UT. Data at 1, 2, 3.75, and 9.4 GHz courtesy of Research Institute of Atmospherics, Toyokawa; data at 408 MHz, 612 MHz, and 17 GHz from Tokyo Astronomical Observatory, Mitaka.

If we compare the theoretical spectra with the observed radio spectra, we can estimate the source parameters $\mathcal{B}$, $\mathcal{L}$, and η if we know the sunspot magnetic field B(0) or the size of radio source. If we put B(0) = 2500 gauss ($\mathcal{B}=1$) in the event of Figure 3, we have $\zeta \cong 10$, $\mathcal{L} \cong 1$, and $1 < \chi < 1/6$ at the maximum phase of the burst. The total number of nonthermal electrons above 100 keV in the whole radio source is thus reduced to about 10^{36}. This is of the same order as estimated from X-ray observation at this event if the mean target density is 10^{10} cm^{-3}. This plasma density seems reasonable in the lower part of the source, but it seems one order high around the upper boundary of the source, so that the mean value in the whole source would be $10^{9 \cdot 5}$ cm^{-3}. Thus the discrepancy is only a factor 3. This small discrepancy may be solved if Γ is 5 or 6 instead of 4, as suggested by Brown (1972), or if the contribution of X-rays emitted from electrons streaming into the chromosphere for a thick target are not negligible (Brown, 1971).

It should be remarked that even if the sources of hard X-rays and microwaves are almost common in a wide sense, the effective radio source at any point frequency is only a small fraction of the whole source, so that it is not common with the X-ray source in a narrow sense.

Another remark is that the altitude of effective center of the hard X-ray source may be lower than the center of the whole radio source, because the target density generally increases with decreasing altitude in the source. There are some evidences showing the altitudes of the radio and hard X-ray sources at the infralimb flares. The altitude of effective radio source at 3 to 4 GHz seems to be 10^4 to $10^{4 \cdot 5}$ km and that of hard X-rays may be slightly lower (Enome and Tanaka, 1971; Γ e 1971; Frost and Dennis, 1971; Kane and Donnelly, 1971).

This is strong evidence against the thick-target model in which the nonthermal electrons are continuously injected into the chromosphere to emit hard X-rays and impulsive microwave bursts, mainly in the chromosphere and the transition layer, since the top of the chromosphere (T $\cong 10^4$ K) may be (2 to 3) $\times 10^3$ km in altitude even in active centers (Simon and Noyes, 1972). On the other hand, one of the objections against the impulsive injection model is the softening of X-ray spectrum during the burst decay phase (Kane and Anderson, 1970). However, Brown (1972) recently presented a model in which the effective target density of Coulomb collision may increase with energy of the nonthermal electrons, if the electrons are trapped in a magnetic flux tube and the higher energy electrons have lower mirror points at which target density is higher. This is reasonable, since acceleration of electrons along the magnetic field lines is more likely. The polarization of hard X-ray bursts observed by Tindo et al. (1970, 1972a, 1972b) model. However, the predominant polarization seems to be concentrated only in the increasing phase of the associated microwave bursts, though the increase in thermal component may seriously reduce the degree of polarization at the later phase.

I have emphasized the impulsive injection model too strongly. However, in the present stage, it seems difficult to say that the hard X-ray component from the chromosphere is much less than that from the lower corona. Those two could be of the same order, since the accuracy of present estimate is not better than a factor of 2.

In some infrequent cases, the flux of microwave impulsive burst increases with frequency at least up to 70 GHz (for example, Croom, 1970). This could be ascribed to the smaller value of electron spectral index Γ in those events. If Γ is between 2 to 1 in the energy range from 100 keV to at least a few MeV, the peak of the radio spectrum may be 70 GHz or more, due to the self-absorption at lower frequencies (previously discussed under Theoretical Radio Spectrum), even if the effective magnetic field in the source is several hundred gauss.

Although the microwave impulsive bursts and hard X-ray bursts are highly correlated, the second phase of the radio bursts, called microwave type IV, is generally not accompanied by appreciable hard X-rays. It would be partly ascribed to the less steep slope of the nonthermal electrons above 100 keV at the second phase. If the spectral index Γ is 2 instead of 4, about 1 percent of nonthermal electrons above 100 keV is enough to emit a radio flux at the second phase comparable with that of the impulsive phase, but the X-rays at 100 keV become 1 percent of the impulsive phase. In addition to this, the source height seems to be higher at the second phase (Kai, 1968; Krivsky et al., 1972) so that target density is lower.

RELATION AMONG NONTHERMAL ELECTRONS, EUV FLASH, AND THERMAL X-RAYS

If we reasonably compromise the observations and models proposed so far by many researchers, we may have the following model: The nonthermal electrons trapped in a magnetic flux tube are thermalized due to Coulomb collisions with ambient thermal electrons to heat up the lower corona to 20 to 40 million kelvin with an emission measure of 10^{48} cm^{-3} (Neupert et al., 1969). This very hot plasma may be cooled down in a few minutes to 10 million kelvin (Horan, 1971) due to conduction and radiation. During these few minutes, strong heat flow along the magnetic field would heat the chromosphere and the photosphere to emit the EUV flash (Hall, 1971), Hα kernels (Vorpahl, 1972) and the white light flare, although part of the nonthermal particles may stream into the chromosphere to participate in the heating and excitation. The time profiles of flash of EUV lines originating from the transition layers seem to be similar to the associated microwave impulsive bursts and hard X-ray bursts (Kane and Donnelly, 1971; Castelli and Richards, 1971; Neupert 1971a,b). From this comparison, however, it seems difficult to exclude the heat flow as the cause of the heating of upper chromosphere.

On the other hand, the energy source to create a more gradual hot coronal condensation with an emission measure of 10^{50} cm^{-3} and temperature of 10 million kelvin, which emits thermal soft X-rays and a gradual microwave burst for a few hours, could not be ascribed to the nonthermal electrons. This is evident from the fact that such hot condensations frequently occur without accompanying, detectable, nonthermal impulsive bursts containing enough electron energy to create such hot condensations.

185

REFERENCES

Brown, J.C., 1971, *Solar Phys.* **18**, 489.

Brown, J.C., 1972, *Solar Phys.* **25**, 158.

Castelli, J.P., and Richards, D.W., 1971, *J.G.R.* **76**, 8409.

Croom, D.L., 1970, *Solar Phys.* **15**, 414.

Enome, S., 1973, These proceedings.

Enome, S., and Tanaka, H., 1971, IAU Symp. 43, *Solar Magnetic Fields* (D. Reidel Publ. Co.), 413.

Frost, K.J., 1969, *Ap. J.* **158**, L159.

Frost, K.J., and Dennis, B.R., 1971, *Ap. J.* **165**, 655.

Hall, L.A., 1971, *Solar Phys.* **21**, 167.

Holt, S.S., and Ramaty, R., 1969, *Solar Phys.* **8**, 119.

Horan, D.M., 1971, *Solar Phys.* **21**, 188.

Kai, K., 1968, *Publ. Astron. Soc. Japan* **20**, ⊥ J.

Kane, S.R., and Anderson, K.A., 1970, *Ap. J.* **162**, 1003.

Kane, S.R., and Donnelly, R.F., 1971, *Ap. J.* **164**, 151.

Krivsky, L., Tlamicha, A., Halenka, J., Lastovicka, J., Triska, P., Pinter, S., and Ilencik, J., 1972, *Bull. Astron. Inst. Czech.* **23**, 94.

Neupert, W.M., 1971a, *Physics of the Solar Corona* (D. Reidel Publ. Co.), 237.

Neupert, W.M., 1971b, *Phil. Trans. Roy. Soc. London* **A270**, 143.

Neupert, W.M., White, W.A., Gates, W.J., Swartz, M., and Young, R.M., 1969, *Solar Phys.* **6**, 183.

Simon, G., and Noyes, R.W., 1972, *Solar Phys.* **22**, 450.

Takakura, T., 1972, *Solar Phys.* **26**, 151.

Takakura, T., and Scalise, E., Jr., 1970, *Solar Phys.* **11**, 434.

Teske, R.G., 1971, *Solar Phys.* **17**, 181.

Tindo, I.P., Ivanov, V.D., Mandel'stam, S.L., and Shuryghin, A.I., 1970, *Solar Phys.* **14**, 204.

Tindo, I.P., Ivanov, V.D., Mandel'stam, S.L., and Shuryghin, A.I., 1972a, *Solar Phys.* **24**, 429.

Tindo, I.P., Valnicek, B., Livshits, M.A., and Ivanov, V.D., 1972b, Levedev Phys. Inst., Spectroscopy Lab. Preprint 43.

Vorpahl, J.A., 1972, *Solar Phys.* **26**, 397.

THEORY OF SOLAR MICROWAVE BURSTS

R. Ramaty
Laboratory for High Energy Astrophysics
Goddard Space Flight Center

ABSTRACT

The theory of solar microwave bursts is discussed in terms of gyrosynchrotron emission and absorption in a magnetoactive plasma and other absorption processes by the background medium. Simplified formulae for all turnover frequencies are given. Above about 2 GHz the most likely absorption processes for large bursts are free-free absorption and gyrosynchrotron self-absorption. The former process is capable of producing flux densities which are flat or slowly varying functions of frequency. The latter process sets absolute upper limits on the intensities of microwave bursts, which at a given frequency, depend only on the magnetic field in the source region.

INTRODUCTION

Large impulsive solar microwave bursts (> 100 sfu) are generally believed to be produced by gyrosynchrotron radiation of nonthermal electrons accelerated in solar flares (Takakura, 1967; Ramaty, 1969). The necessity of nonthermal processes for the production of such bursts follows from upper limits on temperatures and emission measures of solar flare plasmas as determined from X-ray observations. From the excellent time correlation between microwave and hard X-ray bursts, it follows that the microwave emission should be produced by essentially the same electron population as the X-rays; that is, by mildly relativistic electrons of energies less than a few MeV. Such electrons produce radio emission principally by the gyrosynchrotron process.

The application of the theory of gyrosynchrotron emission (Takakura, 1967) to solar microwave bursts, however, is complicated by a variety of suppression and absorption effects which modify the radio spectrum at low frequencies. These effects are: absorption below the plasma frequency, free-free absorption, gyroresonance absorption, gyrosynchrotron self-absorption, and the Razin effect. The first three processes result from the background plasma and do not depend on the radiating electrons; they can be treated independently of the gyrosynchrotron emission mechanism itself. Gyrosynchrotron self-absorption is the consequence of gyrosynchrotron emission, because any emission process is accompanied by a corresponding absorption process. The Razin effect is the term commonly used for the suppression of gyrosynchrotron emission caused by the influence of the background plasma. The last two processes cannot be treated independently of the radiation mechanism, and require a complete theory of emission and absorption in magnetoactive plasma (Ramaty, 1969).

188

In the present paper we first review the background absorption processes and we give simplified formulae for their turnover frequencies (that is, the frequencies of unit optical depth). We then review the theory of gyrosynchrotron emission and absorption in a magnetoactive plasma. Numerical calculations are presented for the intensity of a gyrosynchrotron source and used to justify simplified formulae for the turnover frequencies due to gyrosynchrotron self-absorption and the Razin effect. We then give numerical values for all turnover frequencies in a large solar microwave burst and examine some of the consequences of free-free absorption and gyrosynchrotron self-absorption regarding microwave spectra and maximum intensities. Finally, we examine the peak flux densities of the largest solar microwave bursts and show that the maximum intensity allowed by gyrosynchrotron self-absorption was not exceeded by any of these bursts.

BACKGROUND ABSORPTION PROCESSES

From magnetoionic theory it is well known that radiation does not propagate below the plasma frequency. In a cold electron plasma the ordinary and extraordinary modes are absorbed below ν_p and $\nu_x = (\nu_p^2 + 1/4\,\nu_B^2)^{1/2} + 1/2\,\nu_B$, respectively, where ν_B and ν_p are the gyro and plasma frequencies of the background medium. Even though there are frequency bands below ν_p and ν_x where the index of refraction is real, radiation produced in these bands does not escape from an atmosphere in which the density decreases with distance from the radio source to the observer. Therefore, we consider ν_p and ν_x as the turnover frequencies for absorption below the plasma frequency in the ordinary and extraordinary modes, respectively.

Free-free absorption is the inverse of bremsstrahlung. The free-free absorption coefficient at a frequency ν is $K_{ff}(\nu)$, given by (Ginzburg and Svatskii, 1965)

$$K_{ff}(\nu) \cong 10^{-2}\;\frac{n^2}{\nu^2 T^{3/2}}\left(17.7 + \ln\frac{T^{3/2}}{\nu}\right) \tag{1}$$

where n and T are the density and temperature of the background electrons in cm^{-3} and K, respectively; K_{ff} is in cm^{-1}, and ν is in Hz. The turnover frequency ν_{ff} due to free-free absorption corresponds to unit optical depth ($K_{ff}L = 1$) and is given by (Ramaty and Petrosian, 1972)

$$\nu_{ff} \cong 0.38\,\langle n\rangle\,L^{1/2}\,T^{-3/4}\,X. \tag{2}$$

Here L is the depth of the source in cm, $\langle n\rangle$ is the mean background density, and ν_{ff} is in Hz. The quantity X is the clumpiness factor of the ambient medium, defined as the ratio of the rms density to the mean density, $X = \langle n^2\rangle^{1/2}/\langle n\rangle$. According to some observations (Acton, 1968), this factor in solar flares could be as large as 3 to 5.

The process of gyroresonance absorption was first discussed by Ginzburg and Zheleznyakov (1959) and the absorption coefficient was derived most recently by Takakura and Scalise (1970). As discussed in detail by Takakura (1967), both the ordinary and extraordinary modes are absorbed at the first and second harmonics, whereas only the extraordinary mode is absorbed at the third harmonic. This statement depends on the temperature and density of the thermal electrons, and for higher densities ($> 10^{10}$ cm^{-3}) and temperatures ($> 10^7$ K), absorption at the fourth harmonic is also possible. In the present discussion we shall consider the fourth harmonic as the gyroresonance turnover frequency

$$\nu_g = 4\nu_B \tag{3}$$

GYROSYNCHROTRON EMISSION AND ABSORPTION

The theory of gyrosynchrotron emission and self-absorption in a magnetoactive plasma and its application to solar radio bursts was given in Ramaty (1969). In this treatment, the radio source at the sun was assumed to consist of a homogeneous system of energetic electrons moving in a homogeneous, cold, and collisionless electron plasma permeated by a static and uniform magnetic field. The intensity $I(\nu, \theta)$ as a function of frequency ν can then be written as

$$I_\pm (\nu, \theta) = \frac{j_\pm (\nu, \theta)}{K_\pm (\nu, \theta)} [1 - \exp(-K_\pm L)] \tag{4}$$

where θ is the angle between the direction of observation and the magnetic field in the source, L is the depth of the source along the line of sight, and $j_\pm$ and $K_\pm$ are the gyrosynchrotron emissivities and absorption coefficients in the ordinary (+) and extra-ordinary (-) modes. The quantities j and K were calculated in detail (Ramaty, 1969). These calculations were based on a formula deduced by Liemohn (1965). Recently Trulsen and Fejer (1970) and Ko (1973) have shown that Liemohn's formula contains an erroneous multiplicative term, $1 + (\nu/\mu) \partial\mu/\partial\nu$, where μ is the index of refraction. For the frequencies of interest in Ramaty (1969) and the present paper, this term is of the order of 1. Consequently, for computational simplicity the term $1_+ (\nu/\mu) \partial\mu/\partial\nu$ was neglected in actual numerical calculations of Ramaty (1969), even though it does appear in the radiation formulae given in that paper. The results of the numerical calculations presented below are therefore completely consistent with the corrections of Trulsen and Fejer (1970) and Ko (1973).

In Figure 1 we show the intensity $I(\nu,\theta)$ from a gyrosynchrotron source of the above properties. In these calculations, $\theta = 45°$, the electrons have an isotropic pitch-angle distribution and an energy spectrum which is a power law in kinetic energy with differential spectral index 3. B is the magnetic field in the source in gauss, N is the total number of electrons of energies greater than 100 keV, A is the area of the source in cm^2, and $\alpha = 3/2$ (ν_B/ν_p) is the Razin parameter which takes into account the effect of the ambient medium on gyrosynchrotron emission.

190
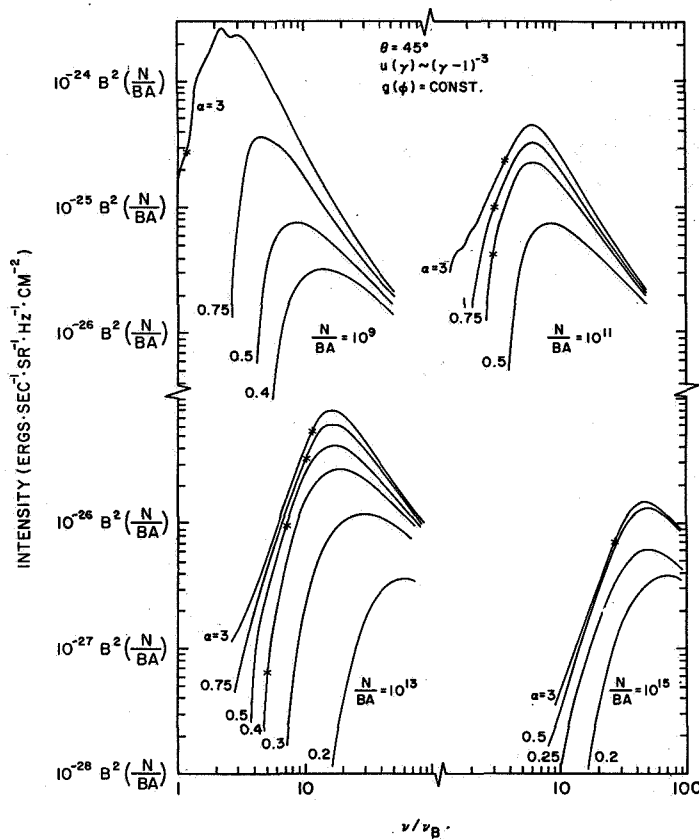
Figure 1. Gyrosynchrotron intensities with effects of self-absorption and suppression the ambient plasma.

The parameter N/BA determines the importance of self-absorption. The larger this parameter, the higher is the turnover frequency due to self-absorption. The asterisks in Figure 1 denote frequencies where the sense of circular polarization reverses. If the source is optically thick, the ordinary mode dominates; if the source is optically thin, most of the radiation is in the extraordinary mode. It has been suggested by Holt and Ramaty (1969) that this reversal could account for the observed reversals of circular polarization of microwave bursts (for example, Scalise, Basu, and Marques dos Santos, 1971).

The parameter α determines the importance of gyrosynchrotron suppression by the ambient medium; the smaller the value of the α, the higher is the turnover frequency due to the Razin effect. A source which is optically thick for a given value of N/BA may become optically thin for a sufficiently low α, because the Razin effect suppresses both the emissivity and the absorption coefficient.

191

Let us now consider approximate formulae for the turnover frequencies due to self-absorption, ν_{sa}, and the Razin effect, ν_R. It is well known (Slish, 1963) that for an ultrarelativistic synchrotron source, ν_{sa} is proportional to the intensity I_m at ν_{sa}, and the constant of proportionality is only a weak function of spectral index. From the paper by Ramaty and Petrosian (1972) we have

$$\nu_{sa} \cong 10^{12.5}\, I_m^{2/5}\, B_\perp^{1/5} \tag{5}$$

where ν_{sa} is in Hz, I_m is in ergs $\cdot$ s^{-1}cm^{-2}sr^{-1}Hz^{-1}, and $B_\perp$ is the perpendicular component of the magnetic field in gauss. In order to test the validity of Equation (5) for a gyrosynchrotron source, we solved it for I_m, $I_m \cong 10^{-15}\, B^2\, (\nu_{sa}/\nu_B)^{5/2}$, and we calculated values of I_m for various values of ν_{sa}/ν_B as obtained from Figure 1. In Table 1 these I_m values are compared with numerical values of the intensity at ν_{sa}/ν_B from Figure 1. As can be seen, at higher harmonics the ultrarelativistic formula is valid to better than 20 percent. At lower harmonics, as expected, the ultrarelativistic formula overestimates the maximum intensity of a gyrosynchrotron source. Since ν_{sa} varies as $I_m^{2/5}$, Equation (5) for ν_{sa} is accurate to better than a factor of 2 even at the lowest harmonics.

Table 1
Gyrosynchrotron Self-Absorption: Comparison of Numerical Calculations
With Equation (5).

N/BA	$\dfrac{\nu_{sa}}{\nu_B}$	I_m/B^2 (ergs $\cdot$ cm^{-2}s^{-1}Hz^{-1}sr^{-1} gauss^{-2})	
		Numerical Calculation	$10^{15}\,(\nu_{sa}/\nu_B)^{5/2}$
10^9	2.5	2.5×10^{-15}	10^{-14}
10^{11}	6	4.5×10^{-14}	9×10^{-14}
10^{13}	16	8×10^{-13}	10^{-12}
10^{15}	45	1.5×10^{-11}	1.4×10^{-11}

For the Razin effect, the turnover frequency ν_R of an ultrarelativistic synchrotron source is given by (Ginzburg and Syrovatskii, 1965)

$$\nu_R = 20\, \langle n \rangle / B_\perp \tag{6}$$

where, as before,$<n>$ is the mean density in cm^{-3} and $B_\perp$ is in gauss. In Table 2 we compare numerical values of ν_R/ν_B from Equation (6) ($\nu_R/\nu_B = 2.3 \ \alpha^2$ for $\theta = 45°$) with the turnover frequencies due to the Razin effect obtained from the numerical calculations presented in Figure 1. As can be seen, the agreement between the ultrarelativistic formula and the numerical calculations is better than 20 percent for all values of α greater than 1.

Table 2

The Razin Effect: Comparison of Numerical Calculations With Equation (6)

$\alpha = 3/2(\nu_B/\nu_p)$	ν_R/ν_B	
	Numerical Calculation	$2.3/\alpha^2$
0.75	4.1	5
0.5	9	9
0.3	26	25
0.2	58	60

DISCUSSION

The turnover frequencies discussed above are summarized in Table 3. Let us consider the numerical values of these frequencies for parameters appropriate for a moderately large microwave burst (for example, Ramaty and osian, 1972): $n = 10^{10}$ cm^{-3}, $B_\perp = 150$ gauss, $T = 10^6$ K, $L = 2 \times 10^9$ cm, $A = 4 \times 10^{1 \prime}$ cm (0.46 arcmin), $S_m = 10^3$ sfu ($S_m = I_m$ Ω, where Ω is the solid angle subtended by the source.) For these parameters we have: $\nu_B = 0.42$ GHz, $\nu_p = 0.9$ GHz, $\nu_g = 1.7$ GHz, $\nu_{ff} = 5.4$X GHz, $\nu_{sa} = 4.3$ GHz, and $\nu_R = 1.3$ GHz. We see that the most important absorption effects are free-free absorption and gyrosynchrotron self-absorption. It is conceivable, however, that for other parameters these effects will be less important. In particular, ν_{ff} can be decreased by decreasing the density and the clumpiness factor or by increasing the temperature.

Ramaty and Petrosian (1972) have recently discussed microwave bursts with flat spectra. They have shown that such bursts could be produced by free-free absorption of gyrosynchrotron emission. Indeed, from the above value of ν_{ff} we see if X is about 5, this turnover frequency could be as large as 25 GHz, in which case free-free absorption would be the most important absorption mechanism in the microwave region. In Figure 2 we show the effect of free-free absorption on the intensity of a gyrosynchrotron source (dashed lines). Except for ν_{ff}/ν_B, all parameters in this figure are the same as those in Figure 1. For the parameters given above, $\nu_{ff}/\nu_B = 13$X. For X between 3 and 5, ν_{ff}/ν_B is between 39 and 65; thus, we see that it is possible to produce by free-free absorption flat or slowly varying flux densities. Such flux densities are consistent with the observed spectra of some microwave bursts.

193

Table 3

Low Frequency Cutoffs

Process	Turnover frequency
Absorption below plasma frequency	
Ordinary mode	ν_p
Extraordinary mode	$\nu_x = (\nu_p^{\ 2} + \frac{1}{4}\nu_B^{\ 2})^{1/2} + \frac{1}{2}\nu_B$
Free-free absorption	Equation (2)
Gyroresonance absorption	Equation (3)
Gyrosynchrotron self-absorption	Equation (5)
Razin effect	Equation (6)

Finally, we would like to consider the implication of self-absorption on the maximum intensity of microwave bursts. From Equation (5) we can calculate the maximum intensity of a gyrosynchrotron source of given magnetic field. Such maximum intensities are given in Table 4 for two frequencies and two values of $B_\perp$. Since the angular sizes of microwave bursts do not seem to exceed about 1 arcmin (Enome, Kakinuma, and Tanaka, 1969), the numerical values for the intensities given in Table 4 may be considered as upper limits on flux densities of microwave bursts.

Table 5 summarizes the peak flux densities of the largest known microwave bursts (data taken from Castelli, Aarons, and Michael, 1968; Nagoya Univ., 1966; and Castelli, J.P., private communication, 1972). By comparing flux densities with the maximum intensities given in Table 4, we conclude that angular sizes on the order of 1 arcmin are indeed appropriate for large microwave bursts, although obviously a great deal of variation of the angular size is to be expected from flare to flare. It is, however, remarkable that whereas in the decimeter region flux densities as large as 0.5×10^6 sfu have been observed (for example, Castelli et al., 1968), in the microwave region the peak flux densities never exceed a few times 10^4 sfu. As discussed in this paper, this should be the result of gyrosynchrotron self-absorption and the small angular size of microwave bursts.

194
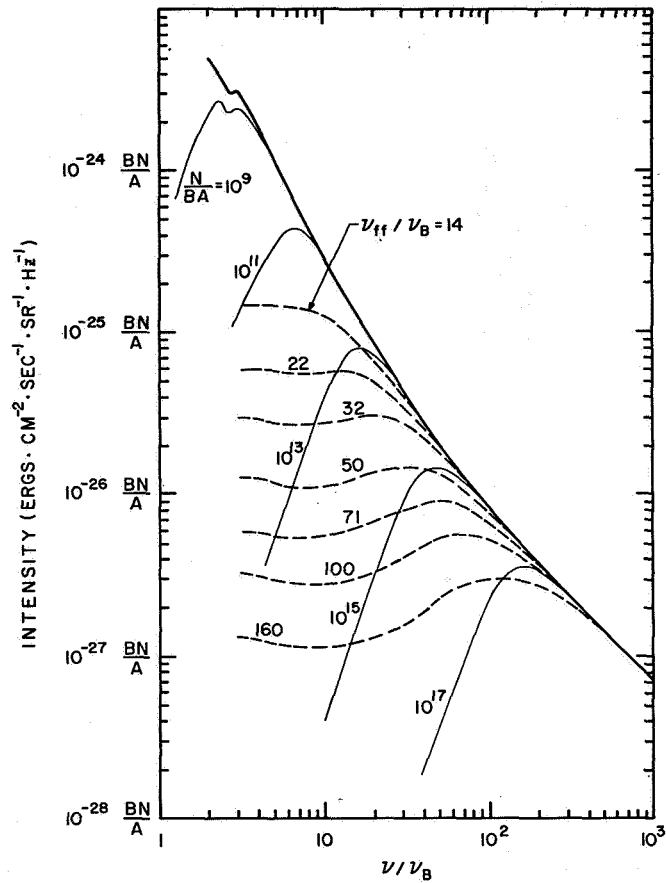
Figure 2. Gyrosynchrotron intensities with effects of
self-absorption and free-free absorption.

Table 4

Maximum Intensity of Gyrosynchrotron Sources

$(sfu \cdot arcmin^{-2})$

$\nu(GHz)$	$B_\perp$ = 100 gauss	$B_\perp$ = 300 gauss
3	2400	1400
10	48000	28000

Table 5
Peak Flux Densities of the Largest Microwave Bursts

Date	Frequency (MHz)	Peak Flux Density (10^{-22} W · m^{-2}Hz^{-1})
Feb 23, 1956	9400	31400
Mar 29, 1960	9500	25000
Nov 15, 1960	9400	24000
Jul 7, 1966	9400	12000
May 23, 1967	8800	23000
Aug 7, 1972	8800	27000
Feb 23, 1956	3770	18000
Mar 29, 1960	3750	8250
Nov 15, 1960	3750	11600
Jul 7, 1966	3750	4500
May 23, 1967	2695	5400
Aug 7, 1972	2695	3900

REFERENCES

Acton. L.W., 1968, *Ap. J.* **152**, 305.

Castelli, J.P., Aarons, J., and Michael, G.A., 68, *Ap. J.* **153**, 267.

Enome, S., Kakinuma, T., and Tanaka, H., 1969, *Solar Phys.* **6**, 428.

Ginzburg, V.L., and Syrovatskii, S.I., 1965, *Ann. Rev. Astron. Astrophys.* **3**, 297.

Ginzburg, V.L., and Zheleznyakov, V.V., 1959, *Soviet Astron. – A.J.* **3**, 297.

Holt, S.S., and Ramaty, R., 1969, *Solar Phys.* **8**, 119.

Ko, H.C., 1973, These Proceedings.

Liemohn, H.B., 1965, *Radio Sci.* **69D**, 741.

Nagoya Univ., Res. Inst. Atmospherics, 1966, *Mon. Rpt. Solar Radio Emission,* July.

Ramaty, R. 1969, *Ap. J.* **158**, 753.

Ramaty, R., and Petrosian, V., 1972, *Ap. J.* **178**, 241.

Scalise, E., Jr., Basu, D., and Marques dos Santos, P., 1971, *Astron. Astrophys.* **13**, 471.

Slish, V.I., 1963, *Nature* **199**, 682.

Takakura, T., and Scalise, E., Jr., 1970, *Solar Phys.* **11**, 434.

Takakura, T., 1967, *Solar Phys.* **1**, 304.

Trulsen, T., and Fejer, J.A., 1970, *J. Plasma Phys.* **4**, 825.

GYROSYNCHROTRON RADIATION FORMULAE

H.C. Ko

Department of Electrical Engineering and
Department of Astronomy
Ohio State University

ABSTRACT

The wave-normal emissivity and the ray emissivity formulae for an electron moving along a helical path in a magnetoactive medium are presented. Simplified formulae for the case of an isotropic plasma are also given. Because of the helical motion of the electron, one must distinguish between the radiated power per unit solid angle and the received power per unit solid angle. The relation between these two quantities in a magnetoactive medium is shown. Results are compared with those obtained by others, and the sources of discrepancies are pointed out.

INTRODUCTION

Electrons gyrating in an external magnetic field emit electromagnetic waves, generally known as gyrosynchrotron radiation. For low-energy electrons the radiation is called gyro radiation, since the radiated energy is mainly confined to the gyro frequency: For highly relativistic electrons, the radiation is called synchrotron radiation, and the radiated energy dominates at the higher harmonics of the gyro frequency. The significance of these radiations in astrophysical phenomena has been recognized for many years. Several excellent reviews on the theory of gyrosynchrotron radiation and its applications to the interpretation of astrophysical problems have been published (Ginzburg and Syrovatskii, 1965, 1969; Wild et al., 1963; Takakura, 1967). Although the theory of gyrosynchrotron radiation in vacuum is well developed, the corresponding theory in a magnetoactive medium is still in an active research stage.

In many astrophysical conditions, the gyrosynchrotron radiation takes place in the presence of an ambient plasma which is often magnetized. The ambient magnetized plasma gives rise to some unusual properties of the gyrosynchrotron radiation because of its dispersive and anisotropic nature. It is well known that, in a magnetoactive medium the direction of energy flow known as the ray direction does not coincide with the wave-normal direction in general (Ginzburg, 1964). It is therefore useful and convenient to introduce the concept of the wave-normal emissivity and the ray emissivity. The wave-normal emissivity of an electron is defined as the energy of those waves having the same wave-normal direction, radiated by the electron per unit of time, frequency interval, and solid angle in the wave-normal direction. The wave-normal emissivity is defined for each of the two polarization modes (ordinary and

extraordinary). Since the energy of these waves does not travel in the wave-normal direction, the directional dependence of the emissivity does not represent the radiation pattern of the electron. On the other hand, the ray emissivity is defined as the energy radiated by the electron per unit of time, frequency interval, and solid angle, traveling in the ray direction. Hence the ray emissivity represents the actual power flow in the true sense of the word. The ray emissivity is defined for each of the two polarization modes.

We present, in the next section, the wave-normal emissivity formulae for the gyrosynchrotron radiation in a magnetoactive medium. We then present the ray emissivity formulae. We will also establish the relation between the radiated power per unit of solid angle and frequency interval and the received power per unit of solid angle and frequency interval. Finally, we present the results for the gyrosynchrotron radiation in an isotropic plasma. In the analysis given, the effects of anisotropy and dispersion of the medium are completely taken into account.

GYROSYNCHROTRON RADIATION IN MAGNETOACTIVE PLASMA

A general treatment of the energy loss suffered by an electron spiraling in a magnetoactive medium was first given by Eidman (1958) using the Hamiltonian method. However, Liemohn (1965) noted that Eidman's analysis did not take into account the dispersion effect explicitly. He derived a new "corrected" formula for the emissivity. Later Mansfield (1967) treated the same problem using the Fourier transform method and indicated that his new calculations agreed with Liemohn's result. During the last several years, Liemohn's formula has been widely quoted in the literature (Ramaty, 1968, 1969; Fung and Yip, 1966; Ginzburg and Syrovatskii, 1969; Wild and Hill, 1971). Unfortunately, Liemohn's corrected formula is in error. (Ko, 1970; Ko, ~~~ z, and Chuang, 1972; Trulsen and Fejer, 1970).

In the Hamiltonian method, the radiation field is represented by a system of harmonic oscillators. Electromagnetic waves can be studied in the cavity and suitable boundary conditions imposed to find the possible normal modes of vibration, each of which is equivalent to a classical harmonic oscillator. The total power radiated by the electron is then given by

$$P = \sum_{i=1}^{2} \int\int\int \eta_i \rho_i \, df \, d\Omega = \sum_{i=1}^{2} \int\int\int j_i \, df \, d\Omega \tag{1}$$

where ρ_i is the normal-mode density function or the number of oscillators per unit volume associated with the wave-normal direction $\overline{k}$, per unit of solid angle and frequency interval. The element of solid angle $d\Omega$ is given by $\sin\theta \, d\theta \, d\alpha$, where θ is the angle between the wave-normal vector $\overline{k}$ and the magnetic field and α is the azimuth angle; η_i is the average power of the harmonic oscillator. The indices i=1 and 2 represent the ordinary and the

extraordinary modes, respectively. The wave-normal emissivity $j_i = \eta_i \rho_i$ is a function of frequency f, direction of the wave-normal θ, and the physical parameters of the medium.

The method is quite straightforward when applied to radiation in vacuum (Fermi, 1932; Heitler, 1954). However, the calculation becomes very complex when the method is applied to the gyrosynchrotron radiation in a magnetoactive medium which is both anisotropic and dispersive. Earlier work by Eidman and Liemohn did not take the dispersion effect into account correctly.

Let us consider an electron moving along a helical path making an angle ϕ with the static magnetic field H directed along the z-axis. The ambient plasma is assumed to be homogeneous and cold. The position and velocity coordinates of the electron along the x, y, z axes are, respectively

$$\bar{r}_e = \left[\frac{\gamma v \sin\phi}{\omega_H} \cos\frac{\omega_H}{\gamma}t, \quad \frac{\gamma v \sin\phi}{\omega_H} \sin\frac{\omega_H}{\gamma}t, \quad (v\cos\phi)t \right]$$

$$\bar{v} = \left[-v\sin\phi\sin\frac{\omega_H}{\gamma}t, \quad v\sin\phi\cos\frac{\omega_H}{\gamma}t, \quad v\cos\phi \right]$$

where $\omega_H = |e|\,H/m_o c$ is the nonrelativistic angular gyrofrequency; $\gamma = (1 - \beta^2)^{-1/2}$ is the Lorentz factor; and $\beta = v/c$.

When the calculation is carried out, taking both the anisotropy and dispersion into account completely and throughout the analysis, one obtains

$$\rho_i = f^2 \left(\frac{n_i}{c}\right)^3 \left(1 + \frac{\omega}{n_i}\frac{\partial n_i}{\partial\omega}\right) \qquad (2)$$

$$\eta_i = \sum_{s=-\infty}^{+\infty} \left(1 + \frac{\omega}{n_i}\frac{\partial n_i}{\partial\omega}\right)^{-1} 2\pi \left(\frac{ecKZ}{n_i}\right)^2 \delta(f - f_s) \qquad (3)$$

$$j_i = \sum_{s=-\infty}^{+\infty} \frac{2\pi n_i}{c} e^2 f^2 K^2 Z^2 \, \delta(f - f_s) \qquad (4)$$

where

$$Z = \left[-\beta\sin\phi\, J_s'(u) + \left(\frac{s\alpha_{y_i}\beta\sin\phi}{u} + \alpha_{z_i}\beta\cos\phi\right) J_s(u) \right] \qquad (5)$$

$$K^2 = \frac{1}{1 + \alpha_{\theta_i}^2} \qquad (6)$$

200

$$u = \gamma n_i \beta \sin\phi \sin\theta \; \frac{f}{f_H} \tag{7}$$

$$f_s = \left(\frac{sf_H}{\gamma}\right) + fn_i \beta \cos\phi \cos\theta \tag{8}$$

$$\alpha_{y_i} = \alpha_{\theta_i} \cos\theta + \alpha_{k_i} \sin\theta$$

$$\tag{9}$$

$$\alpha_{z_i} = \alpha_{k_i} \cos\theta - \alpha_{\theta_i} \sin\theta$$

Strictly, the emission occurs at discrete frequencies

$$f = \frac{sf_H/\gamma}{(1 - n_i\beta \cos\phi \cos\theta)} \tag{10}$$

where s is the harmonic number.

In these expressions, $J_s(u)$ is the Bessel function of the first kind of argument u and order s, and $J_s'(u)$ is its derivative with respect to u. The indices of refraction n_i and the polarization coefficients α_{θ_i} and α_{k_i} are standard parameters in the magnetoionic theory, and we use the same definitions as those given in Liemohn (1965). The wave-normal emissivity j_i in Equation (4) refers to radiation from a single electron. For radiation from a system of electrons, one can calculate the volume emissivity by integrating over the velocity distribution function of the electrons.

The correction factor $(1 + \omega/n_i \cdot \partial n_i/\partial\omega)$ which appears in the numerator of Equation (2) for ρ_i and in the denominator of Equation (3) for η_i represents the effect of the dispersion. Since the wave-normal emissivity j_i is equal to the product of ρ_i and η_i, the dispersion factor cancels out, and disappears in the final formula, Equation (4), for the emissivity. Liemohn used the correct density function as given in (2), but failed to obtain the dispersion factor in (3). Thus Liemohn's final formula for the emissivity contains the extra dispersion factor, which should have been canceled out if he had correctly evaluated the energy of the harmonic oscillator in (3). On the other hand, Eidman ignored the dispersion completely throughout his analysis. However, his final result agrees with the present one in (4), because his errors for ρ_i and η_i cancel out.

Similar conclusions have also been reached by Trulsen and Fejer (1970) who have used an indirect argument without explicitly calculating the dispersion factor in the energy of the harmonic oscillator.

THE RAY EMISSIVITY IN MAGNETOACTIVE PLASMA

It is well known that in a magnetoactive medium, the ray direction coincides with the time-average Poynting vector when spatial dispersion is absent (Ginzburg, 1964). We have calculated the electric and magnetic field of a spiraling electron in the magnetoactive medium using the Hamiltonian method (Ko, Chuang, and King, 1972). From the radiation field, the time-average Poynting vector and the ray emissivity have been obtained. In order to simplify the equation we will eliminate the index i denoting the ordinary and extraordinary modes. In the following equations, only one mode is considered.

Let θ_r represent the angle between the ray direction and the static magnetic field. This angle is different from the wave-normal direction, θ, in general. These two angles are related by the following equation (Ginzburg, 1964)

$$\frac{\partial n}{\partial \theta} \cos \xi = -n \sin \xi \tag{11}$$

where $\xi = \theta_r - \theta$.

The ray emissivity $\tilde{j}_r$ is given by

$$\tilde{j}_r = \sum_{s=-\infty}^{+\infty} \frac{2\pi}{c} ne^2 f^2 K^2 Z^2 ML^{-1} \delta(f - f_s) \tag{12}$$

where

$$M = \frac{\sin \theta \, (K^{-2} \cos \xi - \alpha_\theta \alpha_k \sin \xi) nK^2}{\sin \theta_r \, |(n''-n)\cos \xi + 2n' \sin \xi|} \tag{13}$$

$$L = \left| 1 - \beta \cos \phi \, \frac{\partial(\omega n \cos \theta)}{\partial \omega} \right| \tag{14}$$

In these expressions, $n'' = \partial^2 n/\partial \theta^2$, and $n' = \partial n/\partial \theta$. From the delta function in (12), it is seen that the emission occurs strictly at discrete frequencies, as given in (10).

Since $\tilde{j}_r$ is derived directly by the time-average Poynting vector, it is referred to the power *received* per unit of solid angle and frequency interval. We will denote such quantities with a tilde ($\sim$). In many applications, it is more useful and convenient to use the power *radiated* per unit of solid angle and frequency interval, denoted by j_r. It can be shown that

$$j_r = \tilde{j}_r L \tag{15}$$

202

where L is given in (14). In a vacuum, $n = 1$, $\theta = \theta_r$, and L is reduced to $(1 - \beta \cos \phi \cos \theta)$, which agrees with the result discussed by Scheuer (1968) and Ginzburg and Syrovatskii (1969).

GYROSYNCHROTRON RADIATION IN ISOTROPIC PLASMA

The wave-normal and ray emissivity formulae developed in Equations (4), (12), and (15) are necessarily complicated because of the dispersive and anisotropic nature of the medium. However, the calculation of the emissivity is considerably simplified when the medium may be considered isotropic under certain physical conditions. Thus, when $\omega \gg \omega_H$, and $\omega \gg \omega_p$, where ω_p is the angular plasma frequency, the refractive index and the polarization coefficients are given approximately by

$$n_1^2 \simeq n_2^2 \simeq n^2 \simeq 1 - \frac{\omega_p^2}{\omega^2} \tag{16}$$

$$\alpha_{\theta_i} = \pm 1 \quad \alpha_{k_i} = 0 \quad \xi = 0 \tag{17}$$

Since the medium is isotropic, the wave-normal direction and the ray direction coincide. The wave-normal emissivity in (4) and the ray emissivity in (15) also become identical. Both of these formulae refer to the power radiated. In addition, the distinction between the ordinary and extraordinary modes is no longer required in the power calculation. Thus, by adding the contributions from the two polarization modes, the total power radiated per unit of solid angle and frequency interval becomes

$$j_0 = \sum_{s=-\infty}^{+\infty} \frac{2\pi}{c} ne^2 f^2 \left\{ [\beta \sin \phi \, J_s'(u)]^2 + \left[\frac{\cos \theta - n\beta \cos \phi}{n \sin \theta} J_s(u) \right]^2 \right\} \delta(f - f_s) \tag{18}$$

where j_0 is the emissivity in the isotropic plasma in terms of the power radiated. The emissivity in terms of the power received can be obtained directly from (12), or from (15) and (18)

$$\tilde{j}_0 = j_0 \left[1 - \beta \cos \phi \cos \theta \, \frac{\partial (\omega n)}{\partial \omega} \right]^{-1} \tag{19}$$

Using (19), one can readily calculate the total power received per unit solid angle at the sth harmonic by integrating with respect to the frequency:

$$\tilde{p}_s = \frac{2\pi}{c} e^2 n \frac{s^2 f_H^2 (1 - \beta^2)}{(1 - n\beta \cos \phi \cos \theta)^2} \left\{ [\beta \sin \phi \, J_s'(u)]^2 + \left[\frac{\cos \theta - n\beta \cos \phi}{n \sin \theta} J_s(u) \right]^2 \right\} \left(1 - \frac{\beta}{n} \cos \phi \cos \theta \right)^{-2} \tag{20}$$

203

In deriving (20), we have used the relation $\partial(\omega n)/\partial\omega = 1/n$ for isotropic plasma. It is easily verified that, when $n = 1$, (20) is identical to the familiar equation for vacuum given in Equation (2.7) of Takakura (1967).

In the region of higher harmonics, the radiation spectrum is practically continuous. It is convenient to introduce the spectral intensity ergs $\cdot$ s^{-1}sr^{-1}Hz^{-1} by

$$\tilde{p}_f = \tilde{p}_s \frac{ds}{df} \tag{21}$$

where, using (10)

$$\frac{ds}{df} = \left(1 - \frac{\beta}{n} \cos\phi \cos\theta\right) \frac{\gamma}{f_H} \tag{22}$$

Recently Wild and Hill (1971) presented a general formula for the spectral intensity of gyrosynchrotron radiation in isotropic plasma. Their formula does not agree with the present result shown in (21) since these authors have not taken properly into account the effect of dispersion.

DISCUSSION

In discussing the emissivity of gyrosynchrotron radiation in a magnetoactive medium, it is useful to introduce the concept of the wave-normal emissivity and the ray emissivity. The two emissivities become identical in an isotropic medium. In this paper, we have presented emissivities calculated by using the Hamiltonian method. The full derivation of these formulae, and a critical examination of the Hamiltonian method applied to the anisotropic and dispersive medium will be published elsewhere (Ko, Chuang, and King, 1972).

In addition to the Hamiltonian method, other methods such as the Fourier transform method, dyadic Green's function technique, and plane-wave spectrum representations have also been used by other workers. A critical review of these calculations will be published in a separate paper elsewhere.

Because of the helical motion of the electron, one must distinguish between the power radiated, j, and the power received, $\tilde{j}$. In a magnetoactive medium, these two quantities are related by the factor $[1 - \beta \cos\phi \, \partial(\omega n \cos\theta)/\partial\omega]$. This factor becomes $(1 - \beta/n \cos\phi \cos\theta)$ in the case of isotropic plasma.

In the interstellar and intergalactic medium, the magnetic field is very weak, and the medium can be considered practically isotropic except in the calculation of the Faraday rotation. However, in the solar atmosphere and in some discrete cosmic radio sources, the magnetic field is strong enough so that a more complete analysis is required. The general problem of radiative transfer in an inhomogeneous, magnetoactive medium is very complex.

So far only very simple cases have been discussed (Ginzburg and Syrovatskii, 1969). Further work in this area should contribute greatly to the physics of solar and other cosmic radio emission.

ACKNOWLEDGMENT

REFERENCES

Eidman, V.I., 1958, *Soviet Phys. JETP* **7**, 91.

Fermi, E., 1932, *Rev. Modern Phys.* **4**, 87.

Fung, P.C.W., and Yip,W.K., 1966, *Austral, J. Phys.* **19**, 759.

Ginzburg, V.L., 1964, *The Propagation of Electromagnetic Waves in Plasmas* (New York: Pergamon Press).

Ginzburg, V.L., and Syrovatskii, S.I., 1965, *Ann. Rev. Astron. Astrophys.* **3**, 297.

Ginzburg, V.L., and Syrovatskii, S.I., 1969, *Ann. Rev. Astron. Astrophys.* **7**, 375.

Heitler, W., 1954, *The Quantum Theory of Radiation* (Oxford: Clarendon Press).

Ko, H.C., 1970, IAU 14th Gen. Assembly (Brighton).

Ko, H.C., Chuang, C.D., and King, H.S., 1972, in preparation.

Ko, H.C., King, H.S., and Chuang, C.D., 1972, *Proc. URSI Spring Meeting* (Washington), 92.

Liemohn, H.B., 1965, *Radio Sci.* **69D**, 741.

Mansfield, V.N., 1967, *Ap. J.* **147**, 672.

Ramaty, R., 1968, *J.G.R.* **73**, 3573.

Ramaty, R., 1969, *Ap. J.* **158**, 753.

Scheuer, P.A.G., 1968, *Ap. J.* **151**, L139.

Takakura, T., 1967, *Solar Phys.* **1**, 304.

Trulsen, J., and Fejer, J.A., 1970, *Plasma Phys.* **4**, 825.

Wild, J.R., Smerd, S.F., Weiss, A.A., 1963, *Ann. Rev. Astron. Astrophys.* **1**, 291.

Wild, J.P., and Hill, E.R., 1971, *Austral. J. Phys.* **24**, 43.

NONTHERMAL X-RAYS AND RELATED PROCESSES

H.S. Hudson
Department of Physics
University of California, San Diego

ABSTRACT

The hard X-rays associated with solar flares represent the bremsstrahlung of nonthermal electron streams. In the initial phase of the flare, the X-rays probably come from a dense region in the chromosphere, as a consequence of precipitation from the lower corona. A gradual nonthermal X-ray burst may occur in a later phase, probably caused by the electrons responsible for the type IV burst.

The bombardment of the chromosphere during the early phase of the flare releases a large amount of energy there. This energy can support many of the observed flash-phase phenomena. We therefore consider this picture of flare energetics: The energy initially goes into fast particles. These interact with the chromosphere, which expands to form the hot region observed in the corona. This hot region then provides energy for many of the main-phase flare phenomena, such as Hα emission. The bulk of the energy in the bombardment must reside in the electron component. A clear test of the whole picture lies in its prediction of a strong infrared excess during the flash phase.

INTRODUCTION

The hard X-radiation from a solar flare (Frost, 1973; Kane, 1973) gives information about the energetic particles which cause it. These energetic particles have a particularly important role in the energy balance of the flare (Lin and Hudson, 1971; Syrovatskii and Shmeleva, 1971). Our main central objective in solar flare research must be to describe the energy transformations within the flare. Both the nonthermal electrons and the thermal X-ray source, the latter at temperatures as high as 3×10^7 K, may contain larger amounts of energy than that visible in Hα. Hence we can profitably study models in which the initial release of flare energy occurs in fast particles, from which the other observable phenomena derive their energy supply.

Several ambiguities remain in our understanding of the relationship between the nonthermal electrons and the hard X-rays they produce. The time evolution of the hard X-ray spectrum alone will not resolve the uncertainties, and we must seek auxiliary sources of information. Studies of the X-ray polarization (Tindo et al., 1970) and the spatial distribution of the emitting region (Takakura et al., 1971) have only begun recently. Therefore we must rely upon processes not directly related to the X-ray emission: the ultraviolet, optical, infrared,

and radio spectra; observations of mass motions in the flare, coronal disturbances, and phenomena observed in interplanetary space. The unfortunate consequence is that the interpretation of the relationships among these disparate phenomena requires the framework of a model involving all of them. Any such model must have a high degree of complexity. Furthermore, it must satisfy all of the phenomenology represented in the many decades of observations of solar flares.

In the following we will use the picture which has arisen from the microwave and X-ray observations. This descriptive model envisions the main prompt release of flare energy into 10 to 100 keV electrons. The release takes place in the low corona, but it is not yet known whether the field-line geometry is open and connected into interplanetary space, or closed, in which case the field forms arch-shaped structures. The energetic electrons penetrate the denser layers of the atmosphere, and emit the hard X-rays during their collisional interaction. At this time the impulsive microwave and EUV emissions also emerge. A portion of the chromosphere heats up, rises to the corona, and becomes the hot region or condensation which emits soft X-rays. Hα and the rest of the main phase of the flare depend upon heat conduction downward from this hot region. The coronal phenomena and interplanetary observations must then have an explanation in: a shock front caused by the rapid heating of the chromosphere during the hard X-ray burst, the leakage outward of a small fraction of the fast electrons, or the relativistic particle cloud produced in the corona — apparently independently of the initial energy release.

The model just described serves as a means of organizing the data. It is consistent with that used by Sturrock (1973) and others, but leaves out any description of the initial acceleration of the fast particles. In this paper we first define the X-ray end of the model — the emission mechanisms and interpretation of the data. Secondly, we suggest an observational test for it in the infrared, based upon the description of the white light flare continuum of Hudson (1972). We argue against any mechanism involving energetic protons ($\gtrsim 10$ MeV) for either X-ray production or chromospheric heating.

X-RAY EMISSION PROCESSES

The goal of the hard X-ray observations is the deduction of the electron spectrum at the acceleration source, which becomes the fundamental piece of information necessary for further calculations. For this purpose we have adequate theoretical knowledge of the bremsstrahlung process, and can compute the emissivity of a single electron with reasonable accuracy. However, two problems interfere with the direct deduction of the source spectrum from the observed X-rays. One is that the spectra are distributed, with a typical representation as a power law in energy. The incompleteness and imprecision of the observed X-ray spectrum then prevent us from unambiguously and analytically deducing the electron spectral shape. This leads to the use of a model spectrum approach, which can only establish the consistency of the observations with a specific model. The other main problem comes from the collisional interactions of the electrons, which may greatly distort the instantaneous spectrum and cause it to differ from the injection spectrum.

208

The extent of collisional distortion of the electron spectrum again depends upon the model. Two limiting cases exist, however, which allow us to establish the range of possibilities; these are described as the thin-target and thick-target cases. The thin target corresponds to impulsive injection, and the thick target to continuous injection (Arnoldy, Kane, and Winckler, 1968; Brown, 1971). The thin-target case involves negligible collisional or other energy loss for the electrons, so that their spectrum remains unchanged. In the thick-target case we assume that the electrons lose their total energy in collisions. Of course, any intermediate case may also exist. The collisional range of fast electrons is approximately 2×10^{19} $(E/10 \text{ keV})^2$ electrons $\cdot$ cm^{-2} in an ionized medium. This corresponds, for 20 keV, to the total thickness of the solar atmosphere above a height of 1400 km in a spherically-symmetric model (Athay and Canfield, 1970), at a point with density $\sim 10^{12}$ cm^{-3}.

We present here the formulas for bremsstrahlung, in the Kramers approximation, for the two simple cases. The Kramers approximation gives good values for the electron spectral index, but the resulting number of electrons may be as much as a factor of three too small. However, this is sufficiently precise in view of the other uncertainties discussed below.

For the thick target, a spectral photon flux j_p $(h\nu) = k_p$ $(h\nu)^{-\varphi}$ photons $\cdot$ cm^{-2} s^{-1} keV^{-1} at the earth corresponds to an electron spectral loss rate $n_e(E) = k_e E^{-\delta}$ electrons $\cdot$ s^{-1} keV^{-1} at the sun:

$$\delta = \varphi + 1$$

$$k_e = 2 \times 10^{33} (\delta - 1)(\delta - 2) k_p \text{ electrons} \cdot \text{keV}^\delta \text{ s}^{-1} \tag{1}$$

For the thin target, the same photon spectrum determines a spectral number of electrons $N_e(E) = K_e E^{-\delta}$ electrons $\cdot$ keV^{-1} for a separately specified ion density n_i cm^{-3}

$$\delta = \varphi - 1/2$$

$$K_e = 4 \times 10^{41} (\delta - 1/2) \frac{k_p}{n_i} \text{ electrons} \cdot \text{keV}^{\delta - 1} \tag{2}$$

Either approximation will give similar results for the total number of electrons and their total energy. The main superficial difference lies in the greater steepness of the thick-target electron spectrum; this permits a larger store of energy in the unobservable low-energy range. Physically, the two approximations correspond to very different pictures regarding the location of energy deposition by the electrons. For thick targets, this will be deep in the atmosphere; for thin targets, in the corona. Secondary physical processes will be induced by these large quantities of collisional heating, of the order of 10^5 times the observed energy in X-rays. The amount of heating depends crucially upon the low-energy end of the

nonthermal electron spectrum. These processes will naturally have very different natures depending upon the site of energy deposition.

Several further effects complicate the relationship between the X-ray spectrum and its electron spectrum. These effects, together with others not mentioned, might have a greater effect upon the deduced electron spectrum than the factor of $E^{1.5}$ separating the thick-target and thin-target models:

- There may exist complex cases which do not have an accurate description in either the thick-target or thin-target approximations. One example of this occurs in the model calculated by Brown (1972), which involves the collisional decay of electrons impulsively injected into a magnetic arch. The more energetic electrons, by the assumptions of the model, have smaller pitch angles, and hence decay more quickly in denser layers of the atmosphere. The calculated relationship between the initial electron spectrum and the resulting photon spectrum agrees with neither Equation (1) nor Equation (2); instead very steep electron spectra with $\delta \approx \varphi + 2.25$ result.

- The directivity of bremsstrahlung may become important for higher electron energies. Equations (1) and (2) do not take this factor into account.

- X-ray albedo will contribute significantly to higher X-ray energies, because the absorption cross section becomes very small compared with the Compton cross section. The photons emitted from a source above the photosphere will then be able to scatter many times and emerge again, somewhat degraded in energy. Tomblin (1972) has shown that this process tends to flatten the emitted X-ray spectrum.

In summation, our knowledge of the detailed processes involved in X-ray generation may seem adequate, but our ignorance of the correct model results in a great deal of uncertainty. Any interpretation of the X-ray data must therefore involve some choice of model, preferably through the aid of as much related data as possible.

THERMAL OR NONTHERMAL SOURCES

A traditional debate, which began with the initial observation of hard solar X-rays by Peterson and Winckler (1959), has centered upon the natural interpretation of these X-rays as nonthermal. Chubb (1970) has most recently and forcefully presented the arguments for a thermal source, at very high temperature, and distributed in temperature in such a way as to generate a roughly power-law X-ray spectrum. Kahler (1971) has countered Chubb's arguments, but no firm conclusion has yet been reached. The X-ray data alone cannot decide the issue, although the nonthermal model has the attractive feature of requiring fewer hypotheses. Consequently, here too we need supplementary information from other kinds of observations. However, the models explaining these related phenomena have not

been adequately elaborated, and in the remainder of this paper we shall continue to assume a nonthermal interpretation for the hard X-rays.

THICK OR THIN TARGETS

The X-ray data show that rapid spectral variations occur during both the onset and decay phases of hard X-ray bursts (Kane and Anderson, 1970). This provides clear evidence that most of the observed X-rays come from thick-target interactions.

An independent line of evidence comes from the observation by Kane and Donnelly (1971) that EUV bursts, with total energies comparable to the collisional energy losses of the electrons, come from dense regions and have excellent time correlation with the bursts of bremsstrahlung. The high density of the broadband EUV source could be inferred from its statistical limb darkening relative to the X-ray source. Wood and Noyes (1972) have confirmed this fact by establishing the tendency for chromospheric EUV lines to have impulsive time profiles.

ELECTRON OR PROTON PROCESSES

With the advent of γ-ray observations (Chupp et al., 1972) we have direct information about the proton component of nonthermal particle streams in solar flares. We can use this information a) to examine the hypothesis (Boldt and Serlemitsos, 1969) that proton bremsstrahlung may contribute to flare X-radiation; b) to deduce the total proton energy in comparison with that of the electrons, in order to assess their relative importance in causing secondary effects.

Proton bremsstrahlung produces 10 to 100 keV x-rays from 20 to 200 MeV protons. Chupp et al. (1972) observed inelastic-scattering γ rays (4.4 MeV from ^{12}C and 6.1 MeV from ^{16}O) in the flare of August 4, 1972. Each line had a flux of $(3 \pm 1) \times 10^{-2}$ photons $\cdot$ cm^{-2} s^{-1}. These γ rays arise from interaction by protons of energies similar to those able to produce X-ray emission, so the ratio of γ-ray to X-ray flux will not depend strongly upon the assumed proton spectrum. Making a simple approximation for the ^{16}O cross-section (Lingenfelter and Ramaty, 1967), and assuming an abundance ratio to hydrogen of 5×10^{-4}, we find an X-ray continuum of

$$j_p \, (h\nu) \approx 0.6 \, (h\nu)^{-3.5} \quad \text{photons} \cdot \text{keV}^{-1} \tag{3}$$

per ^{16}O photon, assuming a proton spectrum given by the power law E^{-3} protons $\cdot$ MeV^{-1}. This falls about six orders of magnitude below the hard X-ray spectra typical of such flares, so that we may firmly rule out proton bremsstrahlung as a source of flare X-rays.

One can also obtain an estimate for the total energy in protons from the observed flux in the ^{16}O γ-ray line. For a proton spectrum $AE^{-\delta}$ protons $\cdot$ MeV^{-1}, under the assumption that the protons penetrate the solar atmosphere and lose all of their energy into collisions, the total γ-ray flux becomes

$$J_\gamma = \frac{A}{4\pi(AU)^2\Delta t} \int_{E_o}^{\infty} E^{-\delta} \, dE \int_{E_o}^{E} \frac{\sigma n}{dE'/dx} \, dE' \quad \text{photons} \cdot \text{cm}^{-2}\text{s}^{-1} \tag{4}$$

for an event of duration Δt. The cross section σ (cm^2) varies approximately as $1/E$ above a threshold energy E_o. Assuming $\delta = 3$, the γ-ray flux and duration for the August 4, 1972 event imply $\sim 3 \times 10^{33}$ protons above 10 MeV, corresponding to an energy of $\sim 10^{29}$ ergs. This falls well below the total electron energy estimated for comparable flares. Additionally, because we want to compare the efficiency of protons with electrons for supporting secondary processes in the chromosphere and photosphere, it must be noted that the proton range greatly exceeds the electron range. The heating due to protons therefore becomes greatly diluted relative to that due to electrons.

In view of these decisive new γ-ray observations, only the very low-energy end of the proton energy spectrum could become energetically important. We have as yet no direct way of estimating the number of such protons, with energies < 10 MeV, and will not consider them further.

PENETRATION OF ELECTRONS

Monte Carlo techniques have proven the most favorable approach for studying the diffusive penetration of electrons into an absorbing medium. However, an analytical approximation also exists (Maeda, 1963), for which the heating function has the following form:

$$Q(h) = \int_{0}^{\infty} \frac{N(E') \, dE/dx \, G(\xi_o/\xi)}{A \, \Delta t} \, dE' \quad \text{keV} \cdot \text{cm}^{-3}\text{s}^{-1} \tag{5}$$

where h (cm) represents the height above the photosphere, N(E) the number of nonthermal electrons (keV^{-1}), dE/dx the energy loss of electrons (keV $\cdot$ cm^{-1}), G the Gold integral, A the area of precipitation (cm^2), and Δt its duration (seconds). The argument of the Gold integral is the thickness of the atmosphere ξ_o (electrons $\cdot$ cm^{-2}) above the height h divided by the "attenuation mean free path"

$$\xi = 9.41 \times 10^{16} E^{2.2} \quad \text{electrons} \cdot \text{cm}^{-2} \tag{6}$$

212

Figure 1 shows this heating function normalized to the X-ray flux observed in the May 23, 1967 flare and to the area and duration of the white light emission observed in that flare. The calculation (Hudson, 1972) assumed a power-law electron number spectrum with spectral indices of 3 and 5 chosen to bracket the observed range of values. The qualitative behavior of Q(h) will resemble that of Figure 1 for any reasonable electron spectral distribution or model atmosphere. It must increase toward greater heights. The heating cannot occur in a layer bounded above and below by relatively unperturbed layers, as Najita and Orrall (1970) suggest, unless the magnetic field guides the electrons at a very oblique angle into the atmosphere (Kandel et al., 1971).
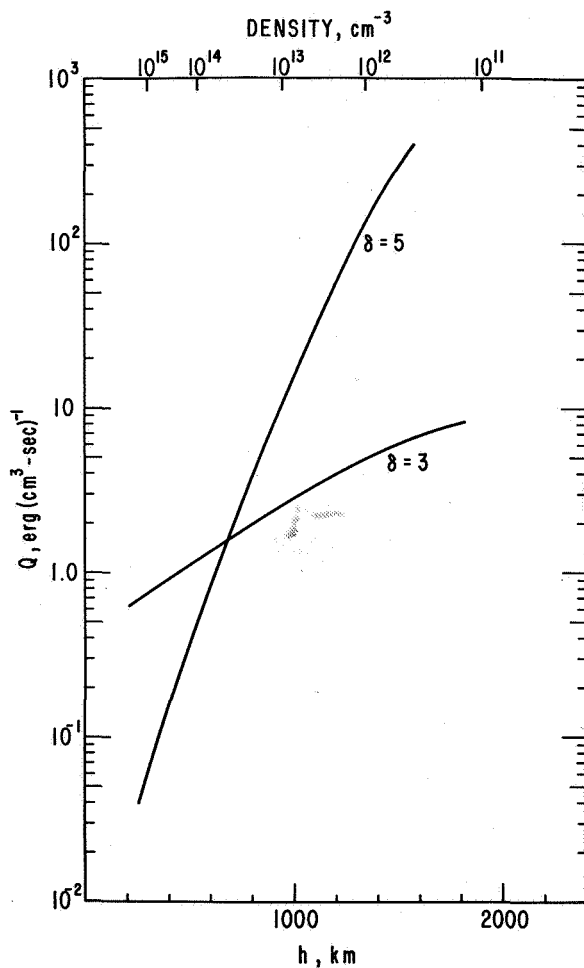
Figure 1. Energy deposition as a function of height in the model atmosphere of Athay and Canfield (1970), for two power-law electron distributions. The energy deposition per unit volume will increase with height for $\delta \gtrsim 2$ up to a height corresponding to any low-energy cutoff in the electron spectrum.

How strong is the heating produced by Q(h)? Most of the excess heat must eventually emerge as radiation, but the details of the conversion process will necessarily be complex. Qualitatively, however, we can see that the ambient emissivity drops off sharply with height because of the reduction in density: the scale height is about 200 km. Therefore the ratio of Q(h) to the emissivity, a crude measure of the rate of temperature increase, must be an even stronger function of height than Q(h) alone. We would then expect that the heating due to the absorption of the electron stream would have a catastrophic effect above some given height, and a negligible effect below that height.

The initial pitch angle distribution and inclination of the field lines with respect to the surface would not have a strong effect on the qualitative conclusions above. One may expect, however, that some fraction of the electrons incident upon the top of the solar atmosphere would recoil out of it before decaying in energy; this fraction may become quite large for suitable pitch-angle distributions and a strongly converging magnetic field pattern. On the other hand, no firm evidence has yet ruled out the possibility that the acceleration actually takes place within the thick target itself. In the former case a large number of electrons could escape into the corona; in the latter case the number escaping would necessarily remain small.

SECONDARY PROCESSES

White Light Flare

The white light flare has remained a puzzle since its discovery more than a century ago (Carrington, 1859; Hodgson, 1859). Recently Svestka (1970), Najita and Orrall (1970), and Hudson (1972) have discussed the possible origin of the visible continuum in heating due to nonthermal particle streams. The predictions of this model provide a good test for the validity of the picture discussed in the preceding sections of this paper.

The 10 to 100 keV electrons do not penetrate to the height corresponding to $\tau = 1$ in the visible continuum. Figure 2 shows the energies of electrons contributing to the heating at a given height. The visible continuum in the strongest disk flares, according to the observations by De Mastus and Stover (1967) of the May 23, 1967 event, must require an energy of some 10^{30} ergs; to include the energy of the EUV flash would increase the requirement to more than 10^{31} ergs. To obtain this much energy we must look at very low electron energies, as low as 5 keV for a very flat spectrum with $\delta = 3$. At the height corresponding to this energy in Figure 2, the assumed model of the solar atmosphere has a total density of $\sim 3 \times 10^{11}$ cm^{-3} and an ambient electron density an order of magnitude smaller. Here the continuum opacity must have a very small value in the visible wavelengths.

No other known component of the nonthermal particle streams contains enough energy to supply the white light continuum. Hence it either must be squeezed out of the > 5 keV electrons in the nonthermal particle stream picture, or else we must discover an entirely new mechanism. Hudson (1972) has argued that strong continuum emission is indeed possible under these conditions, but the details of the radiation process remain vague because of the

214
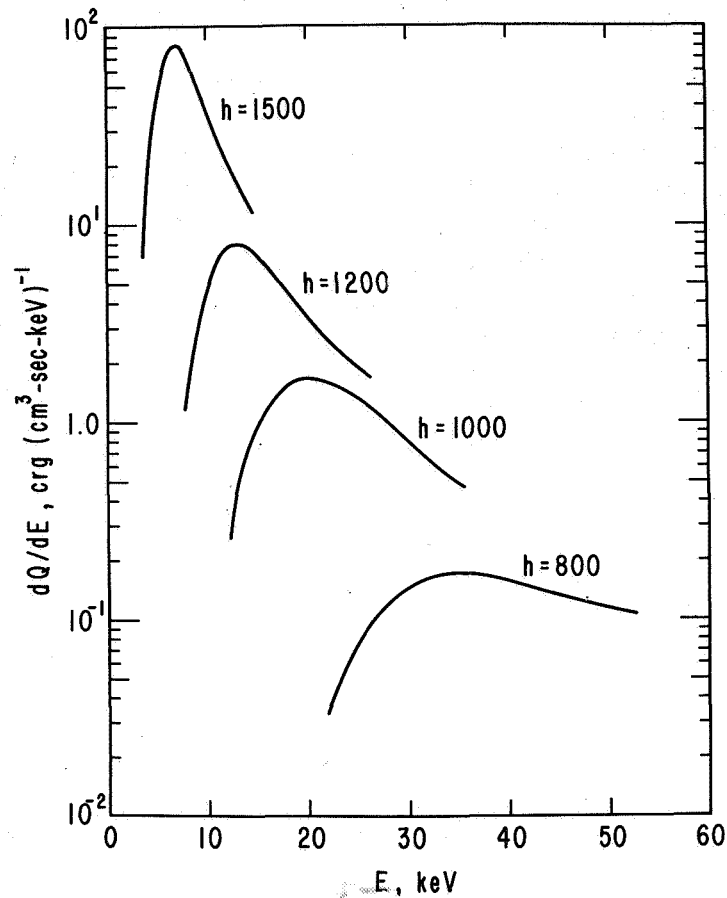
Figure 2. Contributions of electrons at various energies to the chromosphere at the specified altitude (km). These curves correspond to the case δ = 5 in Figure 1.

complexity of the problem. We discuss in the following the mass motions caused by the precipitation itself, for example. However, if the emission does occur at such a high altitude, we can surely conclude that it has small optical depth. Consequently, its spectrum will extend redward from the visible region, and also blueward because it comes from a heated layer. Thus the nonthermal particle stream model predicts both infrared and ultraviolet excesses during white-light flares. The infrared visibility of the heated layer will increase at longer wavelengths because of the Rayleigh-Jeans decrease in the background continuum.

The ultraviolet excess of course does occur in good time correlation with the hard X-ray burst (Kane and Donnelly, 1971). It is of historical interest that Carrington also observed either the ultraviolet or X-ray emission of the first known solar flare, through its simultaneous perturbation of the geomagnetic field.

Formation of Hot Region

The soft X-ray source observed during the main phase of a solar flare coincides with the source of thermal microwave emission (Kawabata, 1960). An argument based upon the large emission measure of the hot region, which may exceed 10^{50} cm^{-3}, shows that the material filling it must originally have come from the chromosphere (Hudson and Ohki, 1972). In the model previously described, the catastrophic heating above some critical height causes this material to rise into the corona. The growth of the thermal X-ray emission does agree in time with the maximum of the hard X-ray burst (Kahler, Meekins, Kreplin, and Bowyer, 1970; McKenzie, Datlowe, and Peterson, 1972). However, a more detailed analysis of Orbiting Solar Observatory-7 (OSO-7) data (Datlowe, D.W., personal communication, 1972) has shown that nonthermal electrons do not supply the bulk of the energy in the hot region, at least for smaller events. These measurements require the existence of some additional source of heating.

Mechanical Effects

To calculate the dynamical response of the solar atmosphere to the bombardment by the precipitating particles, we must have a very detailed model. Some of the input heat goes into ionization, since the chromospheric material begins in a mainly neutral state; subsequently, the heating must cause a rise in temperature. The degree of this temperature rise depends upon the efficiency of the reradiation, convection, and conduction of the excess energy. The mechanical effects in turn depend upon the solution to this complicated problem, and vice versa. The overall problem compounds the difficulty of normal solar atmosphere theory by removing the assumption of a stationary state; however, as a compensating advantage we know something about the height distribut. of the source of heat.

To illustrate the magnitude of the mechanical effects resulting from nonthermal electron precipitation, consider a temperature excess ΔT at some given height. This will produce an upward acceleration $(\Delta T/T)\, g_\odot$. A 10 percent increase in temperature produces an acceleration rapid enough to cause expansion through one chromospheric scale height in 10^2 seconds, a typical duration for large nonthermal X-ray bursts. Yet on the model in Figure 1 for $\delta = 5$, the ratio of heat content to power input reaches the value of 1 second at an altitude of 1000 km, with much shorter heating times at higher altitudes.

In addition to boiling off material to form the coronal hot region, the expansion of the thick target may become explosive enough to initiate the shock front responsible for the meter-wave type II burst and the Moreton-wave phenomenon (Uchida, 1973). No detailed study of this process exists, but a model calculation would be informative. In particular, one might learn what fraction of the kinetic energy of the nonthermal beam would go into mechanical work, and what fraction into heating and radiation.

216

CORONAL PHENOMENA

The thick-target absorption of large numbers of nonthermal electrons seems an established fact, and leads to interesting descriptions of some chromospheric processes as previously described. However, we also have definite evidence for the existence of nonthermal electrons in thin-target situations, in the streams of interplanetary electrons causing type III bursts (Lin, 1973); type IV bursts also require large numbers of high-energy electrons at great altitudes in the corona.

The most striking evidence for thin-target hard X-ray emission comes from the burst of March 30, 1969 (Frost and Dennis, 1971), for which the sun's limb occulted the dense layers. The OSO-5 data for this event showed two phases of nonthermal X-ray emission. The initial impulsive phase resembled the nonthermal spikes detected by OSO-3 (Hudson, Peterson, and Schwartz, 1969) and Orbiting Geophysical Observatory -5 (OGO-5) (Kane and Anderson, 1970), although the differences in energy range and dynamic range among the three X-ray telescopes make comparison difficult. The second phase of the March 30, 1969 event, however, definitely represents a new class of hard X-ray bursts of which other examples have subsequently appeared (Frost, 1973). These long-enduring bursts have extremely close time relationships with meter-wave and microwave type IV bursts. They therefore represent the thin-target bremsstrahlung of the coronal electron population whose high-energy tail produces the observed synchrotron emission. The correlated observations afford an excellent opportunity to describe these electrons, their acceleration and subsequent evolution, in a more complete manner.

The X-ray detection of type III burst electrons remains problematic. The correlated examples thus far discovered (Kahler, 197 'ane, 1973) do not show any identifiable differences from ordinary impulsive X-ray bursts, and thus probably have a thick-target origin at lower altitudes. However, reasonable estimates of the numbers of electrons involved in the type III burst, the density of the medium, and the duration of the stream, suggest that the direct thin-target emission of these electrons is almost detectable.

The discovery of true coronal hard X-ray phenomena in the closing years of the present solar cycle has opened up a new opportunity for the succeeding one. A hard X-ray heliograph, or possibly a coronagraph to eliminate instrumental problems caused by the intense chromospheric X-ray sources, might yield coronal observations rivaling those of the Culgoora radioheliograph.

CONCLUSION

The hard X-ray continuum has provided us with much important information about solar flares. We now understand most of the details of the origin of these X-rays on a microscopic basis. However, ambiguities remain in the interpretation of the data because of our lack of understanding of the correct large-scale picture.

As an example, the X-ray observations should provide information about the spectral distribution and total energy of electrons as inputs to the theory of the acceleration mechanism. The two simple ways to interpret the X-ray data, thick-target and thin-target, give electron spectral indices differing by 1.5. The uncertainty does not end with this, however. Neither simple approximation may be valid; furthermore, complications such as Compton albedo and directivity of bremsstrahlung will have major significance when properly understood. Such a large uncertainty in the spectral index means an uncertainty of an entire order of magnitude in the total energy. In a thin-target model, the total energy produced by the electron acceleration mechanism would be inversely proportional to the lifetime for escape from the X-ray source. This problem has received virtually no attention.

A thick-target model seems preferable on the basis of present X-ray data. The implications of the model for other wavelengths should have greater importance on judging its validity, however. At the present stage of development we need to consider several models as widely as possible so that observations of all kinds can participate in helping to choose the correct physical picture.

ACKNOWLEDGMENTS

REFERENCES

Arnoldy, R.L., Kane, S.R., and Winckler, J.W., 1968, *Ap. J.* **151**, 711.

Athay, R.G., and Canfield, R.C., 1970, *NBS Special Pub.* **332**, 65.

Boldt, E.A., and Serlemitsos, P.J., 1969, *Ap. J.* **157**, 559.

Brown, J.C., 1971, *Solar Phys.* **18**, 489.

Brown, J.C., 1972, *Solar Phys.* **25**, 158.

Carrington, R.C., 1859, *M.N.R.A.S.* **20**, 13.

Chubb, T.A., 1970, *Proc. Leningrad Symp. on Solar-Terrestrial Phys.* **1**, (Dordrecht: Reidel Publ. Co.).

Chupp, E.L., Forrest, D.J., Higbie, P.R., Suri, A.N., Tsai, C., and Dunphy, P.P., 1972, *Nature* (to be published).

De Mastus, H., and Stover, R.R., 1967, *Pub. A.S.P.* **79**, 615.

Frost, K. J., 1973, These Proceedings.

Frost, K.J., and Dennis, B.R., 1971, *Ap. J.* **165**, 655.

Hodgson, R., 1859, *M.N.R.A.S.* **20**, 15.

Hudson, H.S., 1972, *Solar Phys.* **24**, 414.

Hudson, H.S., and Ohki, K., 1972, *Solar Phys.* **23**, 155.

Hudson, H.S., Peterson, L.E., and Schwartz, D.A., 1969, *Ap. J.* **157**, 389.

Kahler, S.W., 1971, *Ap. J.* **164**, 365.

Kahler, S.W., 1972, *Solar Phys.* **25**, 435.

Kahler, S.W., Meekins, J.F., Kreplin, R.W., and Bowyer, C.S., 1970, *Ap. J.* **157**, 389.

Kandel, R.S., Papagiannis, M.D., and Strauss, F.M., 1971, *Solar Phys.* **21**, 176.

Kane, S.R., 1973, These Proceedings.

Kane, S.R., and Anderson, K.A., 1970, *Ap. J.* **162**, 1003.

Kane, S.R., and Donnelly, R.F., 1971, *Ap. J.* **4**, 151.

Kawabata, K., 1960, *Rpt. Ionosph. Space Res.* (Japan) **14**, 405.

Lin, R.P., 1973, These Proceedings.

Lin, R.P., and Hudson, H.S., 1971, *Solar Phys.* **17**, 412.

Lingenfelter, R.E., and Ramaty, R., 1967, in *High Energy Nuclear Reactions in Astrophysics* (New York: W.A. Benjamin, Inc.).

Maeda, K., 1963, *J. G. R.* **68**, 185.

McKenzie, D.L., Datlowe, D.W., and Peterson, L.E., 1972, *Solar Phys.* (to be published).

Najita, K., and Orrall, F.W., 1970, *Solar Phys.* **15**, 176.

Peterson, L.E., and Winckler, J.R., 1959, *J.G.R.* **64**, 697.

Sturrock, P.A., 1973, These Proceedings.

Svestka, Z., 1970, *Solar Phys.* **13**, 471.

Syrovatskii, S.I., and Shmeleva, O.P., 1971, Lebedev Inst. Preprint 158.

Takakura, T., Ohki, K., Shibuya, N., Fujii, M., Matsuoka, M., Miyamoto, S., Nishimura, J., Oda, M., Ogawara, Y., and Ota, S., 1971, *Solar Phys.* **16**, 454.

Tindo, I.P., Ivanov,V.D., Mandel'stam, S.L., and Shuryghin, A.I., 1970, *Solar Phys.* **14**,204.

Tomblin, F.F., 1972, *Ap. J.* **171**, 377.

Uchida, Y., 1973, These Proceedings.

Wood, A.T., and Noyes, R.W., 1972, *Solar Phys.* **24**, 180.

OPTICAL, HARD X-RAY, AND MICROWAVE EMISSION
DURING THE IMPULSIVE PHASE OF FLARES

Joan A. Vorpahl
Big Bear Solar Observatory, Hale Observatories
Sacramento City College

ABSTRACT

A study was made of the variation in hard (E $\geqslant$ 10 keV) X-radiation, H-alpha, and microwave emission during the impulsive phase of solar flares. Most important, the observations showed that there is an *optical* impulsive component in addition to the well-known hard X-ray and microwave spikes discussed by Kane and Anderson (1970). Properties of these Hα kernels are given. Further analysis shows that the rise time in the 20- to 32-keV X-ray spike depends on the slope in the electron spectrum, $E^{-\delta}$ as t_{rise} = 0.11 exp(0.87)δ when thick target theory is used. A picture of the impulsive phase is given that is consistent with observations of the three above emissions.

INTRODUCTION

I will restrict myself initially to the H-alpha impulsive component and its relation to the impulsive X-ray and microwave flux. Then the electron power spectrum will be discussed, along with a presentation of a picture of the impulsive phase that includes the three different emissions: hard X-ray, microwave, and optical radiation.

My study of the impulsive phase of flares began about four years ago. Since that time, I have examined well over 100 impulsive events in detail, comparing hard X-ray data from Berkeley's Orbiting Geophysical Observatory-5 (OGO-5) experiment with Hα films taken by Dr. Zirin's group at the California Institute of Technology and later at Big Bear Solar Observatory. The major results from this analysis will be presented here; for more details, see Vorpahl (1971, 1972a,b).

Most important, the observations showed that there is an optical impulsive component in addition to the well-known hard X-ray and microwave spikes discussed by Kane and Anderson (1970). The optical component consists of an abrupt, very intense increase of Hα emission in one or more knots of the flare. For the study, flares with film available at Hα $\pm$ ½Å were chosen, since the bright kernels are easiest to see off-band due to a better contrast with the background. Using simple events with only one or two bright kernels allowed unambiguous identification of the optical and X-ray components. An isodensitracer at Jet Propulsion Laboratory in Pasadena was used to make contours of light intensity from film taken during the course of three flares. One of these events, that of August 1, 1968, is shown in Figure 1.
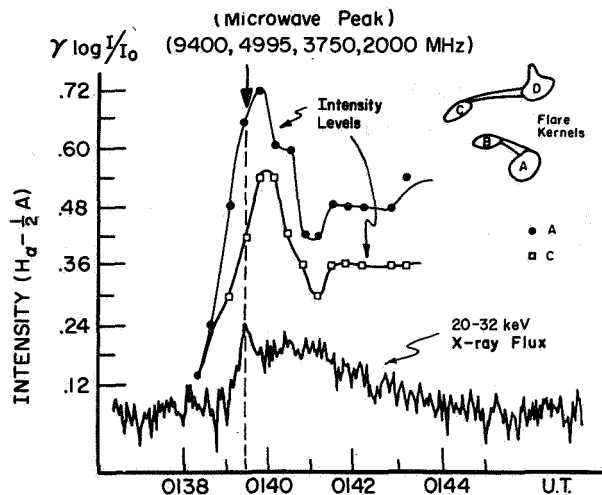
Figure 1. Impulsive X-ray flux (20-32 keV) plotted along with the light curve measured at $H\alpha - 1/2\text{Å}$ during an impulsive flare. Of four potential bright points, only those labeled A and C exhibited the abrupt intensity increase associated with X-ray spikes. I_0 is the local background and γ, with a typical value of 3, is the contrast of the film.

OBSERVATIONS

Flare Emissions

The $H\alpha$ kernels have a luminosity several times greater than the surrounding flare and an intensity rise starting about 20 to 30 seconds before, peaking about 20 to 25 seconds after, and lasting about twice as long as the hard X-ray spike. The effective diameter for the kernels in class $\leqslant 1$ flares is 5 to 10 arcsec, representing one-eighth to one-half the total flare size. Figure 2 is an example of how kernels are located within 6000 km of the boundary separating regions of opposite polarities, often seeming to form near one or both feet of the same tube of flux. (Neutral lines were determined from the $H\alpha$ filament structures in all cases.) Kernels seem confined and often resemble isogauss-contours of the photospheric field indicated on magnetograms; conversely, the thermal part of the optical flare has no special form and expands in an arbitrary fashion.

Figure 3 suggests a possible picture of the impulsive phase that begins with an acceleration of particles at less than 5000 to 6000 km. In this picture, hard electrons move down magnetic field lines towards one or both feet of the flux tubes, through the low chromosphere where they produce microwave and X-ray spikes, along with intense optical emission (the kernel) by collisional excitation. There are several points to be noted in this picture.

222
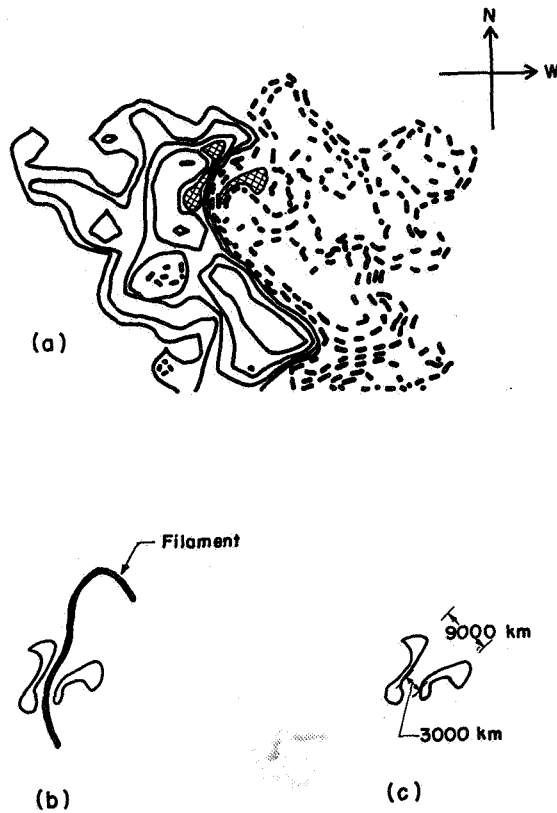
Figure 2. Magnetic field configuration and Hα kernel of July 31 to August 1, 1968 flare (same scale used throughout). (a) Position of impulsive kernels (cross-hatched) with respect to the magnetic field indicated on Mt. Wilson magnetograms. Dotted lines show preceding polarity, and solid lines show following polarity. (b) A filament marks the neutral line in the chromosphere and coincides with the boundary between polarities on the magnetogram. (c) Multiple components in a kernel system are typically less than 5000 to 12,000 km apart.

223
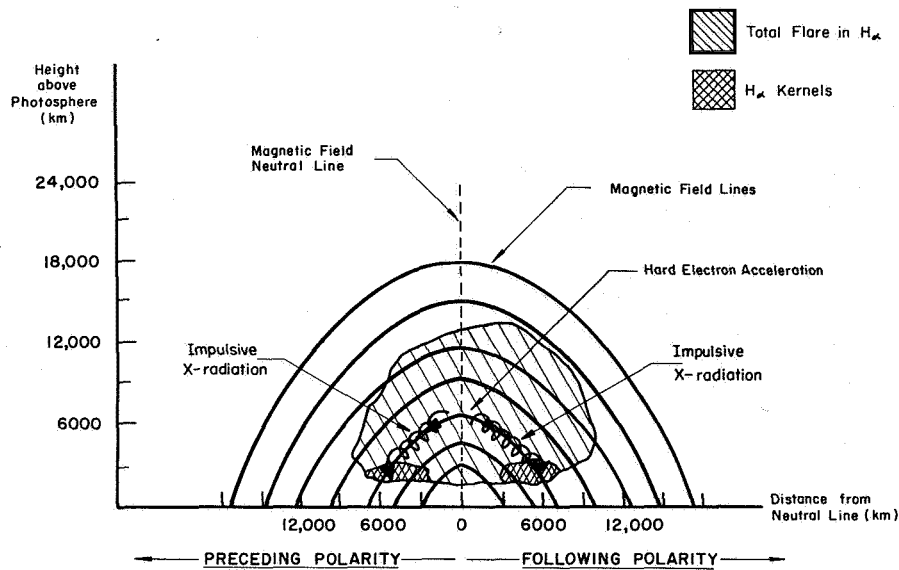
Figure 3. Possible picture of the impulsive phase. After acceleration, the electrons spiral down one or both feet of flux tubes to produce the Hα kernels in the low chromosphere. Field height is assumed to be about one-half the distance between Hα kernels.

First of all, the good time correlation between the Hα kernel and the X-ray spike could be explained either by a compression of cool material at the time when the electrons are accelerated, or by collisional loss from hot electrons moving down through the cooler material. This study cannot distinguish between these two possibilities; however, collisional excitation is consistent with the observations. For example, the bright kernel position is strongly influenced by the magnetic field in the photosphere and low chromosphere; electrons moving down along lines of force could explain this. Furthermore, energy in the hard electrons is more than 50 times that radiated by the kernel during its lifetime, and could therefore explain the optical impulsive flux.

A low source for the impulsive X-ray, microwave, and Hα emission (8000 km or less above the photosphere) is consistent with the observations. First, regarding the Hα kernel:

- In all 15 events observed near the limb, the kernels were located less than 6000 km above the photosphere.

- The fact that kernels closely resemble field contours on magnetograms implies that they occur close to the photosphere, while the remaining part of the flare, having no relation to the magnetograph field, expands to greater heights.

- If the intense Hα kernels are produced by collision, the electrons would have to be accelerated at a height less than the tops of magnetic field arches, that is,

224

h $\leqslant$ 6000 km, if they are to follow the flux tubes down to the kernel site in the low chromosphere. (The field height can be estimated by observing the height of filaments marking the turnover in the field vector. Since filaments are typically one-third to one-half as high as they are long, when observed at the limb, field lines 5000 km in length would be about 2500-km high.)

- The spike-associated kernel, with a line width of more than 2 Å, is much more intense than the remaining part of the flare. This implies that either the temperature of much of the kernel material is less than 20,000 to 25,000 K (where Hα emission is still possible) or the density of neutral hydrogen is high. In either case, a height less than 5000 km is implied.

This describes the Hα kernels, but why are low sites also suggested for the X-ray and microwave emission? This question can be partially answered by referring to the unique time correlation observed between Hα and the higher energy profiles. In order to agree so well, the three regions must either be quite close, perhaps within a few thousand kilometers of each other, or be directly connected by magnetic field lines. Low sites are also suggested by the following:

- Structure is most detailed in the microwave emission at frequencies above 5000 MHz, at those wavelengths least effected by critical plasma densities, by overlying absorption, or by the Razin effect. After considering these three possibilities for cutoff at low frequencies, Zirin et al. (1971) concluded that synchrotron source heights of 3000 to 4000 km were indicated in any case. In addition, the absence of low frequency flux (Zirin et al., 1971; Vorpahl, 1972b) for initial components in some multiple spike events (but not for the later ones), indicates a rising electron source and therefore c   ss subject to plasma effects after each successive burst.

- The peak radio emission is normally at frequencies greater than 7500 MHz, thereby implying a magnetic field of 200 to 300 gauss in the synchrotron source. It would be difficult to explain the existence of a field of several hundred gauss at coronal heights unless the flare explodes, carrying the field upward before the impulsive phase. Observations show that a premature explosion occurs in only a few cases.

Electron Power Spectrum Versus 20- to 32-keV Rise Time

Figure 4 demonstrates how in 36 randomly chosen events the value for δ in the electron power spectrum, $E^{-\delta}$ electrons cm^{-2} s^{-1} keV^{-1}, is related to the 20- to 32-keV spike rise time[*] as $t_{rise} = 0.11 \exp(0.87 \pm 0.03)\delta$. That is, as the rise time becomes shorter, the

---

[*]In the thick foil model, used here to determine the electron spectrum from the hard X-radiation, $\delta = \phi + 1$, that is, the differential electron power spectrum at the point of bremsstrahlung is harder than that at the acceleration site (for example, see Brown, 1971). In the thin target theory, $\delta = \phi - 1$.
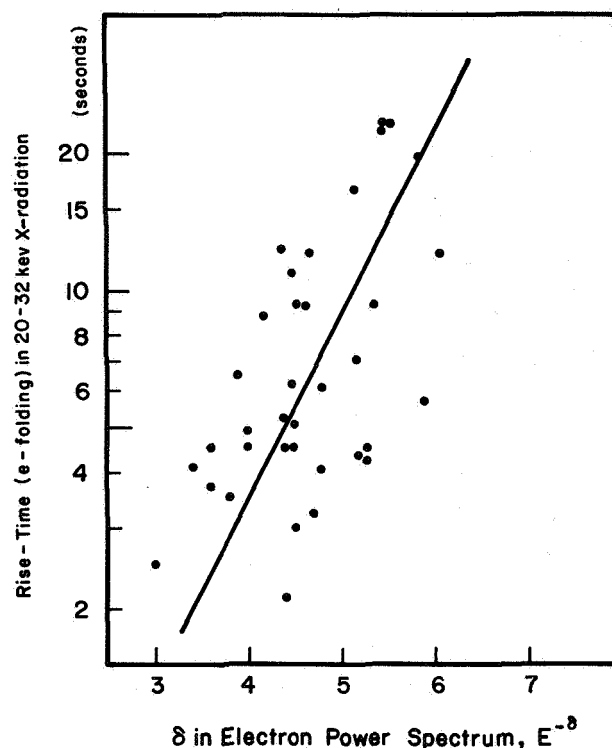
Figure 4. Rise time in 20 to 32 keV X-radiation detected by OGO-5 versus the slope of the electron spectrum.

fraction of hard electrons becomes greater and the probability of higher electron (and photon) energy increases. This implies that the rate at which energy is released is as important, if not more so, than the total energy input if hard electrons are produced.

We can use the relation between rise time and δ to obtain information about the acceleration mechanism: The acceleration rate in the nonrelativistic range is given by

$$dE/dt \simeq C\,E^p$$

where $E = k/mc^2$, C is a constant, $p = 1/2$ for the acceleration due to the electric field or Fermi type, and $p = 1$ for the betatron type (Takakura, private communication). Generally, the electron slope, δ, may be determined by both C and a probability function of time, $W(\lambda)$, for the distribution of effective acceleration times, λ, for individual electrons; the average of λ is of the order of t_{rise}.

For example, if we assume that $p = 1/2$, we have

$$E^{\frac{1}{2}} \simeq C\,\lambda/2 \quad \text{for } E \gg E_0$$

226

for a given electron which had experienced the acceleration over λ, where E_o is the initial energy. Accordingly, the electron energy distribution (electrons cm^{-2} s^{-1} keV^{-1}) for the group of accelerated electrons is determined by the probability distribution $W(\lambda)$, alone, independent of the initial energy distribution of the electrons. This probability function and its importance in the acceleration process will be discussed further in a future paper by Vorpahl and Takakura.

SUMMARY

This study of the impulsive phase of flares includes a discussion of hard X-ray, Hα, and microwave emissions. An abrupt, very intense increase in Hα emission marks the optical impulsive phase. Properties of these Hα kernels include: a) luminosity several times greater than the surrounding flare; b) intensity rise starting about 20 to 30 seconds before, peaking about 20 to 25 seconds after, and lasting about twice as long as the 20 to 32 keV X-ray spike; c) effective diameter of 3000 to 6000 km for class $\leqslant 1$ flares; d) position within 6000 km of the boundary separating opposite magnetic polarities; and e) total radiated energy less than 1/50 that of the hard electrons. Further analysis shows that the rise time in the 20 to 32 keV X-ray spike depends on the slope in the electron spectrum, $E^{-\delta}$, as $t_{rise} = 0.11$ $exp(0.87)\delta$ when thick target theory is used. A picture of the impulsive phase, including hard X-ray, Hα, and microwave emissions, is presented.

ACKNOWLEDGMENTS

REFERENCES

Brown, J., 1971, *Solar Phys.* 18, 489.

Kane, S., and Anderson, K., 1970, *Ap. J.* 162, 1003.

Vorpahl, J., 1971, Ph.D. thesis, Univ. California, Berkeley and California Inst. Tech.

Vorpahl, J., 1972a, *Solar Phys.* 26, 397.

Vorpahl, J., 1972b, "Multiple Hard X-Ray Bursts," to be submitted to *Solar Phys.*

Vorpahl, J., and Takakura, T., 1973, submitted to *Ap. J.*

Zirin, H., Pruss, G., and Vorpahl, J., 1971, *Solar Phys.* 19, 463.

IV: ULTRAVIOLET AND SOFT X-RAY EMISSIONS

THE EXTREME ULTRAVIOLET SPECTRUM
OF SOLAR FLARES

Robert W. Noyes
Harvard College Observatory
Smithsonian Astrophysical Observatory

ABSTRACT

EUV flare observations are discussed, with particular attention to relative variations of spectral features during flares. An approximately equal enhancement of most chromospheric, transition-zone, and coronal lines indicates that thermal conduction may be important at temperatures between 10^5 and 10^6 K in the flare plasma. However, enhancements sometimes appear to be somewhat larger for transition-zone lines and for density-sensitive lines arising from metastable levels. EUV lines characteristic of temperatures between 10^4 and 1.5×10^6 K all show a nearly simultaneous rise in impulsive flares, coincident with the hard X-ray burst. Density increases by factors of 5 to 10 in the transition zone are inferred from emission-measure increases and from line ratios for small flares.

INTRODUCTION

The extreme ultraviolet (EUV) solar spectrum is considered here to extend from about 300 to 1500 Å. The long-wavelength end occurs at the transition between the predominantly photospheric Fraunhofer spectrum at $\lambda \gtrsim$ ¹⁴ Å and the predominantly chromospheric and coronal emission line spectrum at $\lambda \lesssim 1500$ Å. The short-wavelength end at about 300 Å is rather arbitrarily chosen as the practical limit of normal-incidence optics. We shall use the term XUV for the region between 300 Å and the start of the soft X-ray region at 100 Å, below which grating spectrometers give way to crystal spectrometers. Recent reviews of XUV and soft X-ray flare spectra are given by Neupert (1971) and Doschek (1972).

Under nonflare conditions, the solar EUV spectrum originates in regions varying in temperature from photospheric (~ 4000 K) to coronal ($\sim 3 \times 10^6$ K). The chromosphere and the chromosphere-corona transition zone, of intermediate temperature, give rise to a great number of EUV emission lines which convey unique information about the structure of those regions. Current ideas of the structure of the transition zone in particular are due mainly to analysis of EUV data. (For recent reviews of EUV studies of the nonflaring solar atmosphere, see Noyes and Withbroe, 1972, and Noyes, 1971. A recent review of knowledge about the transition zone is given by Athay, 1971.)

In principle, the EUV spectrum of flares can reveal analogous information about the structure and time development of the flare-associated plasma in the temperature range 10^4 K $\lesssim$ T $\lesssim 10^6$ K. For example, it should be possible to determine whether the transition

between flare plasma at chromospheric and coronal temperatures exhibits a steep temperature gradient controlled by thermal conduction, as appears to be the case in the nonflaring sun. Simultaneous flare observations in several EUV lines with different temperatures of emission should reveal the detailed time development of the plasma, including relative timing of heating at various temperatures and densities and the relation of the heating to the time of injection of nonthermal particles of different energies. Relative line intensities, line shifts, and line profiles should provide other diagnostics of density, velocity, and ionization state in the plasma by straightforward extension of techniques normally applied to the nonflaring sun.

The interpretation of the solar EUV spectrum of solar flares, however, rests on a determination of the time-varying ionization state of the gas. The most straightforward assumption is that the ionization state equals the equilibrium value appropriate to the electron temperature at each instant. This assumption is questionable for the low-density parts of the flare volume, at least for impulsive EUV bursts, which are observed to have rise times as short as a few seconds. Kafatos and Tucker (1972) have found that at densities $n_e \gtrsim 10^{10}$ cm^{-3}, the ionization state of highly stripped ions significantly lags the steady-state value during the rise of a flare if the rise time is less than several tens of seconds. For chromospheric and low-transition-zone ions, where the density in the flaring region certainly exceeds 10^{11} cm^{-3} (see following), the use of equilibrium ionization calculations is probably justified, but detailed time-dependent calculations may be required for ions formed in the upper transition zone or low corona.

As already mentioned, important information should be contained in simultaneous flare observations with high time resolution in different individual EUV lines or continua. Unfortunately, only relatively crude approximations to such data exist to date. The Orbiting Solar Observatory-3 (OSO-3) experiment of Hinteregger and his coworkers (Hinteregger and Hall, 1969; Hall, 1971; and Castelli and Richards, 1971) produced light curves of flares with high time resolution, but in only one emission line for each flare. In addition, flare spectra were obtained, but with only 5.4-minute time resolution. Because the instrument received radiation from the entire solar disk, the flare signal-to-noise ratio was decreased by the nonflaring background. The Harvard OSO-4 and OSO-6 experiments obtained moderate (0.5 to 1 arcmin) spatial resolution — and hence good signal-to-noise ratios—and useful time resolution (as good as 30 s); but again, only one line was observed per flare (Wood et al., 1972; Wood and Noyes, 1972). One informative EUV flare spectrum was obtained from OSO-6, and will be discussed below. The University of Colorado OSO-5 experiment (Kelly and Rense, 1973) acquired simultaneous high time-resolution observations over several different EUV bands, but each band was rather broad and contained many different EUV lines. A very high spatial-resolution (~ 3 arcsec) rocket photograph of a flare was obtained by Tousey and coworkers (Purcell and Widing, 1972; and Tousey, 1971); the photograph recorded the emission simultaneously in many lines in the range 170 Å $< \lambda <$ 670 Å. The data were recorded during the decay portion of the flare, however, and give no information on the time development during the impulsive phase. The recent GSFC experiment on OSO-7 records simultaneous images at several EUV and X-ray wavelengths with 20-arcsec spatial resolution and 15-second temporal resolution; preliminary data analysis (Neupert, 1973) shows rather

complex spatial and temporal variations of the flare plasma between 2×10^6 K and 20×10^6 K. While these data will be very useful when fully studied, it is clear that even higher spatial and temporal resolution is ultimately needed.

In spite of the shortcomings of currently available data, a consistent picture of the EUV flare plasma is emerging. From sudden-frequency-deviation (SFD) observations, which respond to the total EUV emission in the range 10 to 1030 Å (Donnelly, 1971, 1973), from broad-band EUV measurements (Kelly and Rense, 1973), and from observations of individual lines (Hall, 1971; Wood and Noyes, 1972), it has been well established that the EUV emission rises impulsively in close synchronism with the hard X-ray burst caused when nonthermal electrons, generated in the transition zone or low corona, impinge on the denser atmosphere below (Kane and Donnelly, 1971). The ratio of electron kinetic energy liberated as X-ray bremsstrahlung to that converted by collisional losses into thermal motions is simply the efficiency factor ϵ for bremsstrahlung, since collisional losses dominate all other energy losses (Lin and Hudson, 1971); ϵ was calculated by Kane and Donnelly (1971) to be $\sim 10^{-5}$ This is approximately the observed ratio between the hard X-ray flux and the total EUV flux and suggests that much of the thermal energy is reradiated in the EUV. Hudson (1972) has argued that the low-energy tail of the nonthermal electron distribution contains enough energy to produce, through collisional losses, not only the EUV emission but also the Hα emission from the low chromosphere, as well as the white-light continuum. For further details on the broadband properties of EUV flare emission and their relation to X-ray, microwave, and optical emission, see Donnelly (1973).

THE EUV SPECTRUM OF SOLAR FLARES

We turn now to a consideration of what can be learned from the detailed EUV flare spectrum, stressing the comparison of two or more emission lines observed simultaneously from the same flare event.

Relative Enhancement of EUV Lines in Flares

The relative enhancement $(I_{flare} - I_{preflare})/I_{preflare}$ of different EUV lines in flares enables models of the flare plasma to be constructed. Because most quantitative photoelectric observations to date have modest spatial resolution at best, it has generally been impossible to isolate and measure the true enhancement of the flare itself, undiluted by nonflaring background emission. Hall (1971) normalized flare enhancements to preflare emission from the entire sun, and Wood et al. (1972) normalized them to the preflare emission within the spectrometer entrance slit.

Some improvement is obtained by normalizing to the measured area of the flare in Hα, under the assumption that the EUV emission is coextensive with the Hα emission. This appears to be a valid assumption, as suggested by the close correspondence between Hα flare filaments and the soft X-ray flare structures seen in the rocket X-ray photographs of American Science and Engineering (Vaiana et al., 1968). By dividing Hall's (1971) EUV enhancements by the fraction of the disk covered by the Hα flare, "true" enhancements

ranging from 50 to 170 can be obtained; the higher enhancement refers to a 1B flare measured in O VI 1032. Similar results are found from the data of Wood et al. (1972).

These enhancements, though large, probably represent a lower limit to the maximum enhancement in a flare, since the observed flux increase is averaged over the total Hα area of the flare; the emission may well be highly nonuniform. For optically thin lines such as O VI 1032 and Mg X 625, the enhancement equals the fractional increase in the quantity n_e^2 Δh averaged over the flare, where Δh, the height range within which the ion in question is near its maximum concentration, varies inversely with the temperature gradient dT/dh. A natural, though simplistic, explanation for the large enhancements is that flare-generated heating of the atmosphere causes the chromospheric and transition-zone temperature rises to occur at deeper levels in the atmosphere, where the density is an order of magnitude higher.

A crude estimate of the relative enhancement of various EUV lines was obtained by Wood and Noyes (1972), who analyzed a set of Hα subflares to find that most lines and continua show roughly the same enhancement at their time of maximum emission. This conclusion is subject to large uncertainties induced by intercomparison of different flares in different lines and must be considered to be only a zero-order approximation (see below). A height-independent enhancement of the emission measure is consistent with a density increase by a constant ratio throughout the flare volume if the temperature gradients in the flare have the same form as in the preflare active region. In an active region, the emission of lines formed between 10^5 and 10^6 K reveals a very steep transition zone having temperature gradients consistent with a height-independent downward conductive flux (Noyes et al., 1970); the constancy of the conductive flux is expected from energy conservation since conduction dominates all other types of energy flow in the transition zone. If the transition zone in the flare region is also characterized by ⅴ ant conductive flux, and if the flare material achieves pressure equilibrium similar to the preflare situation, then flare enhancements would be the same throughout the transition zone. The above results then suggest that, subject to considerable uncertainty imposed by the data and the unknown geometry, thermal conduction plays an important role in defining the temperature profile of the flare plasma between 10^5 and 10^6 K.

Such a conclusion is not unexpected, since simple dimensional analysis leads to a decay time of only a few seconds for a thermal perturbation from the constant conductive flux profile in the transition zone (T ~ 3 X 10^5 K) of an active region. The problem becomes complicated, however, because the conduction is constrained to occur along magnetic-field lines, whose geometry is uncertain. To achieve conductive equilibrium it is necessary, of course, that individual flux tubes entering a region with preflare temperatures of 10^6 K continue through the 10^5 K level and into the chromosphere. Nearly all flare pictures are consistent with such a requirement.

Many individual lines show exceptions to the zero-order approximation stated above. Harvard OSO data show a tendency for slight overenhancement of transition-zone lines relative to coronal lines in flares, although the uncertainties introduced by observing only one line per flare make the results inconclusive. Donnelly et al. (1973), however, have demonstrated

234

from the same data that such effects do occur through comparison of individual line observations with the total EUV flux from 10 to 1030 Å, as revealed by SFD data. They find that in one flare the transition-zone line O VI 1032 is more than a factor of two stronger than that predicted by the SFD data, indicating that either the density or the thickness of the transition zone for this flare was anomalously large.

In addition to intensity variations caused by variations in flare geometry, certain lines arising from density-sensitive metastable levels generally undergo enhancements much larger than average (Hall, 1971). This overenhancement of density-sensitive lines is a valuable diagnostic tool, as we discuss later.

These effects are illustrated in Figure 1, which shows a portion of an OSO-6 spectrum recorded with the spectrometer entrance slit partially covering a class 1B flare. The spectrum was scanned toward shorter wavelengths at the rate of 75 Å min^{-1}, and the flare maximum was determined from SFD data to occur when the spectrometer passed $\sim$ 1275 Å. Thus, the figure illustrates events in the rising and maximum phase of the flare. The observed overall enhancement of $\sim$ 4 compared to the typical "true" value of $\sim$ 50 per unit area of Hα emission suggests that the flaring material covers $<$ 10 percent of the (35 arcsec)^2 slit. After the underlying continuum is allowed for, the lithium-like doublet N V at 1239 and 1243 Å shows an enhancement of 3.4, while the identical transition of Mg X at 625 Å (seen in second order) shows an enhancement of only 0.30. The N V lines are formed at a temperature T $\sim$ 2 X 10^5 K in the low transition zone, while the Mg X line is formed in the
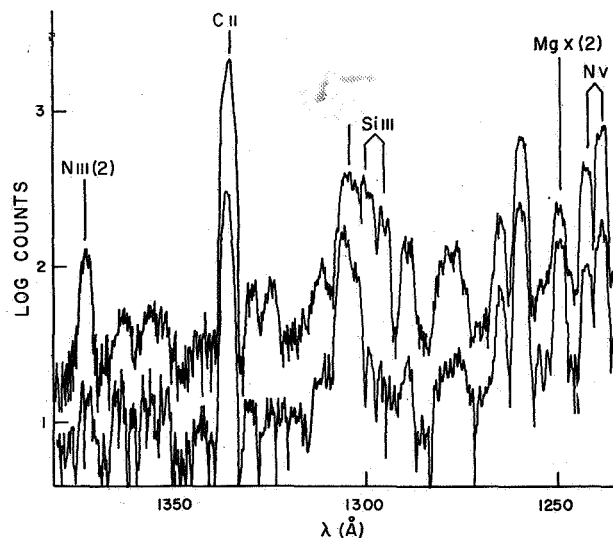
Figure 1. Flare (upper) and preflare (lower) spectra of a portion of a 1B flare obtained by the Harvard OSO-6 EUV spectrometer at 1640 UT, August 23, 1969. Scan rate is 75 Å min^{-1}, from longer to shorter wavelengths. The maximum of the impulsive phase occurred when the spectrum scan was near 1275 Å.

upper transition zone and low corona at T ~ 1.5 × 10^6 K. It is clear that during the impulsive phase of this flare at least, transition-zone lines were much more enhanced than coronal lines.

The greatest enhancements visible in Figure 1 are those of Si III at 1295 and 1299 Å, which increase by a factor of 18; these triplet transitions arise from a metastable level 6.5 eV above the ground state and reflect the density-sensitivity of the population of that level. We shall return to this point later.

Relative Temporal Behavior of EUV Lines in Flares

As mentioned earlier, few simultaneous EUV observations of flares exist in two or more individual emission lines. Donnelly et al. (1973) compared OSO-6 observations of individual lines with SFD data on the total emission from 10 to 1030 Å. They found that impulsive EUV bursts occur simultaneously with the SFD for individual lines emitted at all temperatures from the chromosphere up to 1.5 × 10^6 K, characteristic of Mg X in the low corona. Either of two possible pictures might explain this observation:

(a) Essentially all the energy losses occur in the dense chromosphere, with preflare temperature around 10^4 K; a hot dense region is immediately formed with temperatures well in excess of 1.5 × 10^6 K at the center and lower near the edge. This would give rise to thermal emission at all temperatures up to and beyond 1.5 × 10^6 K.

(b) Collisional heating occurs simultaneously throughout the entire chromosphere-transition zone-low corona region with preflare temperatures in the range from 10^4 to 1.5 × 10^6 K, as a result of electrons thermalizing at various altitudes. Thus, the flare emission at each temperature occurs after collisional heating of gas that previously was in a state only slightly cooler and denser.

Although the observation mentioned above does not by itself rule out either picture, calculations of energy losses by particles impinging on the denser atmosphere from above (Hudson, 1972), as well as densities inferred from line ratios (discussed below), support the second picture.

Kane and Donnelly (1971) have compared the rise time of the total EUV emission as reflected in SFD data with that of nonthermal X-rays of various energies, and found the best match to occur with 9.6- to 19.2-keV X-rays; they suggest, therefore, that the electrons producing these X-rays also produce the bulk of the EUV emission. It is important to extend this type of analysis by obtaining simultaneous observations of chromospheric, transition-zone, and coronal lines with very high time resolution. Such observations should permit deductions about the time variation of the energy spectrum of nonthermal electrons impinging on the atmosphere. Since the level of downward penetration is greatest for the highest energy electrons (Hudson, 1972), and vice versa, EUV observations at different heights provide a coarse energy analysis. For example, it is known (Kane and Anderson, 1970) that the hardest X-rays have the fastest rise times; since these are produced by the highest energy

electrons, we would expect chromospheric EUV lines to have a more rapid impulsive rise than do lines formed in the transition zone or corona. (In this connection, it is interesting that the rise times of two impulsive flares observed in the deep-lying C I 1100 and Si I 1350 continua were among the fastest of all observed by the Harvard OSO-6 experiment.) The time history of impulsive events in the low corona may be complicated by time-dependent ionization effects at the low densities prevailing there (Kafatos and Tucker, 1972).

Observations of the relative timing of EUV emission from the slower postimpulsive phase of flares are less certain, partly because SFD data are not useful for slow changes (Donnelly, 1973). From a statistical study of OSO-3 data on different events, Hall (1971) concluded that coronal lines peak several minutes later than Hα, whereas chromospheric and transition-zone lines peak before. There is no discrepancy between this result and the simultaneity of the impulsive rise in all EUV lines, as mentioned above, if Hall's result refers primarily to the slow nonimpulsive phase of the flare, as suggested by Donnelly et al. (1973).

The gradual postimpulsive EUV rise is seen in individual lines ranging from the chromosphere to the corona (Wood and Noyes, 1972) and appears to exhibit approximately the same temporal behavior as the soft X-ray and microwave postburst increase (Wood and Noyes, 1972). Presumably, all reflect a complicated situation in which thermal conduction from the flare nucleus, shock-wave propagation and deposition, and adiabatic expansion play important roles. Again, observations in individual lines with high time resolution are urgently needed. Here, however, expansion of the flare volume is probably important, so good spatial resolution in all lines is necessary.

Densities Inferred from EUV Flare Observations

As mentioned earlier, a simplistic explanation r the enhancement of EUV lines during flares is that the appropriate temperature for emission occurs at a deeper layer in the atmosphere, where the density is higher. Quantitative determinations of density from the emission-measure increase require a knowledge of the geometry and the temperature profile of the flare volume. A more direct measure of the density, however, is available through ratios of density-sensitive lines. We have already noted (compare with Figure 1) that lines from low-lying metastable levels of ions such as Si III, C III, and O V show greater enhancements during flares than do the resonance lines. For the last two ions, Munro et al. (1972) have calculated the ratio of triplet lines arising from the metastable level (C III 1176, O V 760) to the singlet resonance lines (C III 977, O V 630). These lines were observed in the Harvard OSO-6 flare spectrum scan discussed above. Although the time between observations of the related lines is too long for quantitative conclusions, the trend toward increased density (increased triplet-to-singlet ratio) is clear. For the O V line pair, observed 6 minutes after flare maximum, the density inferred from these lines, averaged over the slit (35 arcsec)^2, was $\langle n_e \rangle = 5 \times 10^{11}$ cm^{-3}, 5 times the preflare value of 1×10^{11} cm^{-3}, 30 times that in a typical nonflaring active region, and 150 times that in the quiet sun. At T ~ 2×10^5 K, characteristic of O V, this corresponds to a gas pressure of 15 dynes cm^{-2}.

Purcell and Widing (1972) studied the density-sensitive ratio of the pair of Fe XIV lines at 211 and 219 Å observed 4 minutes after maximum of an importance 2N flare in the photographic rocket spectrum of Tousey and coworkers (Tousey, 1971); they found that the density increased to $n_e = 3 \times 10^{10}$, corresponding to a gas pressure of 10 dynes cm^{-2} at $T \sim 2 \times 10^6$ K. Similar results were found from the ratio of the 234 and 244 Å lines of Fe XV in the same flare spectrum by Cowan and Widing (1973).

Figure 2 shows part of the spectrum of the same flare as in Figure 1, but at a later time, about 5 minutes after the impulsive peak, when the spectrometer was in the vicinity of the Lyman continuum. The slope of the continuum spectrum shows, relative to the preflare value, a small but a real flattening in the flare decay stage; the difference corresponds to a color-temperature increase of about 1900 K over the preflare value of 7900 K. It has been shown (Noyes and Kalkofen, 1970; Vernazza and Noyes, 1972) that the preflare emission is optically thick and that the measured color temperature is very close to the true electron temperature at optical depth unity in the Lyman continuum. The relatively small temperature increase in the flare does not imply a correspondingly small heating of the chromosphere, for the flare heating may be expected to ionize most of the hydrogen near the level of optical depth unity, causing that level to move to deeper, previously much cooler, regions.
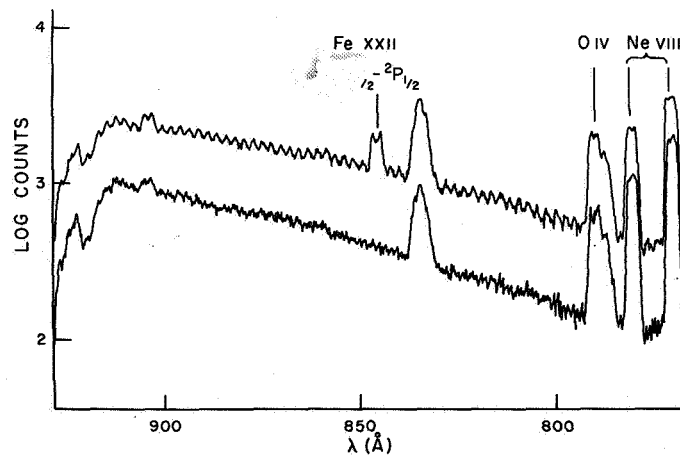
Figure 2. Flare (upper) and preflare (lower) spectra of the same flare shown in Figure 1, but in the region of the hydrogen Lyman continuum, scanned about 5 min after flare maximum. The oscillation in the intensity of the flare (upper) spectrum is due to an instrumental pointing wobble with a period of $\sim$ 1.9 sec and an amplitude of a few arcsec, and indicates the creation of sizable intensity gradients in the flare region.

In principle, one can deduce the density at the height of Lyman-continuum emission in the flares from the observed intensity plus the temperature as determined from the continuum slope, since the intensity is approximately equal to $B_\nu(T)/b_1$, where b_1, the departure coefficient of the ground state of hydrogen, depends on the electron density (Noyes and Kalkofen, 1970). Unfortunately, in the present case that is not possible, because the flare did not fill the entrance aperture and the intensity is diluted by nonflare emission from the active region. One can turn the problem around, however, and conclude from the requirement that b_1 can only decrease in the flare (corresponding to an increase in density) that the flaring area within the slit could occupy no more than 2×10^{17} cm^2. Another possibility, which cannot be ruled out without high spatial-resolution data, is that the flare emission is at a higher temperature, but optically thin, and covers a greater area.

Another point of special interest in Figure 2 is a new line at 845.4 ± 0.2 Å, which has been seen for the first and only time in this spectrum. It has been identified (Kastner, 1971) as the $^2P_{3/2} - {}^2P_{1/2}$ transition in Fe XXII, analogous to the forbidden 5303 Å line of Fe XIV routinely seen in the corona.

SUMMARY AND CONCLUSION

In this paper we have emphasized that simultaneous observations of flares in different EUV emission lines or continua can provide the key to detailed understanding of the behavior of the chromosphere and low corona in response to a solar flare. Several different sets of observations have already shown the close correspondence between impulsive EUV bursts and hard X-ray and microwave bursts, as well as the appearance of a second, more gradual, phase associated with soft X-ray bursts and microwave postburst increases. EUV emission from flares has been seen in individual lines and continua ranging in temperature from 5000 to 1.25×10^7 K. Impulsive EUV bursts occur simultaneously at all temperatures from 10^4 to 10^6 K. Crude spectral analyses suggest that thermal conduction plays an important role in determining the temperature structure of the EUV-emitting flare plasma and that even for small flares the pressure is increased by a factor of 5 to 10 over the preflare value.

It should be clear that real progress awaits simultaneous high time-resolved observations in several emission lines or continuum positions; such data will be relatively straightforward to interpret by use of well-understood diagnostic tools and should produce a clear picture of the response of the chromosphere and low corona to the flare phenomenon.

ACKNOWLEDGMENT

REFERENCES

Athay, R. G., 1971, In *Physics of the Solar Corona*, ed. by C. J. Macris, D. Reidel Publ. Co., Dordrecht, Holland, 36.

Castelli, J. P., and Richards, D. W., 1971, *J. G. R.* 76, 8409.

Cowan, R. D., and Widing, K. G., 1973, *Ap. J.* 180, 285.

Donnelly, R. F., 1971, *Solar Phys.* 20, 188.

Donnelly, R. F., 1973, These Proceedings.

Donnelly, R. F., Wood, A. T., Jr., and Noyes, R. W., 1973, *Solar Phys.*, in press.

Doschek, G. A., 1972, *Space Sci. Rev.* 13, 765.

Hall, L. A., 1971, *Solar Phys.* 21, 167.

Hinteregger, H. E., and Hall, L. A., 1969, *Solar Phys.* 6, 175.

Hudson, H. S., 1972, *Solar Phys.* 24, 414.

Kafatos, M. C., and Tucker, W. H., 1972, *Ap. J.* 175, 837.

Kane, S. R., and Anderson, K. A., 1970, *A*♂ 162, 1003.

Kane, S. R., and Donnelly, R. F., 1971, *Ap. J.* 164, 151.

Kastner, S. O., 1971, *J. Opt. Soc. Amer.* 61, 335.

Kelly, P. T., and Rense, W. A., 1973, *Solar Phys.* 26, 431.

Lin, R. P., and Hudson, H. S., 1971, *Solar Phys.* 17, 412.

Munro, R. H., Dupree, A. K., and Withbroe, G. L., 1972, *Solar Phys.* 19, 347.

Neupert, W. M., 1971, *Phil. Trans. Roy. Soc. London A* 270, 143.

Neupert, W. M., 1973, Las Cruces meeting, Solar Division, AAS. *BAAS*, in press.

Noyes, R. W., 1971, *Ann. Rev. Astron. Astrophys.* 9, 209.

Noyes, R. W., and Kalkofen, W., 1970, *Solar Phys.* 15, 120.

Noyes, R. W., and Withbroe, G. L., 1972, *Space Sci. Rev.* 13, 612.

Noyes, R. W., Withbroe, G. L., and Kirshner, R. P., 1970, *Solar Phys.* 11, 388.

Purcell, J. D., and Widing, K. G., 1972, *Ap. J.* 176, 239.

Tousey, R., 1971, *Phil. Trans. Roy. Soc. London A* 270, 59.

Vaiana, G. S., Reidy, W. P., Zehnpfennig, T., Van Speybroeck, L., and Giacconi, R., 1968, *Science* 161, 564.

Vernazza, J., and Noyes, R. W., 1972, *Solar Phys.* 22, 358.

Wood, A. T., Jr., and Noyes, R. W., 1972, *Solar Phys.* 24, 180.

Wood, A. T., Jr., Noyes, R. W., Dupree, A. K., Huber, M. C. E., Parkinson, W. H., Reeves, E. M., and Withbroe, G. L., 1972, *Solar Phys.* 24, 169.

GROUND-BASED OBSERVATIONS OF EUV FLARE EMISSIONS

Richard F. Donnelly

NOAA Environmental Research Laboratories, Boulder

ABSTRACT

Ground-based observations have established that impulsive extreme-ultraviolet (EUV) flashes occur during solar flares, in close association with hard X-ray bursts and certain impulsive portions of the optical flare. The energy flux radiated in the 10 to 1030 Å wavelength range exceeds that in hard X-rays ($\gtrsim$ 10 keV) by about 10^5, and is roughly comparable to the energy flux radiated at all optical wavelengths. In this paper our current knowledge of EUV flare radiation and ground-based observations of the radiations are reviewed. Several hypotheses are proposed about the interrelation between impulsive EUV emissions and other flare radiations, their spatial location, and association with magnetic fields.

SUDDEN IONOSPHERIC DISTURBANCES

Solar X-ray and EUV radiations produce ionization in the earth's upper atmosphere or ionosphere. Ground-based ionospheric observations provide information about the solar EUV radiation. The ionospheric effects of X-ray and extreme ultraviolet bursts of solar flares, called sudden ionospheric disturbances (SIDs), are observed by a number of techniques, each having its own name for its SID effect, for example, short wave fadeout (SWF) and sudden phase anomaly (SPA). Each of these observing techniques is sensitive to the SID over a particular range of ionospheric heights, and consequently to certain X-ray and EUV wavelength ranges of the solar flare radiation, as evident in Figure 1. SID observations cannot provide high wavelength resolution because monochromatic radiation produces significant photoionization over an appreciable height range, and photoionization at a given height is produced by a wide range of X-ray and EUV wavelengths. Although SID observations cannot provide any spatial resolution of the EUV bursts, certain types of SID observations can provide high time resolution of broadband EUV bursts.

From a solar physics viewpoint, SID observations form two groups. The first and best known group consists of SID effects observed in the ionosphere at D-region heights below 100 km caused by soft X-rays (< 10 Å) and includes SWF, SPA, SCNA (sudden cosmic noise absorption), SEA (sudden enhancement of atmospherics), and so on. These SIDs provide information useful for studying the transient response of the poorly understood D-region (Mitra, 1972) but do not provide data on soft X-ray bursts competitive with recent satellite X-ray measurements.

The second group involves SID effects at heights above 100 km in the well-understood day-time E and F1 regions caused by solar radiation in the 10 to 1030 Å wavelength range. Any

of these SID measurements can currently provide absolute flux intensities accurate at best to about a factor of four. One main portion of this uncertainty is common to any broadband detector, namely that the interpretation of the broadband detector output depends upon the unknown spectrum of the input radiation. About a factor of two of the uncertainty is essentially the same factor-of-two discrepancy that ionospheric physicists find during non-flaring conditions between observed electron densities and values computed from solar flux measurements, using recent measurements of absorption and photoionization cross sections, atmospheric densities, and electron loss rates (Swartz, 1972; Timothy et al., 1972).

CIRA 1965, MEAN MODEL ATMOSPHERE
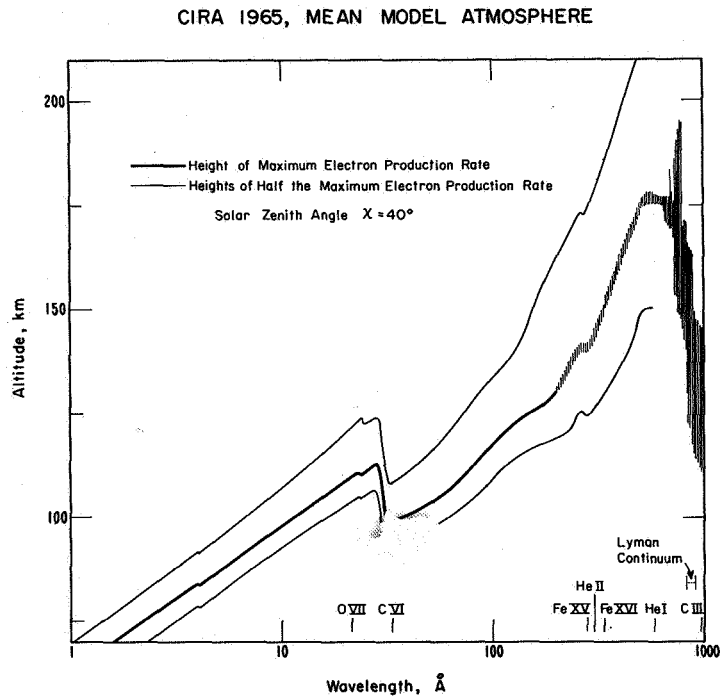
Figure 1. Loci of the heights of peak ionospheric electron production and heights of half the peak production rate as a function of wavelength of the photoionizing solar radiation. At wavelengths greater than 600 Å, the heights fluctuate with wavelength; this fine structure is not shown in detail but is denoted by the hash lines. Radiation at wavelengths greater than about 1030 Å does not efficiently ionize the major constituents of the ionosphere and can therefore be neglected. The sharp change in heights near 30 Å is caused by the K-shell discontinuity in the absorption cross section of N_2. The wavelengths of some solar emission lines are marked.

Soft X-ray bursts involve very large percentage enhancements over the preflare, full-disk solar flux. Once the 1 to 8 Å soft X-ray flux exceeds about 2×10^{-3} ergs·cm^{-2}·s^{-1} at 1 AU (Kreplin et al., 1962), the D-region SID effects tend to involve large percentage increases in ionization relative to preflare values. This threshold effect results from cosmic rays and the solar hydrogen Lyman alpha line being the dominant sources of ionization in the D region, until the soft X-ray flux rises to this threshold value. The 10 to 1030 Å flare radiation and the SID effects above 100 km altitude involve smaller percentage increases but larger absolute increases.

Most of the results on EUV flare radiation deduced from ground-based measurements are based on one observing technique, where the flare effect is called a sudden frequency deviation (SFD). The next section describes the physics of SFDs. A later section describes our current knowledge of EUV bursts based on SFD observations. Because the results from SFDs have recently been reviewed elsewhere (Donnelly 1970, 1971), we emphasize what is not known and what research can be done to further our knowledge of EUV flare emission and its relation to other flare processes.

SUDDEN FREQUENCY DEVIATIONS

Figure 2 shows an example of an SFD and the time dependence of the EUV burst deduced from these data. In an SFD, the received frequency f of a radio wave that propagates through the ionosphere increases suddenly, peaks, and then decays to the transmitted frequency f_0. Note that during the decay in Figure 2, the received frequency decreases below the preflare or transmitted value. The size of the frequency deviation (Δf) is a very small perturbation relative to the transmitted frequency, rarely more than one part per million.
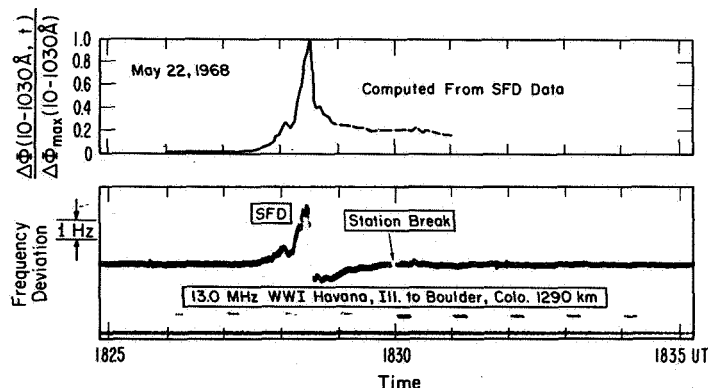
Figure 2. An SFD and the deduced 10 to 1030 Å energy flux enhancement. $\Delta\Phi_{max}$(10 to 1030 Å) ≈ 0.7 ergs cm^{-2}s^{-1} at 1 AU. The rise time ≈ 13 s (1/e to max) and the full pulse width at half the maximum ≈ 17 s.

The physical relation between the EUV burst and the observed SFD is qualitatively as follows: The observed frequency deviation is caused by the time rate of change of electron density in the ionosphere. When an electromagnetic wave propagates through a plasma, the length P of its phase path depends on the frequency, the distance traveled, and the effect of the plasma on the wave propagation, mainly through the interaction of the plasma electrons with the wave. When the electron density in the plasma changes slowly with time, the phase path length also changes in proportion to the change in electron density. The observed frequency deviation (Δf) equals the time rate of change of the phase path and is therefore proportional to the time rate of change of electron density (N_e). Rigorous derivations (Bennett, 1967) give

$$\Delta f = f - f_o = +\frac{f_o}{c} \int_{\text{xmtr, ray path}}^{\text{rcvr}} \cos\alpha \left(-\frac{\partial\mu}{\partial N_e}\right) \frac{dN_e}{dt} \, ds \tag{1}$$

where μ is the phase refractive index given by the real part of the Appleton formula, α is the angle between the wave normal and the ray path, and the integration is along the ray path. Equation (1) can be accurately evaluated numerically by the ray tracing program of Jones (1966). For a radio wave reflected from the ionosphere, the net frequency deviation involves the integration of dN_e/dt over heights up to the height of reflection.

The X-ray and EUV burst increases the photoionization rate in the ionosphere, which causes an increase in the electron density and in the time rate of change of electron density, thereby producing an SFD. Since at E and F1 region heights the ratio of ionization density to neutral density is very small ($< 10^{-4}$), the flare en.̇ ̇ment of ionization produces negligible depletion of the neutral density; hence, the rate of production of ionization is linearly proportional to the radiation flux, Φ. Radiations at different wavelengths produce photoionization over broad height ranges, which vary in height with wavelength, as shown in Figure 1, because the atmospheric photoionization cross sections vary with wavelength. If at wavelength λ the radiation is ϕ (ergs$\cdot$cm$^{-2}\cdot$s$^{-1}\cdot$ A^{-1}) above the earth's atmosphere, then at an altitude h, the rate of production of electrons is

$$\frac{dq}{d\lambda}(h,\lambda) = a(h,\lambda) \, \phi \, (\lambda) \text{ electrons cm}^{-3} \cdot \text{s}^{-1} \cdot \text{A}^{-1} \tag{2}$$

where $a(h,\lambda)$ depends on atmospheric densities, composition, absorption and photoionization cross sections, and the solar zenith angle. Integrating with respect to wavelength from 10 to 1030 Å we obtain q(h) produced by Φ (10 to 1030 Å) ergs$\cdot$cm$^{-2}\cdot$s^{-1} above the earth's atmosphere. From the electron continuity equation

$$\frac{dN_e}{dt} = q - L - \nabla \cdot (N_e \vec{v}) \tag{3}$$

245

where L is the loss rate due to dissociative recombination. At E-region heights, $L \approx \alpha N_e^2$, while at F1 region heights, $L \approx \beta N_e$ (Mitra and Banerjee, 1971). For SFD studies, the last term is neglected since it is estimated to have a small effect in the midlatitude E and F1 regions during the short period of an impulsive EUV burst. Because most SFD events (~ 99 percent) involve small percentage changes, it is useful to express the physical parameters during flares as the sum of a nonflare component (denoted by subscript o) and the flare enhancement (denoted by the prefix Δ). Then

$$\phi(\lambda,t) = \phi_0(\lambda) + \Delta\phi(\lambda,t), \text{ergs} \cdot \text{cm}^{-2} \cdot \text{s}^{-1} \cdot \text{Å}^{-1}$$

$$\Phi(10 \text{ to } 1030 \text{ Å},t) = \Phi_0(10 \text{ to } 1030 \text{ Å}) + \Delta\Phi(10 \text{ to } 1030 \text{ Å},t) \text{ ergs} \cdot \text{cm}^{-2} \cdot \text{s}^{-1}$$

$$q(h,t) = q_0(h,t) + \Delta q(h,t) \text{ cm}^{-3} \cdot \text{s}^{-1}$$

$$N_e(h,t) = N_{eo}(h,t) + \Delta N_e(h,t) \text{ cm}^{-3}; \text{where usually}$$

$\Delta\Phi(10 \text{ to } 1030 \text{ Å},t)/\Phi_0(10 \text{ to } 1030 \text{ Å}) \ll 1, \Delta q/q_0 \ll 1$, and $\Delta N_e/N_0 \ll 1$ for the heights of interest to SFDs. Substituting into (3), and using the fact that $q_0(h,t)$ and $N_{eo}(h,t)$ satisfy (3) by themselves, we find

$$\frac{d}{dt}(\Delta N_e(h,t)) = \Delta q - \frac{\Delta N_e}{t_c} - b(\Delta N_e)^2 \text{ electrons cm}^{-3} \cdot \text{s}^{-1} \tag{4}$$

where t_c is the ionospheric time constant (seconds) for electron losses. Below 160 km, $t_c = 1/[2\alpha(h)N_{eo}(h)]$ and $b = \alpha(h)$, while above 160 km, $t_c(h) = 1/\beta(h)$ and $b = 0$. Typically, $15 \leqslant t_c \leqslant 60$ s. Since $\Delta N_e/N_{eo}$ is usually si the last term is usually negligible and (4) has the same linear form at all heights of interest in SFD data. (The last term in (4) is retained in all our analyses of SFD data, however.) So $\Delta\Phi(10 \text{ to } 1030 \text{ Å},t)$ linearly produces $\Delta q(h)$, which linearly produces $d/dt(\Delta N_e(h,t))$ through Equation 4, which then linearly produces $\Delta f(f_0,t)$ through (1).

The electron loss terms in (4) cause the SFD to be sensitive to how impulsive the EUV burst is, which is illustrated in Figure 3. The solid line represents the time dependence of a hypothetical EUV burst $\Delta\Phi(10 \text{ to } 1030 \text{ Å},t)/\Delta\Phi_{max}(10 \text{ to } 1030 \text{ Å})$ or of the resultant rate of production of electrons $\Delta q(h,t)/\Delta q_{max}(h)$ with a linear rise to a peak in time t_m followed by an exponential decay with a 1/e time constant t_d set arbitrarily equal to $1/2 t_m$. The other curves give the time dependence of $(d(\Delta N_e)/dt)$ normalized to Δq_{max} for three cases of impulsiveness relative to the time constant t_c of ionospheric electron losses. When the EUV burst is fast with respect to t_c, then $d(\Delta N_e)/dt$ and $\Delta f(t)$ have a time dependence essentially the same as that of the EUV burst except that $\Delta f(t)$ becomes negative during the decay stage (See Figure 2). When the EUV burst has rise and decay times comparable to t_c, then $\Delta f(t)$ has a time dependence similar to that of the EUV burst except that the difference increases with time and becomes quite large during the decay stage. Most SFDs fit this case and $\Delta\Phi$ (10 to 1030 Å,t) computed from the SFD data includes the electron loss terms in (4). The

last case in Figure 3 is for a very slow EUV burst where the loss term in (4) nearly equals the production term (Δq) so that $d(\Delta N_e)/dt$ is the small difference between the two terms, and $\Delta f(t)$ is small, smooth, and flat. Hence SFD data are relatively insensitive to slow, smooth EUV bursts. Small frequency deviations caused by nonflare processes make a low signal to noise ratio for $\Delta f(t)$ for such EUV flares; consequently such events are difficult to identify in SFD data. When they are identified, $\Delta\Phi(10$ to 1030 Å,t) is usually not computed because of the small signal to noise ratio in $\Delta f(t)$. Furthermore, studies of the spectra of EUV bursts indicate that the spectra for such slow bursts are distinctly different from the spectra of impulsive bursts, and that the spectra have significant changes with time during the slow burst.
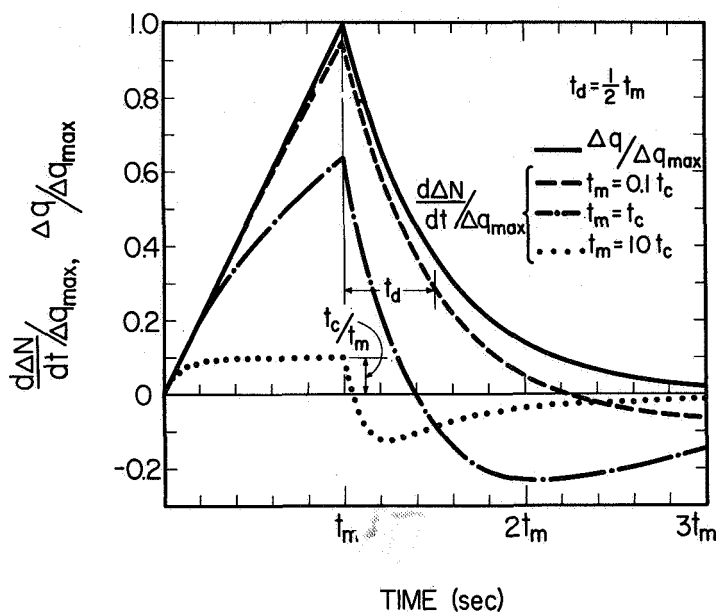
Figure 3. The sensitivity of SFDs to the impulsiveness
of EUV bursts.

Figure 1 showed that radiations at different wavelengths produce ionization at different heights. In equation (1), dN_e/dt and μ are functions of height. The ray path reaches a certain height of reflection depending on the transmitter frequency, the distance between the transmitter and receiver, the ionospheric electron density, and the earth's magnetic field. Furthermore, the solar radiation at different wavelengths produces ionization with varying efficiency. For example, radiation at wavelengths longer than 796 Å is absorbed by the major constituent of the E region (N_2) without producing ionization. Radiation at wavelengths longer than 911 Å is absorbed by the two constituents of highest density in the F1 region (O and N_2) without producing ionization. Conversely, radiation at wavelengths below about 250 Å produces more than one electron-ion pair per incident photon. All of these factors cause the

247

sensitivity of the observed frequency deviation to the incident radiation to vary with the wavelength of the radiation. Figure 4 shows an example of this wavelength dependence for a radio wave reflected at 200 km altitude. The sensitivity function $S(\lambda)$ is defined by

$$S(\lambda) = \frac{\Delta f\,(f_v)}{R_t\,R_\chi\,\Delta\phi(\lambda)\,d\lambda} \quad Hz\,(ergs \cdot cm^{-2} \cdot s^{-1})^{-1} \tag{5}$$

where f_v is the equivalent vertical-incidence frequency of the SFD probing radio wave, R_t is a dimensionless factor that accounts for the time dependence of $\Delta\phi$ (see Figure 3), and R_χ accounts for the solar zenith angle dependence; these additional terms are described elsewhere (Donnelly, 1970). The sensitivity drops with decreasing wavelength below 3 Å, because radiation at those wavelengths produces ionization low in the dense D region, where the freed electrons are rapidly lost via attachment, to form negative ions. Those that remain unattached collide so frequently with the molecules of the neutral gas that they do not interact effectively with the probing radio wave. The sensitivity drops off sharply above 1027 Å, which is the longest wavelength for efficient photoionization of any of the major constituents of the upper atmosphere. Most SFD observations involve paths reflected in the F region with $S(\lambda)$ curves like that in Figure 4. Usually we also have SFD observations from paths reflected from the bottom of the E layer that are sensitive to only the 1 to 10 Å radiation. Since the 1 to 10 Å radiation is much slower than the impulsive EUV bursts studied, the 1 to 10 Å portion is usually removed in our analysis of F-region SFDs in order to determine the 10 to 1030 Å flux as a function of time. In conclusion, SFD observations are effective detectors of impulsive bursts in the wavelength range 10 to 1030 Å.
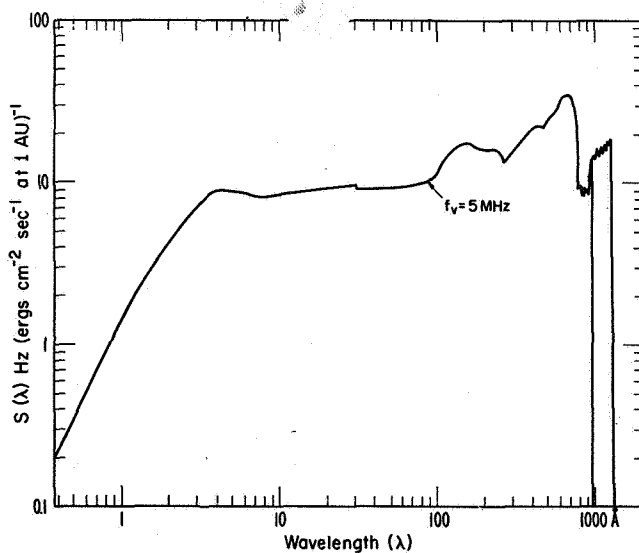
Figure 4. An example of the wavelength dependence of the sensitivity of SFDs to impulsive radiation bursts.

The preceding describes the link between the radiation burst and the observed SFD. The analysis of SFD data involves the reverse process and is described in detail elsewhere (Donnelly, 1970). We now know enough about the spectra of impulsive EUV bursts, and the variations in spectra from one flare to another to permit detailed quantitative evaluation of the errors in $\Delta\Phi(10$ to $1030\,\text{Å},t)$ due to variations in the EUV burst spectra. Recent advances in ionospheric physics now permit us to evaluate quantitatively the details of seasonal and diurnal dependences in the sensitivity of SFDs to EUV bursts.

The best test of the accuracy of the EUV flux enhancements deduced from SFD data would be to compare them with accurate concurrent satellite measurements over the same wavelength range. The closest approach to this ideal test is given by the Orbiting Solar Observatory-5 (OSO-5) measurements (Kelly and Rense, 1972) in the wavelength bands 280 to 370 Å, 465 to 630 Å and 760 to 1030 Å. Figure 5 shows good agreement in the relative time dependences of the SFD-deduced 10 to 1030 Å flux enhancement and data from the OSO-5 760 to 1030 Å channel, including much of the small, fine structure, even though some of this fine structure is about the size of the preflare noise in the 760 to 1030 Å data. The 465 to 630 Å channel exhibited a time dependence similar to, but noisier than the 760 to 1030 Å channel. Note that the ratio of the slow peak near 2010 UT to the impulsive peak near 2008.7 UT is larger in the 10 to 1030 Å (SFD) data than in the 760 to 1030 Å OSO-5 channel. This difference is real; it is caused by the short-wavelength or coronal portion of the 10 to 1030 Å enhancement having a relatively larger flux in the slow enhancement. The OSO-5 280 to 370 Å data exhibited approximately the same flux at the slow peak as that at the impulsive peak. It is not yet clear how well the intensities of the 10 to 1030 Å flux enhancement and the OSO-5 observations agree.
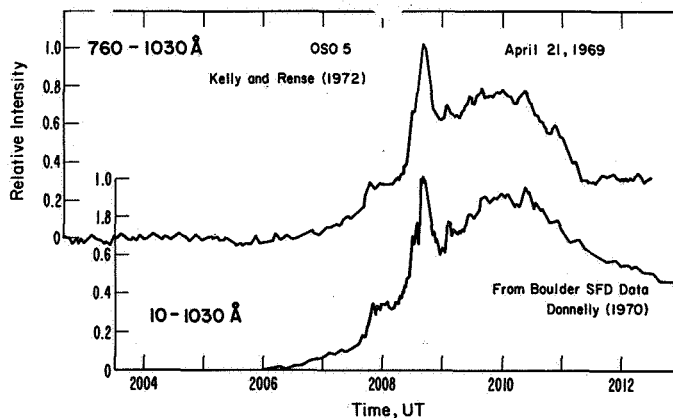
Figure 5. A comparison of time dependences of SFD and OSO-5 broadband EUV observations of a flare. $\Delta\Phi_{max}(10$ to $1030\,\text{Å}) \approx 3$ ergs·cm^{-2}s^{-1} at 1 AU.

EUV SOLAR-FLARE RADIATION

The Relation of EUV Bursts to Other Flare Radiations

The impulsive EUV bursts observed via SFDs have been found to be closely associated with hard X-ray bursts, the early impulsive peaks of the microwave burst, certain impulsive portions of the Hα flare, and, in the case of very large EUV bursts ($\Delta\Phi_{max}$(10 to 1030 Å) $\gtrsim$ 2 ergs·cm^{-2}·s^{-1} at 1AU), with impulsive white light emission (Donnelly, 1971). The impulsive component of the flare illustrated in Figure 6 is seen clearly in the 48 to 80 keV hard X-rays. This component is evident in the 19.2 to 32 keV range but is nearly swamped by slower emissions. The impulsive component is also evident in the 10 to 1030 Å burst and the microwave burst. Concurrent impulsive emission was also evident in the Hα flare (Zirin et al., 1971). The slow emissions dominate the soft X-ray (1 to 8 Å) emission and contribute part of the 10 to 1030 Å emission and microwave emission, especially after 2115 UT. In most flares, there is a significant increase in soft X-ray emission before the onset of the impulsive emissions, which is not true for the flare in Figure 6. In the following sections, we will discuss the impulsive EUV emission (rise times < 100 seconds) and not the slow component at EUV wavelengths, because SFDs are not very sensitive to slow emissions.

Hard X-Ray Bursts

Kane and Donnelly (1971) studied the relation between impulsive hard X-ray bursts and EUV bursts observed via SFDs and found the following:

- The ratio of flux of the impulsive component of hard X-rays ($\gtrsim$ 10 keV) to the 10 to 1030 Å energy flux enhancement is about 10^{-5} for flares located near the solar central meridian, and increases with increasing central meridian distance (CMD) of the associated Hα flare.

- The peak energy flux in hard X-rays ($\gtrsim$ 10 keV) is correlated with the peak 10 to 1030 Å flux enhancement with a correlation coefficient of 0.8 for flares at any CMD involving a range of peak intensities over about three orders of magnitude.

- The total kinetic energy of the energetic electrons in the flare region as deduced from the observed X-ray spectrum is comparable to the energy flux emitted in the 10 to 1030 Å wavelength range.

- The observations indicated that the principal mechanisms for the impulsive emission of 10 to 1030 Å flare radiation are bound-bound, free-bound, and bremsstrahlung emissions from the quasi-thermal plasma produced by the collisional loss of energetic flare electrons in the partially ionized chromosphere at densities $\gtrsim$ 10^{12} cm^{-3}.

- Detailed time comparisons for three flares showed that the rise to peak of the 10 to 1030 Å flux enhancement is closer to that for the impulsive 9.6 to 19.2 keV X-rays than for the higher energy X-rays.

250
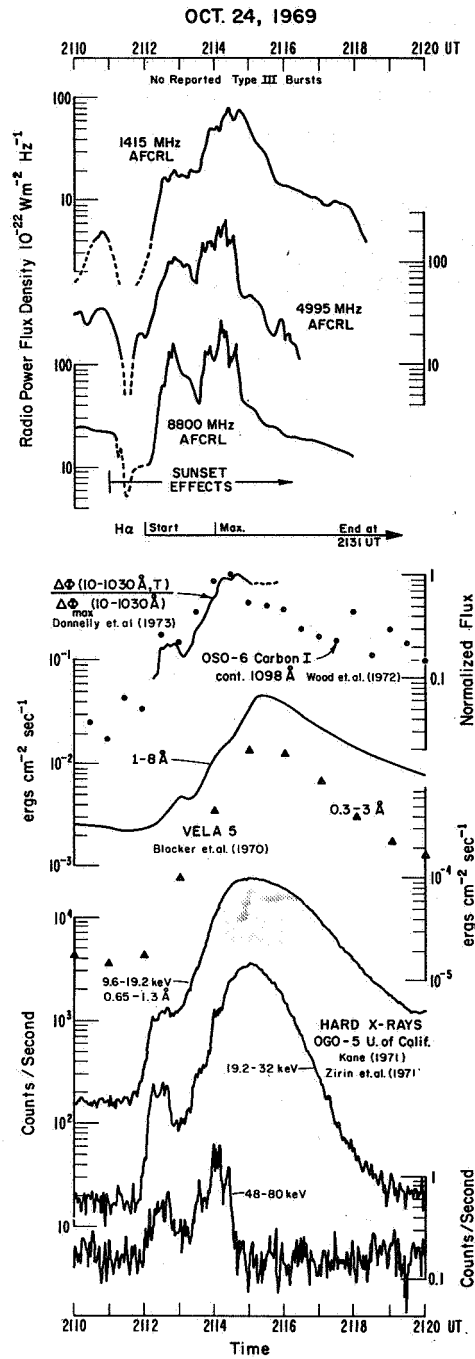
Figure 6. Time comparison of microwave EUV, soft X-ray and hard X-ray solar flare radiations. $\Delta\Phi_{max}$ (10 to 1030 Å) $\approx$ 0.6 ergs·cm^{-2}s^{-1} at 1 AU. The microwave observations are affected by the earth's atmosphere near sunset (Covington, 1972).

Considering that all the energy of the energetic flare electrons $\gtrsim$ 10 keV deduced (thick-target approximation) from the hard X-ray observations, is approximately equal to that radiated in the 10 to 1030 Å range, then probably the flare electrons below 10 keV also contribute to collisionally exciting the EUV source region. This is because the 10 to 1030 Å emission should be only a part of the energy expended by the energetic electrons. The net energy radiated at wavelengths longer than 1030 Å probably exceeds that in the 10 to 1030 Å range (Donnelly, 1971). It is not known what the effective low energy limit is of the distribution of energetic electrons that contribute to the impulsive EUV emission. This is important because most of the energy of the energetic electrons is at the low energy end of their distribution. Kahler and Kreplin (1971) observed in a few flares that the power-law electron energy distribution associated with the impulsive component extended to 3 keV at least. According to Hudson's (1972) calculations of energy deposition in the chromosphere from the corona, electrons of about 1 keV can reach the chromosphere. This result depends on the density model used and the height of the acceleration mechanism in the corona. We conclude that the 10 to 1030 Å burst is excited by the collisional losses at chromospheric densities by the energetic flare electrons, and hypothesize that the effective lower limit to these energetic electrons is about 1 keV for exciting the EUV source region.

It is not yet known how well the time dependence of the impulsive EUV burst agrees with that of the hard X-ray emission as a function of the hard X-ray photon energy during the decay of the impulsive burst. Such a comparison might be possible if flares can be found where the slow emissions do not mask the decay of both the 9.6 to 19.2 keV and the 10 to 1030 Å emissions. Kane and Anderson (1970) observed a progression of both rise and decay times increasing with decreasing photon energy, where the progression is greater in some events than in others. For events having a large progression, if the EUV flare emission is caused primarily by 1 to 10 keV flare electrons, then one would expect the EUV rise and decay to be slower than those of the X-rays $\gtrsim$ 10 keV.

The dependence on central meridian distance of the ratio of the peak 10 to 1030 Å flux to the peak hard X-ray flux has been qualitatively explained as resulting from absorption of the EUV emission in the solar atmosphere (Kane and Donnelly, 1971), but cannot be explained by a spherical shell absorption layer. The increase in this ratio at CMD values below 20 degrees probably involves the spatial structure of both the active region and the flare. Further observational study of the CMD dependence is needed, particularly for CMD $\lesssim$ 20° and > 75°. The decrease in EUV flux near the limb is evident in studies of the percentage of Hα flares accompanied by SFDs (Donnelly, 1971).

Since the EUV emission is from chromospheric densities (Kane and Donnelly, 1971), the hard X-ray emission from the EUV source region must be approximately thick-target emission. How much of the hard X-ray source region for disk flares is thin target and how much is thick is not known. Hard X-ray emission from beyond-the-limb X-ray flares probably are thin-target emission.

Impulsive EUV bursts observed via SFDs are well correlated in time, intensity, and occurrence with microwave bursts (Strauss et al., 1969; Basu and Chowdhurry, 1969; Chan and Villard, 1963; Donnelly, 1970), but their time dependences are usually not identical, and the ratio of their peak energy flux intensities is not constant from one event to another. Takakura (1973) has presented three factors to remove the 10^4 factor between the observed microwave intensity and the larger value computed from the energetic flare electrons determined from hard X-ray observations, namely: a) Difference in energy regimes: The microwave emission depends more on the energetic electrons above 100 keV while most hard X-ray observations involve 10 to 100 keV electrons. A break in the slope in the power law energy spectrum of flare electrons tends to occur at about 100 keV. b) Difference in spatial regions: The microwave burst involves that portion of the hard X-ray source where the magnetic field is strong. c) Microwave suppression or absorption mechanisms: These same mechanisms permit some variation in the relation between microwave and hard X-ray bursts during any event and from one event to another. The impulsive EUV burst is related more to the energetic flare electrons at energies below $\sim$ 20 keV than those above 20 keV, because most of the net energy of these electrons is at the low energy end of their spectrum deduced from hard X-rays (also based on the time dependence studies of Kane and Donnelly, 1971). Adding this to Takakura's picture, one would expect a closer association between impulsive EUV bursts and 10 to 20 keV X-ray observations than between EUV and microwave bursts. On the other hand, the impulsive EUV burst appears (on the basis of the spatial location of con-current optical emissions) to be emitted from small regions located near sunspots or regions of strong magnetic fields with a large radial component. Hence we hypothesize that the impulsive EUV source region is the high dens $\cdots$ bottom of part of both the hard X-ray and the initial impulsive microwave source regions.

Quasi-periodic fine structure has been observed in a few hard X-ray, microwave, and EUV (SFD) bursts (Parks and Winckler, 1969; Donnelly, 1971; and Maxwell, 1972). Because the time dependences of microwave and EUV bursts agree closely for the first peak of a burst and then become less similar (Castelli and Richards, 1971), it would be interesting to compare the microwave and EUV (SFD) quasi-periodic fine structures for a number of events. Since the microwave emission is supposed to be produced mainly from electrons > 100 keV and the EUV excited by electrons mainly < 20 keV, and because the 10 to 100 keV hard X-ray observations sometimes exhibit a progression of increasing rise and decay times with decreasing photon energy, it should be informative to compare the microwave and impulsive EUV time structures in great detail. However, appreciable microwave emission (type IV μ emission), primarily at frequencies below 5 GHz, having impulsive structure, can occur after the flash phase of a flare and not be accompanied by any impulsive EUV emission (that is none $\gtrsim$ 1 percent of the peak of the flash-phase EUV burst).

Hα Flares

Impulsive EUV bursts are closely associated in occurrence and start time with Moreton's explosive phase of the Hα flare (Davies and Donnelly, 1966; Harvey, 1971; Donnelly, 1971) just as hard X-ray and microwave bursts have a similar close association (Moreton, 1964). The explosive phase refers to a time period during the flash phase or rise to maximum of the Hα flare, and to a spatial portion of the Hα flare emission that rapidly expands or explodes ($\sim$ 100 km s^{-1}). However, not all impulsive EUV bursts are accompanied by an Hα feature that involves such a marked expansion of the Hα flare area. Studies of these EUV bursts show there are associated impulsive, small, and very bright Hα emission kernels that are spatially stationary or lie in regions of bright preflare plage, so that rapid expansion in the boundaries of the Hα flare was not apparent in visual examination of the patrol films. The importance of the difference between impulsive Hα flare regions that are spatially stationary and those having rapid expansion of the emission area is not known. It is important that both these types of impulsive Hα regions are located near sunspots or regions of strong magnetic fields. See Vorpahl (1972) for further discussion of impulsive Hα emission and its relation with hard X-ray and microwave bursts. Observations of the impulsive optical emission are very important because they can provide information on the size, shape, and location of the high density portion of the impulsive flare for studies of the relation of this site to the magnetic field structure of the active region. Impulsive EUV bursts consist of emissions from a region like the chromosphere and transition region, hence the impulsive EUV source region should be nearly the same as the source region that emits Hα impulsively.

Optical Spectra

The EUV flare emissions involve source ⁣ ⁣ ⁣ ⁣ ⁣ ⁣ⁿs with temperatures intermediate between those of the X-ray and optical-flare source regions; consequently, one main problem in studying EUV flare emission is to develop its physical relation to the optical emissions. Simultaneous optical and EUV spectra are needed. SFD observations indicate there are quite impulsive EUV bursts with peak flux values that are as large or larger than the peak EUV flux in the slow component. One would expect a similar effect in optical emissions; unfortunately, absolute flux values with high time resolution are available for very few flares even for Hα despite the long history of optical observations.

Whether ground-based optical measurements of flare spectra have ever included the impulsive kernels associated with the hard X-ray, EUV, and microwave impulsive bursts is not known. Most spectra of flares are taken after the flash phase of the Hα flare; and for the few spectra taken during the flash phase (Švestka, 1972), it is not clear whether the small impulsive kernels were included in the field of view of the spectrograph during their impulsive phase. Measurement of the optical spectra of impulsive kernels with moderate time resolution (10 seconds) is difficult; but since it can be done from the ground, it should be less difficult than some of the measurements to be attempted on the ATM satellite.

Švestka (1972) said "Generally, there are no qualitative differences among optical spectra of different flares observed in projection on the solar disk." There are minor differences such

254

as the presence of more emission lines in large flares or effects caused by absorption. I suggest that the optical spectra of impulsive kernels, when adequately observed, will not be drastically different from Švestka's spectra, but will have a significant difference in that emission lines normally emitted from the low chromosphere and from near the temperature minimum region will be strong relative to their intensity at other spatial portions of the Hα flare.

Figure 7 shows an example of an impulsive optical spike (region A) at the wavelength of an Fe I line, 5324 Å, which is normally emitted from the low chromosphere. This spike is the same one seen at EUV wavelengths shown in Figure 5. Any kernels associated with this spike are probably much smaller than region A. Optical spectra measurements like those made to date would probably measure region B after 2010 UT.
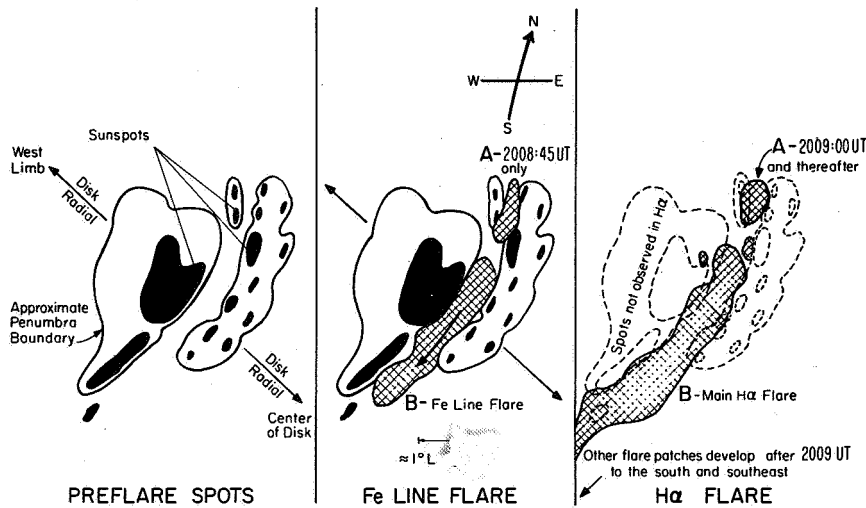
Figure 7. The Hα and 5324 Å Fe I emission regions for the flare of 2010 UT April 21, 1969. The EUV burst is shown in Figure 5. The impulsive Fe emission in region A was concurrent with the EUV spike. The Fe I and Hα observations were made at Lockheed Observatory (Ramsey et al., 1968).

White Light Flares

McIntosh and Donnelly (1972) found a close association in occurrence and timing of the impulsive white-light flare emission and large EUV bursts with 10 to 1030 Å flux enhancements greater than or equal 2.0 ergs·cm^{-2}·s^{-1} at 1AU. The energy flux enhancements of the white-light flash (3500 to 6500 Å) and EUV flash (10 to 1030 Å) were roughly comparable. It is not known whether the ratio of white-light energy flux to EUV flux varies significantly from one flare to another, because white light emission is observable only for a few large events. The white light cores and, hence, the EUV emission cores, were located adjacent to the penumbra of strong sunspots, sometimes covering the umbra of a small spot, but never over the umbra of large strong sunspots.

Švestka (1970) distinguishes two types of white-light flares observed on the disk. His first type is like a bright facula, usually with a shape resembling the Hα flare, and is observed only in flares near the limb. His second type includes flares located far from the limb and consists of one or two short-lived bright points in the penumbral region of sunspots. The impulsive EUV bursts discussed here are associated with his second type of white light flare.

Figure 8 shows the SFD and 10 to 1030 Å flux enhancement for the white-light flare of March 12, 1969. The white light emission consisted of three patches. Two were impulsive and were located near the large spot of the flare region. They were visible during the period marked in Figure 8. The third white light emission was like Švestka's first type of white light flares, that is both types occurred in this flare at 10°N 80°W. The third patch was visible for about 13 minutes. The spectral observations for this flare (Gallegos et al., 1971; Machado, 1971) were at 1744 UT and later; hence, the impulsive white light emission had already subsided. The white light emission observed in the spectrograms was the third patch, the one like Švestka's first type of white light flare. Kelly and Rense's (1972) OSO-5 observations show that the flux enhancement in the 465 to 630 Å and 760 to 1030 Å channels had dropped to about one-fourth their peak flux at 1744 UT.
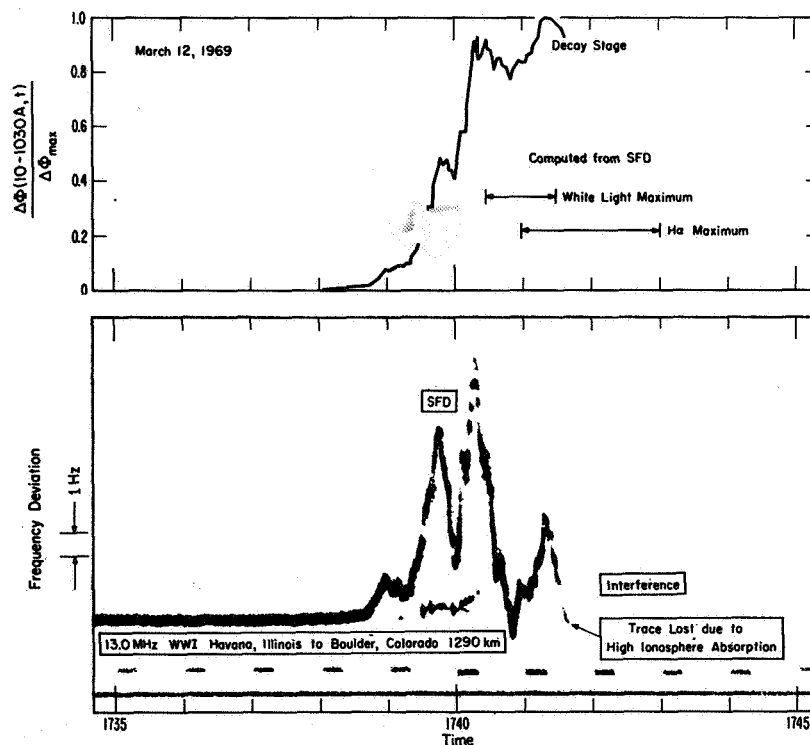
Figure 8. SFD and 10 to 1030 Å burst for the white light flare of March 12, 1969. $\Delta\Phi_{max}$(10 to 1030 Å) ≈ 4 ergs cm^{-2}s^{-1} at 1 AU.

Spatial Location

There have been no EUV observations with high spatial resolution (~ 1 arcsec) of the impulsive emissions of flares. Because the impulsive EUV emission is nearly all line and recombination continuum emissions that are normally emitted from the chromosphere, the impulsive optical kernels must be essentially the same source region as that of the impulsive EUV burst. Hence, these optical emission cores provide information on the spatial location of the impulsive EUV burst.

The importance of having at least a small sunspot in order to have an impulsive EUV burst is evident in the fact that none of the flares of importance ≥ 2 studied by Dodson and Hedeman (1970) that occurred in spotless regions were accompanied by SFDs, while half of those that occurred in regions with very small spots were accompanied by SFDs, which is the same result as for all importance 2 flares. This result, together with the fact that the impulsive Hα and white light emissions associated with EUV bursts are in regions of strong photospheric fields with large radial components, leads us to hypothesize the following: a) Flares with slow soft X-ray enhancements unaccompanied by impulsive hard X-ray or EUV bursts involve emission regions having no underlying sunspots or strong radial component of the magnetic field at photospheric heights. (The active region involved may have sunspots but the emission region is disjoint from them.) b) Flares having impulsive EUV or hard X-ray bursts accompanied by a minimum soft X-ray emission (all flares have some soft X-ray emission) involve emission regions confined to being near or overlying sunspots. c) Flares having both slow soft X-ray emission (seen before the impulsive burst) and impulsive hard X-ray or EUV bursts involve emission regions that are a combination of those cases in a) and b) above. Most flares fit case c), but a ll percentage of events fit cases a) or b).

The location of the impulsive optical cores with respect to the structure of the active region magnetic fields is very important and should be researched thoroughly. Although they occur in regions of strong magnetic fields having large radial components, they are not at the locations of the strongest fields. The white light cores are off to the side of the regions of strongest field intensities or large-scale gradients. I suggest that these emission cores were at the high density base or magnetic flux tubes having less convergence than neighboring tubes when moving along the tube from the corona toward the photosphere, thereby permitting better access of high energy charged particles to high density regions. The decrease in convergence can be caused by nearby magnetic anomalies, like those observed by Rust (1968).

The EUV Spectrum

SFD observations by themselves give little information on the EUV flare spectra. Satellite observations by themselves also have not given a lot of spectral information for the impulsive EUV burst, because measurements with high wavelength resolution were usually made at only one wavelength per flare with high time resolution, or the spectrum was scanned over a time period much larger than the times of impulsive EUV bursts. By comparing these measurements of high time resolution, the 10 to 1030 Å flux enhancement from

SFDs and the satellite measurements at one wavelength for the same flare, we can compare the time dependence and intensity of a given line with that of the 10 to 1030 A flux during impulsive bursts. Similar comparisons for flares observed by satellites while scanning in wavelength give a comparison of intensities for many emission lines. By such comparisons, we can piece together the spectrum of impulsive EUV bursts. Detailed results have been published elsewhere (Donnelly, 1971) and further results will be published soon (Donnelly et al., 1973; Donnelly and Hall, 1973).

This picture puzzle approach would not be very successful if there were no system to the EUV spectra, or if the time dependence of emission lines varied appreciably with respect to $\Delta\Phi(10$ to 1030 A,t) during a particular burst or from one flare to another. Fortunately, there is a system. In fact, like Švestka's (1972) comment about optical flare spectra, there is surprisingly little qualitative variation of the EUV spectra during impulsive bursts. The EUV impulsive burst consists mainly of line and recombination continua of the major solar constituents, H, He, C, O, and N, including many resonance lines.

The EUV burst spectrum is to a first order approximation the same as the preflare spectrum emitted from the chromosphere and the chromosphere-corona transition region (Wood and Noyes, 1972). There are some differences, for example certain density-sensitive lines are enhanced significantly more than the resonance lines (Hall, 1971). No evidence for EUV synchrotron emission has been observed. The reason for this consistency in spectra is probably that when appreciable flare energy is released in the dense chromosphere, it proceeds to radiate it away in accordance with its constituency. In effect, it forms the transition region at higher densities. Details of the spatial structure of EUV bursts are not known, but we should expect that the fibrous structure deduced for optical emissions (Švestka, 1972) will also apply to EUV b   , perhaps in the form of sheets like those in aurora or in the form of fibrous pinched currents. It is not yet known how closely the various impulsive emission lines decay together. It is known that the EUV radiation normally emitted from the corona usually has a much slower time dependence than the impulsive EUV burst. SFDs do not provide useful information on the chromospheric emissions during the early slow rise of the flare or the slow emissions after the impulsive burst.

REFERENCES

Basu, S. and Chowdhurry, S.R., 1969, *J.G.R.* **74**, 4175.

Bennett, J.A., 1967, *J. Atmosph. Terr. Phys.* **29**, 887.

Blocker, N.K., Chambers, W.H., Fehlau, P.E., Fuller, J.C., Kunz, W.E., and Milkey, R.W., 1970, *Vela V and VI Solar X-Ray Atlas II.* September 1, 1969 to January 1, 1970 (Los Alamos Sci. Lab., Rept. LA-4454).

Castelli, J.P. and Richards, D.W., 1971, *J.G.R.* **76**, 8409.

Chan, K.L. and Villard, Jr., O.G., 1963, *J.G.R.* **68**, 3197.

Covington, A.E., 1972, *Solar Phys.* **24**, 405.

Davies, K., and Donnelly, R.F., 1966, *J.G.R.* **71**, 2843.

Dodson, H.W., and Hedeman, E.R., 1970, *Solar Phys.* **13**, 401.

Donnelly, R.F., 1970, *Extreme Ultraviolet Flashes of Solar Flares Observed via Sudden Frequency Deviations,* ESSA Tech. Rept. ERL 169-SDL 14 (U.S. Government Printing Office).

Donnelly, R.F., 1971, *Solar Phys.* **20**, 188.

Donnelly, R.F., and Hall, L.A., 1973, submitted to *Solar Phys.*

Donnelly, R.F., Wood, Jr., A.T., and Noyes, R.W., 1973, *Solar Phys.*, to be published.

Gallegos, H.G., Molnar, H., and Seibold, J.R., 1971, *Solar Phys.* **16**, 120.

Hall, L.A., 1971, *Solar Phys.* **21**, 167.

Harvey, K.L., 1971, *Solar Phys.* **16**, 423.

Hudson, H.S., 1972, *Solar Phys.* **24**, 414.

Jones, R.M., 1966, *A Three-Dimensional Ray Tracing Computer Program*, ESSA Tech. Rept. IER 17-ITSA 17 (U.S. Government Printing Office).

Kahler, S.W., and Kreplin, R.W., 1971, *Ap. J.* **168**, 531.

Kane, S.R., 1971, *Ap. J.* **170**, 587.

Kane, S.R., and Anderson, K.A., 1970, *Ap. J.* **162**, 1003.

Kane, S.R., and Donnelly, R.F., 1971, *Ap. J.* **164**, 151.

Kelly, P.T., and Rense, W.A., 1972, *Solar Phys.* **26**, 431.

Kreplin, R.W., Chubb, T.A., and Friedman, H., 1962, *J.G.R.* **67**, 2231.

Machado, M.E., 1971, *Solar Phys.* **17**, 389.

Maxwell, A., 1972, Microwave Pulsations, read at the Symposium on High Energy Phenomena on the Sun, NASA Goddard Space Flight Center, Greenbelt, Maryland, Sept. 28-30, 1972.

McIntosh, P.S., and Donnelly, R.F., 1972, *Solar Phys.* **23**, 444.

Mitra, A.P., and Banerjee, P., 1971, in *Space Research XI,* ed. by K. Ya. Kondratyev et al. (Berlin, Akademie-Verlag), 1019.

Mitra, A.P., 1972, in *Solar-Terrestrial Physics 1970,* ed. E.R. Dyer, (Dordrecht, Holland, D. Reidel Publ. Co.), Part IV, 1.

Moreton, G.E., 1964, in *AAS-NASA Sym   um on The Physics of Solar Flares,* ed. W.N. Hess, NASA SP-50 (U.S. Government Printing Office).

Parks, G.K., and Winckler, J.R., 1969, *Ap. J.* **155**, L117.

Ramsey, H.E., Smith, S.F., and Angle, K.L., 1968, High Resolution Solar Photography (Lockheed Observatory Rept. LMSC-681495).

Rust, D.M., 1968, in *Structure and Development of Solar Active Regions,* IAU Symp. 35, ed. K.O. Kippenheuer (Dordrecht, Holland, D. Riedel Publ. Co.), 77.

Strauss, F.M., Papagiannis, M.D., and Aarons, J., 1969, *J. Atmosph. Terr. Phys.* **31**, 1241.

Švestka, Z., 1970, *Solar Phys.* **13**, 471.

Švestka, Z., 1972, *Ann. Rev. Astron. Astrophys.* **10**, 1.

260

Swartz, W.E., 1972, *Electron Production, Recombination and Heating in the F-Region of the Ionosphere* (Penn. State Univ., Ionospheric Res. Lab., Sci. Rept. 381).

Takakura, T., 1973, These Proceedings.

Timothy, A.F., Timothy, J.G., Willmore, A.P., and Wager, J.H., 1972, *J. Atmosph. Terr. Phys.* 34, 969.

Vorpahl, J.A., 1972, X-Radiation (E > 10 keV), Hα, and Microwave Emission During the Impulsive Phase of Flares, 26, 397.

Wood, Jr., A.T., and Noyes, R.W., 1972, *Solar Phys.* 24, 180.

Wood, Jr., A.T., Noyes, R.W., Dupree, A.K., Huber, M.C.E., Parkinson, W.H., Reeves, E.M., and Withbroe, G.L., 1972, *Solar Phys.* 24, 169.

Zirin, H., Pruss, G., and Vorphal, J., 1971. *Solar Phvs.* 19, 463.

SOFT X-RAY FLARE SPECTRA

G.A. Doschek and J.F. Meekins
E.O. Hulbert Center for
Space Research
Naval Research Laboratory

INTRODUCTION

Large solar flares produce intense soft X-ray emission ($\approx$ 10 Å), indicating the existence of high temperature plasmas ($> \approx 10 \times 10^6$ K) that coexist in time with the plasmas responsible for the normally observed brightenings in Hα. The time behavior of the X-ray flux, as revealed, for example, by ion chamber detectors on the series of Solrad monitoring satellites, appears to roughly mimic the intensity-time behavior of the Hα flare, insofar as start times, times of maximum flux, and approximate decay times are concerned.

In recent years, soft X-ray spectra of both active regions and solar flares have been obtained by instruments flown on spacecraft such as the Orbiting Solar Observatory (OSO) series. The disbursing elements used were Bragg crystals, and in the 8Å region the resolution is typically $\approx$ 1200. This paper discusses the observed characteristics of X-ray flare spectra and spectroscopic diagnostics for determining electron temperatures, electron densities, and departures from ionization equilibrium within the soft X-ray emitting plasma.

The data discussed have been obtained by three Bragg crystal spectrometers flown by the Naval Research Laboratory (NRL) on OSO . A description of these instruments is given in Doschek (1972), and a much more thorough description of similar instruments flown by NRL on OSO-4 has recently been given by Meekins (1972). Instruments similar to the NRL package have been flown by Neupert and his colleagues on OSO-3 and OSO-5 (Neupert et al., 1967; Neupert, 1971), by Walker and Rugge (1969, 1970) on the OV1-10 and OV1-17 satellites, and by Mandelshtam and his colleagues at the Lebedev Institute (Vasiljev et al., 1971). Very high resolution spectra have recently been obtained in the 10Å region by Parkinson (1971, 1972).

GENERAL CHARACTERISTICS OF SPECTRA

Figure 1 shows typical spectra of active regions and flares obtained by the NRL KAP (potassium acid phthalate, 2d = 26.827Å) spectrometer on OSO-6. The lower spectrum is the sum of nine scans of different active regions, and the top scan is the sum of eight scans of the large limb flare that occurred at $\approx$ 1040 UT November 2, 1969. The flare spectra were obtained during the most intense phase of the burst and spectral differences are evident among the different scans but do not appear in the sum.

Striking differences are immediately evident on comparing the flare spectrum with the spectrum of the active region. The active region spectrum is principally characterized by

262

lines of Fe XVII, Ne IX, Ne X and Mg XI. These ions are formed at relatively low electron temperatures near 6×10^6 K. Only much weaker emission is evident from iron ions more highly ionized than Fe XVII, and from Mg XII, which is formed near 10×10^6 K. During intense flares, however, emission is seen from all iron stages from Fe XVII through Fe XXVI (Fe XXV and Fe XXVI are observed near 1.8A in LiF crystal spectrometer spectra), and from hydrogenlike ions such as Mg XII, Si XIV, S XVI, and Ca XX. A range of temperatures from 10×10^6 K to 30×10^6 K is indicated by the presence of these ions in the plasma, if ionization equilibrium is assumed. The dominant mechanism of the line formation is thought to be collisional excitation from the ground state, while the continuum emission is assumed to be primarily free-free and free-bound emission.
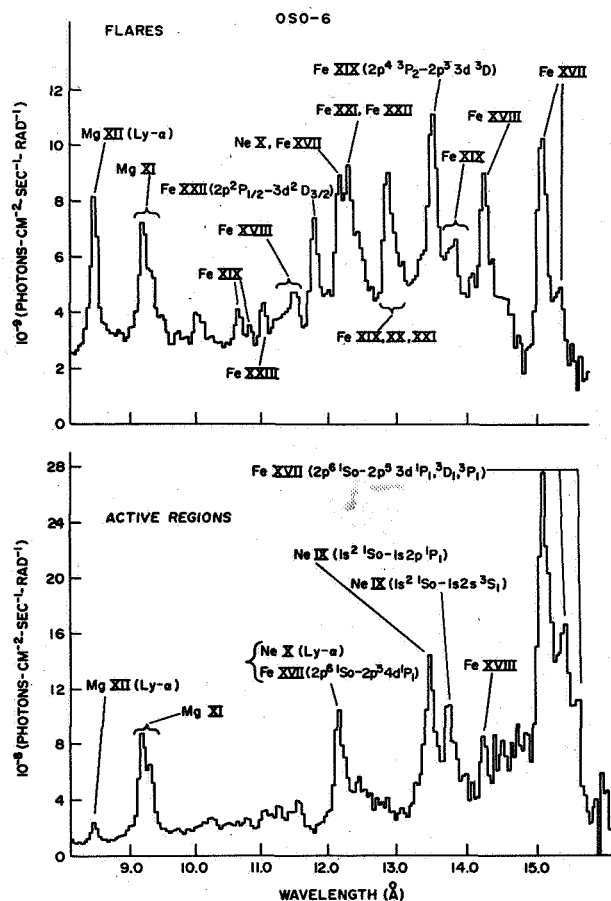
Figure 1. Summed spectra of active regions and flares from OSO-6. Flare spectra show lines from high ionization stages such as Fe XXII, and strong emission from lines of hydrogenlike ions such as Mg XII. The lines of high excitation ions are absent in the active region spectra. Spectra have been corrected using preliminary instrumental efficiencies.

Spectra obtained at different times during a flare show differences, and this is illustrated in Figure 2. The two spectra are from a large limb event that occurred on August 12, 1970, and were recorded near the times shown. (The spectra were obtained by an ethylenediamine d-tartrate (EDDT) spectrometer on OSO-6, $2d = 8.800$Å.) These spectra are not corrected for instrumental efficiencies, and this accounts for the edges seen near 4, 6.7, and 8Å. Since it takes seven minutes to complete a spectral scan, temporal variations of the X-ray flux are also present. Nevertheless, a comparison of these spectra shows that the Lyman-α lines of Ca XX (3.02Å), S XVI (4.73Å) and Si XIV (6.182Å) are noticeably weaker in the bottom scan, indicating lower excitation conditions. If ionization equilibrium is assumed, the ratio of the S XVI line to the S XV lines at $\approx$ 5Å indicates an electron temperature of $\approx 27 \times 10^6$ K, while in the lower scan the corresponding temperature is $\approx 6 \times 10^6$ K lower.
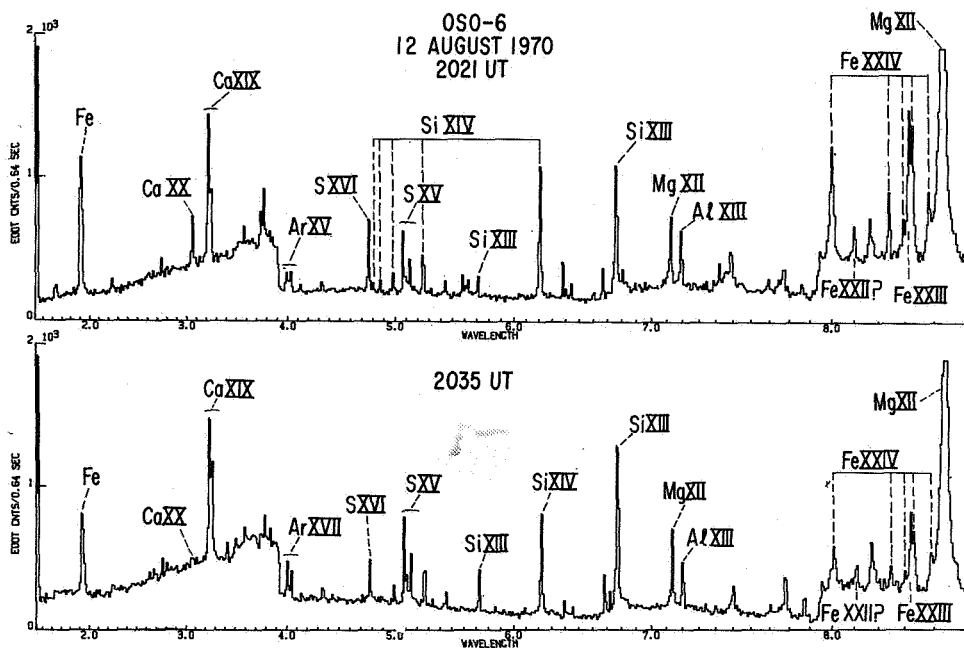
Figure 2. Two spectral scans of a large limb flare that occurred on August 12, 1970. Note the decreased intensity of lines of hydrogenlike ions relative to lines of heliumlike ions in the lower scan. These spectra are uncorrected for instrumental efficiencies.

The principle emission from the heliumlike ions, for instance S XV, and Si XIII, is due to the resonance ($1s^2$ $^1S_0$ - $1s2p$ $^1P_1$), intercombination ($1s^2$ $^1S_0$ - $1s2p$ $^3P_{1,2}$), and forbidden ($1s^2$ $^1S_0$ - $1s2s$ $^3S_1$) lines, in order of increasing wavelength. In the case of S XV, these lines fall at 5.038, 5.063, 5.066, and 5.101 Å (Gabriel, 1972). Gabriel and Jordan (1969a) have shown that the ratios of the forbidden to the intercombination lines of the heliumlike ions are density sensitive.

264

On the four scans which we have for the August 12 event, no change in the ratio of the forbidden to intercombination line greater than statistical fluctuations is evident for Si XIII and S XV, even though the electron temperature appears to be declining markedly. Our line ratio for S XV is close to the value expected for electron densities, Ne, less than $\approx 2 \times 10^{13}$ cm^{-3} (Gabriel, 1972). Furthermore, if we assume that the lack of a change in the forbidden to intercombination line ratio for Si XIII implies that these lines are emitted at densities less than the critical density for silicon, then $N_e \gtrsim 4 \times 10^{12}$ cm^{-3}. (See Gabriel and Jordan, 1969a; Freeman et al., 1971, for a discussion of electron density determination using the lines of heliumlike ions.) Note, however, that the intercombination lines of the heliumlike ions are quite weak, and that the forbidden line is blended with lithiumlike satellite lines. Thus, the measurements are difficult and greater spectral resolution will be required to definitely establish whether or not flare densities can reach values as high as 5×10^{12} cm^{-3}.

Figure 3 shows interpolated time histories of lines of hydrogenlike and heliumlike ions based on the four available spectral scans of the August 12 event. The intensities of the resonance lines of these flare ions appear to reach maximum flux sequentially: The lines of the higher excitation ions reach maximum flux earliest. Although these interpolated curves are necessarily crude, it appears that the lines of the heliumlike ions reached maximum flux about 2.5 minutes later on the average than the lines of the hydrogenlike ions for this particular event. This type of emission line behavior is characteristic of a cooling plasma, and our observations of the spectra of a number of large flares support the conclusion reached by Horan (1971) that the electron temperatures in flare plasmas are highest during the initial phases of events, when the emission measures have not yet reached their maximum values.

We do not have sufficient temporal resolution. sensitivity to study the onsets of events in detail. As an example of our data, Figure 4 shows the beginning of a very large event (2B) that occurred on November 16, 1970. The X-ray flux begins to increase rapidly around ≈ 0050 UT or near 8Å (it takes seven minutes to complete a spectral scan and we were scanning from short to long wavelengths). The slope of the spectrum near 8Å is due mostly to the increasing emission measure. Note that the preflare plasma was evidently preheated before the X-ray flux began to increase rapidly, as is evidenced by the presence of highly ionized ions of calcium and sulfur such as Ca XIX and S XV. The change in slope of the continuum flux appeared first in the LiF spectrum (≈ 3.5Å), which implies that the initial rise in flux was due to a temperature increase and not simply an increase in emission measure. Lines of $\approx$ Fe XXI to Fe XXIV are strong even in the earliest stages of the event. This is not surprising, because at the expected electron densities ($\approx 10^{10}$ cm^{-3}), the ionization of these ions will take only a few seconds at electron temperatures of about 20×10^6 K. Ionization times are much longer for the hydrogenlike and heliumlike ions, however.
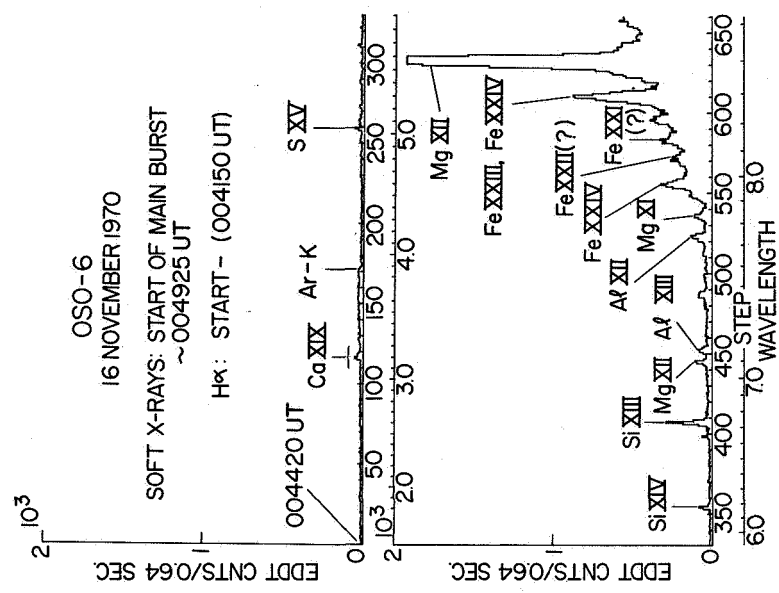
Figure 4. The onset of a large disk flare (≈ 2B) that occurred on November 16, 1970. The continuum appears to begin increasing rapidly ~ 0050 UT (step 550). The flux in the continuum changed slope about 40 seconds earlier near 3.5 Å in the LiF spectrum (obtained simultaneously with the EDDT spectrum). Note the lines of high excitation ions such as Ca XIX that are present in the spectrum appreciably before 0049 UT. The step scale is a function of Bragg angle; 1 step = 6 arcmin.
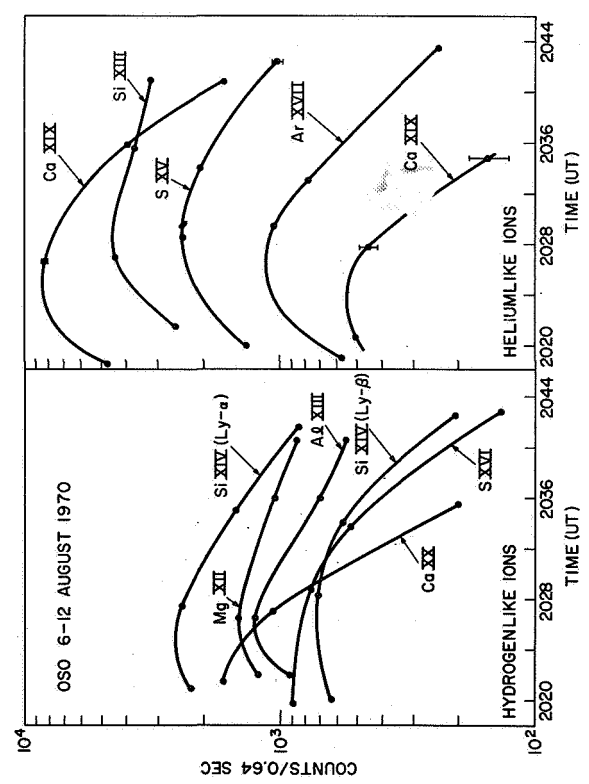
Figure 3. Interpolated time histories of lines of hydrogenlike and heliumlike ions for the flare of August 12, 1970. Most of the lines are the resonance lines, with the exception of the Mg XII and Ar XVII lines, one of the Si XIV lines, and one of the Ca XIX lines, which are transitions originating from the n = 3 level. The data are corrected for the dead time of the detector, but not for other instrumental efficiencies.

PLASMA DIAGNOSTICS APPLIED TO FLARE PLASMAS

The determination of temperatures, densities, and departures from ionization equilibrium in flare plasmas depends on the identification of spectral lines, their relative intensities, and variations of relative line intensities during a flare. An analysis based on continuum emission is more difficult, and is not presently possible with data obtained by the spectrometers flown.

The identification of lines below $\approx$ 8Å is straightforward, with the exception of the satellite lines to be discussed. Most of the emission lines are due to hydrogenlike and heliumlike ions and the wavelengths are well known. Furthermore, the spectrum becomes much less complicated at the short wavelengths and blending of lines is usually not a serious problem. A line list for $\lambda \lesssim$ 8.5Å with identifications based on data obtained by several investigators is given in Doschek (1972).

The spectrum $\sim$ 10Å, however, is much more complicated because of the large number of emission lines in this region due to the range of iron ions present in flare plasmas. Weak lines due to less abundant elements such as nickel will also appear in the spectrum. The situation is further complicated because the spectrometers used so far in this spectral range (KAP) have less resolution than the spectrometers used for the shorter wavelengths. A list of solar flare features near 10Å, with tentative identifications of a few lines and some transition arrays, has been recently submitted for publication (Doschek et al., 1972), and earlier observations and identifications in the 10Å region may be found in Neupert et al. (1967).

Although most of the strong lines at $\lambda \lesssim$ 8Å are easily identifiable and relatively unblended, there are a number of substantially weaker lines that have been identified primarily as satellite lines of the heliumlike ions, that is, innershell emission from lithiumlike ions due to transitions of the form, $1s^2 2\ell$ - $1s2\ell2\ell'$, where ℓ and ℓ' are orbital quantum numbers. The identifications of these satellites were originally suggested by Gabriel and Jordan (1969b) from an analysis of laboratory spectra. Satellites due to doubly excited heliumlike ions may also be present in flare spectra (Walker and Rugge, 1971), but higher spectral resolution and greater sensitivity will be necessary to confirm these tentative identifications.

The lithiumlike satellites necessarily fall close in wavelength to the intercombination and forbidden lines of the heliumlike ions, and for this reason most of them are too badly blended with the much stronger heliumlike features to be identified in the data obtained to date. The exceptions are the satellite lines, $1s^2 2s\ ^2S_{1/2}$ - $1s2p(^1P)2s\ ^2P^0_{1/2,3/2}$, which are just barely resolved in ions such as Si XIII and Ca XIX in some of the data. Also, most of the ironlike satellites near 1.9Å have been resolved by a quartz crystal spectrometer flown on the Intercosmos-4 satellite by Mandelshtam and his colleagues (see Vasiljev et al., 1971).

Gabriel and Jordan (1969b), Gabriel and Paget (1972), and Gabriel (1972) have shown that the dominant mechanism of satellite line formation in most cases is dielectronic recombination of the heliumlike ion. However, in the case of the heavier ions, such as Fe XXIV and Ca XVIII, there is also a non-negligible contribution due to direct innershell excitation of the lithiumlike ion. In fact, in equilibrium some of the lithiumlike satellites are formed primarily by collisional excitation.

In general, in equilibrium there are three classes of satellites: those that can be formed only by dielectronic recombination of the heliumlike ion (at $N_e < 2 \times 10^{15}$ cm^{-3}); those that may contain substantial contributions from collisional excitation as well as dielectronic recombination; and those that are formed primarily by collisional excitation.

Recently, Gabriel (1972) has presented a thorough analysis of the lithiumlike satellites, listing the expected lines and some of the relative intensities for elements of even atomic number ranging from carbon through copper. The results of the analysis are that the relative intensities of some of the satellites to the resonance lines of the heliumlike ions may be used to: a) determine the electron temperature in the plasma, whether or not the plasma is in ionization equilibrium; and b) determine the departure from ionization equilibrium once the temperature is obtained.

Figure 5 shows some of the expected calcium satellites compared with our calcium data for the August 12, 1970 event. The ^{2}P lines (lines 4 and 5) are seen to be just resolvable from the forbidden line, as are the weak lines ≈ 3.22Å, although some blending of lines 4 and 5 with line 6 is probable. The skewed.line just above the abscissa is the estimated continuum and background. These same data may be seen in the middle spectrum of Figure 6.

Lines 6 and 8 in Figure 5 can only be formed by dielectronic recombination since two-electron excitation may be neglected. On the other hand, the resonance line of Ca XIX (line 1) is formed primarily by collisional excitation. Therefore, the ratios of lines 6 and 8 to line 1 depend only on the electron temperature and are independent of the state of ionization equilibrium; that is, the two processes, excitation and recombination, depend differently on temperature, but start with the same ion, namely Ca XIX in this case. Thus, the line ratios are sensitive to temperature, but are independent of the abundance ratio of Ca XVIII to Ca XIX in the plasma, which depends on the state of ionization equilibrium. Similarly, the ratio of lines 10 to the resonance line of Ca XIX (the upper levels are quartet states, see Gabriel, 1972, for a complete and more detailed listing of satellite lines), may be used to obtain the ratio of the abundance of Ca XVIII to Ca XIX, since most of these satellite lines are formed primarily by collisional excitation. A particular ratio of Ca XVIII to Ca XIX corresponds to a particular electron temperature in ionization equilibrium. This temperature may then be compared with the actual electron temperature obtained from the dielectronic lines, and hence the departure from ionization equilibrium may be determined.

Clearly, the data of Figure 5 are not of sufficient quality to fully exploit the technique outlined above. The intensities of the lines shown are the expected intensities in equilibrium relative to an arbitrary resonance line intensity, at the temperature of maximum emitting efficiency of the heliumlike ion, $T_m = 25.4 \times 10^6$ K. However, a few interesting conclusions may be drawn from our data. The ratio of the intercombination line to the resonance line is ≈ 0.52, which is in good agreement with the latest calculations of Gabriel (1972). Since the dielectronic satellites are too badly blended with the forbidden line to be used to obtain an electron temperature, the ^{2}P lines must be used (lines 4 and 5 in Figure 5); and ionization equilibrium must be assumed to derive a temperature because these lines may also be produced by collisional excitation. In this case, from the middle scan of Figure 6, we obtain
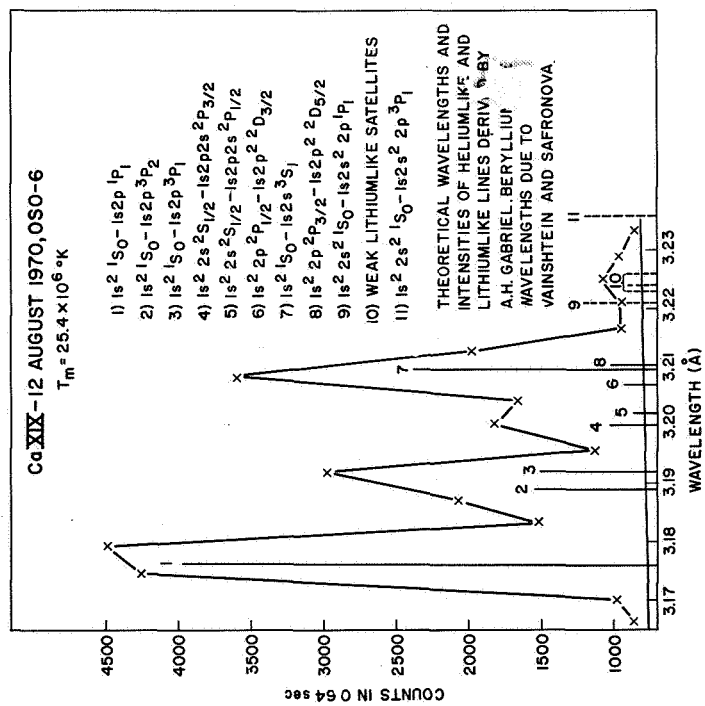
Figure 5. The Ca XIX lines and satellites as observed by OSO-6 for the limb flare of August 12, 1970. The data are corrected for the dead time of the detector. The skewed line above the abscissa is the estimated continuum level. Lines 9, 10, and 11 are too weak to be shown clearly in Figure 5, and therefore the dashed lines only indicate wavelengths and not relative intensities. Part of the emission composing lines 10 are due to transitions of the form $1s^2 2s\ ^2S - 1s2p2s\ ^4P^0$.
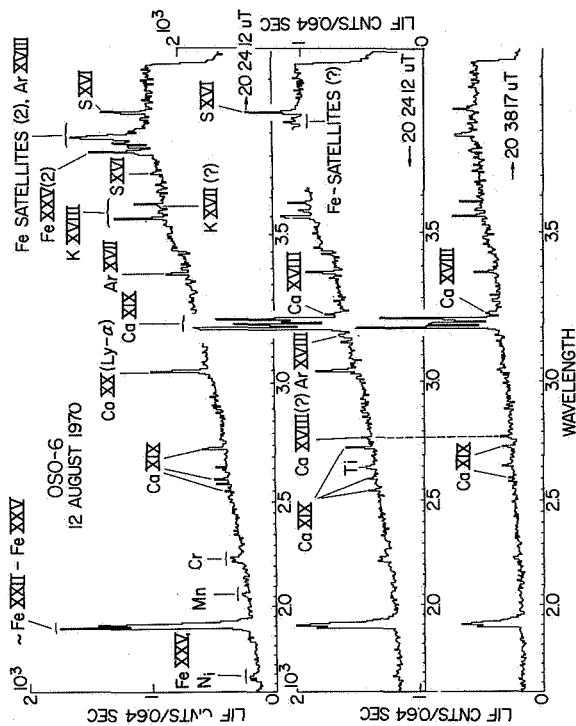
Figure 6. Spectra from ≈ 1.5 Å to ≈ 4 Å obtained by a LiF crystal spectrometer for the August 12 event. The times in each scan are the times when the spectrometer was scanning at ≈ 3.85 Å. The scan rate is 0.64 second per step. The arrows indicate the direction of scan.

an electron temperature of $\approx 20 \times 10^6$ K, which is consistent with a temperature of 25×10^6 K obtained from the ratio of the Lyman-α Ca XX line to the resonance line of Ca XIX, again assuming ionization equilibrium. The ion line ratio temperature should be somewhat higher than the satellite line temperature because the line ratio temperature is an average of the regions emitting Ca XX as well as Ca XIX. However, the measurement of the intensity of the ^{2}P satellite lines is difficult, because these lines are blended somewhat with the longer wavelength lines, and only two data points are involved in the measurement. We considered using the predicted sum of all the lines with wavelengths greater than the intercombination line, but this method will give relatively large errors if there is even a small error in the theoretical intensity of the forbidden line.

Although the ^{2}P line intensities indicate $T_e \approx 20 \times 10^6$ K, the emission in the region of lines 10 is about 5.6 times larger than is expected for a 20×10^6 K plasma in equilibrium. If all of the emission at these wavelengths is due to the lithiumlike ion, then the strength of this feature relative to the Ca XIX resonance line is indicative of a temperature of $\approx 8 \times 10^6$ K. If an isothermal interpretation is adopted and the higher temperature of $\approx 20 \times 10^6$ is assumed to be close to the actual electron temperature, then this result indicates an ionizing plasma, a plasma deviating markedly from ionization equilibrium and in a state of heating. However, from Figure 5, it is also seen that berylliumlike ion lines are predicted to fall near the wavelengths of the lithiumlike lines, and we cannot resolve this blend, if indeed berylliumlike lines are present in the spectra. (The wavelengths of these lines were obtained from Vainshtein and Safronova, 1971.)

If the excess emission near 3.225Å is regarded as purely lithiumlike, then the resultant ionizing condition would have to exist over a time interval of ≈ 7 minutes, implying continual heating of plasma, because a similar enhancement of these lines is observed in another scan ≈ 7 minutes later. Also, if several temperature regions do exist in the flare plasma, then the theory developed by Gabriel will be more difficult to apply. Therefore, instruments flown in the future to measure the satellite lines should probably record simultaneously the intensities of a number of the heliumlike ions and related satellites during a flare.

More extensive spectral data in the region of the Ca XIX lines is shown in Figure 6 for the August 12 event. Telemetry problems account for the data dropout in the two upper scans. The two lower spectra correspond to a cooler plasma than the upper scan, as can be seen from the Ca XX to Ca XIX resonance line ratio, and from Figure 2. According to Gabriel's theory of the formation of the satellite lines, the total intensity of satellite emission should increase relative to heliumlike line emission as the temperature decreases. This appears to be observed in the August 12 data. The total emission of the lines 4 through 8 (see Figure 5) relative to the Ca XIX resonance line seems to be greater in the bottom scan than in the middle scan (≈ 20 percent), but the electron temperature obtained from lines 4 and 5 by assuming equilibrium is about the same in both scans. However, we feel that the blending of lines 4 and 5 with the forbidden line and the other satellites is too severe to allow for an accurate estimate of electron temperature using these lines.

Note that in the two lower scans of Figure 5 there is a weak line at $\approx 2.75\text{\AA}$, just to the long wavelength side of the Ca XIX ($1s^2\ ^1S - 1s3p\ ^1P$) line at $\approx 2.71\text{\AA}$. This line is close to the expected wavelengths of Ca XVIII satellites arising from transitions of the type, $1s^2 2\ell - 1s2\ell 3\ell'$. No other obvious line should appear at this wavelength. The line at $2.75\text{\AA}$ is stronger relative to the $2.71\text{\AA}$ line in the lower scans than in the upper scan. If the $2.75\text{\AA}$ line is in fact Ca XVIII, then this result is consistent with Gabriel's theory, which predicts an increase in total satellite emission relative to heliumlike emission as the temperature decreases. Lines arising from lithiumlike configurations $1s2\ell 3\ell'$ may also be useful as checks on the electron temperature, but autoionization and radiative rates must first be calculated for these configurations.

FURTHER COMMENTS ON IONIZATION EQUILIBRIUM

Electron temperatures have been estimated in flare plasmas by assuming ionization equilibrium, and comparing the relative intensities of resonance lines of hydrogenlike and heliumlike ions of the same element (Meekins et al., 1970). In this section we examine the effect on resonance line temperatures of assuming large departures from ionization equilibrium.

The effects on resonance lines of departures from ionization equilibrium depend on the electron density and temperature as functions of time during the course of an event, as well as on bulk motions of the plasma. Kafatos and Tucker (1972) have considered models in which a plasma is rapidly heated while the density remains constant. However, variations of density with time are equally important in determining the line flux.

Electron densities in flare plasmas are highly uncertain. Purcell and Widing (1972) have estimated electron densities in the flare on November 4, 1969, using density sensitive lines of Fe XIV and Fe XV, and have obtained a value $\sim 3 \times 10^{10}$ cm^{-3}. However, this density determination is based on a relatively low excitation ion. The densities in regions of the flare producing emission from ions such as Fe XXIV could deviate significantly from the above value. Even assuming that the order of magnitude of the electron density is known, variation of density with time during flares is presently completely unknown.

We have attempted to illustrate the effects of density variations on the time-dependent ionization equations, by choosing a relatively simple model based on some observations and an assumption regarding the electron density. We make no claim that this model represents reality; we are attempting to illustrate the effect of departures from ionization equilibrium on the resonance lines of hydrogenlike and heliumlike ions. In this model we assume an isothermal plasma that is heated under the additional assumption that $N_e V = $ constant. If this assumption is not made, then a further assumption involving the heating mechanism in the flare region must be invoked. Since the emission measures of flares increase during the early stages, the assumption of conservation of particles is equivalent to assuming that the plasma is compressed when heated.

We wish to solve the equation

$$\frac{dN_z}{dt} = -N_e N_z (Q_z + \alpha_z) + N_e (N_{z-1} Q_{z-1} + N_{z+1} \alpha_{z+1}) \qquad (1)$$

where N_z is the fractional abundance of a hydrogenlike or heliumlike ion, N_e is the electron density, and Q_z and α_z are the appropriate ionization and recombination rates. (We are neglecting bulk motion of the plasma.) In order to solve Equation (1) we need the electron temperature and density as functions of time. These functions may be obtained from flare data and the previously stated assumptions as follows:

Horan (1971) has derived variations with time of the average electron temperature and emission measure during flares, by analyzing Orbiting Geophysical Observatory-4 (OGO-4) broadband X-ray data in the region from $\approx 0.5\text{Å}$ to 3Å and from 1Å to 8Å. Horan assumes that the radiation between 0.5Å to 8Å is primarily due to free-free and free-bound emission from an isothermal plasma. From the isothermal assumption, the ratio of the flux in the 0.5 to 3Å band to the 1 to 8Å band at a given time uniquely determines the electron temperature at the same instant. (Departures from ionization equilibrium at temperatures, T_e $\approx 20 \times 10^6$ K will not significantly affect the theoretical flux ratio.) Then, from the absolute flux in either energy band and the temperature, the corresponding emission measure, $N_e^2 V$, may also be obtained. Thus, T_e and $N_e^2 V$ may be calculated throughout an event. From the assumption that $N_e V$ is constant, $N_e(t)$ may also be found provided we choose a density at a particular time during the flare.

We chose an event that occurred on October 26, 1967, and performed Horan's calculation to obtain T_e and $N_e^2 V$ as functions of time. The data available are broadband ion chamber data obtained from OGO-4.

We assumed $N_e = 10^8$ cm^{-3} at the onset of the flare, and solved Equation (1) for the flux in the resonance lines of hydrogenlike and heliumlike silicon and sulfur. The results are shown in Figures 7 and 8. Figure 7 gives the electron density, emission measure, and representative fluxes in a few of the lines. Figure 8 shows the fractional abundances of the resonance lines of silicon along with the actual electron temperature as determined from the broadband data. Also shown is the spurious temperature that would be obtained from the ratios of the resonance lines of hydrogenlike silicon and sulfur to the heliumlike resonance lines of these ions assuming ionization equilibrium.

The most noticeable effect of nonequilibrium is that the line ratio temperatures lag considerably behind the actual electron temperature during the early stages of the heating. This is understandable because at these times the electron density is low, and ionization cannot keep pace with the increasing temperature. During the later stages of the event, the temperatures cross and the plasma is only slightly recombining. The density at these times is $\approx 2 \times 10^{10}$ cm^{-3} and recombination can almost keep pace with the declining temperature. A comparison of Figures 7 and 8 shows that, for this particular model, it would be easiest to detect differences between the actual electron temperature and the line ratio temperature,

272
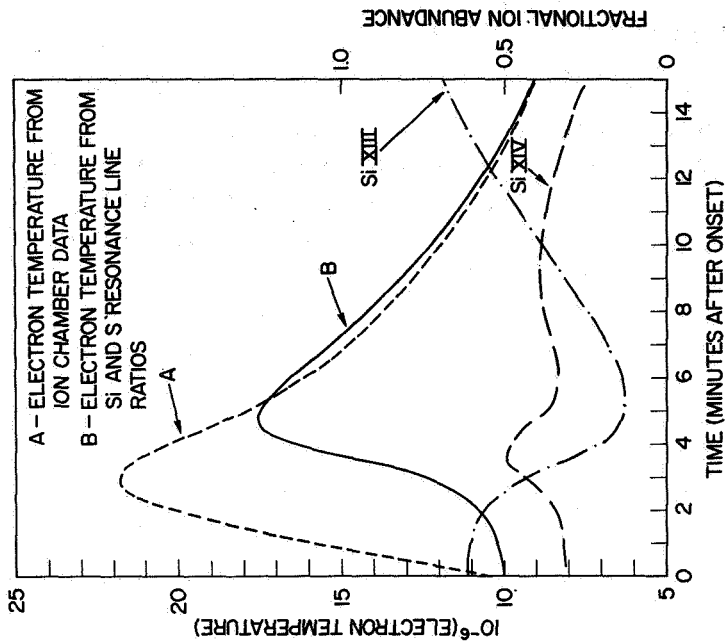
Figure 8. Electron temperatures and fractional ion abundances for the hypothetical model of the October 26, 1967 flare as described in the text. Both the Si and S line ratio temperatures were nearly equal and therefore are shown as only one curve in the figure.
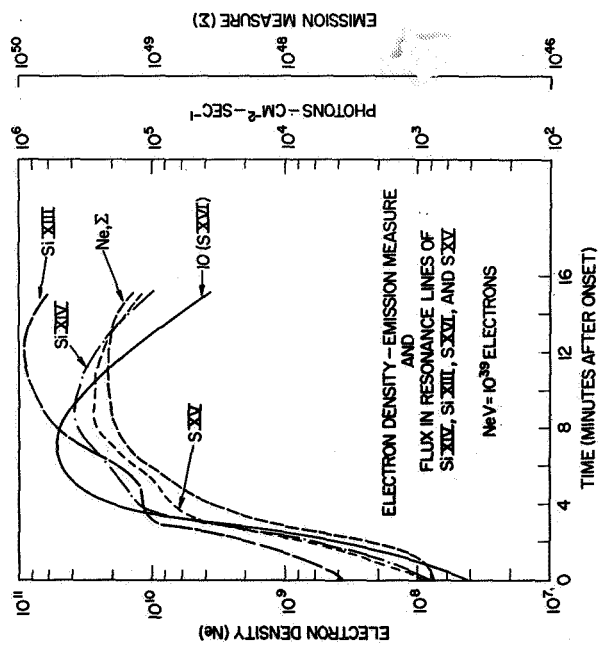
Figure 7. The emission measure, electron density, and resonance line fluxes for the hypothetical model of the October 26, 1967 flare as described in the text. The lines appear at 6.64 Å, 6.182 Å, 5.03 Å, and 4.73 Å for the Si XIII, Si XIV, S XV, and S XVI ions, respectively.

273

T_L, at times near the onset of the event, when the emission measure is still small. A similar conclusion might be expected for any model which involves an initial compression of material during the heating phase.

We wish to again caution the reader against taking this model too literally. In fact, the model implies transient ionization conditions in flare plasmas ($T_e/T_L > 1$), while Gabriel (1972) found recombination conditions from the flare data he had available ($T_e/T_L < 1$). In all likelihood the actual situation in flares is complex, perhaps with both ionizing and recombination conditions existing in different regions of the flare plasma. It may be worthwhile to fly a crystal spectrometer experiment with sufficient sensitivity to obtain spectra when the emission measure is about two orders of magnitude less than the peak value.

ACKNOWLEDGMENTS

REFERENCES

Doschek, G.A., 1972, *Space Sci. Rev.* 13, 765.

Doschek, G.A., Meekins, J.F., and Cowan, R.D., 1972, *Solar Phys.*, (in press).

Freeman, F.F., Gabriel, A.H., Jones, B.B., and Jordan, C., 1971, *Phil. Trans. Roy. Soc. London A.* 270, 127.

Gabriel, A.H., and Jordan, C., 1969a, *M.N.R.A.S.* 145, 241.

Gabriel, A.H., and Jordan, C., 1969b, *Nature* 221, 947.

Gabriel, A.H., and Paget, T.M., 1972, *J. Phys. B.* 5, 673.

Gabriel, A.H., 1972, *M.N.R.A.S.* 160, 99.

Horan, D.M., 1971, *Solar Phys.* 21, 188.

Kafatos, M.C., and Tucker, W.H., 1972, *Ap. J.* 175, 837.

Meekins, J.F., Doschek, G.A., Friedman, H., Chubb, T.A., and Kreplin, R.W., 1970, *Solar Phys.* 13, 198.

Meekins, J.F., 1972, Naval Research Lab. Report 7423, July 1972.

Neupert, W.M., Gates, W., Swartz, M., and Young, R., 1967, *Ap. J. (Letters)* **149**, L79.

Neupert, W.M., 1971, in *Physics of the Solar Corona,* ed. C.J. Macris (Dordrecht, Holland: D. Reidel Publishing Co.), 237.

Parkinson, J.H., 1971, *Nature Physical Sci.* **233**, 44.

Parkinson, J.H., 1972, *Nature Physical Sci.* **236**, 68.

Purcell, J.D., and Widing, K.G., 1972, *Ap. J.* **176**, 239.

Vainshtein, L.A., and Safronova, U.I., 1971, *Soviet Astron, AJ* **15**, 175.

Vasiljev, B.N., Grineva, Yu. I., Zitnik, I.A., Karev, V.I., Korneev, V.V., Krutov, V.V., and Mandelshtam, S.L., 1971, *XIVth Plenary Meeting of COSPAR,* Seattle, 1971.

Walker, A.B.C., Jr., and Rugge, H.R., 1969, *Solar Flares and Space Research* (North Holland, Amsterdam), 102.

Walker, A.B.C., Jr., and Rugge, H.R., 1970, *Astron. and Ap.,* **5**, 4.

Walker, A.B.C., Jr., and Rugge, H.R., 1971, *Ap. J.* **164**, 181.

FURTHER RESULTS ON COOLING MECHANISMS
FOR SOFT X-RAY FLARES

I.J.D. Craig, J.L. Culhane
Mullard Space Science Laboratory,
Dept. of Physics and Astronomy
University College, London

K.J.H. Phillips
Goddard Space Flight Center

J.F. Vesecky
Astronomy Department, University of Leicester

INTRODUCTION

Broadband observations of solar flare X-ray spectra with energies $\gtrsim 10\,\text{keV}$ have indicated the existence of plasma heated to temperatures of $\sim$2-4 $\times$ 10^7 K. Time profiles of temperature T and continuum emission measure $\int n_e^2\,dV$ have been presented during the course of flares by a number of workers using scintillation detectors (Milkey et al., 1971), ionization chambers (Horan, 1971), and proportional counters (Culhane and Phillips, 1970; Kahler et al., 1970). Generally, the procedure used has been to compare spectral slopes as derived by these detectors with the computations of free-free and free-bound continua of Culhane (1969) or the convenient algebraic form dir   d by Culhane and Acton (1970).

Culhane et al. (1970) and more recently Brinkman and Shaw (1972) have examined mechanisms by which the hot plasmas cool, and have found that energy loss by both radiation (principally in soft X-rays) and conduction to the cool chromospheric regions may operate. Analysis of the decay of temperature leads to plausible values for electron density n_e and the source volume V for one or other of these processes. Culhane et al. (1970) also considered a collisional process proposed by Hudson et al. (1969) in which, immediately after the flare plasma has been energized, the electron temperature temporarily exceeds the ion temperature and decays until a mutual equilibrium is restored. An electron Maxwellian distribution is brought about very quickly by electron-electron collisions, whereas the time to attain mutual equilibrium through electron-ion collisions is longer by a factor of approximately 2000.

TWO EVENTS WITH DISCONTINUOUS TEMPERATURE DECAYS

Analysis of data from the soft X-ray proportional counter spectrometer on OSO-4 has been continued along the lines of earlier work (Culhane and Phillips, 1970; Culhane et al., 1970). The instrument, which was constructed at University College, London and Leicester University, has been described by Culhane et al. (1969).

276

It was noticed that the time profiles of X-ray counts from the OSO-4 instrument's 1 to 3 Å detectors for two events showed a very rapid initial decay after maximum, followed by a much more slowly falling section. At least in the case of the larger of the two events, the change of slope seems quite definitely to be discontinuous (Figure 1). Table 1 summarizes data for each event, and Figure 1 depicts the counting-rate and temperature time profiles for the larger event.

Temperatures and emission measures for both flares have been derived, as in Culhane et al. (1970), by fitting an emission function to eight-channel count histograms which form the output of the 1 to 3 Å detectors, analyzed into eight energy intervals by pulse-height analysis. The computer program described in Culhane et al. (1970), developed at the Lockheed Palo Alto Laboratories, has been used here. It employs temperature and continuum emission measures in the Culhane-Acton formula and the flux in the 6.7 keV (1.9 Å) iron-line feature as free parameters, adjusting them by small amounts in successive iterations until the original histogram is approximately reproduced. A χ^2-test is used to examine the agreement between histograms and terminates the iteration accordingly. Account is taken of the proportional counters' energy resolution in the fitting process.
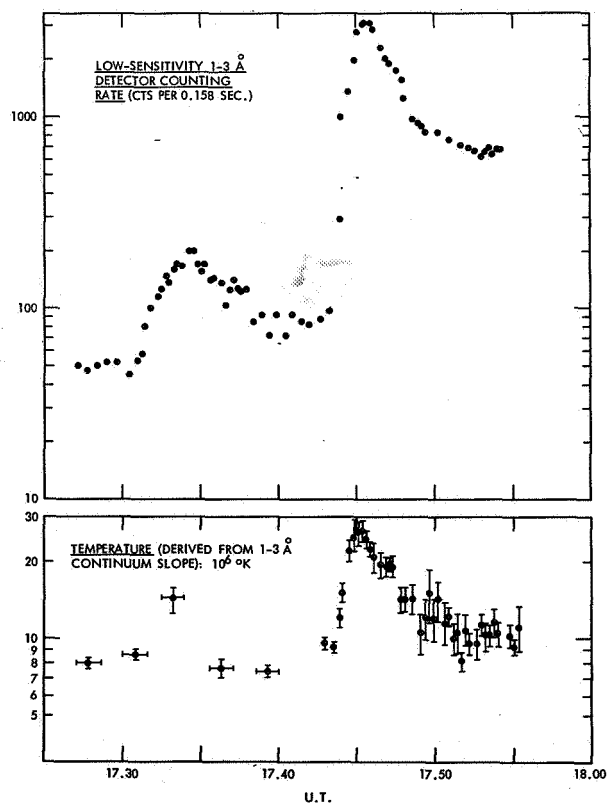
Figure 1. Time profiles of counting rate and temperature for December 1, 1967, X-ray burst. Data from University College/Leicester proportional-counter spectrometer on OSO-4.

277

Table 1

Two X-ray Events With Discontinuous Temperature Decays.

Date	December 1, 1967	March 24, 1968
Soft X-ray event (1 to 3 Å)		
UT of start	17.43	05.57
Maximum	17.46	06.06
End	>17.54	06.12
Peak X-ray flux, $\lambda \simeq 3$ Å		
(4keV) (ergs $cm^{-2} s^{-1} Å^{-1}$)	7×10^{-4}	6×10^{-6}
Hard X-ray event		
(12.5 to 22.5 keV)[*]		
UT of start	17.42	?
Maximum	17.45	?
End	>17.50	?
Hα flare event [†]		
UT of start	17.45	None
Maximum	17.50	
End	17.52	
Class	Sn	

[*] H. S. Hudson, private communication to J. L. Culhane, 1968.

[†] ESSA, Solar-Geophysical Data.

Figure 1 illustrates how the temperature decay profiles track the discontinuous counting-rate profile for the December 1, 1967 event. For the March 24, 1968 flare, which is much smaller, a discontinuous temperature is less obvious but the temperature decay is much more rapid immediately after maximum than at the end of the event. Although it was pointed out in Culhane et al. (1970) that the rapid initial decline of temperature is a characteristic of conduction cooling, the theoretical profiles in that work do not predict a discontinuous fall. We have, therefore, analyzed the two sections on either side of the discontinuity separately to see if different processes were operating in each.

We have considered the three cooling processes of Culhane et al. (1970): radiation, conduction to chromospheric regions, and the collisional process of Hudson et al. (1969). Radiation energy loss occurs principally in the soft X-ray region for $T_e \simeq 10^6$- 10^7 K. In Culhane et al. (1970), an integration of X-ray continua calculated by Culhane (1969), together with line fluxes given by Cox and Tucker (1969), were taken as an estimate of total radiative power, $P(T)$ (ergs cm^{-3} s^{-1}), but we shall use the recent work of Tucker and Koren (1971) which give $P(T)/n_e^2$ directly for coronal plasmas in the temperature range of interest. With temperature falling from a maximum value T_m with e-folding time t_{rad}, we estimate electron density from

$$n_e = \frac{3kT_m}{t_{rad}[P(T_m)/n_e^2]} \qquad (1)$$

where k is Boltzmann's constant. Combining this value with the continuum emission measure ($\simeq n_e^2$ V) we may estimate the emitting volume V and thus the angular dimensions of the flare. For conduction cooling we follow Culhane et al. (1970) in which the hot plasma is assumed to be in the form of a magnetic flux tube of length L. The mirror points of particles in the conducting cylinder are considered to be within the chromospheric regions, so that the temperature gradient from the top of the cylinder to a mirror point is approximately $T/(L2)$, where T is the temperature of the X-ray emitting plasma. T decays with time according to

$$T = (T_m^{-5/2} + \alpha t)^{-2/5} \qquad (2)$$

in which α is related to n_e and L by

$$\alpha = \frac{2 \times 10^{10}}{n_e L^2}$$

Estimating α by comparing the observed decay with that calculated from (2) and knowing the emission measure gives n_e and L. Finally the collisional process of Hudson et al. (1969) is considered by comparing the e-folding time of the observed temperature with the electron-ion "time of equipartition" as defined by Spitzer (1962), which for a coronal plasma is

$$t_{eq} = \frac{12.5 \, T_e^{3/2}}{n_e} \qquad (3)$$

The dependence on the ion temperature and density is very weak. With the observed maximum temperature substituted for T_e, we may again find n_e and thus the dimensions of the emitting region.

Table 2 gives results of calculations for the two events of Table 1. The two sets of estimates of n_e and the flare dimensions refer to each section of the temperature decay: (a) to the initial part and (b) the final. We substitute the flare maximum temperature for T_m in (1) and (2) and T_e in (3) for the initial section, and the temperature at which the discontinuity occurs for the final section.

Table 2

X-ray Flare Dimensions for Three Cooling Mechanisms.

Event	December 1, 1967		March 24, 1968	
	(a)	(b)	(a)	(b)
e-folding time (s)	360	880	530	2900
Temperature (10^6 K)from which event decays	24.0	13.6	10.5	8.3
Collisional-cooling process (Hudson et al., 1969):				
n_e (cm^{-3})	4×10^9	7×10^8	8×10^8	1×10^8
V (cm^3)	2×10^{28}	9×10^{29}	3×10^{28}	8×10^{29}
Angular lengths of filaments *				
(20 arcsec diameter)	2′.9	>1°	4′ 3	>1°
(2 arcsec diameter)	>1°	>1°	>1°	>1°
Radiation cooling				
n_e (cm^{-3})	2×10^{12}	6×10^{11}	8×10^{11}	1×10^{11}
V (cm^3)	8×10^{22}	2×10^{24}	3×10^{22}	5×10^{23}
Angular lengths of filaments (arcsec)				
(20 arcsec diameter)	0.001	0.015	0.0002	0.004
(2 arcsec diameter)	0.07	1.5	0.02	0.39
Conduction cooling (Culhane et al., 1970):				
α	8×10^{-21}	3×10^{-21}	2×10^{-20}	5×10^{-21}
Angular lengths of filaments (arcsec)				
(20 arcsec diameter)	90	180	144	204
(2 arcsec diameter)	19	42	31	44
n_e (cm^{-3}) (20 arcsec diameter)	3×10^9	6×10^9	9×10^7	2×10^8
(2 arcsec diameter)	6×10^{10}	1×10^{11}	2×10^9	4×10^9

* At distance of 1 AU (solar diameter = 32.0 arcmin).

In determining the X-ray flare's angular dimensions, we have assumed that the emitting volume has the type of structure visible in the X-ray flare photographs obtained by Vaiana et al. (1968). A broad envelope of emission, several arcminutes long and 20 arcsec wide surrounds two narrow filaments, each 2 arcsec across. In Table 2 we have given the lengths of cylindrical volumes with diameters of 15,000 km and 1500 km, equivalent to 20 arcsec and 2 arcsec, respectively.

DISCUSSION

To explain the temperature decay of the two events in the light of results in Table 2, we cite three possibilities:

(a) For the first 400 or 500 seconds after the temperature maximum of each event, the electrons and ions of the X-ray emitting plasma had not reached a mutual equilibrium, thus giving a rapid decay of electron temperature as described by Hudson et al. (1969). Conduction of thermal energy to the chromosphere as discussed by Culhane et al. (1970) may have occurred throughout the decay phase of both events, so that the rapid decrease of temperature in each case arises from cooling by both conduction and the collisional process. The collisional process does not appear to operate in phase (b) of either event.

(b) Culhane et al. (1970) argued that the collisional process was not significant for the events in their study because the implied emissive volumes were too large. Thus the energizing of the hot plasma was probably sufficiently gradual for a mutual equilibrium between ions and electrons to be set up before maximum temperature. If this is so for the two flares studied here, conduction over both temperature-decay sections may be taking place; but in that case a sudden change in conduction rate, perhaps as a result of a change in flare dimensions, must have occurred, particularly f   .ie December 1 event.

(c) The rapid initial fall of temperature is due to conduction, but the more gradual decay results from cooling by radiation, with the flare filamentary structure of a diameter much smaller than can be resolved in the photographs of Vaiana et al. (1968). Conduction may have been suddenly arrested because of a sudden change of the flare loop configuration, for example, a ballooning instability arising from continued particle injection as described by Benz and Gold (1971). It may even be possible that magnetic field fluctuations can account for a substantial reduction in the conductivity, as considered in a solar wind context by Hollweg and Jokipii (1972).

It may not be possible to distinguish between (a), (b), and (c) using these broadband soft X-ray data. However, circumstantial evidence might be provided by $H\alpha$ cinematographic film in investigating changes in the $H\alpha$ flare volume considering possibility (b). $H\alpha$ limb flares with X-ray counterparts showing discontinuous temperature profiles may actually show sudden expansions as considered in (c), though of course it is unlikely that the $H\alpha$ -emitting region is identical with that giving soft X-ray emission.

ACKNOWLEDGMENTS

REFERENCES

Benz, A.O. and Gold, T., 1971, *Solar Phys.* **21**, 157.

Brinkman, A.C. and Shaw, M.L., 1972, *Solar Phys.* **23**, 120.

Cox, D.P. and Tucker, W.H., 1969, *Ap.J.* **157**, 1157.

Culhane, J.L. 1969, *M.N.R.A.S.* **144**, 375.

Culhane, J.L. and Acton, L.W. 1970, *M.N.R.A.S.* **151**, 141.

Culhane J.L. and Phillips, K.J.H., 1970, *Solar Phys.* **11**, 117.

Culhane, J.L., Sanford, P.W., Shaw, M.L., Phillips, K.J.H., Willmore, A.P., Bowen, P.J., Pounds, K.A., and Smith, D.G., 1969, *M.N.R.A.S.* **145**, 435.

Culhane, J.L., Vesecky, J.F., and Phillips, K.J.H., 1970, *Solar Phys.* **15**, 394.

Hollweg, J.V. and Jokipii, J.R., 1972, *J.G.R.* **77**, 3311.

Horan, D.M., 1971, *Solar Phys.* **21**, 188.

Hudson, H.S., Peterson, L.E., and Schwartz, D.A., 1969, *Ap.J.* **157**, 389.

Kahler, S.W., Meekins, J.F., Kreplin, R.W., and Bowyer, C.S., 1970, *Ap.J.* **162**, 293.

Milkey, R.W., Blocker, N.K., Chambers, W.H., Fehlau, P.E., Fuller, J.C., and Kunz, W.E., 1971, *Solar Phys.* **20**, 400.

Spitzer, L., 1962, *Physics of Fully Ionized Gases*, 2nd edition, New York, Interscience Publ. 135.

Tucker, W.H. and Koren, M., 1971, *Ap.J.* **168**, 283.

Vaiana, G.S., Reidy, W.P., Zehnpfennig, T., Van Speybroeck, L., and Giacconi, R., 1968, *Science* **161**, 564.

V: NUCLEAR REACTIONS IN FLARES

SOLAR GAMMA RAY AND NEUTRON OBSERVATIONS

E.L. Chupp

Max Planck Institute for Physics and Astrophysics
Institute for Extraterrestrial Physics

D.J. Forrest and A.N. Suri

Department of Physics
University of New Hamphsire

ABSTRACT

The present status of knowledge concerning the impulsive and the continuous emission of solar gamma rays and neutrons is reviewed in the light of the recent solar activity in early August 1972. The gamma ray spectrometer on Orbiting Solar Observatory-7 (OSO-7) has observed the sun continuously for most of the activity period except for occultation by the earth. In association with the 2B flare on August 4, 1972, and the 3B flare on August 7, 1972, the monitor provides evidence for solar gamma ray line emission in the energy range from 300 keV to 10 MeV. A summary of all the results available from preliminary analysis of the data will be given. Significant improvements in future experiments can be made with more sensitive instruments and more extensive time coverage of the sun.

INTRODUCTION

The aim of this discussion is to review the status of the experimental efforts to search for gamma rays and neutrons emitted from the sun. Most of these efforts concern observations during quiet solar periods and during relative small flares $\leqslant$ 2B. At the time Dr. Ramaty organized this conference, we would have had to be content in reviewing the many noble efforts which have been carried out to bring into viable existence a new probe for studying solar phenomena. Fortunately though, the significant solar activity of early August 1972 allows us to review this field while both the sun and some satellite experiments were closely in tune. We therefore will have to consider our remarks in the light of new and interesting observations. Before 1970 the typical limiting flux values for neutrons ($\gtrsim$20 MeV) was $\sim$10^{-2} cm^{-2} s^{-1}. All of these early results referred essentially to continuous emission of neutrons by the sun. Since that time satellite and balloon neutron experiments have been greatly improved, so the neutron flux limit has been reduced by an order of magnitude to $\sim$10^{-3} cm^{-2} s^{-1} for continuous limits. Limiting fluxes for gamma rays (<10 MeV) have remained at the same level; for example, 5 X 10^{-3} cm^{-2} s^{-1} for the 2.2-MeV lines. Efforts to detect π° decay gamma rays (> 10 MeV) have also continued with no clear success. In addition, the realization that mountain-top cosmic ray neutron monitors can potentially detect solar neutrons, coupled with Monte Carlo calculations of solar neutron secondary production in the atmosphere, has allowed continuous search during large events back to 1960. Satellite neutron detectors on Orbiting Geophysical Observatory-6 (OGO-6) and OSO-6 have also extended the time coverage during times of significant solar activity. All of the efforts mentioned above have continued to give only upper limits for solar neutron and gamma ray fluxes under both active and quiet solar conditions.

A new development has just occurred recently with measurements made by a gamma ray monitor on the OSO-7 satellite. Gamma ray lines have definitely been detected during at least two of the several flares which occurred in the period from August 2 to August 11, 1972. Since the neutron-proton capture gamma ray was one of the lines detected, these observations give comprehensive data on both the neutron and gamma ray fluxes with a single instrument.

SUMMARY OF WORK TO AUGUST, 1972

The experimental investigations to detect solar neutrons and gamma rays, which were reported in the literature by 1970, were reviewed previously by Chupp (1971). Up to that time there was no conclusive evidence for either solar neutron or gamma ray fluxes. On the other hand, there were at least three highly disputed claims of observations of both solar neutrons and gamma rays, all in times of modest or low solar activity. None of these possible events occurred in coincidence with the optical phase of any flare. Nonetheless, since they are published as positive fluxes, we should keep the reports in mind and the conditions of solar activity under which they were observed. The Tata result of Apparao et al. (1966) was obtained under very quiet solar conditions; that of Daniel et al. (1967) was made several hours before a subflare. This result was seriously questioned by Holt (1967) since no neutron decay protons were seen by the OGO-A satellite, which was in orbit at the time and should have seen them if the neutron flux was 10^{-1} neutrons cm^{-2} s^{-1} as reported. This criticism has now been countered by Daniel et al. (1971) who have revised their result downward nearly an order of magnitude to 1.5×10^{-2} neutrons cm^{-2} s^{-1}, based on a new measurement of the atmospheric neutron flux which allowed them to convert the measured solar neutron counting rates to an absolute $^{\text{⌐}\text{---}}$. It seems this result persists. In the case of gamma rays, Kondo and Nagase (1969) reported an extremely large (800 percent) increase in the gamma ray flux (3 to 10 MeV) 10 minutes after a 1N flare and associated radio burst. The last positive report of a gamma ray increase was given by Hirasima et al. (1970) who reported a gamma ray line flux coincident with a 1000-MHz radio burst. As satellite experiments in the future continue to search for gamma ray and neutron events, it will be interesting to see if any enhancements are found under similar activity conditions as in the cases just discussed. Then we can decide if indeed these peculiar observations are most probably positive or spurious.

Several significant experiments summarized in Table 1 have been discussed in the literature since the review just mentioned. Joseph (1970) has reported on the results of measurements at Tata using a new type of high energy detector and a plastic scintillator. The basic neutron-detecting element for the new detector consists of a CsI(T1) crystal slab of 11.1 cm diameter by 0.5 cm thickness and associated photomultiplier in a 1-cm thick plastic scintillator anti-coincidence shield. Fast neutrons, 10 MeV $< E_n <$ 500 MeV, produce nuclear reactions, primarily stars, giving rise to proton, alpha particle, or other ion pulses in the slab. Pulse shape discrimination has also been used to separate out neutron-induced star events from gamma-ray events which produce energetic electrons in the crystal. The sensitivity (area $\times$ efficiency) of this detector for fast neutrons is ~ 0.75 cm^2 above 10 MeV. In addition, the

Table 1

Summary of the Recent Solar Neutron and Gamma Ray Observations to August, 1972

Reference	Instrument	Radiation and Energy Range	Neutron or Gamma Ray Flux (cm⁻² s⁻¹)	
			Continuous	Flare Associated
Joseph thesis (1970)	Plastic scintillator telescope with antishield	n 15 to 150 MeV γ 5 to 30 MeV		February 26, 1969 2B, 1N n $<1.2 \times 10^{-2}$ γ $<10^{-2}$
Cortellessa et al. (1971)	Plastic scintillator with antishield	n 10 to 200 MeV	$<5.5 \times 10^{-3}$	June 30, 1970 1N Protons $< 6 \times 10^{32}$ above 30 MeV $P_O = 60MV$
Eyles et al. (1972)	Scintillator recoil telescope with antishield	(i) n 50 to 350 MeV γ >80 MeV (ii) Test of Elliot model	n $<3 \times 10^{-3}$ γ $<4 \times 10^{-4}$	(i) 1B May 29, 1969 n <23 cm⁻² γ < 6 cm⁻² (ii) 2B March 21, 1965 n $<4.2 \times 10^{-3}$ Theo. $\sim 5 \times 10^{-2}$ for Class 4
Sood (1972)	Cerenkov pair telescope with Pb converter	γ >20 MeV		October 17, 1968 1N γ $<2.6 \times 10^{-4}$ (10 min rise) $<1.1 \times 10^{-5}$ (active disc)
Lockwood et al. (1972) OGO-6	He³ proportional counter with antishield	n 1 to 20 MeV	$<1.8 \times 10^{-3}$	Null results
Leavitt et al. (1972) OSO-6	Scintillator recoil telescope	n >40 MeV	$<4 \times 10^{-4}$	Null results

detector is sensitive to gamma rays in the energy range 4 to 30 MeV, but no estimate is given for the efficiency. The properties of the scintillator block were very similar to those previously discussed by Forrest and Chupp (1969). The basic property of this detector needed in this discussion is the sensitivity for solar neutron and gamma rays, which is 22 cm^2 for neutrons (>10 MeV) and 30 cm^2 for gamma rays (5 to 30 MeV). These instruments have been flown in 1969 from Hyderabad (λ_{gm} - 8°N) during coincidental solar activity. During a 2B (and following 1N) flare on February 26, 1969, the plastic block detector observed no increase; therefore, limiting fluxes for solar neutrons were <10^{-2} cm^{-2} s^{-1} (5 to 30 MeV). On April 19, 1969, the smaller volume CsI(Tl) star detector was flown during a 1B flare with no enhancement observed. The corresponding upper limit for solar neutrons in this event was 1.5 X 10^{-2} cm^{-2} s^{-1} which is essentially the same as for the larger plastic block detector. The reason for this is that even though the sensitivity of star detector is much lower than for the former, its background counting rate is correspondingly much lower. All of these limit estimates apply to the case of an assumed neutron spectrum produced by a solar proton exponential rigidity spectrum with P_0 = 60 MV (Lingenfelter and Ramaty, 1967).

Cortellessa et al. (1971) have carried out several careful measurements using an anticoincidence shielded plastic scintillator, which studied both continuous emission possibilities as well as in small flares. The detector was sensitive both to neutrons and gamma rays with the biases for neutrons set at equivalent proton recoil energies of 10 MeV, 20 MeV, and 30 MeV. Self-gating effects due to recoil protons from the surface of the inner detector interacting in the antishield were reduced by surrounding the inner detector with 1 cm of Al. The effective neutron energy range of the detector then was 10 MeV to 200 MeV, with an efficiency for solar neutrons of ~11 percent based on an assumed solar neutron production spectrum due to a solar proton spectrum with characteristic rigidity P_0 = 60 MV. The continuous solar neutron flux limit was 5.5 X 10^{-3} neutrons cm^{-2} s^{-1}, in the energy range of the detector, for flights in 1970. In addition, failure to detect any neutrons in a flight during a 1N flare on June 30, 1970, gave a limit for accelerated protons at the sun of <6 X 10^{32} protons with energies > 30 MeV, for P_0 = 60 MV. In order for these workers to achieve the improved limits (shown in Figure 1), care had to be taken to keep instrumental instability effects on the counting rate B to less than 2 $(BT)^{1/2}$ X 100 for an observing time T. In this case the instability effects were reduced to 0.28 percent.

Eyles et al. (1972) have reported on the results of balloon flights with a recoil telescope designed to test the predictions of Elliot (1969) concerning acceleration of charged particles before the optical flare, with consequent release into the solar atmosphere, thus providing the energy source for the optical flare. The apparatus consists of a polyethylene block of thickness 16.5 gm cm^{-2} as a converter, followed by a recoil proton telescope, all in an anticoincidence shield comprising the neutron telescope. This unit was followed by a Cerenkov element, 1 cm thick, to eliminate 95 percent of relativistic charged particles. The detector's neutron response was effective over an energy range from 50 MeV to 350 MeV with a maximum efficiency at ~190 MeV of ~1.4 percent, falling steeply on

288
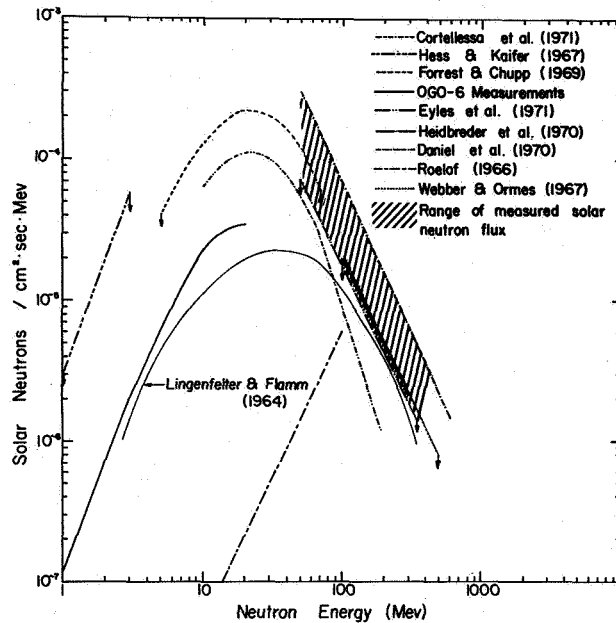
Figure 1. Summary of the upper limits to the differential solar neutron flux at earth. For E>50 MeV the upper and lower limits indicated with a band include many results not shown in the figure. The curve marked Lingenfelter and Flamm (1965) is the calculated time-average solar neutron flux at earth for the last solar cycle.

both sides of the maximum. Using the converter area of ~181 cm^2 gives a maximum sensitivity of ~2.5 cm^2. The telescope half angle for neutrons was ~22°. The detector was also sensitive to gamma rays with energies about 20 MeV. At 100 MeV the gamma ray efficiency was 35 percent. This detector was flown in 1969 to give limits both during active periods and quiet periods. The neutron and gamma ray limits for continuous emission are 3 × 10^{-3} cm^{-2}s^{-1} (50 to 350 MeV) and 4 × 10^{-3} cm^{-2}s^{-1} (~20 MeV) respectively. This neutron limit is even lower than that mentioned above by Cortellessa et al. (1971). Even though the sensitivity is an order of magnitude lower for the telescope, the background is much lower. During a 1B flare on November 1, 1969, the limiting neutron and gamma ray fluxes found were ≤4 × 10^{-2}cm^{-2} s^{-1} and ≤10^{-2}cm^{-2} s^{-1} respectively.

There was, however, an opportunity to test to some extent the predictions of Elliot's model (Elliot,1969),four hours before a 2B flare on March 21, 1969. No neutron flux was detected above a limit of 4 × 10^{-3} neutrons cm^{-2} s^{-1}. Since Elliot's model predicts a flux of ~5 × 10^{-2} neutrons cm^{-2} s^{-1} for a class 4 flare, the authors do not consider this example as a real test of the preflare acceleration model: even much lower fluxes are expected for smaller optical class flares.

Sood (1972) has also conducted a search for high energy gamma rays from the sun in order to test the Elliot model (Elliot, 1969). His instrument consisted of a pair telescope with a Pb converter. In addition, unidirectional Cerenkov elements were used to detect the relativistic electrons. The instrument was not sensitive to photons with energies <20 MeV but had an overall efficiency for π° gamma rays of ~38 percent; the area solid angle factor was 22 cm^2 sr. Several flights were carried out in 1967 and 1968 from Kampala, Uganda, while the sun was moderately active. For a generally active solar disk, the limiting flux was $\leqslant1.1 \times 10^{-4}$ gammas cm^{-2} s^{-1} (>50 MeV), and for a 1N flare on October 19, 1968, the limiting flux was 2.6×10^{-4} gammas cm^{-2} s^{-1} assuming a 10-minute burst. One flight took place ~8 hours before a 2B flare on October 31, 1968, but since no 350 MeV protons (π° threshold) were observed in space following this flare, the author does not consider this a definite test of the Elliot model. In any case, if one did, the limiting flux would be 1.1×10^{-4} gammas cm^{-2} s^{-1}.

In 1969 the OGO-6 satellite carried out neutron monitoring measurements in the energy range 1 to 20 MeV from June, 1969 to December, 1969 (Lockwood et al., 1972). The detector was a high pressure He-proportional counter in a plastic scintillator moderator to thermalize the fast (MeV) neutrons. The anticoincidence charged-particle shield consisted of 22 proportional counters. Typical sensitivities for solar neutron spectra with characteristic rigidities $P_O = 60$ MV and 125 MV are 0.38 cm^2 and 0.37 cm^2, respectively. By carefully selecting the lowest background data (primarily low latitude) and using only data in a 6-month period when no solar proton events were evident, a quiet time limit of 1.8×10^{-3} neutrons cm^{-2} s^{-1} was obtained. This result is about an order of magnitude lower than previously available in the same energy range. In additon, several small flares occurred during the experiment's lifetime, but no positive evidence for enhanced neutron fluxes was seen. No limit estimates were given for flares because of large statistical uncertainties. Figure 1 summarizes the current results on the continuus flux limits for solar neutrons as summarized by Lockwood (1972, personal communication).

A recoil proton telescope was also flown on the OSO-6 satellite to search for solar neutrons. Details on the instrument are not currently available, but continuous flux limits have been presented (Leavitt et al., 1972) as $<4 \times 10^{-4}$ cm^{-2} s^{-1} for solar neutrons with energies greater than 40 MeV. Observations made by this instrument during solar activity are inconclusive.

A very interesting and new approach has recently been described by Kirsch (1972) using mountain altitude cosmic ray neutron monitors. Monte Carlo calculations (Alsmiller et al., 1968) have been carried out which give the conversion efficiency of solar neutrons in the earth's atmosphere for yielding secondary neutrons as a function of atmospheric depth. For example, Kirsch has used these basic results and calculated the efficiency for detecting different assumed solar neutron spectra at the altitudes of existing neutron monitors. For example, at 550 g $\cdot$ cm^{-2} atmospheric depth, corresponding to the Chacaltaya monitor, the secondary neutron flux is 32 percent of the primary neutron flux, assuming the producing-proton spectrum at the sun has a characteristic rigidity $R_O = 125$ MV. Of particular interest

here is the study made of the Chacaltaya and Mina Aquilas monitor data during the November 12, 1960 event for which Lingenfelter and Ramaty (1967) have predicted significant neutron fluxes. They predicted a flux of 10 to 30 neutrons $cm^{-2}s$ at the earth as a result of solar neutron production in the slowing down phase after particle acceleration. Kirsch's analysis (1972) indicates that the observed solar neutron flux is smaller by a factor of 10^{-2} to 10^{-3}. Therefore, it is concluded that the assumption of isotropic proton emission from the solar flare region is not fulfilled. One of the basic difficulties with this technique is the fact that any solar neutron effect must override the diurnal variation of cosmic rays.

OSO-7 OBSERVATIONS

We will now discuss in more detail the recent observations of solar gamma ray lines during the solar activity of early August, 1972, recently reported as preliminary observations (Chupp et al., 1973).

The seventh Orbiting Solar Observatory (OSO-7) carries in one of its wheel compartments the University of New Hampshire gamma ray monitor designed to study solar and cosmic gamma radiation in the energy range 0.3 to 10 MeV. The instrument has been described in detail by Higbie et al., (1972).•It consists of a 7.6 cm by 7.6 cm NaI (T1) crystal surrounded by a cup-shaped anticoincidence shield of CsI (Na). The energy resolution of the instrument for line radiation is ~8 percent at 662 keV. The instrument is calibrated regularly each orbit at day/night and night/day transitions with a Co^{60} source. The calibration gives photopeaks at 1.17, 1.33 meV, and the sum peak at 2.50 MeV. With this calibration system we can determine the energy of a well-defined peak to within 2 percent anywhere in the pulse height spectrum.

During the normal mode of operation the pu... height spectra are accumulated over ~90 wheel rotations (~3 minutes) in the solar and background quadrants (Figure 2), and pulse height is analyzed with a 377-channel quadratic pulse height analyzer (Burtis et al., 1972).

During the recent solar activity, beginning on August 2, 1972, we have observed gamma ray line and continuum emission from the sun, associated with the 2B flare on August 4, and 3B flare on August 7, 1972. A 2B Hα flare on August 4 began at 0621 UT, reaching maximum at 0638 UT (Preliminary Report SESE-PRF-Boulder 092, 093). The OSO-7 gamma ray detector observed this flare until 0633 UT, when the satellite was eclipsed by the earth. Figure 3 shows a plot of the spectra which were taken just before the start of the optical phase of the flare (bottom), during the rise and just after the commencement of the satellite night. The total accumulation time of each pair of these spectra is ~9 minutes and the live time ranges from ~80 to 100 seconds. Figure 3(a) and (b) cover the spectral range ~430 to 620 keV and 2.1 to 2.4 MeV respectively. It is evident from the figure that during the rise of the reported flare there is significant enhancement in both the ~0.5 and 2.2 MeV spectral regions as well as in the continuum to above 2 MeV below the line features. Analysis of the data in other spectral regions shows possible evidence for the emission lines at 4.4 MeV and 6.1 MeV.

291

Figure 3. The OSO-7 gamma-ray pulse height spectrum is shown for the energy regions 460 to 620 keV and 2.1 to 2.4 MeV on August 4, 1972. The lower spectrum was taken in the daytime before the start of the 2B Hα flare, and the central spectrum was taken during the rise of the optical flare. The spectrum at the top was taken just as the satellite was occultated by the earth. The accumulation time intervals are shown for each spectrum.
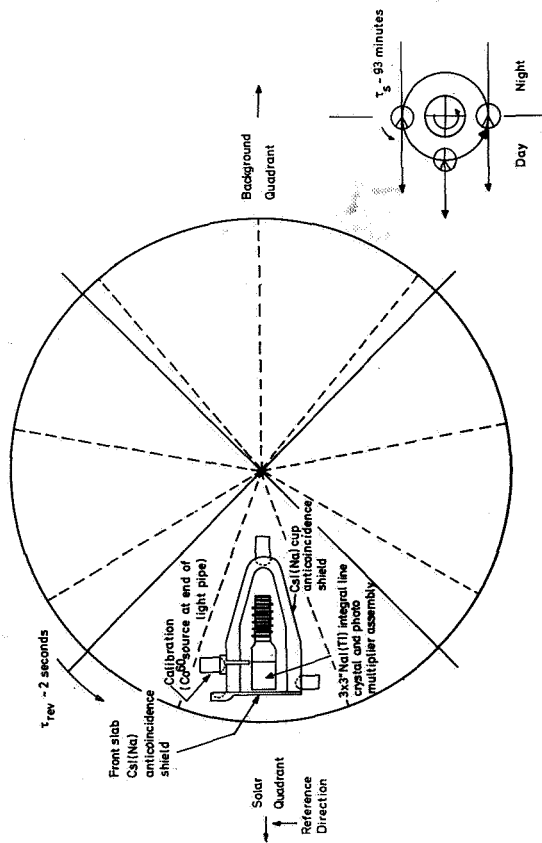
Figure 2. A schematic drawing of the gamma ray spectrometer is shown with the OSO wheel in the position for viewing the sun. The solar and background quadrant identifications are also shown. The small inset at the right shows satellite aspect at sunrise and at noon and at sunset.

The gamma ray monitor has an auxiliary X-ray detector, NaI (Tl) crystal of diameter 3.2 cm and thickness 0.6 cm, covering the energy range 7.5 to 120 keV in four steps. Figure 4 is a plot of the counting rate of X-ray Channel 4 (60 to 120 keV) versus time as recorded during the flare of August 4. Also plotted in Figure 4 are the counting rates (above the continuum) of the line features 0.5 MeV and 2.2 MeV as a function of universal time.
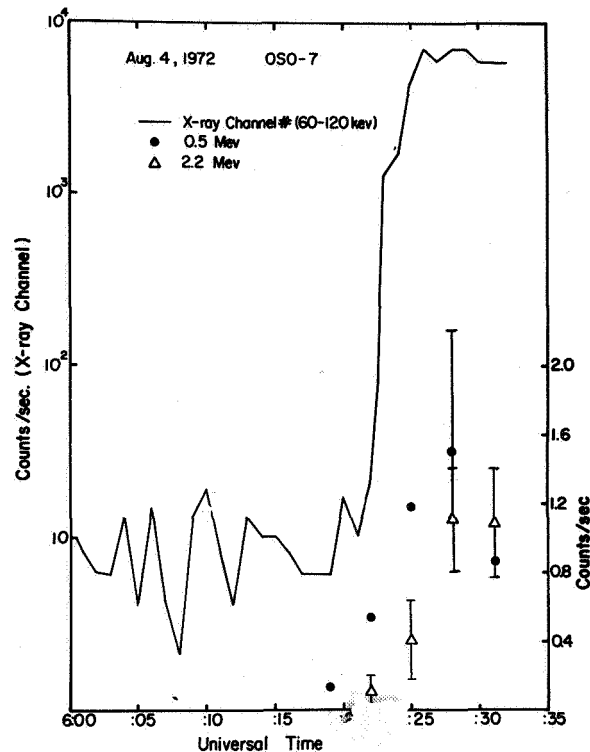
Figure 4. The August 4, 1972, time profile for the counting rate in one X-ray channel (60 to 120 keV) is shown covering the period of satellite day from about 20 minutes before the optical onset until the satellite went into eclipse. Also shown are the time profiles for the counting rates in the five channels corresponding to gamma ray lines at 0.5 MeV and 2.2 MeV. (Preliminary data from OSO-7.)

In addition to the discrete line emission, we also observe significant enhancement of gamma ray radiation over the energy range 0.4 to 8 MeV. This is shown in Figure 5 where the average differential spectra (solar and background quadrants) measured during the rising phase of the flare are plotted. Also shown in the figure is the quiet time solar spectrum recorded just before the onset of the flare. It can be seen from Figure 5 that the quiet time solar spectrum and the background spectrum are almost identical, while the solar spectrum measured during the flare shows significant enhancement in the continuum below the line features.
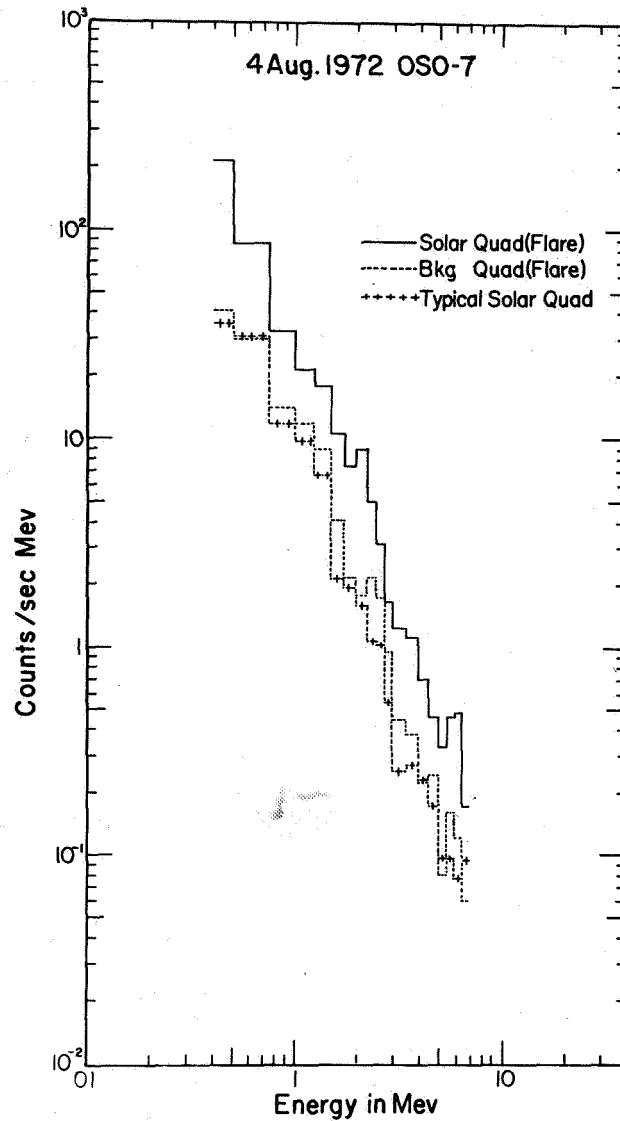
Figure 5. Differential pulse height spectra from OSO-7 (solar and background quadrants) observed during the 2B flare on August 4, 1972. The spectra were measured after the onset of the flare and cover the period 0623 to 0632 UT. Also shown is a typical solar quadrant spectrum taken just before the onset of the flare.

294

The interpretation of these observations implies production of discrete gamma ray lines by a variety of high energy processes taking place in the solar atmosphere. The probable sources of the gamma ray lines are positrons and neutrons produced in the nuclear reactions and high energy protons. Annihilation of positrons with electrons produces the 0.51 MeV annihilation line, while the 2.23-MeV line results from the capture of neutrons by the hydrogen atoms. Inelastic scattering of fast protons on the less abundant, C, N, O, and Ne nuclei produce a large number of weaker deexcitation gamma ray lines: 4.43 MeV (C^{12}*) and 6.13 MeV (O^{16}*) are likely to be the most prominent. We believe that the line features we observe in the 2B Hα flare are the annihilation line (0.51 MeV), the neutron capture line (2.23 MeV) and the deexcitation lines of C^{12}* (4.43 MeV) and O^{16}* (6.13 MeV).

The enhanced continuum shows a large number of unresolved line features. At this stage we are not sure whether the continuum (particularly the high energy end) is due to electron bremsstrahlung or summation of unresolved line features.

It is appropriate to point out here that the gamma ray emission in solar flares could be of more complex character than has been assumed in the past (Lingenfelter and Ramaty, 1967). As discussed by Shima and Alsmiller (1970), the inelastic scattering of protons (50 MeV) on C^{12} produces a line at ∼2 MeV in addition to the 4.43 MeV line, while the 15 MeV protons on O^{16} yield prominent lines at ∼4.4 MeV and ∼5.2 MeV in addition to the 6.13 MeV line. Thus the possibility that more than one source is contributing to the observed line features cannot be ruled out.

The 3B flare of August 7 provides additional evidence for the emission of 0.5 and 2.2 MeV in solar flares. The 3B flare began in Hα at ∼1500 hours UT (Preliminary Report SESC-PRF-Boulder 092, 093) when the OSO-7 satellite was behind the earth. Approximately 40 minutes after the onset of the flare, the satellite emerged into sunlight, and enhanced counting rates in the spectral regions around ∼0.5 and 2.2 MeV were observed. Figure 6 is a plot of the counting rate spectra measured during the onset (nighttime) and declining phase (daytime) of the flare. The first solar spectrum measured after the commencement of the satellite day shows enhancement in the regions corresponding to the photon energies of 0.5 and 2.2 MeV. Although the enhancement is not as large as observed for the August 4 event, but since it appears only in the solar spectrum, it can be argued that it could not arise due to local satellite or atmospheric effects.

The enhancement in the background quadrant ∼0.5 MeV region in the upper spectrum of Figure 6(a) is perhaps genuine. During this time the detector was looking at the earth with good aspect and picked up 0.51 MeV annihilation radiation from the atmosphere.

Table 2 lists tentative fluxes at the Earth for the gamma ray lines observed during the flares of August 4 and 7.

In conclusion, it is clear that the gamma ray production expected during the solar flares has now been observed, and in addition, the presence of simultaneous neutron production is indirectly confirmed through the observation of the 2.2-MeV gamma ray line. When taken
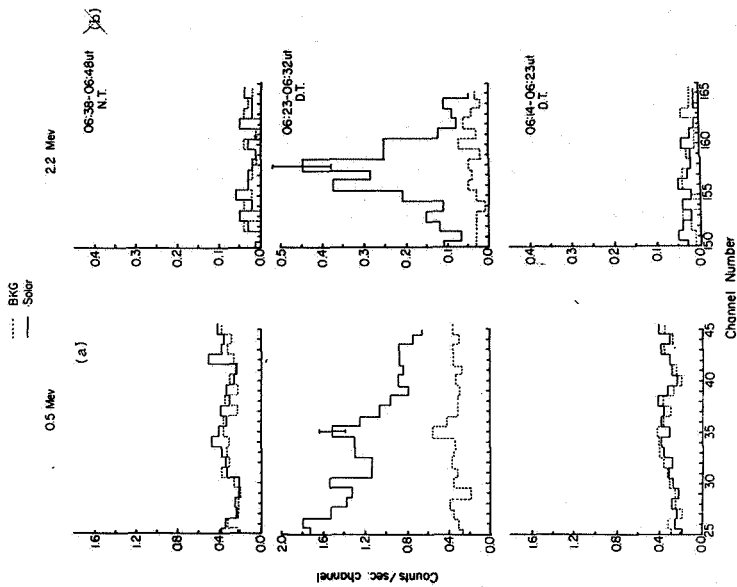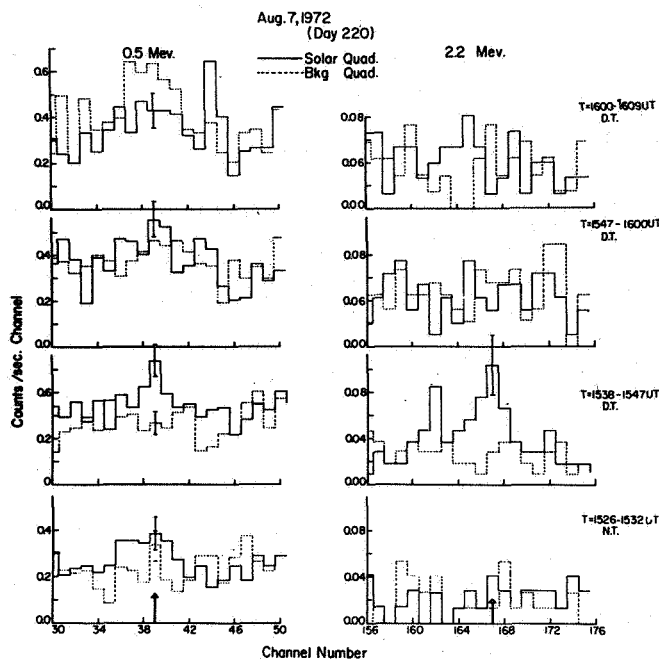
Figure 6. The gamma ray pulse height spectrum is shown for the energy regions 440 to 610 keV and 2.1 to 2.4 MeV on August 7, 1972. The lower spectrum was taken at nighttime just before the satellite sunrise, but while the 3B optical flare was in progress. The second spectrum from the bottom was taken just after the sunrise calibration and during the declining phase of the optical flare. The top two spectra were taken at later times in the same orbit during the satellite daytime. The accumulation time intervals are shown for each spectrum.

Table 2

Tentative Designations and Preliminary Solar Flux at 1 AU

Associated Flare and Time of Observations	Flux (photons · cm⁻²s⁻¹)			
	0.5 MeV	2.2 MeV	4.4 MeV	6.1 MeV
2B (Hα) Aug. 4, 1972 0623 to 0632 UT (Before Hα Max)	$(7 \pm 1.5) \times 10^{-2}$	$(2.2 \pm 0.2) \times 10^{-1}$	$(3 \pm 1) \times 10^{-2}$	$(3 \pm 1) \times 10^{-2}$
3B (Hα) Aug. 7, 1972 1538 to 1547 UT (After Hα Max)	$(3.4 \pm 1.1) \times 10^{-2}$	$(4.6 \pm 1.3) \times 10^{-2}$	$<1.5 \times 10^{-2}$	$<1.5 \times 10^{-2}$

296

with correlated observations of the other radiations emitted during the flare, we believe these gamma ray observations have opened a new dimension into the study of the overall solar flare and solar cosmic ray phenomena.

THEORETICAL IMPLICATIONS

In view of the lack of any believable positive results prior to August 1972, concerning solar neutrons or solar gamma ray fluxes, it had become increasingly evident that some revision was necessary in the simple models describing neutron and gamma ray production in the solar atmosphere. Essentially all the model calculations assumed an isotropic release of accelerated particles into the solar atmosphere. This model gives the largest yield of gamma rays and neutrons, but Lingenfelter and Ramaty (1967) have also considered the production during acceleration in a low density medium where the yield is relatively low. From the failure to detect either gamma rays or neutrons during any solar activity since 1960, it is at least necessary to conclude that the isotropic-release model for solar protons is untenable. This conclusion is supported most strongly by the work of Kirsch (1972).

Until the August 1972 solar flares, there had not been a good opportunity to test the preflare acceleration ideas of Elliot (1969). With the observation of strong emission of gamma ray lines during the rise of the August 4 event, it is likely the particle acceleration also occurred during this time. Since the data now exists from the OSO-7 experiment, a careful search will be made to see if there is any evidence for preflare acceleration of protons during the whole activity period from August 2 to August 12; therefore, a definitive answer on the Elliot model should be soon forthcoming.

Several interesting inferences are now available from the OSO-7 observations. From the time profile of the 0.5 and 2.2 MeV lines shown in Figure 4, we can put an experimental upper limit on the acceleration time for solar protons during the flare of August 4. Since the time resolution of the instrument for the gamma lines is 3 minutes, one can see that the 0.5-MeV radiation rises to its maximum in no longer than about 10 minutes and it could be shorter. Unfortunately, the statistics are not good enough on the 4.4- and 6.1-MeV lines to plot a time-profile curve. Such lines should show a time profile that is exactly that of the protons, since these are prompt reemissions. Further analysis of this data may improve this.

From elementary considerations we may also estimate the flux of protons at the sun required to produce the observed gamma ray intensity, assuming protons are released toward the photosphere. This is most easily done using the measured intensity of the 4.4- and 6.1-MeV gamma ray lines, since they are predominantly produced by protons in the energy range $E_p \sim 10$ to 50 MeV where the excitation cross section is significant. The basic process giving rise to the gamma rays is inelastic scattering: the protons on C^{12} populate the first excited state at 4.4 MeV, followed by prompt deexcitation of the excited nucleus, with a characteristic emission line at 4.4 MeV. This process is denoted as C^{12} (P, P^1, γ) and source strength, S, at the sun may be expressed as

$$S\left(\frac{\text{gammas}}{s}\right) = N\,(n_i t)\,\sigma$$

where N is the number of protons per second incident on the solar atmosphere, $(n_i t)$ is the thickness of the target measured in the number of carbon nuclei cm^{-2}, and σ is the average inelastic excitation cross section over the energy range 10 to 50 MeV. The target area density $(n_p t)$ may be expressed as

$$(n_i t) = f_c R/m_p$$

where f_c is the fractional solar atmospheric atomic abundance of carbon relative to hydrogen $\sim 5.3 \times 10^{-4}$, R is proton range in hydrogen for 50 MeV protons, and m_p is the proton mass (grams).

The source strength obtained from the observed flux is $S(4.4) \sim 10^{26}$ photons per second emitted isotropically from the sun. Using this result, $R(50\ MeV) = 1\ g \cdot cm^{-2}$ and $\sigma(4.4) \sim 1.2 \times 10^{-25}\ cm^2$, the proton current in the solar atmosphere is $N \cong \times 10^{30}$ protons per second. This means that over approximately the 1000 seconds the main burst lasted, about 2×10^{33} protons of energy 10 to 50 MeV were impinging into the denser solar atmosphere.

Deuteron production in the solar atmosphere from neutron capture may also be estimated from the observed flux of 2.2 MeV photons which also gives directly the production rate of such photons on the sun. Since this production rate is the capture rate of neutrons, it is also the production rate of deuterons by this source, and for the observed flux of 2×10^{-1} photons $cm^2\ s^{-1}$, we find $\sim 6 \times 10^{26}$ deuterons produced per second by neutron capture. This is undoubtedly a very small source of deuterons since many more must be produced in the He breakup reactions which produced the neutrons in the first place (Lingenfelter and Ramaty, 1967).

Further analysis of the OSO-7 solar events will be required before we can be sure of final conclusions and interpretations. One of th   incipal goals of further analysis is to determine if nuclear line emission is only observable in very large events or if they are more frequent and their frequency correlated with the frequency of the larger (X class) X-ray bursts. In addition, the gamma ray spectra will have to be studied very carefully for evidence for Doppler line shift or broadening. Finally, by correlating with solar proton observations, we hope to learn more about the spectrum of the protons accelerated at the sun.

CONCLUSION

Since the prediction of solar flares is still a somewhat shaky art, it is clearly advisable to keep gamma ray monitoring experiments continuously in space as the solar cycle advances. Without question it is also possible to greatly improve on the present instruments with the capabilities of existing spacecraft. The most desirable detector improvements that should be made are background reduction, increased sensitivity, and improved energy and time resolution, all of which are easily attainable.

ACKNOWLEDGMENT

REFERENCES

Alsmiller, R.G., Jr. and Boughner, R.I., 1968, *J.G.R.* 73, 4935.

Apparao, M.V.K., Daniel, R.R., Vijayalakshmi, B., and Bhatt, V.L., 1966, *J.G.R.*, 71, 1781.

Burtis, D.W., Aalami, D., Evelyn-Veere, R.H., and Sarkady, A., *IEEE Trans. Nucl. Sci.* NS-19, 613.

Chupp, E.L., 1971, *Space Sci. Rev.* 12, 486.

Chupp, E.L., Forrest, D.J., Higbie, P.R., Suri, A.N., Tsai, C., and Dunphy, P.P., 1973, *Nature* 241, 333.

Cortellessa, P., Benedetto, D.P., and Paizis, C., 1971, *Solar Phys.* 20, 474.

Daniel, R.R., Joseph, G., Lavakare, P.J., and Sunderrajan, R., 1967, *Nature* 213, 21.

Daniel, R.R., Gokhale, G.S., Joseph, G., and Lavakare, P.J., 1971, *J.G.R.* 76, 3152.

Elliot, H., 1969, in *Solar Flares and Space Research*, ed: C. De Jager and Z. Švestka (Amsterdam: North Holland Publ. Co.), 356.

Eyles, C.J., Linney, A.D., and Rochester, G.K., 1972, *Solar Phys.* 24, 483.

Forrest, D.J. and Chupp, E.L., 1969, *Solar Phys.* 6, 339.

Higbie, P.R., Chupp, E.L., Forrest, D.J. and Gleske, I.U., 1972, *IEEE Trans. Nucl. Sci.* NS-19, 606.

Hirasima, Y., Okudaira, K., and Yamagami, T., 1970, *Acta Phys. Hung.* 29, Suppl. 2, 683.

Holt, S.S., 1967, *J.G.R.* 72, 3507.

Joseph, G., 1970, thesis (Univ. of Bombay, India).

Kirsch, E., 1972, *Solar Phys.* (to be published).

Kondo, I. and Nagase, F., 1969, in *Solar Flares and Space Research*, ed. C. De Jager and Z. Švestka (Amsterdam: North Holland Publ. Co.), 134.

Leavitt, C.P., Robb, D.S., and Young, F., 1972, *Bull. Amer. Phys. Soc.* 17, 687.

Lingenfelter, R.E., and Ramaty, R., 1967, in *High Energy Nuclear Reactions in Astrophysics,* ed: B.S.P. Shen (New York: W.A. Benjamin Press), 99.

Lockwood, J.A., Ifedili, S.O. and Jenkins, R.W., 1972, *Solar Phys.* (in press).

Shima, Y. and Alsmiller, R.G., Jr., 1970, *Nucl. Sci. Eng.* **41**, 47.

Sood, R.K., 1972 *Solar Phys.* **23**, 183.

NUCLEAR GAMMA RAYS FROM SOLAR FLARES

R. Ramaty
Laboratory for High Energy Astrophysics
Goddard Space Flight Center

R. E. Lingenfelter
Institute of Geophysics and Planetary Physics
University of California, Los Angeles

ABSTRACT

The theory of gamma-ray line emission from solar flares is reviewed and revised. It is shown that the recently observed (Chupp et al., 1972) line emissions at 0.5, 2.2, 4.4, and 6.1 MeV are due to positron annihilation, deuterium deexcitation following neutron capture on hydrogen, and the deexcitation of excited states in carbon and oxygen. From the observed relative line intensities it is possible to determine the spectrum of accelerated protons in the flare region. This spectrum is found to be very similar to that of charged particles from the flare observed near earth. The total numbers of protons at the sun is deduced from the observed absolute line intensities for various interaction models. It is found that if the protons at the sun have a spectrum which is an exponential in rigidity, the total energy in protons is a few times 10^{28} ergs if the gamma rays are produced by protons moving down into the sun, and about 10^{30} ergs if the g ⁓ a rays are produced at the site of the acceleration.

INTRODUCTION

Solar gamma-ray line emissions at 0.5, 2.2, 4.4, and 6.1 MeV were detected during the flare of August 4, 1972, by a gamma-ray monitor flown on orbiting Solar Observatory-7 (OSO-7) (Chupp et al., 1972). Line emissions at 0.5 and 2.2 MeV were also detected on August 7, 1972, but only upper limits could be set on the 4.4 and 6.1 MeV lines from this flare. In previous papers (Lingenfelter and Ramaty, 1967; Cheng, 1972), the theory of nuclear reactions in solar flares was treated in detail, and predictions were made as to the expected fluxes of gamma rays and high energy neutrons at earth from such reactions at the sun. Following the discovery by Chupp et al. we have reviewed and updated these calculations including more recent nuclear cross sections. By comparing the predicted emissions with the observations, we can show that the observed lines at 0.5, 2.2, 4.4, and 6.1 MeV are produced, respectively, by positron annihilation, deuterium deexcitation following neutron capture on hydrogen, and the deexcitation of the first nuclear levels of C^{12} and O^{16}. Furthermore, from the comparison of the calculated and observed line intensities we can

deduce the spectrum of the accelerated particles at the sun, independent of the assumed interaction model. The total number of accelerated particles required to produce the observed line emission, however, does depend on this model. In the subsequent treatment we shall use two limiting models: a thick-target model in which the accelerated particles move from the flare region downwards into the sun, undergoing nuclear interactions as they slow down in the solar atmosphere; and a thin-target model in which the spectrum of accelerated particles is not modified during the time in which the nuclear interactions take place. The latter model assumes that either the total path length traversed by the particles at the sun is small in comparison with their interaction length, or that the particle energy loss from ionization and nuclear interactions is just balanced by energy gains from acceleration.

We have recalculated the fluxes of various gamma-ray lines expected from accelerated particle interactions in solar flares: at 0.511 MeV from positron annihilation, at 2.23 MeV from neutron capture on hydrogen, and at 1.63, 1.99, 2.31, 4.43, 5.5, and 6.14 MeV from deexcitation of nuclear levels in C, O, N, and Ne. These calculations are based on an ambient solar composition given by $H:He:C:N:O = 1:10^{-1}:5.3 \times 10^{-4}:10^{-4}:9.2 \times 10^{-4}$ (Cameron, 1967), and an accelerated particle population consisting of protons with spectrum

$$N(P) = P_o^{-1} \exp(-P/P_o) \tag{1}$$

Here P is rigidity, P_o is a characteristic rigidity which we treat as a free parameter, and N(P) is the total number of protons per unit rigi* In the calculations N(P) is normalized at the sun to one particle of rigidity greater than zero.

For the thick-target model, the yield of secondaries from a particular type of interaction is given by

$$Q_s = \eta \int_0^\infty dP \ N(P) \int_0^x dx' \ \sigma(P') \ \exp(-(x-x')/L) \tag{2}$$

where η is the number of target atoms per gram of solar material, σ is the cross section as a function of rigidity, and x and L are the stopping range and nuclear interaction length of protons of rigidity P (both measured in g cm^{-2}). This yield has the units of secondaries per incident proton of rigidity greater than zero.

For the thin-target model, the instantaneous production rate of secondaries from the same type of interaction is

$$q_s = n \ c \int_0^\infty dP \ N(P) \ \beta \ \sigma(P) \tag{3}$$

302

where n is the number density of the ambient solar material in cm^{-3}, and $c\,\beta$ is the velocity of a proton of rigidity P. The units of q_s are secondaries per second per proton of rigidity greater than zero.

PHOTON PRODUCTION

Line emission at 0.511 MeV is produced from the annihilation of positrons. The principal source of positrons in solar flares is nuclear reactions of accelerated particles with the ambient solar atmosphere. These reactions produce π^+ mesons and a variety of radioactive isotopes which decay by positron emission. The main positron emitters, their formation reactions, threshold energies, half-lives and maximum positron energies are given in Table 1. Except for the reactions N^{14} (p,n) O^{14} (Andouze et al., 1967) and N^{14} (p,α) C^{11} (Jacobs et al., 1972), the cross sections for these reactions were given in Lingenfelter and Ramaty (1967). The resultant positron yields are given in Figures 1 and 2, for the thick- and thin-target models respectively.
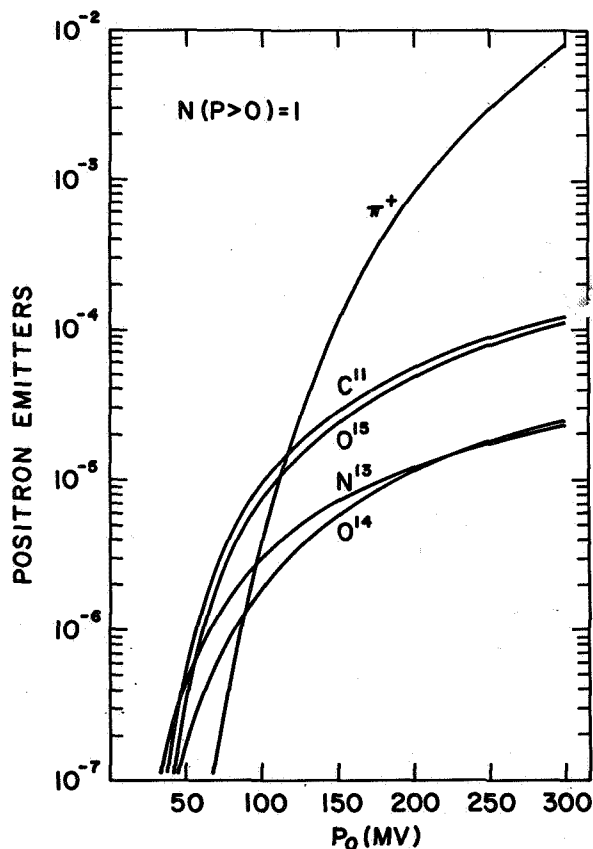
Figure 1. Yield of positron emitters at the sun for the thick-target model.

The intensity of the 0.511 MeV line depends on the number of positrons that annihilate at the sun. For the thick-target model it is reasonable to assume that all the flare produced positrons will ultimately annihilate at the sun. For the thin-target model, however, it is possible that a significant fraction of the positrons will escape from the sun before they annihilate. The determination of this fraction, however, is beyond the scope of the present paper and we defer the discussion on this for future research. For simplicity, in the subsequent calculations we assume that all flare-produced positrons annihilate at the sun, but keep in mind that this assumption may lead to too many 0.511 MeV photons in the case of the thin-target model.

The annihilation radiation yield at 0.511 MeV also depends on the mode of positron annihilation. Positrons annihilate either directly with a free electron or in a bound state of positronium. In the latter case, the annihilations proceed from

303

Table 1
Positron Emitters

$\beta+$ Emitter and Decay Mode	Maximum Positron Energy, MeV	Half-life (min)	Production Mode	Threshold Energy, MeV
$C^{11} \rightarrow B^{11} + \beta^{+} + \nu$	0.97	20.5	C^{12} (p,pn) C^{11}	20.2
			N^{14} (p,2p2n) C^{11}	13.1
			N^{14} (p,α) C^{11}	2.0
			O^{16} (p,3p,3n) C^{11}	28.6
$N^{13} \rightarrow C^{13} + \beta^{+} + \nu$	1.19	9.96	N^{14} (p,pn) N^{13}	11.3
			O^{16}(p,2p,2n) N^{13}	5.54
$O^{14} \rightarrow N^{14} + \beta^{+} + \nu$	1.86	1.18	N^{14}(p,n)O^{14}	6.4
$O^{15} \rightarrow N^{15} + \beta^{+} + \nu$	1.73	2.07	O^{16}(p,pn)O^{15}	16.54

a ^{1}S state leading to two 0.511-MeV photons, or from a ^{3}S state leading to a 3-photon continuum. Since the 3-photon continuum does not contribute to line emission at 0.511 keV, and because the probability of forming the ^{3}S state is three times that of the ^{1}S state, positronium formation and its annihilation produces on the average only one-half of a 0.511-MeV photon per positron as compared to two photons for free annihilation. This point was discussed in detail by Stecker (1969) for positron annihilation in interstellar space. However, in the much higher density and temperature of the solar atmosphere, we do not expect that positrons will annihilate from the ^{3}S state of positronium, because the collision frequency of positronium with ambient electrons is sufficiently high either to dissociate the positronium, or to cause a transition to the ^{1}S state before the annihilation of the ^{3}S state. By allowing two photons per positron at the sun, the time-integrated 0.511-MeV line intensity at earth for the thick-target model is

Figure 2. Production rate of positron emitters at the sun for the thin-target model.

$$F(0.511) = \frac{1}{2\pi R^2} [Q_s (\pi^+) + Q_s (C^{11}) + Q_s (N^{13}) + Q_s (O^{14}) + Q_s (O^{15})] \qquad (4)$$

where the various Q_s's are given in Figure 1. The units of F are photons cm^{-2} per proton of rigidity greater than zero. For the thin-target model we obtain an equation similar to (4), with F and Q_s replaced by the instantaneous rates ϕ and q_s. The units of ϕ are photons cm^{-2} s^{-1} per proton of rigidity greater than zero. The resultant 0.511-MeV photon fluxes are given in Figures 3 and 4, for the thick- and thin-target models respectively.

Next we consider the 2.23-MeV line resulting from the deexcitation of deuterium following neutron capture on hydrogen. The principal neutron-producing reactions and their cross

Figure 3. Time integrated photon fluxes at earth in
the thick-target model.

sections were discussed in Lingenfelter
and Ramaty (1967) and references there-
in. To these reactions we have added the
reaction N^{14} (p,n) O^{14} mentioned pre-
viously, which is important for low en-
ergy protons ($<$ 15 MeV). The neutron-
producing reactions are summarized here:

Reaction	Threshold Energy Mev/Nucleon
H^1 (p,nπ^+) H^1	292.3
He^4 (p,pn) He^3	25.9
He^4 (p,2pn) H^2	32.8
He^4 (p,2p2n) H^1	35.6
C^{12} (p,n...	19.8
N^{14} (p,n...	6.3
O^{16} (p,pn...	16.5
Ne^{20} (p,pn...	17.7

The total neutron yields for the thick-
and thin-target models are then obtained
by using the appropriate cross sections in Equations (2) and (3). Having obtained the neu-
tron yields, we have to consider the propagation of neutrons in the solar atmosphere, since
2.23-MeV photons are not produced if the neutrons escape from the sun or decay in the
solar atmosphere.

Neutron propagation in the solar atmosphere is determined predominantly by scattering
(elastic and inelastic) and capture by protons. The total neutron-proton scattering cross
section σ_s is essentially constant at 20 barns for neutron energies from 1 eV to 10^5 eV,
and then drops to about 0.1 barn at 100 MeV (Hughes and Schwartz, 1958). The capture
cross section is inversely proportional to velocity and is given by $\sigma_c \simeq 2.2 \times 10^{-6} \beta^{-1}$,
where σ_c is measured in barns and $c\beta$ is the velocity of the neutron. Since for all energies
of interest $\sigma_s \gg \sigma_c$, the neutron mean free path in the solar atmosphere is determined
principally by neutron-proton scattering. Using the columnar density of the solar atmos-
phere as given by Allen (1963), we find that a 10-MeV neutron moving radially outward

from the sun will probably escape from the solar atmosphere before making even one collision, if it is produced in a region of density less than 10^{17} cm^{-3}. This density corresponds to a depth of about 300 km below the base of the chromosphere. Since solar flares occur in the chromosphere or corona, it is reasonable to assume that for both interaction models, all upward moving neutrons are going to escape from the sun. The downward moving neutrons, on the other hand, decay or are captured, depending on whether the capture time is greater or smaller than the half-life of the neutrons. From the capture cross section σ_c, the capture time t_c is given by

$$t_c = (c\beta n\sigma_c)^{-1} \simeq \frac{1.5 \times 10^{19}}{n\,(cm^{-3})}\ s \qquad (5)$$

Figure 4. Instantaneous photon fluxes at earth in the thin-target model.

As can be seen, t_c is independent of energy and is inversely proportional to the density n of the region where the neutrons interact with the ambient medium. From the preceding discussion it follows that downward directed neutrons probably will not collide with the ambient gas till they reach the photosphere, where n is of the order 10^{17} cm^{-3}. Thus $t_c \simeq 150$ seconds and since the half-life of the neutron is 720 seconds, it follows that most of the neutrons will be captured before they decay. Furthermore, since the neutron capture occurs at a columnar depth of about 10^{24} cm^{-2} or 1.6 g cm^{-2}, while the stopping range of a 2.2-MeV photon is about 25 g cm^{-2}, all the upward moving photons resulting from deuterium deexcitation will escape from the sun. Assuming isotropic production of neutrons in the interaction region, the 2.23-MeV line intensities at earth, for the thick- and thin-target models, respectively, are:

$$F (2.23) = \frac{1}{4\pi R^2}\ \frac{1}{2} Q_s\,(n) \qquad (6)$$

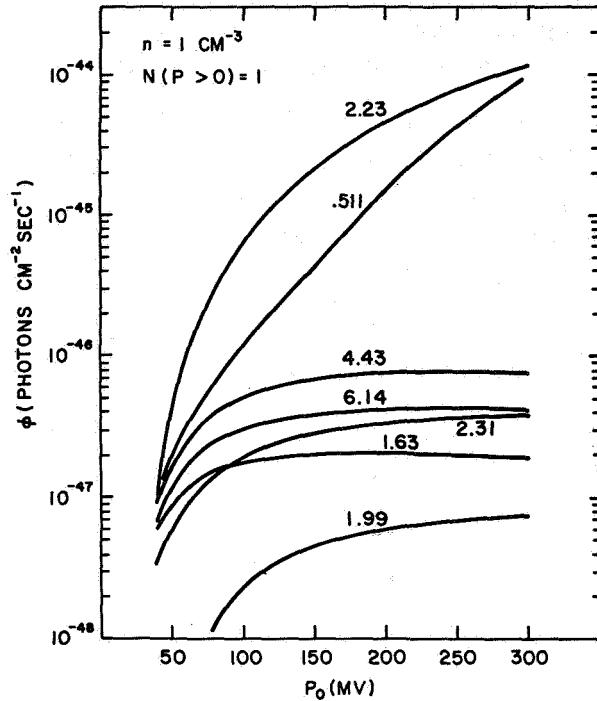$$\phi (2.23) = \frac{1}{4\pi R^2}\ \frac{1}{2}\ q_s\,(n) \qquad (7)$$

where $Q_s(n)$ and $q_s(n)$ are the total neutron yields as calculated from Equations (2) and (3).

The calculations of the other intensities at 1.63, 1.99, and 2.31, 4.43, 5.5, and 6.14 MeV in Figures 3 and 4 is straightforward. Unlike the 0.511 and 2.23 MeV lines, these emissions are prompt, meaning that the excited states or secondary products decay by photon emission in a time scale much shorter than any characteristic time of the flare process.

Line emission at 4.43 and 6.14 MeV results from the deexcitation of the first nuclear levels of C^{12} and O^{16}, respectively. The intensity of the 6.14 MeV line is the same as calculated in Lingenfelter and Ramaty (1967). The intensity of the 4.43-MeV line is about 50 percent greater, because it is possible to produce $C^{12\,(4.43)}$ by the spallation of O^{16}, a process which Lingenfelter and Ramaty (1967) neglected. The calculations for this process given in Figures 3 and 4 are based on cross sections measured by Zobel et al. (1968).

Radiation at 2.31 MeV corresponds to the first nuclear level of N^{14} The 2.31-MeV line is produced by the direct excitation of the first and second levels of N^{14} The latter is at 3.94 MeV and it deexcites 96 percent of the time through the first level, thereby producing a 1.63 photon in addition to the 2.31-MeV photon. In addition to direct excitation, the first level of N^{14} can also be populated by the decay of O^{14} which is produced by the reaction $N^{14}(p,n)O^{14}$. O^{14} beta decays 99.4 percent of the time to $N^{14\,(2.31)}$ and hence each beta decay is accompanied by a 2.31-MeV photon. As previously mentioned, the 1.63-MeV line is formed by the deexcitation of $N^{14\,(3.94)}$. In addition, this line is also produced by the deexcitation of the first level of Ne^{20}. Finally the 1.99-MeV line results from the deexcitation C^{11} which is formed from the spallation of C^{12}. The cross-section for this process is given by Zobel et al. (1968).

The principal reason for showing the 1.99- and 2.31-MeV lines is that for detectors of poor energy resolution these lines could in principle confused with the deuterium deexcitation line. As can be seen from Figures 3 and 4, however, the $C^{11\,(1.99)}$ MeV line is negligible in comparison with the deuterium line. On the other hand, the 2.31 MeV line from N^{14} could compete with the 2.23 MeV line at low P_0's. If all the emission at $\sim$2.2 MeV is from N^{14}, however, the intensities of the 4.43 MeV and 6.14 MeV lines should be about the same as that of the 2.2 MeV line. As will be discussed, this was not the case for the August 4, 1972 event. Therefore, for this flare at least, we conclude that the 2.2 MeV line is produced almost entirely by neutron capture.

We have summarized in Table 2 the principal mechanism leading to line emission in the solar atmosphere. In addition to the lines given in Figures 3 and 4, we have listed in Table 2 lines at 5.2 MeV from O^{15} and N^{15} and at 7.12 MeV from O^{16} From the cross sections of Zobel et al. (1968), the intensities of both these lines should be approximately 50 percent of the 6.14 MeV line intensity.

DISCUSSION

Let us now compare the results of our calculations with the observations of Chupp et al. (1972) for the August 4, 1972 flare. We defer the discussions on the August 7, 1972 observations, since the gamma rays from this flare were observed only after the flare maximum

Table 2
Gamma-Ray Line Emission Mechanisms.

Photon Energy (MeV)	Origin	Production Mode
0.511	Positron Annihilation	(See Table 1)
2.23	Deuterium deexcitation following neutron capture	(See listing of neutron producing reactions in section on photon production)
1.63	$Ne^{20}(1.63)$ deexcitation	$Ne^{20}(p,p') Ne^{20}(1.63)$
2.31	$N^{14}(3.94) \Rightarrow N^{14}(2.31)$ deexcitation	$N^{14}(p,p'_i) N^{14}(3.94)$
2.31	$N^{14}(2.31)$ deexcitation	$N^{14}(p,p') N^{14}(2.31)$
		$N^{14}(p,p') N^{14}(3.94) \Rightarrow N^{14}(2.31)$
		$N^{14}(p,n) O^{14} \Rightarrow N^{14}(2.31)$
4.43	$C^{12}(4.43)$ deexcitation	$C^{12}(p,p') C^{12}(4.43)$
5.2	$O^{15}(5.20)$ deexcitation	$O^{16}(p, \ ) O^{15}(5.20)$
	$N^{15}(5.28)$ deexcitation	$O^{16}(p, \ ) N^{15}(5.28)$
6.14	$O^{16}(6.14)$ deexcitation	$O^{16}(p,p') O^{16}(6.14)$
7.12	$O^{16}(7.12)$ deexcitation	$O^{16}(p,p') O^{16}(7.12)$

and hence they require a more detailed treatment of the time dependence of the gamma-ray intensities.

In Figures 5 and 6, the shaded areas represent the time-averaged ratios of the measured 0.5, 4.4, and 6.1 MeV line intensities to the measured 2.2 MeV line. The curves represent the calculated ratios as functions of the characteristic rigidity P_0, for the thick-target model in Figure 5 and the thin-target model in Figure 6. As can be seen, the calculated 4.43 and 6.14 curves are strong functions of P_0. Therefore, the comparison of these ratios with the measurements allows us to deduce the value of the characteristic rigidity P_0. We find that for both models P_0 has to be in the range 70 to 80 MV. This range of P_0's should be compared with values of P_0 as obtained from charged particle observations near earth.

According to Bostrom et al. (1972), the peak proton intensities after the flare of August 4, 1972 were: $J(> 10\ \mathrm{MeV}) = 10^6\ \mathrm{cm^{-2}s^{-1}}$, $j(> 30\ \mathrm{MeV}) = 2.6 \times 10^5\ \mathrm{cm^{-2}s^{-1}}$, and $j(> 60\ \mathrm{MeV}) = 8 \times 10^4\ \mathrm{cm^{-2}s^{-1}}$. From these intensities we can deduce the local proton density u in the interplanetary medium. If $u(P) \propto \exp(-P/P_0)$ and if the protons are nonrelativistic

$$u(>P) = j(>P)\ (mc/e)\ (P+P_0)^{-1} \tag{8}$$
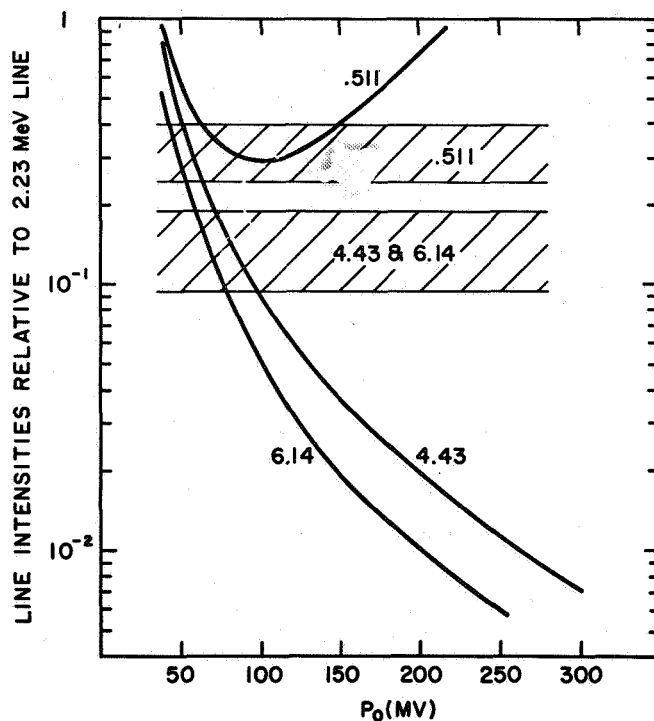
Figure 5. Relative line intensities for the thick-target model.
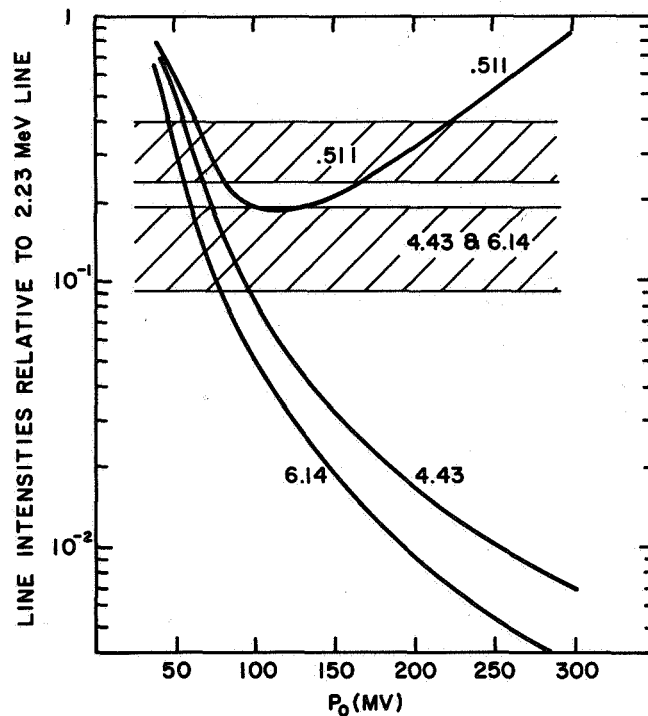
Figure 6. Relative line intensities for the thin-target model.

From (8) and the integral intensities j(> P) given above, we can calculate values of u(> P) for various P_o's. For P_o = 65 MV we obtain proton densities as follows: u(> 10 MeV) = 1.53 X 10^{-4}, u(> 30 MeV) = 2.67 X 10^{-5}, and u(> 60 MeV) = 6.13 X 10^{-6}. These numbers are plotted in Figure 7 as functions of P. The straight lines are exponentials in rigidity with P_o = 60 MV and P_o = 70 MW and they bracket the observed proton densities. The charged particle observations at the peak of the proton event are therefore consistent with a characteristic rigidity of about 60 to 70 MV. Furthermore, this characteristic rigidity remains essentially the same for the remainder of the particle event (J. King, private communication, 1972).

The similarity between the proton spectrum as observed near earth and the proton spectrum at the sun as deduced from the gamma-ray observations, seems to imply that, at least for the August 4, 1972 flare, both the escape of particles from the flare region and their propagation in the interplanetary medium are essentially independent of energy.

Let us now calculate the total number of protons at the sun. In the case of the thick-target model this calculation is independent of the ambient density n but requires the knowledge of the time-integrated photon flux from the flare. According to Chupp et al. (1972) the average intensity of the 2.2 MeV line from 0626 UT to 0632 UT on August 4, 1972, was 0.22 photons $cm^{-2}s^{-1}$ and thus the total photon flux in the 6 minute time interval was 80 photons cm^{-2}. This is only a lower limit because OSO-7 went into earth eclipse at 0632 before the termination of the gamma-ray event. The total gamma-ray flux, however, was probably not much larger, since as indicated by the microwave data (Toyokawa Observatory,
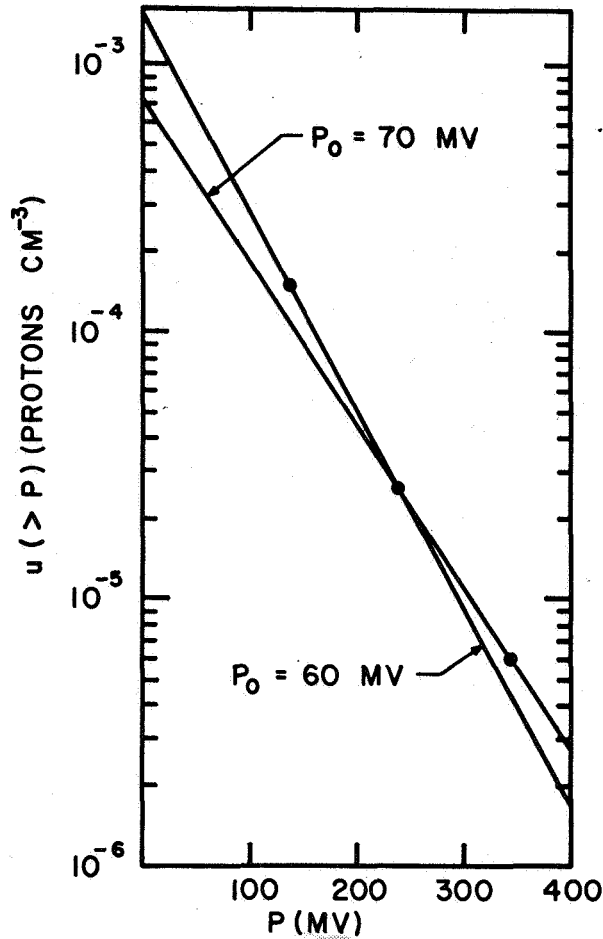
Figure 7. Proton densities in the interplanetary medium
from local particle measurements.

private communication, 1972), the acceleration of the charged particles probably ceased at 0635 UT, 3 minutes after the eclipse of OSO-7.

For a flux of 80 photons cm^{-2} and P_0 ranging from 60 MV to 70 MV, we find from Figure 3 that $N(> P)$ is between 1.4 and 6×10^{33} These numbers should be compared with the number of protons released from the flare based on measurements of the proton flux near earth. This number can be obtained from the local densities shown in Figure 7 if we assume that the particles fill some volume V in the interplanetary medium to that density. A conservative estimate of this volume would be to assume that it is a cone of opening angle 30° with vertex at the sun and height 1.5 AU. This is consistent with the fact that the August 4 flare was located at 15° N latitude on the sun, and that some charged particles were observed on the Pioneer-10 space probe at 2 AU from the sun (B.J. Teegarden, private communication, 1972). The volume V is therefore ~ 10^{39} cm^3 and from Figure 7, $N(> P)$ is 7×10^{35} and 1.5×10^{36} for P_0 equal to 70 MV and 60 MV respectively. When compared with the values of $N(P > 0)$ deduced above from the gamma-ray observations for the thick-target model, we

312

see that possibly not more than about 1 percent of the flare-accelerated protons could have escaped downward into the sun. However, we should note that this conclusion is strongly dependent on our estimate of the total number of protons at the sun based on the local proton observations. Clearly a more detailed understanding of the source function of flare protons in the interplanetary medium is required.

In the case of the thin-target model, the instantaneous photon flux at earth directly determines the emission measure at the sun, that is, the product $nN(P > 0)$. From Figure 4 we find that the observed flux of 0.22 photons $cm^{-2} s^{-1}$ implies that nN is 1 to $2 \times 10^{45} cm^{-3}$ for P_0 ranging from 70 MV to 60 MV. Then using the values of $N(P > 0)$ as deduced from the proton flux near earth, we get $n = 1.5$ to $3 \times 10^9 cm^{-3}$. As before, note that this density is subject to the uncertainty in the total number of protons at the sun obtained from the local observations.

Let us finally evaluate the total energy in the flare-accelerated protons that produce gamma rays at the sun. For the spectrum given in (1) and nonrelativistic protons, the average proton energy is P_0^2/Mc^2. Therefore, for the thick-target model, the energy in the 1.4 to 6×10^{33} protons as deduced above is 1.2 to 3.7×10^{28} ergs.

For the thin-target model, both the instantaneous gamma-ray production rate and the instantaneous proton energy loss rate depend on the product of the ambient density n and the total number of protons at the sun. The ratio of these two rates, therefore, is independent of both n and N and depends only on the spectrum of the accelerated particles, P_0 in our calculations. This point was first made by Lingenfelter (1969). For the proton distribution in (1) normalized to one proton of rigidity greater than zero, the instantaneous energy loss rate W to ionization, excitation, and nuclear interactions in ambient hydrogen of unit density is:

P_0(MV)	W(erg s^{-1})
20	2×10^{-18}
30	2×10^{-18}
40	1.9×10^{-18}
60	1.8×10^{-18}
80	1.6×10^{-18}
100	1.5×10^{-18}
120	1.4×10^{-18}
200	1.2×10^{-18}
300	1.1×10^{-18}

As can be seen, for P_0's between 60 to 70 MV, W is very closely equal to 1.7×10^{-18} ergs s^{-1}. Using the values of Nn given above, we see that gamma-ray production by flare accelerated protons is accompanied by the dissipation of 1.7 to 3.4×10^{27} ergs s^{-1}. For the time

interval of 6 minutes during which gamma rays were observed, the total dissipated energy is 0.6 to 1.2×10^{30} ergs.

This energy is comparable to the total of $\sim 2 \times 10^{30}$ ergs emitted in Hα by the flare of August 4, 1972 (H. Zirin, private communication, 1972) and is consistent with the suggestion of Gordon (1954) that the optical energy from flares results from ionization losses of accelerated particles. On the other hand, in the thick-target model, the ionization losses of the gamma-ray producing protons is only a few percent of the observed optical energy; in this case additional energy loss may be expected from electrons.

REFERENCES

Allen, C.W., 1963, *Astrophysical Quantities*, Athlone Press, London.

Audouze, J., Ephere, M., and Reeves, H., 1967, *High-Energy Nuclear Reactions in Astrophysics*, ed. by B.S.P. Shen, W.A. Benjamin, New York, 255.

Bostrom, C.O., Kohl, J.W., and McEntire, R.W., 1972, *The Solar Proton Flux—August 2-12, 1972* (The Johns Hopkins University, Applied Physics Laboratory).

Cameron, A.G.W., 1967, *Origin and Distribution of Elements*, ed. by L.H. Ahrens, Pergamon Press, London.

Cheng, C.C., 1972, *Space Sci. Rev.* 13, 3.

Chupp, E.L., Forrest, D.J., Higbie, P.R., ~ ~ ~, A.N., Tsai, C., and Dunphy, P.P., 1972, *Nature* (in press).

Gordon, I.M., 1954, *Dokl. Akad. Nauk SSSR* 96, 813.

Hughes, D.J. and Schwartz, R.B., 1958, *Neutron Cross Sections*, Brookhaven National Laboratory, Upton, New York.

Jacobs, W.W., Bodansky, D., Cameron, J.M., Oberg, D., and Russo, P., 1972, *Bull. Amer. Phys. Soc.* 17, 479.

Lingenfelter, R.E. and Ramaty, R., 1967, *High-Energy Nuclear Reactions in Astrophysics*, ed. by B.S.P. Shen, W.A. Benjamin, New York, 99.

Lingenfelter, R.E., 1969, *Solar Phys.* 8, 341.

Stecker, F.W., 1969, *Astrophys. Space Sci.* 3, 479.

Zobel, W., Maienschein, F.C., Todd, J.H., and Chapman, G.T., 1968, *Nuc. Sci. Eng.* 32, 392.

SOLAR FLARE ACCELERATED ISOTOPES OF HYDROGEN AND HELIUM

J.D. Anglin, W.F. Dietrich, and J.A. Simpson

Enrico Fermi Institute and Department of Physics
University of Chicago

ABSTRACT

This paper reports new measurements of solar flare hydrogen, deuterium, tritium, helium-3, and helium-4 in the energy range $\sim$ 10 to 50 MeV per nucleon obtained with University of Chicago instrumentation on the IMP-4 and IMP-5 satellites, and discusses studies based on these results which place several constraints on theories of solar flare particle acceleration. A brief review of previous work and the difficulties in studying the rare isotopes of hydrogen and helium is also included. Particular emphasis is placed on the fact that the information to be obtained from the solar flare products of high energy interactions is not available through either solar wind observations where both the acceleration mechanism and the coronal source of the nuclear species are different, or optical measurements of solar active regions. The principal results are:

- Helium-3 has been separated clearly from helium-4 in large flares. For example, in the energy range 10 to 50 MeV per nucleon, the abundance ratio for the flare of November 2, 1969 is $\Gamma(^3\text{He}/^4\text{He}) = (7.7 \pm 2.0) \times 10^{-2}$.

- The ratio $\Gamma(^3\text{He}/^4\text{He})$ from these events is approximately one to two orders of magnitude above probable ambient solar atmos ric values, and must be the consequence of production by high energy interactions rather than from the ambient ^3He arising from the burning of ^2H in earlier stages of solar evolution.

- The measured upper limits for relative abundances of ^2H and ^3H are approximately a factor ten to fifty lower than earlier values and are consistent with expected yields based on the observed Γ ($^3\text{He}/^4\text{He}$).

- A self-consistent model leads to prompt secondary production in the chromosphere below $\sim$ 5000 km in $\sim$ 100 seconds by ^1H on ^4He (at rest) and ^4He on ^1H (at rest) interactions above the threshold energies of $\sim$ 25 to 30 MeV per nucleon. This process would dominate over all alternative mechanisms such as the preflare buildup of ^3He. Model calculations point to an acceleration mechanism continuously operative in the target gas in order to account for the observed high ^3He yields and energy spectra of the parent nuclei.

- A variation of at least a factor five from flare-to-flare is observed in Γ ($^3\text{He}/^4\text{He}$). This is expected from the variation in several flare parameters, including spectral shape of the parent nuclei, relative abundances of accelerated ^1H and ^4He, and the mean path length for nuclear interactions in the solar gas.

The paper raises several new questions that must be answered by future research. The value of solar neutron experiments based on the unique radial and energy dependence of neutrons decaying in the interplanetary medium is discussed.

INTRODUCTION

In recent years we have come to recognize the crucial relationship of high energy charged particles to nonequilibrium explosive phenomena on all astrophysical scales. We believe that by understanding the most accessible of these phenomena, namely the solar flare, we may find clues to the general problem of particle acceleration in astrophysics. However, even with the dramatic increase in the quality and kind of solar flare observations and theories reported in recent years, the basic mechanism remains obscure and continues to elude us. Fortunately, new channels for investigating particle acceleration are opening. Especially promising is the analysis of the products of accelerated protons and helium nuclei interacting with the solar gas. These products are principally gamma rays, positrons, neutrons, and the normally rare isotopes of hydrogen and helium, namely, deuterium, tritium, and helium-3. The known generic relationship of the H and He isotopes and a knowledge of the nuclear physics involved at solar flare energies make the study of these light isotopes especially attractive, since the predicted yields are highly model dependent. From a knowledge of the relative abundances and energy spectra of the H and He isotopes, it is possible to determine from model calculations:

- The mean path length in g/cm^2 of material traversed by particles observed at the orbit of earth at a given energy. This path length can be related to the mean density ρ of solar matter in the interaction region and the time interval during which particles traverse this material.

- The ambient abundances of ^2H, ^3H, and ^3He in solar active centers.

- The role of acceleration and particle storage at the sun in shaping the energy spectra of the isotopes.

These studies may also provide a fresh attack on the old puzzle of the greater than 100 to 1 variation in the abundance ratio of protons to helium-4 from flare to flare.

Lingenfelter and Ramaty (1967) have comprehensively reviewed the possible high energy nuclear reactions under solar flare conditions, and the experimental attempts through 1967 to obtain evidence for the products of nuclear reactions. By radiochemical analysis of material returned from the Discoverer-17 satellite, which was exposed to radiation from the solar flare of November 12, 1960, evidence was obtained for ^3He by Schaeffer and Zähringer (1962) and for ^3H by Fireman, DeFelice and Tilles (1961). However, only within the past few years has charged particle detection instrumentation in satellites made it feasible to attack these problems on a broad scale. Using data from the University of Chicago charged particle telescope on the satellite IMP-4, Hsieh and Simpson (1970) found that they could separate ^3He from ^4He and derive energy spectra for a group of seven solar

316

flares in 1967. They obtained a ratio of helium isotopes $\Gamma(^3He/^4He) = (2.1 \pm 0.4) \times 10^{-2}$ which was not only consistent with nuclear production in the solar atmosphere, but also consistent with the observed ambient solar chromospheric abundance ratios (Greenstein, 1951; Namba, 1965)*. Clearly the next step was to discover if there is experimental proof for the products of nuclear interactions in solar flares, or if the experiments are consistent only with the acceleration of ambient solar gas isotopes in solar active regions.

It is the purpose of this paper to report on new experimental studies on these questions and to discuss their implications for theories of solar flare acceleration mechanisms. Although this paper is not a complete review, we have included all the review references which, in turn, will guide the reader not acquainted with this topic to all that has been done up to the present. We emphasize that these are only the first primitive steps toward quantitative studies of the solar isotopic abundances of high energy particles. It will become apparent later in the discussion that they provide a unique channel of information essential to the development of solar physics.

THE CHARGED PARTICLE TELESCOPE AND THE
PROBLEM OF ISOTOPE SEPARATION

University of Chicago instruments were carried on the satellites IMP-4 (launched May 1967) and IMP-5 (launched June 1969). Except for the addition of a Cerenkov counter in the IMP-5 satellite experiment, the two instruments are essentially identical. The IMP-5 telescope, whose cross section of detector elements is shown in Figure 1, is composed of an array of solid-state detectors and anti-coincidence scintillators (D5 and D6) arranged to separate and identify the nuclear charge number Z of the elements and isotopes of H and He by simultaneous measurements of energy-ia and residual particle energy. Events which do not trigger the anticoincidence detector D6 are classified according to the range of the particle in the detector stack. In the energy range ~ 10 to 30 MeV/nucleon, detectors D1 and D2 are pulse height analyzed and the events are classified either ID2 or ID3 depending on whether detector D3 is triggered or not. In the energy range ~ 30 to 100 MeV per nucleon, detectors D1, D2, and D4 are pulse height analyzed and the events are classified ID4. For example, in Figure 1 trajectory A shows the path of an incident particle stopping in detector D4; hence we simultaneously measure the energy loss in D1 and D2 and the resiual energy in D4. This trajectory belongs to an allowed group designated by the telescope logic as a D1 D2 D3 D4 $\overline{D5}$ $\overline{D6}$ or ID4 event. Trajectories B and C are excluded by the telescope logic since they pass through the anticoincidence detector D6 which defines a 50° cone of acceptance. (For further details see Hsieh, Mason and Simpson, 1971).

Hereafter we designate the ratio of two isotopes by Γ, for example, $\Gamma(^3He/^4He)$, $\Gamma(^2H/^1H)$.

Isotope analysis is accomplished by performing sums along the expected track distributions in the various pulse height matrices. In these matrices, the track of a heavier isotope will extend beyond the end-of-range point of a lighter isotope with the same charge. We later discuss the importance of this end-of-range technique in separating isotopes and eliminating background.

In many ways, the measurement of the ^{2}H, ^{3}H, and ^{3}He components of high energy particle radiation from solar flares is more difficult than earlier work leading to the discovery of ^{2}H in the galactic cosmic rays (Fan, Gloeckler and Simpson, 1966), or the separation of galactic ^{3}He from ^{4}He. For example, Figure 2 shows the galactic ^{2}H peak distribution as obtained from satellite data (Hsieh, Mason and Simpson, 1971). Clearly,

UNIVERSITY OF CHICAGO
IMP-5
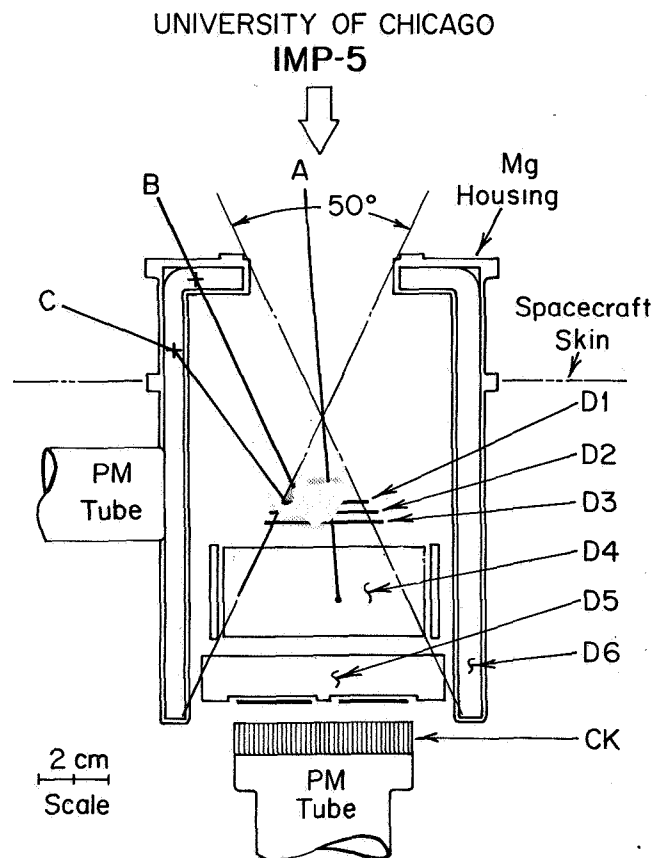
Figure 1. Cross-section view of the detector elements of the University of Chicago charged particle telescope in the IMP-5 satellite. Except for the Cerenkov counter, the telescope on the IMP-4 satellite was essentially identical to the telescope on IMP-5. Trajectory A is an allowed particle trajectory, whereas Trajectory B and C are rejected for analysis by the D6 anticoincidence shield. For details see Hsieh, Mason, and Simpson (1971) and Garcia-Munoz, Mason, and Simpson (1973).

318

NUMBER OF EVENTS PER CHANNEL

IMP-3
(0.9 cm²-ster)
JUN-DEC.1965
150
DEUTERONS

IMP-4
(1.6 cm²-ster)
JUL.-OCT. 1967
204
DEUTERONS

IMP-5
(1.6 cm²-ster)
JUN.-SEP. 1969
44
DEUTERONS

RELATIVE CHANNEL NUMBERS CENTERED ON DEUTERON TRACK
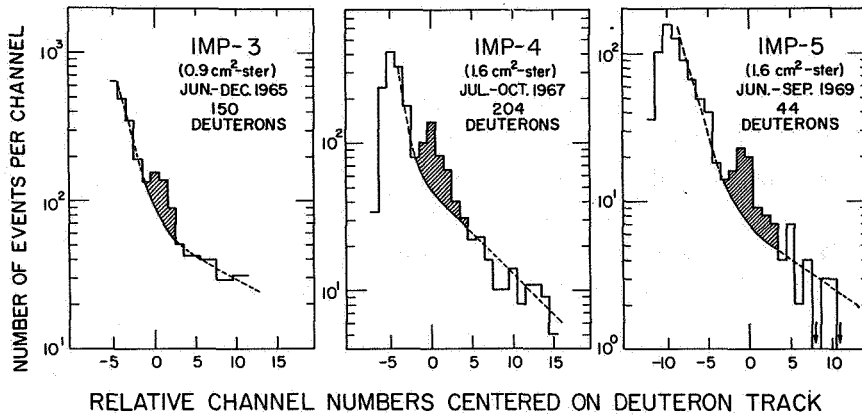
Figure 2. Histograms of deuterium in the galactic cosmic radiation in the presense of high background of ^{1}H events (from Hsieh, Mason, and Simpson 1971).

the determination of the background to be subtracted is the principal limitation on the accuracy of the ^{2}H measurements. The galactic ^{3}He and ^{4}He distributions are shown in Figure 3 for the same type of analysis (Hsieh, 1970) for later comparison with the distributions from solar flares. Solar flare ^{2}H, ^{3}H, and ^{3}He measurements are different from the

IMP-IV   The University of Chicago
~ 30-100 MeV/nucleon He³ and He⁴ Separation

Number of Events per Channel

He⁴(46-58)
He³(61-77)

He⁴(69-84)
He³(94-111)

He⁴(84-93)
He³>111
MeV/nucleon
excluded by
range
measurement

He⁴(36-46)
He³(46-61)

He⁴(58-69)
He³(77-94)

He⁴(25-36)
He³(29-46)

Relative Channel Number in D2 Centered on He⁴ Track
(▲ indicates predicted He³ track center)

Figure 3. Histograms of ^{3}He and ^{4}He in the galactic cosmic rays, illustrating the ID4 resolution and the end-of-range analysis in the ^{4}He energy/nucleon range of 84-93 MeV per nucleon (from Hsieh, 1970).

319

corresponding galactic measurements in a number of ways. Steep solar flare spectra eliminate most nuclear interaction background found in galactic periods, but the high counting rates introduce other types of background such as pulse pile-up which interferes with ^{2}H and ^{3}H analysis. The IMP-4 and IMP-5 instruments have better isotopic separation at lower energies. However, as a result of having only two-detector analysis in the energy interval $\sim$ 10 to 30 MeV per nucleon, the background level is higher than in the energy interval $\sim$ 30 to 100 MeV per nucleon. Since the ratios $\Gamma(^2H/^1H)$ and $\Gamma(^3He/^4He)$ observed in solar flares have been found to be smaller than previous galactic results, often by more than a factor ten, finding individual flare events with adequate ^{2}H, ^{3}H, and ^{3}He statistics has been very difficult and background subtraction has become a critical problem.

There are also important differences in the interpretation of isotopic ratios derived from galactic and solar flare observations, primarily due to the entirely different energy spectra of the parent nuclei. By parent nuclei, we mean the accelerated ^{1}H and ^{4}He which undergo nuclear interactions with the gas of the medium through which they pass. The galactic cosmic rays have a mean energy of a few GeV per nucleon and a spectrum which falls off as a power law in total energy, $W^{-2.6}$, whereas the solar flare particle spectra fall steeply with increasing energy and have mean energies below a few MeV per nucleon (that is, flux $\propto E^{-\gamma}$; wit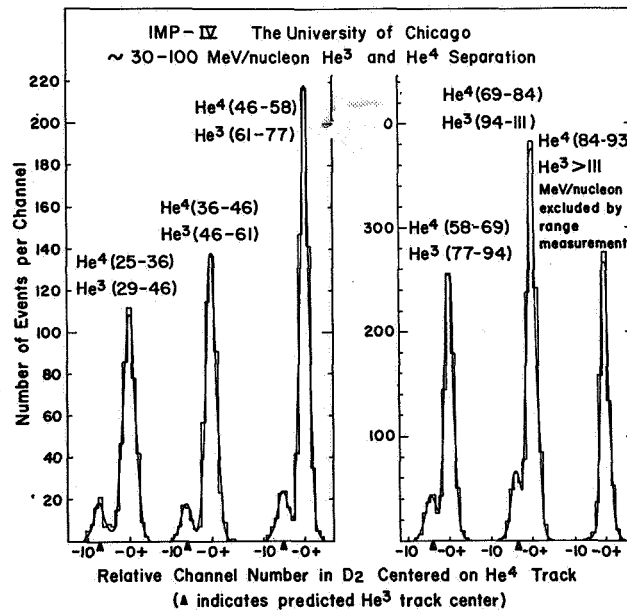h $\gamma \approx$ 2 to 5). These two types of spectra produce entirely different yields of secondary isotopes per gram of matter penetrated. This can be understood by considering the following factors. The principal nuclear interactions and their energy thresholds for producing ^{2}H, ^{3}H, and ^{3}He are given in the listing shown on the following page. Using the energy dependent cross-section data available up to 1971, J.P. Meyer (1971) has obtained the overall or resultant formation cross-sections for ^{2}H and ^{3}He as functions of energy, as shown in Figure 4. From this figure, it is obvious that only a small fraction of the solar flare acceler-
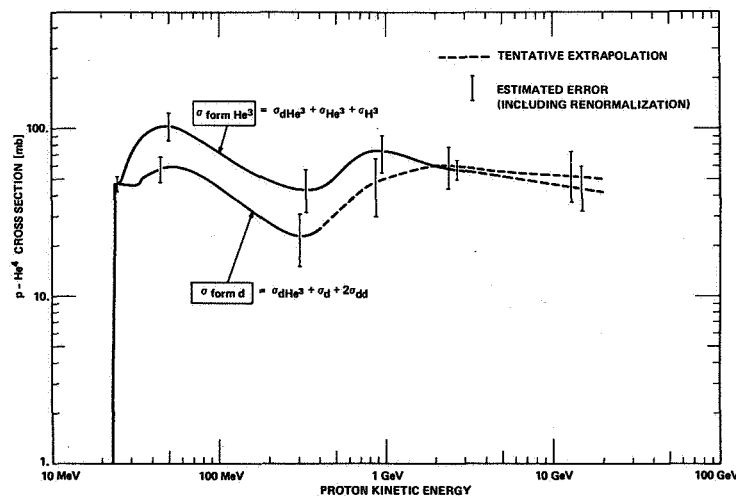
Figure 4. Cross-sections as a function of kinetic energy for the reactions in the nuclear fragment producing reactions listing leading to the formation of ^{2}H and ^{3}He (from J.P. Meyer, 1971).

Nuclear Fragment Producing Reactions*

Reaction	Threshold Energy Mev/Nucleon
Deuteron producing reactions	
H^1 (p, π^+) H^2	284.9
He^4 (p, He^3) H^2	23.0
He^4 (p, 2pn) H^2	32.8
He^4 (p, pd) H^2	30.0
C (p,d ...	17.9
N (p,d ...	8.9
O (p,d ...	14.2
Ne (p,d ...	15.4
Triton producing reactions	
He^4 (p, 2p) H^3	24.9
C (p,t ...	25.3
N (p,t ...	23.9
O (p,t ...	21.7
Ne (p,t ...	20.8
Helium-3 producing reactions	
He^4 (p,d) He^3	23.0
He^4 (p, pn) He^3	25.9
C (p, He^3 ...	21.3
N (p, He^3 ...	5.1
O (p, He^3 ...	16.2
Ne (p, He^3 ...	16.3

*From Lingenfelter and Ramaty (1967).

ated parent nuclei have sufficient energy to reach the thresholds required for the nuclear reactions leading to rare isotope production. On the other hand, over ninety percent of the galactic cosmic ray particle flux is capable of producing secondaries. Although ^{1}H on ^{4}He (at rest) and ^{4}He on ^{1}H (at rest) have the same energy per nucleon thresholds for the reactions in the previous listing, the energy distributions of the nuclear products in the laboratory coordinate-frame are different, especially near threshold energies. Hence the reaction kinematics at low energies play a major role in determining the values of the Γ's and

the slopes of the differential energy spectra in solar flare events. They must be taken into account in all calculations of nuclear product yields and energy spectra. Indeed, because the energy distribution of secondary isotopes from incident ^{1}H is different from the energy distribution of secondary isotopes from incident ^{4}He, and because $\Gamma(^1$H$/^4$He) varies greatly from flare to flare*, the relative contribution of the two reactions to the observed energy spectra may vary significantly. We note that even though the cross-sections for production of these isotopes by ^{1}H on C, N, O, and Ne are large, the small relative abundances of the heavier nuclie make their contribution to the observed yields negligible.

RELATIVE ABUNDANCES AND SPECTRA OF ^{1}H, ^{3}He, AND ^{4}He

Since the separation of ^{2}H and ^{1}H from the ^{1}H background is much more difficult than the separation of ^{3}He from ^{4}He, we first investigate ^{3}He solar flare abundances and energy spectra. We defer to a later section the studies of ^{2}H and ^{3}H.

As we pointed out in the first section, the results of Hsieh and Simpson (1970) were not sufficient to allow any conclusive decision between ^{3}He production by nuclear interactions at the time of flare particle acceleration, and ^{3}He as a preflare component of the ambient solar gas in active regions. The next step was to search for flares containing adequate ^{3}He statistics in order to measure abundance ratios and energy spectra in individual events. To accomplish this, twelve more flares were analyzed using IMP-5 satellite data. Of the twelve flares, five (Table 1) were found to have produced almost all of the analyzed ^{3}He nuclei. The data from these five flares have been summed and displayed as a histogram in Figure 5. This is a histogram of the number of analyzed helium nuclei per channel versus the relative channel number with respect to the centers of the ^{3}He and ^{4}He pulse height peak distributions. Figure 6 is the equivalent histogram i⁶ ʰe remaining seven flares listed in Table 2. The events distributed over channels to the left of the ^{4}He peak in Figure 6 include a few ^{3}He events and the background. Analysis periods in each flare were terminated before the solar helium flux dropped low enough to require correction for the galactic ^{3}He cosmic radiation. Dietrich (1973) has shown that the maximum background correction to the ^{3}He data reported here is less than ten percent. Hence, we have not subtracted any background in these figures or in our calculations of abundance ratios. Tentatively, we have called the five flares summed in Figure 5 the "^{3}He-rich" flares, and the seven flares summed in Figure 6, the "^{3}He-poor" flares. Among the ^{3}He-rich flares, the flares of November 2, 1969 and January 25, 1971 were outstanding. Their ^{1}H, ^{3}He, and ^{4}He energy spectra are shown in Figures 7 and 8. Under the assumption that the spectra may be represented by power laws in kinetic energy, spectral indices have been calculated and they are included in Table 3. Although there is considerable uncertainty in the slopes of the ^{3}He spectra, the data indicate that these spectra are at least as flat as the corresponding ^{4}He spectra. The alternate assumption that the spectra are exponentials in magnetic rigidity R does not change this conclusion [that is flux $\propto \exp(-R/R_0)$].

---

* It is known that Γ (^{1}H$/^4$He) varies from $\sim$10:1 to $\sim$200:1, with at least one case of 7000:1 (flare of Sept. 25, 1969: Dietrich and Simpson, unpublished).

322

Table 1

Five ³He-Rich Flares Observed by IMP-5

Flare Date	Optical onset Day, hour (GMT)	D1 rate max (c/s)	D2 rate max (c/s)	D4 rate max (c/s)	D6 rate max (c/s)	Location	†Importance
Nov 2, 1969	306,10:28	30k	1700	1900	85k	*N16, W90	3B
March 29, 1970	88,00:10	2k	85	28	10k	N13, W36	2B
May 30, 1970	150,2:46	4k	84	2	1k	S 9, W29	2B
Aug 14, 1970	** —	30k	600	8	6.5k	** —	**
‡Jan 25, 1971	24,23:14	10k	1550	750	75k	N19, W50	2B

*Flare location is behind the limb of the sun.

**No definite onset time or location of the flare can be given, since the rates increased for a period of two days, during which several major flares occurred near the east limb.

†From *Solar Geophysical Data*.

‡While the optical onset occurred late January 24, low energy particle fluxes were not observed on IMP-5 until early January 25. This flare has been labeled January 25, 1971, throughout this paper and in the thesis of Dietrich (1973).

Table 2

Seven ³He-Poor Flares Observed by IMP-5

Flare Date	Optical Onset Day	Hour (GMT)	D2 rate max (c/s)	D4 rate max (c/s)	Location	**Importance
Jan 29, 1970	29	10:25	5.9	2.8	S15, W41	1B
Jan 31, 1970	31	15:08	45	10.6	S22, W65	2B
March 6, 1970	65	*15:30	7.8	1.2	— —	—
March 23, 1970	82	15:44	14.7	3.0	N18, W61	1B
July 7, 1970	188	16:48	5.5	1.6	N23, W90	—
July 23, 1970	204	18:32	29	28	N 9, E 8	1B
Nov 5, 1970	309	3:08	100	3.4	S12, E36	3B

*Onset of this flare has been taken from the D2 counting rate.

**From *Solar Geophysical Data*.
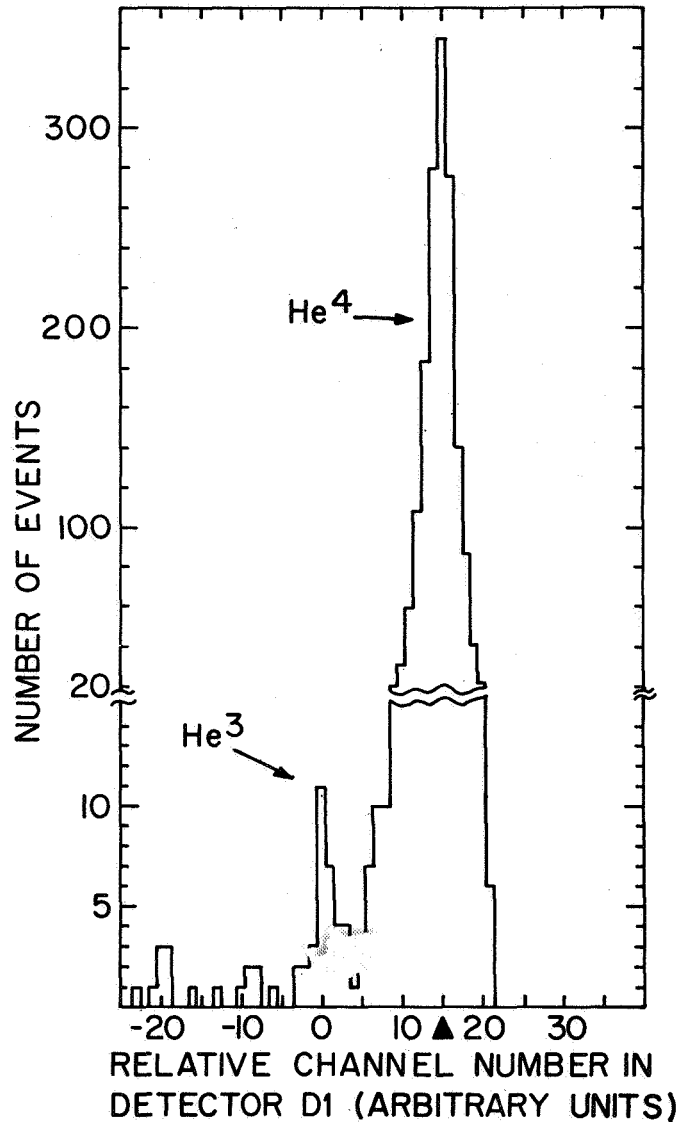
Figure 5. Histograms of analyzed ^{3}He and ^{4}He nuclei from the solar flares listed in Table 1. These are the so-called "^{3}He-rich" flares. Note the change of scale on the vertical axis.

The abundance ratios in the energy range 10 to 50 MeV nucleon for the November 2, 1969 and January 25, 1971 flares are $\Gamma(^3\text{He}/^4\text{He}) = (7.7 \pm 2.0) \times 10^{-2}$ and $(2.0 \pm 1.0) \times 10^{-2}$ respectively. These ratios are compared in Table 4 with IMP-4 work, the ^{3}He-poor flares (Figure 6), spectroscopic upper limits for the solar atmosphere, solar wind measurements, and calculated estimates.* From this comparison, it is clear that $\Gamma(^3\text{He}/^4\text{He})$ for the

---

* E.C. Stone of this Symposium reported the measurement of Γ $(^3\text{He}/^4\text{He}) \approx 0.1$ at $\sim$ 4 MeV/nucleon with instrumentation on the OGO-6 satellite. This confirms the work on IMP-4 and IMP-5 data and also shows that the yield is consistent with nuclear production. This high value for Γ suggests that the spectral slope for ^{3}He may not be significantly flatter than for ^{4}He.

324
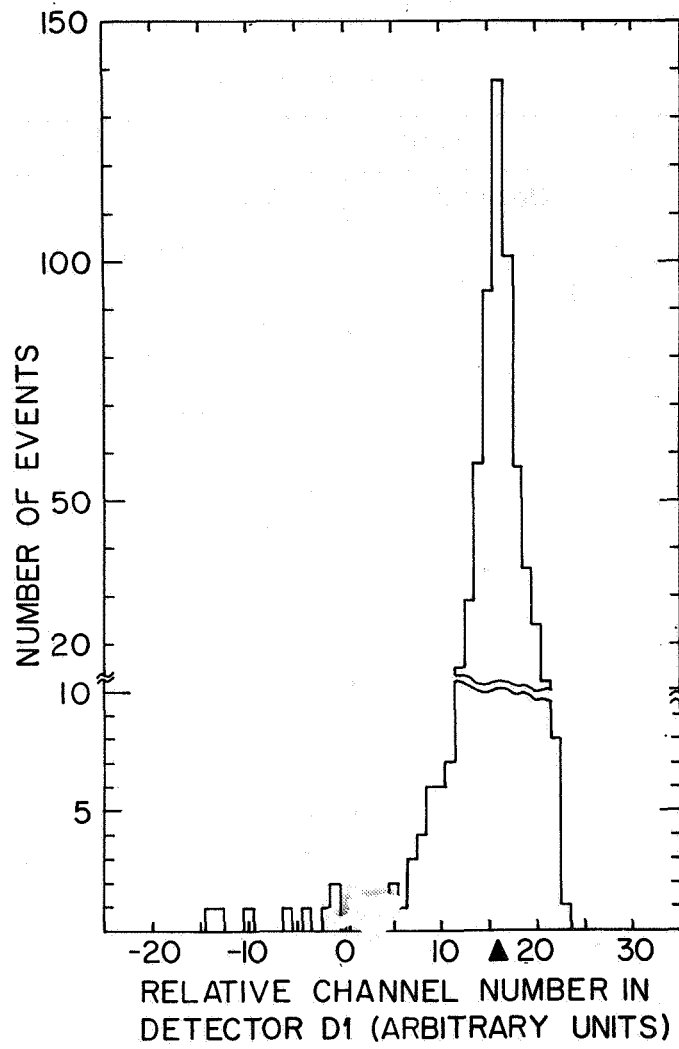
Figure 6. Histograms of analyzed ^{3}He and ^{4}He nuclei from solar flares listed in Table 2. These are the "^{3}He-poor" flares.

Table 3

Observed Spectrums

If Spectrum is of form exp $(-R/R_0)$ $R_0(MV)$				If Spectrum is of form $AE^{-\gamma}$ Relative Flux		
Flare	^{3}He	^{4}He	^{1}H	^{1}H	^{4}He	^{3}He
Nov 2, 1969	76 ± 30	58 ± 6	55	$1.4 \times 10^6 E^{-2.5 \pm .05}$	$2.9 \times 10^5 E^{-3.5 \pm 0.2}$	$1.8 \times 10^2 E^{-1.9 \pm 0.6}$
Jan 25, 1971	98 ± 30	75 ± 3	72	$5.7 \times 10^5 E^{-2.3 \pm .05}$	$8.5 \times 10^4 E^{-3.5 \pm 0.3}$	$1.9 \times 10^2 E^{-2.1 \pm 0.8}$

Table 4

Solar Isotopic Abundance Ratios

Location	$\Gamma(^3He/^4He)$		$\Gamma(^2H/^1H)$	$\Gamma(^3H/^1H)$
	Observed	Calculated		
Chromospheric	[a]$(2 \pm 3) \times 10^{-2}$ [c]$\leqslant (1.0 \pm 0.5) \times 10^{-2}$	[b]$\sim 1.5 \times 10^{-3}$		
Photospheric active regions			[d]$\sim 1 \times 10^{-4}$	
quiet regions			[e]$< 5 \times 10^{-4}$ [f]$< 5 \times 10^{-6}$	
Solar wind...	[g]$\leqslant 4 \times 10^{-4}$ [i]4×10^{-4}		[h]$< 2 \times 10^{-5}$	
Solar flare...	[j]$(2.1 \pm 0.4) \times 10^{-2}$ [m]$\leqslant 2 \times 10^{-3}$ [o]2.2×10^{-2} [p]$(7.7 \pm 2.0) \times 10^{-2}$ [q]$(2.0 \pm 1.0) \times 10^{-2}$ [r]1.5×10^{-2} [s]3.3×10^{-2}	[k]$< 3 \times 10^{-3}$	[l]$< 3 \times 10^{-3}$ [n]$\leqslant 2 \times 10^{-3}$ [o]$\leqslant 8 \times 10^{-5}$	[l]$< 10^{-3}$ [n]$< 6 \times 10^{-4}$ [o]$\leqslant 4 \times 10^{-5}$

Notes: [a]Greenstein (1951)

[b]Wagoner, Fowler, and Hoyle (1967)

[c]Namba (1965)

[d]Severny (1957)

[e]Geiss and Reeves (1972)

[f]Grevesse (1969)

[g]Bame et al. (1968)

[h]Epstein and Taylor (1970)

[i]Geiss et al. (1970) (1972)

[j]10 - 100 MeV/nucleon, Hsieh and Simpson (1970)

[k]Biswas and Fichtel (1965)

[l]Biswas et al. (1962) (25-48 MeV/nucleon)

[m]Extrapolated to 1 MeV/nucleon; Hsieh and Simpson (1970)

[n]Waddington and Freier (1964) ($>$50 MeV/nucleon)

[o]Present work; sum of seventeen IMP-4 flares

[p]Present work; flare of 2 November 1969

[q]Present work; flare of 25 January 1971

[r]Present work; sum of seven ^{3}He-poor flares

[s]Present work; sum of five ^{3}He-rich flares

Figure 7. Relative differential energy spectra of ^{3}He, ^{4}He, and ^{1}H for the flare November 2, 1969. Spectral characteristics are given in Table 3.

November 2, 1969 flare event exceeds chrom??? eric upper limits (Namba, 1965) by at least a factor of five, and solar wind values (Geiss, Eberhardt, Buehler, Meister, and Signor, 1970; Geiss, Buehler, Cerutti, Eberhardt, and Filleux, 1972) by a factor of 100. We take this as strong evidence that the high values of $\Gamma(^3\text{He}/^4\text{He})$ which we have measured are the result of high energy nuclear interactions in the solar atmosphere, as distinguished from the ambient solar ratio arising from ^{2}H burning during solar evolution.

MODELS FOR THE PRODUCTION OF SOLAR HIGH ENERGY ^{3}He

A search for the origin of the secondary ^{3}He observed in a given solar flare leads to two alternatives which we must consider; namely, preflare production and prompt production in the flare. There are two alternatives for preflare production:

- High energy interactions might lead to the temporary and cumulative buildup of ^{3}He confined within an active center, so that a sample of the gas is accelerated when a large flare occurs.

- It could be the result of relatively long-term magnetic field storage of high energy nuclei in the corona with a gradual buildup of secondary nuclei from interactions. They would later escape to the interplanetary medium in a solar flare.
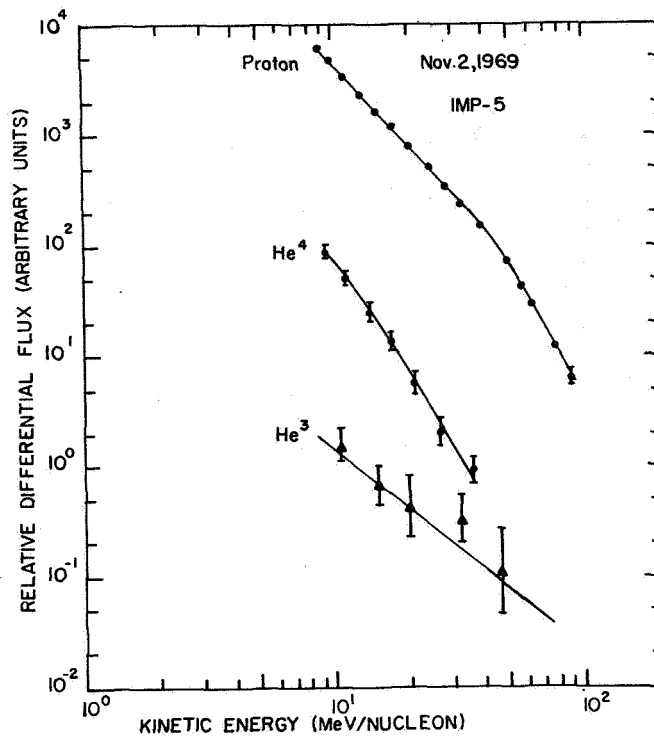
327
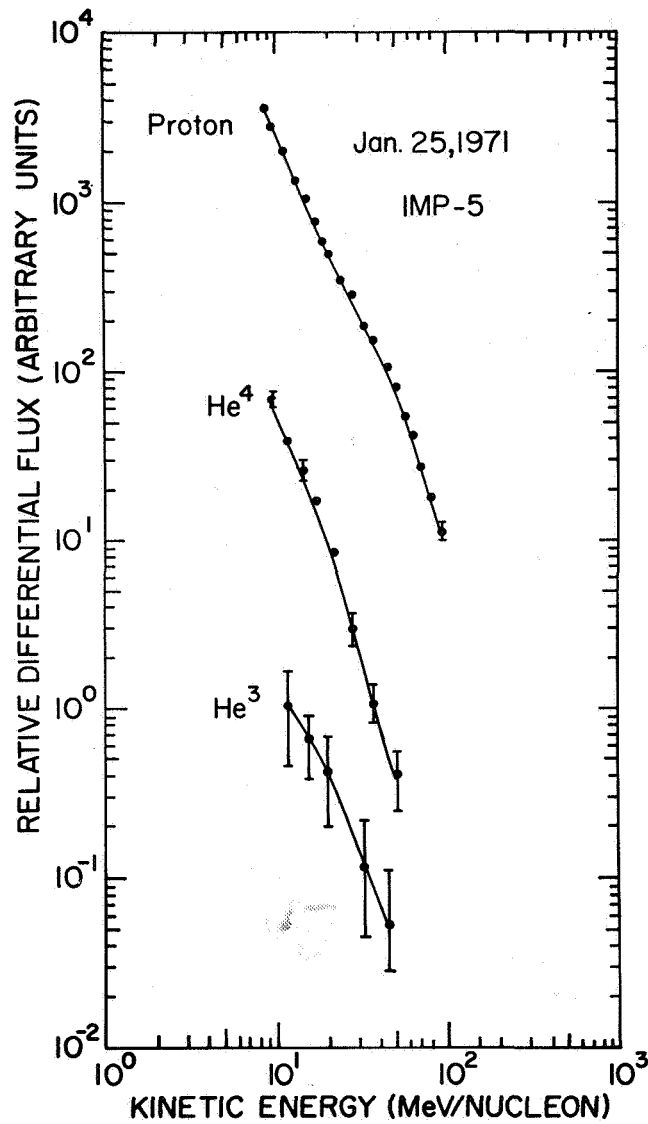
Figure 8. Relative differential energy spectra of ^{3}He, ^{4}He, and ^{1}H for the flare January 25, 1971. Spectral characteristics are given in Table 3.

There are also two general alternative models for prompt ^{3}He production:

- The parent nuclei are accelerated while interacting with the chromospheric gas by the release of flare energy.

- The parent nuclei are accelerated and stored in the corona at energies about ~ 25 MeV per nucleon in events prior to the flare. At the onset of the flare, they are dumped into the chromosphere (Elliot, 1969) to produce the observed ^{3}He.

Because of the high observed ^{3}He yields and the short time periods allowed for interaction, prompt production probably occurs in the chromosphere.

It is not within the scope of this paper to consider in detail all these alternatives or their implications. However, we point out that, on the one hand, the physical conditions required for preflare production are extremely difficult to meet, primarily because of the necessity for maintaining the high time-averaged abundances in the source against a variety of important loss mechanisms. On the other hand, the observed spectra and high ratio for helium isotopes can be accounted for readily by prompt production in the chromosphere under conditions which are self-consistent with known flare phenomena. This conclusion is based on the calculations of expected ^{3}He yields in the chromosphere.

All models for calculating the secondary production require an initial assumption regarding the spectral shapes and relative intensities of the accelerated parent ^{1}H and ^{4}He nuclei at the time of the interactions. We know that spectra measured at 1 AU may be modified by propagation effects, especially in interplanetary space after convection and adiabatic deceleration effects set in. However, using propagation conditions which include energy loss by ionization at the sun, and convection and adiabatic deceleration in the solar interplanetary magnetic field, Englade (1971) has shown that the source spectra of ^{1}H and ^{4}He nuclei above $\sim$ 20 MeV per nucleon are expected to be similar to the spectra observed in the early decay phase of flare particle intensity at the orbit of earth. In our calculations of secondary isotope production, therefore, we used the flare spectra given in Table 3 as the initial input spectra (that is, we assumed magnetic rigidity spectra above $\sim$ 30 MeV per nucleon with $R_0 \approx 75$ MV). We determined the yield of secondary nuclei in a chromospheric gas target of uniform density ρ and composition $\Gamma(^1$H$/^4$He$) = 10:1$, taking into account all ^{1}H on ^{4}He and ^{4}He on ^{1}H reaction cross-sections, inelastic loss cross-sections, and energy loss by ionization in the ambient gas. The computations included the kinematical energy distribution functions discussed by Ramaty and Lingenfelter (1969) and were carried out in 0.1 gm/cm^2 steps using the methods developed by Comstock, Hsieh and Simpson (1972). We assume that thereafter a fraction of the parent nuclei and their reaction products escape the chromosphere to the interplanetary medium and propagate to $\sim$ 1 AU without any change in the relative abundances of the helium isotopes. If we also assume that the time interval when particles are undergoing nuclear interactions is approximately the time defined by the flash phase and by the microwave and hard, nonthermal X-ray bursts (that is t $\sim$ 100 s), then the calculated mean path length determines the density ρ and an approximate scale height in the solar atmosphere where the interactions must have occurred.

There are several variations of the above model which may be considered, two of which we discuss here to illustrate the constraints they place on the acceleration process.

Case 1: We assume that there is no electromagnetic acceleration of the secondary ^{2}H, ^{3}H, and ^{3}He after their production in the target gas by accelerated parent nuclei. Under these conditions the secondary nucleus, whose initial energy is determined by the nuclear interaction kinematics, loses energy by ionization and suffers inelastic collisions from the time of production to the time of

escape ($\lesssim$ 100 seconds). Propagation calculations including the previous assumptions indicate that the observed shapes of the ^{1}H and ^{4}He spectra are quickly destroyed above 10 MeV per nucleon by even small amounts of matter, and it is not possible to produce the observed yields of ^{3}He with any path length through solar material. This result can be easily understood by noting that the range of a 70 MeV per nucleon ^{3}He in ionized hydrogen is ~ 1 gm/cm^2. Clearly, the small amounts of ^{2}H, ^{3}H, and ^{3}He produced are rapidly degraded in energy. Thus models which produce ^{3}He by dumping preflare accelerated ^{1}H and ^{4}He nuclei into the chromosphere are open to question.

Case 2: We assume that the acceleration mechanism is continuously operative within the target gas for t ~ 100 seconds. Therefore, the products of nuclear interactions start out with their kinematical energy and, in addition, gain energy from the acceleration process for the time remaining in the 100-second interval. Since we do not know the details of the rates of energy gain from the acceleration process, nor the rates of energy loss, we have made the minimal assumption that the rate and magnitude of energy gain is equal to the energy losses. This also implies that the initial spectral form of the parent nuclei is unmodified throughout the acceleration period. Under these assumptions, we find that the observed ^{3}He yields for the November 2, 1969 and January 25, 1971 flares are obtained with a mean path length of ~ 5 gm/cm^2 and a gas density of ~ 10^{12} atoms/cm^3 at chromospheric heights of 2000 to 4000 km. (See the density versus altitude dependence shown in Figure 5 of the review by Pagel, 1964). If the higher local densities at flare sites discussed by de Jager (1968) exist at these times, then even higher altitudes on the chromosphere may be the site of these nuclear reactions. Using this model, Dietrich (1973) has calculated differential energy spectra for ^{3}He which are not inconsistent with the observed spectra.

Lingenfelter and Ramaty (1967) have also calculated yields of ^{2}H, ^{3}H, and ^{3}He in solar flares for different characteristic spectral rigidities. For example, they found for $R_0 \approx 145$ MV that a minimum of 8 gm-cm^{-2} was required to produce the $\Gamma(^3\text{He}/^4\text{He}) \approx 0.2$ observed by Schaeffer and Zähringer (1962) in the November 12, 1960 solar flare.

The analysis of cases 1 and 2 stresses the importance of acceleration in the target medium. In view of this requirement, models which invoke the acceleration of parent nuclei before their interaction with the target gas apparently have one more acceleration stage than is necessary for the production of secondary isotopes. It is also clear that these secondary isotopes cannot be produced in transit to earth or in any other region where net positive acceleration does not occur.

A consequence of models for prompt production of secondary nuclei by high energy interactions in the chromosphere is that roughly comparable yields of ^{3}He, ^{2}H, and ^{3}H nuclei are predicted. What do we find?

THE ABUNDANCES OF DEUTERIUM AND TRITIUM AS A FUNCTION OF ENERGY

Previous attempts to measure ^{2}H and ^{3}H led to upper limits which are not low enough to test their consistency with the concept of ^{3}He production by nuclear interactions. The background event rate and the close proximity of the proton peak distribution to the location of the deuterium distribution in the data formats from our IMP-4 and IMP-5 satellite experiments place severe limitations on the search for those isotopes. However, it has been possible with a recently developed computer analysis technique by Anglin (1973) to establish upper limit fluxes at a ninety-five percent confidence level. The program also calculates average flux levels consistent with the observed data. In our report here we emphasize that we do not claim particle-by-particle identification of ^{2}H and ^{3}H, but do establish the upper limits of their fluxes as a function of energy and rigidity. The technique of Anglin has been applied to the ^{3}He data from a sum of seventeen flares observed by IMP-4 in the period May 1967 to July 1968 (the seven flares reported by Hsieh and Simpson (1970) plus ten additional flares) and gives $\Gamma(^3\text{He}/^4\text{He}) = 2.2 \times 10^{-2}$. For the ^{3}He data from the sum of the seven ^{3}He-poor flares listed in Table 2, this method leads to an average value for $\Gamma(^3\text{He}/^4\text{He}) = 1.0 \times 10^{-2}$ and a ninety-five percent confidence upper limit for $\Gamma(^3\text{He}/^4\text{He})$ of 2.4×10^{-2} at the same energy per nucleon. Table 5 contains all our abundance ratios as determined at the same energy per nucleon. We see that the results of analysis of the same data by two independent techniques are consistent.

Anglin's method has been applied to ^{2}H and ^{3}H for the seventeen flares taken from IMP-4 data. Figure 9 contains two histograms from the solar flare sum centered on the expected ^{2}H distribution. Figure 9a illustrates the typical ^{2}H solar flare resolution of the IMP-4 instrument in the ^{2}H energy interval 7.3 to 8.8 MeV per nucleon. The large peak centered at channel -11 is mostly ^{1}H events in the en   interval 10.8 to 14.1 MeV per nucleon. Pulse pile-up from the proton track may be a problem in this ^{2}H energy interval. Of special importance are the ^{2}H and ^{3}H end-of-range energy intervals in which the ^{2}H and ^{3}H tracks extend beyond the end of the ^{1}H track in the ID2 and ID3 data matrices (see Hsieh, Mason and Simpson, 1971 for a further discussion of data matrices). The histogram in Figure 9b shows the low background level and hence the ^{2}H resolution in the energy interval 10.7 to 13.2 MeV per nucleon. This energy interval is comprised primarily of ID2-ID3 end-of-range data. The spectra shown in Figure 10 are represented as a function of magnetic rigidity since we believe a meaningful comparison of the relative abundances of isotopes with different mass-to-charge ratios can be made in equal intervals of magnetic rigidity. The upper bars on each data point are the ninety-five percent confidence upper limits, the data symbols are average fluxes, and the arrows point to the zero data levels (that is, the result obtained by inserting one event in the computation of the relative flux (Anglin, 1973)). Solid data symbols in Figure 10 indicate end-of-range analysis. There appear to be small amounts of ^{2}H in our flare data; however, until we have clear-cut proof, we rely only on the upper limit values for the fluxes.

Table 6 contains solar flare abundance ratios observed on IMP-4 and IMP-5 for the magnetic rigidity interval $\sim$ 300 to 400 MV. In the construction of Table 6, we have assumed that ^{1}H and ^{4}He have the spectral form $A\exp(-R/R_o)$. The ratios of relative abundances we

Table 5

Solar Isotopic Abundance Ratios

Satellite and Flare Period(s)	$\Gamma(^3\text{He}/^4\text{He})$	$\Gamma(^2\text{H}/^4\text{He})$	$\Gamma(^3\text{H}/^4\text{He})$	$\Gamma(^3\text{He}/^1\text{H})$	$\Gamma(^2\text{H}/^1\text{H})$	$\Gamma(^3\text{H}/^1\text{H})$
*IMP-4 sum of seven flares (May 1967-Dec 1967)	$(2.1 \pm 0.4) \times 10^{-2}$					
**IMP-4 sum of seventeen flares (May 1967-Aug 1968)	2.2×10^{-2}	$\leqslant 8 \times 10^{-3}$	$\leqslant 4 \times 10^{-3}$	2×10^{-4} $\leqslant 4 \times 10^{-4}$	$\leqslant 8 \times 10^{-5}$	$\leqslant 4 \times 10^{-5}$
†IMP-5 Nov 2, 1969	$(7.7 \pm 2.0) \times 10^{-2}$	**$(\leqslant 5 \times 10^{-1})$				
†IMP-5 Jan 25, 1971	$(2.0 \pm 1.0) \times 10^{-2}$					
†IMP-5 Sum of five ³He-rich flares	3.3×10^{-2}					
†IMP-5 sum of seven ³He-poor flares	1.5×10^{-2}	**$(\leqslant 2.4 \times 10^{-2})$				

*Hsieh and Simpson (1970); 10 to 100 MeV/nucleon.

**Anglin (1973); upper limits are 95 percent confidence level and weighted for end-of-range data.
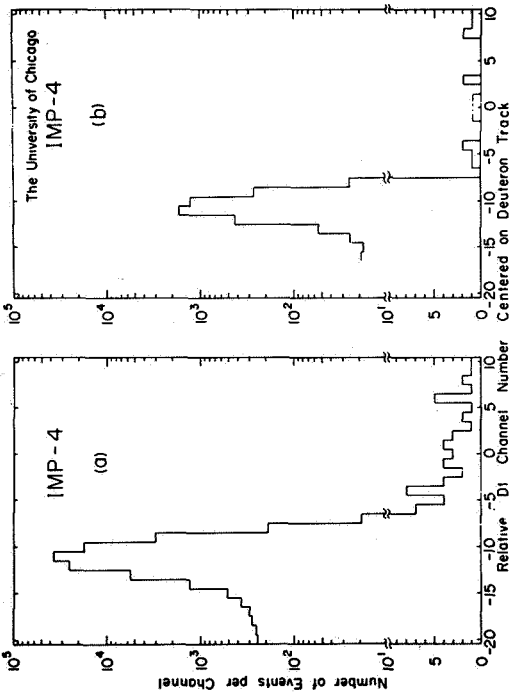
†Dietrich (1973); 10 to 50 MeV/nucleon.

Figure 9. Histograms of analyzed ^{1}H and ^{2}H nuclei from a solar flare sum including seventeen solar flares observed by IMP-4 in the period May 1967 to July 1968. Figure 9(a) contains ^{2}H data in the energy interval 7.3 to 8.8 MeV/nucleon from the ID2 matrix above the proton track. The large peak centered at channel -11 is mostly ^{1}H events in the energy interval 10.8 to 14.1 MeV/nucleon. The analysis program indicates that the data in the histogram is consistent with an average ^{2}H flux of 8.22 counts and a ninety-five percent confidence ^{2}H upper limit of 18.1 counts. Figure 9(b) contains ^{2}H data in the energy interval 10.7 to 13.2 MeV/nucleon primarily from the end-of-range regions in the ID2-ID3 pulse height matrices. The height of the ^{1}H peak is more than a factor of ten smaller than in Figure 9(a) principally because ^{1}H events may enter only in a very narrow energy band. For this histogram, the analysis program indicates that the data are consistent with an average ^{2}H flux of 2.56 counts and a ninety-five percent confidence ^{2}H upper limit of 6.41 counts. Note the change of scale on the vertical axis.

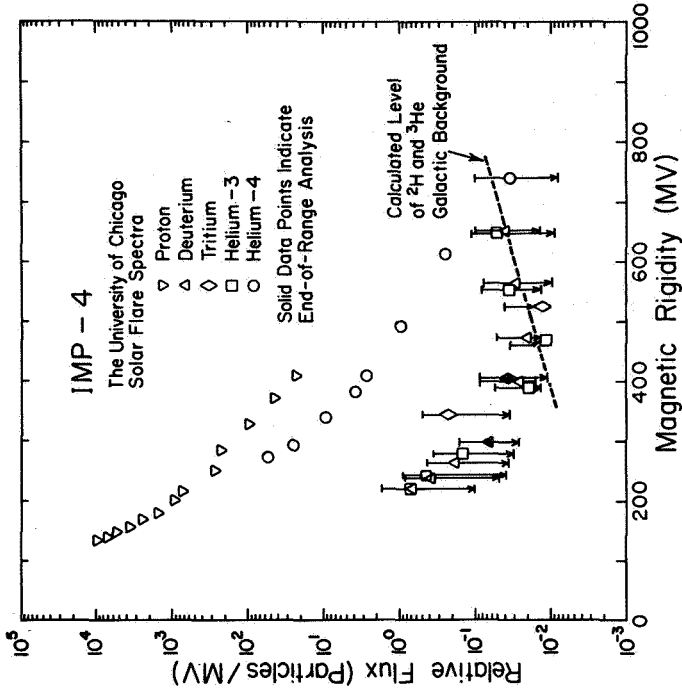Figure 10. Relative differential magnetic rigidity spectra for the sum of 17 IMP-4 solar flares. For ^{2}H, ^{3}H and ^{3}He nuclei, the upper error bars are the ninety-five percent confidence upper limits and the data points are the average fluxes consistent with the observations. ^{1}H and ^{4}He spectra have been corrected for the estimated galactic background flux. See the text for further details.

333

Table 6

Solar Isotopic Abundance Ratios

Satellite and Flare Period(s)	$\Gamma(^3\text{He}/^4\text{He})$	$\Gamma(^2\text{H}/^4\text{He})$	$\Gamma(^3\text{H}/^4\text{He})$	$\Gamma(^3\text{He}/^1\text{H})$	$\Gamma(^2\text{H}/^1\text{H})$	$\Gamma(^3\text{H}/^1\text{H})$	$\Gamma(^4\text{He}/^1\text{H})$
*IMP-4 sum of seventeen flares (May 1967-Aug 1968)	1.5×10^{-2} (350 MV)	$\leqslant 3 \times 10^{-2}$	$\leqslant 5 \times 10^{-2}$	$\leqslant 2 \times 10^{-3}$	$\leqslant 6 \times 10^{-3}$	$\leqslant 6 \times 10^{-3}$	1.3×10^{-1} (350 MV)
**IMP-5 Nov 2, 1969	4×10^{-2}						1×10^{-1}
**IMP-5 Jan 25, 1971	2×10^{-2}						1×10^{-1}
IMP-5 sum of five ^{3}He-rich flares	1.1×10^{-2}						
**IMP-5 sum of seven ^{3}He-poor flares	$\leqslant 3 \times 10^{-3}$						

* Anglin (1973); upper limits are 95 percent confidence levels for the rigidity interval of $\sim$ 300 to 400 MV.

** Dietrich (1973); rigidity interval is $\sim$300 to 400 MV.

report in Tables 5 and 6 for ^{2}H and ^{3}H reduce by a factor of ten to fifty the upper limits so far published for high energy particle data. Due to the lack of knowledge concerning solar flare acceleration and propagation in the interplanetary medium of particles with different A/Z, there may be considerable error in extrapolating our observed energy spectra and abundances back to the sun, especially at low energies. Also, the production curves for ^{2}H, ^{3}H, and ^{3}He at low energies are quite different and very sensitive to the characteristic rigidity R_0 assumed for the spectra of the parent nuclei (for example, Lingenfelter and Ramaty, 1967). With these qualifications, data in Tables 5 and 6 are consistent with the yields predicted from prompt nuclear production models to within a factor ten.

SUMMARY, QUESTIONS, AND NEW DIRECTIONS

We may summarize the present status of our solar flare light isotope studies as follows:

- Helium-3 has been separated clearly from helium-4 in large flares. For example, in the energy range 10 to 50 MeV per nucleon the abundance ratio for the flare of November 2, 1969 is $\Gamma(^3He/^4He) = (7.7 \pm 2.0) \times 10^{-2}$

- The ratio $\Gamma(^3He/^4He)$ from these events is approximately one to two orders of magnitude above probably ambient solar atmospheric values and must be the consequence of production by high energy interactions rather than from the ambient ^{3}He arising from the burning of ^{2}H in earlier stages of solar evolution.

- The measured upper limits for relative abundances of ^{2}H and ^{3}H are approximately a factor of ten to fifty lower than earlier values, and are consistent with expected yields based on the observed $\Gamma(^3He/^4He)$.

- A self-consistent model leads to prompt secondary production in the chromosphere below $\sim$ 5000 km in $\sim$ 100 seconds by $_{\sim\alpha}$ on ^{4}He (at rest) and ^{4}He on ^{1}H (at rest) interactions above the threshold energies of $\sim$ 25 to 30 MeV per nucleon. This process would dominate all alternative mechanisms such as the preflare buildup of ^{3}He. Model calculations point to an acceleration mechanism continuously operative in the target gas to order to account for the observed high ^{3}He yields and energy spectra of the parent nuclei.

- A variation of at least a factor of five from flare-to-flare is observed in $\Gamma(^3He/^4He)$. This is expected from the variation in several flare parameters, including spectral shape of the parent nuclei, relative abundances of accelerated ^{1}H and ^{4}He, and the mean path length for nuclear interactions in the solar gas.

These investigations raise new questions which must be answered. For example: Is post-production acceleration of the nuclei a general requirement for obtaining the observed $\Gamma(^3He/^4He)$? Is the production of ^{2}H and ^{3}H consistent with the yields of ^{3}He from flare–to–flare? What is the significance of the observed variation of $\Gamma(^3He/^4He)$ among flares? Is there a minimum value which is representative of the ambient solar gas value? Is the differential energy spectrum for ^{3}He flatter than for ^{4}He as indicated in Figure 11 by present observations, or will a more precise measurement of these spectra show that they are similar? Are the flares with high yields of ^{3}He always flares in which $\Gamma(^4He/^1H)$ is high?
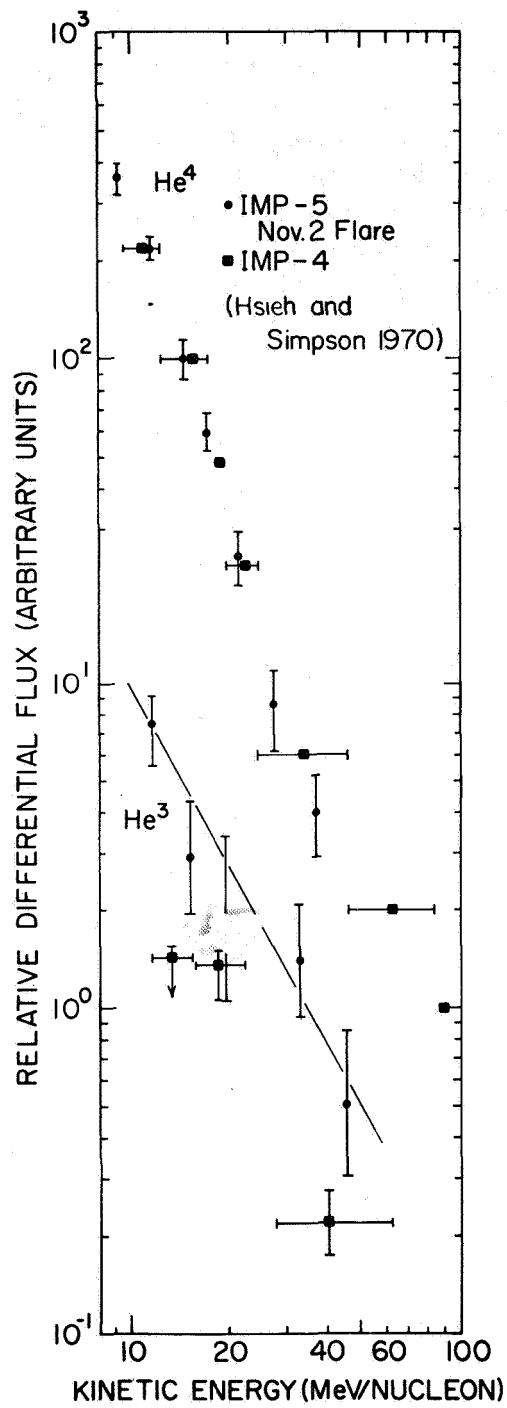
Figure 11. Relative differential energy spectra from the November 2, 1969 flare (Figure 6) normalized at 10 MeV/nucleon to the ^{3}He and ^{4}He spectra from the sum of seven solar flares in 1967 (Hsieh and Simpson, 1970).

In view of the evidence that the rare isotopes of H and He are the result of high energy nuclear interactions, it becomes particularly important to renew the search for other products of these interactions and to reexamine the experimental conditions required for their detection. For example: a) measurable yields of Li, Be and B are predicted from their parent ^{1}H and ^{4}He interactions with ambient solar C and O (see Biswas, 1964 for earlier estimates),* b) high yields of nuclear excitation gamma rays are predicted,* and c) neutron yields in the kinetic energy range ~1 -50 MeV (Simpson, 1970) may extend at least an order of magnitude above the early estimates obtained by Lingenfelter, Flamm, Canfield, and Kellman (1965).

It is especially important to perform new solar neutron and gamma ray experiments along with simultaneous measurements of the light-isotopes. The measurement of their energy spectra and intensity versus time profiles will make it possible to directly determine several important aspects of the solar flare acceleration mechanism. For example, their linear propagation will allow the separation of the time interval for interactions and the mean density of the interaction region.

The detection and measurement of solar neutrons present special experimental problems. Since the principal flux of neutrons is estimated to lie in the energy region ~ 1 to 20 MeV, the large majority will have decayed before reaching an observer at ~ 1 AU because of their ~ 12-minute mean lifetime. Attempts to measure neutrons above ~ 50 MeV at the orbit of earth have been reviewed recently by Chupp (1971). A different approach to these experimental problems has been proposed (Simpson, 1963, 1969, 1970) which would require a spacecraft to carry neutron detectors and low energy proton and helium particle detectors to a radial distance ≲ 0.4 AU, to search for both the impulsive solar flare neutron bursts and quasi-steady solar neutron production. For example, Figure 12 (Simpson, 1969) illustrates the computed radial dependence of   r neutron fluxes at discrete energies in the kinetic energy range 3 to 50 MeV, taking into account both the neutron mean lifetime and the $1/r^2$ dependence of the surviving neutron flux. The resultant flux dependence on r and kinetic energy is unique for solar neutrons and is an important factor in eliminating local neutron production from the spacecraft. It is clear that measurements at ≲ 0.4 AU significantly increase the possibility for observing solar neutrons at low energies.

A less direct attack on the search for solar neutrons is to measure the energy and radial dependence of the decay product protons, which would appear initially in the interplanetary medium, with a spatial and energy distribution directly related to the decaying neutrons without an accompanying alpha-particle component (Simpson, 1963). Calculated fluxes based on this idea have been obtained by Roelof (1966), and it is possible that proton and alpha-particle measurements with the charged particle telescopes on the forthcoming Mariner Venus/Mercury mission may provide evidence for solar neutrons.

---

* Chupp at this symposium has reported the first observations of nuclear excitation gamma rays obtained in the flare of August 4, 1972: Chupp, E. L., Forrest, D. J., Higbie, P. R., Suri, A. N., Tsai, C., and Dunphy, P. D., 1973, *Nature* 241, 333.
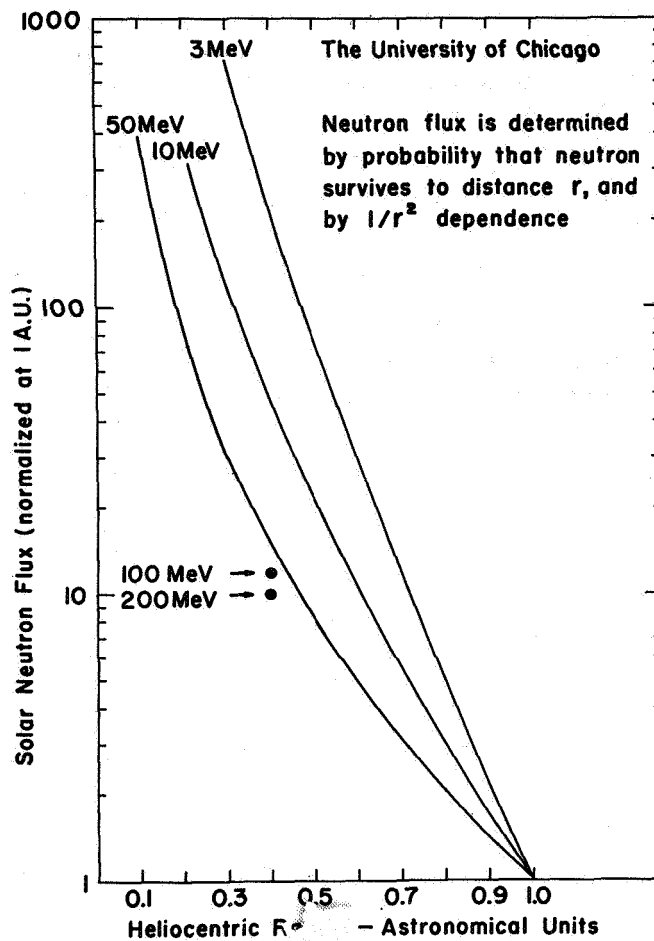
Figure 12. Calculated radial dependence of solar
neutron flux as a function of neutron kinetic energy
(Simpson, 1969).

In summary, the information to be obtained from the solar flare products of high energy
interactions is not available through either solar wind observations, where both the acceler-
ation mechanism and the coronal source of the nuclear species are different, or through
optical measurements of solar active regions.

ACKNOWLEDGMENTS

338

REFERENCES

Anglin, J.D., 1973, Thesis, University of Chicago, to be published.

Bame, S.J., Hundhausen, A.J., Asbridge, J.R., and Strong, I.B., 1968, *Phys. Rev. Letters* 20, 393.

Biswas, S., 1964, *Proc. Intern. Conf. Cosmic Rays,* Jaipur, Bombay Press, 1, 43.

Biswas, S., Fichtel, C.E., and Guss, D.E., 1962, *Phys. Rev.* 128, 2756.

Biswas, S. and Fichtel, C.E., 1965, *Space Sci. Rev.* 4, 709.

Chupp, E.L., 1971, *Space Sci. Rev.* 12, 486.

Comstock, G.M., Hsieh, K.C., and Simpson, J.A., 1972, *Ap. J.* 173, 691.

De Jager, C., 1968, *Mass Motions in Solar Flares and Related Phenomena,* New York, John Wiley and Sons, Inc., p. 171.

Dietrich, W.F., 1973, *Ap. J.* 180, 955.

Elliot, H., 1969, *Solar Flares and Space Research* Amsterdam, North-Holland Pub. Co., 356.

Englade, R.C., 1971, *J.G.R.* 76, 768.

Epstein, S. and Taylor, H.P., 1970, *Geochim. Cosmochin. Acta,* Suppl. 1, 2, 1085.

Fan, C.Y., Gloeckler, G., and Simpson, J.A., 1966, *Phys. Rev. Letters* 17, 3295.

Fireman, E.L., De Felice, J., and Tilles, D., 1961, *Phys Rev.* 123, 193.

Garcia-Munoz, M., Mason, G.M., and Simpson, J.A., 1973, *Ap. J.* (in press).

Geiss, J., Eberhardt, P., Buehler, F., Meister, J., and Signor, P., 1970, *J.G.R.* 75, 5972.

Geiss, J., Buehler, F., Cerutti, H., Eberhardt, P., and Filleux, Ch., 1972, *Apollo 16 Preliminary Science Report,* NASA SP.

Geiss, J. and Reeves, H., 1972, *Astron. and Astrophys.* 18, 126.

Greenstein, J.L., 1951, *Ap. J.* 133, 531.

Grevesse, N., 1969, *Mem. Soc. R. Sci. Liege 8°*, Belgium, **19**, No. 1, 249.

Hsieh, K.C., 1970, *Ap. J.* **159**, 61.

Hsieh, K.C. and Simpson, J.A., 1970, *Ap. J. (Letters)* **162**, L191.

Hsieh, K.C., Mason, G.M., and Simpson, J.A., 1971, *Ap, J.* **166**, 221 and references therein.

Lingenfelter, R.E., Flamm, E.J., Canfield, E.H., and Kellman, S., 1965, *J.G.R.* **70**, 4077.

Lingenfelter, R.E. and Ramaty, R., 1967, *High Energy Nuclear Reactions in Astrophysics*, ed. B.S.P. Shen, New York, W. Benjamin Co., Chapt. 5, p. 99.

Meyer, J.P., 1971, *12th Intern. Conf. on Cosmic Rays*, Hobart, (Tasmania, Australia) **5**, 1740.

Namba, O., 1965, *Ap. J.* **141**, 827.

Pagel, B.E.J., 1964, *Ann. Rev. Astron. Astrophys.* Palo Alto, Calif, Annual Reviews, Inc., **2**, 267 and references therein.

Ramaty, R. and Lingenfelter, R.E., 1969, *Ap. J.* **155**, 587.

Roelof, E.C., 1966, *J.G.R.* **71**, 1305.

Schaeffer, O.A. and Zähringer, J., 1962, *Phys. Rev. Letters* **8**, 389.

Severny, A.B., 1957, *Soviet Astron.* **1**, 324.

Simpson, J.A., 1963, *Semaine d'Etude sur le Probleme du Rayonnement Cosmique dans l'Espace Interplanetaire*, Vatican, Pontificia Academia Scientiarum, 323.

Simpson, J.A., 1969, NASA Document No. SL039 (unpublished).

Simpson, J.A., 1970, *Energetic Particle Measurements at the Environment of Mercury and Venus*, Jet Propulsion Laboratory, JPL 615-5.

Waddington, C.J., and Freier, P.S., 1964, *Phys. Rev.* **136**, B1535.

Wagoner, R.V., Fowler, W.A., and Hoyle, F., 1967, *Ap. J.* **148**, 3.

THE ISOTOPES OF H AND He IN SOLAR COSMIC RAYS

T. L. Garrard, E. C. Stone*, and R. E. Vogt

California Institute of Technology

ABSTRACT

The isotopic composition of H and He in solar cosmic rays has been studied with the Cal. Tech. Solar and Galactic Cosmic Ray Experiment on the Orbiting Geophysical Observatory OGO-6. Averaging over 20 days of data from seven flare events during 1969, we find the ratios $^3He/^4He = 0.10 \pm 0.02$, $D/H < 3 \times 10^{-4}$ and $T/H < 1 \times 10^{-4}$ in the 4 to 5 MeV/nucleon energy range. In addition, we find large variations in the relative abundance of ^3He from event to event, with a maximum ratio of $^3He/^4He = 0.26 \pm 0.08$ observed during October 14–15, 1969. The relative abundance of ^3He and D during this event does not seem to be consistent with existing calculations of the nuclear interaction origin of these isotopes.

INTRODUCTION

The detection of H and He isotopes in solar cosmic rays can provide important information on solar flare phenomena. Since the ambient solar abundances of deuterium, tritium and ^3He are small, larger abundances of these isotopes in solar cosmic rays could be the result of secondary production by the nuclear interaction of energetic protons and alpha particles with the ambient solar medium. The solar flare events may provide a "local" laboratory in which the astrophysical importance of high-energy nuclear interactions can be investigated.

Lingenfelter and Ramaty (1967) have performed extensive calculations of nuclear interaction processes during solar flare events and have been able to deduce the pathlength (g/cm^2) of energetic protons in the flare region. This pathlength is directly related to the density of matter and the residence time of the accelerated particles in the flare region. The pathlengths determined by Lingenfelter and Ramaty from data obtained by others during November 12, 1960 and July 18, 1961 events are summarized in Table 1.

More recently, Hsieh and Simpson (1970) reported measurements of ^3He averaged over seven solar flare events in 1967 which were obtained with a cosmic ray telescope on IMP-4. Their results are also summarized in Table 1. They concluded at that time that the $^3He/^4He$ ratio might be consistent with chromospheric abundances as known then, but that significant ^3He production during solar events could not be excluded. The decreasing relative abundance of ^3He with decreasing energy was noted as being in strong disagreement with

*Alfred P. Sloan Research Fellow.

Table 1
Previously Reported Measurements of Solar Cosmic-Ray H and He Fluxes.

Ratio	Observed	Energy (MeV/nuc)	Pathlength (g/cm²)	Event	Reference
(D/H)	$< 10^{-3}$	25 - 50	$< (0.1 - 1)$	Nov 12, 1960	Biswas et al. (1962)
(D/H)	$< 2 \times 10^{-3}$	> 50	< 3	July 18, 1961	Waddington and Freier (1964)
(T/H)	$< 10^{-3}$	20 - 45	< 0.5	Nov 12, 1960	Biswas (1964)
(T/H)	$< 6 \times 10^{-4}$	> 50	< 1	July 18, 1961	Waddington and Freier (1964)
(^{3}He/^{4}He)	0.2	~ 70	8	Nov 12, 1960	Schaeffer and Zähringer (1962)
(^{3}He/^{4}He)	$(2.1 \pm 0.4) \times 10^{-2}$	10 - 100	$\gtrsim 0.2$	averaged over 7 events (1967)	Hsieh and Simpson (1970)
	$< 1 \times 10^{-2}$	10 - 15			
	$\sim 4 \times 10^{-2}$	15 - 100			

the energy dependence expected from the nuclear interaction calculations (Lingenfelter and Ramaty, 1967).

The present results extend these earlier results in several ways. First, the isotopic abundances are determined at significantly lower energies (~ 4 MeV/nucleon). Second, simultaneous measurements of D, T, and ^{3}He provide the basis for a consistency test of the calculated nuclear interaction origin. Third, individual flare events are compared with the average solar-flare event abundances. Finally, the solar cosmic ray results can be compared with more recent determinations of solar abundances, which are summarized in Table 2.

Table 2
Solar Abundance Ratios

Ratio	Measured Abundance Ratio		Reference
D/H	Photosphere	$\leqslant 5 \times 10^{-6}$	Grevesse (1970), Hall (1972)
	Solar wind	$\leqslant 3 \times 10^{-6}$	Epstein and Taylor (1972)
^{3}He/^{4}He	Solar wind	5×10^{-4}	Geiss (1972)

342

THE EXPERIMENT

The new results are based on data acquired with the Cal. Tech. Solar and Galactic Cosmic Ray Experiment which was launched on the OGO-6 satellite. The instrument included three separate detector systems, but only the dE/dx-Range Telescope will be discussed here. As shown in Figure 1, this cosmic ray telescope consists of a stack of seven silicon solid state detectors and various aluminum and tungsten absorbers surrounded by a plastic scintillator anticoincidence cup. This telescope was designed to measure the differential energy spectra of H and He between ~1 and ~300 MeV/nucleon. Isotopic analysis is possible over a more limited energy range corresponding to those particles which penetrate the first detector (D1) and stop in the second (D2). For these particles, the ionization energy loss of the particle is measured in D1 and the residual energy of the particle is measured in D2 (see Althouse et al. (1967) for more details of the instrumentation).
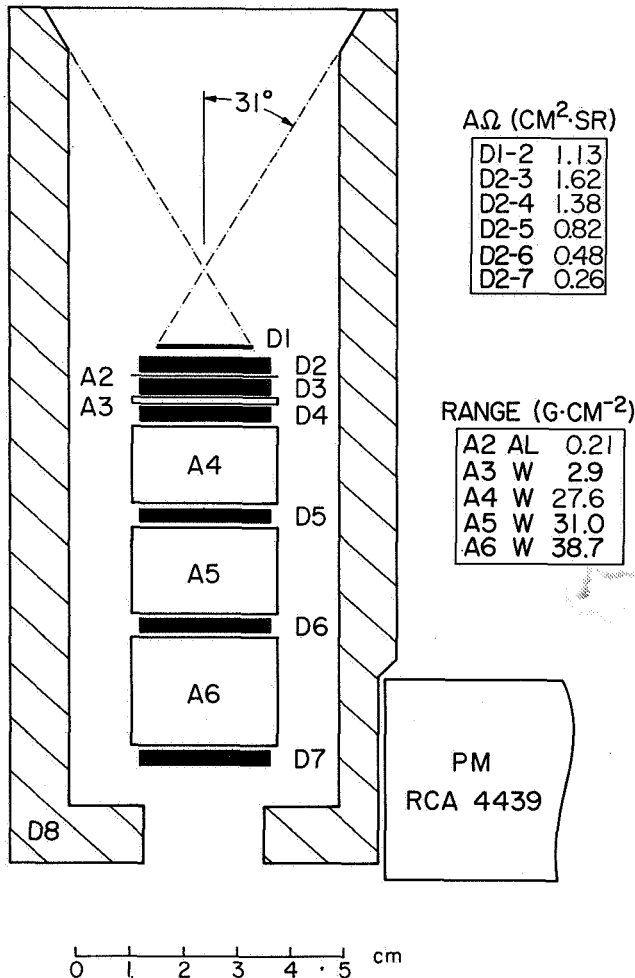
The response of the telescope to solar flare particles is shown in Figure 2, where each analyzed event is sorted according to its energy loss in D1 and the residual energy in D2. A total of ~15,000 H nuclei analyzed during the October 14–15, 1968 event are included. Also shown are the calculated locations (or tracks) of various nuclei based on both flight data and accelerator calibrations. The distribution of events about the theoretical lines for ^{1}H and ^{4}He is due mainly to statistical fluctuations in the ionization energy loss in D1 and to the uncertainty in the particle pathlength in D1 which results from the acceptable range of incidence angles defined by the 31° half-angle cone shown in Figure 1.

$A\Omega$ (CM^2·SR)

D1-2	1.13
D2-3	1.62
D2-4	1.38
D2-5	0.82
D2-6	0.48
D2-7	0.26

RANGE (G·CM^{-2})

A2	AL	0.21
A3	W	2.9
A4	W	27.6
A5	W	31.0
A6	W	38.7

Figure 1. Schematic cross section of the dE/dx-Range Telescope. Detectors D1 through D7 are silicon surface-barrier detectors, while D8 is a plastic-scintillator anticoincidence counter. D1 has a nominal thickness of 100 μm, while D2 through D7 are 1 mm thick. Particle energy loss is measured in D1, D2, and D3.

343

Although theoretical tracks are shown only for integral proton mass numbers, similar tracks can be calculated for any mass. Thus, each two-dimensional bin in Figure 2 corresponds to a range of possible masses which may be subdivided into several smaller mass bins. The events in each two-dimensional bin are then proportionally sorted into the corresponding mass bins, and the resulting mass distribution plotted as a mass histogram, much as is done with a mass spectrometer.
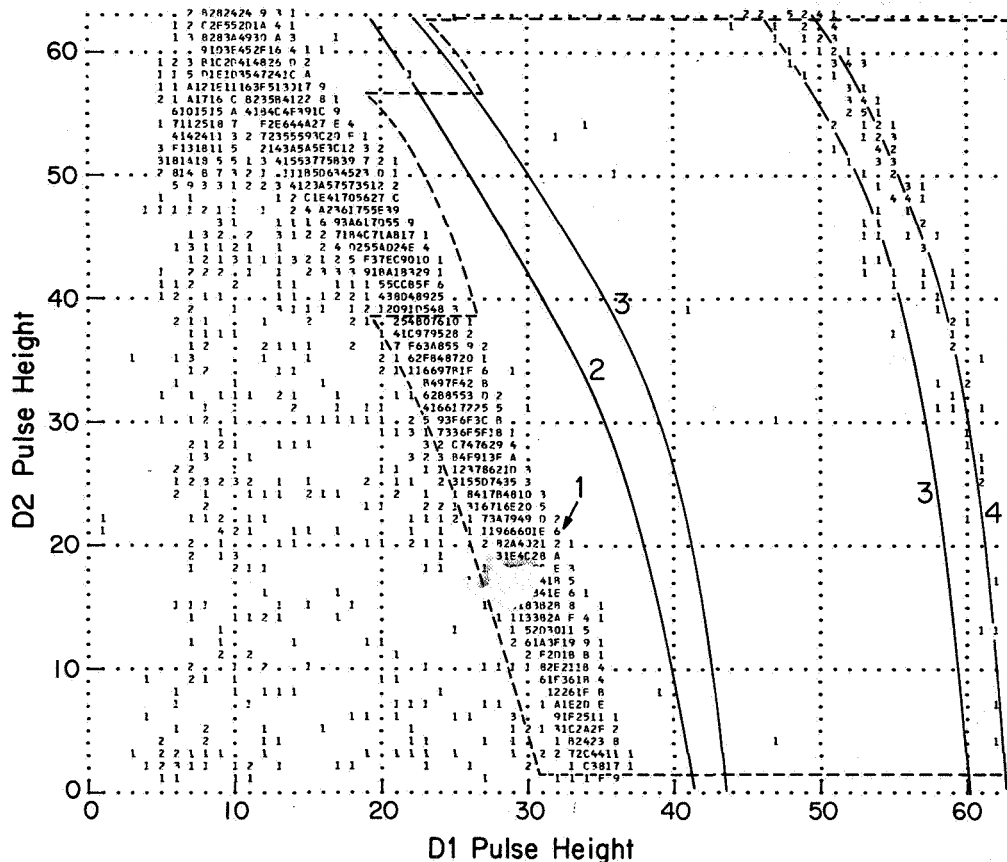
Figure 2. Two-dimensional distribution of analyzed solar-flare particles. Each analyzed event is sorted according to its energy loss in D1 (horizontal axis) and residual energy in D2 (vertical axis), with pseudologarithmic scales on both axes for graphic purposes. The numbers indicate the total number of analyzed events, in hexadecimal notation, corresponding to each value of D1 and D2 response. The dashed line circumscribes the events contained in the mass plots discussed in the text. The solid lines are the expected location of events with masses equal to 2 and 3 proton masses for Z = 1, and 3 and 4 proton masses for Z = 2.

344

The mass resolution in such a histogram is related to the actual width of the data tracks shown in Figure 2.

Also included in Figure 2 is an indication of which events are included in the mass histograms discussed below. The corresponding energy intervals are as follows: H(3.3 to 5 MeV), D(2.2 to 5 MeV/nucleon), T(1.7 to 5 MeV/nucleon), ^{3}He(4 to 6 MeV/nucleon), and ^{4}He(3.5 to 5 MeV/nucleon), measured at D1.

RESULTS

The H and He fluxes have been analyzed for seven solar flare events which occurred between June 5, 1969 and January 2, 1970. As indicated in Table 3, only data from certain periods were selected for analysis. The purpose of the selection procedure was to include only data accumulated when the detector counting rates were relatively low, so that the effects of high-rate anomalies (such as pulse pile-up) could be minimized. The criterion used was that the product of the D1 and D1D2 rates (sec^{-1}) be less than 10^4, which resulted in the analysis of data from 20 of the 40 days of enhanced fluxes.

A total of 88,502 H nuclei were analyzed during the low rate periods shown in Table 3. A mass histogram containing all of these events is shown in Figure 3. The proton peak

Table 3
Periods of Solar Particle Fluxes Included in the
Analysis of Average Abundance Ratios.

Date	H nuclei*	He nuclei**
June 7, 11, 12, 13, 1969	25692	199
Sept 25, 26, 27, 1969	15481	18
Oct 1, 2, 3, 1969	9157	71
Oct 14, 15, 1969	7817	163
Nov 6, 7, 1969	9569	188
Nov 24, 26, 27, 1969	14588	60
Dec 31, 1969, Jan 1, 2, 1970	6198	52
	88502	751

*Mainly ^{1}H (3.3 to 5 MeV)
**^{3}He (4 to 6 MeV/nuc) and ^{4}He (3.5 to 5 MeV/nuc)

at $M = 1m_p$, where m_p is the proton mass, is approximately Gaussian with $\sigma_m \approx 0.09m_p$, which is approximately the uncertainty expected from fluctuations in the ionization energy loss in D1 and from amplifier noise. Although there are no obvious peaks at $2m_p$ and $3m_p$, the expected full-width half maximum (FWHM) of the D and T distributions are indicated. The mass histogram is dominated by a rather smooth distribution of background events for masses greater than $1.4m_p$. This background is observed to depend on the detector counting rates and is most likely the result of residual pulse pile-up effects in the analog electronics system.

It is possible to derive a *conservative* upper limit to the D and T fluxes, however, without detailed analysis of the residual background. For this estimate, all events within the indicated FWHM are assumed to be D and T. With this conservative estimate, we find there must be fewer than 25 D and 14 T, yielding

Figure 3. The mass distribution of H events, averaged over 20 days of enhanced solar fluxes. The smooth curve indicates a Gaussian distribution with $\sigma_m = 0.09m_p$. Although no mass peaks are obvious at $2m_p$ and $3m_p$, the horizontal bars indicate the expected FWHM of the D and T mass distributions.

$$\frac{D(2.2-5)}{H(3.3-5)} < 3 \times 10^{-4} \qquad\qquad \frac{T(1.7-5)}{H(3.3-5)} < 2 \times 10^{-4}$$

where the numbers in parentheses indicate the energy intervals in MeV/nucleon. Although these upper limits are as much as a factor of 10 lower than previously measured, examination of Figure 3 indicates that the actual D and T fluxes must be significantly lower than the above limits, since there is no indication of mass peaks of the expected width and location. Further analysis of the background events with improved estimates of the D and T upper limits will be included in a future more extensive treatment of these results.

The 751 He nuclei analyzed during the same low rate period are included in the mass histogram in Figure 4. The ^{4}He distribution can be approximated by a Gaussian with $\sigma_m \approx 0.32m_p$, which is shown in Figure 4. The expected ^{3}He Gaussian distribution is also shown, with $\sigma_m \approx 0.24m_p$. The amplitude of both Gaussians has been normalized to the
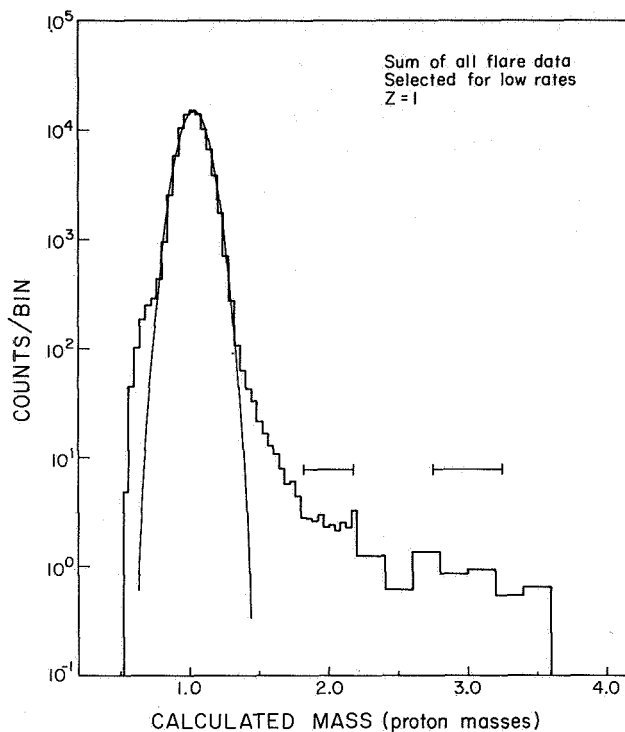
346

data. In both cases, the mass uncertainty is dominated by the uncertainty of the particles' pathlength in D1, which varies by 16 percent over the range of acceptable incidence angles. Because the distribution of possible pathlengths is not Gaussian, the mass distributions are not truly Gaussians. However, the Gaussian approximation is a convenient one for this preliminary report. Also note that no background events have been subtracted from the plotted distributions.

Based on the Gaussian fits in Figure 4, we estimate that there were ~40 ^{3}He nuclei, yielding abundance ratios of

$$\frac{^3\mathrm{He}(4-6)}{^4\mathrm{He}(3.5-5)} = 0.06 \pm 0.01$$

$$\frac{^3\mathrm{He}(4-6)}{\mathrm{H}(3.3-5)} = (5 \pm 1) \times 10^{-4}$$

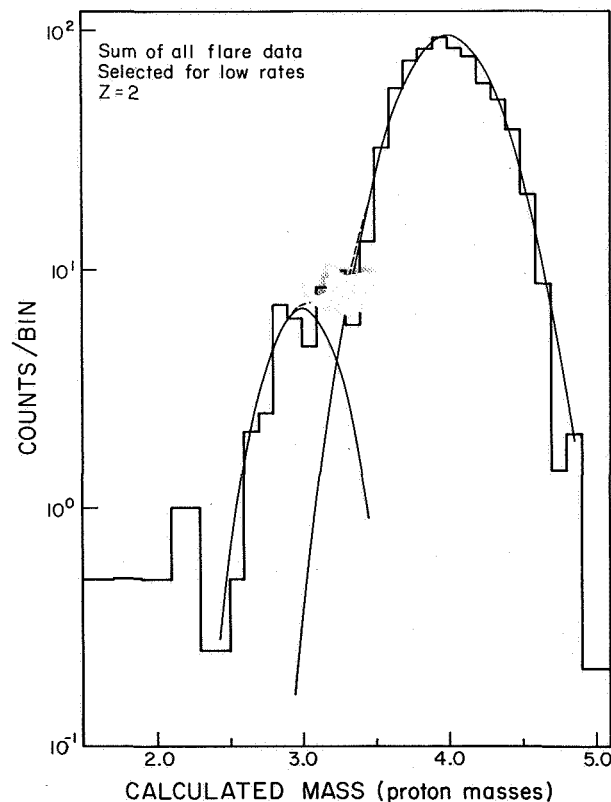$$\frac{^3\mathrm{He}(4-6)}{\mathrm{D}(2.2-5)} > 1.6$$

Figure 4. The mass distribution of He events, averaged over 20 days of enhanced solar fluxes. The smooth curves indicate the expected Gaussian distributions for ^{3}He and ^{4}He.

347

In order to compare these observations with the calculations of Lingenfelter and Ramaty (1967), it is necessary to compare fluxes at the same energy/nucleon. The interval of 4 to 5 MeV/nucleon is common to all of the above observations and was used in calculating the observed ratios in Table 4. The ratio $\Gamma(A,B)$ is defined as

$$\Gamma(A,B) = \frac{N_A}{N_B}$$

where N_A and N_B are the number of observed events of isotopes A and B in the 4 to 5 MeV/nucleon interval. The uncertainties assigned to the $\Gamma(A,B)$ in Table 4 are statistical only ($\pm 1\sigma$), with upper limits given for an 84 percent confidence level. Note that the data in Table 4 are a subset of the data included in the mass plots.

Table 4

Abundances of 4 to 5 MeV per Nucleon Isotopes.

	20-Day Average	Nov 6–7, 1969	Oct 14–15, 1969
H events	36714	4654	3666
D events	$\lesssim 7$	$\lesssim 1$	~ 0
T events	$\lesssim 2$	$\lesssim 1$	~ 0
^{3}He events	22	$\lesssim 2$	12
^{4}He events	223	72	47
$\Gamma(D,H)$	$< 3 \times 10^{-4}$	$< 7 \times 10^{-4}$	$< 5 \times 10^{-4}$
$\Gamma(T,H)$	$< 1 \times 10^{-4}$	$< 7 \times 10^{-4}$	$< 5 \times 10^{-4}$
$\Gamma(^3$He,H$)$	$(6 \pm 1) \times 10^{-4}$	$\lesssim 1 \times 10^{-3}$	$(3 \pm 1) \times 10^{-3}$
$\Gamma(^4$He,H$)$	$(6.1 \pm 0.4) \times 10^{-3}$	$(1.5 \pm 0.2) \times 10^{-2}$	$(1.3 \pm 0.2) \times 10^{-2}$
$\Gamma(^3$He,^{4}He$)$	0.10 ± 0.02	< 0.06	0.26 ± 0.08
$\Gamma(D,^3$He$)$	< 0.5	—	< 0.16

A direct comparison of these ratios with the calculations is complicated by two factors. First, the 4 MeV/nucleon particles observed at earth must have had higher energies at the sun, since the particles lose energy due to adiabatic deceleration as they propagate in the expanding solar wind. Second, the Lingenfelter and Ramaty calculations do not extend below secondary energies of ~ 10 MeV/nucleon. For these reasons, only an illustrative comparison can be made in absence of more detailed calculations.

For such a comparison, we assumed that the observed particles were produced at $\sim$10 MeV/nucleon by protons with a differential rigidity spectrum given by $dJ/dP \propto \exp(-P/P_0)$, with $P_0 = 60$ MV, which is similar to that observed near earth. With these assumptions we used Figures 14 to 16 in Lingenfelter and Ramaty (1967) to determine the total solar material, X(30 MeV), penetrated by 30 MeV protons in producing the observed ^{3}He, D and T. The ^{3}He abundance corresponds to a pathlength X(30 MeV) ≈ 1.5 g/cm^2, while the upper limit D and T fluxes correspond to X(30 MeV) < 0.8 g/cm^2. These numbers are comparable to those determined by Ramaty and Lingenfelter and Hsieh and Simpson (Table 1). However, because of the difficulties discussed above, these pathlength numbers must be considered illustrative and not quantitative. It is not possible with this analysis of average abundances to demonstrate conclusively that the pathlengths required for ^{3}He and D production are either consistent or inconsistent.

In order to further investigate the degree of consistency of the ^{3}He and D observations with a nuclear interaction origin, the data were separated according to individual flare events. Although the data from individual events had larger statistical uncertainties, it was discovered that there were large variations in the ^{3}He relative abundance.* This variation is indicated in the following detailed discussion of data acquired during November 6–7, 1969 and October 14–15, 1969.

The H and He mass histograms from the November 6–7, 1969 interval are shown in Figures 5 and 6. The corresponding ratios for 4 to 5 MeV/nucleon isotopes are included in Table 4. During this two-day period, which is a subset of the low rate data interval in Figures 3 and 4, the ^{3}He relative abundance was significantly lower than the average discussed above. Thus, this was a ^{3}He-poor interval. Any real systematic effect which simulates ^{3}He should be no larger than that shown in Figure 6.

For comparison, the mass histograms for the October 14–15, 1969 interval are shown in Figures 7 and 8, and the corresponding 4 to 5 MeV/nucleon ratios are included in Table 4. This is the richest ^{3}He interval in the above 20-day low-rate period.

We can use the data from the ^{3}He-rich interval to further investigate the origin of ^{3}He, D, and T. Since the $\Gamma(^3$He,H) is $\sim$5 times the average value, the pathlength of 30 MeV protons in solar matter must be $\sim$5 times larger than that calculated above, that is X(30 MeV) $\approx$ 8 g/cm^2. On the other hand, the upper limit for Γ(D,H) is only 1.7 times larger than the upper limit for the average, indicating that X(30 MeV) < 1.4 g/cm^2. Thus, there would appear to be an inconsistency in the relative amounts of ^{3}He and D as calculated and observed.

Since the above comparison was based upon the illustrative calculation described earlier, which had a number of uncertainties associated with it, it may be more useful to make

---

*J. A. Simpson at this Symposium also reported the observation of "^{3}He-rich" and "^{3}He-poor" solar flare events.

Figure 5. The H mass distribution for Nov 6-7, 1969.
This is a subset of the data in Figure 3.

Figure 6. The He mass distribution for Nov 6-7,
1969. This is a subset of the data in Figure 4. It is
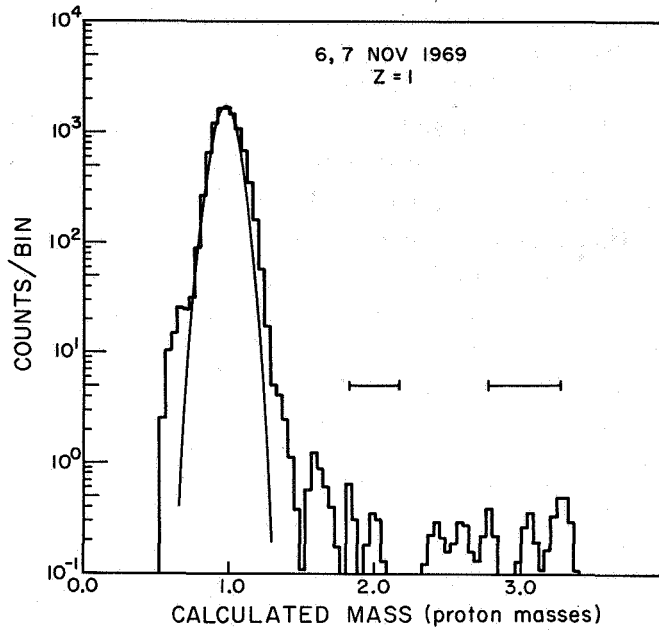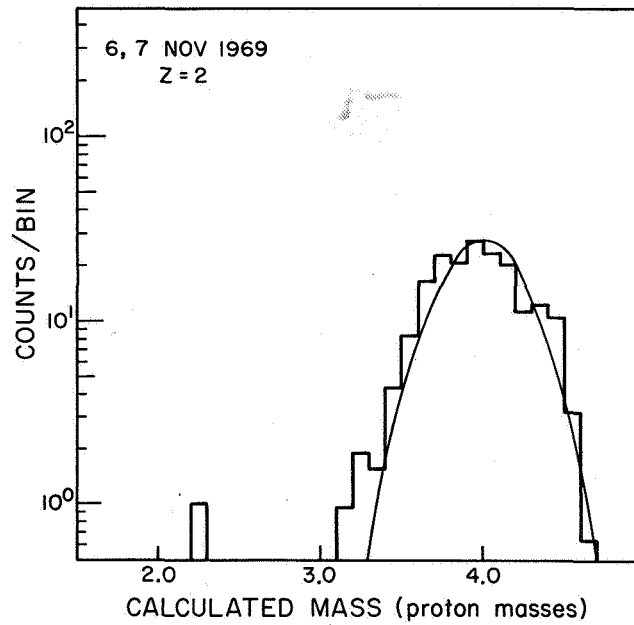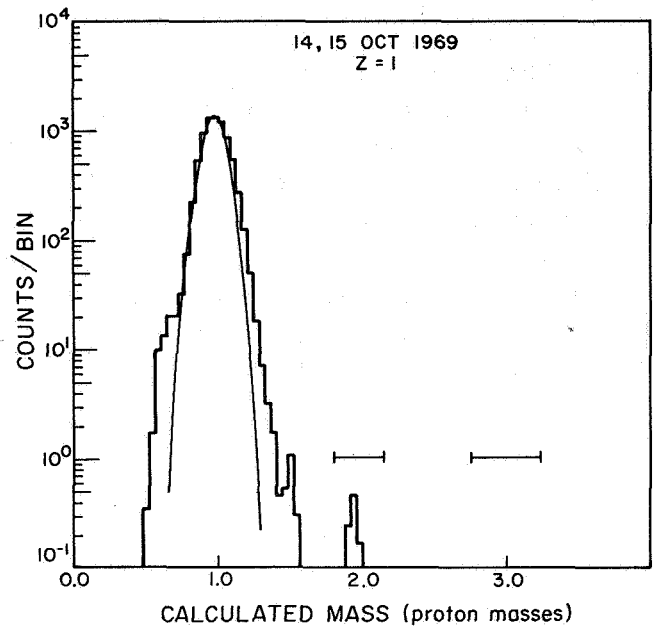an example of a ^{3}He-poor interval.

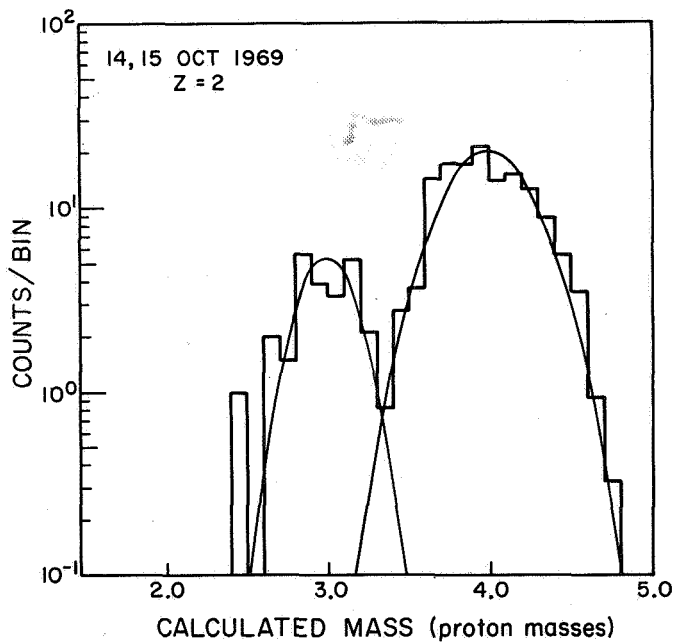Figure 7. The H mass distribution for Oct 14-15, 1969. This is a subset of the data in Figure 3.

Figure 8. The He mass distribution for Oct 14-15, 1969. This is a subset of the data in Figure 4. It is the richest ³He interval observed.

a direct comparison of the observed $\Gamma(^3\text{He,D})$ and the ratio of the production cross sections for ^3He and D. Meyer (1971) has collected the available cross section data for the various reactions resulting from p + ^4He. For low-energy (23 to ~200 MeV) protons, the ratio of production cross sections is $\sigma(\text{D})/\sigma(^3\text{He})$ ~0.9. Thus, it might be expected that approximately equal numbers of D and ^3He should be produced. Since the D and ^3He are not produced with the same distribution of energies, the expected $\Gamma(\text{D},^3\text{He})$ ratio at a given energy/nucleon might be a factor of ~2 smaller, depending on the energy. However, the observed ratio is $\Gamma(\text{D},^3\text{He}) < 0.16$, which is smaller than expected. Thus, this analysis indicates that D and ^3He abundances are not consistent with a nuclear interaction origin as presently calculated. However, the alternative suggestion that the large $^3\text{He}/^4\text{He}$ is characteristic of the solar material which is accelerated during a solar-flare event is inconsistent with the observed solar abundances listed in Table 2.

DISCUSSION

The variable relative abundance of ^3He and the overabundance of ^3He compared to D and ^4He suggests a reexamination of a number of aspects of solar flare phenomena. One possibility may be a variable preferential acceleration of ^3He compared to ^4He, since the Z/A for ^3He is 0.67, while for ^4He it is 0.50. However, such a simple Z/A preferential acceleration would presumably even more enhance H compared to ^4He, since Z/A = 1 for H. However, the $\Gamma(^4\text{He,H})$ for November 6–7, 1969 and October 14–15, 1969 are essentially the same, suggesting that if preferential acceleration is responsible for the inconsistencies, the A- and Z-dependences are not simple.

The inconsistencies may also be the result of the assumption that the nuclear interaction secondaries undergo no additional acceleration after formation. Perhaps the secondaries are produced prior to the final acceleration process, which then accelerates secondary-enriched material. It should be noted, however, that the reaction thresholds are greater than 23 MeV, so that any preflare production would require the presence of protons with reasonably high energies. In addition, there would have to be an enhancement of ^3He compared to D during such a preflare phase.

Another area of possible investigation is the consideration of the detailed kinematics of the secondary particles and their subsequent nuclear interactions. Lingenfelter and Ramaty made the reasonable assumption in their calculation that all of the secondary nuclei emerged from an interaction at the same energy per nucleon which is uniquely related to the energy of the incident particle. Perhaps this assumption is not accurate enough at low energies.

The effects of propagation between the source and earth also require further examination, especially with regard to the effects of adiabatic deceleration on the energies of the particles.

352

SUMMARY

The flux of ^{3}He nuclei with $\sim$4 MeV/nucleon has been measured in solar cosmic rays. The relative abundance of ^{3}He and ^{4}He varies considerably from event to event, with the average being $\Gamma(^3\text{He},^4\text{He})$ = 0.10 ±0.02 and the maximum observed ratio being $\Gamma(^3\text{He},^4\text{He})$ = 0.26 ±0.08. In all cases, only upper limits to the fluxes of D and T were determined, with the average over 20 days giving $\Gamma(\text{D,H}) < 3 \times 10^{-4}$ and $\Gamma(\text{T,H}) < 1 \times 10^{-4}$. These are conservative upper limits; any actual flux is likely to be much smaller. During at least one event, the abundance of ^{3}He was considerably enhanced without a corresponding enhancement in D. The relative abundance of ^{3}He and D was not consistent with expected abundances based on production cross sections, suggesting additional refinement is necessary in the calculation of the origin of ^{3}He, D, and T in solar flares.

ACKNOWLEDGMENTS

REFERENCES

Althouse, W.E., Stone, E.C., Vogt, R.E., and Harrington, T.H., 1967, *IEEE Trans. Nuc. Sci.* **15**, 229.

Biswas, S., 1964, *Proc. Intern. Conf. Cosmic Ra   aipur,* December 1963, I, 43.

Biswas, S., Fichtel, C.E., and Guss, D.E., 1962, *Phys. Rev.* **128**, 2756.

Epstein, S., and Taylor, H.P., Jr., 1972, *Geochim. Cosmochim. Acta* (in press)

Geiss, J., 1972, *Proc. Asilomar Conf. on Solar Wind,* 559.

Grevesse, N., 1970, *Colloque de Liege* **19**, 251.

Hall, D., 1972 (to be published).

Hsieh, K.C., and Simpson, J.A., 1970, *Ap. J.* **162**, L191.

Lingenfelter, R.E., and Ramaty, R., 1967, *High-Energy Nuclear Reactions in Astrophysics,* ed. B. S. P. Shen (New York: W.A. Benjamin, Inc.).

Meyer, J.P., 1971, *Proc. Intern. Conf. Cosmic Rays,* Hobart, Australia, **5**, 1740.

Schaeffer, O.A., and Zähringer, J., 1962, *Phys. Rev. Letters* **8**, 389.

Waddington, C.J., and Freier, P.S., 1964, *Phys. Rev.* **136**, B1535.

VI: ENERGETIC PARTICLES FROM THE SUN

MAGNETIC FIELD RECONNECTION AND PARTICLE ACCELERATION

B. U. Ö. Sonnerup

Radiophysics Laboratory, Dartmouth College

ABSTRACT

After a brief review of steady-state reconnection models, the processes are discussed which place an upper limit on the reconnection rate. In many applications the requirement that the width of the diffusion region exceed the ion gyroradius leads to a severe restriction on this limit. Unless the conductivity is much less than the value given by Spitzer's formula, solar flare times may result which are too long by a factor of 1000 or more. Turbulent and gyro effects which may lead to a reduced conductivity are shown to be operative, but only for sufficiently small ratios of plasma to magnetic pressure in the inflow.

Particle energization processes associated with magnetic-field reconnection and particle reflection by fast shocks are considered briefly. These processes are effective as a first stage in the acceleration of charged particles, but additional multistep processes are needed to reach proton energies above a few MeV.

INTRODUCTION

This paper discusses two topics of fundame *-¹ importance in cosmic physics, namely magnetic-field reconnection and particle accꞈeration. In solar physics, magnetic-field reconnection is often invoked to explain the rapid release of energy in solar flares and efficient particle acceleration processes are needed to account for the associated production of large numbers of energetic particles.

Both topics have been dealt with at great length in the literature. It would be impossible to do justice to all of these researches in the time available. For this reason, the present paper will focus on certain special but important aspects of the two topics. Specifically, the discussion of magnetic-field reconnection is limited to steady-state models and concerns itself primarily with those processes which determine the maximum reconnection flow rate. Similarly, among particle acceleration processes, only acceleration at X-type neutral points and at slow and fast shocks are touched upon, since all of these are directly or indirectly associated with the reconnection process as applied to the solar flare.

TWO MODELS OF FIELD RECONNECTION

Perhaps the best known mathematical model of steady-state magnetic-field reconnection is the one due to Petschek (1964), first described at the AAS-NASA Solar-Flare Symposium

here at Goddard Space Flight Center nine years ago. In order to appreciate some of the ideas to be presented later on, it is desirable to briefly review the main properties of the Petschek model.

In this model, as in most other reconnection models, two oppositely magnetized, highly conducting plasma regions come together at an X-type magnetic null point, and the plasma is ejected with high speed and low magnetization in a direction perpendicular to the inflow. The magnetic field and flow configuration, for simplicity taken to be two-dimensional, is shown in Figure 1(a). The plasma inflow takes place in the $\pm x$ direction, while the ejection flow is along the $\pm y$ direction. The bulk of the plasma is accelerated to the ejection flow speed in a set of magnetohydrodynamic (MHD) slow shock waves, shown by wavy lines in the figure.

The frozen magnetic-field condition holds, except in the vicinity of the X-type magnetic null point, that is, in the usual notation and MKSA units we have

$$\underline{E} + \underline{v} \times \underline{B} = 0$$

This formula implies that an electric field, $E_0 \underline{z}$, must be present in the flow field. Faraday's law further requires that E_0 must be a constant, independent of the coordinates x and y. This being the case, it is clear that the frozen-field condition must be violated at the origin where the magnetic field and the plasma velocity, $\underline{v}$, both vanish. In the vicinity of this point resistive diffusion of the magnetic field through the semistagnant plasma takes place. This region is known as the diffusion region and may be thought of as a small box of dimensions $2x^*$ by $2y^*$, surrounding the magnetic null point. Outside the diffusion region magnetic flux is transported by convection, in accordance with the frozen field condition.

The phrase magnetic-field reconnection or merging may be understood in terms of the frozen-field condition. Pairs of magnetic field lines, such as AB and CD in Figure 1(a), identified via the plasma frozen to them, flow toward the magnetic null point. At that point the field lines are cut and reconnected to form a new pair of lines, $A'C'$ and $B'D'$, in the exit flow.

The term magnetic-field annihilation is sometimes used. It refers to the fact that the magnetic-field energy in the inflow is converted into kinetic and thermal plasma energy via the slow shocks, leaving little magnetic energy in the exit flow. It is because of this energy conversion that magnetic-field reconnection is of interest in solar-flare physics.

The basic formulas governing incompressible flow in the Petschek model are:

$$M_1 \cong v_1/v_{A_1}$$

$$v_2 = v_{A_1}$$

$$B_2 = M_1 B_1 \tag{1}$$

$$x^*/y^* = M_1$$

$$\mu_0 \sigma v_1 x^* = 1$$

Here the indices 1 and 2 refer to conditions in the inflow and outflow regions respectively, as shown in Figure 1. Further, the symbol v denotes flow speed, and v_A is the Alfvén speed. Thus, M_1 is the Alfvén number in the inflow region. This quantity is commonly used as a measure of the magnetic field reconnection rate. The symbols σ and μ_0 denote the electrical conductivity and the vacuum permeability, respectively.

From these formulas it is apparent that B_2, the magnetic field in the ejection region, increases as the reconnection rate M_1 increases. This corresponds to an increase in the (acute) angle between the shock waves, and a readjustment of the magnetic field in the inflow region, as shown qualitatively in Figure 1(b). It is also apparent that the diffusion region, which is extremely elongated in the y direction for small reconnection rates, becomes more square as M_1 increases. At the same time, its absolute size decreases, as is evident from the last of Equations (1). Incidentally, this equation merely assures that the magnetic Reynolds number, based on the inflow speed and the half-width x^* of the diffusion region, is equal to unity, a requirement designed to assure that the diffusion of magnetic field through the semistagnant plasma inside the diffusion region matches the convective flux transport outside.

Noticeable in Figure 1 is the gradual weakening of the magnetic field in the inflow region immediately adjacent to the diffusion region as M_1 increases. By use of an extrapolation into the nonlinear domain of the results of a linear perturbation analysis for the magnetic-field configuration in the inflow region, Petschek estimated that this effect will choke the flow in accordance with the approximate inequality

$$M_1 \leq \frac{\pi}{4\ell n \, (2\mu_0 \sigma v_{A_1} L M_1{}^2)} = \frac{\pi}{4\ell n \, (L/y^*)} \tag{2}$$

where $2L$ is the length of the entire reconnection region, shown in Figure 1(a). This formula depends only logarithmically upon the large quantities σ and L and permits flow rates up to $M_1 \cong 0.05$ under conditions characteristic for a solar flare. These rates are sufficiently large to account for the characteristic energy-release time in a solar flare.
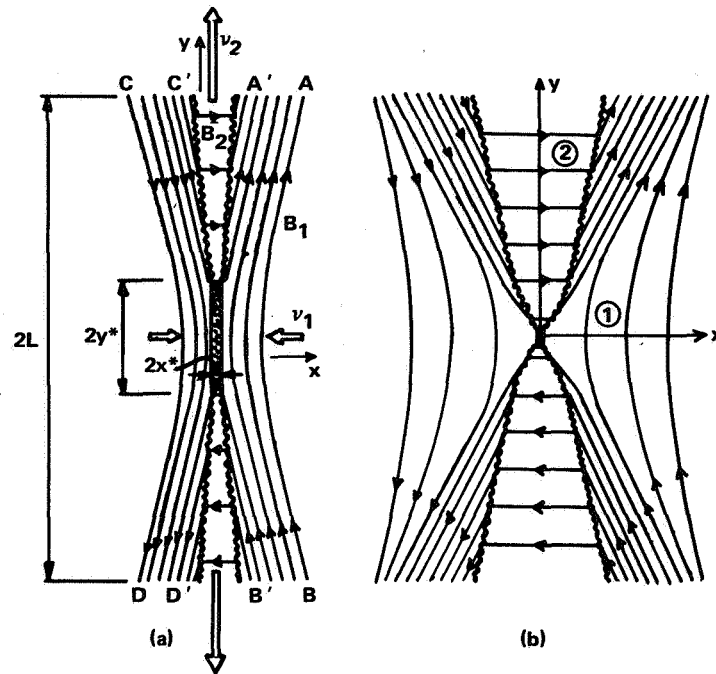
Figure 1. Petschek's reconnection model (a) for small, (b) for
large connection rate.

A somewhat different model of the reconnection process, due to Sonnerup (1970), is shown in Figure 2. It is a special case of a more general family of self-similar reconnection geometries studied by Yeh and Axford (1970). In fact, it is the only nonsingular, and hence the only physically relevant member of the Yeh-Axford family of solutions. It is seen that this model, in addition to the Petschek switch-off waves OA, also involves another set of waves OB. In the incompressible limit these latter waves, like the waves OA, are simply Alfvén waves; in compressible flow they become slow expansion waves forming a fanlike structure centered at B. This implies that such a wave would have to be generated at a precisely located source of disturbance such as a corner in the flow boundary at B. Presumably it would not be present otherwise. Such a boundary condition probably has little practical interest, at least in cosmical physics, and so one would not expect the waves OB actually to be present. Rather the waves OB should be viewed as a mathematical model, lumping all of the MHD interaction in front of the Petschek waves into one line. The advantage of such a model is that it offers an exact solution of the MHD equations, whereas the Petschek model is an approximate one, open to criticism, in particular when applied to large reconnection rates.

The reconnection model shown in Figure 2 has the same general characteristics as the Petschek model: As the reconnection rate increases, the angle between the Petschek waves increases, and the diffusion region shrinks and becomes more square. The equations corresponding to Equations (1) are (Sonnerup, 1970):

$$M_1 \equiv v_1/v_{A_1}$$

$$v_2 = v_{A_1}(1+\sqrt{2})$$

$$B_2 = M_1 B_1/(1+\sqrt{2}) \tag{3}$$

$$x^*/y^* = M_1/(1+\sqrt{2})$$

$$\mu_0 \sigma v_1 x^* = g(M_1)$$

where $g(M_1)$ is a function which decreases monotonically from a value of about seven for $M_1 = 0$ to the value zero for $M_1 = (1+\sqrt{2})$, and for which dg/dM_1 vanishes at $M_1 = 0$. Apart from numerical constants, these equations are the exact counterparts of (1), at least for small M_1 values where $g(M_1)$ is essentially constant. The discrepancy between the value $g(0) \approx 7$ and the value of unity appearing on the right-hand side in the last of (1) is accounted for by a difference in the definition of the size of the diffusion region in the two models, the Petschek model having considerably smaller values of x^* and y^*.

A substantial difference between the two reconnection models is that the present model appears to permit much larger reconnection rates. In fact, the formula replacing (2) is

$$M_1 \leqslant (1 \qquad) \tag{4}$$

The field configuration corresponding to this maximum flow rate is shown in Figure 2(b). The symmetry between the inflow and outflow regions in this figure indicates that no conversion of magnetic energy takes place. It is noted that this maximum flow rate would require a decreasingly small diffusion region.

In constrast to the Petschek model, the maximum flow rate, as given by (4), is independent of both the conductivity σ and the overall scale L, as first pointed out by Axford (1969). But it is conceivable that this discrepancy may be explained by noting that the reconnection rate M_1 is based on the strong magnetic field at infinity in Petschek's model, whereas in the model of Figure 2, M_1 is based on the relatively weak magnetic field in the inflow region. The magnetic configuration shown in Figure 2 may apply only in a thin region adjacent to the diffusion region, with the field at larger $|x|$ values relaxing gradually to a curl-free configuration of oppositely directed uniform fields, which would be considerably stronger than the field B_1.

A definite resolution of this problem must await further calculations. In the next section, it is shown that in many cases the problem is an academic one, since the upper limitation on the reconnection rate in a real collision-free plasma often derives neither from (2) nor (4) but rather from certain restrictions on the minimum size of the diffusion region.

ION GYRO LIMITATION

As pointed out in the previous section, the diffusion region shrinks as the field-reconnection rate increases. Both of the formulas (2) and (4) are derived from magnetohydrodynamics, and assume that there is no lower limit on the size of that region. In fact, in the latter formula the value $M_1 = 1+\sqrt{2}$ would occur only if the linear dimensions x^* and y^* vanish. But a real plasma possesses certain inner length scales, such as the Debye length, the electron and ion gyroradii, and the mean-free path. The question is which of these lengths will pose an appropriate lower limit on the minor dimension, x^*, of the diffusion region.
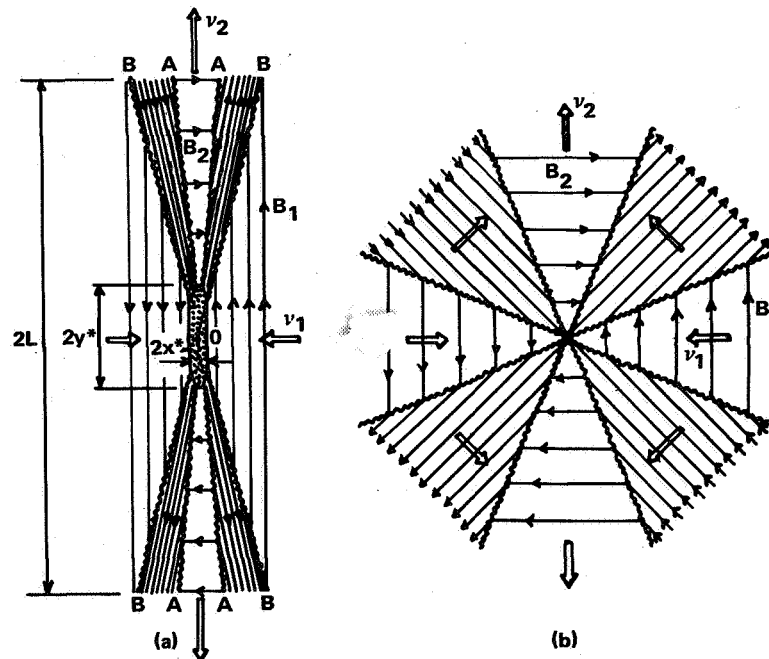

Figure 2. Reconnection model of similarity type (a) for small, (b) for maximum reconnection rate.

In most cosmical applications, including the solar flare, the mean-free path is too long to provide an appropriate lower limit. The ions and electrons perform many gyrations in the magnetic field between collisions. Simple considerations of particle orbits near the X-type

magnetic null point indicate that the current in the diffusion region normally is carried primarily by the ions, and that the proper lower limit on the half-width x^* of that region is of the order of the ion gyroradius R_i. In addition, the shock thickness is also expected to be comparable to the ion gyroradius. Thus, for purely geometrical reasons it is difficult to imagine values of x^* less than R_i, and

$$x^* > R_i = \frac{m_i}{eB_1} \sqrt{2kT_{i1}/m_i} \tag{5}$$

The value of R_i given in (5) represents a lower limit because a) the actual magnetic field adjacent to the diffusion region is expected to be lower than B_1 (for example, Petschek's choking mechanism); b) the ion temperature in the diffusion region is expected to be greater than in the inflow region; and c) the gyroradius should have been based on the total speed $\sqrt{v_1^2 + 2kT_{i1}/m_i}$ of the ions.

Starting from the last of Equations (1) we find that the condition $x^* > R_i$ yields

$$M_1 < \frac{1}{\mu_0 \sigma R_i v_{A_1}} \tag{6}$$

In Table 1 the maximum field reconnection rates resulting from this formula are compared to those obtained from the Petschek formula (2) for two electron densities, temperatures, and magnetic fields of interest in solar physics. The conductivity was calculated from the usual Spitzer formula for a mixture of electrons and protons. In addition to the M_1 values, characteristic flare times, τ_f, corresponding to a flare size $D = 10^4$ km are given, that is, $\tau_f = D/v_1$. The times in the last column are independent of L and depend only logarithmically upon the density.

Table 1

Reconnection Rates, M_1 and Flare Times, τ_f, from
Petschek's Formula (2) and the Ion Gyro Limitation
(6), Using the Spitzer Conductivity

n (cm^{-3})	T (K)	B$_1$ (gauss)	Equation (2) M$_1$	Equation (2) τ_f (s)	Equation (6) M$_1$	Equation (6) τ_f (s)
10^{11}	10^4	100	0.044	328	0.059	246
		500	0.041	71		49
10^9	10^6	100	0.031	47	1.08×10^{-6}	1.34×10^6
		500	0.027	11		2.68×10^5

The numbers in Table 1 indicate that for high temperatures the effect limiting the reconnection rate is the ion gyroradius effect rather than the choking effect described by the Petschek formula, at least in circumstances where the conductivity is given by the Spitzer formula. Futhermore, for the higher temperature, 10^6 K, the resulting flare times are too long by a factor of about 1000. Thus, flare models involving field reconnection in the lower corona or higher run into serious difficulties unless means are found to substantially decrease the electrical conductivity. Two processes which might accomplish this will be discussed.

TURBULENT RESISTIVITY

The electrical conductivity in the diffusion region may be reduced below the value given by the Spitzer formula by a variety of microinstabilities. Dominant among these is the ordinary ion-acoustic two-stream instability, which in suitable circumstances leads to the generation of intense ion-sound turbulence. In order for this instability to occur in a plasma where the electron and ion temperatures, T_{eo} and T_{io}, are equal, it is required that the current drift speed, w_c, obeys the inequality

$$w_c \gtrsim \sqrt{2kT_{eo}/m_e}$$

where the index o denotes conditions in the diffusion region. But the instability, once initiated, is known to heat the electrons preferentially, (Sagdeev, 1967; Smith and Priest, 1972), and as this occurs the threshold drift speed is lowered toward the ion sound speed. Other electron-heating mechanisms are also possible (Coppi and Friedland, 1971). In general, the instability criterion may be written in the form

$$w_c \geq f(T_{eo}/T_{io}) \sqrt{2kT_{io}/m_i} \tag{7}$$

where the function $f(T_{eo}/T_{io})$, for an electron-proton plasma, is plotted in Figure 3 (dashed curve). (The curve is taken from Fredricks, 1969).

The effective conductivity associated with this instability, in a state of turbulent saturation, has been estimated by Sagdeev (1958) as

$$\sigma_{turb} = \frac{ne^2}{m_e} \left(\frac{10^2}{\Pi_i} \frac{\sqrt{kT_{eo}/m_i}}{w_c} \frac{T_{io}}{T_{eo}} \right) \tag{8}$$

where Π_i is the ion plasma frequency, that is

$$\Pi_i = \sqrt{\frac{ne^2}{\epsilon_0 m_i}}$$
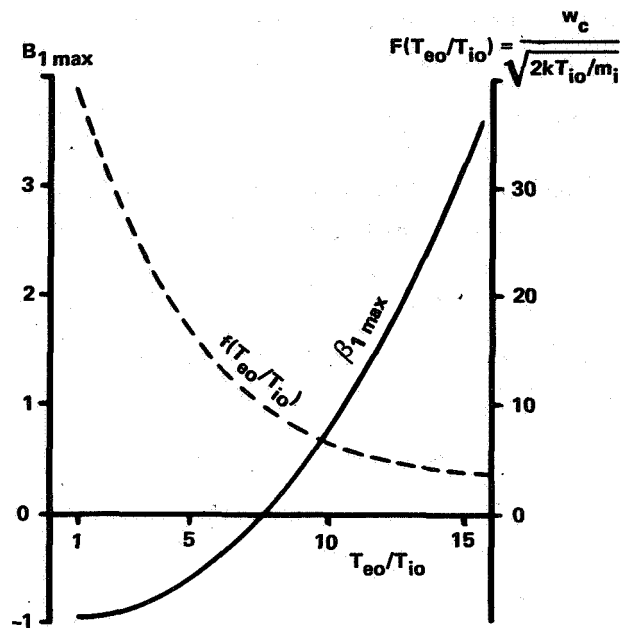
Figure 3. Marginal stability curve for ion-acoustic
two-stream instability (dashed curve), and maximum
β_1 values for turbulent reconnection (solid curve).

Table 2 shows a comparison of reconnection rates and flare times calculated from the ion
gyro limitation, (6), in an electron-proton plasma as well as from Petschek's formula (2),
with the turbulent conductivity given by (8). Also, it has been assumed, arbitrarily, that T_{eo}
= $10T_{io}$ in the diffusion region.

Table 2

Reconnection Rates and Flare Times From Petschek's
Formula (2) and From the Ion Gyro Limitation (6),
Using the Turbulent Conductivity In Equation (8)

n	T	B	Equation (2)		Equation (6)	
(cm^{-3})	(K)	(gauss)	M_1	τ_f (s)	M_1	τ_f (s)
10^9	10^6	100	0.056	26	0.36	4
10^{10}				82		13

It is evident that the effective conductivity is now sufficiently low so that the reconnection process may account for the energy release time in solar flares with a comfortable margin. Further, the Petschek limitation, if correct, again comes into play.

But it is not obvious that the threshold value for the current drift speed w_c given by (6) can be actually reached. The value of w_c may be estimated from Ampere's law. For reconnection rates much smaller than unity, the current in the diffusion region may be viewed as a sheet current with a sheet thickness of $2x^*$. Hence Ampere's law gives

$$(2x^*) \, n_o \, e w_c = 2B_1/\mu_o \qquad (9)$$

where n_o is the electron density in the diffusion region. For small flow speeds v_1 this density may be estimated from a simple static pressure balance across the diffusion region:

$$n_o k \, (T_{eo} + T_{io}) = \frac{B_1^2}{2\mu_o} + n_1 k (T_{el} + T_{il}) \qquad (10)$$

The ion gyro limitation implies that the half width x^* of the diffusion region must exceed the ion gyroradius. It follows from Equations (5), (9), and (10) that

$$w_c < \sqrt{2 \frac{kT_{io}}{m_i}} \left(1 + \frac{T_{eo}}{T_{io}}\right) / (1 + \beta_1) \qquad (11)$$

where β_1 is the ratio of plasma pressure to magnetic pressure in the inflow region, that is

$$\beta_1 \equiv \frac{2\mu_o n_1 k (T_{el} + T_{il})}{B_1^2}$$

Comparison between the inequalities (7) and (11) finally gives

$$\beta_1 < \left[\frac{1 + T_{eo}/T_{io}}{f(T_{eo}/T_{io})} - 1\right] \qquad (12)$$

This inequality derives from two conflicting demands on the width $2x^*$ of the diffusion region: a) the current drift speed must exceed the instability threshold, which requires a small value of x^*, and b) the value of x^* must not be less than the ion gyroradius. The Equation (12) indicates that turbulent diffusion, leading to the high reconnection rates shown in Table 2, is possible only for sufficiently small β_1 values, where β_1 is the ratio of plasma pressure to magnetic pressure in the inflow. The limiting β_1 value is plotted as a function of T_{eo}/T_{io} in Figure 3 (solid curve). Note that a temperature ratio greater than $\cong 8$ must be sustained in the diffusion region if turbulent diffusion is to occur.

While the preceding calculation is by necessity rather crude, it nevertheless contains those physical elements expected to be essential in determining the presence or absence of ion-sound turbulence in the diffusion region.

366

LAMINAR RESISTIVITY

Even in the complete absence of collisions and noise the effective conductivity in the diffusion region is finite, as pointed out by Dungey and Speiser (1969), Speiser (1970), and Sonnerup (1970). The reason for this effect is that the residence time, τ, of a particle in the diffusion region is finite, so that the particle is accelerated in the direction of the electric field E_0 only during a time of the order of τ. The residence time may be estimated as one-half of a gyroperiod in the weak field B_2, in the ejection region. The currents in the diffusion region are predominantly ion currents so that

$$\tau \cong \pi \, \frac{m_i}{eB_2}$$

and the effective laminar conductivity (termed gyroconductivity by Speiser) is

$$\sigma_{lam} \cong \frac{ne^2}{2m_i} \, \tau \cong \frac{\pi}{2} \, \frac{ne}{B_2} \tag{13}$$

(Note that σ_{lam} is in fact independent of whether the current is carried by ions or electrons.)

With this expression for σ, the ion gyro limitation (6) becomes

$$M_1 < \frac{2}{\pi} \, \frac{v_{A_1}}{v_i} \, \frac{B_2}{B_1} \tag{14}$$

where the ion gyroradius is based on the total ion velocity v_i rather than the thermal component alone, that is,

$$v_i = \sqrt{v_1^2 + 2kT_{i\parallel}/m_i}$$

But according to the third of Equations (1) we have $B_2/B_1 \cong M_1$ so that the inequality (14) becomes

$$\frac{v_i}{v_{A_1}} = \sqrt{M_1^2 + \frac{\beta_1}{(1 + T_{e\parallel}/T_{i\parallel})}} \leq \frac{2}{\pi}$$

that is

$$M_1^2 < \frac{4}{\pi^2} - \frac{\beta_1}{1 + (T_{el}/T_{il})} \qquad (15)$$

It follows that reconnection dominated by laminar resistivity is possible only for

$$\beta_1 < \frac{4}{\pi^2} \left(1 + \frac{T_{el}}{T_{il}} \right) \qquad (16)$$

This limitation is a direct result of a conductivity σ_{lam} which, via the magnetic field B_2 in (13), is inversely proportional to the reconnection rate M_1.

It is seen from the inequalities (15) and (16) that laminar resistivity cannot be responsible for the diffusion near the X-type null point for high β_1 values, while for low β_1 values it may play an important role, permitting reconnection rates, M_1, of order unity.

In summary, the β_1 value of the inflowing plasma appears to be an important parameter in determining the occurrence of rapid field reconnection. For low β_1 values, laminar and turbulent resistivity effects will permit large reconnection rates. For large β_1 values the Spitzer resistivity dominates and, via the ion gyro limitation, extremely small reconnection rates may result.

PARTICLE ENERGIZATION IN THE RECONNECTION PROCESS

This section discusses simple one-step particle acceleration processes directly associated with the reconnection geometry. All energy gains given refer to a frame of reference in which the X-type magnetic null point is at rest. Further, in the remainder of the paper all numbers quoted refer to protons. Corresponding values for other particles may be obtained by observing that the energy gains are proportional to the particle mass for the processes dealt with here.

First, it is noted that the plasma as a whole will be accelerated and heated as it passes through the slow shocks in the reconnection geometry. For a maximum-strength slow shock (switch-off shock) the energy gain in the limit of a vanishing field component normal to the shock is given by

$$\Delta\epsilon = \frac{5\gamma - 1}{2\gamma} \frac{m}{2} v_{A_1}^2 \qquad (17)$$

(Kantrowitz and Petschek, 1966). In this formula γ is the ratio of specific heats at constant pressure and volume. Values of $\Delta\epsilon$ for protons are given in Table 3 for a set of magnetic field intensities and densities.

368

Table 3

Proton Energy Gain In Switch-Off Shocks In
An Electron-Proton Plasma With $\gamma = 5/3$

B (gauss)	100			500		
n (cm^{-3})	10^9	10^{10}	10^{11}	10^9	10^{10}	10^{11}
$\Delta\epsilon$ (KeV)	547	54.7	5.47	13.7×10^3	1.37×10^3	137

It is seen that substantial energy gains occur. Thus, the shock-heated plasma provides an abundant supply of particles with a base energy suitable for further acceleration processes.

Second, there is the possibility of direct particle acceleration in the electric field E_0 at the magnetic null point. A particle moving along E_0 across the entire reconnection region would pick up an energy of the order of 10 BeV or more. But the magnetic ejection of particles from the diffusion region, described in the section on laminar resistivity, makes it extremely unlikely for a particle to remain near the null point long enough to pick up even a small fraction of that maximum energy. The average energy gain is estimated to be of about the same order of magnitude as in (17).

Finally, every time a particle is transmitted through one of the slow shocks it gains an amount of energy given by

$$\Delta\epsilon = m v_{A_1} \cos\tilde{\theta} \tag{18}$$

Here $\tilde{v}$ and $\tilde{\theta}$ are the incident speed and pitch angle, respectively, of the particle in a frame of reference, $\tilde{S}$, such that a) the shock is stationary, and b) the electric field E_z vanishes. Equation (18) is based on the assumption that no energy gain occurs in the frame $\tilde{S}$.

All particles incident upon the shock from the high-field region are transmitted to the low-field region. Transmission in the reverse direction also occurs, but only in a restricted pitch and phase angle range (Hudson, 1965). In either case, the value of $\tilde{v}$ in a first step of acceleration is of the order of v_{A_1} and hence the energy gain is of about the same magnitude as in Table 3. A typical situation is one where a particle is first transmitted through one of the slow shocks into the weak-field region and is then transmitted into the high-field region again, perhaps after several internal reflections. This type of process has in fact been dealt with by Speiser (1970) for a field reversal region without switch-off shocks.

In summary, the field reconnection process, by acceleration in one or at most two steps, will lead to the production of numerous protons in the energy range 100 keV to 10 MeV. To reach higher energies multistep processes are needed, such as repeated passages through the

369

shock system. This in turn requires particle scattering off field inhomogeneities, reflection by magnetic mirrors, or looped field lines. Stochastic acceleration of the type discussed by Sturrock (1966) may also be important.

PARTICLE REFLECTION BY FAST SHOCKS

As a final topic we consider acceleration of charged particles by the process of reflection from the front side of a fast shock. This subject has been discussed extensively in the literature (Wentzel, 1963, 1964; Hudson, 1965; Jokipii, 1966; Sonnerup, 1969). It is indirectly connected with the field-reconnection process in two ways: a) at the time of initiation of reconnection in a solar flare, fast shocks propagate outward from the reconnection region; b) the plasma jet ejected radially outward during the reconnection process is likely to be preceded by a shock as pointed out by Sturrock (1967).

Consider a fast shock moving with speed v_s into a stationary magnetized plasma. The shock, as it passes a given volume element of plasma, sets it into motion and changes the plasma properties in accordance with the Rankine-Hugoniot relations. But a few particles, rather than being overtaken by the shock, are reflected against its front side and thus travel ahead of the shock into the stationary plasma. To calculate the energy gain we first transform to a frame of reference, $\tilde{S}$, in which the shock is stationary and the plasma flows along the magnetic field lines. The latter condition guarantees that the electric field $\underline{E} = -\underline{v} \times \underline{B}$ vanishes on both sides of the shock. In this frame of reference the plasma flow speed into the shock is $v_s/\cos\alpha$, where the quantity α is the angle between the shock normal and the magnetic field in front of the shock.

We next ask by what process a particle may be reflected. For low energies the gyroradius of the particle is comparable to the shock thickness, and the reflection may involve electric or magnetic turbulence or an electrostatic barrier in the shock front, as well as magnetostatic reflection. For much greater particle energies the reflection in all likelihood is predominantly magnetostatic, and is possible (Hudson, 1965) only if the magnetic field behind the shock is greater than that ahead of it, as is the case for shocks of the fast mode. Only the case of magnetostatic reflection will be considered here, and for simplicity, attention is restricted to the nonrelativistic case. In the chosen frame of reference, $\tilde{S}$, the particle energy after reflection must then be the same as before. Thus, if the incident particle has speeds $\tilde{v}_{/\!/_1}$ and $\tilde{v}_{\perp_1}$ parallel and perpendicular to the magnetic field, and upon reflection these are changed to $\tilde{v}_{/\!/_2}$ and $\tilde{v}_{\perp_2}$, then we have

$$\tilde{v}_{/\!/_1}^{\,2} + \tilde{v}_{\perp_1}^{\,2} = \tilde{v}_{/\!/_2}^{\,2} + \tilde{v}_{\perp_2}^{\,2} = \tilde{v}^2$$

Returning to the frame of reference, S in which the plasma is stationary ahead of the shock, we find the energies before and after reflection to be

$$\epsilon_1 = \frac{m}{2}\left[(\tilde{v}_{/\!/_1} - v_s/\cos\alpha)^2 + \tilde{v}_{\perp_1}^{\,2}\right] \Bigg\}$$

$$\epsilon_2 = \frac{m}{2}\left[(\tilde{v}_{/\!/_2} + v_s/\cos\alpha)^2 + \tilde{v}_{\perp_2}^{\,2}\right] \Bigg\}$$

The energy gain becomes

$$\Delta\epsilon = \epsilon_2 - \epsilon_1 = mv_s (\tilde{v}_{/\!/_1} + \tilde{v}_{/\!/_2})/\cos\alpha$$

Introducing the pitch angles $\tilde{\theta}_1$ and $\tilde{\theta}_2$, in the frame $\tilde{S}$, before and after reflection via the relations

$$\cos\tilde{\theta}_1 = \tilde{v}_{/\!/_1}/\tilde{v} \qquad\qquad \cos\tilde{\theta}_2 = \tilde{v}_{/\!/_2}/\tilde{v}$$

we find

$$\Delta\epsilon = mv_s\tilde{v}\,(\cos\tilde{\theta}_1 + \cos\tilde{\theta}_2)/\cos\alpha \tag{19}$$

In order to calculate the energy gain from this formula, the pitch angle $\tilde{\theta}_1$ must be chosen such that reflection in fact occurs, and $\tilde{\theta}_2$ must be the associated reflected pitch angle. Information concerning these quantities may be found in Hudson (1965), who calculated the magnetostatic reflective properties of shock waves which are thin compared to the particle gyroradius. Figure 4 shows the ranges of incident pitch angle $\tilde{\theta}_1$ for which reflection occurs as a function of the angle α for a fast shock with the ratio of tangential magnetic-field components after and before the shock equal to three. Since for strong shocks (excluding switch-on shocks) this ratio approaches $(\gamma +1)/(\gamma-1)$, γ being the ratio of specific heats, the value three corresponds to an infinitely strong shock in a gas with $\gamma = 2$ or a shock of more moderate strength in a medium with $\gamma < 2$.

Figure 4 shows a dashed curve and two solid curves. The former gives the critical pitch angle, below which no particles are reflected, and above which all particles are reflected, in the case of adiabatic reflection. The two solid curves, which have been generated from Hudson's calculations, apply to the case of magnetic reflection at a discontinuity in the tangential magnetic field. All particles with pitch angles below the lower solid curve are transmitted through the shock without reflection, while all those above the upper solid curve are reflected. For particles with pitch angles between the two curves, reflection or transmission may occur, depending on the phase angle of the particle in its gyration around the magnetic field at the moment of impact. It is seen that the minimum pitch angle for which reflection is possible is $\tilde{\theta}_1 \simeq 22°$ which occurs at $\alpha \simeq 55°$. Also, for α approaching $90°$ the reflection at a discontinuity occurs nearly adiabatically.
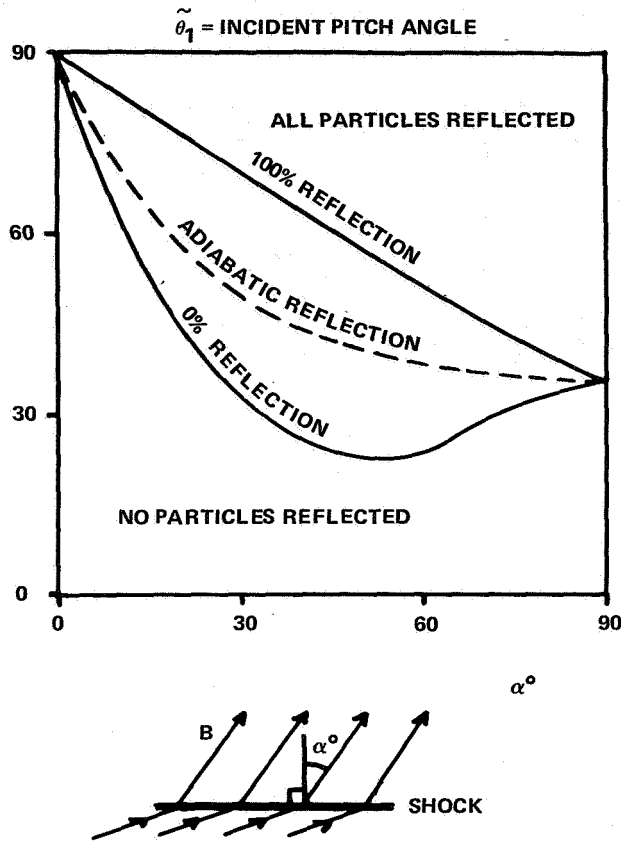
$\widetilde{\theta}_1$ = INCIDENT PITCH ANGLE

Figure 4. Reflective properties of a strong shock of
the fast mode.

In the frame of reference S, in which the plasma ahead of the shock is at rest, a certain minimum energy is needed in order to produce a given incident pitch angle $\widetilde{\theta}_1$ in the shock frame $\widetilde{S}$. This minimum energy is obtained by writing the incident energy ϵ_1 in the form

$$\epsilon_1 = \frac{m}{2} \, [(\widetilde{v} \cos \widetilde{\theta}_1 - v_s/\cos\alpha)^2 + (\widetilde{v} \sin \widetilde{\theta}_1)^2]$$

and then minimizing it with respect to $\widetilde{v}$ keeping $\widetilde{\theta}_1$, v_s and α constant. The result is

$$(\epsilon_1)_{min} = \frac{m}{2} \, \frac{v_s^{\,2}}{\cos^2 \alpha} \, \sin^2 \widetilde{\theta}_1 \qquad\qquad (20)$$

which occurs for $\widetilde{v} = v_s \cos \widetilde{\theta}_1 /\cos \alpha$ Figure 5 shows this threshold energy as a function of the angle α, with $\widetilde{\theta}_1$ corresponding to the 0 percent and 100 percent reflection curves in Figure 4. The lowest threshold energy is found to be 0.34 $(mv_s^2/2)$ at $\alpha \cong 45°$, and it becomes

extremely large as α approaches $90°$. As an example, for $v_s = 1000$ km/s the energy $mv_s^2/2$ for a proton is about 5 keV. Thus, the threshold energy at $\alpha = 45°$ is 1.7 keV, while at $\alpha = 80°$ it is 49 keV.
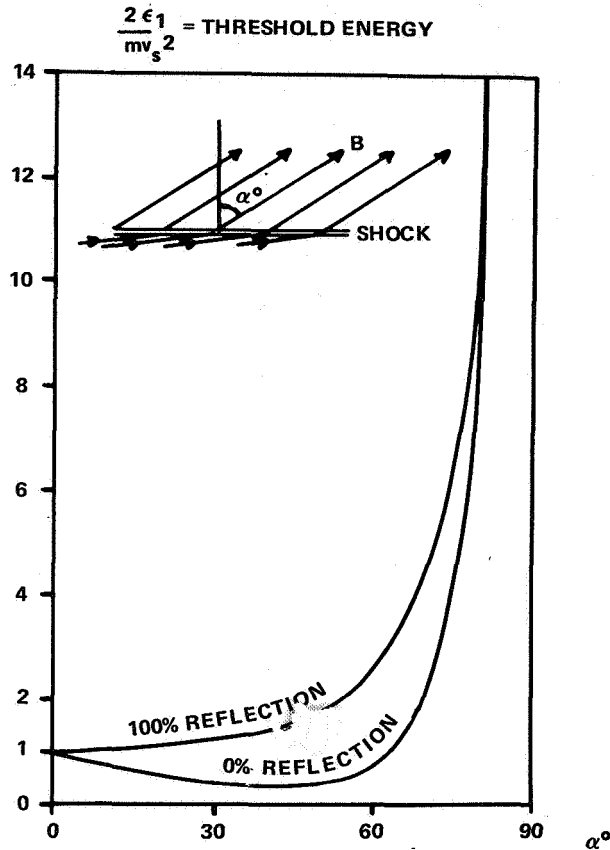

Figure 5. Threshold energy for reflection from a strong shock of the fast mode.

Finally, the energy ratio ϵ_2/ϵ_1 when ϵ_1 is equal to the threshold energy becomes:

$$\epsilon_2/\epsilon_1 = 1 + 2\cot^2\tilde{\theta}_1 \left(1 + \frac{\cos\tilde{\theta}_2}{\cos\tilde{\theta}_1}\right) \tag{21}$$

The pitch angle after reflection, $\tilde{\theta}_2$, may in principle be obtained from Hudson's (1965) work. Generally, the value of $\tilde{\theta}_2$ varies considerably with the phase angle of the particle at the moment of impact, except for $\alpha \to 90°$ where $\tilde{\theta}_2 \cong \tilde{\theta}_1$. For simplicity we shall use $\tilde{\theta}_2 = \tilde{\theta}_1$ for all α values in calculating the energy ratio (21). When this is done, and the values for

$\tilde{\theta}_1$ corresponding to the 0 percent and 100 percent reflection curves in Figure 4 are used, the diagram in Figure 6 results.

This figure demonstrates that the largest energy ratios are obtained at the 0 percent reflection line, with an absolute maximum of $\epsilon_2/\epsilon_1 \cong 25$ occurring at $\alpha = 55°$. (To the extent that $\tilde{\theta}_2$ is less or greater than $\tilde{\theta}_1$ for an individual particle, somewhat larger or smaller energy ratios may obtain, but the values given in Figure 6 are fairly representative.) Along the 100 percent reflection line the energy ratios are more moderate. The two curves meet at a value $\epsilon_2/\epsilon_1 \cong 9$ for $\alpha = 90°$.
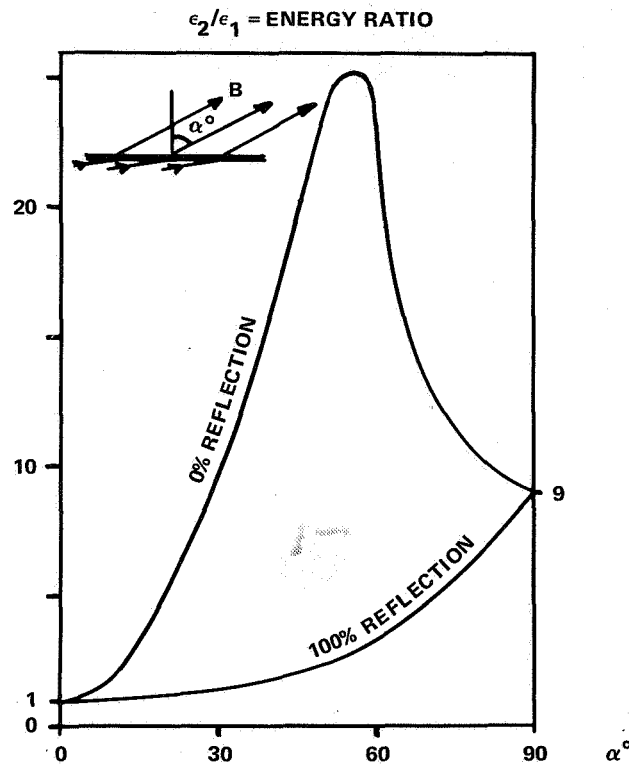

Figure 6. Energy gain above the threshold energy in reflection from a strong shock of the fast mode.

To illustrate this result numerically, we consider a proton near the 0 percent reflection pitch angle at $\alpha = 55°$. With $v_s = 1000$ km/s its initial (minimum) energy is $\epsilon_1 = 2.2$ keV, and the energy after reflection is $\epsilon_2 = 55$ keV. At $\alpha = 80°$ the corresponding numbers are $\epsilon_1 = 47$ keV, $\epsilon_2 = 510$ keV.

In summary, single reflections from fast shocks in the solar atmosphere may produce protons with energies up to perhaps a few MeV. To reach higher energies multiple reflections would be required. This might occur in a variety of field and shock geometries, but one difficulty is that the pitch angle of a nonrelativistic particle after a single reflection is such that subsequent reflections are unlikely to occur. For this reason, acceleration to energies beyond a few MeV requires the presence of an effective pitch-angle scattering mechanism.

ACKNOWLEDGMENT

REFERENCES

Axford, W. I., 1969, *Rev. Geophys.* 7, 421.

Coppi, B., and Friedland, A. B., 1971, *Ap. J.* 169, 379.

Dungey, J. W., and Speiser, T. W., 1969, *Planet. Space Sci.* 17, 1285.

Fredricks, R. W., 1969, *J. G. R.* 74, 2919.

Hudson, P. D., 1965, *M. N. R. A. S.* 131, 23.

Jokipii, J. R., 1966, *Ap. J.* 143, 961.

Kantrowitz, A., and Petschek, H. E., 1966, in *Plasma Physics in Theory and Application*, ed. W. B. Kunkel, New York, McGraw Hill Book Co., 148.

Petschek, H. E., 1964, in *Physics of Solar Flares*, ed. W. N. Hess, NASA SP-50, 425.

Sagdeev, R. Z., 1958, *Plasma Physics and Problems of Controlled Thermonuclear Reactions*, Moscow, USSR, 4, 454.

Sagdeev, R. Z., 1967, *Proc. Symp. Appl. Math.* 18, 281.

Smith, D. F., and Priest, E. R., 1972, *Ap. J.* 176, 487.

Sonnerup, B. U. Ö., 1969, *J. G. R.* 74, 1301.

Sonnerup, B. U. Ö., 1970, *J. Plasma Phys.* **4**, 161.

Speiser, T. W., 1970, *Planet. Space Sci.* **18**, 613.

Sturrock, P. A., 1966, *Phys. Rev.* **141**, 186.

Sturrock, P. A., 1967, *Proc. Int. School of Phys. Course XXXIX, Plasma Astrophysics,* London, Academic Press, 168.

Wentzel, D. G., 1963, *Ap. J.* **137**, 135.

Wentzel, D. G., 1964, *Ap. J.* **140**, 1013.

Yeh, T., and Axford, W. I., 1970, *J. Plasma Phys.* **4**, 207.

COMPOSITION AND ENERGY SPECTRA OF SOLAR PARTICLES

P. B. Price

Department of Physics
University of California, Berkeley

INTRODUCTION

For several years my group has been studying "modern" and "ancient" energetic particles emitted in solar flares. This paper is a brief overview of some of the areas that are currently of interest to us. It is a pleasure for me to record my indebtedness to D. Braddy, J. Chan, R. Cowsik, H. J. Crawford, I. D. Hutcheon, and J. D. Sullivan, who are associated with the work on recent flares; and to D. J. Barber, I. D. Hutcheon, J. D. Macdougall, D. O'Sullivan, P. P. Phakey, and R. S. Rajan, who are associated with the studies of ancient flares. Without them this paper could not have been written.

Heavy ions (those with $Z \geqslant 2$) emitted during solar flares are important for a variety of reasons:

- If they are completely stripped during acceleration and propagation, then all the species from He up to Fe have almost exactly the same charge to mass ratio, ~ 0.5, and respond in the same way to electromagnetic forces. If an unbiased sample of the solar atmosphere is then injected completely stripped into the accelerating region, and if energy losses due to ionization can be neglected, the sample should reach the vicinity of earth as an unbiased sample of the sun who omposition would be of interest to the astronomer and student of nucleosynthesis.

- If, however, heavy ions were initially incompletely stripped or if a distorted sample of the solar atmosphere (for example, those with the same velocity in a Maxwellian distribution) were to be accelerated, then the composition of the sample, in the vicinity of earth, would vary with energy and also with time. Such a sample would provide clues to processes occurring during the flares as well as in transit from sun to earth.

- Because of the Z^2-dependence of ionization rate, heavy ions account for far more than their share of the radiation damage suffered by material on the surface of the moon and other atmosphereless bodies. There is evidence that the albedo and microscopic erosion rate of the lunar regolith are affected by low-energy heavy ions from the sun.

- Records of ancient solar flares survive in the form of heavy ion tracks in minerals that date back nearly to the beginning of the solar system. We are making a start at deciphering that record. Explanations of the current low solar neutrino luminosity that postulate long-term fluctuations in the solar energy output might find support if long-term fluctuations in solar flare output were to be discovered in the heavy ion track record.

METHODS OF STUDYING HEAVY SOLAR PARTICLES

Fichtel and co-workers (Biswas and Fichtel, 1965; Bertsch et al., 1972) have for about a decade maintained a highly successful sounding rocket program that exposes stacks of nuclear emulsions above the earth's atmosphere during intense flares. They have been able to measure abundances of the more abundant even-Z elements at energies from $\sim$ 15 to $\sim$ 100 MeV/N. They have emphasized that in this interval the composition of solar flare particles appears to be quite similar to that in the photosphere and corona.

Several groups (Armstrong and Krimigis, 1971; Van Allen et al., 1971) have continuously monitored time variations in composition of solar particles at quite low energy ($<$ 1 MeV/N), using single-parameter detectors on the Explorer-35 satellite to separate particles into three categories: p, He, and Z $>$ 2. Large rapid variations of relative abundances appear to occur at low energy.

Mogro-Campero and Simpson (1972) and Teegarden et al. (1973), using two-parameter detectors on satellites, have recently reported abundance data for individual elements in several flares at energies above $\sim$ 10 MeV/N. I shall discuss their results later in the paper.

Our track techniques are based on the principle that energetic heavy ions in solids produce chemically reactive trails of radiation damage that can either be seen directly by transmission electron microscopy (Figure 1 (a)) or made visible by using a chemical reagent (Figures 1(b), (c),(d)). In natural glasses and lunar and meteoritic minerals, only ions with Z $\gtrsim$ 20 produce easily visible tracks, whereas in special plastics it is possible to detect particles with Z as low as 2 at energies such that their ionization rate is nearly at a maximum.

The techniques for identifying tracks of energetic particles in dielectric solids have recently been reviewed (Price and Fleischer, 1971). If one is content with some sacrifice in resolution, it is possible to determine relative abundances of the major even-Z elements (He, C, O, Ne, Si, Fe) at energies down to $\lesssim$ 0.5 MeV/N. The resolution rapidly improves with energy, and it is possible to resolve individual elements at energies above $\sim$ 3 MeV/N. Solid dielectric detectors are thus able to function satisfactorily at energies where fluctuations in composition are suspected to occur (Price et al., 1971) and where ions may be only partially stripped. We will see later that interesting effects indeed occur at energies below several MeV/N.

SOLAR FLARES IN THE FIRST BILLION YEARS OF SOLAR SYSTEM HISTORY

The meteorites formed about 4.6 billion years ago, perhaps somewhat before the sun had stabilized as a main sequence star. It would be exceedingly interesting to have a record of solar flare activity during the infancy of the sun, when it is hypothesized to have been extremely active. Such a record is believed to exist, and we are attempting to quantitatively decipher it. High densities of Fe-group tracks exist in the outer portions of silicate grains found at various depths within many of the gas-rich breccia-like meteorites (Lal and Rajan, 1969; Pellas et al., 1969). Fortunately, the accretion process was sufficiently gentle that the tracks have been preserved. Figure 1(a) gives an example of such tracks. The weight of opinion now is that these meteorites were assembled soon after the silicate grains were
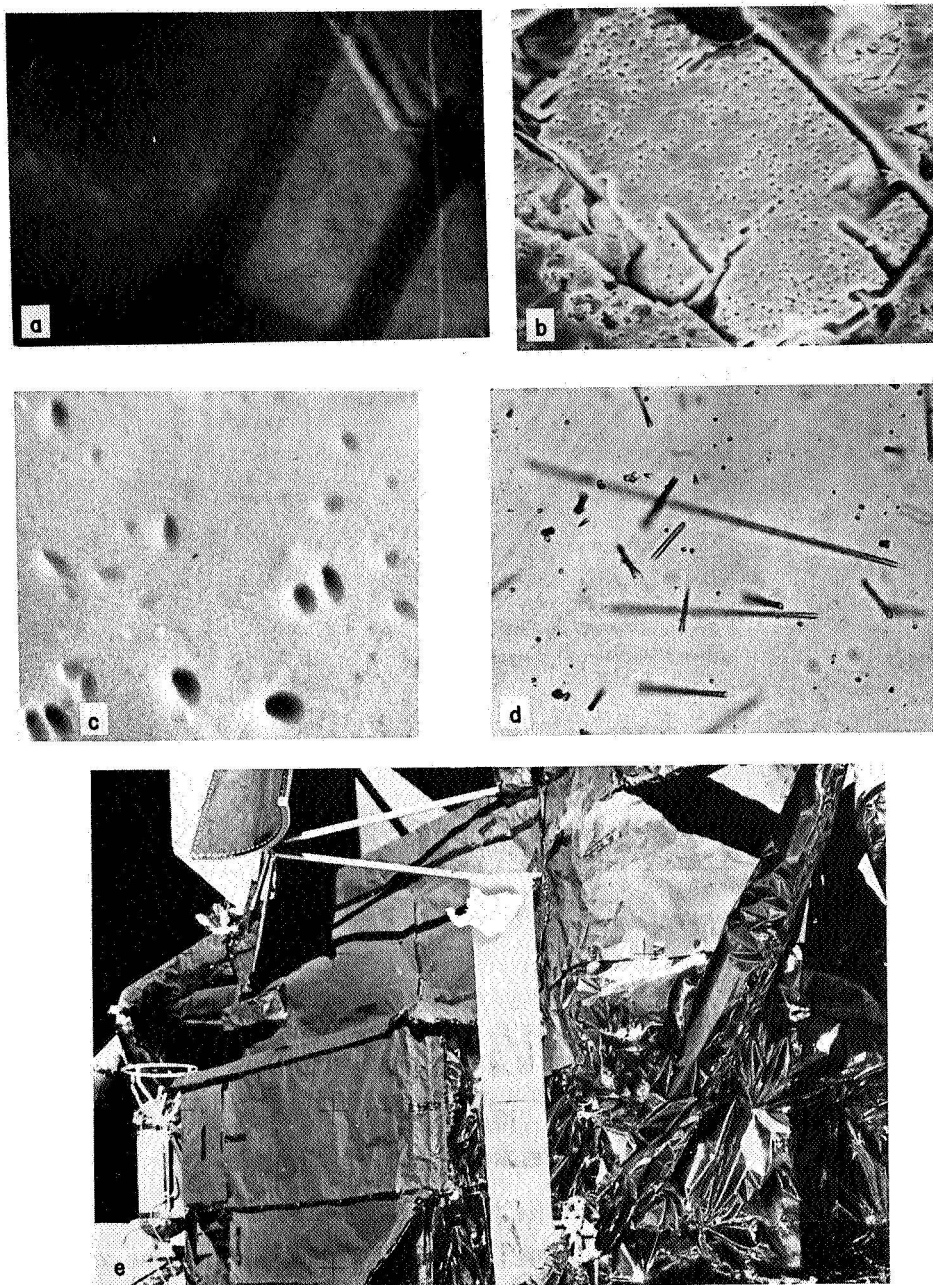
378

Figure 1. Tracks of heavy solar particles: (a) Transmission electron micrograph of solar Fe tracks in a gas-rich meteorite; (b) scanning electron micrograph of etched tracks in a lunar soil grain, each "hole" representing a nucleus with $Z > 30$; (c) scanning electron micrograph of etch pits of Fe-tracks in glass from the Surveyor camera; (d) optical micrograph of etched tracks of nuclei with $Z \geqslant 8$ in a rocket-borne plastic detector exposed four minutes during the August 4, 1972 flare; (e) Lunar Surface Cosmic Ray Experiment (brightly reflecting rectangular array of plastics) used to study a flare during the Apollo-16 mission.

formed and irradiated, at about the same time as the moon and planets were formed. As a result of improvements in our techniques of preparing sections through such meteorites and etching and observing the tracks, we are beginning to obtain energy spectra that extend down to energies as low as 0.1 MeV/N. Gradients of solar Fe tracks in several such meteoritic grains are plotted in Figure 2. As a rough indication of the energies involved, a separate scale for mean energy at each depth is included. Though the information is still fragmentary, the solar flare spectra inferred from these measurements appear to be similar to spectra observed in the present solar cycle (represented by the dashed line in Figure 2).
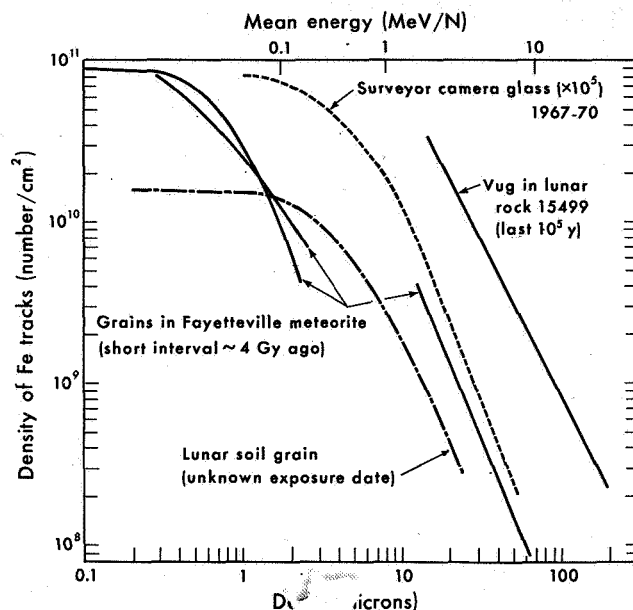

Figure 2. Long-term average depth spectra of solar flare Fe nuclei at various times in the past. None of the ancient flare spectra differs significantly from that observed during a 2.6 year period in 1967-70 (dashed curve). Surveyor glass data are from Price et al. 1971 ; vug data are from Hutcheon et al. (1972); lunar soil data and meteorite data are unpublished results of R.S. Rajan.

Some of the lunar rocks are breccias that consist of consolidated soil grains containing a record of heavy particle fluxes during solar flares that occurred about 3.5 to 4.0 billion years ago. One of the track profiles in Figure 2 was measured in a grain within a breccia from the Apollo-14 landing site. The tracks in the grain predate the time of formation of the breccia, probably about 3.9 billion years ago. A colleague of mine, J. D. Macdougall, has just begun determining relative abundances of Fe and much heavier ions (Z $\gtrsim$ 30) as a function of energy by track measurements in this breccia. The tracks of ions with Z > 30 are much bigger than the Fe tracks and can easily be distinguished. It should thus be possible to determine if there was a systematic change of composition with energy in ancient solar flares.

380

SOLAR FLARES DURING THE LAST 500 MILLION YEARS

Normally track profiles extending in from the surfaces of lunar rocks give a distorted view of solar flare energy spectra, because the surfaces are being eroded away by micrometeorite bombardments. (The track profiles in grains within lunar breccias were of course protected from erosion because they were sealed deep inside.) Fortunately it is possible to circumvent this difficulty by studying track profiles in vugs or cavities in certain rocks. The presence of protective walls means that erosion rates are extremely low at the base of the vug (Hutcheon et al., 1972), so that the observed profile can be used to compute an energy spectrum. In Figure 2 is a profile from a vug in lunar rock 15499, which is estimated to have been exposed to solar flares for about the last 10^5 years. The spectrum is similar to that from solar flares during 1967-70 (dashed curve).

Drill cores containing lunar soil extending to depths of about 2.5 meters have been returned from the Apollo-15 and -16 missions. Though we do not yet have a temporal profile for the dates of exposure of various levels to solar flares, we know that most of the material was irradiated at least 500 million years ago (Russ et al., 1972). Our group intends to map out solar flare spectra at various depths in these cores to look for unusual surges of solar activity as a function of time.

ENHANCED EMISSION OF Fe NUCLEI AT LOW ENERGY DURING 1967-70

The track profile measured by several groups (Crozaz and Walker, 1971; Fleischer et al., 1971; Price et al., 1971) in the neutral density filter from the Surveyor III camera has become a benchmark with which all other track profiles can be compared. It was exposed on the moon for 2.6 years from 1967 to 1970, too short a time for any erosion to have occurred but long enough to integrate over seven major flares and a large number of interplanetary particle enhancements. The dashed curve in Figure 2 gives the profile scaled up by a factor 10^5 for comparison with meteoritic and lunar rock profiles. Though there is no a priori reason why any particular 2.6 year interval of solar activity should be representative of that averaged over longer times such as 10^5 years, such indeed seems to be the case. It seems rather remarkable that the energy distribution in Fe nuclei should be so similar when determined at various times from the present cycle back some 4 billion years. Regularly recurring solar flares in which heavy ions are emitted are apparently characteristic of a main sequence star.

Our group noticed that the total fluence of Fe-group nuclei during the period of exposure of the Surveyor glass was a factor 10 to 20 higher relative to the fluence of He nuclei than the corresponding ratio $(Fe/He)_\odot$ in the photosphere (Price et al., 1971). The He fluence was obtained by summing satellite data of Lanzerotti and co-workers. We could account for the enhancement of the Fe nuclei by assuming that heavy ions are only partly ionized at low energy, with the fractional ionization depending on charge and velocity as a result of capture and loss of orbital electrons during acceleration. Heavier ions would have a smaller fractional ionization, a larger mass to charge ratio and thus a larger rigidity at a given velocity. They should therefore escape more readily from a confining region than would a fully stripped light ion.

Subsequent to our suggestion, several lines of evidence have recently begun to indicate that heavy element enhancements are common at energies below a few MeV/N (Mogro-Campero and Simpson, 1972; Price and Sullivan, 1971; Lanzerotti et al., 1972). We will present some of the evidence below.

STUDIES OF SOLAR FLARES WITH PLASTIC STACKS ON SOUNDING ROCKETS

Though it is known from spectral line observations that in a flare region a certain fraction of ions even as heavy as Fe can be completely stripped (Neupert et al., 1967), we must admit that no one really knows the distribution of charge states during any of the stages of particle acceleration and emission. In examining the conditions under which heavy ions can be preferentially emitted in solar flares, the experimentalist thus has the upper hand and it will be some time before a satisfactory theoretical model can be developed. Fortunately, within the last two years the sun has been extremely active and our group has exposed detectors during four flares ranging over several orders of magnitude in intensity from the rather weak flare that occurred on April 16, 1972 during the Apollo-16 mission to the spectacular series of flares in the first week of August 1972, the largest in the present solar cycle. Figure 3 gives an idea of the large range of proton intensities in the four flares.

The Flare of January 24, 1971

Accounts of our analyses of this flare using rocket-borne plastics have already appeared (Price and Sullivan, 1971; Crawford et al., 1972a). The energy spectra of Fe, Si, and O in Figure 4 are included here so that the reader can appreciate several features of our plastic detector work:

- At high energies, where measurement can be made with nuclear emulsions, our data agree well with those of the Goddard emulsion group.

- Variations of composition with energy can be quite subtle and it is important to be able to make observations down to energies lower than a few MeV/N in order to detect such changes. In Figure 5, where element abundance ratios as a function of energy in several flares are displayed, one can see that the case for a change in the Fe/Si ratio is not strong unless our observations below 15 MeV/N are included.

- The spectra for O, Si and Fe have maxima at $\sim$ 1 to 2 MeV/N, with the fluxes dropping to zero at a few tenths MeV/N. We do not know whether the absence of very low-energy particles is related to a magnetospheric cutoff or to a time-delay in propagation of the slowest particles from the sun. (The rocket was fired 16 hours after onset of the event.) Whatever the reason, we were unable to determine composition ratios in the interesting region below 1 MeV/N where we might expect large differences in fractional ionization of nuclei undergoing stripping and pickup of electrons in a cool region of the solar atmosphere.
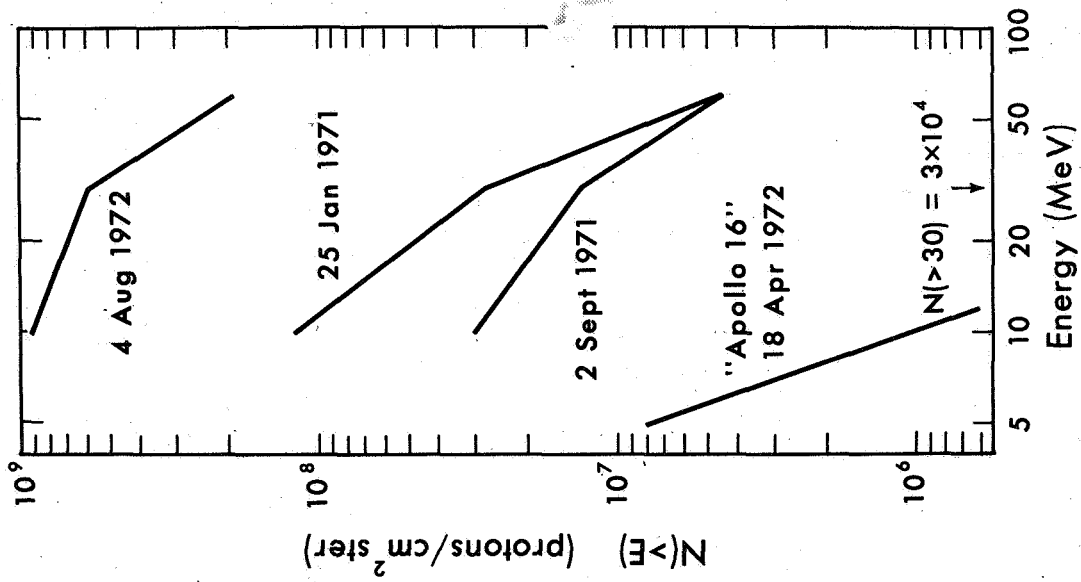
382
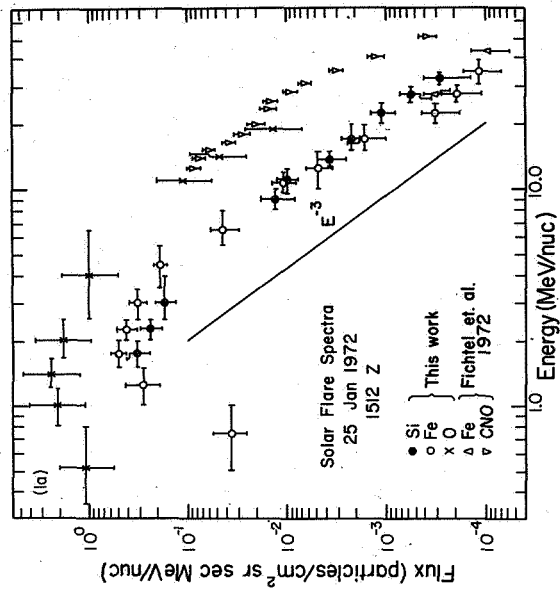
Figure 4. Energy spectra of O, Si, and Fe determined with plastic detectors in the January 25, 1971 flare (Crawford et al., 1972a).

Figure 3. Integral proton intensities in the four flares discussed in the text.

We have adopted the reasonable point of view that the solar particle composition should approach the composition of the solar atmosphere at high energies, at which the solar particles are completely ionized. We, therefore, determined abundances of all even-Z elements above carbon at the highest energies at which we could obtain adequate statistics (13 to 16 MeV/N).
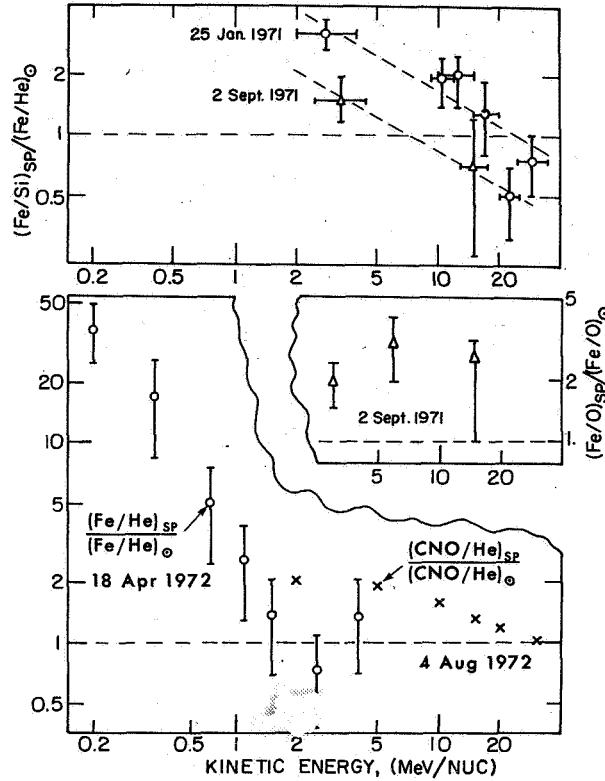

Figure 5. Energy dependence of certain abundance ratios in January 25, 1971 flare (Crawford et al., 1972a); September 2, 1971 flare (Crawford et al., 1972b); April 18, 1972 flare (Braddy et al, 1973); and August 4, 1972 flare (unpublished results of P.B. Price and J.D. Sullivan).

Most astronomers will admit, in the aftermath of a recent drastic upward revision of the photospheric Fe abundance, that solar ·abundance data cannot be regarded as known to better than a factor of three. Our abundances at 13 to 16 MeV/N are barely compatible with photospheric data when this criterion is applied, but only if solar Ne, S, and Ar are revised downward about three-fold. It is very interesting and possibly significant that our abundance data fit rather better the abundances inferred at cosmic ray sources. The correlation is shown in Figure 6. We have conjectured (Crawford et al., 1972a) that gas of solar composition, such as might be found in the interstellar medium, might serve as source material out of which cosmic rays are made. If the sun can emit energetic particles with a particular bias for or against certain elements, cannot cosmic accelerators behave similarly? Kristiansson
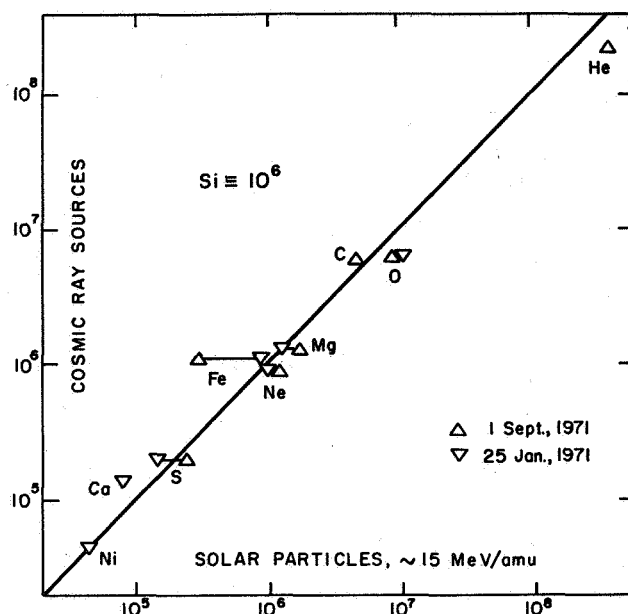
Figure 6. Relative abundances of cosmic ray sources compared with solar particles studied in the January 25, 1971 flare and the September 2, 1971 flare.

(1971, 1972) has recently discussed ways in which certain elements may be selectively accelerated in cosmic rays. A similar discrepancy between the composition of solar particles and of the solar atmosphere was found in a second flare, to be discussed next.

The Flare of September 1, 1971

During this flare the ΔE + (total E) detector of Teegarden et al. (1973) was in operation on the IMP-5 satellite. We were thus able to compare our composition data (Crawford et al., 1972b), obtained during a 4-minute interval 12 hours after onset, with their data summed over the entire flare. As Figure 7 shows, the relative abundances obtained by the two totally different methods agree remarkably well when compared at about the same energies. Our relative abundance of Fe was significantly lower, by about a factor 0.4, in the September flare than in the flare on January 25, 1971. Both sets of data are compared with cosmic ray source abundances in Figure 6. The evidence for a variation of the ratio of Fe/Si with energy in the September flare is marginal (Figure 5), and the Fe/O ratio appears not to change. Because of the sharp decrease in flux below about 2 MeV/N measured at rocket altitude, we could not rule out a variation at lower energies.

The Flare of August 4, 1972

From the photomicrograph in Figure 1(d) one can sense the excitement we felt when we first examined the plastic sheets immediately after chemical processing. In a photograph of a comparable area of plastic exposed during either of the two previous flares the track
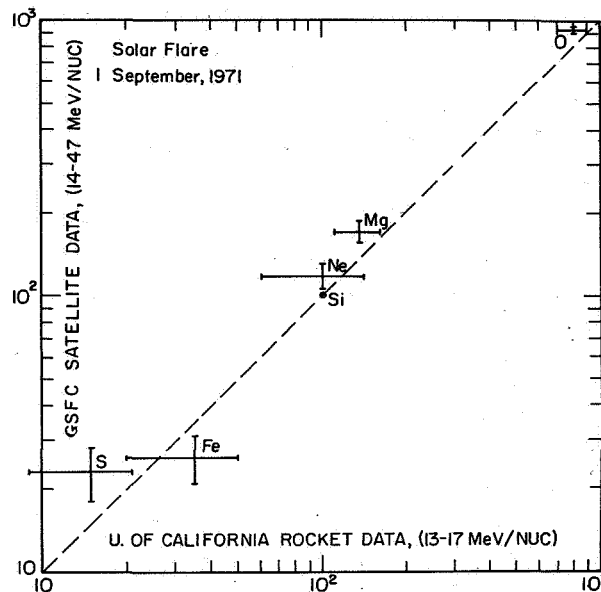
385

Figure 7. Comparison of relative abundances measured with rocket-borne plastic detectors (Crawford et al., 1972b) and with a satellite-based electronic detector (Teegarden et al. 1973) during the flare on September 2, 1971.

density was such that we would usually have seen none or perhaps one track compared with the 25 or so in this picture. All of these tracks were produced by nuclei with $Z \gtrsim 10$ in a 4-minute exposure.

Figure 8 shows the He energy spectrum and preliminary data for the CNO nuclei in a 4-minute interval at 1900 UT on August 4, 1972 when the magnetic field at Fort Churchill was extremely disturbed. The absence of well-defined maxima in these energy spectra is in sharp contrast to the shapes of the spectra shown in Figure 4 for the January 24, 1971 flare. Since the magnetic field at Fort Churchill was not disturbed during the two rocket flights on January 24, 1971 and on September 1, 1971, when particles with energies below $\sim$ 1 MeV/N were absent, we conclude that the shapes of the energy spectra at low energies are determined largely by the local geomagnetic cutoff during the rocket exposures.

Though the analysis is still at an early stage, there appears to be a strong enhancement of heavy nuclei relative to He at energies of several MeV/N but decreasing with energy and disappearing at energies above $\sim$15 MeV/N. The energy-dependence of the CNO/He ratio is shown in Figure 5.
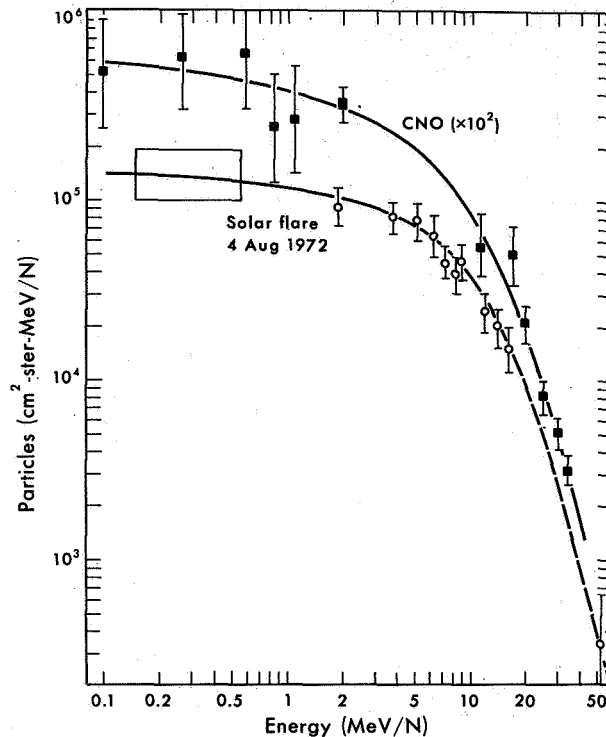
386

Figure 8. Preliminary energy spectra for He and the CNO group measured with plastic detectors during the August 4, 1972 flare (Price and Sullivan, unpublished results). Circles r to He spectrum; solid squares refer to CNO spectrum multiplied by 100.

THE LUNAR SURFACE COSMIC RAY-EXPERIMENT

Figure 1(e) shows the stacks of plastics and other detectors deployed on the side of the Apollo-16 Lunar Module. Our plastics were exposed outside the magnetosphere from April 16 to 23, 1972, during which time a relatively weak solar flare occurred. From Figure 3 one can see that in the April 18 flare the proton intensity above 30 MeV was several orders of magnitude lower and the energy spectrum was considerably steeper than in the other three flares studied.

Because of the long exposure, encompassing the entire duration of the flare, and because of the absence of complications due to terrestrial atmosphere or magnetic field, the experiment has given us important information about the behavior of the sun with respect to charged particle emission in a weak flare. The evidence for an enhancement of the Fe/He ratio at low energies is quite unambiguous, and it has been possible to determine energy spectra extending over about seven orders of magnitude of intensity. The results are summarized in Figure 9. I have included the He spectrum from the August 4 flare; one can see that the difference in intensity between He spectra in the two flares increases rapidly with energy.
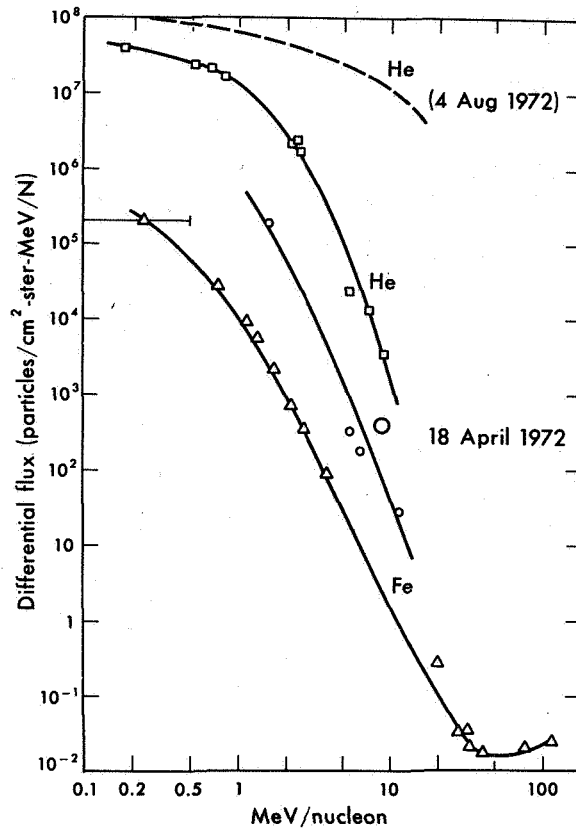
Figure 9. Energy spectra for Fe, O, and He measured in the Lunar Surface mic Ray Experiment on Apollo 16 (Braddy et al., 1973), compared with He spectrum for August 4, 1972 flare. During the mission, on April 18, 1972, a solar flare of moderate intensity occurred.

The Fe/He ratio as a function of energy is displayed in Figure 5. Having detectors capable of particle identification at extremely low energies has thus made it possible to observe a heavy element enhancement that is virtually absent above about 2 MeV/N.

The energy spectra monotonically increase with decreasing energy, with no sign of a maximum such as was observed in the January 25, 1971 and September 2, 1971 flares. At their steepest the spectra fall off as $\sim E^{-5}$ in contrast to the much shallower spectra observed in the rocket flights. Independent satellite data from the University of Chicago detector (J.A. Simpson, private communication, 1972) confirm the steepness of the alpha spectrum.

At energies above $\sim$ 30 MeV/N the flare contribution is below galactic background. In a separate study (Price et al., 1973) we have established that the nuclei above about 30 MeV/N have a composition quite similar to that associated with cosmic rays. The usual spallation products attributed to traversal of several g/cm^2 of interstellar matter were found to be present.

388

DISCUSSION

A rather sketchy view of the sun's long-term emission of heavy particles is beginning to emerge from studies of both ancient and recent tracks in a variety of recording media. Though not in itself decisive evidence for enhanced emission of heavy solar nuclei, the presence of extremely high densities of low-energy Fe tracks in the majority of lunar grains down to the greatest depth sampled ($\sim$2.5 m) (Phakey et al., 1972) is quite consistent with a recurring preference for heavy particle emission over times of at least $\sim 10^9$ years while the lunar soil was being deposited. The strong similarity of track density profiles in grains from a variety of sources — lunar, meteoritic, and Surveyor glass — suggests a long-term stability in the energy distribution in flares.

We do not yet have enough observations to be able to compute the long-term overall mass distribution resulting from energetic particle emission during flares. If frequent, weak flares with steep spectra such as the April 18, 1972 flare, when added together, eject more mass than do the rarer, more energetic flares, then the overall output will be disproportionately rich in heavy nuclei because of the strong inverse correlation of heavy element enrichment with energy. For example, in the April 18 flare, half of the Fe ions had energies less than 0.2 MeV/N and were enriched more than fifty-fold relative to their solar proportions. On the other hand, if strong flares with shallower spectra like the August 4, 1972 flare make the dominant contribution to ejected mass, the enrichment may be much smaller, since a larger fraction of heavy nuclei have higher energy and nearly normal abundance ratios.

The data in Figure 5 suggest that the enrichments are greatest when the difference in atomic numbers is largest, in agreement with our original suggestion (Price et al., 1971). The two largest enrichment factors were found for F/He in the Surveyor glass and for Fe/He in the flare on April 18, 1972. Mogro-Campero anu Simpson (1972) have found that the enrichment factor, averaged over seven flares, increases with Z, though there seems to be considerable variability from one flare to another. In the near future we expect to have compositional data for elements much heavier than Fe and will be able to determine whether such a trend continues on beyond Fe.

By combining data from low-energy detectors on a satellite and from rocket-borne nuclear emulsions, Armstrong et al. (1972) have determined average values for the CNO/He enhancement ratio that agree extremely well with the values we have found for the CNO/He enhancement in the August 4, 1972 flare. The energy-dependence shown in our Figure 5 is quite consistent with the trend in Figure 3 of their paper.

Cartwright and Mogro-Campero (1972) have developed a two-stage acceleration model based on our suggestion (Price et al., 1971) that heavy element enhancements can result naturally from preferential leakage of incompletely ionized heavy nuclei from the accelerating region. In their model, completely stripped nuclei in the very high-temperature flare region are accelerated without bias to intermediate energies ($\sim$1 MeV/N) but then pass through the cool chromosphere where they can reach charge equilibrium by encounters with electrons before finally entering colliding shock trains for a final stage of acceleration.

389

After transport through the cool region, as a result of electron pickup, heavy particles will have higher rigidity at the same velocity than will light particles. Since the process of Fermi acceleration in colliding shock trains requires that a particle have a rigidity greater than a minimum cutoff rigidity, a greater percentage of high-Z nuclei are able to participate in the Fermi acceleration. Quantitative development of the model leads to the predictions that the enhancement varies from flare to flare and is an increasing function of Z.

In its present form their model does not predict an energy-dependence of the enhancement factor. Since the data show a strong inverse correlation of enhancement with energy, it would be useful to explore the model further with this correlation in mind.

I would like finally to comment on the differences in the shapes of the energy spectra for the four flares. The spectra showed definite maxima in the two flares (January 25 and September 1, 1971) during which the magnetic field at Fort Churchill was undisturbed, whereas the spectra continued to rise monotonically with decreasing energy in the April 18, 1972 flare (detector on the moon in the absence of any field) and in the August 4, 1972 flare (geomagnetic field strongly disturbed and magnetic cutoff probably extremely low). If we regard the normal geomagnetic field at Fort Churchill as responsible for excluding low-energy particles in the 1971 flares, we can infer effective charges for the species O, Si, and Fe, for which spectra exist. Based on the daytime rigidity cutoff of $\sim$150 MV calculated by Smart and Shea (1972), we conclude that ions of each species must have been nearly completely stripped of electrons rather than in charge equilibrium with capture and loss of electrons when they began to feel the influence of the geomagnetic field. For example, at 1 MeV/N, the equilibrium charge of an Fe nucleus moving through cool matter is only about 13 instead of 26; with such a charge its rigidity would be 190 MV and it would not have been excluded by the undisturbed field at Fort Churchill

One possible way of understanding the high charge states would be to assume that adiabatic deceleration occurred after the particles moved out of high density regions in the solar atmosphere. If the particles passed through insufficient matter for charge exchange to occur, their charge near the earth could remain the same as it was before deceleration from a higher energy. An Fe nucleus of 1 MeV/N at earth would have had to originate at the sun with an energy of more than $\sim$15 MeV/N in order for its mass to charge ratio to be high enough for it to penetrate the undisturbed field at Fort Churchill. Early in a flare the deceleration would have to occur in leaving the corona; later in a flare it could occur in interplanetary space.

ACKNOWLEDGMENTS

REFERENCES

Armstrong, T.P., and Krimigis, S.M., 1971, *J.G.R.*76, 4230.

Armstrong, T.P., Krimigis, S.M., Reames, D.V., and Fichtel, C.E., 1972, *J.G.R.* 77, 3607.

Bertsch, D.L., Fichtel, C.E., and Reames, D.V., 1972, *Ap. J.* 171, 169.

Biswas, S., and Fichtel, C., 1965, *Space Sci. Rev.* 4, 709.

Braddy, D., Chan, J., and Price, P.B., 1973, *Phys. Rev. Letters* 30, 669.

Cartwright, B.G., and Mogro-Campero, A., 1972, *Ap. J.* 177, L43.

Crawford, H.J., Price, P.B., and Sullivan, J.D., 1972a, *Ap. J.* 175, L149.

Crawford, H.J., Price, P.B., and Sullivan, J.D., 1972b, to be published.

Crozaz, G., and Walker, R.M. 1971, *Science* 171, 1237.

Fleischer, R.L., Hart, H.R., and Comstock, G.M., 1971, *Science* 171, 1240.

Hutcheon, I.D., Braddy, D., Phakey, P.P., and Price, P.B., 1972, *The Apollo 15 Lunar Samples*, ed. by J.W. Chamberlain and C. Watkins, Lunar Science Institute, Houston, p.412.

Kristiansson, K., 1971, *Astrophys. Space Sc*, 485.

Kristiansson, K., 1972, *Astrophys. Space Sci.* 16, 405.

Lal, D., and Rajan, R.S., 1969, *Nature* 223, 269.

Lanzerotti, L.J., Maclennan, C.G., and Graedel, T.E., 1972, *Ap. J.* 173, L39.

Mogro-Campero, A., and Simpson, J.A., 1972, *Ap. J.* 171, L5 and 177, L37.

Neupert, W.M., Gates, W., Swartz, M., and Young, R., 1967, *Ap. J.* 149, L79.

Pellas, P., Poupeau, G., Lorin, J.C., Reeves, H., and Audouze, J., 1969, *Nature* 223, 272.

Phakey, P.P., Hutcheon, I.D., Rajan, R.S., and Price, P.B., 1972, *Proc. Third Lunar Sci. Conf.* 3, The MIT Press.

Price, P.B., and Fleischer, R.L., 1971, *Ann. Rev. Nuc. Sci.* 21, 295.

Price, P.B., Hutcheon, I.D., Cowsik, R., and Barber, D.J., 1971, *Phys. Rev. Letters* **26**, 916.

Price, P.B., O'Sullivan, D., and Thompson, A., 1973, *Nature Phys. Sci.,* (in press).

Price, P.B., and Sullivan, J.D., 1971, *Proc. 12th Int. Conf. on Cosmic Rays,* Hobart, Tasmania, **1**, 449.

Russ, G.P., Burnett, D.S., and Wasserburg, G.J., 1972, *Earth Plan. Sci. Letters* **15**, 172.

Smart, D.F., and Shea, M.A., 1972, *J.G.R.* **77**, 4595.

Teegarden, B.J., von Rosenvinge, T.T., and McDonald, F.B., 1973. *Ap. J.* **180**, 571.

Van Allen, J.A., Venkatarangan, P., and Venkatasan, D., 1971, submitted to *J.G.R.*

A MECHANISM FOR THE ABUNDANCE ENHANCEMENTS
OF HEAVY NUCLEI IN SOLAR FLARE PARTICLE EVENTS

Brian G. Cartwright and Antonio Mogro-Campero

Enrico Fermi Institute, University of Chicago

ABSTRACT

A mechanism is proposed to account for the recently reported abundance enhancements of heavy nuclei in solar flares. The mechanism requires two acceleration stages for its operation: First, fully stripped ions are accelerated to suprathermal energies, and subsequently, a fraction of these ions are Fermi-accelerated to higher energies. It is shown that because injection into Fermi-acceleration is rigidity-dependent and the ions may pick up electrons during transport to the Fermi-acceleration region, an enhancement of the abundances of heavy nuclei can occur. The degree of the enhancement depends on a number of factors particular to each flare, so that the degree of enhancement may be variable from flare to flare, or may be a function of time within a given flare. In some flares, conditions may be such that no enhancement would be expected.

STATUS OF COMPOSITION OBSERVATIONS

Recent measurements have shown an enhancement of the abundances of heavy nuclei in solar cosmic rays when compared with solar photospheric and coronal values. We present here a mechanism which may be operative during the acceleration process in solar flares, which results in a monotonic increase in the enhancements of the abundances of the accelerated heavy nuclei with increasing nuclear charge number. The magnitude of this enhancement is calculated in a simple case where energy loss during acceleration is unimportant.

A review of the observations of the charge composition of solar cosmic rays has been given by Reames (1972) at this symposium. Therefore we discuss this question briefly, and mention only the most recently reported work.

Observations using nuclear emulsions flown on rockets have been performed for many years (Bertsch et al., 1972). It has been concluded that the abundances of the solar cosmic rays are consistent with the solar photospheric and coronal abundances up to the Fe-group at energies $\geq$ 10 MeV nucleon^{-1}. On the other hand, Konyakhina et al. (1972), summarizing their work, report an enhancement over solar abundances of the abundance ratio (Z > 20)/(5 $\leq$ Z < 20) during solar flares from continuous satellite observations using Cerenkov detectors at energies $\geq$ 400 MeV nucleon^{-1}. At a few MeV nucleon^{-1}, an over-abundance of Fe-group nuclei which decreases with increasing energy has been reported by Price (1973) at this symposium; these results were obtained using rocket-borne plastic detectors.

Lanzerotti, Maclennan, and Graedel (1972) have also found an overabundance of heavier nuclei at a few MeV nucleon⁻¹ by comparing satellite results with data from plastic detectors. Continuous satellite observations using solid-state detectors have been reported by Mogro-Campero and Simpson (1972b), and by Teegarden, von Rosenvinge, and McDonald (1972). Mogro-Campero and Simpson find an overabundance of heavy solar cosmic rays which increases monotonically with increasing atomic number over the charge range $6 \leqslant Z \leqslant 26$, at energies $\gtrsim 15$ MeV nucleon⁻¹, for a sum of several solar flares. At approximately the same energies, Teegarden, von Rosenvinge, and McDonald find an enhancement of certain nuclei above the photospheric and coronal values, but their data do not exhibit a systematic enhancement. The variability of the relative abundances of the heavy nuclei in different solar flares has been reported (Mogro-Campero and Simpson 1972b; Konyakhina et al., 1972, Bertsch et al., 1972, Teegarden, von Rosenvinge, and McDonald, 1972), although the magnitude of this variability is still not established.

ENHANCEMENT MECHANISMS PREVIOUSLY SUGGESTED

Price et al. (1971) have pointed out that their measurements may be qualitatively consistent with the preferential leakage of incompletely ionized heavy nuclei from an acceleration region.* Preferential leakage would occur because at low energies particles with the same speed have different charge-to-mass ratios at charge-state equilibrium, and in fact, high-Z nuclei have smaller charge-to-mass ratios than low-Z nuclei. The magnetic rigidity of a particle is given by the mass-to-charge ratio multiplied by a function of the particle speed. Therefore, for example, at low energies an iron ion has a greater rigidity than an oxygen ion at the same speed, and consequently would escape more readily across a magnetic barrier region, provided that the mec̣⁻ˢm of transport is dominated by gradient and curvature drifts, or by scattering from magnetic scattering centers that are small with respect to the size of the particle gyroradius. (If the scattering centers are large with respect to the particle gyroradius, then the corresponding diffusion coefficient is not dependent on the charge-to-mass ratio of the particle. See following section.) This effect becomes less pronounced at higher energies, vanishing altogether when the most probable ionic charge-state is equal to the nuclear charge. Therefore one would expect, on the basis of the preferential leakage model, that the enhancement of the abundances of heavy nuclei would diminish as a function of energy, becoming negligible at the energies at which the ions have become completely stripped of all their electrons. Such an energy dependence of the enhancement has been reported at this symposium by Price (1973).

A detailed quantitative examination of the role which preferential leakage, as opposed to preferential acceleration, may play in creating enhancements of the abundances of heavy nuclei requires a knowledge of the relevant magnetic structures. However, an estimate of the order of magnitude of the enhancement which might result in the case of preferential

* Also, Cowsik (1971) has invoked preacceleration preferential leakage in the context of acceleration of galactic cosmic rays at white dwarf sites.

leakage may be made by considering the ratio of the diffusion coefficients of different species as a function of energy in the scattering case, or the ratio of the drift velocities of different species in the drift case. Drift velocity is proportional to Z/Z^* (where Z = nuclear charge number and Z^* = ionic charge number; this convention will be adhered to throughout this paper.) The diffusion coefficient, for diffusion with scattering centers that are small with respect to the particle gyroradius, varies with $(Z/Z^*)^2$. Using a simple semi-empirical formula to estimate Z/Z^* (see following section), we find the results shown in Figure 1. The ratio $[(Z/Z^*)^2$ (iron)$/(Z/Z^*)^2$ (oxygen)] varies by only a factor of three from 0.1 MeV nucleon^{-1} to 10 MeV nucleon^{-1}. Therefore, if the enhancements depend directly on the diffusion coefficient or drift velocity, then preferential leakage alone may be insufficient to explain the observed degree of enhancement.

Mogro-Campero and Simpson (1972a) have pointed out that even iron nuclei are fully stripped in the 25 to 61 MeV nucleon^{-1} range where their measurements were made, using the University of Chicago Orbiting Geophysical Observatory-5 (OGO-5) experiment. Therefore, they stress that if the excess abundances of high-Z nuclei observed at higher energies are to be attributed to preferential leakage, this leakage must be followed by another acceleration stage. That is, a two-stage process for solar particle acceleration must be invoked.
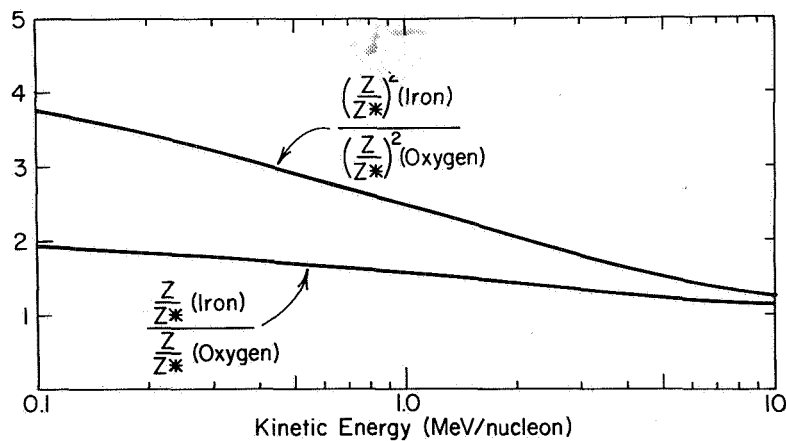

Figure 1. The upper curve represents the ratio of the diffusion coefficients of iron and oxygen for the thin scattering case; the lower curve, the ratio of the drift velocities of iron and oxygen ions in the drift case. In the thick scattering case, the diffusion coefficient does not depend on Z/Z^*.

Enhancements of high-Z abundances also may be obtained by a mechanism first proposed by Korchak and Syrovatskii (1958) for application to the galactic cosmic rays. This mechanism can be important if: 1) the pre-acceleration ions are only slightly ionized; 2) the ions pass through an amount of matter during acceleration sufficient to make energy loss by ionization and excitation an important effect relative to energy gain by the acceleration process; and 3) acceleration is by the Fermi mechanism. This mechanism operates as a result of the fact that an injection threshold for Fermi acceleration exists at the energy at which the rate of energy loss equals the rate of energy gain due to Fermi acceleration. Since the threshold energy is a function of the particle mass, if the ions are only singly or doubly ionized so that the rate of energy loss does not depend on Z, heavy ions may be preferentially accelerated. Indeed, under certain circumstances only heavy ions may be accelerated (see Ginzburg and Syrovatskii, 1964). It should be pointed out that if energy loss is an important effect and the ions are highly ionized prior to acceleration, it becomes practically impossible to accelerate heavy ions by the Fermi mechanism, since under these conditions the energy loss is a function of Z^2. Therefore, under conditions in which energy loss is not negligible during acceleration, the Fermi mechanism is capable of accelerating only heavy ions or of not accelerating heavy ions at all, depending on the initial charge state.

Although the mechanism of Korchak and Syrovatskii cannot be excluded from consideration, it is likely that Fermi acceleration on the sun is of first order, resulting from colliding shock trains. In this case, acceleration may be sufficiently rapid that energy loss effects may be neglected during acceleration. As a result, the Fermi acceleration process is probably "democratic", accelerating light and heavy ions with equal efficacy.

We wish to propose a mechanism for obtaining enhancements under conditions in which energy loss processes may be neglected during acceleration.

THE MODEL

We present here in expanded form a model which we have previously discussed in condensed form (Cartwright and Mogro-Campero, 1972).

We summarize the model qualitatively before considering a simplified quantitative approach for determining the magnitude of the effects expected. We propose that as part of the initial flare process, a region exists where ions are efficiently stripped of all, or nearly all, their electrons. This could result from a particularly violent discharge-like preacceleration phase, or be the result of thermal processes in a plasma heated to temperatures $T \gtrsim 3 \times 10^7$ K. Such localized hot plasmas have been observed both in continuum X-ray emission (for example, Strauss and Papagiannis, 1971) and in the transition lines of hydrogenlike iron (Neupert et al., 1967). Over the charge range considered here ($2 \leqslant Z \leqslant 26$), these ions will all have charge-to-mass ratios of about 2. We suggest that these highly ionized ions are then accelerated to suprathermal energies (up to ~ 1 MeV nucleon^{-1}). Sonnerup (1973) at this symposium has suggested several mechanisms which could accelerate ions to this energy.

It is reasonable to assume that the differential energy spectra of these supra-thermal ions will differ only by constants, namely, the solar abundance ratios, since the charge-to-mass ratio is the same for all of these species. After this first stage of acceleration some fraction of this suprathermal population may traverse a region at approximately chromospheric temperatures, eventually finding its way to a region where colliding shock trains provide efficient first-order Fermi acceleration. Fermi acceleration is often invoked to account for the acceleration of solar cosmic rays to high energies. See for example, Parker (1958) and Wentzel (1964, 1965). Recently McLean et al. (1971) and Wild (1973) at this symposium have interpreted their observations as supporting this view. At this symposium, Sonnerup (1973) has also suggested that a second stage of acceleration after the initial acceleration to suprathermal speeds may be necessary. During transport to the Fermi acceleration region, electron pickup alters the ionization state of the particles from complete ionization in the direction of ionization equilibrium. Therefore, after transport, higher-Z particles will have higher rigidity at the same velocity due to this electron pickup. Since the Fermi-acceleration process requires that a particle have a rigidity greater than a minimum cutoff rigidity for efficient acceleration (Wentzel 1965), a greater percentage of high-Z nuclei are able to participate in the Fermi acceleration.

MAGNITUDE OF EXPECTED ENHANCEMENT

We now perform a simplified calculation in order to obtain an estimate of the magnitude of enhancement which can be expected as a result of our model. We express the number of particles of charge Z which participate in the Fermi acceleration process by

$$N_Z = \int_0^\infty S(Z,Z,T)\, f(Z,T)\, dT \tag{1}$$

where $S(Z,T)$ represents the number of ions of charge Z present with kinetic energy per nucleon T after the initial acceleration to suprathermal velocities; $F(Z,T)$ represents the fraction of these ions of charge Z and kinetic energy per nucleon T which are transported to the region of Fermi acceleration during the time when efficient Fermi acceleration is occurring; and $f(Z,T)$ represents the fraction of ions of charge Z and energy T which are "injected", that is, are efficiently accelerated by the Fermi mechanism. We can approximate $f(Z,T)$ by a step-function with a step at $T_c(Z,R_c)$, the cut-off kinetic energy per nucleon for Fermi acceleration. $T_c(Z,R_c)$ is calculated, of course, from the corresponding rigidity cut-off R_c, which is independent of Z. The Z-dependence of T_c arises because the rigidity of ions with different nuclear charge number Z, but the same velocity is different, owing to the effects of electron pickup. That is, the net ionic charge Z^* differs from Z, so that Z^*/A is different for each species. Equation (1) can therefore be written

$$N_Z = \int_{T_c(Z,R_c)}^\infty S(Z,T)\, F(Z,T)\, dT \tag{2}$$

We represent the suprathermal particle distribution by a power law, that is, $S(Z,T) = C_Z T^{-\gamma}$. This assumption is not necessary, since significant enhancements will occur for any $S(T)$ which decreases sufficiently rapidly as a function of T. C_Z is a constant for each Z which is assumed to be proportional to the photospheric or coronal abundance of the species, since the first stage acceleration is postulated to occur in a region where the ions are completely or nearly completely stripped of all electrons. Since we are interested in the enhancement relative to photospheric and coronal abundances, we do not need to retain the constant C_Z. Thus, we have

$$N_Z \propto \int_{T_c(Z,R_c)}^{\infty} F(Z,T) \, T^{-\gamma} \, dT \qquad (3)$$

We are left with the problem of evaluating $F(Z,T)$, the fraction of ions which arrive at the Fermi-acceleration region. This will depend on the nature of the propagation of the ions through the intermediate region in question. We can enumerate these possibilities:

1) The supra-thermal particles flow through a magnetic field which is so full of waves and irregularities that the particles are scattered many times during transit of the field, and the scale size of the scattering centers is small with respect to the particle gyroradius. We refer to this as the "thin scattering" case.

2) The fields are disordered as in the thin scattering case above, but the scale size of the scattering centers is large with respect to a particle gyroradius. This we call the "thick scattering" case.

3) The intervening magnetic field structure is relatively ordered, and particles traverse the region by gradient and curvature drifts. This we call the "drift" case.

We shall see that all three cases produce qualitatively similar results, and that even the quantitative differences are not great. Following Parker (1963), we find that the diffusion coefficients Q_{thin} and Q_{thick} for cases 1 and 2 are

$$Q_{thin} \propto \left(\frac{Z}{Z^*}\right)^2 \beta^3 \qquad (4)$$

$$Q_{thick} \propto \beta \qquad (5)$$

where β = the speed of the ion in units of the speed of light c, and as before Z is the nuclear charge number and Z^* is the equilibrium ionic charge.

In either of these diffusive cases, if we assume that the transport of particles during the relevant time period is sufficiently small so as not to significantly affect the gradient in the density of these particles, we can write $F(Z,T) \propto Q(Z,T)$. In the drift case, if we assume that effective Fermi acceleration occurs only for a finite period of time, then the number of particles reaching the Fermi region during that period is proportional to the drift velocity, and

$$F(Z,T) \propto \frac{Z}{Z^*} \beta^2 \tag{6}$$

since the drift velocity for both curvature and gradient drifts has this dependence. Thus we may write

$$N_Z \propto \int_{T_c(Z,R_c)}^{\infty} \left(\frac{Z}{Z^*}\right)^{L-1} \beta^L \ T^{-\gamma} \ dT \tag{7}$$

where $L = 1$ for the thick scattering case, $L = 2$ for the drift case, and $L = 3$ for the thin scattering case.

Using the well known relation (Barkas, 1963)

$$Z^* = Z \left(1 - \exp\left(-\frac{130\beta}{Z^{2/3}} \right) \right) \tag{8}$$

to determine the equilibrium ionic charge, and transforming to an integral over β, we have

$$N_Z \propto \int_{\beta_c(Z,R_c)}^{\infty} \frac{\beta^{L-2\gamma+1}}{\left[1 - \exp\left(-130\beta/Z^{2/3}\right)\right]^{L-1}} \ d\beta \tag{9}$$

This equation is meant to apply only in the nonrelativistic domain under consideration; the upper limit of integration has been set to infinity for convenience in the evaluation of the integral. This approximation is valid because the integrand approaches zero rapidly as a function of β in the physical cases considered here. The function $\beta_c(Z,R_c)$ is obtained by solving

$$R_c = \frac{A m_o c^2 \beta_c}{e Z^*} \tag{10}$$

where m_0 is the mass of a nucleon, A is the nuclear mass number of the particle species in question, and e is the elementary charge. Approximating, for the Z ≤ 26 species in question, A = 2Z, we can then write:

$$\frac{R_c e}{2m_0 c^2} \left[1 - \exp\left(-130 \ \beta_c / Z^{2/3}\right) \right] - \beta_c = 0 \tag{11}$$

This equation can be solved numerically for its roots in $\beta_c(Z, R_c)$ by Newton's iterative method.

The integral itself is solved trivially in the thick scattering (L = 1) case:

$$N_Z \propto \beta^{3-2\gamma} \tag{12}$$

For the L = 2 and L = 3 cases, the integral is of the form

$$N_Z \propto \int_{\beta_c(Z, R_c)}^{\infty} \beta^{-n} \left(1 - e^{-\alpha\beta} \right)^{1-L} d\beta \tag{13}$$

where $\alpha = 130/Z^{2/3}$, and where n = 2γ - 3 in the L = 2 case, and n = 2γ - 4 in the L = 3 case. A convergent infinite series expansion for this integral can be obtained for n integral and n ≥ 2 by using the binomial expansion and integration by parts. We find

$$N_Z \propto \sum_{k=1}^{\infty} [k(L-2) + 1] \left\{ \sum_{\ell=1}^{n-1} \frac{(-k\alpha)^{\ell-1} (n-\ell-1)!}{(n-1)!} \frac{e^{-k\alpha\beta_c}}{\beta_c^{n-1}} \right.$$

$$\left. + \frac{(-k\alpha)^{n-1}}{(n-1)!} E_1(k\alpha\beta_c) \right\} + \frac{1}{(n-1)\beta_c^{n-1}} \tag{14}$$

where $E_1(x)$ is an exponential integral

$$E_1(x) = \int_x^{\infty} \frac{e^{-t}}{t} dt \tag{15}$$

We have carried out a numerical evaluation of these expressions in all three cases. Some typical results are shown in Figures 2 and 3. The effects of energy loss during transit to the
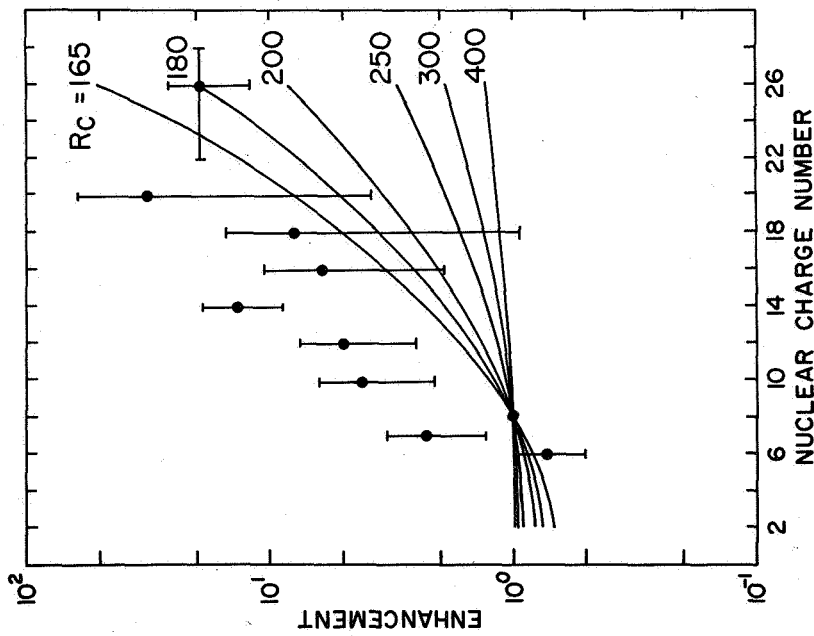
400

Figure 3. Enhancement normalized to oxygen $(N_z/N_{z=8})$ as a function of nuclear charge number, a) for various values of γ with $R_c = 180$ MV and $L = 1$; and b) for the three possible propagation modes $L = 1, 2,$ and 3 with $\gamma = 3$ and $R_c = 180$ MV.

Figure 2. Enhancement normalized to oxygen $(N_z/N_{z=8})$ as a function of nuclear charge number for various values of R_c in MV with $\gamma = 4$ and $L = 1$; These values for $(N_z/N_{z=8})$ correspond to the enhancements $Q(Z)$ observed for a sum of several solar flares reported by Mogro-Campero and Simpson (1972a), which are also shown.
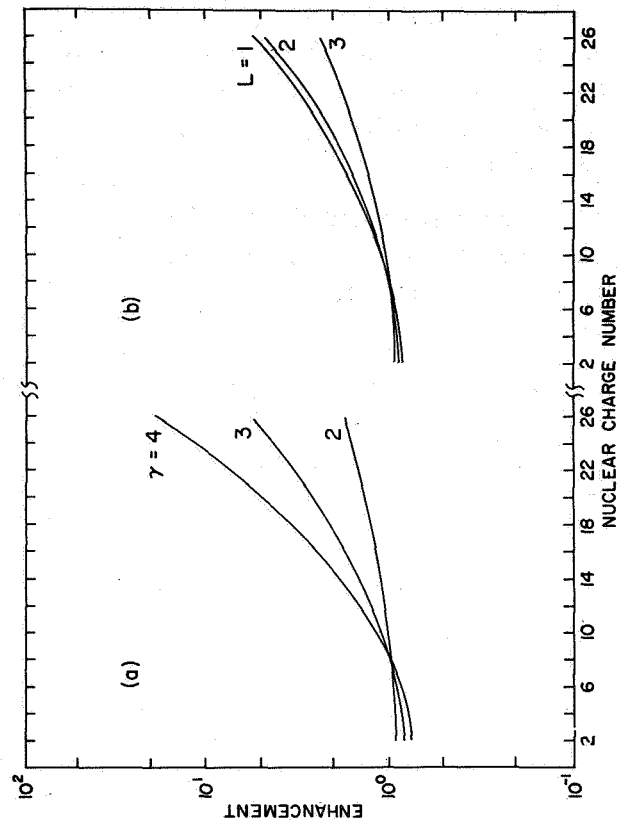
Fermi acceleration region are not included in the calculation we have presented here, but when energy loss becomes important, the enhancements due to this mechanism will be less than those predicted by Equation (14). It is possible that under some circumstances, since the rate of energy loss increases with increasing Z, this enhancement mechanism may be operative only for intermediate Z nuclei.

Since the cutoff rigidity for Fermi acceleration R_c depends on the magnetic configuration of the shocks which accelerate particles, it is expected that this parameter will vary from flare to flare. From Figure 2 we see that relatively small variations in R_c lead to large variations in the enhancement.

The sensitivity of the enhancement to the spectral index of the suprathermal particles is shown in Figure 3(a). From Figure 3(b) we see that the mode of transport to the Fermi acceleration region has a relatively small effect on the predicted enhancement.

CONCLUSION

We have presented a mechanism which could account for the enhancements of the abundances of heavy nuclei observed in some solar flares. A simplified calculation shows that the magnitude of the enhancements expected is similar to the observed enhancements. Considerable variation of the enhancement from flare to flare would be expected if this mechanism is operative.

ACKNOWLEDGMENT

REFERENCES

Barkas, W.H., 1963, *Nuclear Research Emulsions*, Vol. 1 (New York: Academic Press), p. 371.

Bertsch, D.L., Fichtel, C.E., Pellerin, C.J., and Reames, D.V., 1972, NASA/GSFC X-662-72-197.

Cartwright, B., and Mogro-Campero, A., 1972, *Ap. J. (Letters)* 177, L43.

Cowsik, R., 1971, *Proc. 12th Int. Conf. Cosmic Rays*, Hobart, Tasmania, Australia 1, 329.

Ginzburg, V.L., and Syrovatskii, S.I., 1964, *The Origin of Cosmic Rays* (New York: Pergamon Press), 163.

Konyakhina, S.S., Kurnosova, L.V., Logachev, V.I., Razorenov, L.A., and Fradkin, M.I., 1972, P.N. Lebedev Physical Inst. Preprint 74, Moscow.

Korchak, A.A., and Syrovatskii, S.I., 1958, *Soviet Dokl.* **3**, 983.

Lanzerotti, L.J., Maclennan, C.G., and Graedel, T.E., 1972, *Ap. J. (Letters)* **174**, L39.

McLean, D.J., Sheridan, K.V., Stewart, R.T., and Wild, J.P., 1971, *Nature* **234**, 140.

Mogro-Campero, A., and Simpson, J.A., 1972a, *Ap. J. (Letters)* **171**, L5.

Mogro-Campero, A., and Simpson, J.A., 1972b, *Ap. J. (Letters)* **177**, L37.

Neupert, W.M., Gates, W., Swartz, M., and Young, R., 1967, *Ap. J. (Letters)* **149**, L79.

Parker, E.N., 1958, *Phys. Rev.* **109**, 1328.

Parker, E.N., 1963, *Interplanetary Dynamical Processes* (New York: John Wiley and Sons), 170.

Price, P.B., Hutcheon, I., Cowsik, R., and Barber, D.J., 1971, *Phys. Rev. Letters* **26**, 916.

Price, P.B., 1973, These Proceedings.

Reames, D.V., 1972, read at NASA Symposium on High Energy Phenomena on the Sun, Sept. 28-30, Goddard Space Flight Center.

Sonnerup, B.U.Ö., 1973, These Proceedings.

Strauss, F.M., and Papagiannis, M.D., 1971, *Ap. J.* **164**, 369.

Teegarden, B.J., von Rosenvinge, T.T., and McDonald, F.B., 1972, NASA/GSFC X-661-72-222.

Wentzel, D.G., 1964, *Ap. J.* **140**, 1013.

Wentzel, D.G., 1965, *J. G. R.* **70**, 2716.

Wild, J.P., 1973, These Proceedings.

SOLAR COSMIC RAY MICRO-EVENTS

F.B. McDonald and M.A. Van Hollebeke
Goddard Space Flight Center

ABSTRACT

To study small discrete solar particle events, it has proven useful to define a special class such that the proton flux at energies greater than 20 MeV exceed 10^{-4} protons/cm^2-sec-sr-MeV. These increases are termed micro-events. An arbitrary upper limit is placed at 2×10^{-2} protons/cm^2-sec-sr-MeV. By demanding a measurable flux above 20 MeV, a better separation from corotating events is achieved and onset times can in general be determined more precisely. Over an observing period extending from May 1967 through December 1971, approximately 105 events were observed. There are several different sources of these small events. Some are produced by moderate to large solar flares near the east limb or by solar flares on the nonvisible disk of the sun. Others are produced by generally minor solar activity: typically a 1N flare, a group of type III radio bursts and a well defined X-ray burst. A significant number of this latter type are accompanied by type II radio emission. A small sample of the micro-events can be classified as "scatter-free" events. For these the distance traveled by the particles before their initial detection at earth is on the order of 1.5 AU and observed rise and decay times are much less than normal. In this paper examples of these general types of micro-events and their solar association are discussed.

INTRODUCTION

The characteristics of large solar cosmic ray events are well defined. They begin with an optical flare near a complex spot configuration in a large center of activity with almost simultaneous microwave and X-ray bursts followed by a long-lived type IV continuum. As observed at 1 AU, the time-history of the particle event is diffusive with a rise time that is typically on the order of a factor of ten larger than the transit time and decay times that are on the order of 12-24 hours. The crucial question then becomes how do these properties change as one goes to very small solar cosmic ray events and are any new phenomena observed in conjunction with these smaller events.

With the development of more sensitive cosmic ray detector systems, it is now possible to observe solar cosmic rays down to the level of galactic cosmic rays at the same energy. In particular with the Goddard Cosmic Ray Experiment on IMP's 4 and 5, sensitivities down to 2×10^{-5} protons/cm^2-sec-MeV were obtained for differential energy measurements over the 20-80 MeV/nucleon interval. At low energies (that is, 1-20 MeV) small events are less well defined due both to the longer rise and decay times and to confusion with corotating events. It has been found useful in identifying very small events to impose a requirement

404

that the flux of protons $\geqslant 20$ MeV exceed 10^{-4} particles /cm^2-sec-MeV. Those events where the peak flux lies in the range $10^{-4}-2 \times 10^{-2}$ particles/cm^2-sec-MeV for protons above 20 MeV are termed micro-events. The lower part of this range has previously been inaccessible to conventional solar cosmic ray detectors. It is important to emphasize that our definition is one of convenience; the requirement for a measurable flux at 20 MeV is to aid in event and flare identification with the lower intensity limit being defined by the sensitivity of the particular detector system and the upper intensity level is arbitrary.

The IMP-4 and IMP-5 satellites have provided almost continuous coverage in interplanetary space from May, 1967–December, 1971. During that time, some 105 micro-events have been observed. This number is a lower limit since some events which occur soon after a larger event will not be detected. It is found that most micro-events fall into two classes:

- Flare associated events which have favorable propagation conditions between the source and the earth.

- Flare associated events which have unfavorable propagation conditions between the source and the earth. This category includes flares on the non-visible disk of the sun. Many of these have the same time history and solar associations as the larger events; however, in almost every case the flare site is located east of central meridian.

In the latter group, the implication is that had these events occurred at a more favorable solar longitude, they would have appeared much larger and might not be in the micro-event range.

Those events in the first group which appear to have favorable propagation conditions exhibit a wide range of behavior:

- Some proton events exhibit a very rapid rise and decay time and can almost be classified as "scatter-free events".

- For many events the main solar association is a small flare ($\sim$ 1N), a type III radio burst and an X-ray burst.

- Many of the above events are also accompanied by type II radio emissions. In most of these cases there is also a weak continuum present (Dulk, private communication, 1972).

- There are also events that are just at the limit of detectability which display no clear solar association. These sometimes continue for three to four days and may represent very low level sporadic injections.

- While many micro-events appear as isolated cases, there are occasions when an active region may produce 6-10 events over a 14-day period.

It is also interesting to note that on rare occasions there are very small well-defined flare associated events seen at low energies with no detectable flux above 20 MeV.

As one goes to greater sensitivity, it is obvious that not only does the number of events increase but one also observes more complex phenomena. In this paper we attempt to illustrate typical small events and discuss their solar association.

PROPERTIES OF MICRO-EVENTS

The small events of June 27, 1968 (Figure 1) and December 27, 1967 (Figure 2) are used to illustrate some general properties of micro-events. The event on June 27 began with a 1B flare at W87 and a well defined X-ray burst as detected by the University of Iowa 2-12Å X-ray detector on Explorer-35. This is accompanied by a group of type III radio bursts at 0728. In the metric region, Weissenau Observatory reports these are of class 3 intensity and have an underlying continuum. The particle event is so weak that an accurate on-set time cannot be established. The rise time is $\sim$ 7 hours, which is very slow for a western hemisphere flare. The peak differential intensity is 3×10^{-4} proton/cm^2-sec-MeV which corresponds to an integral flux $>$ 19 MeV of 0.01 proton/cm-sec-sr. This is $\sim$ 20 times smaller than the integral galactic cosmic ray flux above the same energy. The integrated flux for the entire event is of the order of 750 proton/cm^2-ster with energies above 19 MeV which is more than a factor of 10^6 smaller than the large events in November, 1960 and August, 1972. The small increase on June 29th is just at the level of detectability and may be produced by the same region which would then be located $\sim$ 25° behind the west limb.

The energy spectra for the June 27th event is of the form $E^{-2.2}$ from $\sim$ 2−60 MeV for the period near the event maximum. Below 2 MeV there is a sharp increase and the spectra is of the form $E^{-5.5}$ from 0.7−2 MeV.
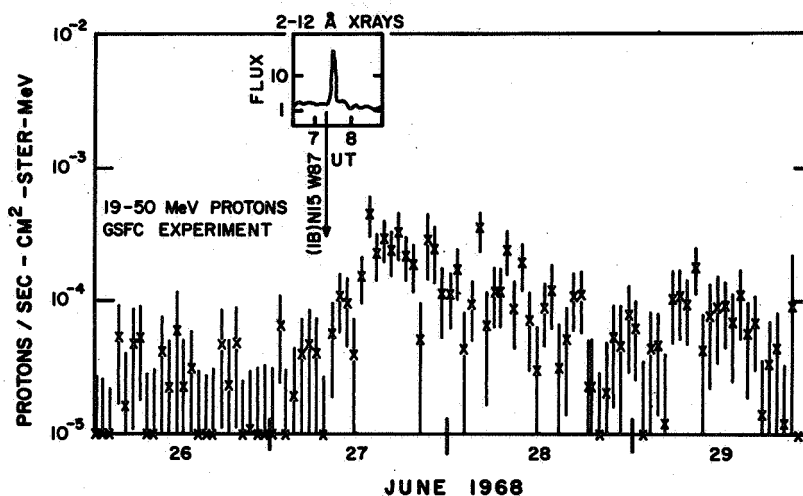

Figure 1. Illustration of a micro-event: the time history of the 19-50 MeV proton intensity from the GSFC IMP IV Cosmic Ray Experiment for the June 1968 event. The top insert shows the 2-12 Å X-rays from University of Iowa data, used as a time marker.
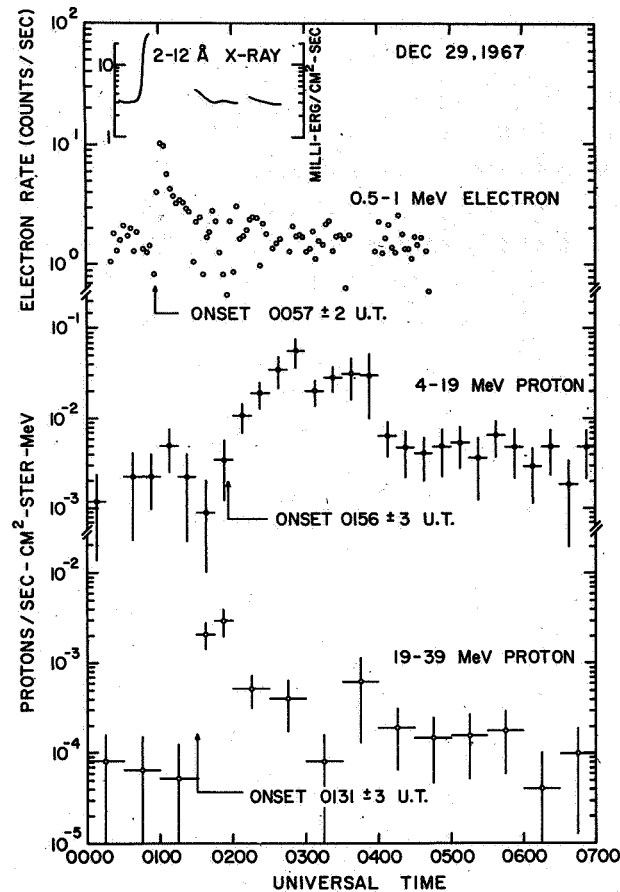
Figure 2. Time profil . the December 29, 1967 microsolar event for the 0.5-1 MeV electrons, 4-19 MeV protons, and 19-39 MeV protons with the measured onset time for each particle group and the 2-12 Å X-rays from University of Iowa data. The time average for protons is half an hour and for electrons 2.7 minutes. These profiles for electrons and high energy protons are typical for a scatter-free proton event.

The event on December 29th started with a 1N flare at 0047 located at S26 W77. Associated with this was a well defined X-ray burst (Figure 2) detected by Explorer-35 and a group of type III bursts in the metric and decametric region (both intensity 2) with type V radio emission (Solar Geophysical Data). The particle event is remarkably different. The 0.5-1 MeV electrons arrive at 0057 (Figure 2). The 19-39 protons have a very rapid rise time (< 1 hour) and the decay time is less than two hours for the period just following the event maximum. The total duration of the 4-19 MeV portion is of the order of 12 hours. To examine whether this is indeed a solar event or perhaps an interplanetary one (although no

407

significant magnetic activity was observed), we have plotted in Figure 3 the particle intensity as a function of distance traveled. Assuming simultaneous release of all particles and having measured the arrival time of different groups of particles, it is possible to determine that the particle release time was 0045 ± 3. The time of the maximum in the X-ray burst is 0042 and the type III burst ends at 0041 (these numbers have been corrected for the transit time from the sun). From Figure 3 it is readily apparent that the data is consistent with a travel distance of some 1.3 AU. This clearly suggests that the particles were of solar origin and propagate very rapidly to the earth. This very short "initial travel distance" as well as the rapid rise and decay times lead us to term this a "scatter-free event". The energy spectra near the event maximum is of the form $E^{-2.5}$ for 2-50 MeV. No sharp increase is observed at low energies and the data is consistent with a flatter spectra at lower energies.
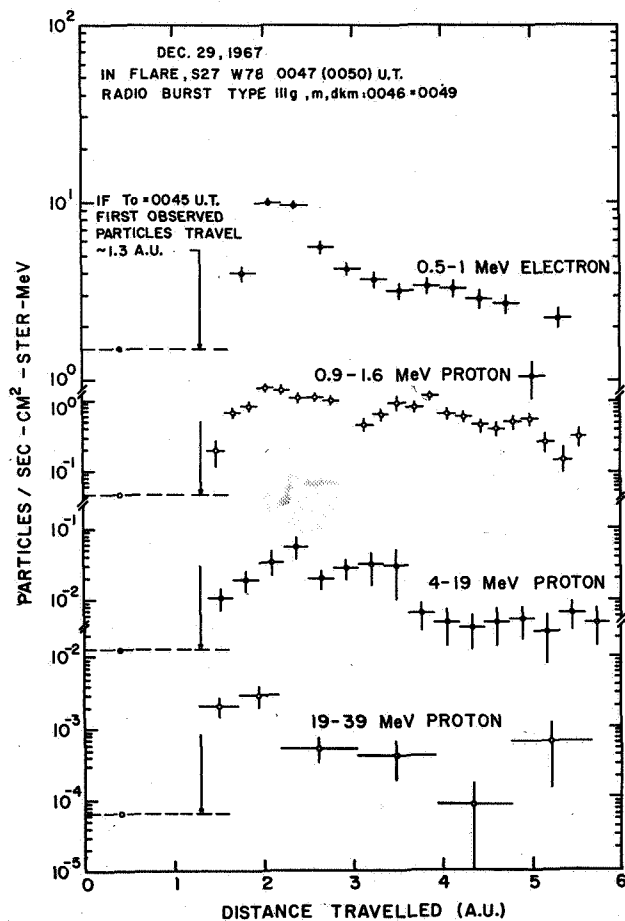

Figure 3. The December 29, 1967 scatter-free micro-event. The intensity of the 0.5-1 MeV electron, and 0.9-1.6 MeV, 4-19 MeV, and 19-39 MeV protons is plotted versus the distance traveled by each particle group. The first observed particles travel less than 1.5 AU. On the top is the relevant flare information.

FLARE-ASSOCIATED EVENTS WITH FAVORABLE PROPAGATION CONDITIONS

The particle events related to the McMath plage 8905 have been chosen as an example of those micro-events which appear as a series of impulsive increases coming from the same active region. This region has been previously studied in detail by Lin (1970) as a source of scatter-free electron events. Figure 4 shows the time histories of the 20-50 MeV, 6-20 MeV, and 0.9-1.6 MeV protons and the 0.5-1.1 MeV electrons. Each arrow indicates the onset times for the different energy groups. Again the University of Iowa Explorer-35 X-ray detector is used as a time marker for the various events. These events are listed in Table 1 with the onset time of the various energy groups and the most probable solar event. Except for two flares on July 29, and August 2, for which the onset of the electron increase cannot be determined, all flares within one hour before the electron onset time and giving both X-ray burst and radio burst were examined as candidates. For all these events except the one
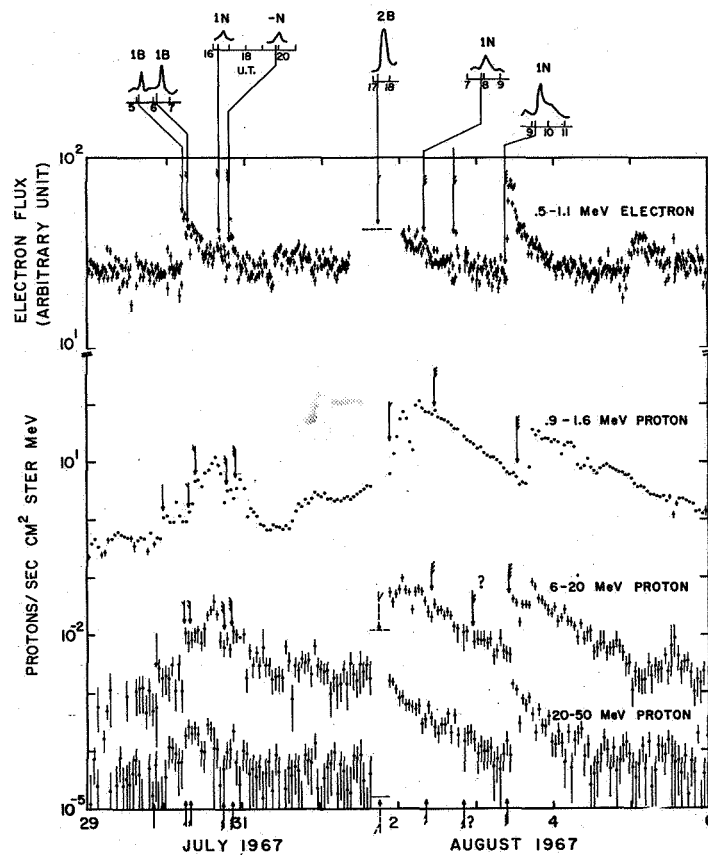

Figure 4 Multiple micro-events associated with McMath region 8905—mostly scatter-free proton events. They are associated with the scatter-free electron events studied by R. Lin, 1970. Each arrow shows the onset of the different particle groups and is associated with an identified solar flare shown here by the 2-12 Å X-rays.

Table 1

Associated Flare Event From McMath Plage 8905

Date 1967	Particles	Onset UT	Maximum Proton Flux (cm^{-2} s^{-1} sr^{-1} MeV^{-1} > 20 MeV)	Associated Flare Importance and Position	X-Ray Burst Onset time (Max Time)	Radio Burst* Type III m, dam, and Time
29 July	E 0.5 - 1.1 MeV P 20 - 40 MeV P 4 - 19 MeV	2100 ± 0030 2215 ± 0030	10^{-4}	1B N23 W21	1940 ± 0003 (1950)	m, dam 1942 = 9003G
30 July	E 0.5 - 1.1 MeV P 20 - 40 MeV P 4 - 19 MeV	0515 ± 0003 0545 ± 0015 0615 ± 0015	3 × 10^{-4}	1B N25 W26	0508 ± 0002 (0512)	m, 0507 = 0518G dam 0508.5 = 0516G
30 July	E 0.5 - 1.1 MeV P 20 - 40 MeV P 4 - 19 MeV	0635 ± 0005 0730 ± 0015 0815 ± 0015	6 × 10^{-4}	1B N28 W30	0616 ± 0002 (0625)	m, 0617 = 0625 dam 0615 = 0622
30 July	E 0.5 - 1.1 MeV P 20 - 40 MeV P 4 - 19 MeV	1634 ± 0003 1745 ± 0015 1830 ± 0030	1.8 × 10^{-4}	1N N26 W36	1622 ± 0002 (1630)	m, dam 1623 = 1639G
30 July	E 0.5 - 1.1 MeV P 20 - 40 MeV P 4 - 19 MeV	1950 ± 0003 2945 ± 0015 2145 ± 0030	3 × 10^{-4}	N N30 W33	1945 ± 0002 (1950)	m, dam 1937 = 1955G
1 August	E 0.5 - 1.1 MeV P 20 - 40 MeV P 4 - 19 MeV	Perigee > 1500 < 2100	> 2.6 × 10^{-3}	2B N27 W62	1728 ± 0002 (1735)	m, dam 1729 = 1738G and V
2 August	E 0.5 - 1.1 MeV P 20 - 40 MeV P 4 - 19 MeV	0845 ± 0015 1045 ± 0030	1.1 10^{-3}	1N N27 W60	0756 ± 0002 (0800)	Not available
2 August	E 0.5 - 1.1 MeV P 20 - 40 MeV P 4 - 19 MeV	1738 ± 0003 — —	7.5 10^{-4}	1N N26 W76	Not available	dam 1729 = 1731.8
3 August	E 0.5 - 1.1 MeV P 20 - 40 MeV P 4 - 19 MeV	0936 ± 0003 1037 ± 0007 1107 ± 0007	2.8 10^{-3}	1B N27 W85	0915 ± 0002 (0932)	Not available

* The intensity of the type III burst is given on a 1 - 3 scale, indicated by the number or horizontal bar separating the onset and the end time. G indicates large group (> 10) burst, g small group, and V indicates type V burst, c mean continuum.

410

on August 3rd there was only one possible flare corresponding to these conditions. For August 3rd, two flares were possible candidates, however, the one more consistent with the particle onset (which is also the largest X-ray producer) has been chosen. For July 29, the more probable flare has been listed; for August 2, the 20-40 MeV proton onset date was used for flare identification. All the particles producing flares were from the region 8905 as Lin (1970) has previously pointed out for the scatter-free electron events. Comparing this list of events with those of the scatter-free electron events, it is interesting to note that all cases of 40 keV electron emission appear to be accompanied by energetic protons when the maximum flux of the 40 keV electron is above 400 particles $(cm^2\text{-sec-sr})^{-1}$. A good assumption would be that the observation of 20-40 MeV protons is still limited by the sensitivity of the detector and that solar processes which accelerate 40 keV electrons also produce MeV protons.

Another interesting feature is that most of the proton events listed in Table 1 can be classified as scatter-free (Figure 4) with rapid rise and decay time (1 to 2 hours) and the observed distance traveled (which ranges from 1.3 to 2.5 AU for 20 to 40 MeV protons). As for the December 1967 "scatter-free" proton event discussed in the previous section, those events are associated with a type III radio burst in meter and decameter wavelength, while there is no indication of any type II or type IV radio burst.

As shown in Figure 5, region 8905 was active before the 29th of July, but no distinct proton events were observed prior to this time. Central meridian passage (CMP) occurred on July 28th. However, the 0.9-1.6 MeV proton intensity starts to increase on the 23rd of July when the 8905 was $\sim 60°E$ (Figure 5). Such increases have been observed before in a large number of cases as the so called corotating event (Bryant, et al., 1965; O'Gallagher and Simpson, 1966; Fan, et al., 1968; McD* ., et al., 1971). This increase may represent the superposition of successive micro-events which were not seen as distinct events until the

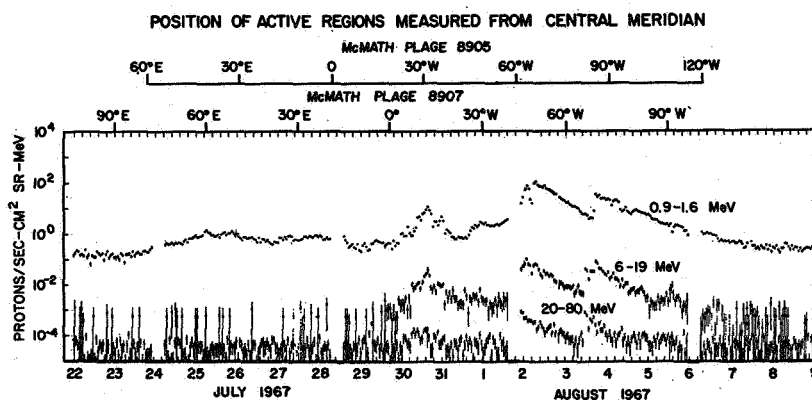
Figure 5. The proton time history is shown for the events associated with McMath plage 8905. While no discrete >20 MeV proton events were observed before July 29, an increase in the low energy emission may represent the superposition of discrete micro-events where the region is east of the central meridian.

411

region was close to central meridian. Note that during this low energy proton increase, the differential proton energy spectrum in the 1-10 MeV interval is of the form $E^{-4.5}$. This value can be compared with the values near the maximum of the multiple impulsive events observed after July 29th which are between -2.7 and -3.5 depending on the particular events.

MICRO-EVENTS ASSOCIATED WITH TYPE II RADIO BURSTS

It is found that $\sim$ 20 percent of the micro-events are associated with type II radio burst as well as type III. Three of these cases are shown in Figure 6. These display more fine structure than seen in the previous cases.

The February 1, 1968 Events

The entire increase lasts less than two days and at least three discrete injections are observed, for which the onset of the different particle groups and the associated solar phenomena are indicated on the right upper portion of Figure 6. The electron onset time is defined within ± 3 minutes. The onset time of the proton events are less well defined. For each of these injections there is an associated X-ray burst. The radio data indicate: a weak decametric continuum starting a few days before the beginning of these events; a large group of type III burst with importance 2 or 3 in metric and decametric wavelengths occurring within ± one minute of the associated optical flare; followed a few minutes later by a type II burst (of intensity 2 or 3 in the metric band). The optical flares are weak and all occur in McMath region 9148 which is $\sim$ 20°W. This region produces larger flares on the 2nd and the 3rd, but no related particle increases were detected. The last detected injection of February 2 (associated with the W23 optical flare) is again a "scatter-free" event in that the calculated traveled distance of the 20-50 MeV proton the 0.5-1.1 MeV electrons is $\sim$ 1.2 ± .5 AU (T_0 = 0538).
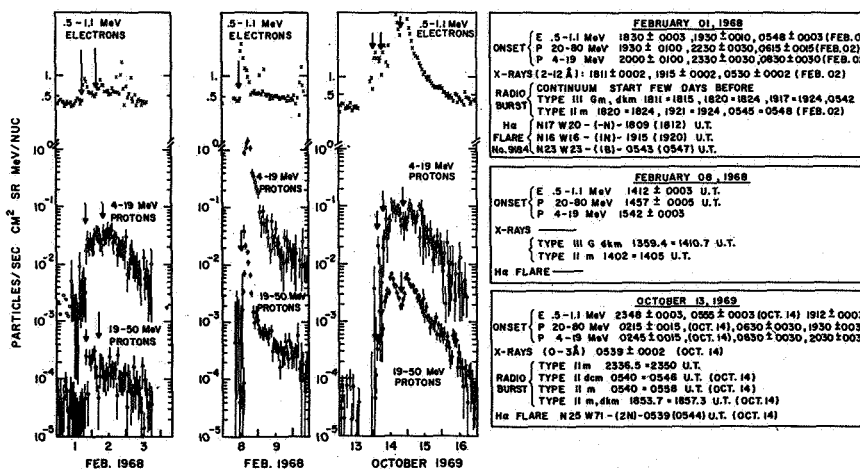

Figure 6. Micro-events associated with types II and III radio bursts. The onset of the 0.5-1.1 MeV electron, 4-19 MeV proton and 19-50 MeV proton emissions are indicated with an arrow. Solar associations are indicated in the right portion of the figure.

412

The February 8, 1968 Event

The event has the same time profile as a "scatter-free" proton event such as December 1967 or February 2, 1968 discussed previously, however, the maximum of the 19-50 MeV proton intensity is larger and after a rapid rise time and decay time, the decay becomes more gradual. The solar information on this event is poor; no X-ray burst was detected and no optical flare could be identified. However, there is a type II (intensity 3) radio burst at 1402 UT which ends at 1405 UT preceeded by a weak decametric continuum at 1359 and a large group of type III in decametric band between 1359.4 and 1410.7. Assuming the same traveled distance for each particle group the time of the release of particle was 1355 UT ± 0005. The energy spectrum can be represented by:

$$\frac{dJ}{dE} = E^{-3} \qquad \text{between 4 and 80 meV}$$

The October 13-14, 1969 Events

These present the same characteristics as the February 1st events, with a fine structure representing three multiple injections. However, the maximum flux in the 20-50 meV proton is about a factor 10 to 20 larger than those of the February 1st events. As for the previous example, the solar information on these multiple injections is poor. Except for the event at 0550 UT on 14th, only radio data can be associated with each of these. The three increases are indicated by the particle onset times given in Figure 6. In all three cases, a type II in the metric band has been reported either by Sidney, or the Harvard Observatory. Again, a group of type III bursts in metric band occurs a few minutes before the type II burst associated with the first and the last increase. Note also that the last event is accompanied by decametric type II and type III radio burst. The increase occurring in the electron intensity at 0555 UT ± 0003 on October 14th produced by a well-identified 2N optical flare at W71. X-rays in the 0-3Å range are observed with a maximum at 0550 UT. No type III or continuum has been reported for this event. The first arriving particle travels less than 1.5 AU, assuming a release time of 0541. However, the rise and decay times for these events are larger and more complex than in the February events. It is possible that some of these events which are unaccompanied by flares may be produced in regions just behind the west limb.

FLARE ASSOCIATED EVENTS WITH UNFAVORABLE PROPAGATION CONDITIONS

Another example of a series of impulsive events coming from a single active region (McMath plage 9740) is illustrated in Figure 7. For each event the position and optical importance of the associated flares are indicated on the top of Figure 7. Each arrow indicates the onset of a flare-associated particle event in a given energy group. All the events presented on this figure are well defined and come unambiguously from McMath plage 9740.

The first discrete particle event from this region was produced late on the 25th by a flare at E32°. The proton intensity actually began to increase some 50 hours prior to this and there was significant solar activity but, similar to the behavior of region 8905, no discrete events could be identified. For the period from the 22nd to the 25th of October, the proton energy
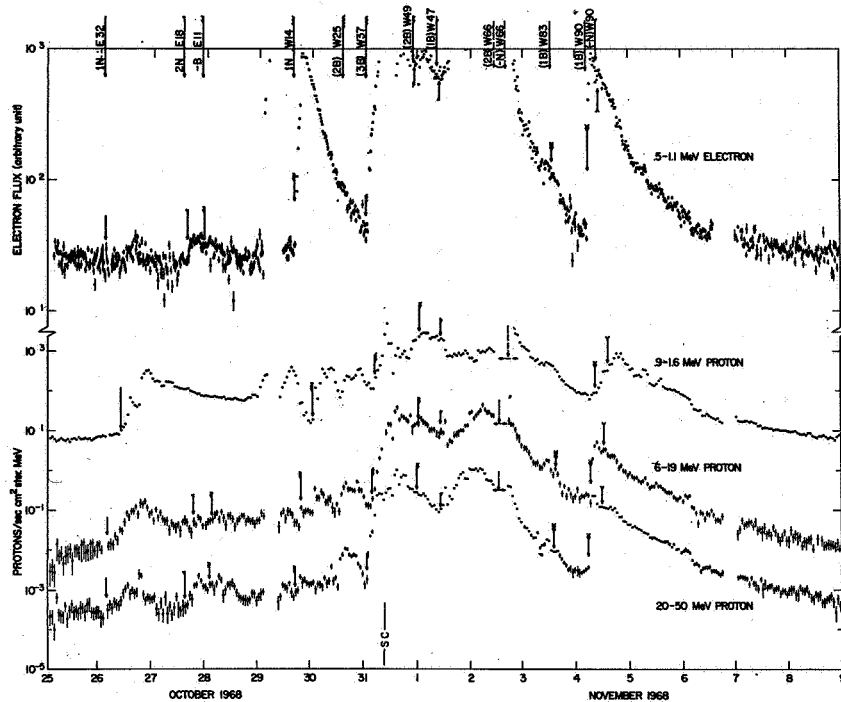
Figure 7. Case of unfavorable propagation. The time history of the multiple micro-events of October and November 1968 is shown for events associated with McMath plage 9740. Importance and longitude of the associated flares are shown on the top of the figure.

spectrum $\frac{dJ}{dE}$ = $E^{-3.9}$. However, in sharp contrast with the 8905 flare-associated events, the micro-events from October 26-31 are associated with medium to large-sized flares and with strong type II and type IV radio emissions and the 2-12 Å X-rays are a factor of 5-20 larger than those associated with 8905. In addition the rise and decay times are much longer and the distance traveled between particle release at the sun and initial detection at the earth is greater than 5 AU. In particular the flares at W14 and W37 produce remarkably different types of particle events. While the electron intensity at 0.5 MeV is approximately equal, the proton intensity from the W14 event is 200 X smaller in the 20-50 MeV interval. These differences in event size and characteristics can be explained in terms of propagation conditions. Figure 8 shows the interplanetary magnetic field measurement (unpublished data, N. Ness and D. Fairfield) from Explorer-34 and -35 during the October 22 to November 8, 1968 time interval. The interplanetary magnetic field from October 26 to 31 is especially disturbed and probably accounts for the adverse propagation conditions. On the 31st there is evidence of an ill-defined sector boundary passage which coincides with the increase in the size of the particle events observed after this time. From the regularity of the magnetic field after November 2, one can expect better propagation conditions and observation of normal size events. The different behavior for October 29 event between electrons and protons may be explained by the small gyro-radius of electrons compared with the 20-50 MeV proton gyro-radius.
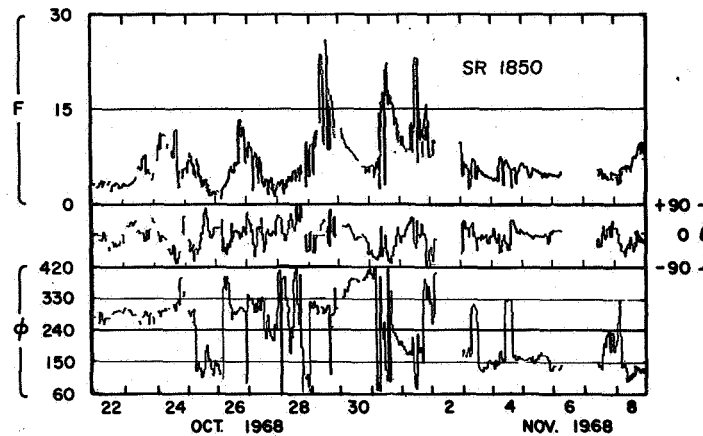
414

Figure 8. Interplanetary magnetic field measurements during the October and November 1968 events; ϕ, θ, and F indicate respectively the azimuthal, latitudinal direction and the intensity (N. Ness and D. Fairfield, unpublished data, 1972). The perturbated magnetic field may account for the unfavorable propagation prior to October 31.

Figure 9 is another example of unfavorable propagation conditions related to an event starting on July 18, 1972. There is strong evidence that this event is from the same region that produced the large events of August 1972. The probable location of the associated flare would be $\sim 160°$W. There is no information on flare activity on the nonvisible disk of the sun, however, there is no indication of any activity on the front side which could account for the observed particle event. During the lifetime of IMP 4 and IMP 5 (June 1967-December 1972), there were several such events with a fairly long rise time (~ 10 hours), and a plateau like maximum which could be associated with back side flares. They generally have quite small amplitude compared to that detected by spacecraft in better positions observing the same event (McKibben, 1972).

DISCUSSION

Previously it has been shown by several observers (for example, Webber, 1962) there is a reasonable correlation between the intensity of type IV radio emission and the size of a solar cosmic ray event. This is consistent with the observations reported here that the continuum becomes almost vanishingly small for micro-events with favorable propagation conditions. To a first approximation there appears to be a general scaling down of solar phenomena for these events — the associated flares are typically 1N or -N and the X-ray bursts are smaller but remain well defined. In almost every case there is one or a group of type III cases that can be directly associated with a specific flare and in a significant number of cases there is type II emission. For many of these events there is a strong suggestion of weak continuum radiation — some events occur in the presence of type I emission, some are listed as type III, indicating an underlying continuum and some have type V emission. Dulk (private communication, 1972) has reexamined some of the type II cases using the University of Colorado's
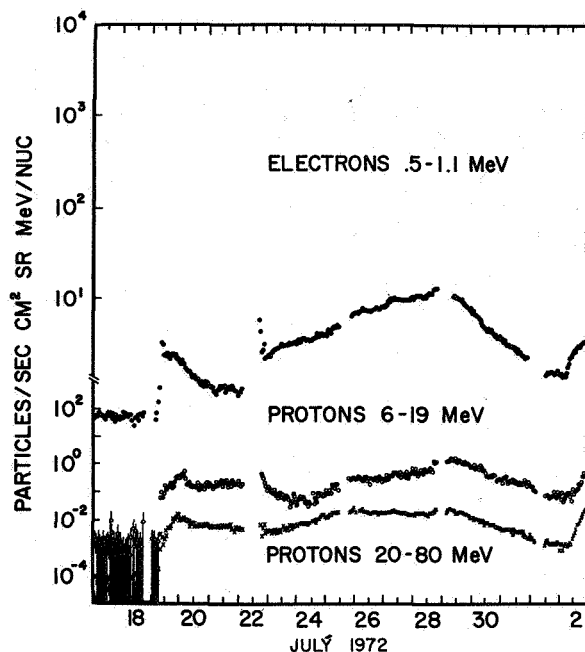
415

Figure 9. A case of unfavorable propagation. This is
the backside event of July 1972, showing time history
of the 0.5-1.1 MeV electrons, 6-19 MeV protons, and
20-80 MeV protons. Note the plateaulike maximum.

7.6-41 MHz scans and finds evidence for weak continuum for all five cases where radio
coverage was available.

This association of solar cosmic ray events with type III emission had been reported previously for electrons by Lin (1970) and Graedel and Lanzerotti (1971) showed a statistical
association for proton events.

Of special importance in the class of micro-events is the so termed "scatter-free" events.
Their association with a group of type III and (or) sometimes with a type II radio burst has
been described in the previous sections. One can wonder if this association and the small
amplitude of the maximum of proton intensity are essential characteristics related to the
necessary conditions of scatter-free events propagation.

To observe these events, a necessary condition is that the interplanetary magnetic field lines
connecting the earth and sun are undisturbed. In the case of big associated flare events, such
connections are probably obliterated by the presence of shocks produced by the interaction
of the fast expanding solar plasma and the spiral magnetic field. Observations on big events,
based on IMP-4 and IMP-5 experiments support this point: The travel-distance of the first
arriving particles is much longer for big events than those reported here for the scatter-free
micro-events. On the other hand, the association with type III radio bursts and the amplitude of the proton intensity in the case of scatter-free events suggests that the proton stream

416

could have been the excitor for these type III bursts, as suggested by D.F. Smith (1970). Smith has estimated the number of approximately 50 MeV protons excitor at 80 MHz required $\sim 6 \times 10^{-4}$ protons/cm^2-sr^{-1} in the vicinity of the earth assuming a source size of 6×10^{11} cm^2. This value is on the order of those observed in the case of micro scatter-free events described here. However, calculations of the wave plasma energy density on more recent observations of type III radio bursts at low frequencies (Fainberg, Evans, private communication, 1972) shows that the flux is too small to explain the observed burst (Smith, 1973).

However, the most important result is that in all these small events including the scatter-free events both electrons and protons are accelerated (protons are present with a velocity of $\geq 0.3c$). This rules out processes such as an electrostatic field and would appear to favor processes like 2nd order type Fermi mechanisms.

It has previously been shown by Krimigis et al. (1971) using observations from several spacecraft that McMath plage 8905 produced a large, complex, corotating particle event. The data presented in this paper suggest very strongly that this stream is maintained by repeated small injections of energetic particles. The exact nature of particle storage close to the sun is probably more complex than that considered previously by McDonald and Desai (1971).

REFERENCES

Bryant, D.A., Cline, T.L., Desai, U.D., and McDonald, F.B., 1965, *Phys. Rev. Letters* 14, 481.

Fan, C.Y., Pick, M., Pyle, R., Simpson, J.A. and Smith, D.R., 1968, *J. G. R.* 73, 1555.

Graedel, T.E., and Lanzerotti, L.J., 1971, *J. G. R.* 76, 6932.

Krimigis, S.M., Roelof, E.C., Armstrong, T.P., and Van Allen, J.A., 1971, *J.G.R.* 76, 5921.

Lin, R.P., 1970, *Solar Phys.* 12, 266.

Lin, R.P., 1970, *J.G.R.* 75, 2583.

McDonald, F.B., and Desai, U.D., 1971, *J.G.R.* 76, 808.

McKibben, B.R., 1972, *J.G.R.* 76, 3957.

O'Gallagher, J.J., and Simpson, J.A., 1966, *Phys. Rev. Letters* 16, 1212.

Smith, D.F., 1970, *Solar Phys.* 15, 202.

Smith, D.F., 1973, These Proceedings.

Webber, W.R., 1963, *NASA Symp. The Physics of Solar Flares*, NASA SP-50.

MODULATION OF SOLAR COSMIC RAYS

L.A. Fisk

Laboratory for High Energy Astrophysics
Goddard Space Flight Center

ABSTRACT

We consider whether the modulation of low energy solar cosmic ray nuclei between the sun and earth can be so extreme that the fluxes observed at 1 AU imply a) that the cosmic ray energy density in the solar atmosphere is comparable to the thermal energy density, and/or b) that the cosmic ray intensity is sufficient in the solar atmosphere to produce detectable fluxes of secondary particles such as low energy positrons. We find that such large modulation is compatible with observations, provided that we confine the modulation to occur principally within a solar envelope lying within $\sim$ 0.2 to 0.3 AU of the sun. There is, however, no compelling observational evidence to require that the modulation is this large.

INTRODUCTION

We observe near earth a nearly continuous flux of low energy solar protons with a differential intensity typically between 0.1 to 10 protons $\cdot$ cm^{-2}s^{-1}sr^{-1}Mev^{-1} at energy $\sim$1MeV (Kinsey, 1970; McDonald, 1970; Krimig's et al., 1971). This flux is the result of long-lived particle streams, as well as numerous disc$\ldots$ $_{\supset}$ solar-flare events. The flux of particles from the sun is of course modulated in the interplanetary medium. The intensity and energy density are reduced as the particles undergo convection, diffusion, and energy loss due to adiabatic deceleration (Parker, 1965; Gleeson and Axford, 1967). It is the purpose of this paper to consider whether current observations are consistent with modulation so extreme that the fluxes observed near earth imply a) that the cosmic ray energy density in the solar atmosphere is comparable to the thermal energy density and thus energetic particles have the potential to influence the dynamics of the corona, and/or b) that the cosmic ray intensity in the solar atmosphere is sufficient to produce detectable fluxes of secondary particles, such as low energy positrons.

Recently, Gregory (1972) has predicted the intensity of cosmic rays at 2 solar radii from the sun and finds for protons the large value of $2.7 \times 10^{8} T^{-4.9}$ (protons$\cdot$cm^{-2}s^{-1}sr^{-1}MeV^{-1}), where T is kinetic energy in units of MeV. This prediction is made assuming that the diffusion coefficient for propagation in the radial direction is independent of radial distance and roughly equal to the diffusion coefficient at 1 AU that was determined by Jokipii and Coleman (1968). The energy density corresponding to this predicted flux ($\sim 10^{9}$ eV$\cdot$cm^{-3}) is not appreciably less than the thermal energy density at several solar radii, provided that cosmic

ray protons are available with energy down to ~ 100 keV. According to Gregory (1972) the predicted flux of cosmic rays interacting with the solar atmosphere is also sufficient to produce the flux of positrons observed at 1 AU between 0.5 and 2 MeV (Cline and Hones, 1970). A solar origin for these positrons is a reasonable possibility since a galactic origin appears to require very large fluxes of cosmic-ray nuclei in interstellar space (Ramaty et al., 1969), or special assumptions concerning supernovae processes (Burger et al., 1970).

In the present paper we consider a model similar to the one discussed by Gregory (1972) and argue that this model results in intensity versus time profiles for solar flare events, and anisotropies at low energies, that are inconsistent with observations. We show, however, that this model can be modified so that these inconsistencies are removed, and yet the large modulation is retained. We take advantage in this modified model of the rapid rate at which cosmic rays can be decelerated within the first few tenths of an AU of the sun, and we confine the region of large modulation to occur within this solar envelope.

ANALYSIS

Consider the modulation that occurs in a quasi-steady stream of solar protons, the same circumstances as were considered by Gregory (1972). Provided that the anisotropy is not large ($\lesssim$ 30 percent), the behavior of the particle number density U, per unit interval of kinetic energy T, can be described by the spherically-symmetric Fokker-Planck equation (Parker, 1965; Gleason and Axford, 1967).

$$\frac{1}{r^2} \frac{\partial}{\partial r} (r^2 V U) - \frac{1}{3r^2} \frac{\partial}{\partial r} (r^2 V) \frac{\partial}{\partial T} (\alpha T U) = \frac{1}{r^2} \frac{\partial}{\partial r} (r^2 \kappa \frac{\partial U}{\partial r})$$ (1)

Here, r is heliocentric radial distance, κ is the diffusion coefficient in the radial direction for scattering by magnetic irregularities (the κ_{rr} term of the diffusion tensor), and V is the radial speed of the irregularities. In the interplanetary medium ($r \gtrsim 0.1$ AU) V is approximately the solar wind speed, whereas in the corona, as we discuss below, V is equivalent to the Alfven speed. The function $\alpha(T) = (T + 2T_0)/(T + T_0)$, where T_0 is particle rest energy ($\alpha \simeq 2$ for the nonrelativistic particles ($T \ll T_0$) that we are considering). The terms in (1) describe from left to right the convection, energy loss due to adiabatic deceleration, and diffusion of the particles. The assumption of spherical symmetry in (1) is of course questionable, since solar activity and interplanetary conditions can exhibit large azimuthal variations. However, since the interplanetary magnetic field between the sun and earth lies predominantly in the heliocentric radial direction, (1) should be a reasonable description of the behavior of particles emitted from a given region on the sun provided that there is no significant cross-field diffusion.

From the sun to earth, the variation of the diffusion coefficient with radial distance is essentially unknown. We consider first that κ is independent of r and equal to the diffusion

coefficient determined from magnetic field power spectra measured near 1 AU. We assume that there is little cross-field diffusion, that is

$$\kappa \simeq \kappa_{\parallel} \sin^2 \Psi \simeq \kappa_{\parallel}/2 \qquad (2)$$

where $\Psi \simeq 45°$ is the angle between the radial and magnetic field directions at 1 AU, and $\kappa_{\parallel}$ is the diffusion coefficient for propagation parallel to the mean magnetic field. We use the form for $\kappa_{\parallel}$ determined by Jokipii and Coleman (1968), or

$$\kappa_{\parallel} \simeq 1.8 \times 10^{20} \ (\alpha T \beta)^{1/2} \qquad (3)$$

where T is in units of MeV and β = v/c with v particle speed and c the speed of light ($\kappa_{\parallel} \propto \beta R^{\frac{1}{2}}$, where R is particle rigidity). In our initial calculations we ignore the current controversy over the validity of the theory used in deriving (3) at low energies (Jokipii, 1972; Klimas and Sandri, 1971, 1973), and we apply this form for $\kappa_{\parallel}$ down to T $\sim$ 100 keV for protons.

We choose V to be constant at 400 km/s for all r. At r $\gtrsim$ 0.1 AU the magnetic irregularities are convected outward at the solar wind speed. At r $\lesssim$ 0.1 AU the solar wind is still being accelerated and here the irregularities propagate outward at the Alfven speed; however, the latter speed is also $\sim$ 400 km/s. We assume here that on the average, irregularities in the corona have their origin in the photosphere (or at least in the bas of the corona) and propagate outward in essentially the radial dirretion.

We have solved (1) numerically for the modulation of protons using the above forms of κ and V. The results are shown in Figure 1. The differential intensity j_0 (= vU/4π) at 2 solar radii ($2r_{\odot}$) from the sun is taken to be $j_0 = 10^7 T^{-4.5}$ (protons·cm^{-2}s^{-1}sr^{-1}MeV^{-1}), where T is in units of MeV. Also shown is the resulting modulated intensity at 1 AU, which has an intensity $\sim$ 10 protrons·cm^{-2}s^{-1}sr^{-1}MeV^{-1} at 1 MeV in agreement with some of the larger fluxes observed. The predicted cosmic ray intensity in the solar atmosphere is roughly a factor of twenty-five lower than that determined by Gregory (1972). The discrepancy results mainly because Gregory normalizes his intensity at 1 AU to be an unusually large value of $\sim 10^3$ protrons·cm^{-2}s^{-1}sr^{-1} MeV^{-1} at 1 MeV.

Shown also in Figure 1 is the radial anisotropy ξ at 1 AU determined from (Gleeson and Axford, 1967)

$$\xi = \frac{3}{vU} \ (VU - \frac{V}{3} \frac{\partial}{\partial T} (\alpha TU) - \kappa \frac{\partial U}{\partial r}) \qquad (4)$$
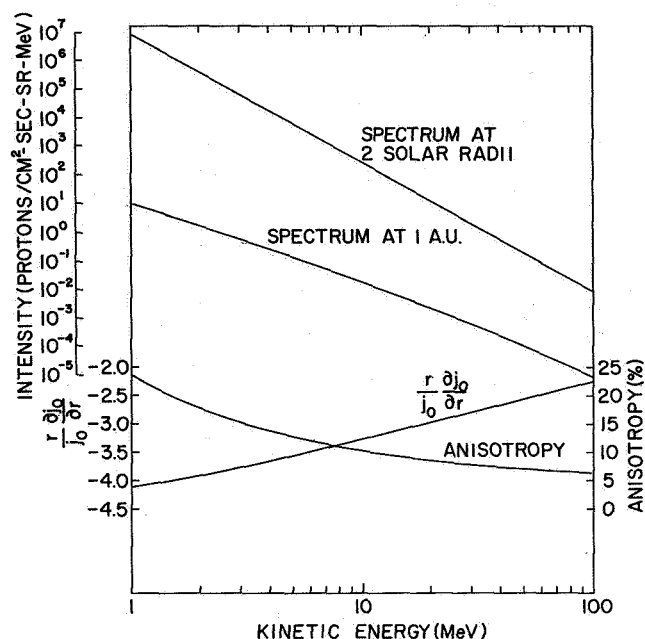
420

Figure 1. The intensity spectrum of protons at 2r .
and the resulting modulated spectrum at 1 AU. Also
shown are the predicted radial gradient and aniso-
tropy at 1 AU.

Note that the anisotropy does not exceed 20 percent down to energies ~ 1 MeV. This re-
sult is in direct conflict with the recent ob͟.   .tions of Krimigis et al. (1971) who find that
the anisotropies in quasi-steady proton streams are typically quite large, often ~ 10:1.

This model, with its continuous scattering between the sun and earth, also predicts risetimes
for solar flare events that are unrealistically long. In Figure 2 we have plotted for two ener-
gies the intensity versus time profiles that result at 1 AU from the impulsive injection of
protons at the sun. The profiles were determined by solving the time-dependent form of
(1) numerically with κ independent of r and T and evaluated for the two energies using (2)
and (3). (In the time-dependent form of (1) a term $\partial U/\partial t$, where t is time, appears on the
left side (Gleeson and Axford, 1967)). The injection spectrum at the sun was taken to be
$U \propto T^{-4}$. As can be seen, the predicted rise times certainly exceed those typically observed
in flares. For example, the intensity of ~1 MeV protons injected from a flare at ~40° to
60°W solar longitude typically reaches maximum at 1 AU within 15 hours (Van Hollebeke,
private communication 1972).

We can modify the above model, however, so that it is consistent with observations and yet
the large modulation is retained. In Figure 3 we have plotted for the above model, versus
radial distance, the energy density in protons >100 keV, the intensity at several representa-
tive energies, and also the mean energy of particles that are injected at the sun in a mono-
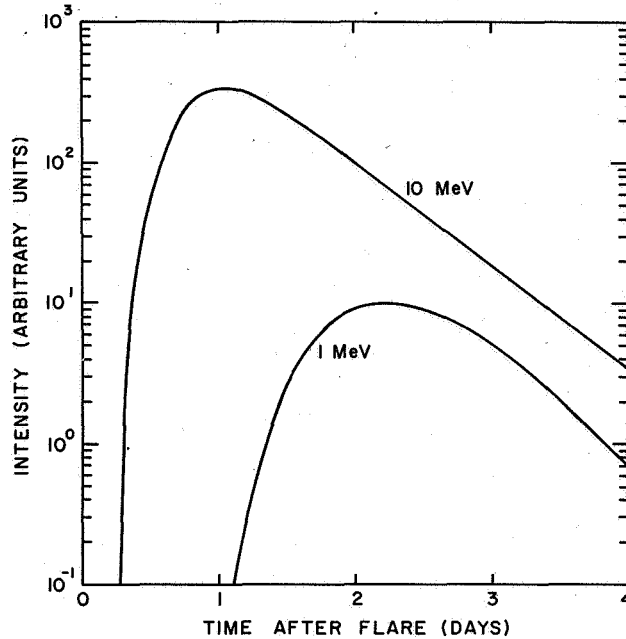
Figure 2. Intensity versus time profiles at several different energies during a model solar flare event.

energetic beam centered at 10 MeV. As can be seen, most of the modulation takes place within the first few tenths of an AU of the sun. Adiabatic cooling, which is principally responsible for the modulation, is greatest near the sun since the irregularities are diverging spherically, and here the volume in which particles are trapped undergoes its largest expansion. In principle then, we can constr⋅ modified model which takes advantage of this strong cooling and accomplishes any reasonable modulation of low energy particles within only a short distance of the sun. We choose the diffusion coefficient near the sun to be quite small, that is, smaller than the above choice and as we will show, we can reduce the differential intensity at low energies by a factor $\sim 10^8$ within only 0.2 to 0.3 AU of the sun. We are then free to have the particles experience relatively little scattering beyond ~ 0.2 to 0.3 AU so that the anisotropies in quasi-steady proton streams are large. Also, the rise time for flare events in our modified model are relatively short.

Consider that the diffusion coefficient near the sun is sufficiently small so that the term on the right side of (1) can be neglected, or

$$\frac{1}{r^2} \frac{\partial}{\partial r} (r^2 V U) - \frac{1}{3r^2} \frac{\partial}{\partial r}(r^2 V) \frac{\partial}{\partial T} (\alpha T U) \simeq 0 \qquad (5)$$

In practice, for (5) to hold we must have $\kappa \ll V r$, which considering that r is small requires truly significant scattering. For an injection spectrum which is a power law in kinetic energy $U = U_0 T^{-\mu}$ at, for example $r = 2r_\odot$, the solution to (5) is simply (Fisk and Axford, 1969; Gleeson, 1971)
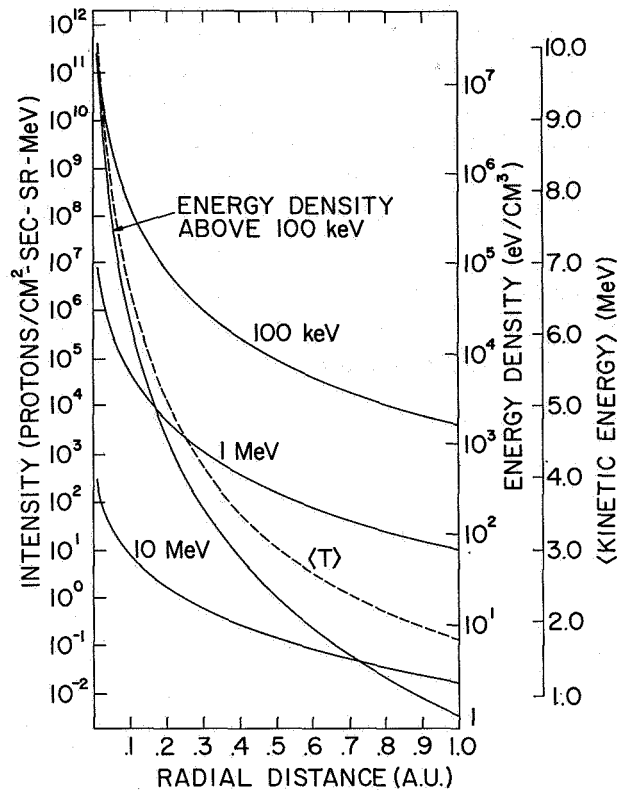
422

Figure 3. A plot versus radial distance of the energy density above 100 keV, the intensity at several different energies (100 keV, 1 MeV, 10 MeV), and the mean energy $\langle T \rangle$ of ions that are injected at the sun at 10 MeV.

$$U = U_o T^{-\mu} \left(\frac{[r^2 V]_{2r_\ominus}}{r^2 V} \right)^C \tag{6}$$

where the term in square brackets is to be evaluated at $2r_\ominus$ and C, the Compton-Getting coefficient, is given by $C = (1 + 2\mu)/3$ on taking $\alpha = 2$ for low energy particles $(T \ll T_0)$.

Note that (6) is independent of the magnitude of V. The particles in this approximation are constrained to move with the magnetic irregularities, and thus experience the total expansion of the irregularities which depends only on the spherical geometry we have assumed. The total energy loss (or modulation) then depends only on the distance the particles are from the sun, not on the speed at which the particles reach this distance. The modulation does depend, however, on the radial variation of V, and would be larger if V was an increasing function of r.

423

As we indicated above, an intensity $\sim 3 \times 10^8 T^{-5}$ protons·$cm^{-2}s^{-1}sr^{-1}MeV^{-1}$ at two solar radii from the sun can account for the positron flux observed at earth (Gregory, 1972), and has an energy density not appreciably less than the thermal energy density of the corona at the same altitude (provided that the flux of $\sim$ 100 keV protons at the sun is not substantially reduced, for example by ionization losses). Compared with a typical flux at 1 AU of $\sim$ 1 proton·$cm^{-2}s^{-1}sr^{-1}MeV^{-1}$ at 1 MeV the required modulation is then by a factor $\sim$ 3×10^8. According to (6), we can achieve this modulation within a distance from the sun of only $\sim 22r_\odot$ ($\sim$ 0.1 AU) on taking μ = 5.5 and V constant. We can consider also that particles undergo some diffusion near the sun in such a way that the spectrum softens to be more consistent with a typical T^{-3} spectrum observed at earth. With such diffusion we should still be able to achieve the required modulation within $\sim$ 0.2 to 0.3 AU of the sun.

Equation (5) has been considered in detail by Gleeson (1971) who shows that the kinetic energy T of particles in this approximation varies with radial distance as

$$T = T_1 \left(\frac{[r^2V]_{r_1}}{r^2V} \right)^{\alpha/3} \tag{7}$$

where T_1 is the energy of the particles at r_1 (the term in square brackets is to be evaluated at r_1). For example, in a region of significant scattering lying between 2 and $22r_\odot$ particles are reduced in energy by a factor $\sim$ 25 (with V constant). The 1 MeV protons we observe at earth are then 25 MeV particles at the sun. We should expect of course that at progressively higher energies particles can diffuse more easily near the sun and thus suffer less energy loss and modulation. Even so, for this large-modulation model to be viable we must require that the sun is able to produce continuously (or store for long periods after flares) significant fluxes of relatively high energy particles.

The energy lost by cosmic rays near the sun is of course absorbed by the magnetic irregularities and in turn by the solar wind. On the average, it is doubtful whether cosmic rays could be important for accelerating the solar wind. However, large fluxes of cosmic rays near active regions could conceivably be partially responsible for high speed solar wind streams.

The assumption in our modified model that low energy particles propagate relatively freely beyond 0.2 to 0.3 AU, thus yielding large anisotropies, is incompatible with the predicted diffusion coefficient at 1 AU given in (2) and (3). However, this diffusion coefficient is probably not applicable at very low energies (< a few MeV/nucleon) since it is determined from a questionable extrapolation of the theory. Of course we must allow in our model for some scattering beyond 0.2 to 0.3 AU so that the anisotropy decays with time during flare events. We might also speculate, as was considered by Goldstein and Fisk (1973), that high-intensity proton streams are special circumstances in which magnetic irregularities are damped, causing the anisotropies to be particularly large.

The rise time of solar flare events predicted in our modified model can also be quite short, in agreement with observations. Particles will be delayed in propagating from sun to earth principally in the region of significant scattering lying close to the sun. However, the particles

traverse this region at $\sim$ speed V; for example, the transit time from 2 to $22r_\odot$ with V = 400 km/s is only $\sim$10 hours. We should also expect that early in flare events particles can diffuse across the scattering region in times < 10 hours because of the large gradients present. Flare particles may also be influenced by shock waves near the sun, or for large flares the particles may have sufficient energy density themselves to affect the coronal magnetic field. Even allowing then for some scattering of the particles at distances greater than several tenths of AU, we should be able to account for rise times in $\sim$ 1 MeV proton flares of $\sim$ 15 hours.

CONCLUDING REMARKS

We find that it is possible for solar cosmic rays to be modulated between the sun and earth to the extreme that the predicted fluxes in the solar atmosphere are an interesting source of energy to the corona, as well as possible source of secondary particles such as positrons. To be consistent with some observations from near earth we must require that most of the modulation occurs within a solar envelope lying within $\sim$ 0.2 to 0.3 AU of the sun. The concept of a solar envelope of scattering is of course not new and was considered some years ago by Lust and Simpson (1957). Also, the heating of the solar wind is thought to occur in an extended region out to $\sim$ $20r_\odot$ and according to Barnes (1969) may result from the damping of hydromagnetic waves. These waves may scatter cosmic rays (Burlaga, 1970), and be responsible for our region of significant scattering.

Although our model is consistent with some observations, we emphasize that there is no compelling observational evidence that requires the large modulation considered here, other than now we can account for the low energy positron observations. We also note that we have not considered some possible observational tests for our model, namely, whether large fluxes of cosmic rays in the corona will red   in the X-ray or radio bands, or whether they produce detectable spallation products. Nor have we provided a plausible explanation as to how the sun accelerates the required copious fluxes of particles to relatively high energies. These concerns will have to await a future study.

We have also not considered the modulation of low energy electrons. However, at energies $\lesssim$ a few MeV the electrons should be scattered by irregularities that affect only very low energy nuclei ($\lesssim$ a few keV/nucleon), which are not of interest to us here. In principle, then, we can consider the modulation of nuclei and these electrons separately. In fact, in order to account for the low energy positron flux at 1 AU, Gregory (1972) must require that $\sim$ 1 MeV positrons experience much less modulation than comparable energy nuclei.

Finally, we comment that even if the solar envelope does not modulate the intensity by the large factors considered here, this region could still significantly affect our estimates of cosmic ray fluxes in the corona, the average energy at the sun of particles seen at earth, and so on.

ACKNOWLEDGMENTS

425

REFERENCES

Barnes, A. 1969, *Ap. J.* **155**, 311.

Burger, J.J., Stephens, S.A., and Swanenburg, B.N., 1970, *Astrophys, Space Sci.* **8**, 20.

Burlaga, L.F., 1970, *Acta Phys. Acad. Sci. Hung.* **29**, Supp. 2, 9.

Cline, T.L., and Hones, E.W., 1970, *Acta Phys. Acad. Sci. Hung.* **29**, Supp. 1, 159.

Fisk, L.A., and Axford, W.I., 1969, *J.G.R.* **74**, 4973.

Gleeson, L.J. 1971, *Astrophys. Space Sci.* **10**, 471.

Gleeson, L.J., and Axford, W.I., 1967, *Ap. J.* **149**, L115.

Goldstein, M.L., and Fisk, L.A., 1973, *J.G.R.*, in press.

Gregory, C.T., 1972, *J.G.R.* **77**, 1316.

Jokipii, J.R., 1972, *J.G.R.* **172**, 319.

Jokipii, J.R., and Coleman, Jr., P.J., 1968, *J.G.R.* **73**, 5495.

Kinsey, J.H., 1970, *Phys. Rev. Letters* 2., ⊦6.

Klimas, A.J., and Sandri, G. 1971, *Ap. J.* **169**, 41.

Klimas, A.J., and Sandri, G., 1973, *Ap. J.*, in press.

Krimigis, S.M., Roelof, E.C., Armstrong, T.P., and Van Allen, J.A., 1971, *J.G.R.* **76**, 5921.

Lust, R., and Simpson, J.A., 1957, *Phys. Rev.* **108**, 1563.

McDonald, F.B., 1970, *Intercorrelated Satellite Observations Related to Solar Events*, ed. D. Reidel, Dordrecht, Netherlands, 34.

Parker, E.N., 1965, *Planet. Space Sci.* **13**, 9.

Ramaty, R., Stecker, F.W., and Misra, D., 1969, *J.G.R.* **75**, 1141.

SOLAR FLARE ALPHA PARTICLES

L. J. Lanzerotti
Bell Laboratories

ABSTRACT

Interplanetary disturbances frequently change the instantaneous values of the low-energy solar flare alpha-to-proton flux ratios (when particles are compared as to equal energy per nucleon). The fluxes of alpha particles ($\sim$ 1 to $\sim$ 12 MeV/nucleon in five differential channels) have been integrated over the duration of seven large solar events occurring between May 28, 1967, and November 6, 1969, in order to investigate the total alpha particle fluxes observed at 1 AU resulting from the flares. The spectra of the event-integrated alphas are always softer than the spectra of the event-integrated protons. As a consequence, the event-integrated alpha-to-proton ratios decrease slightly with increasing energy per nucleon. The ^{4}He/^{1}H ratios averaged over the seven events are found to vary as 0.026 $(E/nucl)^{-0.2}$ in the range 1 to 10 MeV/nucleon. The value of the ratio at 1 MeV/nucleon is less than the helium-to-hydrogen abundance determined from spectroscopic studies of prominences and the chromosphere ($\sim$ 0.06), and is less than the average solar wind helium-to-hydrogen abundance ($\sim$ 0.045).

INTRODUCTION

Observations of the ^{4}He intensity in the solar wind and in solar cosmic rays give a direct measurement of this second most abundant of the solar chemical species. Even though these alpha particle measurements, together with simultaneous proton measurements, give values of the ^{4}He/^{1}H ratios, it is not readily clear how to relate such helium abundances to the solar abundances in the chromosphere, photosphere, and solar interior.

The most detailed studies of the average and instantaneous values of the emitted solar ^{4}He result from measurements of the solar wind. These studies have indicated that the ^{4}He abundance in the wind normally varies over a range from $\sim$0.03 to $\sim$0.1 and is somewhat dependent upon solar wind velocity and temperature. Increases in the velocity and temperature result in increases in the ^{4}He abundance, and an increase in solar wind flux is found to produce a decrease in the ^{4}He abundance (Hirshberg et al., 1972a; Ogilvie, 1972). Large increases in the solar wind helium abundance are often observed after a shock wave from a large flare passes the earth (Gosling et al., 1967; Bame et al., 1968; Ogilvie et al., 1968; Lazarus and Binsack, 1969; Ogilvie and Wilkerson, 1969; Hirshberg et al., 1970; Hirshberg, 1972). An average value of the ^{4}He/^{1}H ratio of 0.045 is given by Hundhausen (1970).

In addition to protons and electrons, solar flares also accelerate ^{4}He to high energies. Early measurements of the solar cosmic ray ^{4}He from balloons and rockets indicated that, for

alpha particles of energy $E_\alpha \gtrsim 25$ MeV/nucleon, the ^{4}He/^{1}H ratio varied from event to event and also within an event when fluxes of particles of equal energy per nucleon were compared (Biswas and Fichtel, 1965). Measurements of solar cosmic ray ^{4}He at lower energies ($\sim$ 1 to 10 MeV/nucleon) by satellite-based instrumentation have confirmed the variability of the ^{4}He/^{1}H ratios both within an event and from event to event (Lanzerotti and Robbins, 1969; Lanzerotti, 1969, 1970, 1972; Armstrong and Krimigis, 1971; Scholer et al., 1972). Some of these ratio changes at the lower energies may be due to interplanetary propagation effects (Lanzerotti and Robbins, 1969; Lanzerotti, 1972; Scholer et al., 1972). Only proton and alpha fluxes when compared as to equal energy per charge have ^{4}He/^{1}H ratios that remain relatively constant throughout many events.

The variability of the solar cosmic ray ^{4}He abundance is illustrated by the data shown in Figure 1. These proton and alpha particle data were obtained from measurements made with instruments flown by Bell Laboratories on the Explorer-34 satellite. Alpha particles, protons, and electrons were separately identified by energy-loss and range considerations as well as by use of an onboard particle identifier (Lanzerotti et al., 1969).

Plotted at the top of Figure 1 are the fluxes of protons and alpha particles measured during three events. The November 1968 flare occurred at N21W87 and was followed approximately two days later by a sudden commencement observed at the earth. Energetic storm particles were seen in the lower energy proton channel as well as shock-accelerated particles at the time of the sudden commencement (Lanzerotti, 1970). The May 1967 particle event followed a flare located at N28W33. Typical energetic storm particles were not seen, although one of the largest reported shock-accelerated particle enhancements was observed about two days after the flare. The April 1969 particle event was observed following a flare at N11E90. The sudden commencement April 12 was associated with the passage of a sector boundary. No energetic storm particles were observed and no shock from the flare was evident at the earth. The particle flux decreases on April 17 accompanied a Forbush decrease in the galactic cosmic ray intensity.

The bottom panels of Figure 1 contain plots of the solar cosmic ray ^{4}He/^{1}H ratios for particles compared as to equal MeV/nucleon, equal MeV/Z, and equal energy for the three events. For both of the flare events (November 1968 and May 1969) which were followed by interplanetary shock waves observed at the earth, the ^{4}He/^{1}H ratios changed during the course of the event for fluxes of particles compared as to equal velocity v (MeV/nucleon) and equal rigidity P (MeV). The particle fluxes remained fairly constant throughout both events for particles compared as to equal v·P (MeV/charge). In particular, no significant changes in the ratios were observed at the time of the shock passage for particles compared as to equal v·P. The time profiles of the particle fluxes following the April 1969 event were independent of particle rigidity and velocity; hence, the ^{4}He/^{1}H ratios were constant throughout the event.

To obtain a measure of the average solar flare ^{4}He abundance from large, discrete flare events, we determined the total flux of solar cosmic ray alpha particles and protons measured following seven events in 1967 to 1969. Three of these events are those shown in Figure 1. The event-integrated ^{4}He/^{1}H ratios are then compared to other measures of the solar
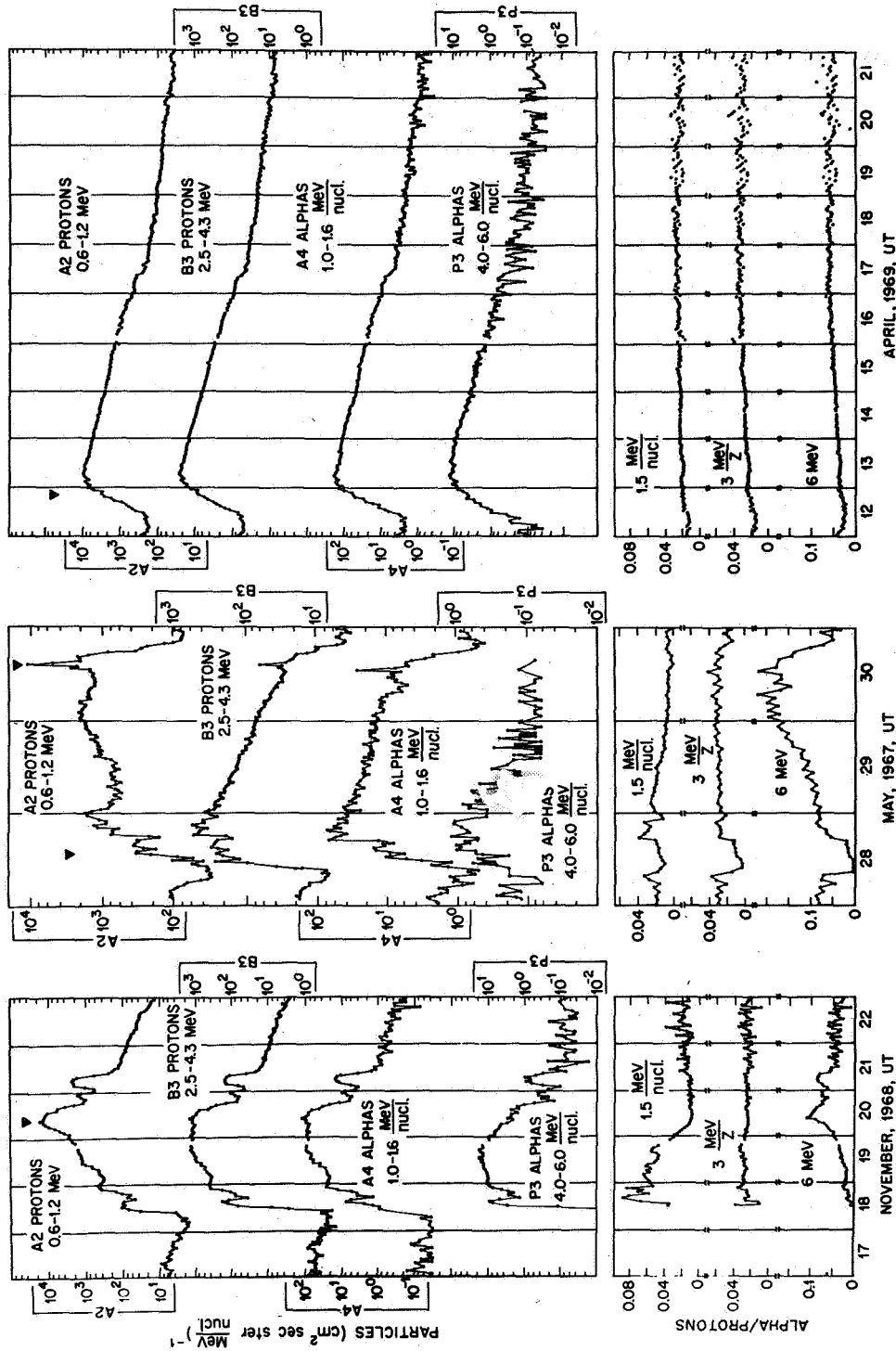
Figure 1. Proton and alpha particle fluxes observed at 1 AU following solar flare events on November 18, 1969, May 28, 1967, and April 10, 1969. At the bottom are plotted the alpha-to-proton flux ratios for particles compared as to equal energy per nucleon, equal energy per charge, and equal energy.

429

helium abundance to obtain information on the abundance from as wide a variety of data bases as possible.

OBSERVATIONS

The event-integrated alpha and proton fluxes were determined following the seven events listed in Table 1. Also listed in the table are the time periods over which the particle flux integrations were made, as well as the flare type, location, and time of occurrence.

Plotted in Figure 2 are the event-integrated alpha particle spectra from each of the seven events. All of the events have an intensity J dependence upon energy that is approximately a power law:

$$\frac{dJ}{d(E/nucl)} \propto (E/nucl)^{-n} \tag{1}$$

where E is the particle kinetic energy. Best-fit power laws of the form of Equation (1) were made to each of the alpha spectra of Figure 2 and to each of the proton spectra (not shown). It was found that, for the protons, n ranged in value from 1.3 to 3.0, and for the alphas, n ranged in value from 1.5 to 3.3. For each individual event, the alpha particle spectrum was harder than the proton spectrum; that is, $n_\alpha > n_p$ for all events. The values of n_α and n_p determined for each of the events are listed in Table 1 and plotted in Figure 3. (Also plotted in Figure 3 are values of n_e, the power-law exponent for fits made to the integral electron spectra for each of the events. The electron energy channels recorded electrons of energy $E > 300$ keV, > 500 keV, and > 1.0 MeV).
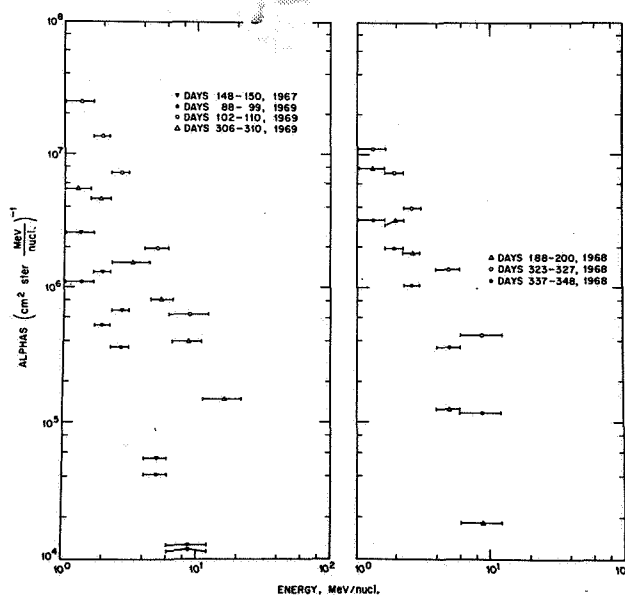

Figure 2. Event-averaged solar alpha particle fluxes
following seven large events in 1967 to 1969.

Table 1

Properties of Charged-Particle Events

| Event	Time	Importance	Location	Flux Summation (days)	n_p	n_α
May 28, 1967 (Day 148)	0527	3B	N28W33	148 – 150	2.1	3.0
July 6, 1968 (Day 188)	0946		N14E89	188 – 200	3.0	3.3
Nov. 18, 1968 (Day 323)	1017	1B	N21W87	323 – 327	1.5	1.8
Dec. 2, 1968 (Day 337)	2116	3N	N18E80	337 – 348	1.6	1.8
March 30, 1969 (Day 89)	0100		N19W10	88 – 99	2.1	3.0
April 10, 1969 (Day 101)	0410		N11E90	102 – 110	1.6	2.0
Nov. 2, 1969 (Day 306)	1028	1N	N13W90	306 – 310	1.3	1.5

431
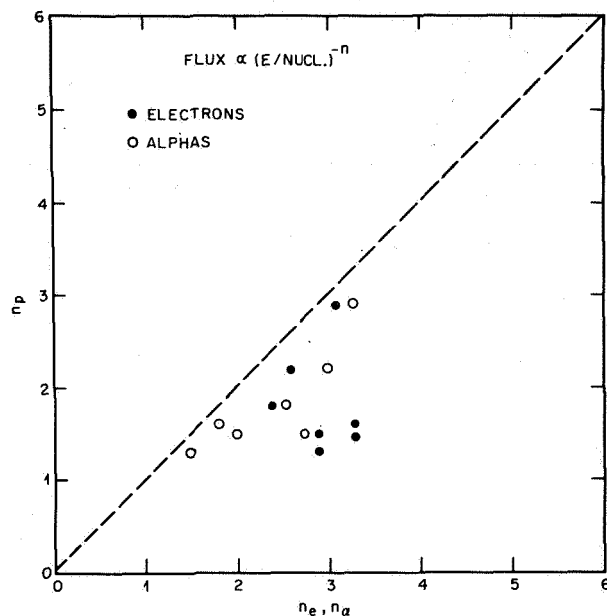
Figure 3. Power-law exponent for the alpha particle and electron flux spectra plotted for each event as a function of the exponent for the proton spectrum for the respective event.

The particle fluxes from the seven events were used to obtain the average proton and alpha particle fluxes measured in interplanetary space in the period May 28 (Day 148), 1967, to November 6 (Day 310), 1969. These averaged spectra are plotted in Figure 4. Over one-half of the alphas and protons in these averaged spectra were produced in the three largest events in this time interval: April 10 (Day 110), 1969; November 18 (Day 323), 1968; and July 6 (Day 188), 1968. There were additional fluxes of flare-produced protons and alphas from numerous flares in the time interval covered by the spectra of Figures 2 and 4. Inclusion of these data could increase the absolute fluxes in the averaged spectra of Figure 4 by perhaps a factor of two. These data would also tend to steepen the spectra, as the less intense flare events produce predominantly lower energy particles.

Power-law fits to the two spectra of Figure 4 give values of $n_\alpha = 1.9$ and $n_p = 1.7$. The least-squares power-law fits to each of the spectra are drawn in the figure.

The [4]He-to-^{1}H ratios for particles of equal velocity were determined as a function of particle energy per nucleon for each of the seven events. These ratios are shown in Figure 5. For all of the events the ratios decrease with increasing particle energy.

Also plotted in Figure 5 is the average alpha-to-proton ratio for the seven events as determined from the spectra of Figure 4. Since the seven-event averaged spectra for both species
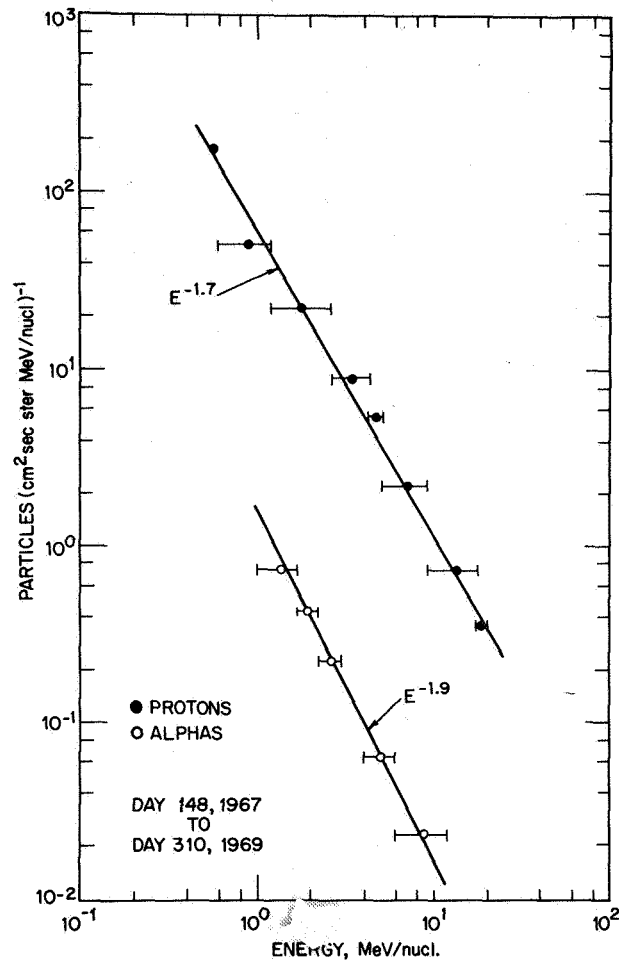
432

Figure 4. Time-averaged proton and alpha fluxes
from the seven flare events.

of particles obeys a power law in energy, the average alpha-to-proton ratio in the range 1 to 10 MeV/nucleon can be expressed as

$$\frac{^4\text{He}}{^1\text{H}} = 0.026 \, (\text{E/nucl})^{-0.2} \tag{2}$$

Hence, the energy dependence of the $^4\text{He}/^1\text{H}$ ratio is found to be small and to vary as the energy to the one-fifth power. In terms of equal kinetic energy particles, the ratio can be written as

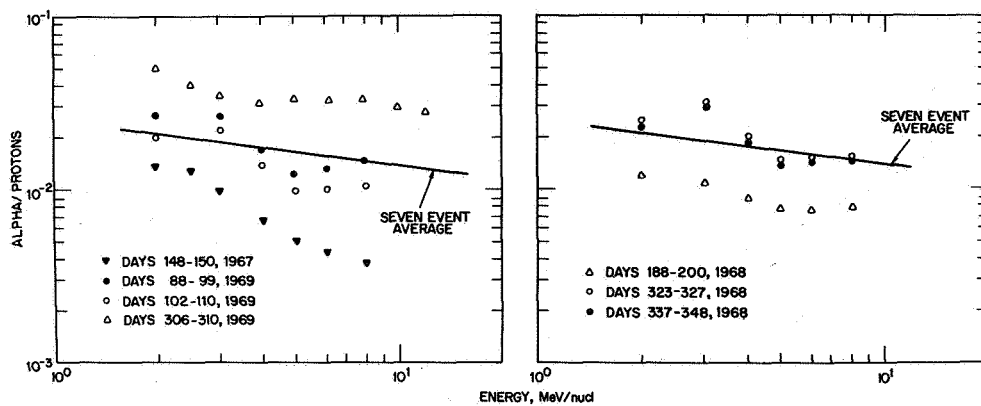$$\frac{^4\text{He}}{^1\text{H}} = 0.1 \, \text{E}^{-0.2} \tag{3}$$

Figure 5. Solar cosmic-ray alpha-to-proton flux ratios for each of the seven flare events. The solid line is the seven-event-averaged $^4\text{He}/^1\text{H}$ ratio as a function of particle energy per nucleon.

As indicated in the Introduction, it is not completely clear at present which particle-energy representation is most suitable for comparing the solar cosmic-ray fluxes with other measures of the solar helium abundance. In terms of past work, the $^4\text{He}/^1\text{H}$ ratio has always been expressed in terms of equal energy per nucleon. However, if the shock-associated propagation effects noted earlier in connection with the data of Figure 1 are important (as they appear to be), then comparison of particles in terms of equal energy per charge Z should be made. In this case

$$\frac{^4\text{He}}{^1\text{H}} = 0.05 \left(\frac{\text{MeV}}{Z}\right)^{-0.2} \tag{4}$$

DISCUSSION

Information about the solar helium abundance has been obtained previously by four principle methods:

- Helium abundance determinations from prominences and the chromosphere give a $^4\text{He}/^1\text{H}$ ratio of ~ 0.06 (Hirayama, 1971). The photospheric temperature of ~ 6000 K apparently precludes ionizing sufficient helium for conventional spectroscopic studies of the photospheric helium abundance.

- The average solar wind $^4\text{He}/^1\text{H}$ ratio is ~ 0.045 (Hundhausen, 1970) although this value varies considerably with changing wind conditions (see Introduction). The helium abundance is found to increase with increasing solar activity (Hundhausen, 1970; Ogilvie, 1972). The post-shock associated helium enhancements are found to give values of $^4\text{He}/^1\text{H}$ as high as twenty percent or more (Hirshberg et al., 1972b).

434

● At energies of $\sim$ 25 MeV/nucleon and higher, the abundance of helium to Z > 3 nuclei has been reported to remain relatively constant (Biswas and Fichtel, 1965; Durgaprasad et al., 1968). These observations of the cosmic-ray helium to medium (C, N, O) ratios have been used, together with spectroscopic determinations of the hydrogen to C, N, O abundance, to obtain a ^{4}He/^{1}H abundance ratio of $\sim$ 0.06 on the surface of the sun (Lambert, 1967; Durgaprasad et al., 1968). The Z > 3-to-^{4}He ratios have been found to deviate from the spectroscopic values at energies of a few MeV/nucleon (Price et al., 1971; Armstrong and Krimigis, 1971; Lanzerotti et al., 1972; Von Rosenvinge et al., 1972). Hence, the intercomparisons of cosmic ray and spectroscopic determinations in order to arrive at a solar photosphere ^{4}He/^{1}H ratio are probably not valid for solar cosmic rays of a few MeV/nucleon.

The relative fluxes of solar cosmic ray alpha particles and protons were summed from seven flare-events in 1967 (Hsieh and Simpson, 1970). Power law fits to the summed spectra between 10 and 100 MeV/nucleon indicated that n_p = 2.7 and n_α = 3. These are considerably softer spectra than reported here for ^{1}H and ^{4}He in the energy range 1 to 10 MeV/nucleon. The Hsieh and Simpson ^{4}He/^{1}H ratio varies as $E^{-0.3}$, an energy dependence close to that reported here ($E^{-0.2}$). At 10 MeV/nucleon, Hsieh and Simpson report ^{4}He/^{1}H $\sim$ 10^{-2}, a value smaller than that reported here at 10 MeV/nucleon ($\sim$ 1.7 X 10^{-2}).

● Iben (1969) used the upper limit on the solar neutrino fluxes as established by Davis et al. (1968) to infer a ^{4}He/^{1}H ratio of $\sim$ 0.07 in the interior of the sun. Theoretical models of the sun place the ^{4}He/^{1}H ratio in the interior at $\sim$ 0.09 (Morton, 1968).

Recently Lanzerotti et al. (1973) have compared the alpha particle abundances of Figure 4 with the alpha fluxes inferred from the abundance of the radionuclide ^{59}Ni in lunar rock samples. ^{59}Ni is produced in the reaction ^{56}Fe(α,n) ^{59}Ni and has a half-life of 80,000 years. They concluded from this comparison that the fluxes of solar flare-produced alphas have been a constant over the last $\sim$ 10^5 years. The analyses of lunar rocks for the radionuclides ^{26}Al (half-life 7.4 X 10^5 years) and ^{53}Mn (3.7 X 10^6 years) produced by proton-induced reactions appear to indicate that solar flares have produced cosmic-ray protons with similar fluxes and spectra over the past one million years (Shrelldalff, 1970; Finkel et al., 1971; Lavrukina and Ustinova, 1971). Hence, the solar cosmic ray alpha-to-proton ratio appears to have been approximately a constant for the last $\sim$ 10^5 years.

The seven-event-average solar alpha-to-proton ratio results presented here for particles compared as to equal energy per nucleon (Figure 5) fall substantially below other determinations of the solar helium abundances discussed previously. For 1 MeV/nucleon particles, the average ^{4}He/^{1}H ratio is $\sim$ 0.026 and the ratio decreases at higher energies. The average cosmic ray helium abundance for particles of equal v·P (^{4}He/^{1}H $\sim$ 0.05 at 1 MeV/Z) is more compatible with several of the other abundance determinations. However, Equations (3) and (4) point up clearly the difficulties in interpreting solar cosmic ray alpha particle abundances in terms of solar abundances, when little is known of the physics of the acceleration and propagation processes.

In summary, the average solar cosmic-ray ^{4}He/^{1}H ratio determined from seven large flares during the maximum of solar cycle 20 has a dependence upon particle (energy/nucleon)$^{-0.2}$ in the energy range 1 to 10 MeV/nucleon. The average cosmic ray ^{4}He abundance is smaller than both the average solar wind abundance and a spectroscopic abundance determination from prominences. In terms of astrophysical processes, the average helium abundance in both the solar wind and solar cosmic rays is below the $\sim$ 7 to 9 percent helium abundance thought to be the normal content of stellar interiors (Faulkner, 1971) and as obtained from models of the solar interior (Sears, 1964; Morton, 1968). In view of the present astrophysical controversies concerning the helium problem, among them a) the question of departures from local thermodynamic equilibrium in interpreting spectroscopic measurements (Burbidge, 1971; Worrall and Wilson, 1972), and b) the decreasing upper limit on the solar neutrino fluxes (Davis, 1972), it is of great importance to continue to investigate the relationship of helium observations in the solar wind, and in solar cosmic-rays to helium abundance determinations made spectroscopically and calculated theoretically.

REFERENCES

Armstrong, T. P. and Krimigis, S. M., 1971, *J. G. R.* **76**, 4230.

Bame, S. J., Asbridge, J. R., Hundhausen, A. J. and Strong, I. B., 1968, *J. G. R.* **73**, 5761.

Biswas, S. and Fichtel, C. E., 1965, *Space Sci. Rev.* **4**, 709.

Burbidge, G., 1971, *Highlights of Astronomy*, Ed. C. de Jager (D. Reidel, Holland) **2**, 328.

Davis, R., Jr., Harmer, D. S. and Hoffman, K. C., 1968, *Phys. Rev. Letters* **20**, 1205.

Davis, R., Jr., 1972, *Bull. Am. Phys. Soc.* **17**, 527.

Durgaprasad, N., Fichtel, C. E., Guss, D. E. and Reames, D. V., 1968, *Ap. J.* **154**, 307.

Faulkner, J., *Highlights of Astronomy*, Ed. C. de Jager (D. Reidel, Holland) **2**, 269, 1971.

Finkel, R. C., Arnold, J. R., Imamura, M., Reedy, R. C., Fruchter, J. S., Loosli, H. H., Evans, J.C., Delany, A.C., and Shedlovsky, J.P., 1971,*Proc. Second Lunar Sci. Conf.* **2**, 1773.

Gosling, J.T., Asbridge, J.R., Bame, S.J., Hundhausen, A.J. and Strong, I.B., 1967, *J.G.R.* **72**, 1813.

Hirayama, T., 1971, *Solar Phys.* **19**, 384.

Hirshberg, J., 1972, *Proc. Asilomar Solar Wind Conf.*, NASA SP-308, 582.

Hirshberg, J., Alksne, A., Colburn, D.S., Bame, S.J., and Hundhausen, A.J., 1970, *J.G.R.* **75**, 1.

Hirshberg, J., Asbridge, J.R. and Robbins, D.E. 1972a, *J.G.R.* **77**, 3583.

Hirshberg, J., Bame, S.J. and Robbins, D.E., 1972b, *Solar Phys.* **23**, 467.

Hsieh, K.C., and Simpson, J.A., 1970, *Ap. J.* **162**, L191.

Hundhausen, A.J., 1970, *Rev. Geophys. Space Phys.* **8**, 729.

Iben, I., Jr., 1969, *Ann. Phys.* **54**, 164.

Lambert, D.L., 1967, *Nature* **215**, 43.

Lanzerotti, L.J., 1969, *J.G.R.* **74**, 2851.

Lanzerotti, L.J., 1970, Report UAG-9, (World Data Center A, U.S. Dept. of Commerce, NOAA, Boulder, Colorado).

Lanzerotti, L.J., 1972, NASA-TM-2440, 193.

Lanzerotti, L.J. and Robbins, M.F., 1969, *Solar Phys.* **10**, 212.

Lanzerotti, L.J., Lie, H.P. and Miller, G.L. 1969, *IEEE Trans. Nucl. Sci.* **NS-16**, 343.

Lanzerotti, L.J., Maclennan, C.G., and Graedel, T.E., 1972, *Ap. J.* **173**, L39.

Lanzerotti, L.J., Reedy, R.C. and Arnold, J.R., 1973, *Science* **179**, 1232.

Lavrukina, A.K. and Ustinova, G.K., 1971, *Nature* **232**, 463.

Lazarus, A.J. and Binsack, J.H., 1969, *Ann. IQSY* **3**, 378.

Morton, D.C., 1968, *Ap. J.* **151**, 285.

Ogilvie, K.W., 1972, *J.G.R.* **77**, 4227.

Ogilvie, K.W. and Wilkerson, T.D., 1969, *Solar Phys.* **8**, 435.

Ogilvie, K.W., Burlaga, L.F. and Wilkerson, T.D., 1968, *J. Geophys. Res.* **73**, 6809.

Price, P.B., Hutcheon, I., Cowsik, R. and Barber, D.J., 1971, *Phys. Rev. Letters* **26**, 961.

Scholer, M., Hovestadt, D. and Hausler, B., 1972, *Solar Phys.* **24**, 475.

Sears, R.L. 1964, *Ap. J.* **140**, 477.

Shrelldalff., 1970, Proc. Apollo 11 Lunar Sci. Conf., *Geochim. Cosmochim. Acta,* Suppl. 1, 2, 1503.

Von Rosenvinge, T.T., Teegarden, B.J. and McDonald, F.B., 1972, *Bull. Am. Astron. Soc.* **4**, 390.

Worrall, G. and Wilson, A.M., 1972, *Nature* **236**, 15.

THE RELATIONSHIP OF SOLAR FLARE ELECTRONS TO THE FLARE FLASH PHASE AND TYPE III RADIO BURSTS

R. P. Lin

Space Sciences Laboratory
University of California, Berkeley

ABSTRACT

The energy spectrum and temporal behavior of the 10-100 keV solar flare electrons observed at 1 AU are interpreted in terms of: 1) the location of the acceleration region; 2) the time of acceleration and duration of the injection into the interplanetary medium; and 3) type III radio burst origin at the sun and at 1 AU. For at least some and possibly the majority of electron flare events the density of the acceleration region is $\sim 2 \times 10^9$ cm^{-3}; the time of acceleration and release coincides to within minutes of the flash phase as indicated by the type III radio burst, and the duration of the release is $\lesssim 3$ minutes. Evidence for the origin of type III radio bursts in 10-100 keV electron streams is shown and discussed.

INTRODUCTION

Recent studies of the flash phase acceleration of electrons in small flares, based on X-ray, radio, optical and particle data, have greatly increased our understanding of the rapid and substantial energy release in this phase of solar flares. (Lin and Hudson, 1971; Kane and Anderson, 1970; Kane and Donnelly, 1970). Here we review and expand on the clues to this acceleration and subsequent release of electrons in these flares provided by the low energy particle observations available from spacecraft. In particular, we will discuss 1) the location of the acceleration region; 2) the time of the release and its duration; and 3) the origin of type III radio bursts.

The particle observations are from University of California experiments aboard the IMP-4, -5, and -6 spacecraft and the Apollo-15 and -16 subsatellites. The instrumentation is described in detail elsewhere (Lin, 1970; Lin et al., 1972; Anderson et al., 1972); here we only note that the IMP experiments provide measurements above ~ 20 keV with varying degrees of energy resolution, while the Apollo experiments provide measurements as low as 0.5 keV energy for electrons.

LOCATION OF ELECTRON ACCELERATION REGION

Measurements of the electron energy spectrum observed at 1 AU down to low energies can be interpreted in terms of an upper limit to the amount of material traversed by the accelerated particles. We assume that the electrons are accelerated at a height, h, in the solar

atmosphere, and then pass through the overlying material to reach the vicinity of 1 AU. The minimum amount of material traversed (in number of ions/cm^2) is given by

$$\int_h^{1 \, AU} n_i(x) \, dx$$

Then, assume the electrons travel through fully ionized hydrogen so that the energy loss formula is given by Trubnikov (1965)

$$\frac{dE}{dt} = 4.9 \times 10^9 \, n_i \, E^{-\frac{1}{2}} \, keV/s$$

where E is in keV and n_i in cm^{-3}. Then for nonrelativistic electrons

$$\frac{dE}{dx} = 2.6 \times 10^{-18} \, \frac{n_i}{E} \, keV/cm \tag{1}$$

Integrating from height h to 1 AU

$$\int_{E_1}^{E2} E \, dE = 2.6 \times 10^{-18} \int_h^{1 \, AU} n_i(x) \, dx \equiv K(h)$$

and

$$E_2 = (E_1{}^2 - 2K)^{\frac{1}{2}} \tag{2}$$

where E_1 is the initial accelerated energy of the electron and E_2 its energy at 1 AU. If the spectrum of the freshly accelerated electrons at the sun is given by a power law in energy, as would be consistent with the X-ray observations,

$$\frac{dI}{dE_1} \, \, AE_1{}^{-\gamma} \tag{3}$$

then the spectrum of the electrons observed at 1 AU will be

$$\frac{dN}{dE_2} = \frac{AE_2}{(E_2^2 + 2K)^{(\gamma + 1)/2}} \tag{4}$$

This spectrum will have a maximum at

$$E_{2M} = (\frac{2K}{\gamma})^{\frac{1}{2}} \tag{5}$$

The location of the maximum will be at this energy or higher because:

● The direct radial distance outward through the solar atmosphere is used in the calculation without taking into account the helical paths followed by the particles.

440

- Scatterings which change the particle's direction are far more effective for low energy particles than for high energy particles and will subject the low energy particles to longer path lengths.

- No other energy loss mechanisms such as generation of radio or plasma waves are taken into account.

We proceed now to evaluate K for a small electron event observed on April 27, 1972, by the Apollo-16 subsatellite. Figure 1 shows the time history of the event in five energy intervals. Although no flare was reported for this event in the preliminary listing of the Solar Geophysical Data bulletins, the solar origin of the event is confirmed by the analysis of the path length traveled by the particles (shown in Figure 2) and the observation simultaneously by IMP-6 of a type III radio burst at low frequencies beginning at the onset of this particle event. (Fainberg, Stone and Evans, private communication, 1972). The analysis of Figure 2 is made under the assumption that the particles at different energies are injected at the same
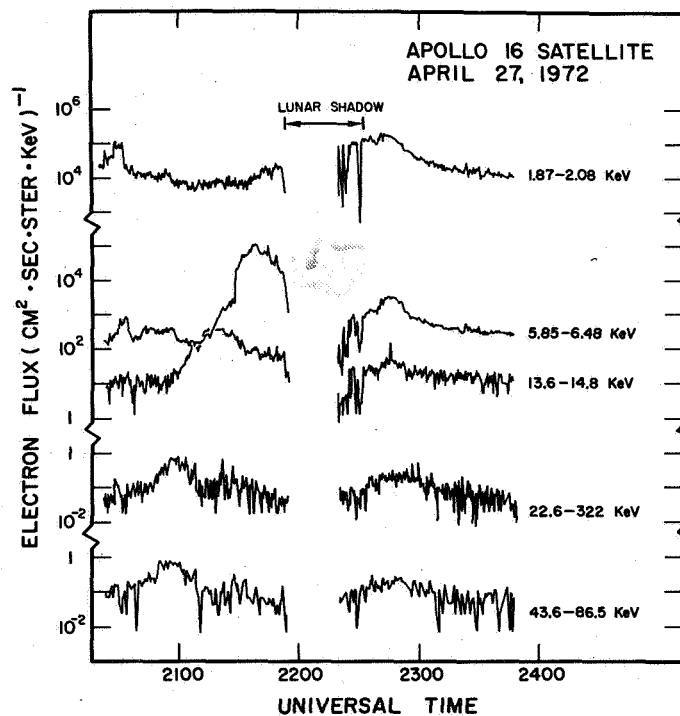

Figure 1. A solar flare electron event observed in five energy channels of the Apollo-16 subsatellite particles experiment. Part of the time (indicated in the figure) the spacecraft is on field lines passing through the moon so that the electrons from the sun are unable to reach the spacecraft.
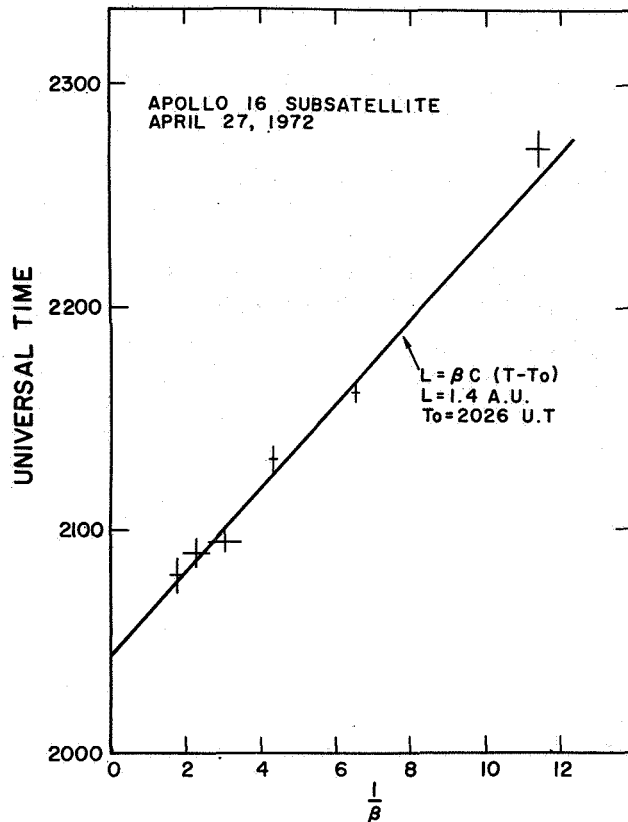
Figure 2. A plot of the time of maximum flux in each
energy channel versus $1/\beta$ = c/v. The points lie on a
straight line, indicati̶ng a common distance traveled,
L ~1.4 AU, and a common injection time T_0 ≈ 2026
UT.

instant and travel approximately the same total distance. Then the times T_i of the peak flux
of particles of velocity $\beta_i c$ are related to the time of injection T_0 and the distance traveled
L by

$$\frac{L}{c} \frac{1}{\beta_i} = T_i - T_0 \tag{6}$$

so that a plot of T_i versus $1/\beta_i$ should produce a straight line with slope L/c and T_0 at
$1/\beta_i$ = 0. Figure 2 clearly shows that the five energy intervals fall on a straight line with
L ≈ 1.4 AU and T_0 ≈ 2026 UT.

This value of L is quite reasonable for a scatter-free event (Wang et al., 1972) and this event
certainly shows the characteristics of such an event (note the rapid initial decay). The energy
spectrum of the event at the peak (converted for anisotropy) is shown in Figure 3. Although
some modifications of this spectrum are required to obtain an injected spectrum at the sun,
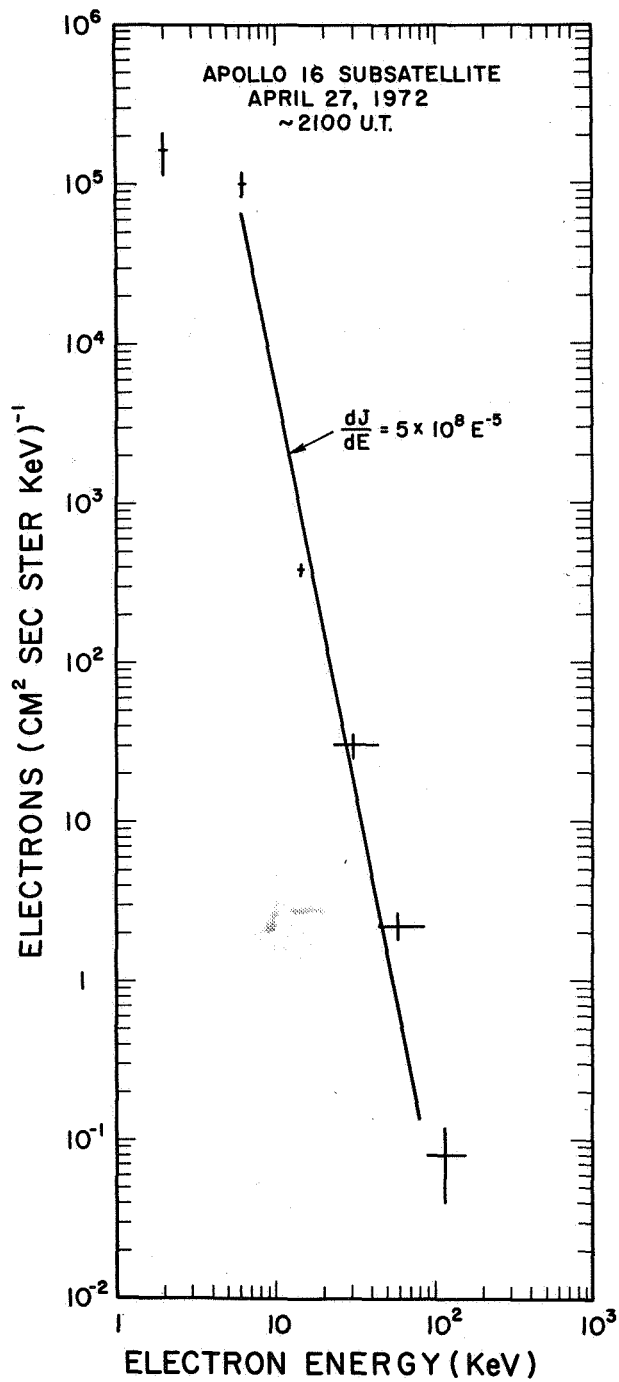
442

Figure 3. The differential energy spectrum of the April 27, 1972 event at the maximum of each energy channel (that is, taking into account velocity dispersion). The directional detectors have been corrected so the values shown are averaged over all directions.

these modifications are minor* and do not change the main conclusion drawn from this spectrum: that the injected spectrum does not have a turnover at low energies before ~6 keV. Using Equation (5) we find, placing $E_{2M} \lesssim 6$ keV, and $\gamma = 5$,

$$K \lesssim 90$$

$$\int_h^{1 \, AU} n_i(x) \, dx \lesssim 3.5 \times 10^{19} \text{ cm}^{-3}$$

For hydrogen this is $\lesssim 60$ $\mu g/cm^2$ of material traversed. The ambient density of material in the corona at the acceleration region is then $\lesssim 2 \times 10^9$ cm^{-3} and the height is $\lesssim 0.04$ $R_\odot$ or ~3 $\times$ 10^4 km above the photosphere for a 10X Baumbach-Allen active region density model. Clearly the electron acceleration in this event must have occurred in the lower corona. We wish to reemphasize that this estimate is a *lower* limit to the actual height of acceleration, since all the effects which were not taken into account would tend to increase the minimum energy of the peak. Although this is only one event and only a few events have been observed to energies below ~20 keV, we note that in no events to date has a turnover been observed at higher energies. This suggests that it is quite likely the electron acceleration at the flash phase is generally a coronal phenomenon. In view of the substantial amount of energy contained in the non-thermal electrons, comparable to the total energy in the rest of the flare for these small (subflares or class 1) flares (Lin and Hudson, 1971) it is likely that the primary flare energy conversion mechanism itself is located in the lower corona. This location would be consistent with the observed starting frequencies of type III bursts (typically several hundred megahertz).

TIME OF ELECTRON ACCELERATION AND RELEASE AND ITS DURATION

It is difficult in particle observations near 1 AU to separate the effects of a prolonged injection of particles at the sun from effects due to propagation in the interplanetary medium. In order to obtain the most accurate estimate of the time of acceleration and/or release of the electrons and its duration, we have chosen those events in which the effects of the interplanetary and coronal propagation of these particles are known to be negligible or easily corrected. These events are those scatter-free electron events whose associated flares are located near the footpoint of the spiral field line connecting the earth. The two events shown in Figure 4 (from Wang et al., 1971) have the additional advantage of being sufficiently intense to provide accurate observations to energies above ~400 keV even though a steep spectral slope is present above ~200 keV (Figure 5). A comparison of the times of peak flux in an analysis similar to that performed in the previous section on the event of April 27, 1972 gives a travel distance of ~1.2 AU and injection times of 1623 and 1938 UT (Figure 6). These times are within a minute of the onset times of the type III burst at the sun. Because the various detectors respond to a range of particle energies, the time profile will show a duration which is the sum of the injection duration and the velocity dispersion

---

*Since this is a scatter-free event, the number of electrons released at the sun is approximately proportional to the flux observed at 1 AU integrated over the peak.
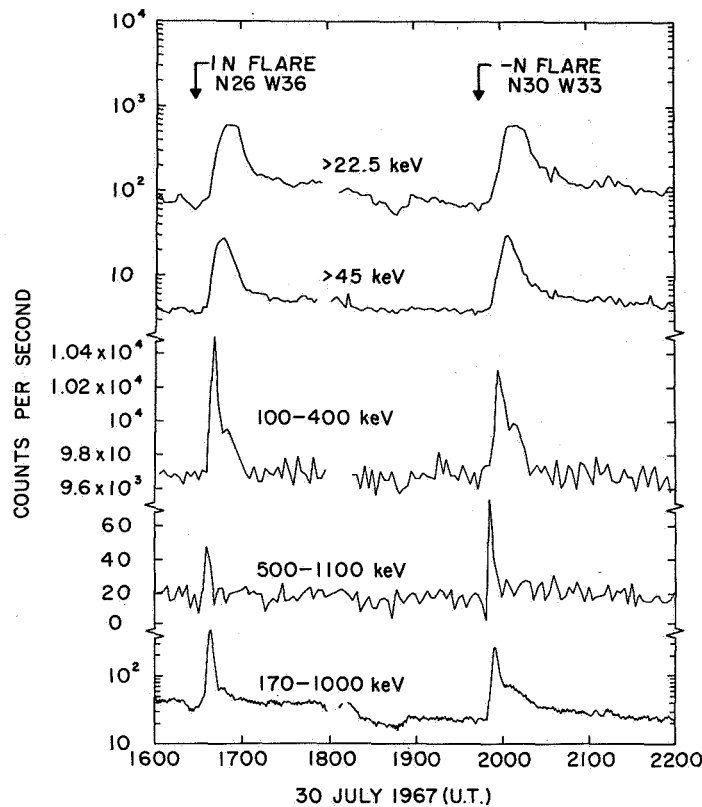
444

Figure 4. Two scatter-free events observed up to ~500 keV in electron energy. These events come from flares located near the footpoint of the interpl̶ ᵣy field line connecting the earth so that the effects of coronal diffusion are minimized as well. The width of the peaks at high energies is ≲5 minutes total. (From Wang et al., 1971.)

of the particles in traveling a distance of ≳ 1.2 AU. By comparing the different energy channels Wang et al., 1971 obtain a maximum duration of injection, consistent for all energy channels, of ≲ 3 minutes. Thus the acceleration and/or injection of these electrons occurs at the flash phase and lasts for ≲ 3 minutes.

TYPE III BURSTS

There is at the present time strong evidence for the electron hypothesis for type III burst excitation. At the sun the remarkable temporal correlation of type III bursts to non-thermal impulsive X-ray events for many bursts can be taken as evidence that electrons are certainly present exactly at the time of type III burst. Figure 7 shows several examples of X-ray type III events in a short time period (from Kane, 1972). In the interplanetary medium the ~40 keV solar electron events observed at 1 AU appear to be closely correlated with kilometric
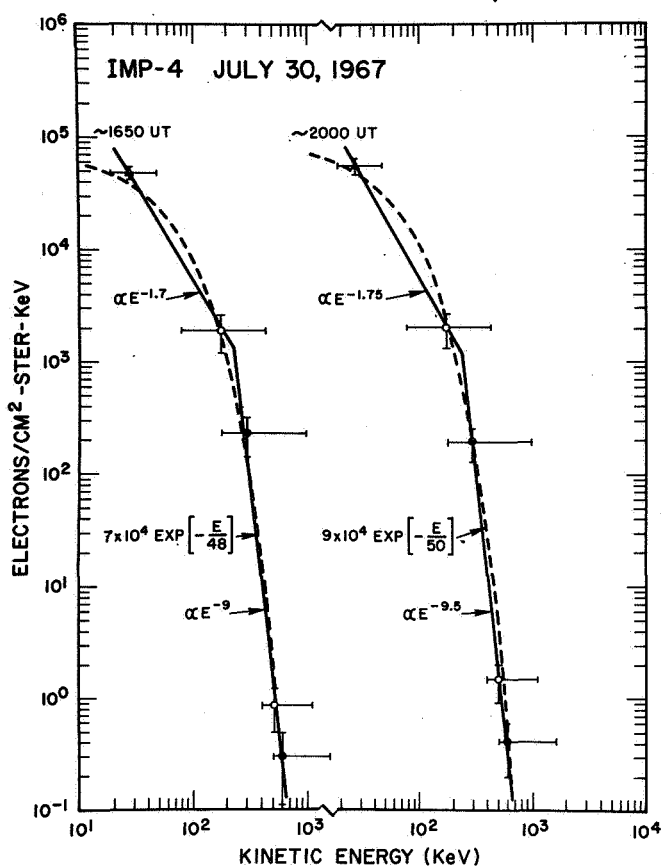
Figure 5. The energ ... ctra of the two events of
Figure 4. These spectra are rapidly falling above ~200
keV, which is typical of the flash phase electron
events.

wavelength type III bursts, if propagation effects are taken into account (Alvarez, et al., 1972). These observations, however, do not rule out the presence of a small energetic proton flux in these events below the observational background of the particle detectors.

Under the electron exciter hypothesis, plasma waves near the plasma frequency are excited by the beam of electrons with a peak in its velocity distribution near ~0.3c, and these plasma waves then generate electromagnetic radiation near the plasma frequency and at its second harmonic through scattering on thermal fluctuations in the plasma and on other plasma waves (combination scattering) (Ginzburg and Zheleznynkov, 1968). Two problems remain, if the evidence for electrons as the type III bursts exciter is accepted. The first problem is illustrated in Figure 3; that is, that no peak appears to be present at ~40 keV in the spectrum of the accelerated and released electrons as would be expected from the velocities derived from the radio observations. The second problem is that theoretically it appears difficult to stabilize an electron beam (Smith, 1970).

446
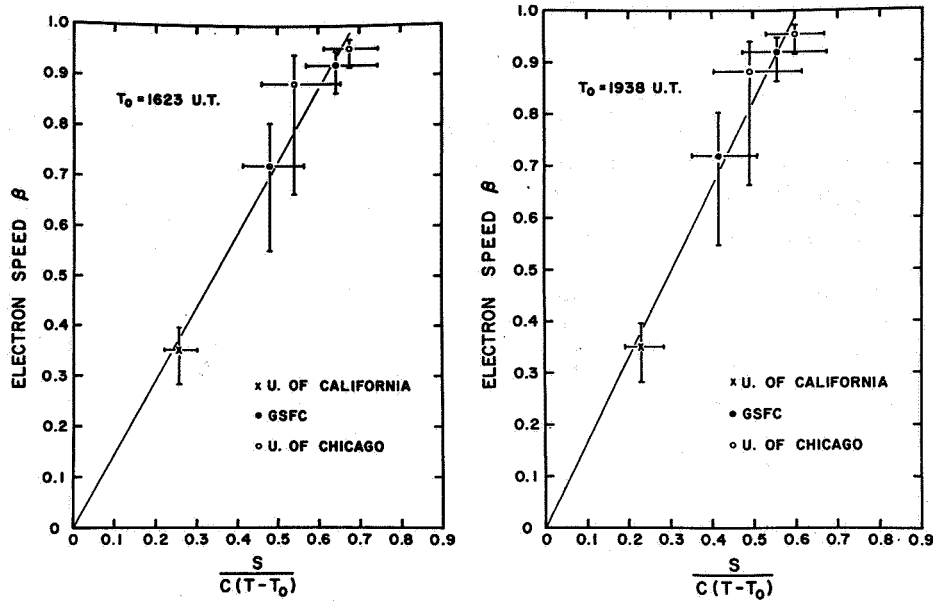
Figure 6. A time versus velocity analysis similar to that shown in Figure 2, but for the events of Figure 4. The times of injection, 1623 and 1938 UT, compare with type III burst start times at the sun of 1623 and 1937 UT. (From Wang et al., 1971.)
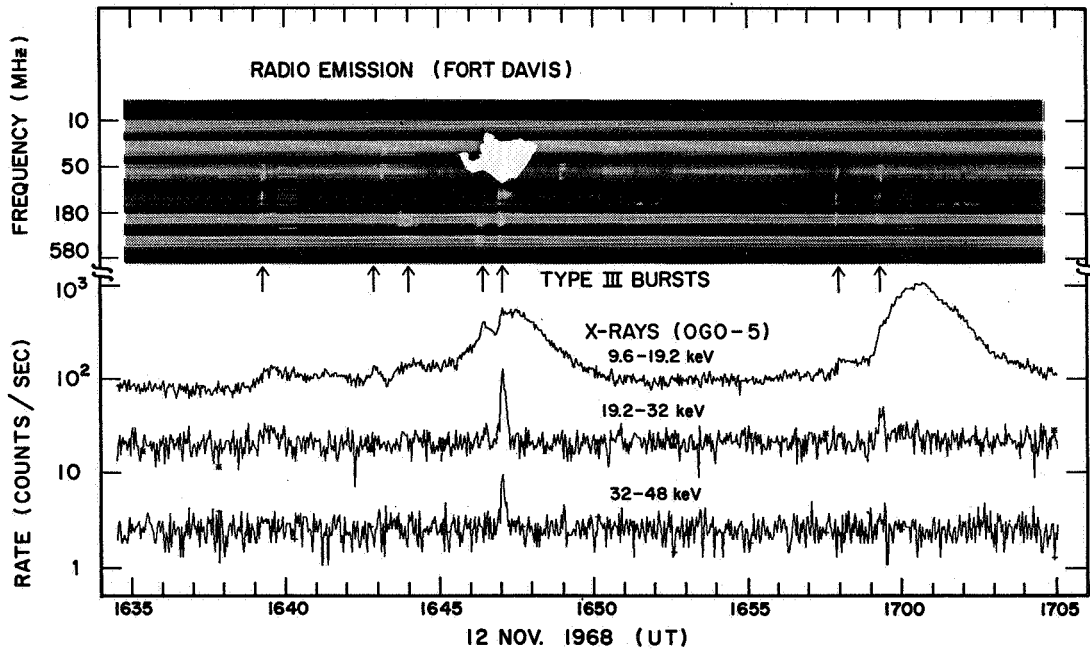
Figure 7. The coincidence in time between type III bursts and nonthermal impulsive X-ray bursts is illustrated here (from Kane, 1972). The X-ray bursts are not always observed to accompany type III bursts, presumably because the burst is too small to observe above background. The bremsstrahlung X-ray emission is proportional to the ambient density, so that variations in the height of the electron region will vary the intensity of the emission.

Figure 8 shows observations of the energy spectrum of a solar electron event observed by IMP-6 at 1 AU. Clearly a peak in the energy spectrum exists above detector threshold (18 keV) for a substantial duration. These peaks are generated by the arrival of the high energy electrons prior to the low energy electrons, that is just velocity dispersion due to the traversal of the $\gtrsim$ 1.2 AU spiral field line by the electrons. The transitory nature of the peak may, in fact, prove necessary to the stabilization of the electron beam (Zaitsev et al., 1972).

Radio observations at 55, 44, and 30 kHz show a type III burst whose onset corresponds to the onset of the > 18 keV electrons at 1 AU (Fainberg, Stone and Evans, private communication, 1972). The location of the source of radiation at these frequencies is near or around the spacecraft at 1 AU, since the radio observations, which are obtained with a directional (dipole) antenna, show no spin modulation at these frequencies. It is likely that the second harmonic of the plasma frequency is generated as well as the fundamental and may even dominate the fundamental. If the ~ 55 kHz radiation is second harmonic produced near the spacecraft, then the observed lack of modulation would be consistent with typical solar wind plasma densities measured near 1 AU. The radio emission at these low frequencies continued to increase in intensity until all traces of the peak disappeared from the electron observations (lower threshold 18 keV).

IMP-6 SOLAR ELECTRON EVENT, MAY 16, 1971
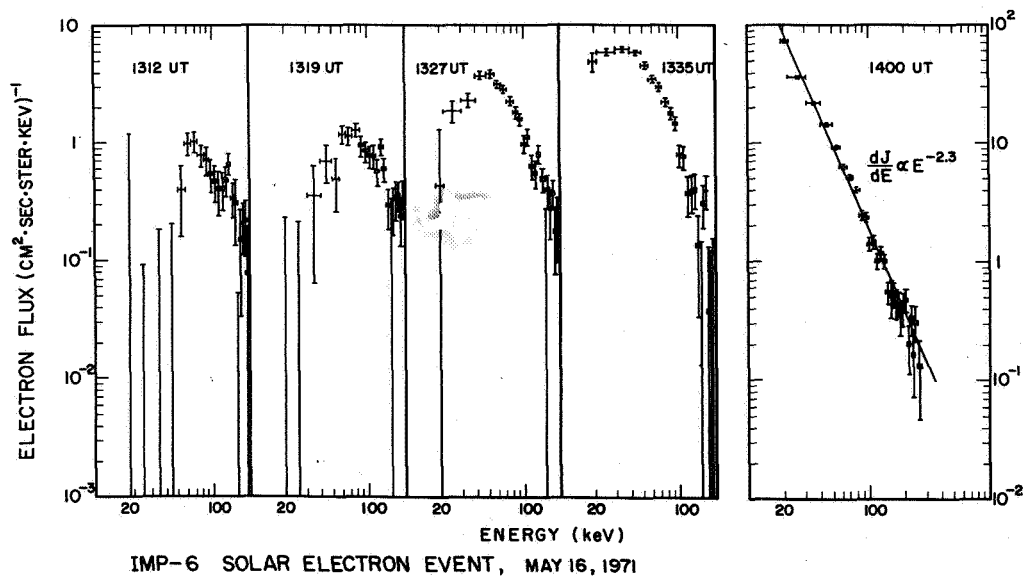
Figure 8. A sequence of energy spectra taken during the rising portion of a solar electron event observed by IMP-6. The experiment provides 64-channel pulse height analysis with ~8 keV per channel resolution. The onset of the type III radiation at 55 kHz is 1307 UT, the same time that the particle event begins. The type III radiation continues to increase until the peak disappears from the >18 keV electron spectra. (Radio times from Fainberg, Stone and Evans, private communication, 1972.)

ACKNOWLEDGMENTS

REFERENCES

Alvarez, H., Haddock, F. and Lin, R.P., 1972, *Solar Phys.*, in press.

Anderson, K.A., Chase, L.M., Lin, R.P., McCoy, J.E., and McGuire, R.E., 1972, *J.G.R.* 77, 4611.

Ginzburg, V.L., and Zheleznyakov, V.V., 1968, *Astron. Zh.* 35, 694.

Kane, S.R., 1972, *Solar Phys.*, in press.

Kane, S.R., and Anderson, K.A., 1970, *Astrophys. J.* 162, 1003.

Kane, S.R., and Donnelly, R.F., 1971, *Astrophys. J.* 164, 151.

Lin, R.P., 1970, *Solar Phys.* 12, 266.

Lin, R.P., Anderson, K.A. and Cline, T.L., 1972, *Phys. Rev. Letters* 29, 1035.

Lin, R.P., and Hudson, H.S., 1971, *Solar Phys.* 17, 412.

Smith, D.F., 1970, *Solar Phys.* 15, 202.

Trubnikov, B.A., 1965, *Rev. Plasma Phys.* 1, 105.

Wang, J.R., Fisk, L.A., and Lin, R.P., 1971, 12th Int. Conference on Cosmic Rays, Hobart, Tasmania, Australia.

Zaitsev, V.V., Mityakov, N.A., and Rapoport, V.O., 1972, *Solar Phys.* 24, 444.

VII: MAGNETIC FIELDS
AND PARTICLE STORAGE

CORONAL MAGNETIC FIELDS AND ENERGETIC PARTICLES

Gordon Newkirk, Jr.

High Altitude Observatory,
National Center for Atmospheric Research

ABSTRACT

Magnetic fields in coronal and interplanetary space play a critical role in determining the propagation and storage of energetic particles from the flare site to 1 AU. The current investigation is designed to determine how several characteristics of solar energetic particle emission are influenced by the detailed configuration of the coronal magnetic fields below $2.5 R_\odot$.

For this purpose, particles are followed in the ambient magnetic field from their injection above a flare until they either

- impact on the photosphere,

- escape into interplanetary space, or

- mirror at some distant location in the corona.

We use the guiding center approximation but neglect drifts, pitch angle diffusion, and scattering from magnetic inhomogeneities. Energy loss by Coulomb collisions is included for a model corona. The ambient magnetic fields are calculated using a potential model incorporating Mount Wilson photospheric magnetic data.

We apply the calculations to 46 flares of reported importance >2+ which occurred in the period 1959 to 1971 at times when good magnetic data were available. Of these, 27 occurred in the western hemisphere and included:

- 14 flares without proton events

- 6 flares with long duration (lifetimes in excess of 3 days at 100 Mev) or with recurrent proton events

- 7 flares with impulsive proton events

Typical examples of such field line calculations for an injection surface placed at 1.3 $R_\odot$ covering a sector $36^\circ \times 36^\circ$ centered on the flare are displayed. A statistical examination of these calculations shows that many particles ($\sim$ 60 percent) find themselves initially mirroring in closed magnetic arches, that a smaller fraction (16 to 40 percent) escape immediately, and that a still smaller fraction (1 to 15 percent) impact onto the photosphere.

However, only a small number ($\sim$ 4 percent) of the injected particles would find themselves mirroring on field lines which extend above 2.0 $R_\odot$.

Possible differences in the ambient magnetic field configurations between proton and nonproton flares are also examined, with the conclusion that proton flares have significantly more open field lines emerging from the injection surface than do flares of the same importance which do not produce protons at 1 AU. We conclude that the ambient field configuration influences whether or not protons escape from a given flare.

Comparing our calculation of the average spread in longitude of field lines opened by the solar wind at 2.5 $R_\odot$ with observations of protons and electrons at 1 AU, we conclude that the present model cannot account for the observed longitude distribution of energetic particles.

The mean electron density encountered by particles mirroring in the magnetic field permits us to determine the probability that particles injected from the flare regions will encounter a mean electron density smaller than any given value. Mean electron densities smaller than $\sim$ 3 $\times$ 10^7 cm^{-3} occur for less than 10 percent of the mirroring particles. This implies that storage of 10 Mev particles for longer than 1 day and of 3 Mev particles for longer than a few hours is extremely unlikely. Thus, particle storage in high magnetic arches cannot account for the long duration (1 to 50 days) of particles with energies $\widetilde{<}$ 10 Mev at 1 AU. Such particles must be generated by a continuously-operating acceleration mechanism.

INTRODUCTION

There exists ample evidence that magnetic fields, especially those in the corona, are intimately related to many aspects of ergetic phenomena on the sun. A few specific examples are immediately apparent: Coronal magnetic fields appear to constitute the primary reservoir for the energy released during a flare. Open magnetic field line configurations emerge as the channels along which type III radio burst particles are conducted from their point of origin low in the corona out into interplanetary space. The field determines the propagation through the corona of flare-produced magnetohydrodynamic (MHD) shock waves and the appearance of these shocks as type II radio bursts and Moreton waves. The temporary containment of energetic particles in closed magnetic loops is evident from pulsations in microwave bursts. Finally, the field configuration is critical for storage of particles in the corona. The goal of this investigation is to examine how the detailed magnetic configuration of the corona affects energetic solar particles.

CORONAL FIELDS

Our current knowledge of coronal magnetic fields depends almost exclusively upon their calculation from observed line-of-sight fields at the photospheric level. Since the details of these calculations and their limitations have been extensively discussed in the literature

(Schmidt, 1964; Newkirk et al., 1968; Schatten et al., 1969; Altschuler and Newkirk, 1969; Schatten, 1971) they need not be repeated here. It is sufficient to remember that these calculations represent the potential (current-free) coronal field, with a zero potential sphere placed at $R_w \sim 2.5\ R_\odot$ to simulate the influence of the solar wind. Thus, these calculations cannot include any information about the disruption of the fields by flare phenomenon, and moreover, may become inaccurate during periods when the photospheric fields are evolving rapidly.

Nevertheless, several lines of evidence suggest that these calculations give us at least the broad outlines of the magnetic fields present in the corona. The fact that the density structure of the corona seen at eclipse often closely resembles the configuration of the calculated magnetic field lines (Figure 1) suggests that much of the corona is made up of magnetic tubes of different densities of coronal gas. (Such comparisons also let us determine
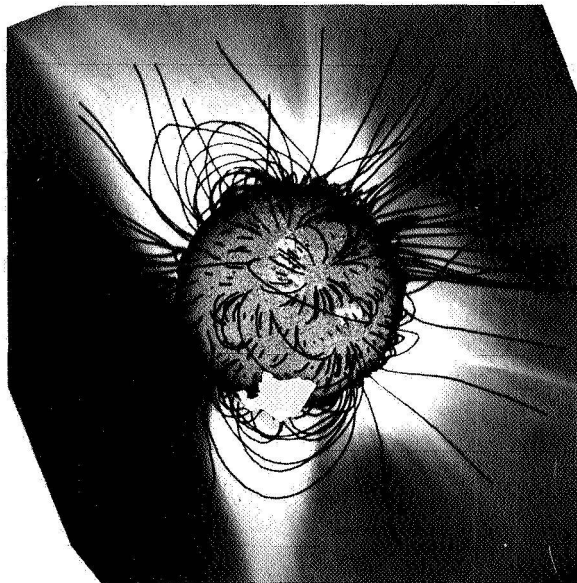

Figure 1. Calculated coronal magnetic field lines with $R_w = 2.5\ R_\odot$ superposed on a white light photograph of the corona of November 12, 1966 and the corresponding Hα filtergram (Sacramento Peak).

the appropriate radius R_w, at which field lines become radial, to be used in field calculations.) Those few cases (Lantos-Jarry, 1970; Trotter and Newkirk, 1971; Dulk, 1971; Smerd and Dulk, 1971) in which the configuration of the field has been inferred from radio data have generally shown agreement between the inferred and calculated coronal fields.

The Hα filtergram placed over the image of the moon (Figure 1) as well as a second Hα-magnetic field superposition (Figure 2) show many of the characteristics of coronal fields and their relationship to familiar surface phenomena. Note, for example, that extensive diverging field patterns are associated with active regions and that widely separated active centers are connected by magnetic fields. Arcades of magnetic loops and corresponding arches in the coronal density also appear as characteristic features.

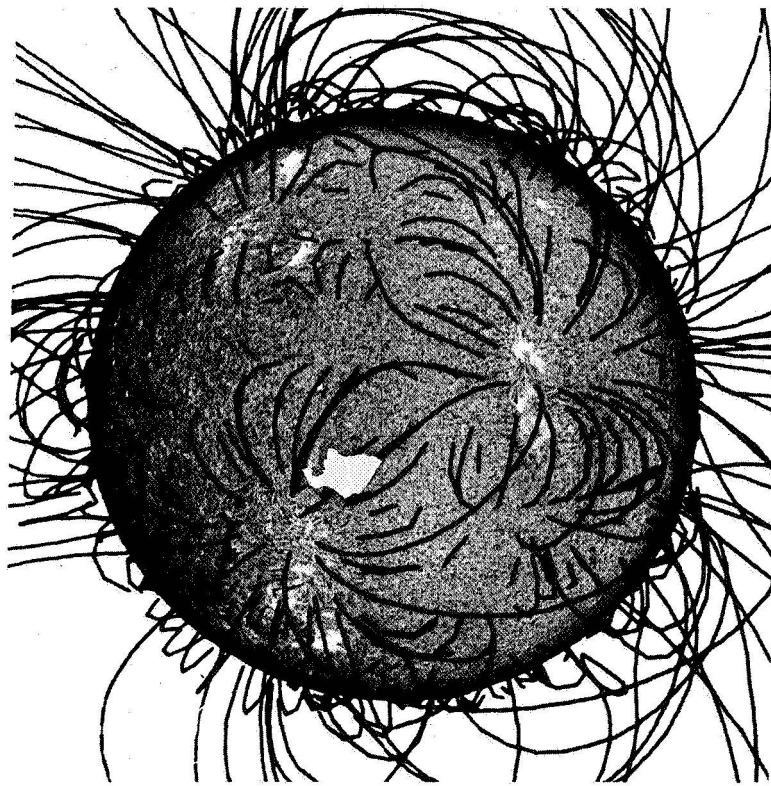

Figure 2. A calculated coronal magnetic field map superposed on the corresponding Hα filtergram (Sacramento Peak) demonstrates the diverging fields associated with active regions and the magnetic connection between widely separated centers.

456

One aspect of coronal fields which is not represented in these calculations is the small scale fibrous nature which the density structure of the corona and its fields undoubtedly possess. Evidence for a fine scale density structure comes to us from radio burst observations (Kundu, 1965; Warwick and Dulk, 1969; Fainberg and Stone, 1970; Wild and Smerd, 1972; Steinberg et al., 1971; Aubier and de la Noe, 1971), coronal spectroscopy and photography (Leroy, Rosch and Trellis, 1968; Jefferies, Orrall and Zirker, 1972; Koutchmy and Laffineur, 1970; Newkirk and Lacey, 1970), discrete cosmic radio source scattering (Cohen and Gunderman, 1969; Hewish and Symonds, 1969; Hewish, 1971; Jokipii and Hollweg, 1970; Lovelace, Salpeter and Sharp, 1970), and from observation of the propagation of satellite radio signals through the corona (Levy et al., 1969). We suggest in Figure 3 that some of this fibrous structure originates at photospheric levels through the concentration of
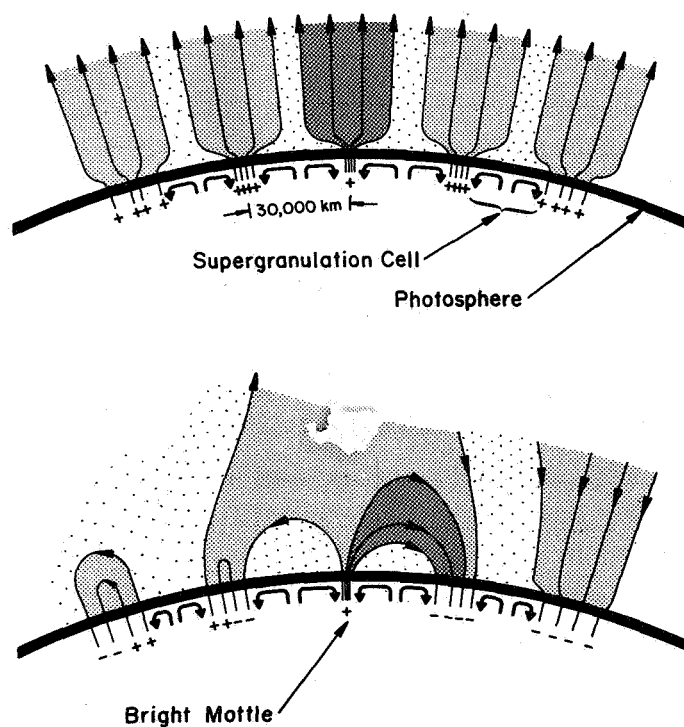

Figure 3. A schematic representation of the coronal field above the supergranulation structure for uniform polarity (upper) and mixed polarity (lower). Current sheets of extremely small thickness can be expected to form above the closed loops.

457

the magnetic field into small knots of high intensity. In the upper panel we represent a region in which the field is all of the same polarity. Here the fields from a given knot expand to form tubes with characteristic dimensions of 30,000 km, which appear as polar plumes and rays in the corona (Newkirk and Harvey, 1968). Since such tubes trace the large scale field represented by our calculations, and since their dimensions are much larger than the particle gyroradii, their presence has little influence on particles of energy below 1 Gev. However, over much of the solar surface the polarity of the field is mixed, as represented in the lower panel of Figure 3.

A simple comparison of the magnitude of the horizontal field energy-density in such configurations with the coronal energy-density shows that current sheets will occur above the tops of the closed magnetic loops displayed in the figure. These sheets are similar to those associated with helmet streamers in the outer corona. The theory of such sheets (Pneuman, 1972; Smith and Pneuman, 1972) suggests that they are extremely thin with a characteristic thickness $\sim$ 500 km and a radius of curvature of the transverse field in the sheet of only tens of kilometers. Since the local field strength is low, the radius of gyration of energetic particles exceeds this radius of curvature; and such current sheets could act as effective scattering and conducting plates for particles much in the manner suggested by Fisk and Schatten (1972).

Thus, we picture the magnetic corona as a system of many thin current sheets which follow the overall geometry of the magnetic field as approximated by the potential field calculation. As mentioned earlier, the influence of these coronal current sheets is not included in our present calculations.

INFLUENCE ON ENERGETIC PARTICLES

Energetic particle emission from the sun exhibits many characteristics (for example, Webber, 1964; McCracken and Rao, 1970; Axford, 1972) which cannot be reviewed in this paper, and which will require a complete model of the coronal and interplanetary magnetic structure for proper explanation. Here we examine how large scale magnetic fields in the corona affect three of the most obvious characteristics:

- Among apparently identical flares, some produce copious energetic particles at 1 AU while others produce none. Does the geometry of the ambient field explain this phenomenon?

- Flares far removed from the source of the approximately spiral field lines connecting the earth to the sun may transmit energetic particles to the earth. Is the divergence of field lines from the neighborhood of an active region sufficient to explain this effect?

- Energetic particles are received at the earth from some regions for days or weeks following an impulsive particle event and any obvious flare activity. Are the closed magnetic arches revealed by the calculations and also seen in the corona capable of storing particles for extended periods of time?

458

To answer these questions we have constructed a preliminary model for the propagation of particles in the coronal magnetic field below 2.5 $R_\odot$, by using the guiding center approximation and assuming that particles are introduced in the mirroring condition at an injection sector placed at a radius R_{in} with dimensions $36^\circ \times 36^\circ$ centered on a flare. Dissipation of energy by Coulomb collisions in a completely ionized corona is included, but cross-field drifts of the guiding center, pitch-angle and cross-field diffusion by collisions, and scattering by magnetic irregularities are not treated. Various aspects of the model and estimates of the importance of these latter mechanisms are discussed in the Appendix.

The model has been applied to forty-six flares which occurred between 1959 and 1971 as summarized in Table 1. An example of a typical calculation of particle trajectories appears in Figure 4, in which field lines of three kinds are easily distinguished: (a) those permitting

NORTH POLE VIEW
$R_{IN} = 1.3 R_\odot$

CENTRAL MERIDIAN
VIEW
$R_{IN} = 1.05 R_\odot$

CENTRAL MERIDIAN
VIEW
$R_{IN} = 1.3 R_\odot$

✗ Flare
Site

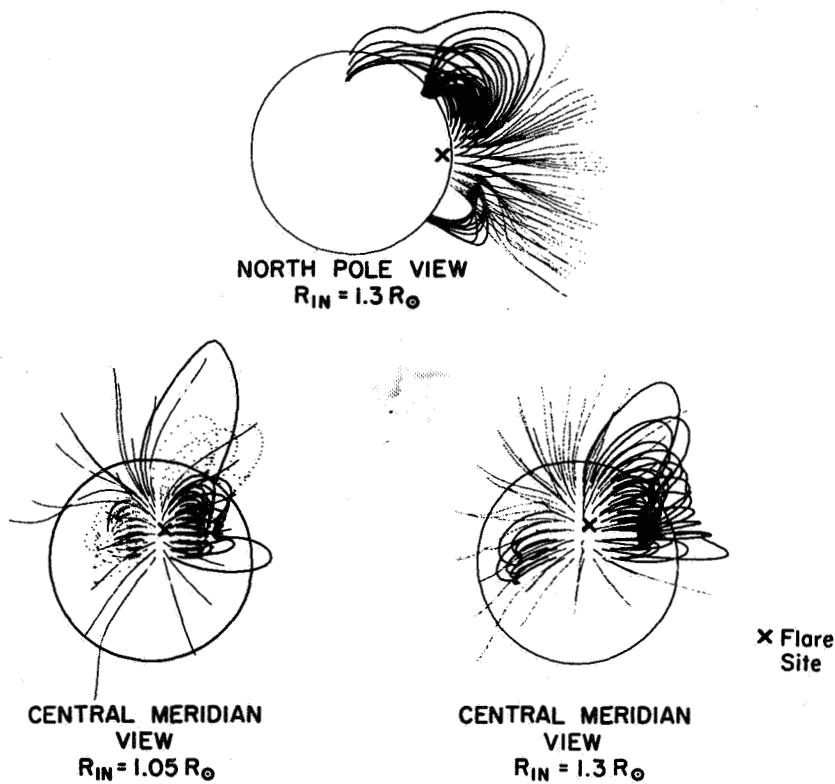Figure 4. A typical example of the trajectories of particles originating at a $36^\circ \times 36^\circ$ injection surface centered on a flare (X) for two different values of R_{in}. Mirroring particle trajectories appear as heavy solid lines; escaping trajectories, as light solid lines; and impacting trajectories, as dotted lines. The particular event displayed is the long duration proton flare of April 20, 1971.

459

Table 1

Flares Examined for Ambient Coronal Field Configuration.

Date	Start Time (UT)*	McMath Plage Number	Latitude	Position From Central Meridian	Longitude	Importance	Type**
1959 Aug 23	2233	5339	N 17	E 28	129	2+	
Sep 1	1923	5354	N 12	E 60	351	2+	Proton
Nov 28	2006	5476	N 12	E 31	299	3	
1960 Apr 1	b0123	5627	N 15	E 68	56	2+	
Apr 28	b0130	5645	S 05	E 34	93	3	Proton
May 6	1404	5653	S 09	E 07	15	3+	Proton
Jul 1	b0332	5726	N 08	E 37	323	2+	
Sep 2	b0620	5822	N 18	W 23	270	2+	
Sep 3	0037	5838	N 18	E 88	146	2+	Proton
Oct 14	2033	5896	S 25	E 56	357	2+	
Oct 29	1026	5909	N 22	E 27	188	3	Proton
Nov 15	0207	5925	N 25	W 35	26	3	Proton, L
1961 Mar 26	1012	6069	S 1	E 74	349	3	
Apr 26	1646	6098	S 11	E 53	323	3	
Jul 18	0920	6171	S 07	W 59	57	3+	Proton, I
1963 Oct 28	0135	7003	N 12	W 24	200	3	
1966 Mar 19	0338	8207	N 21	E 25	152	3n	
Jul 07	0025	8362	N 35	W 48	210	2b	
Sep 02	0542	8461	N 24	W 87	216	3b	Proton, L
1967 Jan 11	0137	8632	S 27	W 45	246	3b	
Feb 13	1747	8687	N 21	W 11	138	3b	
Feb 18	0943	8698	N 22	W 11	50	3n	
Mar 26	1630	8740	N 26	E 05	302	3b	
May 6	0435	8791	S 20	W 34	89	3n	
May 28	0529	8818	N 28	W 32	176	2b	Proton, I

Table 1 (Concluded)

Date	Start Time (UT)*	McMath Plage Number	Latitude	Position From Central Meridian	Longitude	Importance	Type**
1968 Jun 09	0830	9429	S 14	W 09	254	3b	Proton, I
Jul 08	1708	9503	N 13	E 58	163	3b	Proton, ?
Sep 29	1617	9678	N 17	W 51	255	2b	Proton, L
Oct 30	2340	9740	S 14	W 37	192	3b	Proton, L
Dec 02	2202	9802	N 19	E 80	000	3n	
1969 Jan 24	0706	9879	N 20	W 08	110	3n	
Mar 1	0251	9957	S 26	W 05	353	2b	
Mar 27	1315	9994	N 20	W 69	74	2b	
Apr 21	2004	10035	N 24	W 33	68	3b	
Sep 27	0350	10352	N 09	E 02	90	3b	Proton
Nov 21	2120	10432	N 03	W 03	90	2b	
Nov 27	1928	10432	N 16	W 82	90	2b	
1970 Jan 31	1512	10543	S 23	W 62	294	2b	Proton, I
Mar 29	0032	10641	N 13	W 37	238	2b	Proton, I
Apr 15	0404	10670	N 13	W 86	63	2b	Proton, I
Aug 01	1024	10851	N 06	W 43	33	2b	
Sep 25	0019	10960	N 14	W 67	49	2b	
Nov 17	0731	11029	N 16	W 38	41	2b	
1971 Jan 24	2215	11128	N 18	W 49	236	3b	Proton, L
Apr 8	b0325	11221	S 19	W 19	311	2b	
Apr 17	b0513	11256	N 20	W 20	133	2b	Proton, L

*b indicates flare already in progress at time noted.

**Western Hemisphere flares are subdivided into I = impulsive and L = long duration according to the definition in the text.

the immediate escape of particles to the interplanetary medium at 2.5 $R_\odot$, (b) those permitting the temporary trapping of particles, and (c) those permitting immediate loss of particles by impact on the photosphere. The extreme divergence of field lines of type (a), and the large area of the solar surface covered by field lines originating from the injection surface, are typical. As expected, location of the injection surface at R_{in} = 1.05 $R_\odot$ rather than 1.3 $R_\odot$ reduces the proportion of field lines which reach out into interplanetary space and increases the proportion from which particles impact on the photosphere.

The Ambient Field and the Escape of Particles

The average characteristics of particles originating above the several types of flares contained in Table 1 are of interest and can be determined by examining the fate of particles originating at the injection surface. Since the foot points of the field lines are chosen at equal intervals in sine-colatitude and longitude, the probability of an injected particle having a particular fate is proportional to the number of field lines classified as "mirroring", "escaping", or "impacting", as displayed in Tables 2 and 3. Several conclusions are

Table 2

Probability of Injected Particles Having a Particular Fate

(36° Injection Sector at 1.05 $R_\odot$)

	Escape	Impact	Mirror with $R_{max} < 2R_\odot$	Mirror with $R_{max} > 2R_\odot$	Remain at Sun
All Flares > 2+ (38)	0.12 *454*	0.19 *733*	0.67 *2533*	0.01 *52*	0.88 *3318*
Western Hemisphere Flares > 2+, non-proton (14)	0.07 *93*	0.25 *340*	0.67 *929*	0.01 *18*	0.93 *1287*
Western Hemisphere Flares > 2+, long duration proton (4)	0.16 *62*	0.18 *70*	0.66 *265*	0.01 *3*	0.84 *338*
Western Hemisphere Flares > 2+ impulsive proton (5)	0.18 *92*	0.19 *93*	0.63 *315*	0 *0*	0.82 *408*

Note: The division between impulsive and long duration proton flares is taken as a reported lifetime of 3 days for 100 MeV protons. Number of flares appears in parenthesis while number of field lines appears in italics.

462

Table 3

Probability of Injected Particles Having a Particular Fate

$(36° \text{ Injection Sector at } 1.3 \text{ R}_\odot)$

	Escape	Impact	Mirror with $R_{max} < 2R_O$	Mirror with $R_{max} > 2R_O$	Remain at Sun
All Flares > 2+ (46)	0.28 *531*	0.002 *3*	0.68 *1287*	0.04 *79*	0.72 *1369*
Western Hemisphere Flares > 2+, non-proton (14)	0.16 *222*	0.001 *1*	0.80 *1127*	0.04 *50*	0.84 *1178*
Western Hemisphere Flares > 2+, long duration proton (6)	0.24 *143*	0.003 *2*	0.74 *441*	0.02 *14*	0.76 *457*
Western Hemisphere Flares > 2+, impulsive proton (7)	0.39 *276*	0.004 *3*	0.58 *405*	0.02 *16*	0.61 *424*

Note: The division between impulsive and long duration proton flares is taken as a reported lifetime of 3 days for 100 MeV protons. Number of flares appear in par͏ ͏ ͏sis while number of field lines appears in italics.

immediately apparent. First, a high proportion of the particles (60 to 80 percent) find themselves initially trapped in closed magnetic configurations; for only a minor fraction (1 to 4 percent) of these particles does the field line extend above 2 $R_\odot$. Second, many (7 to 40 percent) of the particles escape immediately to the zero potential surface and to the spiral magnetic field of the interplanetary medium. Such particles presumably account for the scatter-free phases of the impulsive particle event (Lin, 1970a, b, c; Wang, 1972). Finally, restricting our attention to western hemisphere flares in order to minimize any bias caused by interplanetary field lines from the eastern hemisphere not reaching the earth, we see an increasing probability for the immediate escape of particles as we consider successively: nonproton flares, long duration proton flares, and impulsive proton flares. To test the statistical significance of this effect, we calculate χ^2 for the contingency tables, comparing the number of field lines which would force particles to remain at the sun (columns 6), with the number allowing immediate escape (columns 2) for the western hemisphere flares. The values of χ^2 for these 2 X 3 or 2 X 2 tables together with P, the probability that such an association might have arisen by pure chance, appear in Table 4. For $R_{in} = 1.05$ $R_\odot$, the role of the configuration of the field in determining whether a flare

463

appears as a proton or nonproton flare is well established, while its role in determining whether a flare appears as an impulsive or long duration event is unclear. For $R_{in} = 1.3\ R_{\odot}$, however, both the greater proportion of escaping particles for proton flares as compared to nonproton flares, as well as the increased proportion for impulsive proton flares as compared to long duration proton flares, are well established. Thus, we conclude that the undisturbed ambient field configuration does determine whether energetic particles escape from a given flare to 1 AU, and as the proportion of open field lines increases, the probability that an impulsive particle event will be observed also increases.

Table 4

χ^2 Tests of Significance of the Association
between Ambient Field Configuration and Energetic
Particle Events

Comparison of Escaping vs Remaining Particles for:	$R_{in} = 1.05\ R_{\odot}$	$R_{in} = 1.3\ R_{\odot}$
Nonproton vs Proton Flares	$\chi^2 = 61$ $P < 10^{-3}$	$\chi^2 = 144$ $P < 10^{-3}$
Western Hemisphere Nonproton vs Long Duration Proton vs Impulsive Proton Flares	$\chi^2 = 52$ $P < 10^{-2}$	$\chi^2 = 36$ $P < 10^{-3}$
Western Hemisphere Long Duration Proton vs Impulsive Proton Flares	$\chi^2 = 1.3$ $P = 0.25$	$\chi^2 = 104$ $P < 10^{-3}$

The Distribution in Longitude of Proton Flares

Although energetic particles may be trapped for a time in closed magnetic arches in the corona, open field lines represent the sole channel of escape into interplanetary space. We ask if smooth propagation along such open field lines as they diverge from the injection surface can account for the observed spread in longitude of flares which deliver energetic particles to the earth. To investigate this hypothesis we determine the relative frequency distribution of open field lines at 2.5 $R_{\odot}$ with longitude counted from the center of the flare. Only field lines within the latitude band $\pm 30^{\circ}$ at 2.5 $R_{\odot}$, where they presumably are swept out into the solar wind, are included, and the distribution function is summed for 10° intervals of the absolute magnitude

$$\mid \phi_{flare} - \phi_{line} \mid$$

in the longitude difference.

These distribution functions for R_{in} = 1.05 $R_\odot$ and 1.3 $R_\odot$ appear in Figure 5, together with the distributions in longitude for flares designated as the sources of electron events with energy greater than 40 keV (McCracken and Rao, 1970), for prompt electron events (Lin, 1970a), and for the proton flares from Table 1. The field line distribution function is centered at F (60° west longitude) to represent the average location of the spiral field line connecting the earth to the sun. As expected, open field lines originating at an injection surface at 1.3 $R_\odot$ are more radial and yield a narrower distribution function than those originating at 1.05 $R_\odot$. However, the spread in longitude of open field lines characterized by a full-width-at-10 percent of 60° to 75° (or a full-width-at-50 percent of 10° to 20°) is far from sufficient to explain the observed distribution of energetic particle events. Thus, we conclude that either: (1) The flare event does disrupt the ambient magnetic field; or (2) open field lines far from the injection surface are fed energetic particles by cross-field
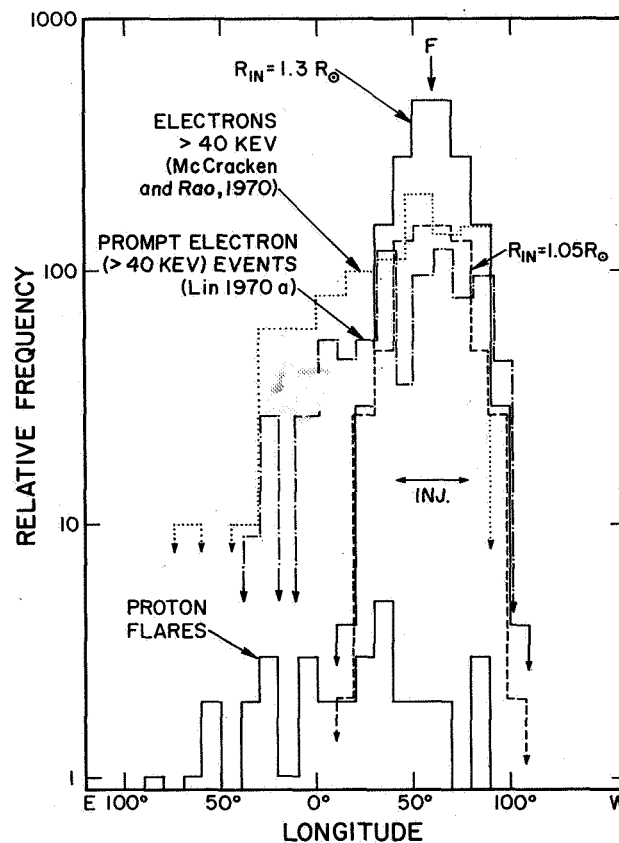

Figure 5. The relative frequency distribution in longitude of escaping particles for a synthetic flare at F compared to that of energetic electron events and proton flares. The angular spread of escaping field lines is insufficient to explain the observed longitudinal distribution of particles.

drift or diffusion (Reid, 1964); or (3) the injection surface used in the model is too small; or (4) field line meandering and diffusion in interplanetary space accounts for most of the observed spread. These alternatives require discussion.

Since the energy responsible for a flare may originate in the relaxation of coronal magnetic fields from a force-free to a nearly potential configuration, some readjustment of the coronal field following a flare is to be expected. Current data are insufficient to determine how extensive or frequent this adjustment might be although coronal photographs (Dunn, 1971; Wagner, 1972; Brueckner, 1972) show that it does occur. Valdez and Altschuler (1970) found an opening of the magnetic fields from active regions due to changes in the surface fields following proton flares. However, their conclusion was based on magnetic field calculations similar to ours and show no wider spread of the open field lines. Disruption of the field as a direct consequence of the explosive force of the flare can be expected in the largest flares (see Appendix). However, we conclude that whatever field disruption may occur is not sufficient to destroy the relationship between ambient field configuration and the escape of particles. Alternative (2) is specifically omitted from our current model. However, particles escaping by such an indirect route would be expected to have passed through many orders of magnitude more coronal plasma than the 10^{-6} to 10^{-5} g cm^{-2} encountered by particles released directly along open field lines. The recent observation of Krimigis (1969) and of Krimigis and Verzariu (1971) — that 10 MeV protons have encountered less than 2×10^{-5} g cm^{-3} by the time they reach 1 AU — suggests that such particles leave the sun more or less directly. Little can be said concerning alternative (3) except that, for particles accelerated in such shock waves as give rise to type II bursts, our injection surface may be both too small and incorrectly located. For alternative (4) to be important, a major fraction ($\sim 40°$) of the observed deviation must be considered as due to meandering of field lines in interplanetary space. Although a similar magnitude for the random walk of field lines has been obtained by Burlaga (1967), such large diffusion has been criticized (Axford, 1972) as being orders of magnitude too large to be consistent with the observed anisotropy of the particles and the presence of a core in the longitudinal spread of energetic electrons. We suggest that diffusion occurs over relatively small dimensions in the solar system consistent with the coefficient $K_1 \sim 10^{20}$ cm^{-2} s^{-1} suggested by simultaneous observation from separated spacecraft (O'Gallagher, 1970), but that large scale distortions of the interplanetary field produced by the interaction of fast and slow streams in the solar wind (Hundhausen, 1972; Gosling et al., 1972) account for the major portion of the longitudinal spread of particles from flares.

The Storage of Energetic Particles

Considerable evidence exists for the emission of energetic particles from some active regions for days (for protons of 30 to 100 Mev) or weeks (for protons < 10 Mev) following a major flare outburst (Fan et al., 1968; Lin, Kahler, and Roelof, 1968; Krimigis, 1969; Krimigis and Verzaiu, 1971). Of the two alternative mechanisms suggested to account for this phenomenon — continuous injection or storage — the latter encounters serious difficulty

466

since the lifetime of particles of energy < 10 MeV appears to be limited to less than a day by Coulomb collisions with the ambient coronal gas (Ahluwalia, 1972). Other investigators (McDonald and Desai, 1971; Simnett, 1971) maintain that if one chooses the highest, stable coronal arches as the reservoir, calculated storage times can be brought into close agreement with the observations. The present study approaches this question by examining the statistical properties of the lifetimes of particles trapped in the closed magnetic loops originating above the flares contained in our list (Table 1). Before examining the details of that analysis, we ask if our calculations present a true picture of the closed magnetic loops present in the corona. Specifically, do closed arches higher than the 2.5 $R_\odot$ limit of the model exist?

As seen in the corona at eclipse, closed, coronal arches extend out to a maximum of 2.2 $R_\odot$ from the center of the sun (Newkirk, 1967). Judging from the lifetimes of coronal streamers, with which arches always appear to be associated, of from one to several solar rotations, and from the small velocities (< 4 km/s) (Bugoslavskaya, 1949) present, such arches possess long term stability although they may be temporarily disrupted during the most violent flares. High, transient, coronal arches are seen at 3 to 6 $R_\odot$ (Brueckner, 1972) with space borne coronagraphs, and the existence of similar features is inferred from radio scattering data (Schatten, 1970). However, the lifetimes of such arches appear limited to a few hours or at most a day. U bursts at radio wavelengths, which are interpreted as plasma oscillations set up by a burst of energetic particles travelling along a closed arch, have a mean height of 1.6 $R_\odot$ (Takakura, 1966) although one such event is reported at 35 $R_\odot$ (Stone and Fainberg, 1971). However, there is no evidence that these higher U bursts take place in stable magnetic features. Stationary type IV bursts, attributed to the synchrotron or plasma emission of mildly relativistic cles trapped in stable magnetic arches and precipitating into the corona, last for hours or days (Wild, Smerd, and Weiss, 1963; Kundu, 1965; Wild and Smerd, 1972). Such bursts do not occur at distances above ~ 2.0 $R_\odot$. On the other hand, closed magnetic configurations containing mildly relativistic particles are expelled from the sun to great distances (Riddle, 1970; Dulk and Altschuler, 1971) in the form of moving type IV bursts. Such features travel outwards with speeds ~ 1000 km/s (Kundu, 1965) and last for at most a few hours and, thus, cannot be invoked as permanent reservoirs of trapped particles. Moving type IV bursts, which become stationary after an hour or so, can, perhaps, be interpreted as such clouds moving out into the highest, closed magnetic arches. However, even these events appear to stall at distances of ~ 2 $R_\odot$ (Krishnan and Mullaly, 1962; Weiss, 1963). Thus, the present evidence requires that stable, closed loops be limited to a maximum height of ~ 2.5 $R_\odot$. It is for this reason that we set our zero-potential sphere at that radius.

Of course, the open field lines shown in Figures 1 and 2 must ultimately close in interplanetary space (Gold, 1963); and we naturally ask if they close in a form which might trap particles in the outer corona. The geometry of field lines in the corona above ~ 2.5 $R_\odot$ is determined by the steady state interaction of the field and the solar wind and has been studied by Pneuman (1972) and Smith and Pneuman (1972). Their analysis demonstrates

that the field eventually closes in the form of a cusp containing a current sheet of extremely small thickness ($\sim$ 500 km at 2 to 3 $R_\odot$) with radii of curvature of the transverse field of the order of 1 km. Since energetic particles would be effectively scattered and probably conducted along such sheets (Fisk and Schatten, 1972), long term trapping would not occur. (A simple calculation shows that the scattering by such sheets is enhanced as one moves above the 2 to 3 $R_\odot$ considered by Smith and Pneuman.) Thus, we conclude that the magnetic configurations found above $\sim$ 2.5 $R_\odot$ are inimical to the long-term storage of energetic particles.

Returning to our model and consulting Tables 2 and 3, we find that although a large (60 to 80 percent) fraction of the initially injected particles are trapped in closed magnetic configurations, only a small (1 to 4 percent) fraction find themselves on magnetic loops which extend beyond 2 $R_\odot$. Thus, these tables tend to support the conclusion that long term storage near the sun does not occur. To place the statistics represented by these tables in more quantitative form, we consider each of the closed magnetic loops in which trapping may occur, and using a realistic electron density model (equation (6), Appendix), calculate the mean electron density $\overline{N_e}$ (equation (5) Appendix) which would be encountered. The probability that trapped particles from a given group of flares will encounter a mean density less than any particular value is then

$$P(<N_e) = \frac{\text{Number of trapping field lines in which } \overline{N_e} < N_e}{\text{Total number of trapping field lines}}$$

Graphs of $P(< N_e)$ for $R_{in} = 1.05$ $R_\odot$ and $R_{in} = 1.3$ $R_\odot$ for the proton and nonproton flares of our list appear in Figure 6. As expected, the probability that $\overline{N_e} < 10^8$ cm^{-3} is greater for $R_{in} = 1.3$ $R_\odot$ than for $R_{in} = 1.05$ $R_\odot$. Somewhat surprisingly, these probabilities seem rather insensitive to whether proton or nonproton flares are being considered. The quantity P ($< N_e$) may be related to the expected lifetime of injected particles by calculating the lifetime τ_c against Coulomb collisions in a completely ionized corona of electron density N_e (Equation (4), Appendix) provided the density is low enough that particles completely traverse the magnetic loop before losing a significant fraction of their energy. Lifetimes τ_c for particles with a variety of energies for $10^5 \leqslant Ne \leqslant 10^{10}$ cm^{-3} together with the equivalent position in the corona also appear in Figure 6. Comparison of the P ($< N_e$) and τ_c relations demonstrates that for $R_{in} = 1.3$ $R_\odot$ the probability that 3 MeV protons can endure longer than $\sim$ 2 $\times$ 10^4 s (8 hours) is less than 10 percent. Stated another way, less than 40 percent of the initially trapped 30 MeV particles will have lifetimes in excess of 3 days; less than 1 percent of the 10 MeV particles and $< <$ 1 percent of the 3 MeV particles will have such a lifetime. Thus, we must conclude that the long duration output of the sun for particles of energy $<$ 10 MeV cannot be the result of storage in closed magnetic arches in the corona and that some continuous replenishment of these particles must occur. This conclusion may be questioned on several grounds which should be examined. It might be argued that the magnetic arches included in our calculation are abnormally devoid of coronal gas, or that storage occurs only at the tops of the arches, or

that they are predominantly filled with energetic particles (Anderson, 1972; Lin, 1972). In all three cases, the rate of energy loss due to Coulomb collisions would have been overestimated in our calculations.
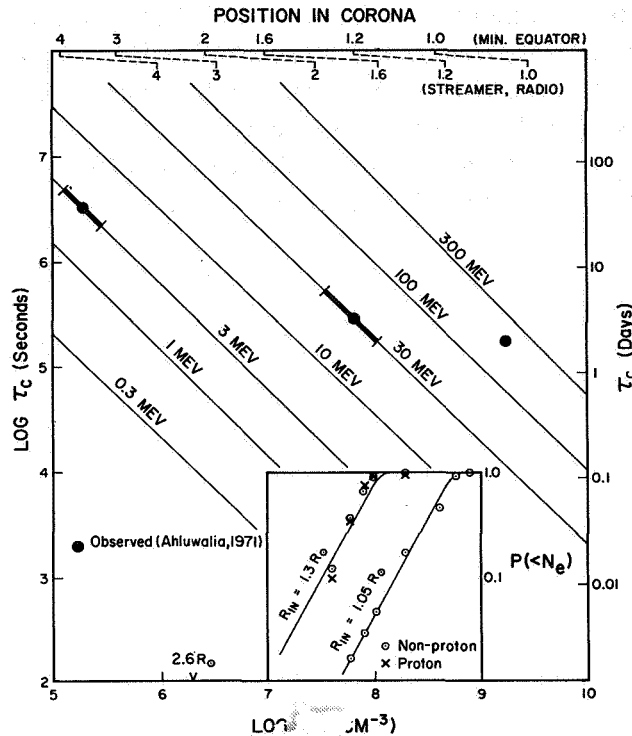

Figure 6. The lifetimes of protons of various energies moving in a completely ionized corona of density N_e together with the equivalent position in the corona for each density. The inset shows the probability that temporarily trapped particles will encounter an average density less than N_e.

Regarding long duration storage in vacant magnetic arches, the cosmic ray data themselves argue against this possibility independently of the collisional lifetime. In a typical long duration proton event at low energy, the number of stored particles which leak out over a period of days or weeks exceeds the number which arrive directly (2 to 4 hours for 3 MeV protons) by one to two orders of magnitude or more. Thus, we should require that the probability of immediate escape be < 1 percent rather than the 20 to 40 percent shown for proton flares in Tables 2 and 3. With respect to the argument that pitch angle diffusion rapidly raises the mirror points above the injection surface so that trapping occurs only at

the tops of the magnetic arches, we note that such a hypothesis would require the presence of a scattering mechanism 10^3 to 10^4 times more effective than Coulomb scattering to increase the mirror point motion to the required value. Although such scattering may occur, the lifetime of 3 MeV protons would still be only 2×10^4 to 2×10^5 seconds (Figure 6) rather than the 3×10^6 seconds observed. Moreover, such a mechanism could not increase the total ratio of stored to escaping particles above that indicated in Tables 2 and 3. The interesting suggestion of Anderson and Lin — that the flare elevates the entire plasma contained in the storage region to $\sim$ 30 KeV, so that collisional losses are orders of magnitude below those calculated for the ambient corona — must be examined in detail before its full application to the entire storage problem can be ascertained. Specifically, we might question whether the increased lifetime these authors find for 30 KeV protons has any influence on the storage of particles in the 1 to 10 MeV range. Although these questions still remain, present data support the conclusion that long term storage cannot explain the observations below 10 MeV.

ACKNOWLEDGMENTS

APPENDIX

Guiding Center Approximation

The guiding center approximation is valid only if both the radius of curvature of the field and the scale length (for example, the characteristic dimension of the field gradients) are large compared to the Larmor radius (14 km for 100 MeV protons in a 1 gauss field) and if the total energy density of the particles is well below that of the field. The dimensional requirements of the field are automatically satisfied by our model except for the neglect of scattering in current sheets. To estimate the energy restriction, let us consider a hemispherical bubble of radius r centered on the flare and containing energetic particles of total energy E. The condition for equivalence of particulate and magnetic energy density is then

$$B_{crit} = 3.46 \ E^{1/2} \ r^{-3/2} \tag{1}$$

Taking $E \sim 10^{30}$ erg for a class 2 flare (De Jager, 1972) and $r = 2.3 \times 10^{10}$ cm $= 0.33 \ R_{\odot}$, we find $B_{crit} \sim 0.3$ gauss, which is sufficiently below the $\sim$ 10 gauss (Newkirk, 1967) expected at this height above active regions. Thus, we may expect the guiding center approximation to be valid for all but the most violent flare events.

Injection Surface

Particles are introduced on the injection surface in the mirroring condition, and thus the proportion of particles which find themselves mirroring along some field line is overestimated, compared to a more realistic model in which particles are injected isotropically in a volume between R_{in} and $R_{in} + \Delta R$. The reflection coefficient for particles injected isotropically at a point where the field has a value B_1 is (Spitzer, 1956)

$$K = 1 - \frac{B_1}{B_m} \tag{2}$$

where B_m is the field at the mirror point. For $R_{in} = 1.3\ R_\odot$ and $\Delta R = 0.1\ R_\odot$, $B_1/B_m \sim$ 0.4 and $K \sim 0.6$. A thicker injection volume will, of course, produce a large reflection coefficient. Thus, our calculation may overestimate the proportion of isotropically injected particles which will initially mirror by perhaps a factor of two to five.

The dimensions of the injection surface, $36° \times 36°$, are considerably larger than the area covered by the Hα flare and the field annihilation volume envisioned by most flare theories. How can such a large surface be justified? First, the spatial resolution of our magnetic calculations is restricted by the total number of Legendre coefficients which may be conveniently handled to $\sim 6°$ in latitude and $\sim 20°$ in longitude. Thus, the location of the flare within the magnetic field is uncertain by a similar amount. Second, the actual source of energetic particles in the large scale magnetic field is very uncertain. Particles initially accelerated in a very small volume may experience considerable scattering in the immediate vicinity of the flare. Moreover, radio observations (Smerd, 1972) demonstrate that MHD shock waves, considered to be another source of energetic particles (Smith, 1971), frequently cover a large volume of the corona and appear far removed from the flare. If such shocks are the principal source of energetic particles in the corona, the dimensions of our injection surface may, in fact, be too small.

Coulomb Collisions

The lifetime of protons with energy less than 1 GeV trapped in the corona is largely influenced by Coulomb collisions with the ambient gas (Benz and Gold, 1971). Nonrelativistic protons in completely ionized hydrogen lose energy at a rate (Ginzburg and Syrovatskii, 1964)

$$- \frac{dE}{dt} = 7.62 \times 10^{-9}\ N_e \left(\frac{1.876 \times 10^3}{E} \right)^{1/2} \left\{ \ell n \left(\frac{E}{938.2} \right) \right.$$

$$\left. - \frac{1}{2}\ \ell n\ N_e + 38.7 \right\} (eV/s) \tag{3}$$

Thus, energetic particles may be characterized approximately by an e-folding lifetime

$$\tau_c = \frac{3.04 \times 10^{12} E^{3/2}}{N_e \left\{ \ell n \dfrac{E}{938.2} - \dfrac{1}{2} \ell n \, N_e + 38.7 \right\}} \tag{4}$$

where τ_c is in seconds, N_e in cm^{-3}, and E in MeV.

Since protons with energies above 0.3 MeV have a mean free path in the corona ($N_e \sim 10^8$ cm^{-3}) of ~ 1 $R_\odot$, a mean electron (or proton) density

$$\overline{N}_e = \frac{1}{L} \int_{\ell_{in}}^{\ell^\star} N_e(R) \frac{d\ell}{\sqrt{1 - \left| \dfrac{B}{B_i} \right|}} \tag{5}$$

is a suitable approximation for use in Equation (4) for the lifetime. Equation (5) considers that the actual distance traversed by a particle for a distance $d\ell$ along a field line depends upon the local value of the field B and the field at the injection surface B_i. Here ℓ_{in} and $\ell^\star$ are points along the field line at injection and at the conjugate mirror point and $L = |\ell^\star - \ell|$. Electron densities are given by

$$N_e = (4.20 \times 10^4) \, 10^{4.32/R} \, \text{cm}^{-3} \tag{6}$$

where R is in units of the solar radius $R_\odot$. Equation (6) (Newkirk, 1961) is for the undisturbed corona at sunspot maximum away from active regions or streamers, and represents a mean corona between the denser and more tenuous regions which a field line may penetrate.

Particle Drifts

Cross field drift of the guiding center occurs with a velocity (Welch and Wittaker, 1959)

$$W_{DR} = \frac{m_0 \, c \, w^2}{Z \, e \, B} \frac{1}{\mathcal{R}} \left(1 - \frac{1}{2} \frac{B}{B_i} \right) \, \text{cms}^{-1} \tag{7}$$

where m_0 is the rest mass of the particle, Z its charge, w its speed, $\mathcal{R}$ the radius of curvature of the field, and B the local field strength. Combination of (4) and (7) gives an approximate relation for the drift that particles of energy E will experience during their lifetime

$$W_{DR} \, \tau_c \sim 2.8 \times 10^{25} \frac{E^{5/2}}{B \, \mathcal{R} \, N_e} \left(1 - \frac{1}{2} \frac{B}{B_i} \right) \, \text{cm} \tag{8}$$

where the constant is chosen for E in MeV. Taking $\mathcal{R} = R_\odot$, $N_e = 10^{-7}$ cm^{-3}, B = 1 gauss, we find for 100 MeV protons,

$$W_{DR} \, \tau_c \sim 4 \times 10^{12} \text{ cm}$$

and for 10 MeV protons

$$W_{DR} \, \tau_c \sim 10^{10} \text{ cm}$$

We conclude that our model is valid for protons of energy $\stackrel{\sim}{<} 30$ MeV but is seriously compromised by the neglect of cross field drifts of trapped particles of larger energy.

Pitch Angle Diffusion

Pitch angle diffusion raises or lowers the mirror points of a particle as a result of Coulomb collisions or scattering from magnetic irregularities. The velocity of the mirror point caused by the accumulated effect of many small deflections by Coulomb collisions is

$$V_m = - \frac{K (1 - \beta^2)}{w^3} \frac{|B_i|}{\left(\dfrac{dB}{d\ell} \right)_i} \times$$

$$\int_{\ell_{in}}^{\ell^\star} N_e \left(\left| \frac{B_i}{B} \right| - 2 \right) \frac{d\ell}{\sqrt{1 - \left| \dfrac{B}{B_i} \right|}} \tag{9}$$

where $K \sim 9 \times 10^{12}$ for a completely ionized corona (Benz and Gold, 1971) and $\beta = w/c$. Clearly, the sign of the integral expresses the fact that a dominance of collisions near the injection surface will cause the mirror points to descend, while a dominance of collisions far from this surface will cause an opposite effect. Evaluation of (9) for some representative magnetic arches shows that the large-scale height of the corona generally induces upward motion of the mirror points. However, combination of (4) and (9) for the mirror point motion during the particle lifetime yields

$$\frac{V_m \, \tau_c}{1 - \beta^2} \sim 3.9 \times 10^{-4} \frac{1}{L \, \overline{N_e}} \frac{|B_i|}{\left(\dfrac{dB}{d\ell} \right)_i} \int_{\ell_i}^{\ell^\star} \left(\left| \frac{B_i}{B} \right| - 2 \right) \frac{N_e \, d\ell}{\sqrt{1 - \left| \dfrac{B}{B_i} \right|}} \tag{10}$$

which for a typical coronal arch and injection above the chromosphere amounts to only about 100 km. Since cross-field diffusion occurs at a similar rate, we conclude that both cross-field and pitch-angle diffusion from Coulomb collisions during a particle's lifetime in the corona may be safely ignored. In the case of diffusion produced by small scale magnetic irregularities, V_m may be increased by many orders of magnitude above the Coulomb case and a serious modification of the model is required.

REFERENCES

Anderson, K. A., 1972, Submitted to *Solar Phys.*

Ahluwalia, H. S., 1972, *Proc. 12th Int. Conf. on Cosmic Rays*, Hobart, Tasmania.

Altschuler, M. D., and Newkirk, G. Jr., 1969, *Solar Phys.* **9**, 131.

Aubier, M., and de la Noe, J., 1971, *Astron. Astrophys.* **12**, 491.

Axford, W. I., 1972, *Solar Terrestrial Physics*, Part II, E. R. Dyer, Ed., (Dordrect: D. Reidel Publ. Co.), 110.

Benz, A. O., and Gold, T., 1971, *Solar Phys.* **21**, 157.

Brueckner, G. E., 1972, *Proc. 15th Plenary Meeting of COSPAR*, Madrid (submitted for publication).

Bugoslavskoya, E. Y., 1949, *Publ. Sternberg Inst.* **19**.

Burlaga, L. F., 1967, *J. G. R.* **72**, 4449.

Cohen, M. H., and Gunderman, E. J., 1969, *Ap. J.* **155**, 645.

De Jager, C., 1972, *Solar Terr. Phys./1970*, E. R. Dyer, ed., 1.

Dulk, G. A., 1971, *Austral. J. Phys.* **24**, 217.

Dulk, G. A., and Altschuler, M. D., 1971, *Solar Phys.* **20**, 438.

Dunn, R. B., 1971, *Physics of the Solar Corona*, Macris, C. J., ed., (Springer-Verlag).

Fainberg, J. and Stone, R. G., 1970, *Solar Phys.* **13**, 433.

Fan, C. Y., Pick, M., Pyle, R., Simpson, J. A., and Smith, D. R., 1968, *J. G. R.* **73**, 1555.

Fisk, L. A., and Schatten, K. H., 1972, *Solar Phys.* 23, 204.

Ginzburg, V. L., and Syrovatskii, S. I., 1964, *The Origin of Cosmic Rays*, McMillan Book Co., New York.

Gold, T., 1963, *Pontif. Acad. Sci. Scripta Varia* 25, 431.

Gosling, J. T., Hundhausen, A. J., Pizzo, V., and Asbridge, J. R., 1972, *J. G. R.* 77, 5442.

Hewish, A., 1971, *Ap. J.* 163, 645.

Hewish, A., and Symonds, M. D., 1969, *Planet. Space Sci.* 17, 313.

Hundhausen, A. J., 1972, submitted to *J. G. R.*

Jefferies, J. T., Orrall, F. Q., and Zirker, J. B., 1972, *Solar Phys.* 22, 327.

Jokipii, J. R., and Hollweg, J. V., 1970, *Ap. J.* 160, 745.

Koutchmy, S., and Laffineur, M., 1970, *Nature* 226, 1141.

Krimigis, S. M., 1969, *Proc. 11th Int. Conf. Cosmic Rays*, Budapest 2, 125.

Krimigis, S. M., and Verzariu, P., 1971, *J. G. R.* 76, 792.

Krishnan, T., and Mullaly, R. F., 1962, *Austral. J. Phys.* 15, 87.

Kundu, M. R., 1965, *Solar Radio Astronomy*, Interscience Publishers.

Lantos-Jarry, M. F., 1970, *Solar Phys.* 15, 40.

Leroy, J. L., Rosch, J., and Trellis, M., 1968, *Proc. IAU Symp.* 35, K. O. Kiepenheuer, ed., 346.

Levy, G. S., Saito, T., Seidel, B. L., Stelzried, C. T., Ohlson, J. E., and Rush, W. V. T., 1969, *Science*, 166, 596.

Lin, R. P., 1970a, *J. G. R.* 75, 2583.

Lin, R. P., 1970b, *Solar Phys.* 12, 266.

Lin, R. P., 1970c, *Solar Phys.* 15, 453.

Lin, R. P., Kahler, S. W., and Roelof, E. C., 1968, *Solar Phys.* 4, 338.

Lin, R. P., 1972, *Proc. Solar Terrestrial Relations Conf.* Calgary (in press).

Lovelace, R. V. E., Salpeter, E. E., and Sharp, L. E., 1970, *Ap. J.* **159**, 1047.

McCracken, K. G., and Rao, U. R., 1970, *Space Sci. Rev.* **11**, 155.

McDonald, F. B., and Desai, U. D., J., 1971, *J. G. R.* **76**, 808.

Newkirk, G. Jr., 1961, *Ap. J.* **133**, 983.

Newkirk, G. Jr., 1967, *Ann. Rev. Astron. Astrophy.* **5**, 213.

Newkirk, G. Jr., Altschuler, M. D., and Harvey, J. W., 1968, *Proc. IAU Symp.* **35**, 379.

Newkirk, G. Jr., and Harvey, J., 1968, *Solar Phys.* **3**, 321.

Newkirk, G. Jr., and Lacey, L., 1970, *Nature* **226**, 1096.

O'Gallagher, J. J., 1970, *J. G. R.* **75**, 1163.

Pneuman, G. W., 1972, *Solar Phys.* **23**, 223.

Reid, G. C., 1964, *J. G. R.* **69**, 2659.

Riddle, A. C., 1970, *Solar Phys.* **13**, 448.

Schatten, K. H., 1971, *Cosmic Electrodynamics* **2**, 232.

Schatten, K. H., 1970, *Solar Phys.* **12**, 484.

Schatten, K. H., Wilcox, J. M., and Ness, N. S., 1969, *Solar Phys.* **6**, 422.

Schmidt, H. U., 1964, *NASA Symp. Physics of Solar Flares*, SP-50, 107.

Simnett, G. M., 1971, *Solar Phys.* **20**, 448.

Smerd, S. F., 1973, These Proceedings.

Smerd, S. F., and Dulk, G. A., 1971, *Proc. IAU Symp.* **43**, Paris.

Smith, D. F., 1971, *Ap. J.* **170**, 559.

Smith, D. F., 1973, *Proc. Conf. Flare Produced Shock Waves in the Corona and Interplanetary Space*, National Center for Atmos. Res., Boulder, in press.

Smith, D. F., and Pneuman, G. W., 1972, *Solar Phys.* 25, 461.

Spitzer, L. Jr., 1956, *Physics of Fully Ionized Gases*, Interscience Publishers, New York.

Stainberg, J. L., Aubier-Gieraud, M., Leblanc, Y., and Boischot, A., 1971, *Astron. Astrophys.* 10, 362.

Stone, R. G., and Fainberg, J., 1971, *Solar Phys.* 20, 106.

Takakura, T., 1966, *Space Sci. Rev.* 5, 80.

Trotter, D. E., and Newkirk, G. Jr., 1971, *Solar Phys.* 20, 372.

Valdez, J., and Altschuler, M. D., 1970, *Solar Phys.* 15, 446.

Wagner, W. J., 1973, *Proc. Conf. Flare Produced Shock Waves in Corona and Solar Wind*, National Center for Atmos. Res., Boulder, in press.

Wang, J. R., 1972, NASA/GSFC, X-661-72-76.

Warwick, J. W., and Dulk, G. A., 1969. *Ap* ˙ ˙58, 123.

Webber, W. R., 1964, *Proc. AAS-NASA Symp. Solar Flares*, W. N. Ness, ed., p. 215.

Weiss, A. A., 1963, *Austral. J. Phys.* 16, 526.

Welch, J. A. Jr., and Whitaker, W. A., 1959, *J. G. R.* 64, 909.

Wild, J. P., and Smerd, S. F., 1972, *Ann. Rev. Astron. Astrophys.* 10, 159.

Wild, J. P., Smerd, S. F., and Weiss, A. A., 1963, *Ann. Review Astron. Astrophys.* 1, 291.

A LOWER LIMIT TO THE ALTITUDE OF CORONAL PARTICLE STORAGE REGIONS DEDUCED FROM SOLAR PROTON ENERGY SPECTRA

S.M. Krimigis
The Johns Hopkins University
Applied Physics Laboratory

ABSTRACT

The spectrum of low energy protons observed at 1 AU following solar flares shows little or no evidence of energy degradation down to ~ 0.3 MeV. Such observations may be used to set a lower limit on the altitude of hypothetical coronal particle storage regions, ranging from 2 to 7 R_s (Krimigis and Verzariu, 1971; Verzariu and Krimigis, 1972). It is pointed out that closed coronal magnetic loop structures are observed to extend to < 2 R_s, so that long-term (> 1 day) storage of low energy protons does not take place in the immediate vicinity of the sun. It is further suggested that in the few cases where the proton spectrum appears to be degraded at low energies, the energy loss may be due to adiabatic deceleration in the expanding solar wind (Parker, 1965). The alternative of continual acceleration is suggested as a plausible substitute for the particle storage hypothesis.

INTRODUCTION

The question of particle storage in the solar corona versus long-term (a few days) acceleration following a solar flare is a relatively old one. It was debated during the last Goddard Symposium on Solar Flares in 1963, with the apparent consensus that long-term (several days) trapping of solar protons does take place, particularly in coronal active regions corotating with the sun (for example, Bryant et al., 1963; Warwick, 1963). It was also assumed, at that time, that electrons must clearly be trapped in the vicinity of the sun, since solar electrons had not as yet been observed at 1 AU. Since these early deductions with regard to particle storage at the sun, there has been a large increase in the amount and quality of data which makes possible a much improved analysis of the observations.

The main observational evidence which is presently thought to favor a storage region close to the sun lies principally in two areas: a) The unusually long duration (a few days) of low energy (E $\leqslant$ a few MeV) solar particle events; and b) the longitudinal range over which solar particles seem to be present as measured at the orbit of earth and beyond. Apparent delays in the propagation of electrons have also been interpreted as indicating long-term storage (Simnett and Holt, 1971).

478

An obvious observational test of the storage hypothesis is to examine the solar particle energy spectrum for possible degradation due to ionization energy loss in the presumed storage region. That is, Δt seconds after acceleration and trapping, some particles will have traversed sufficient material to have their energies substantially degraded or to have been completely stopped. It follows that if the source energy spectrum following acceleration is of the form $dj/dE = KE^{-\gamma}$ where j is the directional intensity, E the particle kinetic energy and K, γ are constants, particles at low energies will be eventually removed and a seriously degraded or even peaked spectrum will result at the low energy end. In applying such an observational test, care must be exercised in identifying propagation effects such as those due to velocity dispersion or adiabatic energy losses.

Some tests of the storage hypothesis using the energy loss criterion were applied by Lin et al. (1968) and McDonald and Desai (1971), but at relatively high energies ($\sim$ 3 MeV) where the particle lifetimes are relatively long ($\gtrsim$ 4 days) even at low coronal altitudes (2.4 R_s). McDonald and Desai (1971, p. 826) concluded that " . . . storage of energetic particles is a characteristic feature of many solar centers of activity." It is evident that in deciding in favor of or against the storage hypothesis, the particle energy at which the observations are obtained is the most important parameter. For example, if the McDonald and Desai (1971) observations had extended down to $\sim$ 0.3 MeV and no degradation in the energy spectrum had been found, their conclusion would probably have been quite different.

Observations of proton energy spectra down to $\sim$ 0.3 MeV have recently been published by Krimigis and Verzariu (1971) and Verzariu and Krimigis (1972). The authors found that in several events during 1969, proton energy spectra did not exhibit significant degradation down to energies of $\sim$ 0.3 MeV. They suggest that if storage of energetic protons is postulated to exist, the storage region ⋅ ⋅ ⋅ ⋅ d have to be located at altitudes $\gtrsim$ 3 to 7 R_s, where stable closed magnetic field structures have not been observed directly as yet. Further Verzariu and Krimigis (1972) point out that adiabatic energy losses could degrade a power law spectrum in a manner similar to that due to ionization energy loss in a coronal storage region. In the remainder of this paper, the results at these low energies are reviewed and the implications are discussed in the context of recent work on solar particle acceleration, confinement, and propagation.

OBSERVATIONS AND INTERPRETATIONS

Figure 1 gives the time history of $0.32 \leqslant E_p \leqslant 6.3$ MeV protons for the event of January 24, 1969 as observed by Explorer-35 in the interplanetary medium. The particles most probably originated in the flare indicated on the figure and were detected at Explorer-35 $\sim$ 1.5 hours after the flare, with maximum intensity occurring at $\sim$ 2000 UT on the same day. The arrows on the solid curve in Figure 2 show those times for which energy spectra were obtained over the earth's polar caps with the Injun-5 spacecraft.

A detailed history of the energy spectrum is given by Krimigis and Verzariu (1971). Figure 2 shows two of these spectra late in the event, for which the degradation in the spectrum due
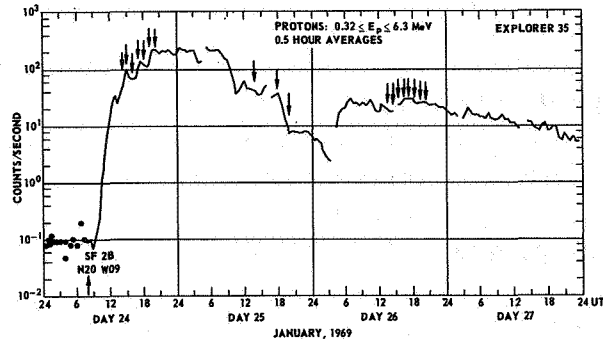
Figure 1. The intensity versus time profile of $0.3 \leqslant E_p \leqslant 6.3$ MeV protons as seen on Explorer-35 outside the magnetosphere. Arrows indicate times for which Injun-5 data are available over the earth's polar caps (Krimigis and Verzariu, 1971).
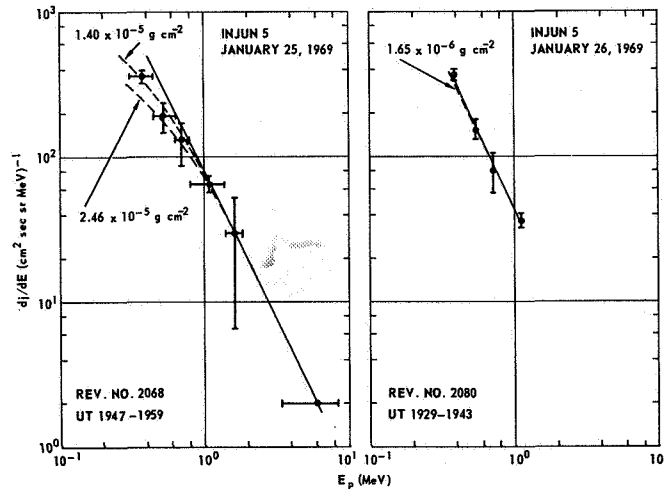

Figure 2. The calculated energy degradation of the adopted spectrum whose slope coincides with the observed one at high energies $(E_p \geqslant 1.1$ MeV) is shown. The calculations have been carried out for thicknesses of 1.65, 14.0, and 24.6 micrograms cm^{-2} of fully ionized hydrogen. One observes that best fit to the observations is obtained for 14×10^{-6} g cm^{-2} for January 25 and 1.65×10^{-6} g cm^{-2} for January 26, 1969 (Krimigis and Verzariu, 1971).

480

to ionization energy loss in a fully ionized hydrogen plasma has been calculated. It is seen that for the spectrum on January 25, the best fit to the observations is obtained for a thickness of (traversed) material equivalent to $14 \, \mu g \, cm^{-2}$. This thickness corresponds to the range of a 0.3 MeV proton. For the spectrum on January 26 the equivalent thickness is $\sim 1.6 \, \mu g \, cm^{-2}$, corresponding to the range of a 0.1 MeV proton.

Density of Storage Region

Using this information, it is now possible to calculate the density in the postulated storage region. The expression for energy loss in fully ionized hydrogen plasma is

$$- \frac{dE}{dx} = \frac{4\pi n_0 Z_1^2 e^4}{mv^2} \ln \frac{2mv^2}{\hbar \omega_0} \tag{1}$$

where E is the particle kinetic energy; x is the particle path length; n_0 is the density of local atoms; e, m, are electronic charge and mass, respectively; $Z_1 e$ is the charge of the incident particle; v is the particle velocity; and ω_0 is the local plasma frequency. By substituting $dx = vdt$ and $de = Mv \, dv$ where M is the proton mass, we have that

$$- M \frac{dv}{dt} = \frac{4\pi n_0 e^4}{mv^2} \ln \frac{2mv^2}{\hbar \omega_0} \tag{2}$$

By integrating (2) as the proton velocity changes from v_0 to 0, we have

$$n_0 \Delta t = \frac{v_0^3 m M}{240 \pi e^4} \tag{3}$$

where v_0 is the velocity of 0.3 MeV protons or 0.1 MeV protons, corresponding to the spectra of January 25 and 26, respectively. The equivalent values of $n_0 \Delta t$ are

$$n_0 \Delta t = 1.65 \times 10^{10} \, s \, cm^{-3} \quad \text{January 25} \tag{4}$$

$$n_0 \Delta t = 4.5 \times 10^9 \, s \, cm^{-3} \quad \text{January 26} \tag{5}$$

The resulting densities in the presumed storage region derived from (4) and (5) range from $4 \times 10^5 \, cm^{-3}$ to $3 \times 10^4 \, cm^{-3}$ for confinement times of 4×10^4 sec (Δt between flare and maximum intensity) and 1.6×10^5 s (Δt up to January 26), respectively. These densities correspond to altitudes of 3 to 6 solar radii ($1 \, R_s = 7 \times 10^5$ km).

The relative lack of degradation of the proton energy spectrum during the January 24, 1969 event appears as a feature in many other events as well. Several particle events during 1969 and 1970 have been examined by Verzariu and Krimigis (1972), and in most cases the proton spectrum is monotonically decreasing with energy and shows little or no evidence of energy degradation. There exist, however, cases where significant departures from a power law in energy are present in the proton spectrum, which cannot be attributed readily to other effects (for example, velocity dispersion). One such case of degraded spectra was obtained during the April 26-28, 1968 event (Simnett, 1972). Another case was observed during the March 6, 1970 event, where the spectrum remained degraded some two days after the intensity onset (Verzariu and Krimigis, 1972). It may be significant to note that for both of these events there were no optical flares on the visible hemisphere of the sun and the origin of the particle increase was attributed to flares beyond the west limb.

Figure 3 shows the energy spectrum observed during the March 1970 event. In Figure 3(b), the degraded spectra resulting from passage through 24.6 and 54.3 micrograms cm^{-2} are shown, together with the observed data points and the extrapolated power law. Neither of the two spectra shown fit the data well, so that an intermediate value corresponding to the range of ~ 0.4 MeV protons is taken as the best fit. Using Equation (3) it is found that the deduced coronal densities correspond to altitudes of ~ 2 to 3 R_s.

Continuous Acceleration and Emission

It is possible, however, that the observed departure of the proton spectrum from a power law at low energies may not be due to ionization losses in a storage region, but rather to adiabatic energy loss in the interplanetary medium. Parker (1965) has calculated the energy loss of energetic particles released continuously from a source at a rate N/s and cooled adiabatically in a uniform radial solar wind of speed w. The energy loss at a given radial distance r is inversely proportional to the magnitude of the diffusion coefficient κ, as shown in Figure 3(c), where n is a relativistic correction factor and equals 2 for nonrelativistic particles. If one assumes that at 1 AU $\kappa = \kappa_o$ v, we find that

$$8nwr/3\kappa = C(E)^{-\frac{1}{2}}$$

where C is a constant and E is the energy of the particle at 1 AU (Verzariu and Krimigis, 1972). By choosing the value of C appropriately, the degraded spectrum can be transformed into a source spectrum which fits a power law down to the lowest observable energies, as shown in panel 3d. This value of C results in a diffusion coefficient for 10 MeV protons (w = 350 km/s) of 1.9×10^{20} cm^2 s^{-1}, which is in reasonable agreement with the prediction of Jokippii and Coleman (1968). Thus, the reasonable value of the diffusion coefficient supports the essential correctness of this calculation.
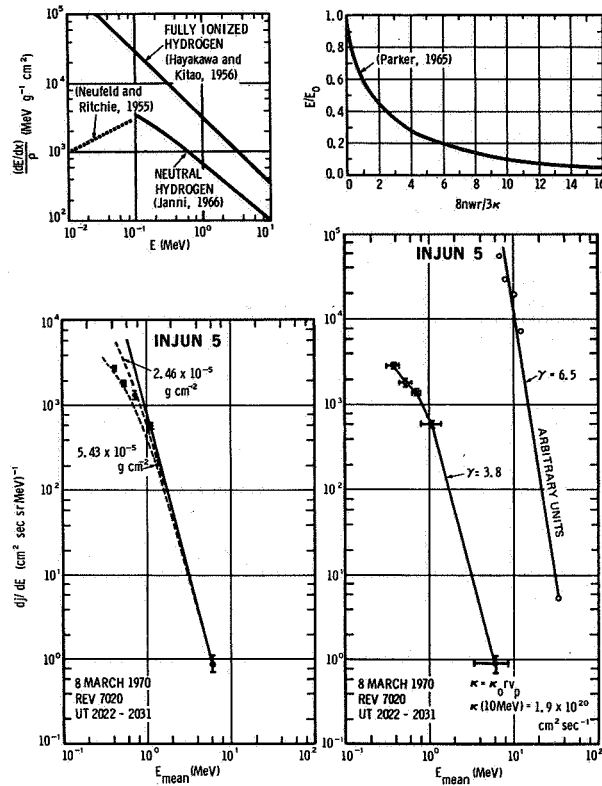
482

Figure 3. The calculated energy degradation of the spectrum measured on March 8, 1970, where the observed distortion is assumed to be due either to ionization losses in a presumed storage region in the vicinity of the sun or to adiabatic deceleration in the solar wind of energetic particles which are continuously accelerated and released at the site of an active region. For both cases the source spectrum is assumed to fit a power law ($\sim E^{-\gamma}$). The rate of energy loss in fully ionized and neutral hydrogen (Krimigis and Verzariu, 1971) and the energy loss curve in a uniform radial solar wind having velocity w (Parker, 1965) are shown at the top (Verzariu and Krimigis, 1972).

DISCUSSION AND CONCLUSIONS

It is evident from the data discussed in the preceding sections that degradation of solar flare proton spectra at energies down to ~ 0.3 MeV is a relatively infrequent phenomenon. When some energy loss can be shown to have occurred, and if it is assumed that it is due to ionization energy loss in a presumed storage region, it is found that the altitude of such a region is $\geqslant 3$ to 6 R_s. These altitudes were derived by using the quiet-sun electron density radial profiles. Since densities over solar active regions are typically greater by a factor of 10

483

than the surrounding coronal plasma, the altitude at a given density (that is 3×10^4 cm^{-3}) can easily exceed 10 R$_s$. In addition, if we assume that flare protons are restricted to mirror-type magnetic field configurations, they will lose most of their energy by ionization in the vicinity of the mirror point, where they interact with the denser ambient plasma. Thus, the altitudes of the storage region derived in the preceding section should be taken as *lower limits*, since most of the effective trapping volume lies above the computed altitudes.

A review of observational evidence on long-lived closed magnetic loop structures over solar active regions reveals that such loops never appear at heights $\gtrsim 2$ R$_s$ above the solar surface (a detailed discussion is given by Verzariu and Krimigis, 1972). Since it is generally assumed that such closed structures are necessary for long-term particle confinement, and since the data demonstrate that a lower limit to the altitude of the storage region is $\gtrsim 3$ to 10 R$_s$, one must conclude that effective trapping of low energy protons *does not take place* in the immediate vicinity of the sun.

Recently Simnett (1971) has proposed that low rigidity ($\leqslant 50$ Mv) particles are stored at altitudes of 3-5 R$_s$ following acceleration. Most of the evidence cited by Simnett is based on the morphology of $0.3 - 0.9$ MeV electrons whose rigidities are ~ 0.7 Mv, although the model is extended to cover protons up to ~ 1.4 MeV (~ 50 Mv). It has been demonstrated in the preceding sections that protons down to 0.3 MeV are observed at 1 AU and that the energy spectrum is rarely degraded at these energies, so that Simnett's model is clearly in conflict with observations on this point. Trapping of electrons may still be possible, since their rigidities are a factor of ~ 40 less than protons in this energy range, although alternative explanations to the evidence cited by Simnett are more plausible (that is Warwick, 1973).

The ultimate tests for any storage mechanism have to be the evaluation of effects which are known to exist in particle trapping configurations. These include the effects of particle drifts, pitch angle scattering, plasma instabilities, cross-field diffusion, and so forth. Even if these effects are not considered, quantitative evaluation of particle trajectories show that trapping lifetimes in typical solar magnetic field loop structures are generally limited to < 1 day (Newkirk, 1973). Thus the hypothesis of coronal storage of energetic particles meets with severe observational and theoretical difficulties, although it must be continuously re-examined as our observational and theoretical understanding of solar particle phenomena continues to improve.

It was demonstrated in the preceding section that adiabatic energy loss of particles emitted continuously at the sun could explain the observations in the few instances when the proton energy spectrum appears degraded at low energies. Abundant evidence for long-term acceleration has been recently demonstrated to exist for several types of solar particle events (Roelof and Krimigis, 1973). In addition McDonald (1973) has shown data which support the view that continual acceleration does indeed take place, with maximum proton energies in excess of 20 MeV. Thus the hypothesis of continual acceleration appears to be an excellent substitute to that of particle storage, and merits our most careful attention in the future.

484

REFERENCES

Bryant, D.A., Cline, T.L., Desai, U.D., and McDonald, F.B., 1963, *AAS-NASA Symposium on Solar Flares*, NASA SP-50, 289.

Jokipii, J.R., and Coleman, P.J., 1968, *J.G.R.* 73, 5495.

Krimigis, S.M., and Verzariu, P., 1971, *J.G.R.* 76, 792.

Lin, R.P., Kahler, S.W., and Roelof, R.C., 1968, *Solar Phys.* 4, 338.

McDonald, F.B., 1973, These Proceedings.

McDonald, F.B., and Desai, U.D., 1971, *J.G.R.* 76, 808.

Newkirk, G.A., 1973, These Proceedings.

Parker, E.N., 1965, *Planet. Space Sci.* 13, 7.

Roelof, E.C., and Krimigis, S.M., 1973, *J.G.R.* 78.

Simnett, G.M., 1971, *Solar Phys.* 20, 448.

Simnett, G.M., 1972, *Solar Phys.* 22, 189.

Simnett, G.M., and Holt, S.S., 1971, *Solar Phys.* 16, 208.

Verzariu, P., and Krimigis, S.M., 1972, *J.G.R.* 77, 3985.

Warwick, J.W., 1973, These Proceedings.

Warwick, J.W., 1963, *AAS-NASA Symposium on Solar Flares*, NASA SP-50, 441.

CORONAL PROPAGATION OF ENERGETIC CHARGED PARTICLES

E.C. Roelof

Department of Physics
University of New Hampshire

ABSTRACT

A technique for estimating the equatorial connection longitude of interplanetary field lines to the corona is applied to quasi-stationary low-energy solar charged particle (LESP) events to reconstruct their coronal injection profile. Comparison with synoptic charts constructed from Hα chromospheric absorption features for solar rotation 1524 reveals that the inferred chromospheric equatorial magnetic neutral line structure strikingly orders the LESP coronal injection profiles of $\geqslant 0.3$ MeV protons for this period (August 1967), allowing the identification of acceleration processes lasting several days and well-defined coronal transport over $\geqslant 100°$. It is also proposed that LESP observations offer a unique tool for studying the magnetic structure of the transition region from the low corona to interplanetary space.

INTRODUCTION

My colleagues and I believe we now have at hand the techniques necessary to study directly the acceleration histories of low energy solar charged particles (LESP) and the structure of the magnetic fields that determine their propagation in the solar corona. The techniques are based on four points, justifiable both observationally and theoretically:

1) LESP undergo negligible diffusion across field lines in interplanetary space and hence their coronal injection longitude is essentially that of the field line;

2) Although interplanetary field lines are locally distorted by dynamical processes during transport by the solar wind between the sun and 1 AU, their large-scale ($\gtrsim 0.1$ AU) structure is essentially that of the bulk motion of the solar wind;

3) Solar wind plasma observed in the ecliptic originates near the equator and the source longitude for slowly evolving streams may be estimated with $\sim 10°$ accuracy;

4) Absorption features observable in Hα solar photographs delineate neutral lines that are boundaries (the more strongly marked extending into the corona) of large-scale polarity cells in the chromospheric magnetic field (McIntosh, 1972).

Point 1 implies that the bulk velocity of LESP *perpendicular* to field lines must equal the velocity at which the field line is convected by the solar wind, although the motion of LESP *parallel* to the lines is determined independently by their scattering along the line (a transport process we have called "collimated convection"). Therefore the longitude at which LESP are injected into the interplanetary medium must be the same as the origin of the field line on which they are observed. Point 2 relates the source longitude of the field to that of the plasma convecting the field, and Point 3 (to be discussed in more detail below) implies that knowing the coronal source longitude and longitude of the plasma, we may "map" the LESP event histories back to their equatorial injection profile in the corona. If coronal magnetic structure inferred from solar observations then orders the inferred LESP injection profiles, we have a self-consistent justification of the techniques. Point 4 offers the possibility of comparing low coronal magnetic structure with LESP injection profiles, and I shall demonstrate in this paper that well-defined chromospheric equatorial neutral-line structure did indeed order LESP data during the summer of 1967. However, when Hα equatorial structure is weak (as during solar minimum), the neutral-line structure may not correspond to LESP data or interplanetary magnetic field sector boundaries, since it is then less likely that such weak structure will delineate the equatorial coronal field.

Detailed evidence for Point 1 from multiple spacecraft observations was first offered by Lin et al. (1968) and further observations are summarized by McCracken and Rao (1970). Kavanagh et al. (1970) emphasized that the small-scale structure ($\lesssim 10°$ in azimuth) in LESP events also verifies Point 2, as did Krimigis et al. (1971) who showed that such small-scale magnetic structure is preserved in 0.5 MeV quasi-stationary field-aligned proton events over 0.3 AU. Regarding Point 3, theoretical arguments such as those of Siscoe and Finley (1969, 1970) support the contention that the solar wind observed in the ecliptic originates within 10° latitude of the solar equator.

Our estimate of solar wind source longitude is obtained by the method originally proposed by Snyder and Neugebauer (1966). The difference between the connection longitude and the satellite longitude $\Delta\phi$ is approximated by taking the product of the sun's sidereal angular velocity Ω and r/V, the approximate "transit time" of solar wind with observed velocity V at a distance r from the sun. Nolte and Roelof (1972) justify this approximation (which they call the "extended quasi-radial hypervelocity," or EQRH approximation) for the source longitude by comparison with recent theoretical calculations of Goldstein (1971), Sakurai (1971) and Matsuda and Sakurai (1972). In this approximation, $\Delta\phi$ is the same as if the field lines were constructed by instantaneous ideal Archimedean constant-velocity spirals. However, Nolte and Roelof (1972) emphasize that the applicability of the EQRH approximation for $\Delta\phi$ does not imply that interplanetary field lines are ideal spirals. Quite to the contrary, they show that the approximation for $\Delta\phi$ is adequate only because the two main effects that cause the actual solar plasma trajectories to deviate from an ideal constant-velocity spiral tend to cancel: (1) the acceleration of the solar wind *increases* $\Delta\phi$ from the EQRH approximation, while (2) the corotation of the solar plasma inside the MHD critical points tends to *decrease* $\Delta\phi$.

487

Direct observational evidence in support of Point 3 is found in the identification by Krieger, et al. (1972) of a source of a particular recurrent solar wind stream on a 3-35 Å and 44-51 Å X-ray photograph taken by an American Science and Engineering rocket flight November 24, 1970 (Figure 1). The EQRH mapping of the solar wind data from two spacecraft ~ 50° apart located the stream source with an accuracy of < 10° as the equatorial portion of a low density, magnetically open coronal "hole" (Figure 2). Roelof and McIntosh (1972) have reported more evidence for Points 2 and 3 in the form of an improved correlation of interplanetary and chromospheric polarities (deduced from the technique of Point 4) using the EQRH extrapolation (Figure 3). The correlation during July to September 1967 peaks strongly within 10° of the equator, and equator-crossing neutral lines well marked by Hα filaments agree with the origin of interplanetary sector boundaries within 10°. However, such a strong correlation is not expected when Hα features are weak in the solar equatorial regions (as during solar minimum).

Further establishment of all four points taken together comes directly from the association of long-lived, field-aligned LESP event time histories with equatorial coronal structure inferred from Hα polarity synoptic charts using the EQRH approximation to obtain the coronal connection longitude for the interplanetary magnetic field. And that is the subject of this paper.

CHARACTERISTICS OF LESP EVENTS

Our earliest information on the acceleration and coronal transport of solar charged particles was derived from the temporal behavior of near-relativistic solar flare protons. More recently, the intimate relationship among solar radio and X-ray bursts and near-relativistic electrons have been exploited to construct models of densities and magnetic fields in the regions where electron acceleration occurs. Then, beginning with the observations of solar protons with energies below 1 MeV that exhibited 27-day recurrence patterns (Bryant, et al. 1965a; Fan, et al. 1966), there has been a growing realization that these particles may not be associated with occasional large solar flares, but rather with the general dynamics of solar active regions (Fan, et al. 1968; Krimigis, 1969; McCracken and Rao, 1970; McDonald and Desai, 1971; Pick, 1972). Moreover, a number of workers have emphasized the existence at these energies of "delayed" events (Lin, et al. 1968; Anderson, 1969; Lanzerotti, 1969; McCracken and Rao, 1970) which are intermediate between a flare event (appearing several days later) and recurrent events. It has also been argued that post-flare "energetic storm particle" events (Bryant, et al. 1962, 1965b; Rao, et al. 1967) may also be an intermediate class of events, depending (as do the delayed events) on the relative longitude of the observer and the flare active region (Kahler, 1969; McCracken and Rao, 1970).

The immediate implication of the first three points listed in the Introduction is that these long-lived LESP events provide an indication of the *injection profile* of the particles into the interplanetary medium (as a function of longitude) from the equatorial corona. The striking variations of the event time histories is then seen not to be "noise" due to (unspecified) "random" processes, but actually to be a deterministic signal, each significant variation reflecting a definite coronal magnetic structure.

488
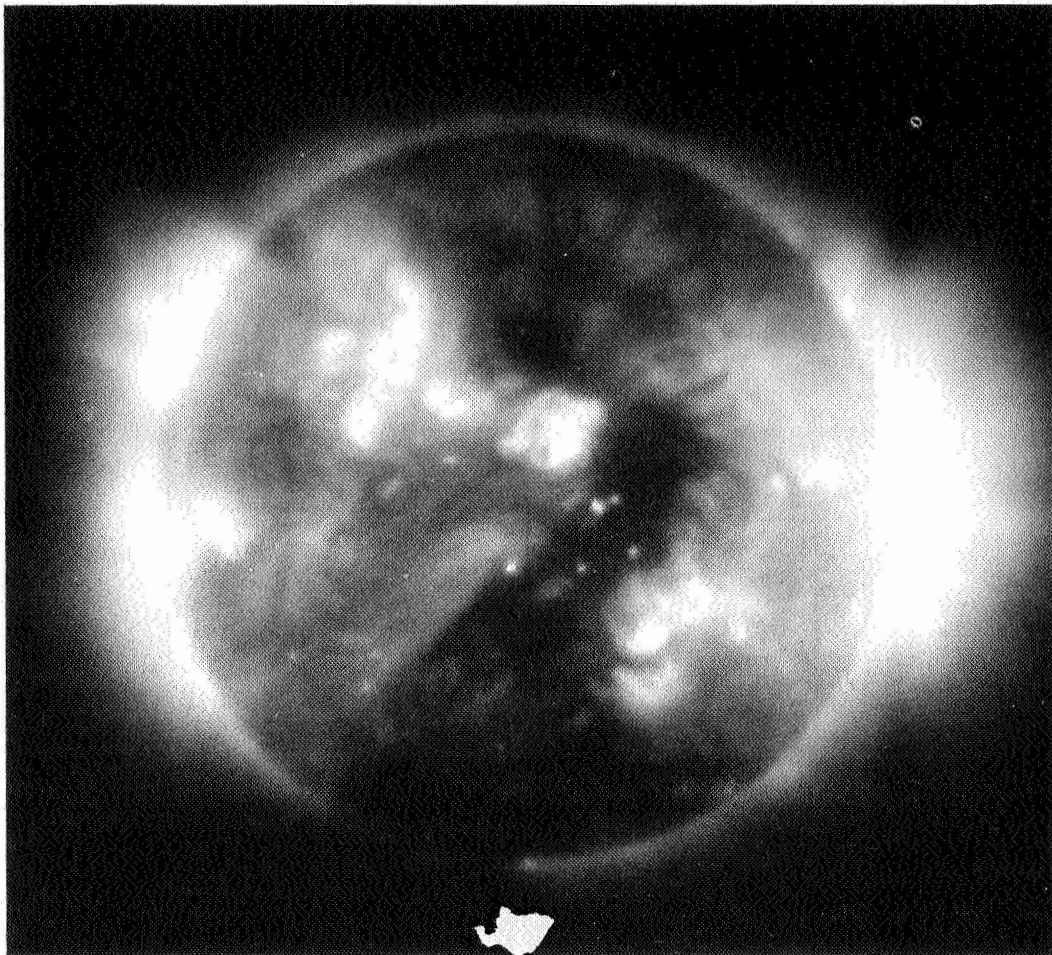
24 NOVEMBER 1970
2047 UT
EXPOSURE: 9.5 SEC
NOMINAL PASSBAND (1% TRANSMISSION):
3-35,44-51Å

Figure 1. A photograph of the sun in 3-35Å and 44-51Å wave bands obtained on November 24, 1970 (258° CMP). East is toward the left, heliographic North is 3.4° CW on the top of the page. The coronal "hole" extends from 280° near the equator southeastward to the southern limb. From Krieger, et al. (1972).
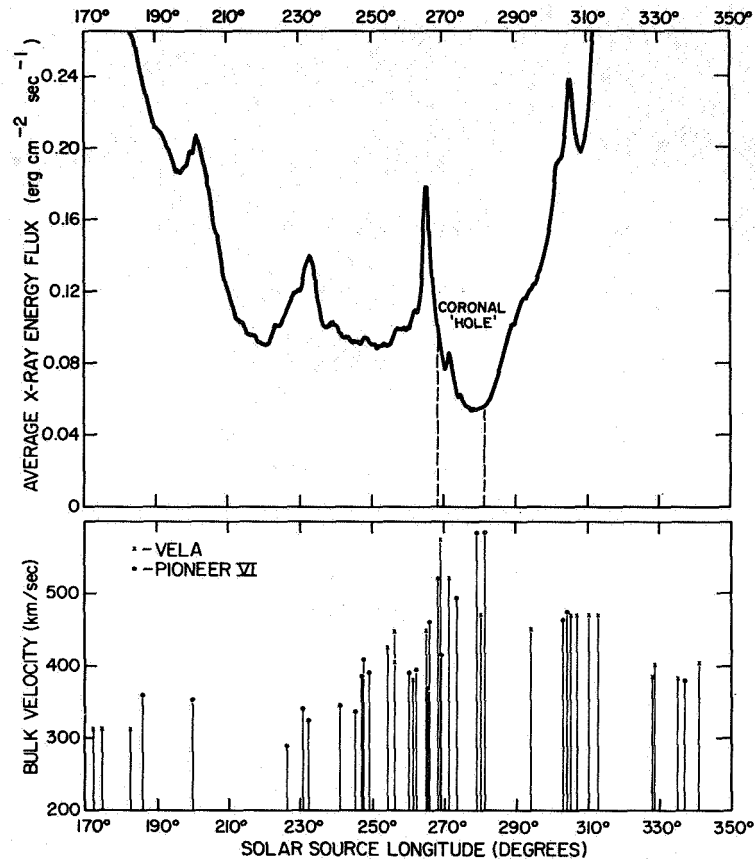
Figure 2. Comparison of (a) the intensity in the wavebands 3-35Å and 44-51Å emitted from an equatorial swath extending 4 arcmin in latitude and with a 4-arcsec longitudinal sampling interval, and (b) the solar wind bulk velocity measured from Pioneer-6 and Vela with connection longitudes inferred from the EQRH approximation. (Pioneer-6 data courtesy of A.J. Lazarus, Vela data from the NOAA/ERL Reports of Solar-Geophysical Data, No. 316, Part 1, 1970.) The inferred source of the velocity stream and the longitude of the hole will agree within 10° only at equatorial latitudes due to the nonmeridional boundaries of the hole (see Figure 1). From Krieger, et al. (1972).

An early attempt at such an association using the EQRH approximation from two spacecraft is given by Roelof (1972a). Clearly, however, before such associations can be made, we must unambiguously identify temporal variations in the injection as well as modification of flux profiles due to distortion of the local interplanetary field and plasma configuration.

We have carried out such an analysis and synthesis of coronal and interplanetary energetic particle, plasma and magnetic field observations over three solar rotations (Roelof and Krimigis, 1972, which I shall refer to as Paper II) based on particle data from three widely separated spacecraft in 1967 (Mariner-4 and -5 and Explorer-35) presented with preliminary
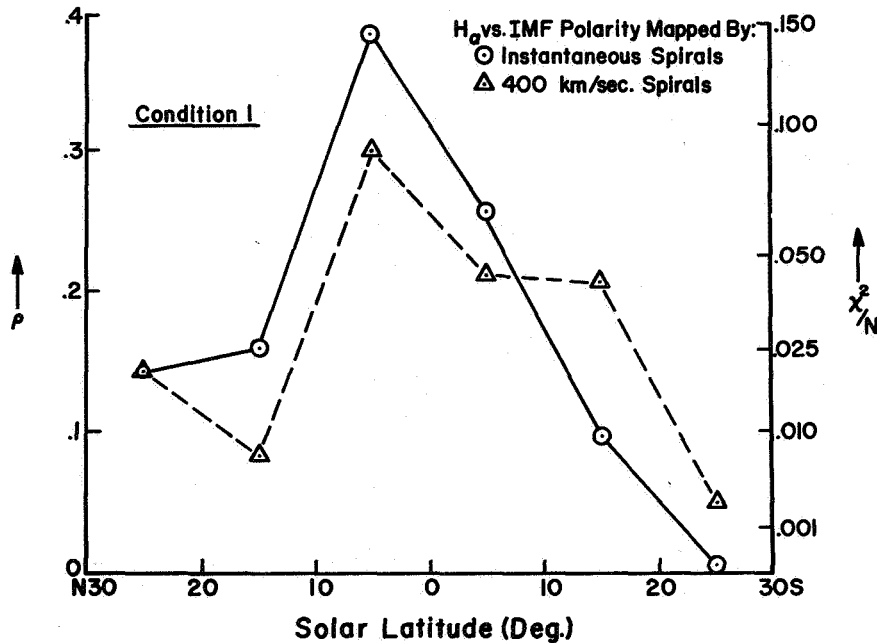
490

Figure 3. Cross-correlation coefficient ρ between polarities of the interplanetary magnetic field measured on Mariner-5 (courtesy of L. Davis, Jr.) and the chromospheric magnetic field inferred from $H\alpha$ filtergrams (courtesy of P.S. McIntosh) for Carrington Rotations 1523-5 (July-September, 1967). Chromospheric polarities were assigned to areas $10° \times 10°$ and the correlation was done in longitude for all three rotations on each $10°$ swath in latitude. The χ^2/N for each correlation of N polarities (N $\simeq$ 100) is given on the right-hand vertical axis. Interplanetary polarities were mapped back to the sun using both the EQRH (instantaneous spiral) approximation for $\Delta\Phi$ (circles) and a fixed lag corresponding to a constant 400 km/sec solar wind (triangles). From Roelof and McIntosh, 1972.

analysis by Krimigis, et al. (1971, which will be referred to here as I). In II we did identify and compensate for the effects of "collimated convection" identified in I, but I shall refer the interested reader to those papers and pass on to selected results from II more pertinent to this symposium, namely the resulting deductions on LESP active region acceleration and coronal propagation from event histories (the next section) and chromospheric $H\alpha$ structure (the following section).

ANALYSIS OF LESP EVENTS DURING AUGUST 1967

Of the three Carrington rotations analyzed in II (1523-1525) I have chosen 1524 as a sample of our findings. The particle data for this rotation (August 1967) are presented in Figure 4 where the intensities of protons ≥ 0.3 MeV measured on Mariner-4 and -5 and Explorer-35 are plotted together. Also given is the first harmonic amplitude A_0 of the four-sector ecliptic anisotropy measurement on Explorer-35 along with the theoretical convective (Compton-
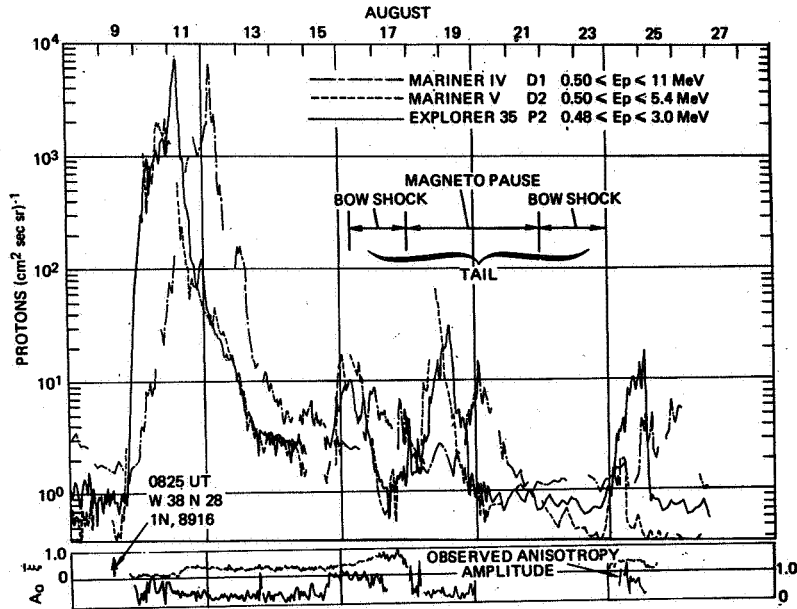
491

Figure 4. Top — Hourly averages of the intensities in the designated energy intervals from Mariners-4 and -5 and Explorer-35 for days 220 to 239. The intensities are those for ~ 0.5 MeV protons, although the anisotropy measurements represent those for ~ 0.3 MeV protons at Explorer-35. The background counting rates represent equivalent fluxes of 1.0, 0.66, and 0.18 $(cm^2 \ sec \ sr)^{-1}$ for Mariner-4, Explorer-35 and Mariner-5, respectively. Note that the anisotropy during days 230 to 231 is small, and is not representative of the interplanetary anisotropy, because Explorer 35 is located inside the magnetotail. Bottom — A_o is the amplitude of the first harmonic of the particle anisotropy in the ecliptic plane measured at Explorer-35. $\bar{\xi}$ is the theoretical Compton-Getting convective anisotropy calculated from the solar wind velocity at Explorer-34 and particle spectral ratio at Explorer-35. After Roelof and Krimigis, 1972.

Getting) anisotropy $\bar{\xi}$ which is the theoretical energy-dependent anisotropy $\bar{\xi}$ averaged over the energy range 0.32 MeV to 6.3 MeV and calculated with the solar wind velocity measured at the same time on Explorer-34 (courtesy of K. Ogilvie). Note that the interplanetary anisotropy cannot be measured reliably while Explorer-35 is in the earth's magnetotail (August 16-23).

The four particle events of rotation 1524 show directly the influence of coronal structure. Only the first event (August 9) displays the customary rapid rise of a flare-associated event, but as we shall see, its maximum and decay reflect the coronal injection profile. All flares for rotations 1523-5 with importance ≥ 1N are listed in Table 2 of I. The remaining three events have their time histories dominated by coronal structures, for their shapes are clearly unlike "classical" flare events, having decays that are as fast as (or faster than) their rises.

492

In fact, although the event of August 9 (associated with a 1N flare in McMath region 8916), has a hard spectrum and a rapid rise beginning $\sim$ 1500 UT at Mariner-5 and Explorer-35 (agreeing within the $\sim$ 6 hour transit time for these protons after the Hα flare maximum at 0825 UT), by the time the maximum is seen at Mariner 4, $\sim$ 0600 UT on August 12 some three days later, the event has assumed a considerably more symmetric time history but with a comparable peak flux (see Figure 4). The spectrum softens abruptly at both Mariner 5 and Explorer 35 with the passage of the peak. Thus even this flare-associated event must reflect a coronal injection profile that is established over a period $\sim$ 3 days on the field lines passing through Mariner-4 which connect it to the corona $\sim 20°$ west of those through Mariner-5 and Explorer-35 (for a solar wind velocity of $\sim$ 400 km/s). This assertion is strongly supported by the striking similarity of the post-maximum profile at all three spacecraft, particularly the ancillary peak that appeared at Mariner-5 and Explorer-35 late on August 11. The delays in the appearance of the ancillary peak between Explorer-35 and Mariner-5 at 0.89 AU of $\sim$ 7 hours and Mariner-4 at 1.35 AU of $\sim$ 24 hours agree with a convection of this field-aligned event over almost 0.5 AU with a solar wind velocity $\sim$ 600 km/s, which is indeed the observed velocity at Mariner-5 late on August 11. However, we demonstrated in II that the slower "shoulder" decay following the convected ancillary peak is essentially longitude-independent. This curious behavior can be explained only after studying the coronal configuration (Section 4).

One of the inescapable implications of the detailed agreement of the event profile, seen at Mariner as late as August 13 some four days after the associated flare on August 9 with negligible change in intensity, is that 0.5 MeV protons are being accelerated during this period. It is worth remarking at this point that nonflare associated protons observed July 12-15 on the previous rotation were identified in II with Region 8880, the predecessor of 8916. Coronal storage after impulsive injection cannot by itself explain the event profile prior to the ancillary peak; even though similar time histories could be the result of the profile of the storage structure, the intensity would be lower at Mariner-4 one day later (due to the loss of particles at the sun). For the same reason, interplanetary storage is not acceptable, because typical decay times for events at these energies are $\sim$ 1 day. Indeed, the usual diffusion-convection theory cannot explain this event because both 1) the gradient along the convected field lines is essentially zero and 2) the direction of the anisotropy (not shown, see II) remains essentially aligned with that of the interplanetary field throughout the decay of the event.

The three smaller events (August 15, 18, and 24) are field-aligned and are convected past all three spacecraft (see Figure 4). The interplanetary gradients along the convected field lines are negative in the first two events, while the event of August 24 is clearly evolving, steadily increasing in width as it is seen by spacecraft successively further outward. However, we established in I that the sharp drop at the end of the event was a convected feature, so the fluxes must be spreading steadily *westward* in the corona from an eastern boundary. The anisotropy (when it can be measured outside the magnetotail in two out of the three events), is extremely large, with five to ten times as many particles coming from the sun as

returning towards it, that is these protons are undergoing nearly *scatterfree* propagation near 1 AU for periods of several days.

The symmetric history of the first two small events and particularly the increasing fluxes of the third again have their simplest explanation in acceleration of the protons during the lifetime of the event. There are no intimate flare associations with the first two events, the only flares greater than importance 1 prior to August 15 being a 2B in Region 8926 (S24) on August 12, and the next two have maxima at 0610 and 2106 UT on August 17, ~ 15 hours before the sharp increase at ~ 1200 UT at Mariner-5 on August 18. This is consistent with the soft spectrum of the first small event, and the somewhat harder (more flare-like) spectrum of the second.

The only flare association for the third event (onset at Mariner-5 ~ 2000 UT, August 23) is an importance 2N flare in Region 8942 with maximum at 1242 UT on that day. Since the flare at that time is at N25 E41 and the profile at Explorer 35 rises more slowly and with a softer spectrum than expected for a flare event, we did not make an association in I. However, as we pointed out in II and shall see in the next section, consideration of coronal structure does indeed offer the possibility of transport of these protons across ~ 100° in longitude from the flare region (perhaps explaining the slow rise and soft spectrum).

The remainder of the rotation is anomalously quiet in 0.3 MeV protons, but even this *absence* of particles has an explanation in coronal structure, as we shall now see.

SYNTHESIS OF EVENT HISTORIES WITH CHROMOSPHERIC Hα STRUCTURES

The techniques required for the construction of a synoptic chart of magnetic neutral lines inferred from Hα filtergrams have been reviewed by McIntosh (1972). Two additional characteristics deserve emphasis here. Hα features (filaments, filament channels, fibril patterns, and so on) undergo considerable evolution even during disc transit, so if a synoptic chart is to be used for correlation with near-Earth interplanetary data the Hα configurations should more closely represent the patterns when they are ~ W60 rather than central meridian passage (the latter being the case for most synoptic charts). Moreover, the inference of the location of a neutral line can range from a strong one (marked by an extended dark filament) to a moderate one (marked by a filament channel) to a weak one (marked by fine structure or required for continuity with stronger features).

The synoptic chart for Carrington Rotation 1524 displayed in the center panel of Figure 5 (taken from II) was constructed by P.S. McIntosh of NOAA/ERL for comparison with interplanetary data and explicitly indicates filaments (cross-hatched), clearly inferred neutral lines (solid lines) and neutral lines inferred from fine structures or continuity (dashed lines). Features present at east-limb passage but not present near W60 (such as the evolving connection at N30, 170°) are indicated by dotted lines; plages (in Hα emission) are stippled and sunspots are marked by solid dots. The plus and minus signs indicate field polarities out and into the sun, respectively. Relevant McMath Regions are indicated.
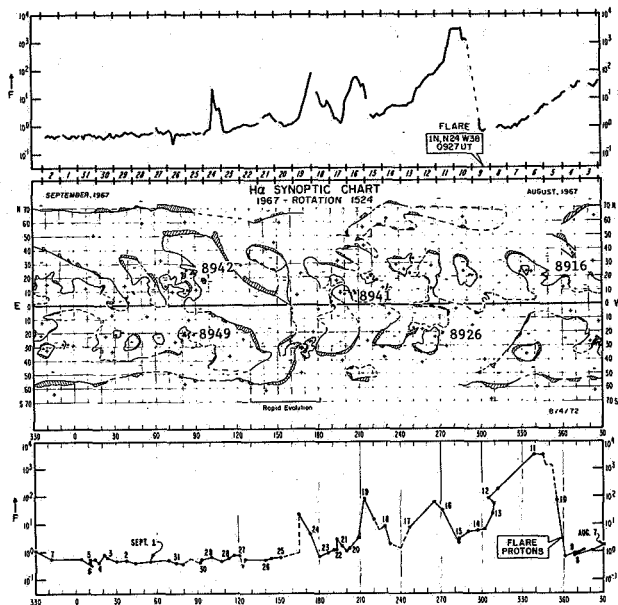
494

Figure 5. Mapping of ⩾ 0.31 MeV proton fluxes observed at Mariner-5 back to magnetic structures identified in the chromosphere, using the EQRH approximation and solar wind velocities measured at Mariner-5. Top — Particle intensity as a function of time, but using the central meridian passage (CMP) of the features in the synoptic charts as the time axis (time increases from right to left). Major flares are identified. Center — Synoptic chart of magnetic field features in the chromosphere derived from Hα "filtergrams" for Carrington rotation 1524 prepared by P.S. McIntosh, August 4, 1972. McMath Regions referred to in the text are indicated by number. Bottom — Intensities shown in the upper panel are now plotted at their Carrington connection longitude. The plotted points are twelve hours apart and the numbers give the day of the observation. From Roelof and Krimigis, 1972.

To aid the reader in understanding the transformation from satellite time to solar longitude, the ⩾ 0.32 MeV proton fluxes measured at Mariner-5 are plotted in the upper panel of Figure 5 on the convenient time scale given by the CMP time (as seen from earth) of the Hα structures. (Note that this time scale increases from right to left.) In the lower panel, the intensity for a given time t (chosen near 00 hours UT and 12 hours UT and indicated by a dot with the date of the month and an unlabeled dot, respectively) is plotted at the

Carrington longitude corresponding to the longitude of Mariner-5 plus $\Delta\phi(t) = \Omega r(t)/V(t)$ calculated from the solar wind velocity $V(t)$ measured by Mariner-5 when it was at a distance $r(t)$ from the sun. For example, the peak flux at 00 UT on August 19 (read top panel in Figure 5) occurred concurrently with a solar wind velocity of 600 km/s when Mariner-5 was at Carrington $176°$ and radius 0.88 AU. Therefore we infer the coronal connection point for the field line through Mariner-5 carrying these protons was

$$176° + (14.3°/day) \ \frac{(0.88 \text{ AU}) (1.5 \times 10^8 \text{ km/AU})}{(600 \text{ km/s}) (8.64 \times 10^4 \text{ s/day})} = 212°_{\text{Carrington}}$$

and that is where it is plotted on the bottom panel.

We are told that "a picture is worth a thousand words," so I have included a Table 1 (condensed from Tables 2b and 3b of II) containing a summary of the analyses of particle characteristics (condensed from Section 3) and of the coronal characteristics deduced from Figure 5 and given below in this section. Also given in Table 1 are our conclusions, drawn from a synthesis of the interplanetary and coronal analyses.

Comparing the upper and lower panels of Figure 5, we see that the variability of the solar wind velocity can considerably distort the profile of an individual event, that is the expansion of the coronal profile of the fluxes of August 10-12 due to the rapid increase in solar wind velocity during the first half of August 11 (evident by the $30°$ jump in connection longitude). The opposite kind of distortion occurs in the same event when the coronal profile of fluxes from August 12-14 is compressed to a region of only $10°$ (instead of the average $27°$ spread for two days) due to a steady decay of the solar wind velocity during this period. I have called this characteristic behavior a "dwell" in solar connection longitude associated with the decay of a solar wind stream and have analyzed nearly 40 of them that occurred during the years 1965-1967 (Roelof, 1972b). In other cases, events occurring during high speed solar winds are mapped appreciably further to the east (for instance, our example of August 19 where $\Delta\phi = 37°$) than the usual $\Delta\phi \cong 60°$ for low solar wind velocities (that is the event of August 24). Considering these distortions, we find it striking that equatorial neutral line structure organizes so well the EQRH-mapped intensity profiles.

The peak fluxes of flare-associated protons of August 10 map to the positive cell from $340°-360°$ bounded above by the neutral line through region 8916 (N24, $347°$). The abrupt flux drop early on August 11 corresponds to the $30°$ shift eastward of the connection point (noted in the previous paragraph). The convected ancillary flux peak of August 12 (discussed in conjunction with Figure 4) then marks the beginning of the exponential "shoulder" decay while the connection dwells near $305°$, *outside* the positive polarity cell to the west which was the particle source for the main intensity peak. It then appears that this decay represents the escape of particles on these field lines from the outer solar system since (as we saw from Figure 4) there is no significant interplanetary gradient along field lines between 0.9 AU and 1.35 AU at this time. The event at Mariner-4 thus still exhibits an

Table 1
Syntheses of Particle and Coronal Analyses for Carrington Rotation 1524 (August 1967)

| Day and Date (1967) | Particle Characteristics (Analysis) | | | Carrington Connection Longitude (deg) | Coronal Characteristics (Analysis) | | Conclusion (Synthesis) |
	Intensity History	Spectral Ratio M5 & E35	Gradient (Along Field Lines)		Associated Flare and/or McMath Region	Equatorial Hα Structure	
221-223 Aug 9-11	Flare injection (221) evolving into quasi-stationary profile with abrupt drop following "ramp"	Hard in rise. Softens afterward.	~ zero (M5-E35)	300-360	8916 (return of 8880) 1N Flare 0827 UT Aug 9 (N24, W38)	Large positive cell bounded by neutral line passing thru 8916	Flare-initiated flux increase. Protons contained in positive cell since intensity drops at eastern boundary
224-225 Aug 12-13	Ancillary peak (224). Convected and exponential "shoulder" decay extrapolated from E35 to M4	Constant at typical value	~ zero (M5-E35) = + 80% / AU or some time dependence in 24 hr (E35-M4)	~305	8916 (?)	Convoluted equator crossing of neutral line from 8916	Exponential decay during dwell with low field-aligned anisotropy with small positive gradient due to loss of particles through scattering regions beyond 1.4 AU
227-229 Aug 15-17	Symmetric non-impulsive profile with small-scale distortions	Unusually soft	Large and negative (M5-E35-M4)	245-295	New active regions 8926 (?)	Equator-crossing neutral lines at 250° and 285°	Quasi-stationary coronal injection profile bounded by neutral line crossings, but distorted by evolving three-dimensional interplanetary field
230-232 Aug 17-19	Symmetric non-impulsive profile similar at M5, E35 and M4 Exponential "shoulder" decay and increase	Harder than than usual	Large and negative (M5-E35-M4)	200-245	Possibly return of regions associated with fluxes days 205-209. 1B Flares 0610 UT and 2106 UT Aug 17 in 8941	Equator-crossing neutral lines at 200° and 225° passing thru 8941	Quasi-stationary coronal injection profile associated with neutral-line complex of 8941, perhaps initiated by flares of Aug 17
236-238 Aug 24-26	Evolving structure with termination convected from M5 to E35 and probably to M4	Soft	Strongly evolving	120-170	New active region born Aug 24, N10, 155°. 2N Flare 1232 UT Aug 23 in 8942	Rapidly evolving filament from 8942 crossing equator at 160°	Evolving field-aligned population, possibly associated with birth of active region or flare in 8942

497

undecayed main (cell) peak and ancillary (boundary) peak, while the fluxes from the exterior coronal region continue to decay exponentially, further revealing the eastern boundary of the ancillary peak. The chromospheric neutral line therefore marks the boundary between two populations of protons with differing time behavior, protons interior to the cell being quasi-constant, those exterior decaying exponentially.

The neutral lines are also successful in organizing the coronal profiles of the next three small events, as indeed they should since these events are quasi-stationary and thus their histories must be determined by coronal structure. The first event profile is centered over 265° where there is a narrow double neutral line corridor just above the equator. Since the inferred eastern neutral line (near 260°) leads southward to pass close to region 8926 (270°,S25), the occurrence of the most immediately preceding importance 1 flare in this same region (albeit on August 12) suggests that the protons seen on August 15-17 may be from subsequent activity in 8926, transported northward along the coronal structure above the neutral line running from 8926 to the equator. The very strong field-aligned anisotropies (see Figure 4) rule out any possibility of storage in interplanetary space.

The peak of the coronal profile (August 19) of the second quasi-stationary event falls near 210°, close to the longitude (205°) of the equatorial (N10) region 8941 in which there were two flares on August 17. Although the interplanetary anisotropy could not be measured for this event, the simplest explanation for these fluxes is continued activity in 8941 since the fluxes first appear on August 18 when the connection longitude first approaches the neutral line leading northeastward from the equator through 8941.

The coronal profile of the third small event, shown in I and II to be steadily expanding westward in time with a fixed eastern boundary after an associated 2N flare at E41 in region 8942 (1242 UT, August 23), offers a most interesting possibility for coronal transport. The deduced eastern boundary falls on the equatorial crossing at 160° of a long neutral line that leads northeastward back through region 8942 (80°, N25), some 80° away. The agreement of the event onset time ($\sim$ 2000 UT, August 23) with the flare maximum (plus the proton transit time) now seems more significant. Even more interesting is the path the particles would have taken, since they seemed to be preferentially excluded from the coronal structure above the large negative cell west of 8942. During disc passage the neutral line, which ran more or less directly from 8942 to the equator at 160° when first visible, evolved by west limb passage to incorporate the small negative cell centered at 145°, N35. The dotted lines in Figure 5 are the east-hemisphere appearance. Thus the particles may have traveled a convoluted, indirect route to the equator at 160°, perhaps explaining the gradual evolution of the profile. However, we also mentioned in II an alternative (but, I feel, less likely) explanation for this flux increase. We noted that new active regions were born along the neutral line near N10 on August 21 and 24, perhaps accelerating protons.

No significant 0.3 MeV proton flux increases were detected over the next half a rotation (from 150° eastward). This anomalous absence of protons is, however, in agreement with the observations of Lin (1970) who observed a peculiar absence of $\geqslant$ 45 keV electron events

498

during this period even though region 8942 steadily produced ≥ 20 keV X-ray bursts during its disc transit. The anomaly is heightened by the strong association of X-ray bursts with the many electron events observed on the previous rotation from flares in regions 8905 and 8907 which coalesced to produce 8942. In II we showed that our proton events of the previous rotation 1523 suggest open coronal structure consistent with the electron events from 8905-7 (and dominated by the same neutral line that we just discussed). Lin suggested that the absence of ≥ 45 keV electrons in the presence of ≥ 20 keV X-ray bursts implied a closed coronal structure over 8942. The avoidance of the negative cell west of 8942 by our protons and their absence while the connection longitude moved eastward 180° is certainly consistent with Lin's implication from the X-ray data of closed structure. Complementary information on this coronal configuration is found in a very small increase (near the Explorer-35 background) of > 0.8 MeV protons observed on Explorer-35 beginning 0500 UT on August 26 (M.A. Shea and D.F. Smart, private communication, 1972). The event had a "classic" flare profile and can be associated with a 1B flare with maximum at 0022 UT in region 8949. However, this region is in the southern hemisphere (80°, S19) with rather indirect neutral line connection to the equator near the connection longitudes for August 26-28, which dwell near 120°, indicating a completely different coronal structure than that in the northern hemisphere.

SUMMARY AND CONCLUSIONS

Table 1 summarizes our analysis and synthesis of the interplanetary and coronal observations for rotation 1524. In II we required that our conclusions be not only consistent within the data set of a given rotation, but also that they be consistent with the evolution of particle, plasma and coronal features from rotation to rotation, 1523-5. I cannot emphasize strongly enough the importance of such extended consistency. Some particular aspect of an event, such as the development and decay of the amplitude of the particle anisotropy, may have a number of plausible explanations. However, when one requires a consistent explanation for the time history, spectral energy dependence, anisotropy amplitude and direction, interplanetary magnetic field direction, and variations in solar wind velocity, the multiplicity of explanations is rapidly reduced, particularly when similar data from separated spacecraft are compared.

We claim that, after this demanding process of intercomparison of data is carried out with strict consistency criteria, the LESP data are strikingly ordered by Hα neutral-line equatorial structure using the four points of analysis listed in the Introduction. Since all four points are still under discussion by workers in solar, interplanetary, and cosmic ray physics, we believe that the ordering of LESP data by their use constitutes a self-consistent justification of them taken as a whole, strongly supplementing their individual verification (as cited in the Introduction) for at least the period July to September 1967.

If our results conflict with some current opinions of other workers, at least there is a small additional judgmental argument on the side of continuing to analyze LESP events using the four-point technique. Our techniques open new possibilities for studying the sun and interplanetary medium, while conflicting views would deny us these simple, direct analytical techniques. As we wrote in the last paragraph of II:

> "The explanation of this ordering must lie in the faithful mapping of these chromospheric structures out through the corona and into the interplanetary medium. If so, LESP provide a unique tool for studying the otherwise invisible magnetic structure of this transition region from the low corona to interplanetary space."

ACKNOWLEDGMENTS

REFERENCES

Anderson, K.A., 1969, *Solar Phys.* 6, 111.

Bryant, D.A., Cline, T.L., Desai, U.D., and McDonald, F.B., 1962, *J.G.R.* 67, 4983.

Bryant, D.A., Cline, T.L., Desai, U.D., and McDonald, F.B., 1965a, *Phys. Rev. Letters* 14, 481.

Bryant, D.A., Cline, T.L., Desai, U.D., and McDonald, F.B., 1965b, *Ap. J.* 141, 478.

Fan, C.V., Lamport, J.E., Simpson, J.A., and Smith, D.R., 1966, *J.G.R.* 71, 3289.

Fan, C.V., Pick, M., Pyle, R., Simpson, J.A., and Smith, D.R., 1968, *J.G.R.* 73, 1555.

Goldstein, B.E., 1971, (preprint MIT CSR-P-71-63).

Kahler, S.W., 1969, *Solar Phys.* 8, 166.

Kavanagh, Jr., L.D., Schardt, A.W., and Roelof, E.C., 1970, *Rev. Geophys. Space Phys.* **8**, 389.

Krieger, A.S., Timothy, A.F., and Roelof, E.C., 1972 (preprint, ASE 3029A), *Solar Phys.*, in press.

Krimigis, S.M., 1969, Trudi Mezdunaradrovo Seminara, *Proc. Ioffe Physico-Technical Inst.* (Leningrad), 43.

Krimigis, S.M., Roelof, E.C., Armstrong, T.P., and Van Allen, J.A., 1971, *J.G.R.* **76**, 5921.

Lanzerotti, L.J., 1969, *J.G.R.* **74**, 2851.

Lin, R.P., Kahler, S.W., and Roelof, E.C., 1968, *Solar Phys.* **4**, 338.

Matsuda, T., and Sakurai, T., 1972, *Cosmic Electrodyn.* **3**, 97.

McCracken, K.G., and Rao, U.R., 1970, *Space Sci. Rev.* **11**, 155.

McDonald, F.B., and Desai, U.D., 1971, *J.G.R.* **76**, 808.

McIntosh, P.S., 1972, *Rev. Geophys. Space Phys.* **10**, 837.

Nolte, J.T., and Roelof, E.C., 1972 (abstract), *EOS* **53**, 506 (Solar Phys., to be published).

Pick, M., 1972, in *Solar Terrestrial Physics*, 1970, ed. Dryer, Part I (D. Reidel, Holland), 61.

Rao, U.R., McCracken, K.G., and Bukata, R.P., 1967, *J.G.R.* **72**, 4325.

Roelof, E.C., 1972a in *Solar Wind*, eds. Sonett, Coleman, Jr., and Wilcox, NASA SP-308, 140.

Roelof, E.C., 1972b (abstract), *EOS* **53**, 506 (manuscript in preparation).

Roelof, E.C., and Krimigis, S.M., 1972 (preprint APL/JHU), *J.G.R.* **78**, in press.

Roelof, E.C., and McIntosh, P.S., 1972 (abstract), *EOS*, **53**, 1113 (manuscript in preparation).

Sakurai, T., 1971, *Cosmic Electrodyn.* **1**, 460.

Siscoe, G.L., and Finley, L.T., 1969, *Solar Phys.* **9**, 452.

Siscoe, G.L., and Finley, L.T., 1970, *J.G.R.* **75**, 1817.

Snyder, C.W., and Neugebauer, M., 1966, in *The Solar Wind,* ed. Mackin, Pergamon Press, 25.

Wibberenz, G., 1972, *Proc. 12th Conf. Cosmic Rays* (Invited and Rapporteur Papers).

ENERGETIC PARTICLE STORAGE ON THE SUN

G.M. Simnett

*Physics Department and Institute of Geophysics
and Planetary Physics, University of California,
Riverside*

INTRODUCTION

The question of energetic particle storage in the solar corona has frequently been discussed either with a view to creating solar flares (Elliot, 1964) or to explain some of the long lived features of solar particle events (Fan et al., 1968; Anderson, 1969; McDonald and Desai, 1971; Simnett and Holt, 1971; Simnett, 1971). Whereas Elliot's model is concerned with storing protons of energies ≈ 1 GeV, the observations of recurrence and long-lived events are for the most part concerned with protons and electrons $\lesssim 30$ MeV. This article discusses the latter.

When a long lived (1 to 2 weeks) energetic particle event is seen at 1 AU, the dominant reason for the duration of the event must be either extensive diffusion and/or convection following impulsive release from the sun or extended release from the sun. The events of about two weeks duration are certainly not the result of transport processes entirely in the interplanetary medium, if for no other reason than the sweeping effect of the solar wind; neither are the recurrence events discussed by McDonald and Desai (1971). Therefore these events can only be accounted for by continuous or quasi-continuous release from the sun. The problem now divides into two issues: either particles can be stored in the corona for periods of $\gtrsim 1$ week, or there must be continuous acceleration process for electrons, to $\gtrsim 10$ MeV, and for protons, to $\gtrsim 30$ to 100 MeV. The long-lived events never contain protons > 100 MeV on a scale comparable to the emission from a large flare. On the other hand, the > 12 MeV electron intensity can be within an order of magnitude of the largest direct flare increase reported by Datlowe (1971). In a storage model, it would appear easier to store electrons than protons, which is a natural consequence of a magnetic trapping regime where escape is rigidity dependent. In a continuous acceleration model it would appear that the acceleration process must be almost as effective as that occurring in a major flare for electrons, but not for protons.

Storage times equivalent to a solar rotation are unnecessary to explain recurrence events, as it is plausible to occasionally repopulate the storage region with particles. During a solar rotation there is generally more than one flare with identical signatures to a known particle producing flare; yet many such flares do not appear to release particles into interplanetary space.

We now discuss the requirements and restrictions for long term coronal storage of electrons and protons up to ≈ 30 MeV. As the acceleration mechanism for particles on the sun is still unknown, continuous acceleration must be retained as a possible, although in our opinion unlikely, alternative to storage.

ENERGY AND PARTICLE LOSS PROCESSES IN THE CORONA

The most plausible region for storing energetic charged particles is in a magnetic bottle or arch extending high into the corona. Evidence for transient structures of this nature has been reported (Schatten, 1970; Riddle, 1970) out to 5 to 10 $R_\odot$. There is little or no evidence for closed magnetic field lines at altitudes of 1 to 2 $R_\odot$, but there are also no observations, as opposed to inferences, of coronal magnetic fields above these altitudes. All distances refer to heights above the photosphere. The length of time a given particle population can exist in such a region depends on the various loss processes. These are ionization losses, escape into interplanetary space (leakage), scattering into the sun, and bremsstrahlung and synchrotron radiation losses (for electrons). Loss into the sun and leakage involve the removal of the particle; the other loss processes move it from one energy interval to another, thereby modifying the energy spectrum of the trapped particles. The limit to this occurs when the particles become indistinguishable from those in thermal equilibrium in the storage region.

It is important first to put a realistic lower limit on the altitude of the storage region. In the subsequent discussion 5×10^5 seconds, or 6 days, is arbitrarily chosen as a storage time. Allowing for diffusion and/or convection for 4 days after the particles are released, this would account for an event at 1 AU of 10 days duration.

Table 1 gives proton lifetimes against ionization loss at mean densities equivalent to 1, 2, 3, 4, and 6 $R_\odot$. Clearly trapped particles do not move in a medium of constant density; however, precise calculations of energy loss cannot be made without postulating the detailed structure of the trapping field. For the present discussion, an order of magnitude estimate is sufficient to indicate the ionization losses. For a 3 MeV proton to survive for 5×10^5 seconds, the lowest part of its orbit, at which it spends a disproportionate amount of time, must not be below about 2 $R_\odot$. (Here we have assumed a magnetic field configuration such that the mirror points are at the lowest altitude.) At 2 $R_\odot$ the lifetime is 1.4×10^6 seconds, so that allowing for part of the orbit to be at higher altitudes, it will survive without more than ≈ 25 percent energy loss in 5×10^5 seconds. A similar argument for 1 MeV protons would put a lower altitude limit of 4 $R_\odot$.

These limits assume that the proton differential energy spectral index should remain unchanged. However, there is evidence of spectral degradation in some events below ≈ 1 MeV (Verzariu and Krimigis, 1972). This could, however, result from a number of causes, among which are adiabatic deceleration in interplanetary space, a rigidity dependent release unfavorable to low rigidities, and ionization losses in the source. If the latter hypothesis is adopted, the storage region must extend below 4 $R_\odot$, and therefore we postulate a lower

Table 1
Proton Lifetimes in the Corona

Particle Density (cm^{-3})	Equivalent Altitude $R_\odot$	Proton Lifetime (seconds)			
		1 MeV	3 MeV	5 MeV	10 MeV
2.5×10^4	6	4.3×10^6	1.7×10^7	4.1×10^7	1.1×10^8
7.0×10^4	4	1.5×10^6	6.2×10^6	1.5×10^7	4.1×10^7
1.4×10^5	3	7.6×10^5	3.1×10^6	7.3×10^6	2.0×10^7
3.2×10^5	2	3.3×10^5	1.4×10^6	3.2×10^6	8.9×10^6
2.5×10^6	1	4.3×10^4	1.7×10^5	4.1×10^5	1.1×10^6

limit to this region of around 3 $R_\odot$ from which escape is probable, at least for protons. This would demand field line closure at ≈ 5 to 10 $R_\odot$, which does not conflict with current knowledge of the coronal field.

Ionization and bremsstrahlung losses for electrons > 0.5 MeV stored above 2 $R_\odot$ are negligible because of the small amount of matter traversed. Moving at the speed of light, c, in a medium of density, ρ, 3×10^5 H atoms cm^{-3}, the matter traversed in $t = 5 \times 10^5$ seconds is

$$\frac{\rho c t}{N} = \left[\frac{(3.10^5) \times (3.10^{10}) \times (5 \times 10^5)}{(6.10^{23})} \right]$$

$$= 8 \times 10^{-3} \text{ g cm}^{-2}$$

(1)

N is Avagadro's number. In the same time the synchrotron radiation loss of a 20 MeV electron in a 2-G field perpendicular to its motion is ≈ 3 MeV. As this field is certainly an overestimate, and energy loss $\alpha H_\perp^2$, synchrotron radiation does not limit electron storage.

Particles trapped in a magnetic field experience drifts which alter the plane of the orbit. Drift is negligible for electrons, as a 0.5 MeV electron would take $\gtrsim 10^7$ seconds to drift 1 $R_\odot$ if the radius of the orbit is > 1 $R_\odot$ and the field gradient is ≈ 1 $G/R_\odot$. The drift rate for 10 MeV protons is around 100 times faster, so this may become an important consideration in long term storage of protons. However, a suitable configuration to the trapping field would eliminate this potential difficulty.

Electrons, and less likely, protons may be lost through Coulomb scattering into the sun or onto open field lines. The amount of matter traversed by electrons (1) is 2×10^{-4} radiation length in hydrogen (58 g cm^{-2}). The rms angle of scattering is then only $\approx 10°$ for a 1 MeV electron (Rossi, 1952). Therefore scattering is not a dominant loss mechanism for electrons and it is negligible for protons.

Leakage into space could occur through scattering off irregularities in the trapping field. The gyroradius of a 10 MeV proton in a 0.1 G field is around 50 km, which is small on the scale we are considering for the storage region. We choose 0.1 G as a probable lower limit to the field at any point in the trapping volume. It is possible that the more energetic protons would gradually leak into space; however, electrons are only likely to escape through decay of the trapping field. This would naturally lead to a soft proton spectrum when the trapping field finally decays and the particles are released.

There is a limit to the number of energetic particles a given magnetic field can contain before the motion of the particles dominates the field. Simnett and Holt (1971) showed that around 10^4 MeV $\cdot$ cm^{-3} was a realistic limit to the density of particles that could be contained by a 1 G field. In a trapping volume of 10^{31} cm^3, $> 10^{34}$ particles of energy $\gtrsim 1$ MeV can be contained without violating energy constraints. A larger volume can contain more particles, while with a weaker field the number is reduced. It is envisioned that a typical storage region is considerably in excess of 10^{31} cm^3. Energy density is not a limiting factor in the interpretation of storage events.

ENERGETIC PARTICLES AND SOLAR RADIO OBSERVATIONS

Many events observed at 1 AU cannot be identified with a specific source on the sun; some of these, together with the very long-lived events, may result from the release of trapped particles. One example of a long-lived event is illustrated in Figure 1, which shows intensity versus time histories of electrons and protons from December 3 to 14, 1968. A 3N flare, at N21° E80° at 2116 UT December 2, 1968 was probably responsible for accelerating the particles (Datlowe, 1971; Simnett, 1971). Note the 3 to 4 day rise-time, and the almost symmetrical time profile of the intensities. Protons > 100 MeV were present in this event (Datlowe, 1971). This event has similarities in form to the EDP events discussed by Anderson (1969). The centroid of the particle flux is well defined and occurs earlier for the electrons than for protons. There is a 3.5 percent decrease in the sea level neutron monitor intensity, a signature noted by Anderson (1969). Shown in Figure 2, 169 MHz radio emission has a distinct maximum on December 5 and 6, correlated with maximum electron intensity at the earth. Simnett (1971) showed that the low energy proton spectrum tended to flatten after December 6, consistent with degradation due to ionization losses. There is no evidence that relativistic electron acceleration is occurring continuously from December 3 to 6 or later. If we interpret this event as quasi-stable storage with excessive leakage onto a co-rotating tube of field lines, both the sudden commencement and the associated particle increase on December 5 can be attributed to the passage of the earth into the magnetic flux tube. The radio noise storm reaches maximum at the time of the greatest particle loss.

Figure 3 shows a rather different event in July 1968, which has been interpreted by Simnett and Holt (1971) as evidence for stable trapping of relativistic electrons and probably low energy protons for 4 to 5 days. Using a wealth of additional data, they argued that the 0.3 to 45 MeV electron increase that peaks on July 13 could not have been accelerated later
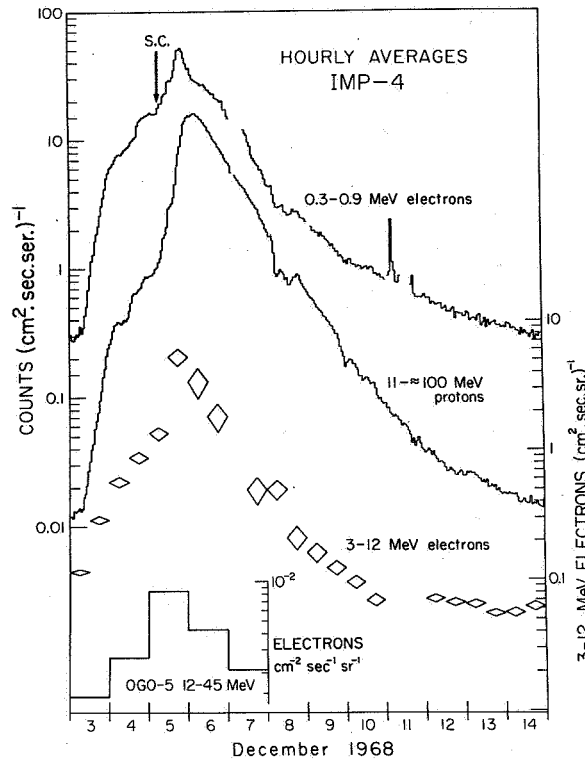
Figure 1. Intensity-time histories for electrons and protons following the 3N flare at E80° on December 2, 1968 (after Datlowe, 1971, and Simnett, 1971).
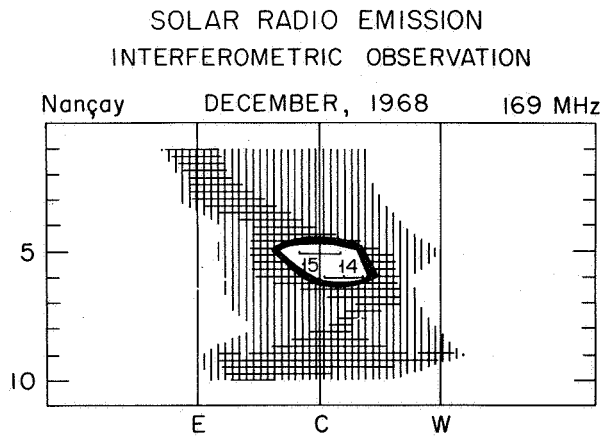

Figure 2. 169-MHz solar radio interferometer data from the Nançay Observatory, France (reproduced from ESSA bulletin No. IER-FB-293, January 1969).
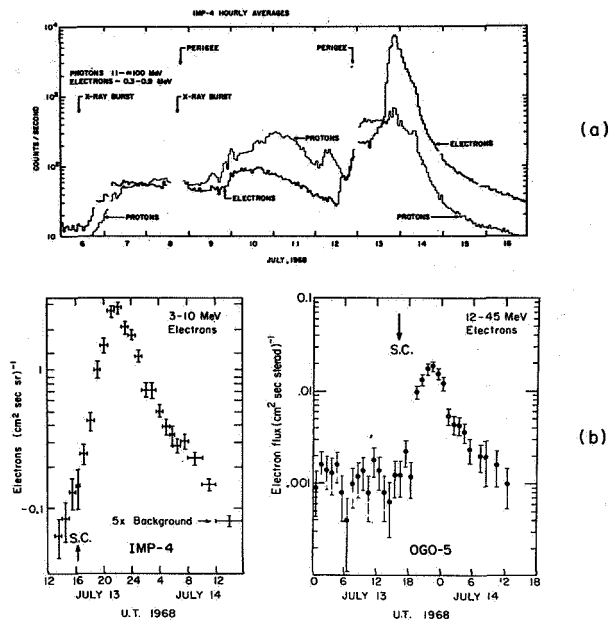
Figure 3. (a) Intensity-time histories from IMP-4 of
0.3 to 0.9 MeV electrons and 11 to ≈ 100 MeV
protons for July 6 to 16, 1968 (after Simnett, et al.,
1970). (b) Intensity-time histories of 3 to 10 MeV
and 12 to 45 MeV electrons around the maximum of
the July 13, 1968 event (after Simnett et al., 1970,
and Datlowe, 1971).

than July 8, at the time of the X-ray burst indicated in Figure 3. The majority of electrons were stably trapped, with negligible leakage but probably significant energy loss, until the middle of July 12, when the release commenced. Protons were associated with the electrons, but the intensity was negligible above 90 MeV (Datlowe 1971). There was an additional increase associated with the sudden commencement, not unlike that seen in December 1968.

Interpretation for the propagation for this event is that the main electron release began on July 12, with the majority of electrons streaming out along a tube of field lines. Scattering makes the low energy component spatially broader than the highly relativistic component. As this structure co-rotates and slowly evolves, earthbound spacecraft map what is effectively the spatial profile, which suggests that the highly relativistic electrons are propagating in a narrow, well-collimated beam. The phase of the electron anisotropy vector was typically 50° west of the earth-sun line for around 10 hours either side of the maximum, and amplitude of the anisotropy was around 60 percent for three hours prior to the sudden commencement (Allum, private communication, 1972). This is consistent with most of the particles streaming out along the field lines and is certainly indicative of particle release from the sun.

508

Figure 4 shows that the 169-MHz radio emission is greatly enhanced during the proposed storage time, but falls abruptly following the maximum particle intensity at earth. It would be a remarkable coincidence if this radio noise were not connected to the observed electrons.
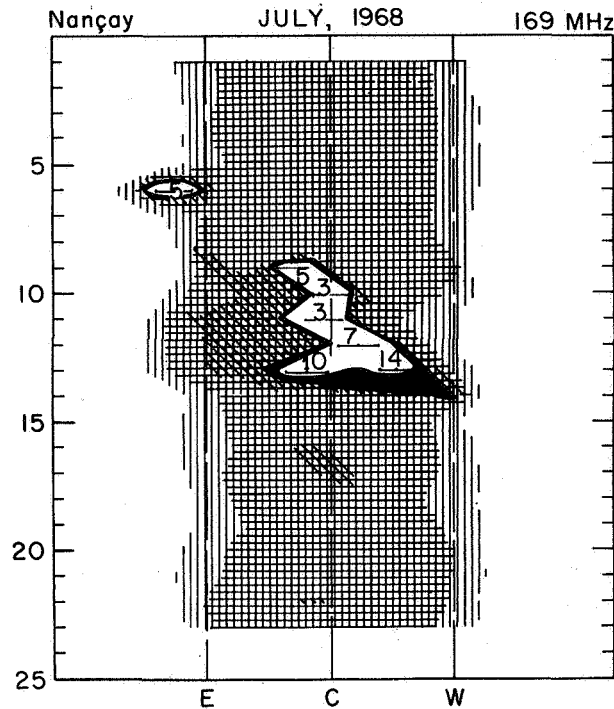

Figure 4. 169-MHz solar radio interferometer data from the Nançay Observatory, France (reproduced from ESSA bulletin No. IER-FB-288, August 1968).

Solar radio observations frequently indicate that accelerated electrons do not escape from the corona, and they are often suggestive of large scale magnetic loop structures. Wild (1969) interpreted an event on November 22, 1968, in terms of an expanding magnetic arch with electrons trapped in orbits near the top of the arch. Sources of 80 MHz radiation were seen at the feet of the arch, corresponding to electrons whose mirror points lay below the 80-MHz plasma level. Radio emission observed at $02^h 49^m 50^s$ on March 30, 1969 by Smerd (1970) is shown in Figure 5, and a hypothetical magnetic field is illustrated schematically, with field line closure at 4 to 6 $R_\odot$. The microwave burst from the (backside) flare started at 0247 and intense emission at the base of the hypothetical magnetic loop continued for $\approx$ 10 to 15 minutes. The type II burst which appears between the two major radio features in Figure 5 was observed to move outwards at 3080 km/s (Smerd, 1970). As energetic particles were
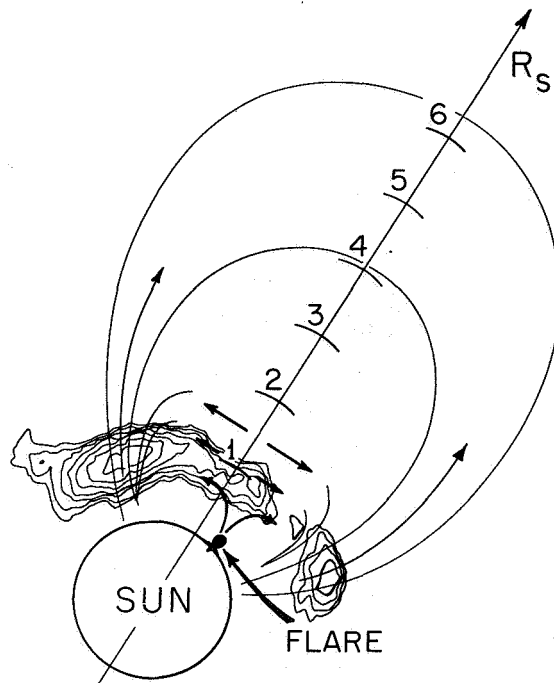
509

Figure 5. 80-MHz radio data from the March 30,
1969 event, at $02^h49^m50^s$ U.T. (after Smerd, 1970).
A hypothetical coronal magnetic loop structure ex-
tending out to 6 $R_\odot$ is superimposed. The emission
from the base of the loop is long-lived (see text) but
the central region is a type II burst moving outwards
at ≈ 3080 km s^{-1}.

subsequently observed in large numbers at 1 AU, it is likely that this disturbance destroyed
the magnetic loop. However, it is interesting to note that the exponential decay of the
subsequent 0.3 to 0.9 MeV electron event had a decay constant of 125 hours.

Several features in the solar radio data are relevant to a particle storage model. Radio events
are very rarely accompanied by > 300 keV electron events at the earth. This is true for type
I, II, and IV bursts, although type III bursts are frequently accompanied by electrons > 45
keV (Lin, 1970). Figure 6 shows the occurrence of noise storms at 169 MHz and > 300
keV electron events at the earth for the period of July 1967 to April 1969. The 169 MHz
data is from *Solar Geophysical Data* and includes only those events with intensities above 4
flux units. Storms correlated with electron events are shown as solid bars. Times when
electron events and noise storms are coincident are rejected if the noise storm is not close to
the flare that produced the observed electrons. Such radio noise storms may be caused by
electrons of a few keV (Takakura, 1963); however, as we have only used the more intense

storms, it would seem remarkable that the electron spectrum was always so steep that the intensity above 300 keV was unobservable. Figure 6 suggests that regions which produce noise storms do not release 300 keV electrons into space. The few cases where the correlation is good tend to be associated with long-lived electron events, such as those discussed above, or the beginning of a series of events, such as September 26 to October 4, 1968.
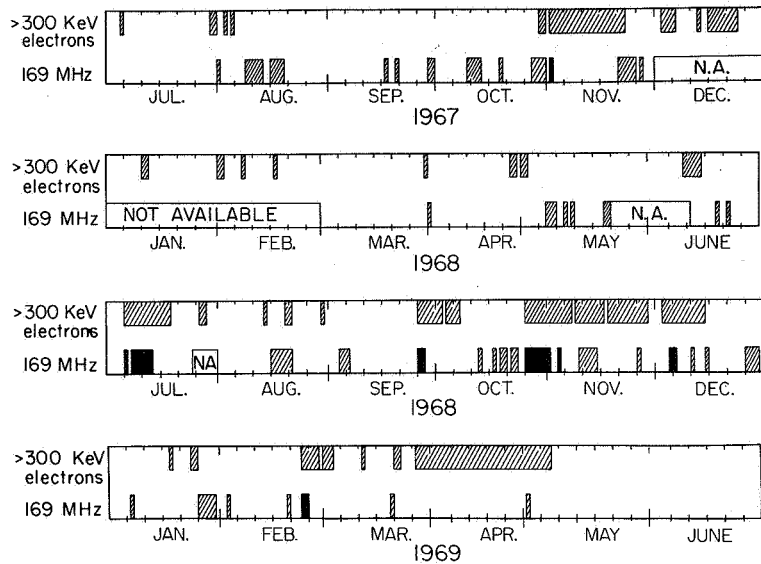

Figure 6. Occurrence of 169-MHz noise storms and electron events at the earth above 300 keV, from July 1967 to May 1969. The solid bars represent events which can be identified with a known source of interplanetary electrons.

Table 2 shows the correlation between 12 moving type IV bursts observed by Smerd and Dulk (1971) and > 300 keV electrons at earth. Smerd and Dulk interpret the type IV emission as coming from electrons in the range 0.1 to 1 MeV. In only one event were 0.3 to 0.9 MeV electrons observed above an intensity level of 0.2 electrons $\cdot$ cm$^{-2} \cdot$ s$^{-1} \cdot$ sr^{-1}. In one other event, on October 26, 1968, a small electron event was recorded with a maximum intensity < 0.2 electrons $\cdot$ cm$^{-2} \cdot$ s$^{-1} \cdot$ sr^{-1}. Table 2 appears to be clear evidence that few, if any, of the electrons responsible for most moving type IV bursts are released into space. Although this may in part be due to unfavorable propagation in the interplanetary medium, the identified flares in Table 2 are sufficiently dispersed that this is unlikely to be the dominant reason.

Figure 7 shows a model of the corona developed to account for unusual features of solar electron events (Simnett, 1971, 1972). The coronal field is envisaged as extending out to a radial distance of ≈ 5 R$_{\odot}$ before taking on the Archimedian spiral pattern characteristic of

511

Table 2
Moving Type IV Bursts and Electrons
> 300 keV at the Earth

Date	Flare	Electrons at Earth		Type IV Velocity
		Prompt	Delayed	
1968				
Feb 25	1B W17	No	No	400 km/s
Sep 4	1N W14	No	No	760
Oct 23-24	2B E59	No	No*	1400
Oct 26	1N E32	No**	No*	480
Nov 22	1N E39	No	No	334
1969				
Mar 1-2	1N W89	No	No	270
Mar 21	2N E16	Yes	No	980
Aug 29-30	1B E38	No	No	480
Oct 10		No	No	650
Dec 17	2B E36	No	No	700
				260
1970				
Mar 21	2N E69	No	No	290
Apr 29	2N E46	No	No	820

*Electrons observed on October 29.

**See text.

the interplanetary field. While the field may be predominantly radial in the lower corona (Newkirk and Altschuler, 1970), higher in the corona it becomes more random in direction, and provides a barrier to the release of low rigidity solar particles. There may be strong, quasi-permanent features which could be responsible for long-lived interplanetary phenomena, such as the magnetic sector structure and recurrent proton streams (released from weak points in the field). Subsequent to a large flare, the plasma heating carries the field into space, allowing the escape of low rigidity particles. However, until the plasma wave can reach ≈ 5 $R_\odot$ there is considerable azimuthal diffusion, which populates the corona with particles. Leakage of the latter forms the co-rotating component of solar cosmic ray events. Moving type IV events may be from disturbances not turbulent or energetic enough to open up the coronal field; instead they propagate slowly outwards, expanding a magnetic arch, until an equilibrium situation is reached. It is significant that the derived speeds of moving type IV bursts are generally $< 10^3$ km · s^{-1}, which is considerably slower than observed velocities of disturbances from major events (compare with March 30, 1969). Flares with a
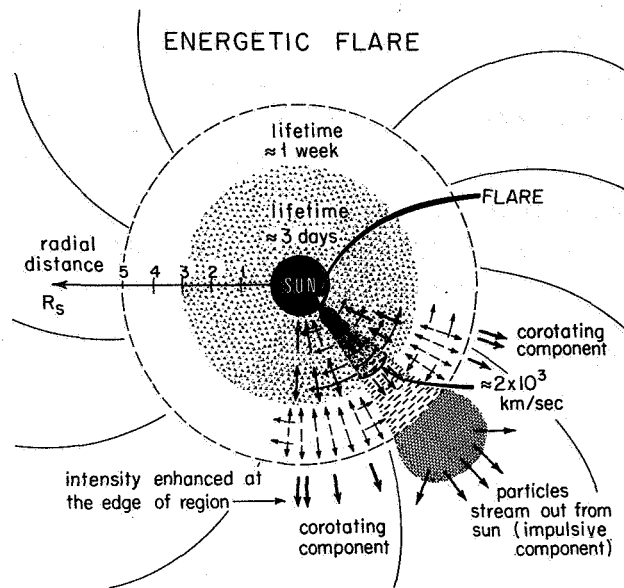
Figure 7. Model of the corona at the time of a large solar flare, shown as a plan view in the ecliptic plane. Low rigidity solar cosmic rays from the flare are denied access to interplanetary space until the plasma wave penetrates the coronal field and reaches open field lines. Meanwhile, the trapped particles diffuse azimuthally in the lower corona; some of these particles later escape to form the co-rotating component of solar cosmic rays.

small energy release may often be unable to overcome the local coronal field, thus preventing the release of particles entirely. On the occasions where prompt electron events are seen following type III bursts, (Lin, 1970) we interpret these as originating in a part of the corona with open field lines. Such a situation is perhaps the exception, rather than the normal.

CONCLUSIONS

We conclude that energetic particle storage is very likely to occur on the sun provided closed field lines or other suitable trapping configurations are present in the high corona. Although the attempted correlation of 169 MHz noise storms with 300 keV electron events may be tenuous, the same cannot be said with relation to moving type IV bursts. Therefore not only does the radio data provide evidence for magnetic arches, but it also indicates nonrelease of electrons. It is an interesting feature of solar events that although recurrent proton events are seen at 10 MeV, there is little evidence for recurrent electron events (McDonald et al, 1972). However, it has been shown that once in a storage region where ionization losses are

unimportant, loss mechanisms for electrons, either through synchrotron radiation or scattering into the sun, are much more severe than for protons. Leakage losses, on the other hand, are much greater for protons. It has been emphasized previously (Simnett, 1971) that of particles present in the storage region, it is normally only the protons that escape into interplanetary space.

A storage model offers a consistent solution to a wide range of different phenomena; without it the problems of explaining some observations with continuous acceleration and complex transport in interplanetary space appear overwhelming.

ACKNOWLEDGMENTS

REFERENCES

Anderson, K.A., 1969, *Solar Phys.* **6**, 111.

Datlowe, D., 1971, *Solar Phys.* **17**, 436.

Elliot, H., 1964, *Planet. Space Sci.* **12**, 657.

Fan, C.Y., Pick, M., Pyle, K.R., Simpson, J.A., and Smith, D.R., 1968, *J.G.R.* **73**, 1555.

Lin, R.P., 1970, *Solar Phys.* **12**, 266.

McDonald, F.B., and Desai, U.D., 1971, *J.G.R.* **76**, 808.

McDonald, F.B., Cline, T.L., and Simnett, G.M., 1972, *J.G.R.* **77**, 2213.

Newkirk, G., and Altschuler, M.D., 1970, *Solar Phys.* **13**, 131.

Riddle, A.C., 1970, *Solar Phys.* **13**, 448.

Rossi, B., 1952, *High Energy Particles*, Prentice-Hall, New York.

Schatten, K.H., 1970, *Solar Phys.* **12**, 484.

Simnett, G.M., Cline, T.L., Holt, S.S., and McDonald, F.B., 1970, *Acta. Phys. (Hungary)* **29**, Suppl. 2, 649.

Simnett, G.M., and Holt, S.S., 1971, *Solar Phys.* **16**, 208.

Simnett, G.M., 1971, *Solar Phys.* **20**, 448.

Simnett, G.M., 1972, *Solar Phys.* **22**, 189.

Smerd, S.F., 1970, *Proc. Astron. Soc. Austral.* **1**, 305.

Smerd, S.F., and Dulk, G.A., 1971, *Solar Magnetic Fields*, ed. R. Howard, 616.

Takakura, T., 1963, *Publ. Astron. Soc. Japan* **15**, 462.

Verzariu, P., and Krimigis, S.M., 1972, *J.G.R.* **77**, 3985.

Wild, J.P., 1969, *Solar Phys.* **9**, 260.

VIII: RADIO EMISSIONS
IN THE CORONA AND INTERPLANETARY SPACE

SOLAR RADIO BURSTS AT KILOMETER WAVELENGTHS

R.G. Stone and Joseph Fainberg

Laboratory for Extraterrestrial Physics
Goddard Space Flight Center

INTRODUCTION

The dynamic spectra of solar radio bursts are observed over the frequency range from 10 MHz to 30 kHz with satellite experiments located above the terrestrial plasmasphere. For traveling radio phenomena such as type II and type III bursts, this frequency band corresponds to emission occurring over the range from approximately 10 solar radii to one astronomical unit from the sun. The combination of ground-based and space observations offers the opportunity to study the properties of the corona and interplanetary medium as well as the propagation of energetic particles and shock waves from the photosphere out to 1 AU. Dynamic properties of the interplanetary medium, such as the large-scale magnetic field configuration, can also be studied, since the characteristic time scales involved are often long compared to the propagation time of the traveling radio event. In those instances where the disturbance producing the radio emission passes the vicinity of the earth, the radio observations can also be related to in situ field and particle measurements obtained by space probes.

The first section of this paper is a general survey of the characteristics of type III radio phenomena observed at hectometer and kilometer wavelengths. A brief discussion is also included here of the relationship between type I meter noise storms, decametric continuum, and type III hectometric storms. The second section deals with the analysis of type III bursts to show how these data provide information about the average energy, dispersion, and trajectory of energetic particles, as well as about the interplanetary density scale and magnetic field configuration. The third section is a brief description of the recent observations of type II shock wave phenomena at kilometer wavelengths. The summary outlines current research as well as the direction of future observations.

OBSERVATIONS OF TYPE III EVENTS

In contrast to the situation at short wavelengths where an array of complex radio phenomena is observed, radio emissions at hectometer and kilometer wavelengths consist essentially of type II and III traveling bursts. The complex emission at shorter wavelengths arises in part because of particle confinement in closed magnetic field configurations which can exist close to the sun. However, beyond ten solar radii, where the energy density of the expanding solar wind exceeds that of the imbedded magnetic field, an open field

configuration will occur. The energetic particles which produce type III emission can propagate through the interplanetary medium guided by such open field lines.

Indeed, except for the rare occurrence of a type II event, the prominent phenomena observed at long wavelengths are type III bursts occurring individually, in groups, and in storms. Within this type III classification, the variability of burst characteristics such as intensity, rise and decay time, drift rate, and bandwidth reflect dynamic conditions occurring in the medium, and the injection and propagation properties of the exciter particles.

Individual Bursts and Groups of Bursts

Conservatively estimated, many thousands of individual or groups of type III bursts, such as those shown in Figure 1, have been observed in the hectometer wavelength range during each year near the last solar maximum. The upper part of the figure illustrates computer-developed dynamic spectra, while the lower part of the figure shows the intensity profiles at six selected frequencies. These data were obtained with the Radio Astronomy Explorer satellite, RAE-1. The horizontal lines through the contour plots correspond to these frequencies, while the crosshatched region is the low frequency limit imposed by observing conditions for this experiment. Figure 1(a) illustrates typical rise, decay, and drift times for a simple type III burst in this wavelength region. Figure 1(b), showing a complex group of bursts, illustrates a common situation in which individual bursts tend to merge, particularly at lower frequencies.
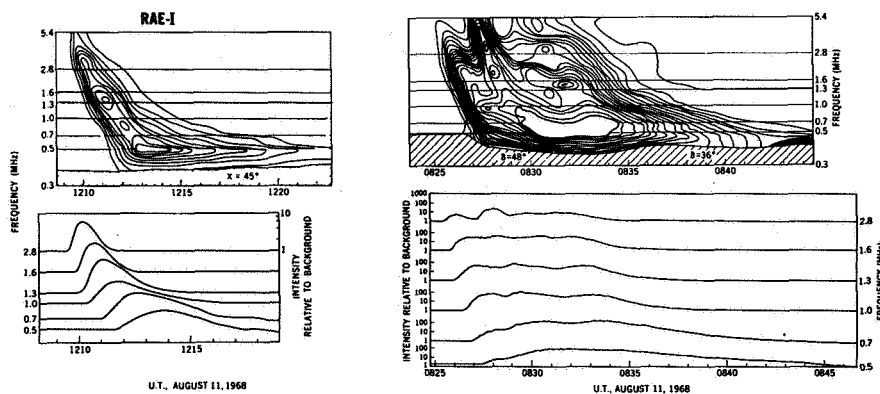

Figure 1. Dynamic spectra of type III bursts at the hectometer wavelengths observed with the RAE-1 satellite. The upper figure shows computer-developed dynamic spectra from 5.4 to 0.3 MHz with 1-db intensity contours. The lower figure shows the intensity profiles at six frequencies corresponding to the horizontal lines through the upper figure. (a). A single type III burst which is shown to illustrate typical rise, decay and drift times in this part of the spectrum. Figure (b). illustrates the complex structure resulting from the merging of groups of single events.

520

The spectral range over which type III bursts are observed depends on the trajectory over which the energetic particles propagate and also on the ability of the radio emission to reach the observer. For a large number of events, the burst can be observed over the entire spectrum from meter through kilometer wavelengths. Quite often, however, a burst observed at shorter wavelengths is seen over only a part of the long wavelength region, or not at all. The converse situation frequently occurs in which a long wavelength burst does not have a short wavelength counterpart. An example of a type III event observed only between 1 MHz and 30 kHz is shown in Figure 6, which is discussed in detail later. These cutoffs seem to be produced not by propagation conditions for the exciter particles but instead by the escape conditions of the radio emission relative to the observer. The influence of the interplanetary medium on the scattering, absorption, and refraction of the radio emission has been considered, for example, by Steinberg et al. (1971).

By far the majority of type III bursts observed in this part of the spectrum show a continual drift to lower frequencies, implying that the exciter particles travel outward along open field lines extending through the interplanetary medium. However, there are a few occasions where the dynamic spectra suggest more complicated field configurations. The example shown in Figure 2 may be recognized as a U-burst in which the emission drifts first to lower and subsequently to higher frequencies. This type of spectrum can be produced by exciter particles confined to move along a magnetic loop structure. Assuming an exciter speed of 0.3 c, the loop structure shown in Figure 2 is inferred, for which the turning point is located at about 35 solar radii (Stone and Fainberg, 1971). Less than ten U-bursts have been observed in the analysis of three years of RAE-1 data. This may imply that such large-scale magnetic bottles occur infrequently. On the other hand, the rarity of U-bursts may also be due to observational effects or exciter electron propagation conditions. Many bursts have an L-like dynamic spectra. These may be U-bursts with a poorly developed or no-return branch. There are also cases where a type III event drifts to a low frequency, dwells there for a short period of time, and then continues to drift down in frequency. This may imply a field configuration with a bend in its structure.

Storm Events

Type III storms are composed typically of thousands of individual drifting bursts superimposed on a continuum background component (Fainberg and Stone, 1970a, 1971b). The burst distribution shows a hierarchy of intensities with a preponderance of smaller sizes. The individual burst may exist over only a limited band of frequencies. In many ways the characteristics resemble those of type I meter storms. A number of storms have been observed for the whole transit across the disk of the associated active region. In some cases the storm activity is observed again when the active region reappears on the east limb. Figure 3 shows dynamic spectra for a storm in August 1968 when the active region is near central meridian, and when it is located about 60° east. Near central meridian, the observed occurrence rate of individual bursts is about one every ten seconds.
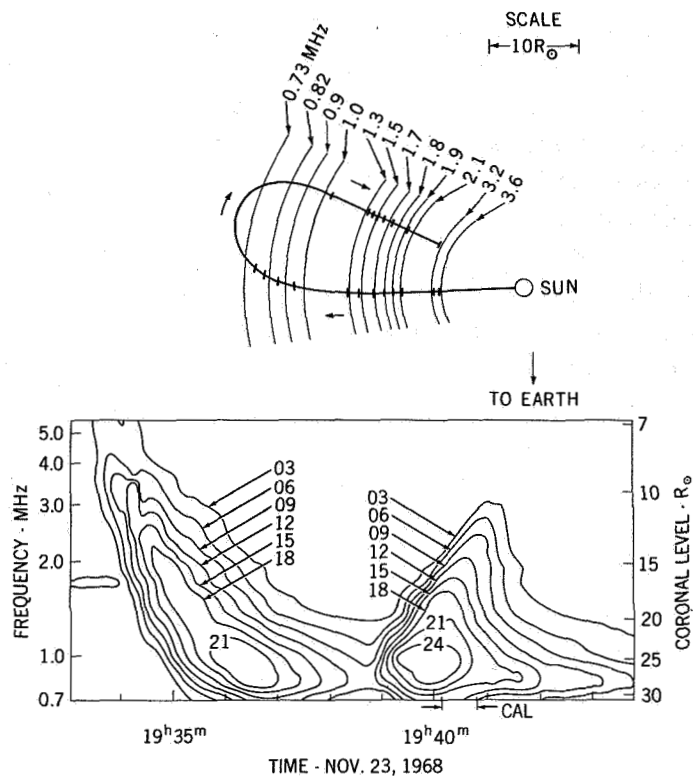
Figure 2. (a). Dynamic spectrum of a hectometer U-burst. Numbers on the figure indicate intensity in decibels relative to cosmic noise background. Note the frequency limit of the return branch. (b). The magnetic bottle inferred from the U-burst. The model is based on the RAE-1 density scale (see text) and an assumed exciter speed of 0.3 c. Bars on the figure show the positions determined from the dynamic spectrum relative to the start of the burst.

The distribution of continuum can be seen in Figure 4, which shows both the average and minimum flux observed at six frequencies for the August 1968 storm. The average flux consists of both the continuum and burst components. The minimum flux obtained by determining the enhancement of the smooth background (relative to the cosmic noise level) in the absence of bursts is a measure of the storm continuum component (Fainberg and Stone, 1971b). The data in Figure 4 also illustrate in a general way the dependence of observed storm activity on heliographic longitude. This type of decrease in activity away from central meridian passage (CMP) is expected as a consequence of a combination of radiation beaming and the influence of the medium on the propagation of radiation from source to observer (Steinberg, 1972). However, the data obtained from a single storm must be used with caution in attempting to study this effect quantitatively, because of the difficulty in separating time variations at the source from real longitude dependence.
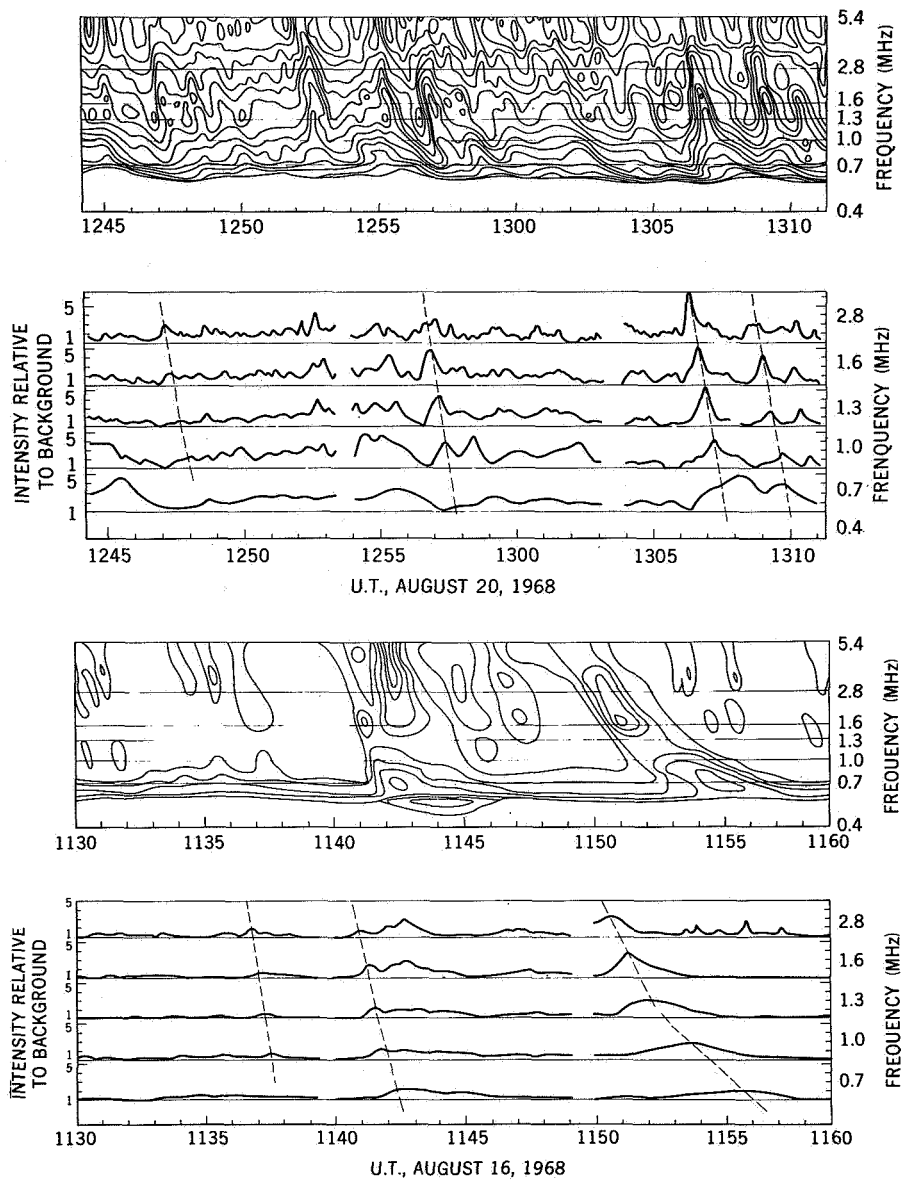
Figure 3. Dynamic spectra for the hectometer type III storm of August 1968.
(a) A 30-minute segment of data when the active region was approximately 60°
east of CMP. (b) A 30-minute segment of data observed near the peak of storm
activity close to CMP.

Relation to Shorter Wavelength Observations

A close correlation exists between hectometric storms and decametric continuum.
Apparently they are the manifestation of the same phenomenon, that is, the outward
propagation of energetic electrons producing radio emission at widely separated distances in
the corona and interplanetary medium. This clearly supports the contention of Warwick
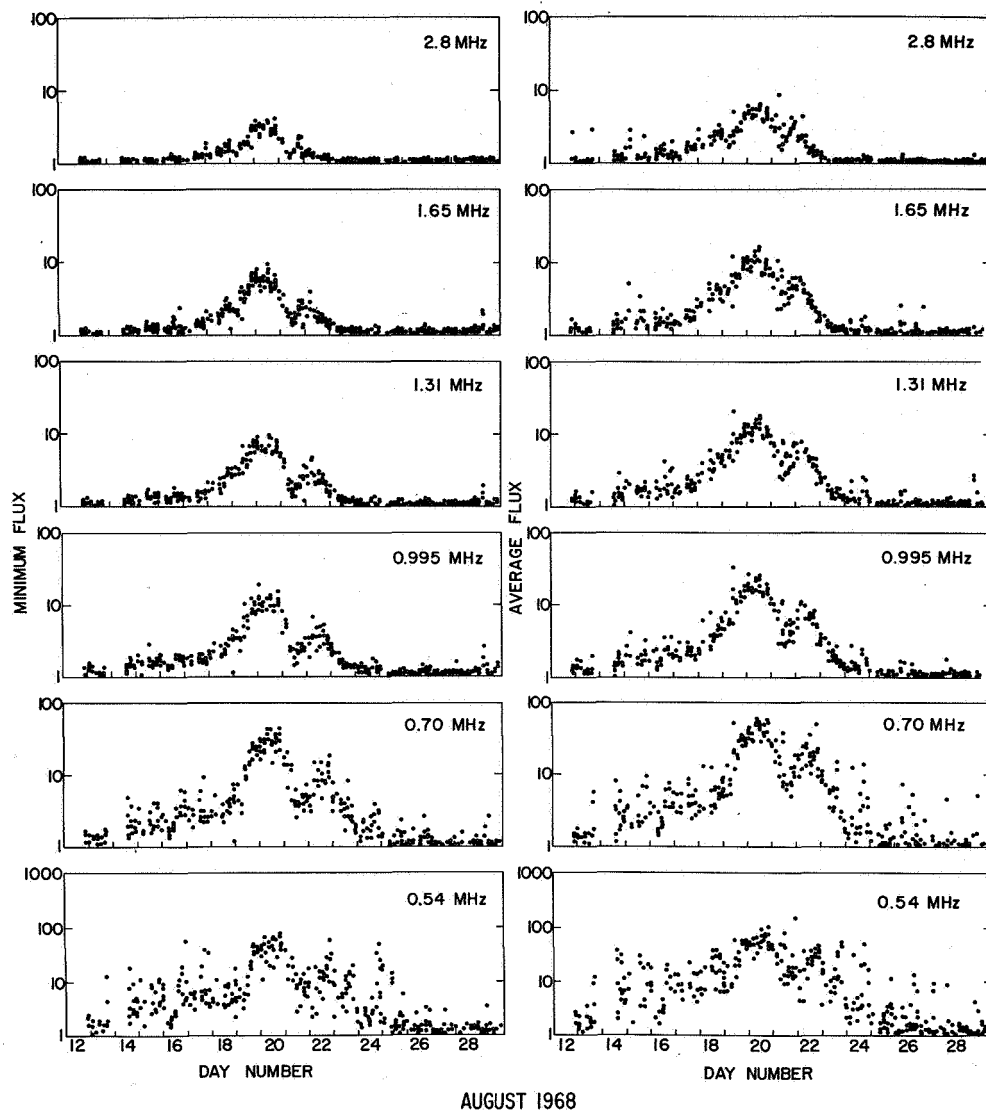
Figure 4. The average and minimum flux for the August 1968 storm as a function of heliographic longitude (day number) of the associated active region. The average flux consists of both continuum and burst components, while the minimum flux is essentially the continuum component alone.

(1965) that the occurrence of decametric continuum indicates the escape of exciter particles into the interplanetary medium. Furthermore, there is evidence that meter and decameter storms are also generated by these same electrons (Boischot et al., 1970). Thus a very close correlation should exist between meter and hectometer storm activity. Analysis of approximately one year of RAE-1 data from June 1968 to June 1969 shows in fact an almost perfect correlation between the occurrence of 169 MHz type I noise storm activity and 1.65 MHz hectometric type III storm activity. The important conclusion to be drawn from this observation is that the field configuration is such that at least some of the

electrons responsible for this type I emission are able to escape from the trapped region and propagate along channeled paths through the interplanetary medium where they are observed as long wavelength storm activity. There is also some support to the suggestion that these streams of exciter electrons do in many cases propagate along neutral sheets, that is, sector boundaries (Sakurai and Stone, 1971).

Judging from the large number of meter to hectometer storms observed during the years of maximum solar activity, it would appear that streams of superthermal electrons should be a common occurrence during such periods, although it must be noted that the density of particles in such streams is probably quite small (Evans et al., 1971) and they presumably do not contribute to the dynamics or heating of the solar wind.

ANALYSIS OF TYPE III BURSTS

Frequency versus Time Characteristics (Drift Rate)

The burst drift rates obtained from dynamic spectra can be analyzed to deduce the average exciter speed or the interplanetary density scale. Without some form of directivity, it is necessary to assume a model for one or the other of these quantities. Suppose that over the height range of interest the electron density N (cm^{-3}) variation with distance $R_\odot$ (solar radii) is represented by a power law

$$N = N_o R^{-\alpha} \tag{1}$$

Then the drift rate will be (Papagiannis, 1970)

$$\frac{df}{dt} = - \frac{\alpha\beta c f^{(\alpha + 2)/\alpha}}{2(1-\beta \cos\theta)\, R_\odot\, (81 \times 10^{-6}\, N_o)^{1/\alpha}} \tag{2}$$

where it is assumed that the exciter travels radially outward at a speed $\beta = V/c$, at an angle θ to the sun-earth line. From this equation it is clear that to deduce a density scale, the exciter speed and trajectory must be known or assumed. On the other hand, assuming a density scale, information about the average exciter speed or the particle trajectory can be deduced.

The combination of long term hectometric storm activity from the same solar active region and the dependence of burst drift rate on heliographic longitude provided a method of partially solving this problem. The drift rate effect, shown in Figure 5, can be understood in the following way: Suppose that an exciter moves radially outward from the limb position. The radio emission produced at two plasma levels whose frequencies are f_1 and f_2, where $f_1 > f_2$ is generated first at f_1 and, at a time Δt later, at f_2. For an observer near the earth, the propagation paths from the two plasma levels are essentially the same, so that the received radiation will be delayed approximately by the time Δt. On the other hand, for the same situation near CMP, the path lengths from the plasma levels to the observer will be different by an amount $\beta\Delta t$. Thus the radiation at f_1 will have to travel this additional path length to the observer. Thus the delay between radiation at f_1 and f_2 will be decreased and

the drift rate will appear shorter. This is the reason for the cos θ term in Equation 2. Utilizing this effect, a least squares analysis of 2500 bursts from the August 1968 storm was conducted by Fainberg and Stone (1970b, 1971a). From this analysis it was possible to show that the average exciter speed between 10 and 40 solar radii was 0.37c. Furthermore, a power law density scale of the form

$$N(R_\odot) \cong 5.52 \times 10^7 \, R_\odot^{-2.63} \tag{3}$$

was derived for the same height range. These results will be considered again in light of the recent IMP-6 directional observations.

In considering data such as that shown in Figure 4 at several frequencies, it was also noted that central meridian passage (CMP) as determined by the minimum drift rate, was delayed at lower frequencies. This is to be expected if the exciter moves outward along a nonradial path such as a spiral. The delay is consistent with an average solar wind bulk speed of 380 km/s.
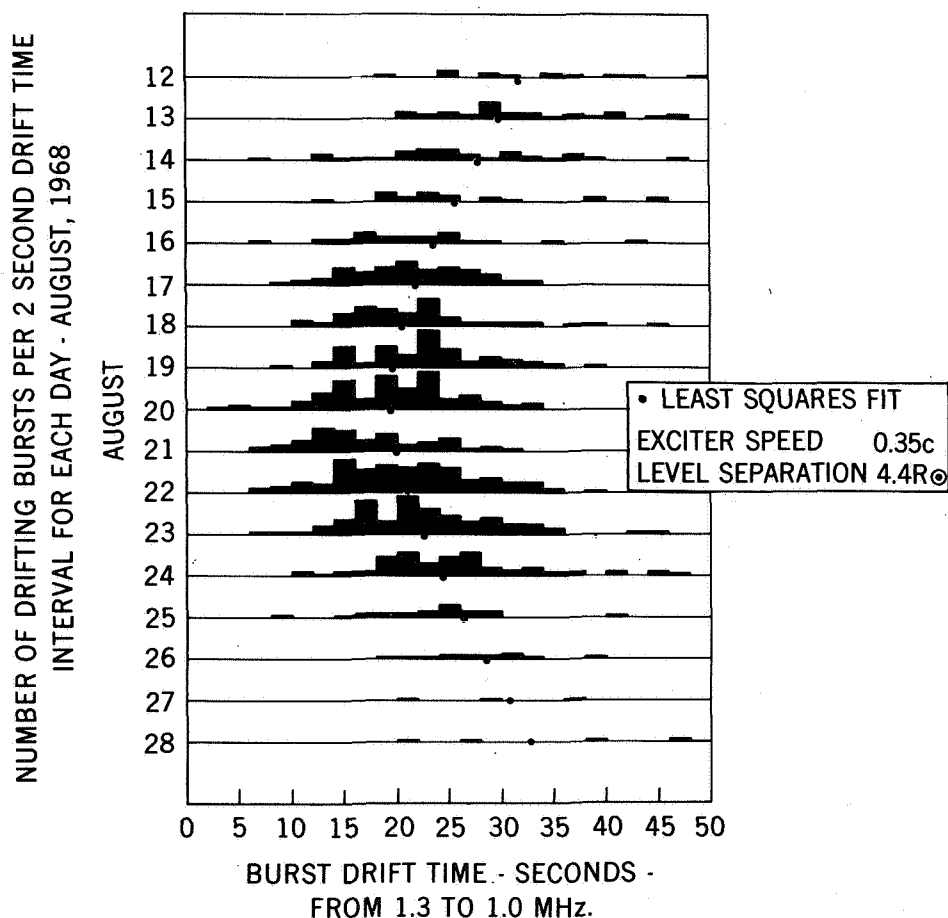
Figure 5. The dependence of burst drift rate between 1.3 and 1.0 MHz on heliographic longitude for the August 1968 storm. The least squares fit, indicated by black circles in the figure, gives a level separation of 4.4 $R_\odot$ and an average exciter speed of 0.35 c.

While the RAE-1 observations of dynamic spectra discussed above do not directly yield source size or direction, information about these parameters has been obtained recently from the IMP-6 radio experiment which gives dynamic spectra down to 30 kHz. This spacecraft is spin stabilized with the spin axis perpendicular to the ecliptic plane. The experiment dipole antenna spins in the ecliptic plane so that incoming signals from radio sources near the plane are modulated by the dipole reception pattern. If the known reception pattern function is cross-correlated with the received signal, and the phase adjusted for maximum correlation, this phase can be simply related to a reference direction such as the center of the sun. With this technique, source direction can be determined to an accuracy of one degree. An estimate of source angular size can also be obtained from the depth of modulation of the received signal. As the angle subtended by the source increases, the nulls of the reception pattern become filled in and the modulation decreases. There is an ambiguity associated with attempting to determine source angular size by this method because of the nature of a dipole reception pattern. It is not possible, for example, to uniquely determine whether one is observing a small source located out of the ecliptic or an extended source in the ecliptic, since both could result in the same percentage of modulation.

An example of a type III burst observed with the IMP-6 experiment to 30 kHz is shown in Figure 6, where the insert figure also shows the original spin modulated data at 250 kHz (Fainberg et al., 1972). Only the envelope of the bursts is shown in the main figure to clearly illustrate the drift of the burst as well as the systematic increase in rise and decay times. The time scale involved may be appreciated by noting that a type III burst which has a duration of seconds at meter wavelength lasts in excess of 3 hours at 30 kHz.

For this event, the directions of arrival have been determined between 737 kHz and 67 kHz. Above 737 kHz the burst amplitude was too weak to apply the analysis, while below 67 kHz there was insufficient modulation to apply the program. The absence of modulation is an indication of the nearness of the source to the observer and consequently its very large angular extent. The directions of arrival for the radio emission at the various frequencies are shown in Figure 7. In order to fix the position of the source in space, however, it is necessary to use a density versus distance scale, and to relate the emission frequency to the plasma frequency (or its second harmonic as discussed later). If the density scale derived from the RAE-1 observations is used and extrapolated to 1 AU, the trajectory shown as solid circles in Figure 7 is obtained. If, on the other hand, one simply chooses the point of closest approach of the direction line to the sun, the trajectory with open circles is obtained. In either case the curved trajectory of the exciter through interplanetary space is quite apparent. For the event depicted in Figure 7 an associated flare was not visible, suggesting an extreme west limb position of the event. Nor were there any high frequency type III observations, because for this case the escape conditions of the radiation would not allow high frequency radiation to reach the observer. By contrast, Figure 8 illustrates two type III bursts which are flare-associated. The arrows indicate the flare site. For the event near central meridian, the exciter path spirals far to the east, and the lowest frequencies are not observed because of the escape conditions for low frequency radiation.
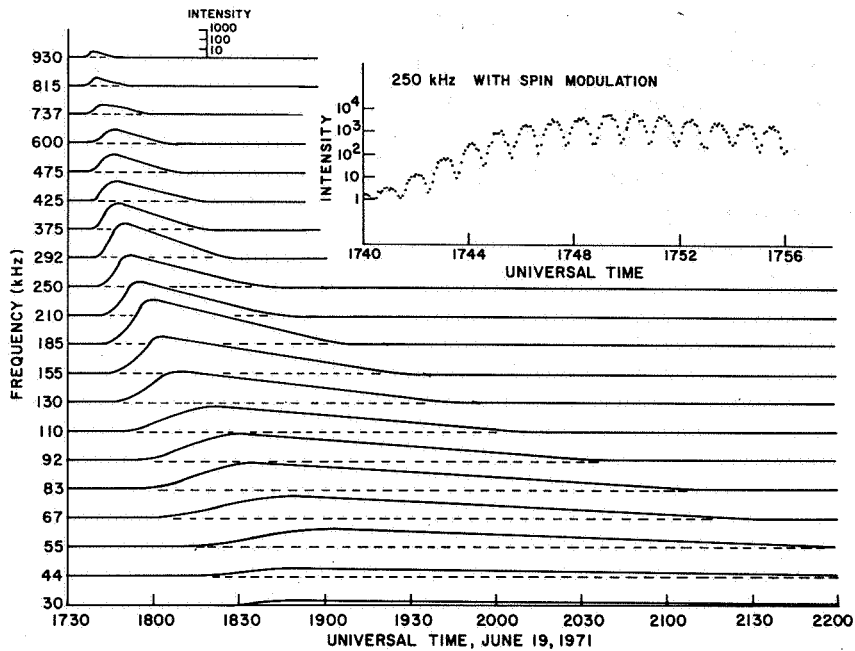
Figure 6. A type III burst observed between 1 MHz and 30 kHz by the
IMP-6 radio experiment. The insert figure illustrates the observed spin
modulation at a frequency of 250 kHz, while for the main figure, only
the burst envelopes are shown for clarity.

One of the perplexing issues has been the choice of an appropriate density scale for the interplanetary medium. This problem is summarized in Figure 9 (Fainberg et al., 1972) where the upper solid line is the density scale derived from the RAE-1 analysis (Equation 3) and extrapolated to 1 AU. This density is enhanced by a factor of about eight, relative to models of the ambient solar wind. It has been suggested for a number of years that type III bursts are observed when they propagate along enhanced density regions or streamers. The open circles in the figure are the density values corresponding to the open circle trajectory shown in Figure 7. The difficulty with these density scales is that they are not consistent with values obtained by other means such as in situ satellite measurements. To emphasize this point, the lower solid line in Figure 9 is an interpolated density scale which makes use of the density derived from light scattering observations at 10 solar radii (Michard, 1954; Blackwell, 1956; Blackwell and Petford, 1966) and in situ solar wind density measurements (long term average) at 1 AU (Hundhausen, 1968). If the radiation occurs at the plasma frequency, it is not possible to reconcile the discrepancy in density shown by these two curves. If, on the other hand, the emission occurs not at the plasma frequency but at its second harmonic, then the open circles in Figure 9 will map into the squares and the picture is more consistent. Although the second harmonic hypothesis is appealing, the issue is not yet decided. The analysis of a very large number of type III bursts in the long wavelength region has as yet shown no clear evidence for the occurrence of both fundamental and second harmonic emission. The second harmonic hypothesis has previously been proposed by Haddock and Alvarez (1971).
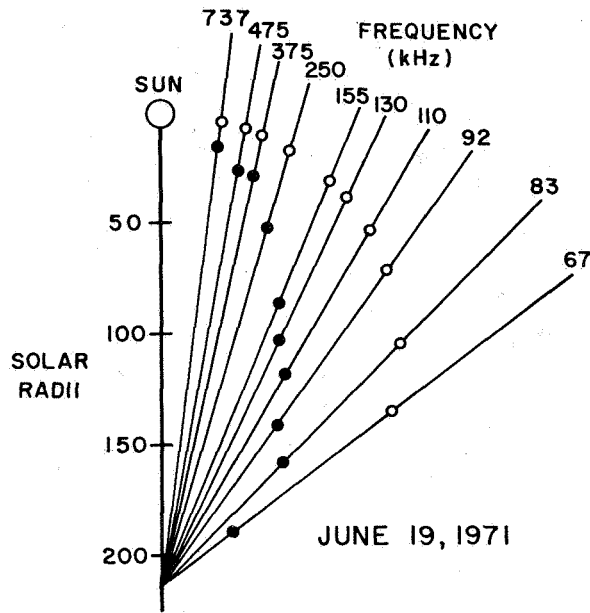
528

Figure 7. Directions of arrival (in the ecliptic plane) determined from the spin modulation for the burst in Figure 6. The trajectory shown by the black dots is fixed by using the RAE-1 density scale (see text). The trajectory shown by the open circles is determined by the distance of closest approach permitted by the arrival direction. The curved path of the interplanetary magnetic field can be seen in either case.

By utilizing the density scale and the measured drift time of the burst from one frequency to another, the speed of the exciter particles can be determined. These data are shown in Figure 10 for the June 19, 1971 burst. If the exciter consists of a packet of particles of different energies, then the burst onset, which should correspond to radiation produced by the faster particles, is shown by the upper set of points. The burst peak shown by the lower set of points more nearly represents the average speed of the exciter packet. It must be emphasized again that these results were obtained from the analysis of a single burst, and are presented here only to illustrate the order of magnitude of the exciter speed as well as the apparent deceleration of the exciter particles. If this were a real deceleration, it would correspond to a 75 percent loss of energy over 1 AU. On the other hand, if the particles undergo scattering, the radial component of speed would appear smaller and this is the only component determined by this method.

Intensity versus Time Characteristics

The time profile of a burst contains information about the properties of the exciter stream of particles and their interaction with the interplanetary medium. Specifically, parameters which can be investigated include the length of the exciter stream, the energy dispersion of
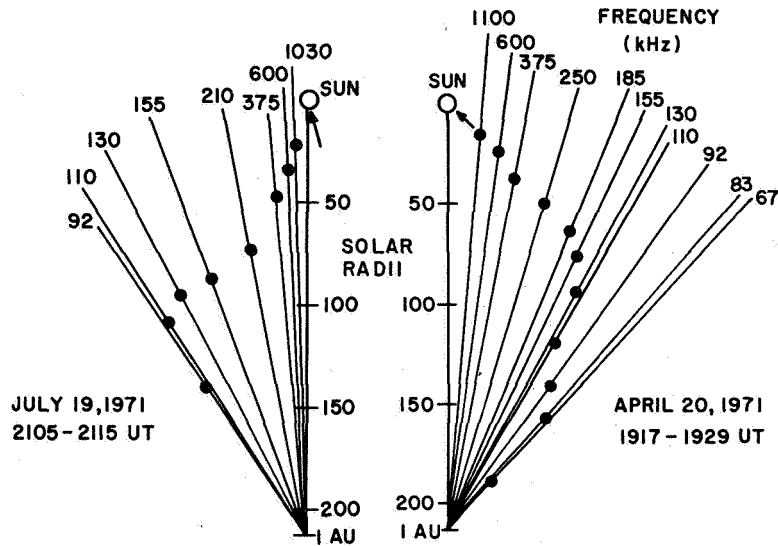
529

Figure 8. Two events which are flare associated. The arrows show the position of the flare site. The July 19 event also indicates the low-frequency cutoff (below 92 kHz in this case) observed for events whose trajectory is to the east of CMP. The anomalous positions at 92 and 110 kHz are probably caused by refraction in the medium.
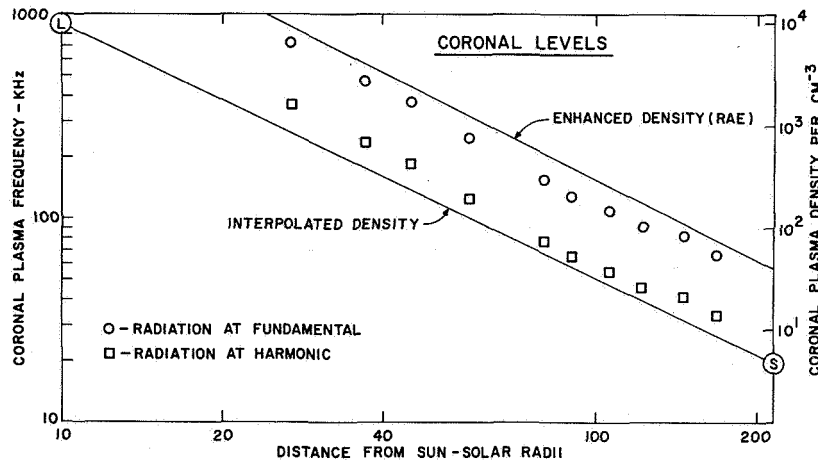

Figure 9. Interplanetary density and plasma frequency scale as a function of distance in solar radii. The interpolated density scale is given by a line between the value determined by light scattering observations, labeled L, and that from space probe measurements, labeled S. The circles are the density scale corresponding to the closest approach trajectory shown in Figure 7, assuming radiation occurs at the plasma frequency. These points map into the squares if radiation occurs at the second harmonic of the plasma frequency.
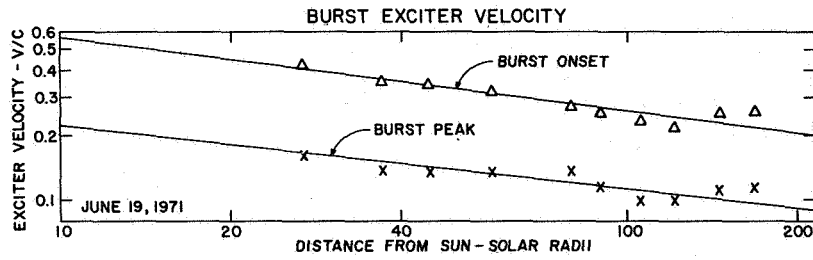
Figure 10. Average burst exciter velocity (v) divided by the velocity of
light (c), as a function of distance from the sun for the trajectory of
closest approach. Corrections were made for the travel time of light.
The burst onset times yielded the values labeled by triangles and
correspond to the faster particles in the exciter. The burst peak times
yielded the values labeled by X and correspond to particles producing
most of the radio burst energy. These results are based on the analysis
of only one burst, that shown in Figure 6.

the packet and the damping time of the radio emission. The problem of relating the
characteristics of a packet of particles to the properties of type III bursts has been
considered recently by Aubier and Boischot (1972). Provided that the particle packet is of
limited duration and that the decay of the radio emission is exponential, they show that the
intensity of the radio emission I(t) is related to the particle profile P(t′) and t, the
characteristic damping time, through the relation

$$I(t) = \int_{o}^{t} P(t') \; e^{-(t-t')/t} \; dt' \tag{4}$$

If the exciter ends at a time t* this equation becomes

$$I(t) = (\text{constant}) \; e^{-t/t} \quad \text{for } t > t^* \tag{5}$$

The time t* can be evaluated from a plot of ℓn I(t) versus t since the curve will be linear for
t > t*. Therefore the exciter duration can be measured as a function of plasma frequency,
and through a density model as a function of distance. If it is assumed that the emission
bandwidth is small, the exciter time duration at one frequency is directly related to the
exciter length. Evans et al., (1973) using RAE-1 and IMP-6 observations, have determined
the exciter duration in this manner and compared their results with mathematical models
for this quantity. One parameter that can be determined from this analysis is the velocity
dispersion $\Delta V/V$ which is found to increase with distance from the sun. However, in view of
the discussion in the previous section (see Figure 10) concerning the apparent decrease of
velocity with distance, these results are also consistent with a constant velocity dispersion of
the order of 0.4, at least for the low frequency data.

The damping frequency for the radio emission is obtained from the burst decay rates.
Particularly below 1 MHz, the burst decay is found to be exponential over a large intensity

range, which suggests that the damping is not a function of burst intensity or time. This suggests that the conversion to radio emission is also independent of these variables.

The mechanisms which have been proposed for the decay process are Landau and collision damping. However, the present formulations of Landau damping (Zaitsev et al., 1972) do not give results which show an exponential decay in time, and thus appear to be inconsistent with observations at long wavelengths. On the other hand, collision damping (Spitzer, 1962) has been utilized frequently to account for burst decay (Malville, 1962; Hughes and Harkness, 1963; Hartz, 1969; Alexander et al., 1969; Aubier and Boischot, 1972). The coronal temperatures derived by this means, however, appear to be too low (Hundhausen et al., 1970), although as pointed out by Evans et al. (1973), enhanced noncollisional coupling may explain the observed decay.

Comparisons have recently been possible between kilometer type III bursts and solar electron events in the 10 to 100 keV energy range. The evolution of the electron spectrum can be compared to that of the radio burst. Lin (1973) notes that the onset of the type III radio emission at a frequency of the order of 50 kHz corresponds to the onset of electrons with energies > 18 keV, and that the radio burst continues to increase until the peak disappears from the > 18 keV spectra. Continued correlations of this kind may eventually lead to an understanding of the type III radiation and beam stabilization process involving superthermal electrons (for example, Evans and Fainberg, 1973).

TYPE II BURSTS

The identification of type II emission at hectometer and kilometer wavelengths has occurred only recently (Malitson et al., 1973). The difficulties associated with the identification of type II bursts result from the low probability of occurrence of these events, and from their characteristics in the long wavelength region.

In the analysis of RAE-1 data, solar radio events were observed which showed slowly drifting structure with derived velocities of the order of 1000 km/s. However, this drifting structure did not appear to be an independent phenomenon but rather an enhancement, over a specific frequency range, of a group of type III bursts. As the series of type III bursts occurred later in time, the region of enhanced emission occurred at progressively lower frequencies. An example of such an event is shown in Figure 11 where the solid line through the sequence shows the region of enhanced emission as it drifts to lower frequencies. Note that for the latter part of the event enhanced emission is seen, although the lower frequency parts of the type III bursts are not observed. For the event shown in Figure 11, the velocity, assumed constant and obtained from the observed drift rate is about 1100 km/s, and extrapolates back to a flare which occurred at about 0953.

This type of enhanced drifting structure, observed in the decametric wavelength region by Lacombe and Møller-Pederson (1971), has been attributed to the effects of type III interaction with the shock wave. The physical conditions resulting from the shock-wave interaction presumably result in enhanced type III emission.
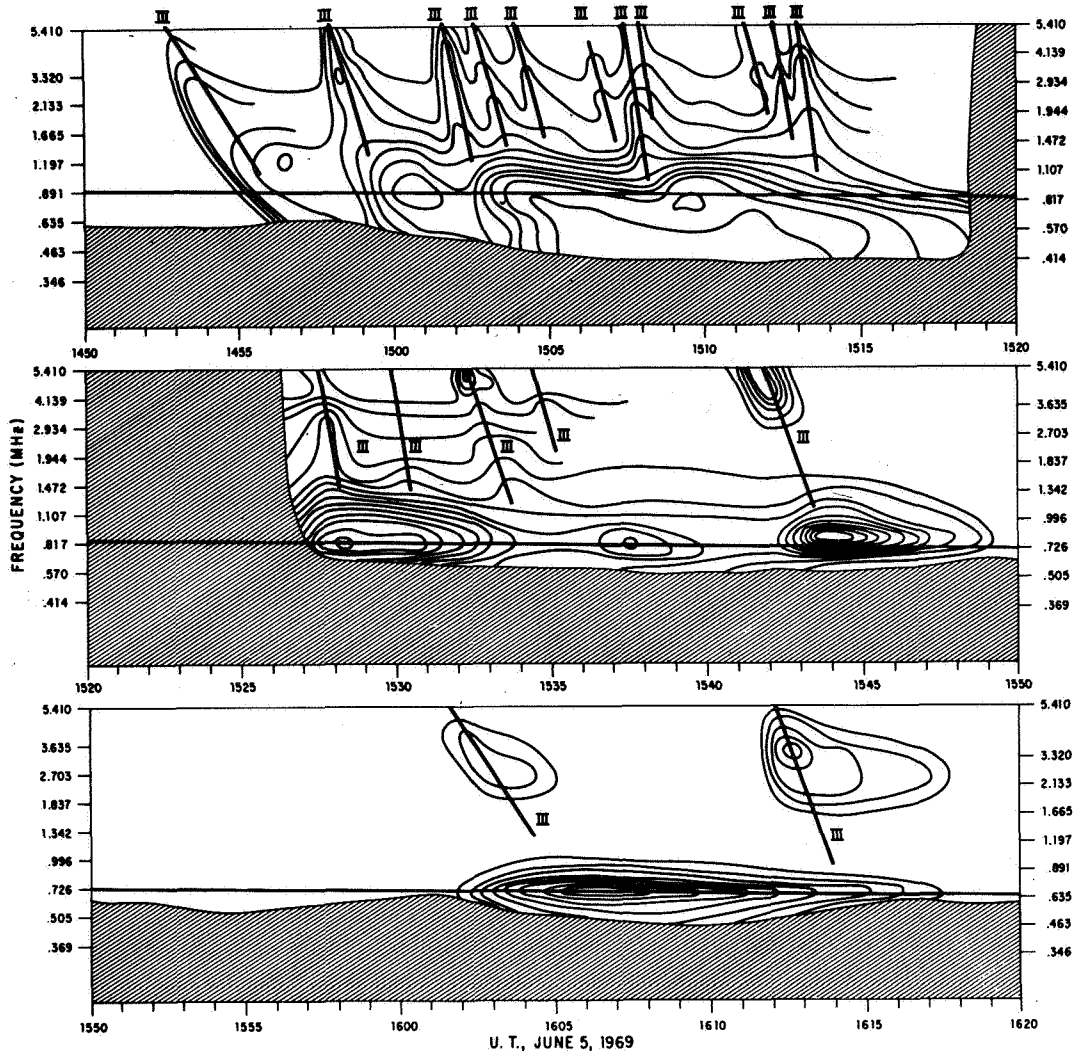
532

Figure 11. Dynamic spectrum of a slow-drift event, presumably a shock wave, which is illuminated by the passage of type III bursts. The line through the time sequence shows the enhanced region of emission and the drift to lower frequencies. Towards the end of sequence, the disturbance apparently is illuminated by the exciter particles, although the type III burst is not observed at the lower frequencies.

However, there now appears to be more direct evidence for type II emission which does not necessarily have this dependence on the existence of type III emission. Figure 12 illustrates a type II burst observed with the IMP-6 experiment for which both the fundamental and harmonic can be observed. The solid lines show the drift of the event through the time sequence. Although type III bursts occur within this time, it does not appear that they are necessarily associated with the type II event. The figure also illustrates that in this wavelength region, type II emission is not continuous; that is, it is observed only sporadically. This type II gives a drift rate of about 635 km/s and extrapolates back to a flare (at 0117) with a long duration, two maxima, and an unusually long X-ray emission.
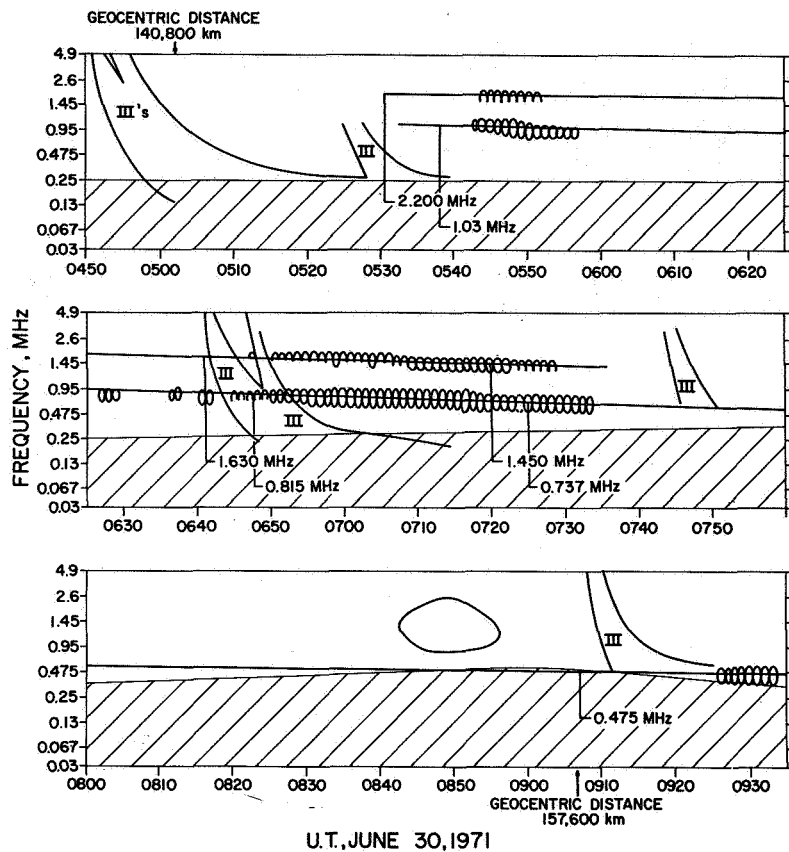
Figure 12. Dynamic spectrum of a type II slow-drift in which both the fundamental and harmonic are observed. The burst is observed sporadically, but is not necessarily dependent on the passage of a type III event for illumination. The intensity ovals of the type II burst are caused by the spin modulation. The similar modulation patterns of the type III bursts are omitted.

The results shown in this section are of a preliminary nature. It may well turn out that the shock wave phenomena shown in Figures 11 and 12 have different basic characteristics, for which one type of shock wave must be made visible by the passage of type III exciter particle, while the second type of shock wave is self-radiating.

CONCLUSION

The potential value of traveling solar radio bursts for the investigation of energetic particle propagation and for the probing of the interplanetary medium has been demonstrated. The most complete utilization of this technique must await a comprehensive theory of the emission processes involved. Certainly this is borne out in the case of type III bursts by the key questions concerning whether emission occurs at the fundamental or harmonic of the plasma frequency, as well as what processes are responsible for damping. The long

534

wavelength observations will certainly aid theoretical analysis, particularly since it is now possible to compare radio observations with field and particle measurements within the source region. Smith (1973) has considered the present state of knowledge concerning the type II and III emission processes.

The direction-finding capability, although giving only one-dimensional information, represents a major advance. Although a density scale must be used in conjunction with the directional data, it is now possible to track shock waves and energetic electron streams through the interplanetary medium. Currently the technique is being used to study dynamic changes in the large-scale magnetic field. Future experiments can extend the direction finding method to two and three dimensions. The two dimensional method would employ a dipole configuration which would scan in and out of the ecliptic plane. The three-dimensional extension requires two well-separated spacecraft and would permit the determination of emission regions through direct triangulation. Such experiments would have the capability of fixing the trajectory of radio bursts traveling out of the ecliptic plane. In this manner, through the remote sensing techniques of radio astronomy, a three-dimensional description of the solar wind and interplanetary magnetic field could be obtained in and out of the ecliptic between 0.05 and 1 AU from the sun.

REFERENCES

Alexander, J.K., Malitson, H.H., and Stone, R.G., 1969, *Solar Phys.* **8**, 388.

Aubier, M. and Boischot, A., 1972, *Astron. Astrophys.* **19**, 343.

Blackwell, D.E., 1956, *Mon. Not. Roy. Astron. Soc.* **116**, 57.

Blackwell, D.E., and Petford, A.D., 1966, *Mon. Not. Roy. Astron. Soc.* **131**, 399.

Boischot, A., de la Noë, J., and Møller-Pederson, B., 1970, *Astron. Astrophys.* **4**, 159.

Evans, Larry G., Fainberg, Joseph, and Stone, R.G., 1971, *Solar Phys.* **21**, 198.

Evans, Larry G., Fainberg, Joseph, and Stone, R.G., 1973, submitted to *Solar Phys.*

Evans, Larry G., and Fainberg, Joseph, 1973, presented at the Solar Physics Division, AAS Meeting, Jan. 8–10, 1973.

Fainberg, Joseph, and Stone, R.G., 1970a, *Solar Phys.* **15**, 222.

Fainberg, Joseph, and Stone, R.G., 1970b, *Solar Phys.* **15**, 433.

Fainberg, Joseph, and Stone, R.G., 1971a, *Solar Phys.* **17**, 392.

Fainberg, Joseph, and Stone, R.G., 1971b, *Ap. J.* **164**, L123.

Fainberg, Joseph, Evans, Larry G., and Stone, R.G., 1972, *Science* **78**, 743.

Haddock, F.T., and Alvarez, H., 1971, Bulletin AAS, 3(1),6 (Abstract).

Hartz, T.R., 1969, *Planet. Space Sci.* **17**, 267.

Hughes, M.F., and Harkness, R.L., 1963, *Ap. J.* **138**, 239.

Hundhausen, A.J., 1968, *Space Sci. Rev.* **8**.

Hundhausen, A., Bame, S., Asbridge, J., and Sydoriak, S., 1970, *J.G.R.* **75**, 4643.

Lacombe, C., and Møller-Pederson, B., 1971, *Astron. Astrophys.* **15**, 406.

Lin, R.P., 1973, These Proceedings.

Malitson, H.H., Fainberg, J., and Stone, R.G., 1973, *Astrophysical Letters,* in press.

Malville, J.M., 1962, *Ap. J.* **136**, 266.

Michard, R., 1954, *Ann. Astrophys.* **17**, 429.

Papagiannis, M.D., 1970, NATO Advanced Study Institute on Physics of the Solar Corona, Athens, Greece.

Sakurai, Kunitomo, and Stone, R.G., 1971, *Solar Phys.* **19**, 247.

Smith, D., 1973, These Proceedings.

Spitzer, Lyman, 1962, *Physics of Fully Ionized Gases,* (New York: Interscience Publishers).

Stone, R.G., and Fainberg, Joseph, 1971, *Solar Phys.* **20**, 106.

Steinberg, J.L., Aubier-Giraud, M., Leblanc, Y., and Boischot, A., 1971, *Astron. Astrophys.* **10**, 362.

Steinberg, J.L., 1972, *Astron. Astrophys.* **18**, 382.

Warwick, J.W., 1965, in *Solar System Radio Astronomy,* ed. J. Aarons (New York: Plenum Press).

Zaitsev, V.V., Mityakov, N.A. and Rapoport, V.O., 1972, *Solar Phys.* **24**, 444.

DECAY TIME OF TYPE III SOLAR BURSTS

Hector Alvarez and F. T. Haddock

University of Michigan

Type III bursts were observed by the University of Michigan radio astronomy experiment aboard the Orbital Geophysical Observatory-5 (OGO-5). The observing frequencies were 3.5, 1.8 MHz, 900, 600, 350, 200, 100, and 50 kHz. We analyzed 64 bursts that drifted to frequencies below 600 kHz between March 1968 and February 1970.

Decay times (from peak intensity to 0.37 of peak) were measured and combined with published data ranging up to about 200 MHz. Because of receiver saturation, our values are considered to be upper limits. Using Hartle and Sturrock's (1968) solar wind model, we computed collisional decay times for distances out to 1 AU. Comparison with observations reveals that the observed decay times increase with decreasing frequency but at a rate considerably slower than that expected from Coulomb collisions (see Figure 1). The observed decay time τ, seconds, varies with frequency f, Hz, approximately according to $\tau f^{1.0} = 10^{7.7}$. This discrepancy had been noticed before by other observers who at higher frequencies tried to deduce coronal temperatures; at 50 kHz the discrepancy in decay times attains a factor of about 100.

By fitting power functions to the computed and observed decay times, and using the local plasma hypothesis, we found that the ratio ρ of computed to observed values varies with heliocentric radial distance according to a power function $\rho = 3r^{0.7}$, assuming fundamental emission, and $\rho = 2r^{0.7}$, assuming second harmonic emission. This functional dependence is approximately valid between a few solar radii and 1 AU. It is similar to the ad hoc function $\rho = r^{0.7}$ used by Wolff, Brandt, and Southwick (1971) to increase the electron-proton collisional energy exchange, and make their theoretical results agree with the measurements of electron and proton temperature near the earth. The radio and theoretical results are quantitative and complement each other. Together they cover a continuous range of distances from the base of the corona to 1 AU. The similarity of the results suggests that they represent the same phenomenon whose nature is still unknown.
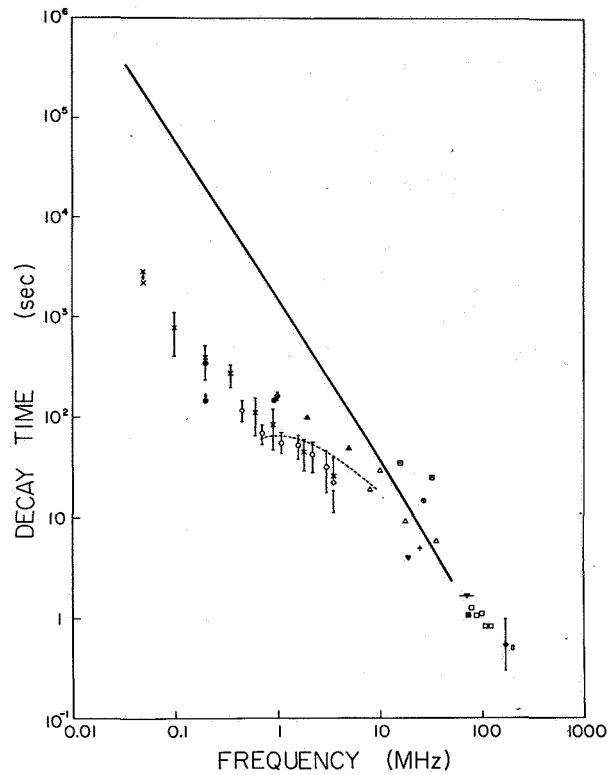
Figure 1. Decay times of type III bursts. The key to the authors is: X, this paper; ●, Slysh (1967); Δ, Boischot (1967); ⊡, Boischot *et al* (1960); ◊, Haddock and Graedel (1970); ▭, Elgaroy and Rodberg (1963); □, Wild (1950); ⊙, Riihimaa (1963); +, Malville (1962); ○, Alexander *et al* (1969); ■, Williams (1948); ◆, Bougeret; (1970); , De Jager and Van't Veer (1957); ▼, Payne-Scott (1949); ▲, Hartz (1964); ---, Hartz (1969). The solid line curve corresponds to values computed from Hartle and Sturrock's model, assuming collisional damping.

REFERENCES

Alexander, J.K., Malitson, H.H., and Stone, R.G., 1969, *Solar Phys.* **8**, 388.

Boischot, A., 1967, *Ann. Astrophys.* **30**, No. 1, 85.

Boischot, A., Lee, R.H., and Warwick, J.W., 1960, *Ap. J.* **131**, 61.

Bougeret, J. L., Caroubalos, C., Mercier, C., and Pick, M., 1970, *Astron. Astrophys.* **6**, 406.

De Jager, C., and Van't Veer, F., 1957 *IAU Symp. 4*, Ed. H. C. van de Hulst, 366.

Elgaroy, O., and Rodberg, H., 1963, *Astrophys. Norw.* **8**, 271.

Haddock, F. T., and Graedel, T. E., 1970, *Ap. J.* **160**, 293.

Hartle, R. E., and Sturrock, P. A., 1968, *Ap. J.* **151**, 1155.

Hartz, T.R., 1964, *Ann. Astrophys.* **27**, 831.

Hartz, T.R., 1969, *Planet Space Sci.* **17**, 267.

Malville, J.M., 1962, *Ap. J.* **136**, 266.

Payne-Scott, R., 1949, *Austr. J. Sci. Res.* A2, 214.

Riihimaa, J.J., 1963, *Ann. Acad. Sci. Fennicae*, Series A, **VI**, Physica, No. 131.

Slysh, V.I., 1967, *Sov. Astronomy*, **11**, 389.

Wild, J.P., 1950, *Austral. J. Sci. Res.* A3, 541.

Williams, S.E., 1948, *Nature* **162**, 108.

Wolff, C.L., Brandt, J.C., and Southwick, R.G., 1971, *Ap. J.* **165**, 18.

ON THE DENSITY OF THE CORONA IN REGIONS OF TYPE III ACTIVITY

T. B. H. Kuiper

Clark Lake Radio Observatory
Astronomy Program
University of Maryland

ABSTRACT

The east-west positions of 190 type III bursts have been measured between 30 and 65 MHz with the log-periodic array at Clark Lake. A method is described to find the intrinsic variation of position with frequency of type III bursts based on the comparison of the positions of the bursts measured at any two arbitrary frequencies. It is found that the variation of position with frequency agrees with the behaviour expected from coronal density models. This suggests that the measured positions were not seriously affected by scattering in the corona. Knowing the functional form of the variation of position with frequency for type III bursts, it is shown that the observed burst positions can be corrected for the effects of ionospheric refraction.

INTRODUCTION

Coronal Density in Active Regions

The density of the corona according to various models is plotted in Figure 1. Allen (1947) and van de Hulst (1950) have given essentially identical models for the corona in the equatorial regions at the maximum phase of the solar cycle, based on the observations of Baumbach (1937). More recently, Newkirk (1959) presented models for the quiet corona and for active regions based on K-coronameter observations taken around the 1958 solar maximum. Newkirk's model for the quiet corona has densities which are about twice those of Allen and van de Hulst.

In determining the density in active regions, Newkirk assumed that the active region could be described by a cone whose apex was at the center of the sun. The apex angle was taken to be 25 degrees. The enhancement of the electron density in the active region over that in the quiet corona was then found to be approximately a factor of two. The amount of enhancement is dependent, however, on the geometry assumed for the streamer.

In the height range relevant to the present observations ($\sim 10^7$ to 5×10^7 electrons cm^{-3}), all the models vary with radial distance from the center of the sun in the same way (see Figure 1). This variation can be described approximately as $N \propto R^{-6}$, which is similar to the empirical formula given by Allen (1947).
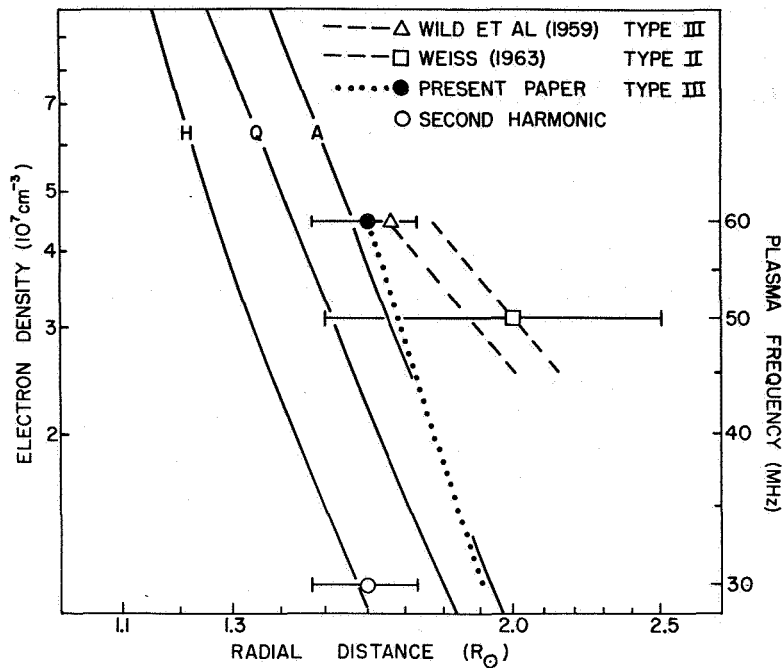
Figure 1. Various determinations of the coronal density near solar maximum. Models based on observations of the K-corona: H — Van de Hulst (1950) for a quiet corona, Q — Newkirk (1959) for a quiet corona, A — Newkirk (1959) for a streamer. Models based on radio observations are identified in the figure. (See text for an interpretation of the present results.)

Coronal Density from Radio Bursts

Wild, Sheridan, and Neylan (1959), for a large sample of type III bursts, plotted the difference between the positions at 45 and 60 MHz, p_{45} and p_{60}, as a function of the position at 60 MHz. They found that when the burst occurred on the east limb, the 45 MHz position was more easterly than the 60 MHz position, on the average. Similarly, the 45 MHz positions measured on the west limb were more westerly than the 60 MHz positions. They concluded that the 45 MHz radiation came from higher in the corona than the 60 MHz radiation. It was found that, on the average

$$\frac{p_{45} - p_{60}}{p_{60}} = 0.2$$

If we neglect possible effects of refraction and scattering in the corona, and of refraction in the ionosphere, and further assume that bursts move radially outward on the average, then

$$\frac{R_{45} - R_{60}}{R_{60}} = 0.2$$

541

where R_{45} and R_{60} are the heights of the radiation at 45 and 60 MHz, measured from the center of the sun. In the plasma hypothesis, the radiation occurs at the local plasma frequency, f_p (MHz) $= 9 \times 10^{-3} \sqrt{N}$. Let the coronal density fall as $N \propto R^{-\beta}$. Then

$$R \propto N^{-1/\beta} \propto f^{-2/\beta} \tag{1}$$

so that, for $(R_{45} - R_{60})/R_{60} = 0.2$, $\beta = 3$. These observations therefore suggested a corona in which density decreases more slowly with height than indicated by the models based on K-corona data.

By observing that the number of bursts seen at 60 MHz fell sharply for distances exceeding 1.66 $R_\odot$ from the center of the disk, Wild et al. (1959) deduced that $R_{60} \simeq 1.66 \, R_\odot$, or that N $(1.66 \, R_\odot) \simeq 5.5 \times 10^7$. Newkirk's model for a streamer gives a density of 3×10^7 for this height. It was concluded that type III bursts probably originated in coronal streamers.

Weiss (1963) made a similar analysis for 22 type II bursts measured between 1958 and 1961. He also found that $(p_{45} - p_{60})/p_{60} \simeq 0.2$, that is, that $\beta \simeq 3$, and suggested that Newkirk's streamer model was perhaps not correct above 2 $R_\odot$. Since the type II bursts analyzed were associated with flares, Weiss was able to show that $p_{50}/p_{flare} = 2 \pm 0.5$ for the fundamental bands, where p_{flare} is the east-west coordinate of the associated optical flare. Thus, $R_{50} = 2 \pm 0.5 \, R_\odot$, indicating a density which appears to be three times the density in Newkirk's streamer. The uncertainty in this determination is such, however, that the observed density could also be consistent with Newkirk's quiet corona model (see Figure 1).

In summary, these observations suggested that type III bursts originate in coronal streamers whose density at $1.5 - 2 \, R_\odot$ is about twice that of Newkirk's streamer model, and that the density in these streamers falls as R^{-3} instead of R^{-6}. When an electromagnetic wave propagates through a region whose plasma frequency is near the wave frequency, strong refraction occurs and even small inhomogeneities will cause considerable scattering of the radiation (Steinberg et al., 1971; Riddle, 1972). The effect of scattering is to make limb sources appear further from the center of the disk. This effect may be expected to be a function of frequency, and hence, since the radiation itself is close to the plasma frequency, of height in the corona. If scattering were more important at lower frequencies, it would explain the departure of the form of the radio-derived density model from that of the K-corona models.

OBSERVATIONS

The present observations of type III bursts were made with the log-periodic array at Clark Lake Radio Observatory. Sixteen log-periodic antennas are uniformly spaced over a 3300 meter east-west baseline. The antennas are lightly coupled at intervals of 219.99 ± 0.01

meters to a traveling wave transmission line having a velocity factor of 0.99932. It can be shown that a source with hour angle HA and declination δ would be located in one of the interferometer maxima if

$$f(MHz) = \frac{1.362695 \, k}{\sin \theta + 1.00062} \tag{2}$$

where $\sin \theta = \cos \delta \, \sin HA$, and k is an integer (Erickson and Kuiper, 1972). A swept-frequency receiver is scanned from 65 MHz to 20 MHz once per second and the receiver output is recorded on a facsimile record. By measuring the frequencies at which maxima of the response occur, the interferometer angle θ of the source is determined. Since as many as thirty different fringe orders, k, are measured, we are able to determine the position as a function of frequency. There is no difficulty in choosing the correct order for each fringe.

The data are observations of 190 type III bursts recorded in March and April of 1971. Insofar as we are able to separate them temporally, all bursts in a group were measured separately. We have attempted to distinguish type V bursts, and these have been eliminated from the data. For each burst, measurements of all the fringes yield the apparent displacements from the center of the sun as a function of frequency. To first order, we might assume that all the radiation comes from the same position in the sky, and that any variation of position with frequency is due to ionospheric refraction. The bursts are fitted to a function of the form

$$\rho = A + Bf^{-2} \tag{3}$$

where ρ is the apparent displacement from the center of the sun in solar radii, and A and B are suitable constants resulting from the fit. In this paper we will show that, on the average, type III bursts can better be fitted to a function of the form

$$\rho = A \, f^{-1/3} + Bf^{-2} \tag{4}$$

where the first term comes from the variation of frequency with height in the corona (see Equation (1)) and the second term represents ionospheric refraction. The data are also fitted to function (4). The parameters were stored on cards and used in the analysis to be described.

ANALYSIS

Geometry

If a type III exciter moves radially outward from the sun, then, as is demonstrated below, the component measured by the interferometer ρ bears the same proportion to the height R

543

at all frequencies. We derive below the relationship between ρ and R. Consider that the exciter moves radially outwards from a flare having a latitude λ and a meridian distance MD. Let us choose a sun-centered coordinate system in which z is the sun's rotation axis and the x-axis is chosen so that the earth is in the xz-plane. The position of a source at height R is then given by

$$\vec{R} = R \; [\; \cos \lambda \cos MD \; \hat{x} + \cos \lambda \sin MD \; \hat{y} + \sin \lambda \; \hat{z} \;]$$

Now let P denote the position angle of the axis of rotation measured counterclockwise from celestial north, B_o be the heliographic latitude of the center of the disk, and ϕ be the position angle of the interferometer fringes measured clockwise from celestial north. The position angle, ϕ, depends on the position of the sun,

$$\sin \phi = \tan HA_\odot \tan \delta_\odot$$

where $HA_\odot$ and $\delta_\odot$ are the hour angle and declination of the sun. If a coordinate transformation is made to a system where $\hat{z}'$ is aligned with the interferometer fringes and $\hat{x}'$ points towards the earth, then the interferometer measures

$$\rho = \vec{R} \cdot \hat{y}' = R \; [\; \cos \lambda \cos MD \sin (P+\phi) \sin B_o + \cos \lambda \sin MD$$

$$\cdot \cos (P+\phi) - \sin \lambda \sin (P+\phi) \cos B_o \;] \tag{5}$$

If the coronal density falls off with height as $N \propto R^{-\beta}$ and we observe the disturbance at the plasma frequency or its harmonic, then by Equation (1),

$$\rho \propto f^{-2/\beta} \tag{6}$$

Thus, using the assumption of radial motion and neglecting possible refraction and scattering in the corona, the observed position of the burst can be described by

$$\rho = Af^{-2/\beta} + Bf^{-2}$$

where the second term represents ionospheric refraction. Choosing $\beta = 6$ according to the coronal models led to the choice of Equation (4) to fit the measured $\rho(f)$ values. We will verify that this choice is correct.

Average Variation of Position with Frequency

Let the average variation of position with frequency for a type III burst have the form

$$\rho = Af^{-\alpha} + \overline{B} f^{-2}$$

544

where A is unspecified and related to the direction of motion of the exciter, $\bar{B}$ describes the average ionospheric refraction, and α, the intrinsic variation of position with frequency of type III bursts. Consider a type III burst, which we will label i, whose position has been measured at two frequencies, f_1 and f_2. Then

$$\rho_{1i} = A_i f_{1i}^{-\alpha} + B_i f_{1i}^{-2}$$

$$\rho_{2i} = A_i f_{2i}^{-\alpha} + B_i f_{2i}^{-2} \tag{7}$$

where A_i now represents the position of the burst on the disk and B_i the ionospheric refraction at the time of observation. On the average, we expect that

$$\left(\frac{\rho_1}{\rho_2}\right) = \frac{A f_1^{-\alpha} + \bar{B} f_1^{-2}}{A f_2^{-\alpha} + \bar{B} f_2^{-2}}$$

Thus, given the measurement ρ_{2i}, we would expect that

$$\rho_{1i} = \left(\frac{\rho_1}{\rho_2}\right)_i \rho_{2i} = \frac{A_i f_{1i}^{-\alpha} + \bar{B} f_{1i}^{-2}}{A_i f_{2i}^{-\alpha} + \bar{B} f_{2i}^{-2}} \rho_{2i}$$

where A_i is found from solving the set of Equations (7). In any particular case, however, ρ_{1i} will be larger or smaller, depending in part on the measurement error, but more importantly on the ionospheric refraction at the time of observation. In order to determine the best values of α and $\bar{B}$, we minimize the quantity

$$\chi^2 = \sum_{i=1}^{N} \frac{1}{\sigma_i^2} \left[\left(\frac{\rho_1}{\rho_2}\right)_i \rho_{2i} - \rho_{1i} \right]^2 \tag{8}$$

where σ_i is the standard deviation of the difference $\langle\rho_1/\rho_2\rangle_i \, \rho_{2i} - \rho_{1i}$, obtained by propagating the errors of the measured positions. It can be shown that

$$\sigma_i^2 = \sigma_{\rho_{1i}}^2 \left[\frac{\rho_{2i} f_{2i}^{-2}}{\xi_{2i}} \left(f_{1i}^{-\alpha} - \left(\frac{\rho_1}{\rho_2}\right)_i f_{2i}^{-\alpha} \right) - 1 \right]^2$$

$$\sigma_{\rho_{2i}}^2 \left[\frac{\rho_1}{\rho_{2i}} - \frac{\rho_{2i} f_{1i}^{-2}}{\xi_{2i}} \left(f_{1i}^{-\alpha} - \left(\frac{\rho_1}{\rho_2}\right)_i f_{2i}^{-\alpha} \right) \right]^2 \tag{9}$$

where $\xi_{2i} = (\rho_{1i}\, f_{2i}^{-2} - \rho_{2i}\, f_{1i}^{-2})\, f_{2i}^{-\alpha} + \bar{B}\, f_{2i}^{-2}\, (f_{1i}^{-\alpha}\, f_{2i}^{-2} - f_{1i}^{-2}\, f_{2i}^{-\alpha})$. The quantity χ^2 is minimized by searching parameter space for the best values of α and $\bar{B}$.

This procedure was used on a set of 190 type III bursts observed in March 1971. For convenience in the data processing, the bursts were fitted to Equation (3) and the parameters, along with their standard deviations, were stored on cards. In a subsequent processing, the positions at the highest and lowest observed frequencies for each burst were generated from the parameters. These were used to generate χ^2 according to Equation (8). A minimum value of χ^2 was found at $\alpha = 0.285 \pm .045$ and $\bar{B}/(60\ \text{MHz})^2 = -0.0175 \pm .0075$. From this result it is apparent that Equation (4) is better than Equation (3) for fitting type III bursts. Strictly speaking, we should use $\alpha = 0.285$ instead of $\alpha = 0.333$ in Equation (4) but the slight difference between these functions is not significant.

To confirm this result, the procedure was repeated using positions interpolated from Equation (4). Figure 2 shows contours of χ^2 plotted versus α and $\bar{B}/(60\ \text{MHz})^2$ for this case. A minimum value of $\chi^2 = 10220$ occurred at $\alpha = 0.26 \pm .04$ and $\bar{B}/(60\ \text{MHz})^2 = -0.016 \pm .0075$. We note that reduced χ^2 is much greater than unity, so that the standard deviations, σ_i, used in Equation (8) underestimate the true dispersion of the data from the best fit. The σ_i were based solely on the measurement errors in the positions, and more scatter is apparently introduced by the ionosphere. To evaluate positional uncertainty due to random ionospheric refraction, the positional uncertainty was redefined by

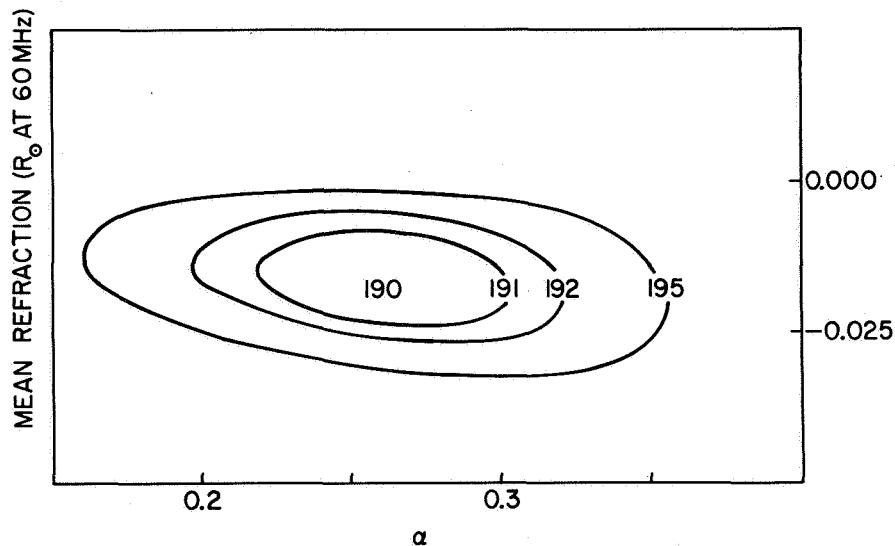$$\sigma_\rho^2 \to \sigma_\rho^2 + (\sigma_B^2\, f^2)^2$$

Figure 2. Contours of χ^2 as a function of α and $\bar{B}/(60\ \text{MHz})^2$. The contour units are $(\chi^2/\chi_{min}^2)\ *N$, where $N = 190$, the number of data points in the sample. The standard deviations of the parameters are determined by contour 191.

546

assuming that the excess in χ^2 is attributable solely to the ionosphere. These new standard deviations were propagated by means of Equation (9) to obtain new σ_i's. It was found that the minimum value of reduced χ^2 became unity for $\sigma_B/(60 \text{ MHz})^2 = 0.1 \text{ R}_\odot$. Thus, at 60 MHz, we do not find a significant systematic refraction, but there is a random component with a dispersion of about $0.1 \text{R}_\odot$.

Variation of Coronal Density with Height

In a simple interpretation which neglects refraction and scattering in the corona, we would relate α directly to β (see Equation (1)) which would have a value of 7.8 ± 1.2. This agrees very well with the value of $\beta \simeq 6$ which is based on the coronal models. Our result does not agree with the value of $\beta \simeq 3$ deduced from previous radio observations (Wild et al., 1959; Weiss, 1963). The suggestion by Weiss that the coronal models might fail above 1 $\text{R}_\odot$ is not borne out.

On the assumption that the amount of scattering of radiation is a function of frequency, and hence of the height of emission, it would appear that scattering did not play an important role in the bursts observed. Only if the source displacement due to scattering scaled as $f^{-\alpha}$, where $\alpha \simeq 1/3$, would the effect have been undetected in the data. There are two reasons why the effects of scattering might not have been detected. It is possible, and indeed likely, that the bursts observed near the limb were predominantly harmonics. Wild et al. (1959) have noted that the percentage of recognizable harmonic pairs increases from the center of the disk to the limb. The sudden drop of recognizable pairs at the limb is attributed to the absence of fundamentals, whose radiation is directed more or less radially outwards from the sun by the refractive properties of the corona. The other possibility is that type III radiation is generated in regions of enhanced density, that is, streamers. In this case, when the radiation emerges from the streamer, its frequency could be sufficiently above the local plasma frequency that the effects of scattering would be diminished.

Mean Height of Type III Bursts at 60 MHz

Of the groups of bursts observed, four coincided with flares published in *Solar Geophysical Data* (1971). Examination of the Big Bear Solar Observatory Hα films yielded three more. In Figure 3 the positions of the flares in the direction of resolution of the array, computed using Equation (5), are plotted versus the burst positions corrected for refraction (see following section). Assuming that the exciters moved radially from the flare, we conclude that $\text{R}_{60} = 1.6 \pm .13 \text{ R}_\odot$. In Figure 1, the height of the bursts is plotted for the cases of fundamental band and second harmonic radiation. The height of the bursts at 60 MHz agrees with the height determined by Wild et al. (1959) to within experimental error. If the bursts measured near the limb are predominantly fundamental band, then the type III sources must have occurred in regions of enhanced density (see previous subsection). In this case, the density appears to correspond to Newkirk's streamer model (1959).

Since harmonic radiation is favoured for limb sources, because of the refractive properties of the corona, it seems likely that the bursts measured were predominantly harmonics, and
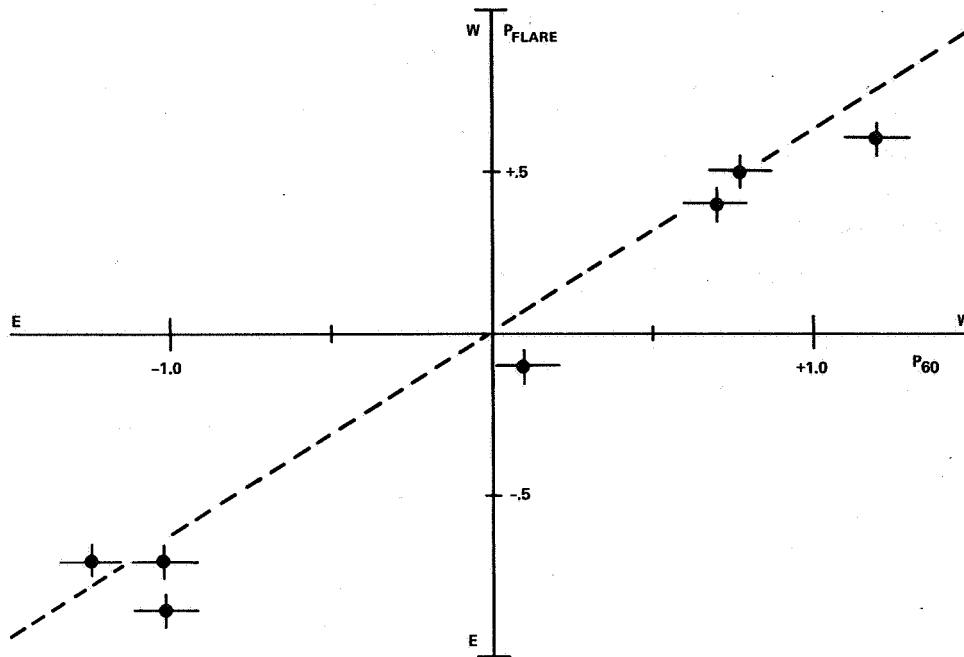
Figure 3. Positions of the associated flares, p_{flare}, measured from the center of the sun in the direction of resolution of the array in solar radii, versus the 60 MHz positions of groups of type III bursts, p_{60}. The best slope, given by the dashed line, is $p_{60}/p_{flare} = 1.6 \pm 0.13$.

that the observed height corresponds to the 30 MHz plasma level. Smerd et al. (1962) and Stewart (1972) have shown that harmonic radiation appears from a lower position in the corona than its true position, as if reflected from near the plasma level. Thus, the true height of the source cannot be known until detailed model calculations are made. In this case, however, the possibility that the source occurs in a region of normal coronal density cannot be ruled out.

CORRECTION FOR IONOSPHERIC REFRACTION

In the previous section it was shown that the variation of position with frequency for type III bursts is well described by Equation (4). If the departure of the exciter's trajectory from the radial is not large, then A should represent the component of the burst's path in the direction of the array axis, while B represents the amount of ionospheric refraction suffered by the burst. If the technique is successful then $A \, f^{-1/3}$ should be a better representation of the burst's position than ρ. For demonstration we have selected the activity of March 9, 1971, when the path of the exciters appeared to be nearly perpendicular to the line of sight, in order to minimize the possible scatter due to nonradial motion. In Figure 4, the 60 MHz position lines of the type III groups are plotted before correcting for refraction (that is, ρ_{60}). Also plotted are the position lines for which the refraction-corrected positions $(A * (60 \text{ MHz})^{-.33})$ were determined to an accuracy of 0.1 $R_\odot$ or better. In the latter case, the scatter is significantly reduced.
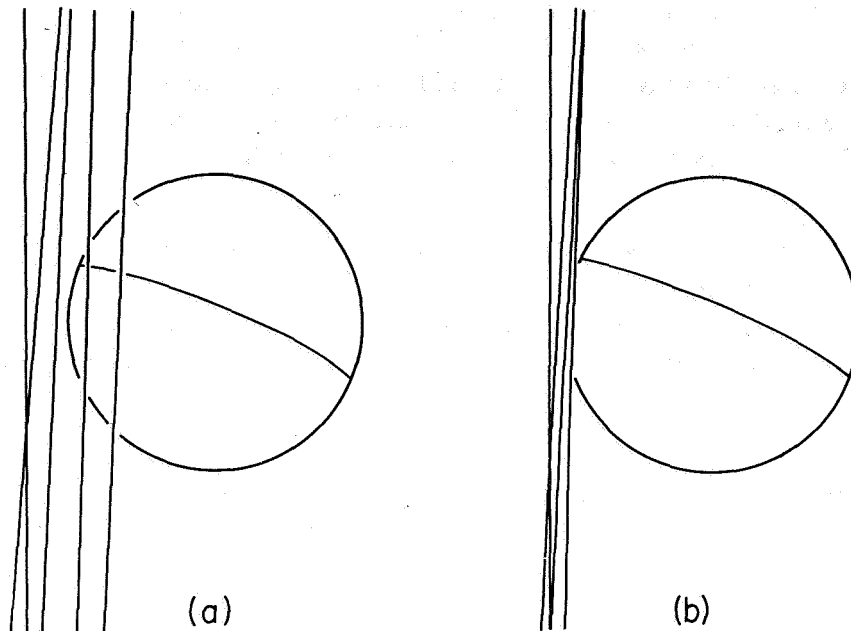
548

Figure 4. Correction of positions of type III bursts for ionospheric refraction.
The position lines measured for groups of type III bursts on March 9, 1971,
are shown relative to the sun (a) including ionospheric refraction, and (b)
with ionospheric refraction removed. Celestial north is at the top of the
figure. The solar equator is also shown.

CONCLUSION

A method has been developed to find the intrinsic variation of position with frequency for
solar radio bursts, based on the comparison of the positions measured at two frequencies.
Unlike the method of Wild et al. (1959), the two frequencies need not be the same for all
the bursts. Such a method is necessary for instruments, such as the Clark Lake radiohelio-
graph now under construction, which are continuously tunable over a wide frequency range
and therefore will not always observe at the same frequencies.

The method has been applied to 190 type III bursts observed at Clark Lake in March 1971.
It is found that the position of type III bursts varies as the (0.26 ± .04)th power of
frequency. If one neglects effects of refraction and scattering in the corona, then this
implies that the coronal density decreases with radial distance as the (7.8 ± 1.2)th power.
This result differs from those reported previously (Wild et al., 1959; Weiss, 1963). The good
agreement between the observed functional dependence and that of models based on
K-corona observations implies that coronal scattering did not significantly affect the
positions observed for the bursts. It is concluded that events near the limb are either
predominantly second harmonics, or that the bursts occurred in regions of enhanced
density.

549

By comparing the positions of the type III bursts with the positions of associated flares, and assuming that the exciters moved radially from the flare site, it was found that the average radial distance of the bursts was $1.6 \pm 0.13 \, R_{\odot}$. Because of the difficulty in knowing whether a burst was observed at its fundamental frequency or its second harmonic, and of assessing the effects of refraction and scattering, it is not possible to know the actual density. Both the streamer and the quiet corona models are consistent with these observations.

Since the intrinsic dependence of type III positions on frequency is about $f^{-1/3}$ and the amount of ionospheric refraction varies as f^{-2}, one can separate these two terms if the burst has been observed with sufficient accuracy over a range of frequencies. We have shown that, in this way, the observed positions can be corrected for the effects of ionospheric refraction.

ACKNOWLEDGMENTS

REFERENCES

Allen, C. W., 1947, *MNRAS* **107**, 426.

Baumbach, S., 1937, *Astr. Nachr.* **263**, 121.

Erickson, W. C., and Kuiper, T. B. H., 1972, Clark Lake Radio Observatory preprint.

Newkirk, G., 1959, *Paris Symposium on Radio Astronomy,* R. N. Bracewell, ed., Stanford, 149.

Riddle, A. C., 1972, *Proc. Astron. Soc. Austral.* **2**, 98.

Smerd, S. F., Wild, J. P., Sheridan, K. V., 1962, *Austral. J. Phys.* **15**, 180.

Solar Geophysical Data, 1971, **325**, *Part II, 3.*

Steinberg, J. L., Aubier-Giraud, M., Leblanc, Y., and Boischot, A., 1971, *Astron. Astrophys.* **10**, 362.

Stewart, R. T., 1972, *Proc. Astron. Soc. Austral.* **2**, 100.

Van de Hulst, H. C., 1950, *Bull. Astron. Inst. Neth.* **11**, 135.

Weiss, A. A., 1963, *Austral. J. Phys.* **16**, 240.

Wild, J. P., Sheridan, K. V., Neylan, A. A., 1959, *Austral. J. Phys.* **12**, 369.

A STORM OF TYPE III BURSTS OBSERVED BY RAE-1 IN AUGUST 1968

Edward G. Howard

Martin Marietta Corporation (Denver)

ABSTRACT

Curves of the number of type III bursts as a function of time are presented for six fixed frequencies (2.8, 1.65, 1.31, 0.995, 0.700, and 0.54 MHz). The curves peak at approximately 0500 UT August 20, 1968, and are symmetrical on both sides. Sakurai (1971) has shown that this time correlates well with the CMP of the McMath Region 9597. The maximum rate of bursts is approximately 150 per hour at the higher frequency of 2.8 MHz. Over 20,000 bursts were counted during the 15-day period from August 13 to August 27 when the active region was visible to the earth. A least-squares normal curve has been fitted to the observational data and calculations of variance and standard deviation are given.

DISCUSSION

The RAE-1 (Explorer-38) satellite was equipped with more than one type of radiometer. However, the present analysis was done using data from the 37-meter dipole antenna and the fixed-frequency burst radiometers (BRs). The fixed frequencies were 2.8, 1.65, 1.31, and 0.995, 0.70, and 0.54 MHz. Each channel was sampled by the telemetry system twice a second. Every 10 minutes additional measurements were made for calibration. Details of the antenna and radiometer systems can be found in Weber et al. (1971). The morphology of type III solar radio burst storms observed at hectometer wavelengths has been described by Fainberg and Stone (1970).

Even though the RAE-1 spacecraft was in a circular orbit at 5860 kilometers inclined 59 degrees to the equator, this orbit was within the ionosphere for a considerable time. To ensure the highest quality data for comparison at all six frequencies, only data frames were used when the spacecraft was above 30-degrees geomagnetic (GM) latitude. The 30-degree value was chosen after preliminary study of the data, to minimize possible effects of high ambient plasma density and changes in antenna impedance at the lowest frequency, 0.54 MHz. The only disadvantage of using data of the 30-degree GM or greater value was a loss of time resolution. Although the data are continuous throughout the orbit, with the latitude restriction above, resolution is limited to six frames of 10-minute duration each, during every orbit—that is, every 3 hours, 46 minutes.

Although the procedure used to analyze burst data was direct, it required counting over 20,000 bursts for the six frequencies. Since no convenient method was found to automate the procedure, burst counts were done visually and the numbers tabulated by hand using the procedure described in the following paragraphs.

First the time period of August 10 to August 30, 1968 was examined. Prior to August 13 and beyond August 27 no storm bursts above background could be detected. Within the 15-day period from August 13 to August 27, the times when the spacecraft was above 30-degree GM latitudes were found. These 92 periods are termed data windows and Table 1 shows the universal times of these periods. For each of the six channels (corresponding to the six fixed frequencies) there were six, 10-minute frames per window.

All separate bursts that could be recognized above the background intensity level of that particular frame were counted and cataloged, and certain counting precautions were taken. These included covering other frequencies when counting one, so adjacent frequencies would not influence the visual count. Duplicate counts of data windows were made at different times to insure counting consistency. Frames were also counted in and out of chronological sequence to prevent time trends.

Table 1

Start Times for 6 Satellite Windows Shown for Each Day of the August 1968 Type III Storm. Times Shown Are the Start of the First of 6 Successive Data Frames of 10 Minutes Duration for Each Frame.

Date 1968	Start Times of Frames Greater than 30° GM							Consecutive Data Windows
	Windows							
13 Aug.	0122 UT	0420	0816	1203	1540	1926	2303	1-7
14 Aug.	0300	0646	1024	1400	1806	2143		8-13
15 Aug.	0120	0517	0850	1240	1617	2003	2330	14-20
16 Aug.	0336	0723	1110	1447	1823	2210		21-26
17 Aug.	0157	0524	0930	1257	1654	2040		27-32
18 Aug.	0017	0443	0750	1137	1524	1900	2247	33-39
19 Aug.	0224	0620	1017	1344	1721	2117		40-45
20 Aug.	0104	0441	0827	1214	1551	1947	2324	46-52
21 Aug.	0301	0648	1044	1421	1888	2145		53-58
22 Aug.	0141	0518	0905	1251	1638	2015		59-64
23 Aug.	0001	0348	0725	1112	1508	1845	2223	65-71
24 Aug.	0218	0615	0942	1318	1715	2052		72-77
25 Aug.	0029	0455	0802	1158	1545	1922	2318	78-84
26 Aug.	0245	0642	1019	1405	1742	2148		85-90
27 Aug.	0205	0520						91 & 92

The average number of bursts per 10-minute frame was calculated for each of the 92 data windows. This was just the total number of bursts for six frames divided by six. These averages were then plotted as the data points shown in Figures 1 through 6 corresponding to the six fixed frequencies.
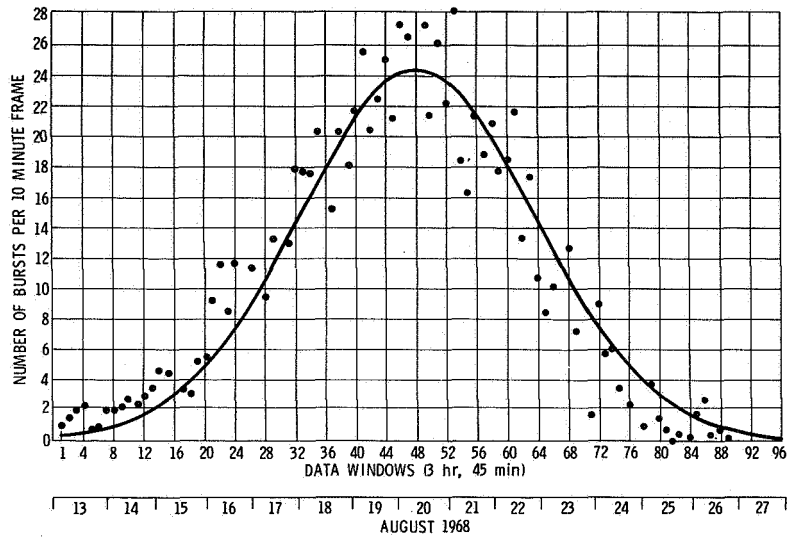

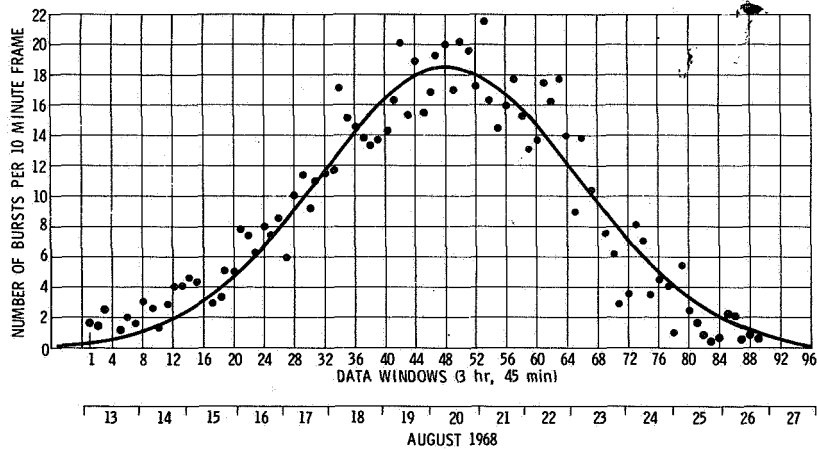Figure 1. Number of type III bursts versus time, frequency = 2.8 MHz.

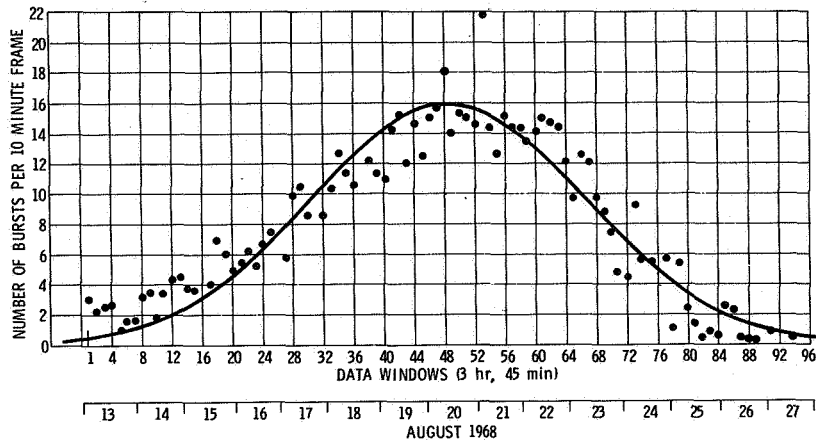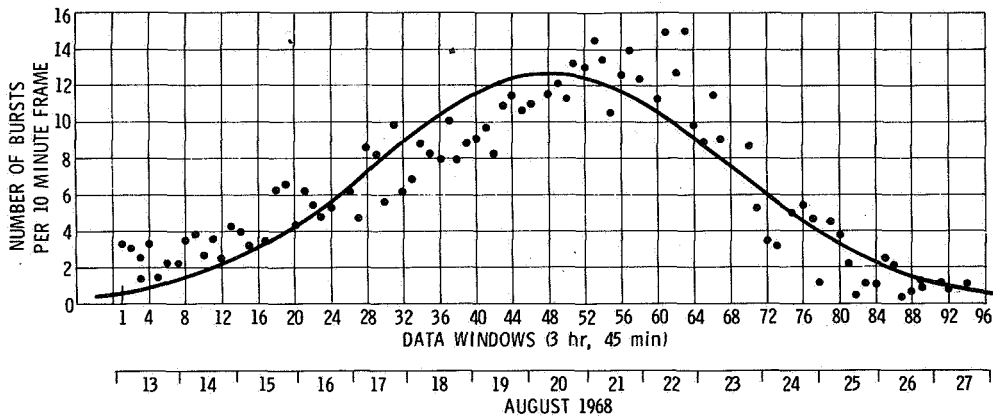Figure 2. Number of type III bursts versus time, frequency = 1.65 MHz.

554

Figure 3. Number of type III bursts versus time, frequency = 1.31 MHz.

Figure 4. Number of type III bursts versus time, frequency = 0.995 MHz.

It would be possible to convert time of the burst's occurrence to their approximate heliocentric longitude positions by using CMP at 0500 UT August 20 and a rate of 13.2 degrees per day corresponding to the active region location of 16 degrees south latitude. However, the curves are left in time of the 92 data windows—time window 1 corresponds to 0122 to 0222 UT August 13, time window 47 to 0441 to 0541 August 20 as can be found from Table 1—with the windows running consecutively from 1 to 92. The approximate date in days in August 1968 is also shown on the curves.

A normal curve fitted to the data points for each frequency is shown by the solid line. Values of skewness and kurtosis that differed very little from those of a normal curve were found. Numerical values corresponding to the curves are given in Table 2.
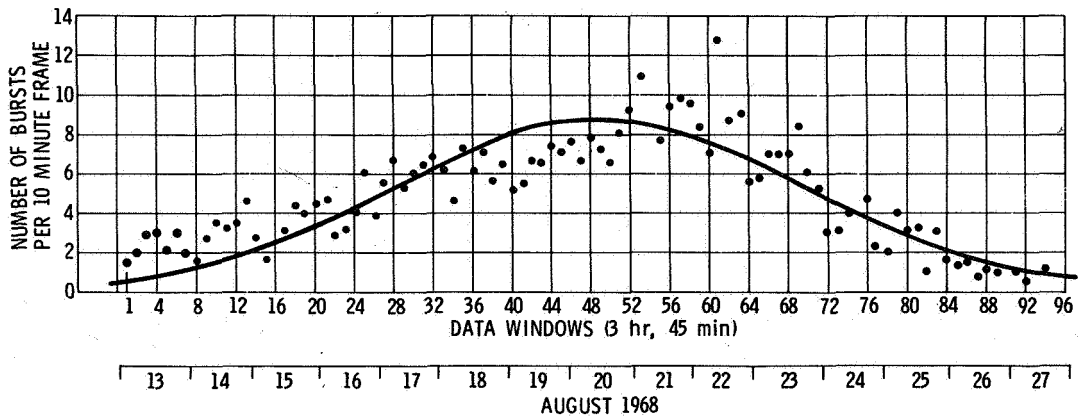
Figure 5. Number of type III bursts versus time, frequency = 0.70 MHz.
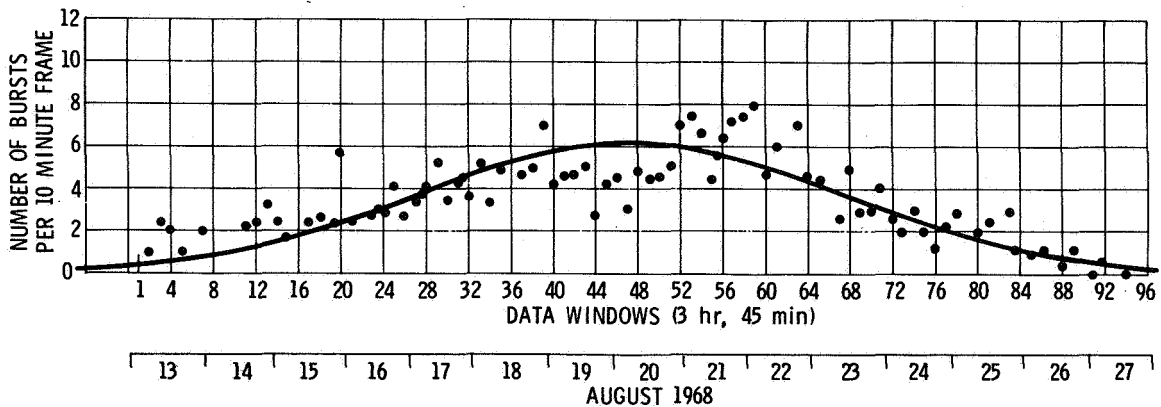

Figure 6. Number of type III bursts versus time, frequency = 0.54 MHz.

The time of maximum of the fitted curves agrees well for all six frequencies (that is, the time of maximum differs by only a little more than the time between data points). Although the observational data points show some scatter, it is not expected they could be further smoothed. The peak of curve 1 indicates about 150 bursts per window. One could expect a variance of $\sqrt{150} \approx 12.2$, that is, a variation of ≈ 2 per 10 minutes. This is approximately the variance shown on the curves.

These curves are believed to be as accurate as may be obtained from spacecraft observations of a type III storm of this kind. Such number distribution curves have not been readily available before from ground-based or spacecraft observations. From the ground, such type III number distribution curves often suffer from insufficient numbers and tend to be from different regions resulting in nonhomogenous data. It is hoped that Figures 1 thru 6 will prove useful to other investigators of type III bursts and refraction and scattering in the solar corona. A physical explanation of these curves will be published elsewhere (Howard et al., 1973).

556

Table 2

Results of Normal Curve Fitting for the Number VS Time Distribution Curves
of Figures 1 Thru 6.

Frequency, MHz	Time of Maximum, Hours UT	Maximum No. of Bursts per 10 Minutes	Width of Normal Curve at 1σ (60.6% of Maximum)
	20 Aug 1968		hours
2.8	05:04	24.38	59.2
1.65	05:31	18.45	64.8
1.31	06:12	15.95	68.6
0.995	05:45	12.70	72.9
0.700	07:47	8.74	78.0
0.540	03:10	6.16	76.0

ACKNOWLEDGMENTS

REFERENCES

Fainberg, J., and Stone, R.G., 1970, *Solar Phys.* 15, 222.

Howard, E.G., Stone, R.G.,and Fainberg, J., 1973, to be submitted to *Solar Phys.*

Sakurai, K., 1971, *Solar Phys.* 16, 125.

Weber, R.R., Alexander, J.K., and Stone, R.G., 1971, *Radio Sci.* 6, 1085.

TYPE II AND TYPE III BURST THEORY

Dean F. Smith

High Altitude Observatory
National Center for Atmospheric Research (Boulder)

ABSTRACT

The present state of the theory of type III bursts is reviewed by dividing the problem into the exciting agency, radiation source, and propagation of radiation between the source and the observer. In-situ measurements indicate that the excitors are electron streams of energy about 40 KeV which are continuously relaxing. A theory which takes into account both Landau damping by the background plasma and the stream itself, both of which are important at low frequencies ($\sim$ 500 KHz) does not exist. An investigation of neutralization of an electron stream indicates that $n_s \leqslant 10^{-5} n_e$, where n_s is the stream density and n_e the coronal electron density. In situ observations are consistent with this result. An analysis of propagation of electrons in the current sheets of coronal streamers shows that such propagation at heights greater than 1 $R_\odot$ is impossible. The mechanisms for radiation are reviewed; it is shown that fundamental radiation at high frequencies ($\sim$ 100 MHz) is highly beamed in the radial direction and that near the earth second harmonic radiation must be dominant. Because of beaming of the fundamental at high frequencies, it can often be quite weak near the limb so that the second harmonic is dominant. In considering propagation to the observer, the results of scattering of radiation are discussed. It is concluded that the whole question of inferring densities from type III bursts needs to be reexamined taking into account dominant second harmonics near the limb at high frequencies, dominant second harmonics everywhere at low frequencies and scattering.

The present state of the theory of type II bursts is reviewed in the same manner as type III bursts. The exciting agency is a collisionless shock wave with Alfven Mach number $M_A \gtrsim 2$ whose plane makes a slight angle (for example, 3.5°) with respect to the magnetic field. This allows only fast electrons created in the shock by ion-acoustic turbulence to escape ahead of the shock and form a beam. The beam relaxes leading to highly nonthermal plasma waves. Radiation near the fundamental is relatively weaker than in type III bursts because it can be amplified less, and second harmonic radiation is stronger because of a more isotropic distribution of plasma waves. Apparently, backward radiation near the second harmonic may be dominant in some cases because of absorption of direct radiation in the shock.

INTRODUCTION

The theories of type II and, especially, type III solar radio bursts are in a state of rapid development due both to the stimulus of better measurements at high ($\sim$ 100 MHz) and low

558

(~ 500 kHz) frequencies, and to recent developments in plasma physics. Thus our intent here is to present and comment on developments in the last five years, and to indicate what remains to be done rather than to present finished theories which do not exist at the present time. Although there are many differences, both observationally and theoretically, between type II and type III bursts, the radiation is due to conversion of electron plasma waves into radiation in both cases (Wild, Sheridan, and Neylan, 1959; Weiss, 1963). This link provides the rationale for considering these bursts together. No attempt will be made to review the observations of type II and type III bursts here except for those points directly connected to theoretical developments since this has already been done by Wild (1973) and Stone (1973).

For both type II and type III bursts, we can divide the theory into three parts — the nature of the source of plasma waves, the mechanisms of conversion of plasma waves into radiation, that is, the nature of the radiation source, and the propagation of radiation from the source to the observer. Thus the plan of this paper is to consider these three parts in turn for both bursts, starting with type III bursts since they are in many ways simpler.

TYPE III BURSTS — NATURE OF THE EXCITING AGENCY

Until very recently (Lin, 1973), there was no firm evidence to support either an electron or proton stream hypothesis for the exciting agent for type III bursts. The spectra of type III bursts were or could be interpreted as implying an excitor with a constant velocity (Stewart, 1965; Alexander, Malitson, and Stone, 1969). This was taken as evidence by several theoreticians (Kaplan and Tsytovich, 1967; Smith, 1970a, b; Melrose, 1970b) that the exciting stream must be stabilized, that is, the two-stream instability must be suppressed. Since analyses (Zheleznyakov and Zaitsev, 1970a; Smith and Fung, 1971) showed that proton streams were favored for such stabilization, proton streams appeared more attractive from a theoretical viewpoint (Smith, 1970b). It was not readily apparent how a relaxed electron stream could lead to a source with an apparently constant velocity, although it was known that such a source limited in space and time would continue to be unstable relative to the production of plasma waves (Baldwin, 1964; Zheleznyakov and Zaitsev, 1970a).

We now have firm evidence of an electron stream which has perfect time correspondence with a simultaneously measured type III burst (Figure 8 of Lin, 1973). Although 50 MeV protons are also often present at the time of type III bursts (McDonald and Van Hollebeke, 1973), their flux is too low to excite sufficient numbers of plasma waves to explain the observed bursts. Thus, we conclude on the basis of our present knowledge that electrons must be the exciting agent. Moreover, since electron streams cannot be stabilized (Zheleznyakov and Zaitsev, 1970a; Smith and Fung, 1971), the stream must be relaxed to the extent that it has time to relax at each point in the corona. Clearly the beam observed by Lin (Figure 8 of Lin, 1973) has not relaxed very much initially because the relaxation rate is very slow due to the low beam density (~10^{-7} cm^{-3}). We see that as the beam density increases, the extent to which the beam appears to be relaxed (spread towards lower velocities) also increases. Using the assumption of a completely relaxed beam everywhere (Figure 1), Zheleznyakov and Zaitsev (1970a) treated the case of an electron exciter at high frequencies (~ 100 MHz) where

559

collisions constantly remove slow electrons, leading to continuous reformation of a weak beam. It was not, however, apparent from their analysis why the speed of the excitor should appear constant. Using the same assumption of a completely relaxed beam (Figure 1), Zaitsev, Mityakov and Rapoport (1972) treated the case of an electron exciter at low frequencies (~500 kHz). At the head of the beam fast electrons are continuously overtaking slow electrons, leading to the reformation of a weak beam and production of plasma waves. At the tail of the beam there is a dearth of fast electrons so that to maintain a plateau (Figure 1), the slower electrons must absorb energy from the plasma waves. However, this model does not reproduce the decay phase of low frequency type III bursts properly (Fainberg, private communication).
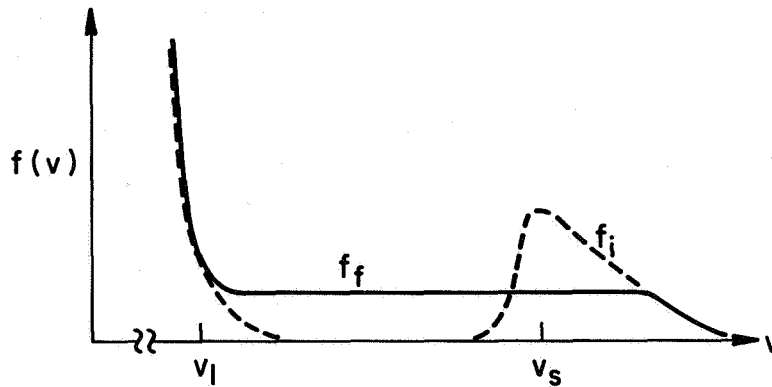

Figure 1.   Electron distribution function before (dotted) and after (solid) quasi-linear relaxation. In the completely relaxed state f_f, a plateau is formed from the initial beam of velocity v_s.

Recently, Harvey and Auber (1972) have shown that at low frequencies (<3 MHz) Landau damping of plasma waves by the background corona is much more important than collisional damping. Their analysis does lead to an exponential decay which is what is observed at low frequencies, but with an abrupt cutoff which occurs after a time comparable with the observed e-folding time. This cutoff has not been observed.

We might hope that inclusion of Landau damping by both the exciting stream and the background corona would lead to results more consistent with observations. This remains to be done. Even so, we might ask if this were done, what physics would we be leaving out of the problem and to what extent is it important? For example, how is the stream neutralized and to what extent is the stream guided by a current sheet? The problem of neutralization was treated by Smith (1972a) who showed that a large amplitude plasma wave would be excited at the head of the stream, the amplitude being dependent on the ratio of stream density n_s to the background plasma density n_e. This analysis showed that unless $n_s < 10^{-5}$ n_e, the amplitude would be sufficiently large to cause significant stream deceleration which has not been observed. It is possible that the large amplitude plasma wave at the head of the stream is related to the precursor phenomenon reported by De la Noe and Boischot (1972) and De la Noe (1973).

560

It was suggested by Wild (1964) that the electrons causing type III bursts might be guided along current sheets and this possibility was analyzed by Weiss and Wild (1964). Their analysis, however, allowed for no transverse field in the sheet and no bending of the sheet due, for example, to the rotation of the sun. Thus, it is only applicable to the low corona $(r < 2R_\odot)$ where these effects are not important. Recently, Smith and Pneuman (1972) analyzed this problem, taking into account both the transverse field in the sheet (Figure 2) deduced by Pneuman (1972) and a B_ϕ field due to solar rotation. They found that electrons could not drift across field lines sufficiently fast in the center of the sheet nor could they drift out of the sheet sufficiently fast to explain a type III burst. Moreover, the presence of a $B\phi$ field stopped the well known bouncing property of a plane neutral sheet (Wild and Weiss, 1964; Spieser, 1965), so that particles drift out of the sheet readily, though not sufficiently readily to explain a type III burst. Thus, while electrons may be channeled along current sheets in the low corona $(r < 2 R_\odot)$, there is good reason to believe that they must leave the central regions of current sheets further out. In other words, type III sources at low frequencies may have quite large angular extents and be traveling along normal interplanetary field lines, that is, not in the vicinity of any special surfaces such as current sheets. We shall attempt to resolve this result with the high densities which are often inferred from observations in the next section.

TYPE III BURSTS — NATURE OF THE RADIATION SOURCE

The mechanisms for radiation near the fundamental and second harmonic of the plasma frequency are now well known and agreed upon by most theoreticians. Near the fundamental the process is scattering on the polarization clouds of ions (Tsytovich, 1970; Smith, 1970a; Melrose, 1970b) which can be represented schematically by

$$p + i \rightarrow t + i'$$ (1)

Here p is a plasma wave, t is a transverse wave or radiation, and i and i' are the polarization cloud of an ion (electron density fluctuation) before and after the scattering, respectively. Process (1) can be either spontaneous or induced and the absorption coefficient can be negative, that is, the possibility of amplification exists. Such amplification must be invoked to explain the dominance of fundamental radiation at high frequencies (Wild, Sheridan, and Neylan, 1959). There is no validity in the conjecture of Zheleznyakov and Zaitsev (1970b) that emission near the second harmonic of the plasma frequency is dominant at high frequencies. This was based on an incorrect analysis of amplification by process (1).

Near the second harmonic of the plasma frequency, the radiation mechanism is a combination of two excited plasma waves (Sturrock, Ball, and Baldwin, 1965; Zheleznyakov and Zaitsev, 1970b; Smith and Fung, 1971) which can be represented schematically by
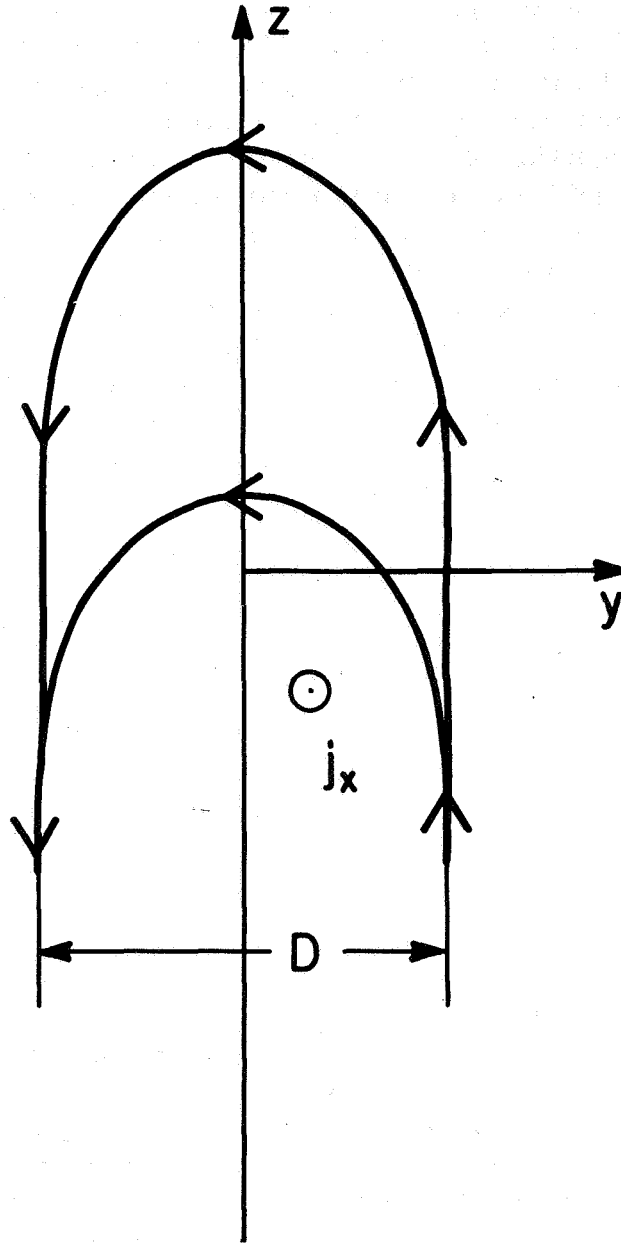
$$p + p \rightarrow t (2\omega_p)$$ (2)

Figure 2. Schematic configuration of a current sheet model which has a small, but finite transverse (B_y) field. A current density j_x maintains the current sheet which has a thickness D.

Unlike process (1), the absorption coefficient for process (2) can only be positive (Smith, 1970a) and hence there is no possibility of amplification. While the observations at high frequencies clearly point to the dominance of fundamental radiation, there is no similar evidence at low frequencies. In fact, since amplification by process (1) depends sensitively on the energy density in plasma waves W^P, and since this must decrease with increasing height as the stream becomes weaker, we expect amplification by process (1) to become unimportant at low frequencies. Due to the same decrease of W^P, the nonlinear process of induced amplification of one plasma wave p' by another plasma wave p

$$p + i \to p' + i'$$ (3)

becomes very weak. Since the two plasma waves in process (2) must meet almost head-on (Smith, 1970a), weakening of induced process (3) leads to a decrease in radiation by process (2). This occurs because the excited plasma waves are produced with directions close to the stream direction and one of the plasma waves in (2) must be produced by process (3). At low frequencies, we expect that only spontaneous scattering by process (3) will be important. Thus, to determine approximately the ratio of the total emission near the fundamental J_{T1} to that near the second harmonic J_{T2}, we can use the spontaneous emission only from process (1) (Smith, 1970a) and the emission due to process (2), taking into account only the spontaneous emission from process (3) (Zheleznyakov and Zaitsev, 1970b; Smith 1972a). This leads to

$$\frac{J_{T1}}{J_{T2}} \simeq 10^{-20} \frac{n_e^{3/2}}{W^P T_e^{1/2}}$$ (4)

where n_e and T_e are the electron density and temperature, respectively.

With the help of Equation (4), we can investigate which radiation should be dominant at low frequencies. The only undetermined factor is the energy density in plasma waves W^P. Some lower limits can be put on W^P by assuming that emission near the second harmonic is dominant and giving the source a reasonable maximum size, that is, a radius of 10^{12} cm at 1 AU. We can then check to see whether or not emission near the second was dominant via Equation (4) a posteriori. For the electron event observed by Lin (1973), the corresponding type III close to the earth had a total power near 55 kHz of about 4.6×10^9 erg·sec⁻¹ in a bandwidth of 20 Hz (Evans and Fainberg, private communication). The 20-Hz bandwidth corresponds to a height of about 2×10^9 cm. Thus, with a source area of 3.1×10^{24} cm² (corresponding to a source radius of 10^{12} cm), the total emissivity would have to be 6.9×10^{-25} erg·cm⁻³·sec⁻¹. The total volume emissivity for process (2) in the case that only spontaneous scattering by process (3) is important is (Smith, 1972b)

$$J_{T2} \simeq \frac{(3)^{1/2} \omega_{oe}^5 \langle v_{ph} \rangle (W^P)^2}{80 (2\pi)^{1/2} \nu_{eff} n_e^2 m_e c^5 v_i}$$ (5)

where ω_{oe} is the plasma frequency, $<v_{ph}>$ is the average phase velocity of plasma waves, ν_{eff} is the effective collision frequency, n_e is the electron density and v_i is the ion thermal velocity. With $<v_{ph}> \approx 10^{10}$ cm s⁻¹, $n_e = 9$ cm⁻³ corresponding to a 55 KHz second harmonic, and $\nu_{eff} \approx 10^{-5}$ s⁻¹ and $v_i = 4 \times 10^6$ cm·s⁻¹ corresponding to a temperature $T_e \simeq T_i = 1.6 \times 10^5$ K, we find

$$J_{T2} \simeq 1.5 \times 10^5 \; (W^P)^2$$

Thus to obtain 6.9×10^{-25} erg·cm⁻³·s⁻¹, W^P would have to be 2.1×10^{-15} erg cm⁻³. Putting this value of W^P into Equation (4) with n_e and T_e as above, we find $J_{T1}/J_{T2} \simeq 3 \times 10^{-7}$. Thus, the assumption that second harmonic emission is dominant is well justified. At high frequencies, second harmonic sources near the limb may also be dominant (Labrum, 1971).

We have not investigated in detail where the transition from the dominance of fundamental radiation to the dominance of second harmonic radiation occurs. Indeed, although the necessary data such as the sizes of sources at various frequencies exists, it has not been analyzed sufficiently for this purpose. Nevertheless, it is well to discuss a point of possible confusion which properly overlaps with the next section, namely the observed burst frequency versus projected position on the sun for bursts around 1 MHz. A typical distribution is shown in Figure 3. We see that there are fewer bursts observed near the limb. However, such a distribution does not necessarily argue for the dominance of a directive source such as near the fundamental, since it could equally well result from propagation effects coupled with a minimum threshold for detectability. For example, the radiation from a second harmonic source at the limb at a height of 100 $R_{\odot}$ must travel more than twice the distance of the radiation of the same kind of source at the center of the disk.

Returning to the high frequency region where amplification of the fundamental is important, we can ask how directive we expect the source to be. A recent computation (Smith, 1973) in which rays were traced in a model cylindrical source like the one used in Smith (1970a), taking into account amplification and absorption, shows that the source itself is very directive. Results are shown in Figure 4 for a source at the 80 MHz level which is 2541 km high and 100 km in radius. All of the important radiation comes out in a cone of half angle 2.6°.

TYPE III BURSTS — PROPAGATION OF RADIATION BETWEEN SOURCE AND OBSERVER

It is now well established that radiation from type III sources is severely scattered and refracted on its way to the observer (Steinberg et al., 1971; Steinberg, 1972; Riddle, 1972). Thus, observations indicate the size of a scatter image of the true source. We now consider only one aspect of this result, its implications for inferring densities from type III bursts. The densities inferred from type III bursts have generally been higher than those obtained by other means (Newkirk, 1967; Fainberg and Stone, 1971), although it has been shown by

Kuiper (1973) that at high frequencies such an interpretation is not necessary because the scatter of points is large. The results of scattering theory are that scattering will lead to apparent sources which are minutes higher than the true source at the limb at high frequencies, and degrees higher at low frequencies. Thus we expect a priori that direct application of type III observations to density determinations will lead to errors whose magnitudes become increasingly large with decreasing frequency. This is exactly the behavior observed for the discrepancy with other observations, although it should be kept in mind that part of the discrepancy at low frequencies is due to the dominance of second harmonic radiation, and at high frequencies part is due to dominant second harmonic limb sources (Labrum, 1971).
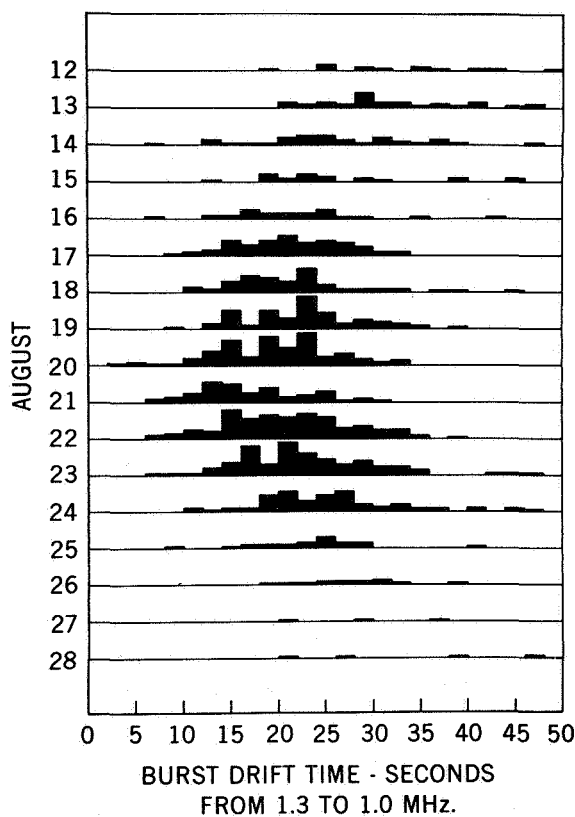

Figure 3. The apparent burst drift rate distribution between 1.3 and 1.0 MHz, which also shows the number of bursts as a function of solar longitude. CMP was August 20 (after Fainberg and Stone, 1970).
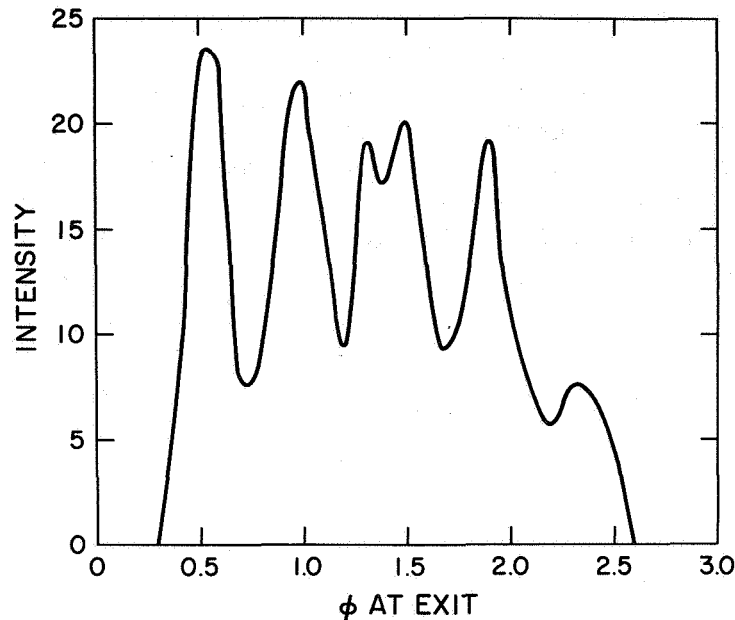
Figure 4. The intensity distribution of fundamental radiation emerging from a cylindrical source at the 80-MHz level as a function of the angle ϕ which is the angle with respect to the radial direction in degrees.

TYPE II BURSTS — NATURE OF THE EXCITING AGENCY

A picture now emerging for the exciter of type II bursts is that linear fast mode magnetosonic waves are excited at some point in a flare and as they travel upward they meet regions of low Alfven velocity such as current sheets where they steepen into shocks (Uchida, 1973). Although this fails to explain the close relation sometimes observed between type II and type IV bursts, it can be used as a starting point. The first question we can then ask of a theory is how large an Alfven Mach number M_A is required before a fast mode shock leads to significant production of electron plasma waves. It was shown by Smith (1971) that significant plasma wave production can not occur in the laminar shock structures invoked by Pikel'ner and Gintsburg (1963) and Zaitsev (1965; 1968), because these structures are too inhomogeneous. Significant plasma wave production can only occur when M_A is about 2 and ion-acoustic waves excited in the shock heat the electrons significantly. When the angle between the plane of the shock and the magnetic field ψ is small (that is, $3.5°$), only the fast electrons heated in the shock can escape forward and thus beams are formed (Figure 5). As in the case of type III bursts, such beams must relax, and since they are initially more well-defined beams, they must relax more violently. This relaxation leads to the copious production of plasma waves whose distribution in k-space can be calculated semiquantitatively (Smith, 1972b).
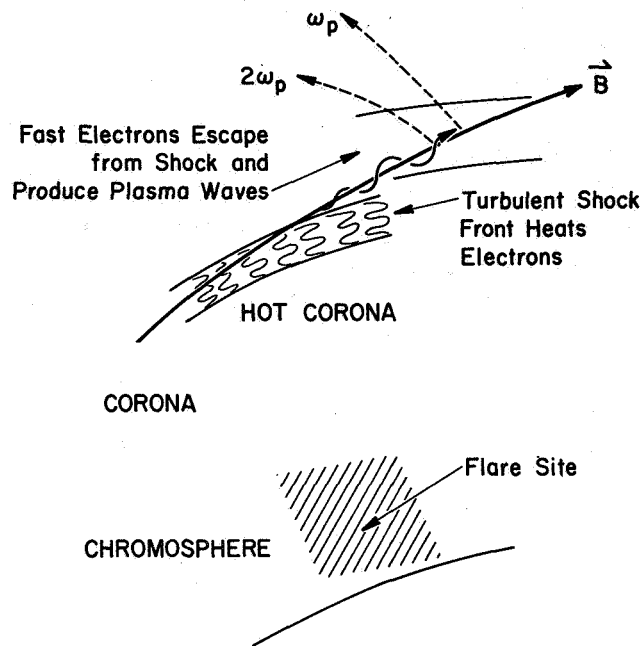
Figure 5. Schematic summary of the processes
occurring in a type II burst.

The extent to which beams are formed and plasma waves produced is a very sensitive function of the angle ψ between the plane of the shock and the magnetic field. For example, a shock with $\psi \approx 15°$ which is dominated by whistler turbulence is very ineffective at selecting only fast particles to produce beams. This sensitivity provides a possible explanation for the "winking" phenomenon observed in type II bursts — one part of the shock front brightens and then fades as another part brightens with time scales as short as 1 second at 80 MHz. This behavior could be a consequence of ψ reaching more optimal values in some parts of the shock front as it moves through the corona. This interpretation seems more likely than one based on variations in M_A since fairly large changes are required to affect the emission in this case. Only one case has been worked out in detail with $\psi = 3°42'$ which is probably close to maximum efficiency (Smith, 1972c). In this case with $M_A = 2.5$, all of the radiation observed in a strong type II burst would require only 4×10^{19} cm^2 of the shock to have this angle.

TYPE II BURSTS — NATURE OF THE RADIATION SOURCE

The basic radiation processes for type II bursts are the same as those outlined in a previous section for type III bursts. However, some specific details must be different because second harmonic emission from type II bursts at high frequencies is much stronger than in type III bursts, making fundamental-harmonic pairs easily discernable at the center of the disk. Two

567

reasons for the apparently reduced strength of the fundamental are the following: First, the amplification lengths for fundamental radiation in induced process (1) are shorter than in type III bursts, because a very distinct beam is formed in the shock and it normally relaxes very quickly as soon as it leaves the shock, that is, in 100 m at 80 MHz. There is still a large region in front of the relaxation region to which plasma waves with sufficient group velocities can escape. However, the size of this region (for example, 139 km at 80 MHz) is still much smaller than corresponding regions in type III bursts (for example, 2350 km at 80 MHz). Secondly, radiation near the second harmonic in type II bursts is stronger than in type III bursts ab initio because the energy density in plasma waves W^P is much larger in and close to the relaxation region. Thus, induced process (3) is much stronger leading to a total emission several orders of magnitude larger than in Equation (5) where only spontaneous process (3) was considered. Because the amplification region for type II bursts is smaller than for type III bursts, radiation near the fundamental is less directive initially although this effect may be masked by propagation effects.

TYPE II BURSTS — PROPAGATION OF RADIATION BETWEEN SOURCE AND OBSERVER

Again, in general propagation is the same as for type III bursts, but there are some details which differ. Specifically, the number of cases in which apparently backward emission of the second harmonic is required to explain the observations (Wild, 1970) is greater than for type III bursts (Stewart, 1972). The statistics are admittedly poor since only four cases of type II bursts in which the fundamental and second harmonic positions were suitable for analysis have been observed. Of these, one observed close to the center of the disk could only be explained by direct propagation of the second harmonic (Riddle, 1970). The remaining three all occurred at solar longitudes greater than 45° from the center of the disk, and all required that the second harmonic be apparently emitted in the backward direction and reflected to be observed. This behavior may be due to a propagation effect rather than any innate property of the emission mechanism. In fact, for plasma waves with phase velocities less than 0.6 c, the radiation from process (2) is effectively isotropic with some scattering. The propagation effect which may explain the absence of a direct second harmonic near the limb is shown in Figure 6. Direct radiation is absorbed in and behind the shock because the high level of ion-acoustic waves there raises the effective collision frequency by several orders of magnitude (Smith, 1972b).

DISCUSSION

Direct measurements of type III bursts and particles are doing much to clarify type III theory. The results of the theory in turn have important implications for the particle acceleration process. For example, the fact that electrons make it all the way to the earth while continually relaxing means that the electrons had to be produced with a power law or other monotonically decreasing distribution. Otherwise, if they had a beam distribution, for example, there would be an enormous energy density in plasma waves produced when they
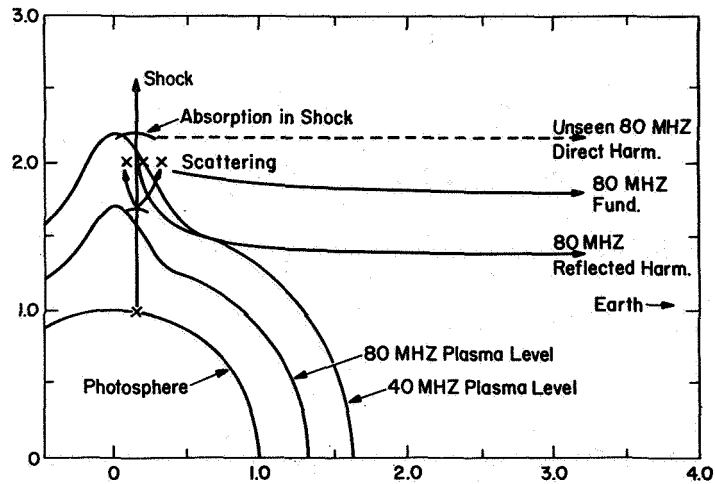
Figure 6. A schematic configuration for explaining the apparent differences in the locations of fundamental and second harmonic sources with the ray paths involved indicated. Direct second harmonic radiation is absorbed in the shock and the region behind the shock, and only the scatter image of the fundamental source is seen.

relaxed, leading to a very intense pulse of radio emission, but such a pulse has not been observed. The view of Zaitsev, Mityakov, and Rapoport (1972) that even if a beam were produced it would relax before leaving the source, would still lead to an intense pulse of radiation. Thus, a beam simply cannot be formed initially. This result is also attractive in that it leads to an explanation of why the starting frequencies of type III bursts are not higher even though the acceleration region may be low. Namely, it takes a certain distance, typically of the order of 50,000 km, for fast electrons to overtake slow electrons sufficiently to lead to highly nonthermal plasma wave production.

The whole question of densities inferred from type III bursts needs to be reexamined. The large spread in points which allowed Kuiper (1973) to conclude that there is no problem at high frequencies is most likely due to dominant second harmonics near the limb and scattering. Both of these effects need to be taken into account before type III bursts can become a useful tool for density diagnostics. At low frequencies the problem should be simpler because second harmonic radiation is most likely always dominant. It may be that no density enhancements are required to explain the observations. This would be consistent with particle trajectory calculations which indicate that it would be impossible for electrons to travel in the central and densest parts of coronal streamers.

Type II theory has seen less progress than type III theory probably because the problem is harder and the observations considerably scarcer. We can expect that in situ measurements near the earth will do much to clarify and stimulate this theory.

REFERENCES

Alexander, J. K., Malitson, H. H., and Stone, R. G., 1969, *Solar Phys.* 8, 388.

Baldwin, D. E., 1964, *Phys. Letters* 12, 202.

De la Noe, J., and Boischot, A., 1972, *Astron. Astrophys.* 20, 55.

De la Noe, J., 1973, These Proceedings.

Fainberg, J., and Stone, R. G., 1970, *Solar Phys.* 15, 222.

Fainberg, J., and Stone, R. G., 1971, *Solar Phys.* 17, 392.

Harvey, C. C., and Aubier, M. G., 1972, *Astron. Astrophys.*, in press.

Kaplan, S. A., and Tsytovich, V. N., 1967, *Astron. Zh.* 44, 1194.(English transl., 1968, *Soviet Astr-AJ* 11, 956).

Kuiper, T. B. H., 1973, These Proceedings.

Labrum, N. R., 1971, *Australian J. Phys.* 24, 193.

Lin, R. P., 1973, These Proceedings.

McDonald, F. B., and Van Hollebeke, M. A., 1973, These Proceedings.

Melrose, D. B., 1970a, *Australian J. Phys.* 23, 885.

Melrose, D. B., 1970b, *Australian J. Phys.* 23, 871.

Newkirk, G., 1967, *Ann. Rev. Astron. Ap.* 5, 213.

Pikel 'ner, S. B., and Gintsburg, M. A., 1963, *Astr. Zh.* 40, 842. (English transl. 1964, *Soviet Astr.-AJ* 7, 639).

Pneuman, G. W., 1972, *Solar Phys.* 23, 223.

Riddle, A. C., 1970, *Proc. Astr. Soc. Australia* 1, 310.

Riddle, A. C., 1972, *Proc. Astr. Soc. Australia* 2, 98.

Smith, D. F., 1970a, *Adv. Astron. Astrophys.* **7**, 147.

Smith, D. F., 1970b, *Solar Phys.* **15**, 202.

Smith, D. F., 1971, *Ap. J.* **170**, 559.

Smith, D. F., 1972a, *Solar Phys.* **23**, 191.

Smith, D. F., 1972b, *Ap. J.* **174**, 121.

Smith, D. F., 1972c, *Ap. J.* **174**, 643.

Smith, D. F., 1973, *Solar Phys.* (to be submitted).

Smith, D. F., and Fung, P. C. W., 1971, *J. Plasma Phys.* **5**, 1.

Smith, D. F., and Pneuman, G. W., 1972, *Solar Phys.* **25**, 461.

Speiser, T. W., 1965, *J. G. R.* **70**, 4219.

Steinberg, J. L., Aubier-Giraud, M., Leblanc, Y., and Boischot, A., 1971, *Astron. Astrophys.* **10**, 362.

Steinberg, J. L., 1972, *Astron. Astrophys.* **18**, 382.

Stewart, R. G., 1965, *Australian J. Phys.* **18**, 67.

Stewart, R. G., 1972, *Proc. Astr. Soc. Australia* **2**, 100.

Stone, R. G., 1973, These Proceedings.

Sturrock, P. A., Ball, R. H., and Baldwin, D. E., 1965, *Phys. Fluids* **8**, 1509.

Tsytovich, V. N., 1970, *Nonlinear Processes in Plasma* (New York: Plenum Press).

Uchida, Yu., 1973, These Proceedings.

Weiss, A. A., 1963, *Australian J. Phys.* **16**, 240.

Weiss, A. A., and Wild, J. P., 1964, *Australian J. Phys.* **17**, 282.

Wild, J. P., 1964, NASA SP-50, 161.

Wild, J. P., 1970, *Proc. Astr. Soc. Australia* 1, 365.

Wild, J. P., 1973, These Proceedings.

Wild, J. P., Sheridan, K. V., and Neylan, A. A., 1959, *Australian J. Phys.* 12, 369.

Zaitsev, V. V., 1965, *Astr. Zh.* 42, 740. (English transl. 1966, *Soviet Astr.-AJ* 9, 572.)

Zaitsev, V. V., 1968, *Astr. Zh.* 45, 766. (English transl. 1969, *Soviet Astr.-AJ* 12, 610.)

Zaitsev, V. V., Mityakov, N. A., and Rapoport, V. O., 1972, *Solar Phys.* 24, 444.

Zheleznyakov, V. V., and Zaitsev, V. V., 1970a, *Astron. Zh.* 47, 60. (English transl. 1970, *Soviet Astr.-AJ* 14, 47.)

Zheleznyakov, V. V., and Zaitsev, V. V., 1970b, *Astron. Zh.* 47, 308. (English transl. 1970, *Soviet Astr.-AJ* 14, 250.)

TIME PROFILE OF TYPE III BURSTS IN DECAMETER AND HECTOMETER RANGE

Tatsuo Takakura and Yoshiharu Naito
Department of Astronomy, University of Tokyo

Kenichiro Ohki
Tokyo Astronomical Observatory, University of Tokyo

INTRODUCTION

It is quite suspicious that the decay time of type III bursts at low frequencies is ascribed to the collisional damping time of plasma waves excited by a beam of fast electrons.

I would like to propose the following new hypothesis: The decay time, τ, of plasma waves is much shorter than the time scale of type III bursts especially at low frequencies. Accordingly, the time variation of radio flux at a given frequency merely corresponds to the flux of fast electrons passing through the corresponding plasma layer.

DECAY TIME OF PLASMA WAVES

One possibility for the plasma waves to have such a short decay time is that the radio waves are emitted preferentially from the dense and fine filamentary irregularities along the streamer. Suppose that the plasma waves are excited in the filament by a fast electron with a speed u traveling along the filament. If we take into account the Landau damping, the effective range of phase velocity v_ϕ of the plasma waves is given by

$$4\,v_T \lesssim v_\phi \leqslant u \tag{1}$$

where v_T is the rms speed of thermal electrons. The corresponding frequency range ω of plasma waves is given by

$$1.03\,\omega_p > \omega \gtrsim 1.002\,\omega_p \tag{2}$$

if $T_e = 10^6$ K and $u = c/3$, since $\omega^2 = \omega_p^2 \left[1 - (v_T/v_\phi)^2\right]^{-1}$. The corresponding range of the group velocity v_g is given by

$$1700\,\text{km} \cdot \text{s}^{-1} \gtrsim v_g \gtrsim 500\,\text{km} \cdot \text{s}^{-1} \tag{3}$$

573

since $v_g = v_T^2/v_\phi$. Therefore, the wave-packet of those plasma waves propagates almost perpendicularly to the velocity u of the electron since the Cerenkov cone angle θ of the wave-packet is

$$\sin \theta = <v_g>/u \ll 1$$

If the radius of the filament is a, the wave-packet propagates through the filament in a time

$$\tau_1 = a/<v_g>$$

When the wave-packet gets into the outer rarefied plasma $(\omega_p{}')$, it is suddenly damped due to the strong Landau damping if

$$1.03\,\omega_p{}' < \omega$$

since the relation (2) is not satisfied there.

The observations of scintillation of radio stars have given the typical size, a, of irregularities in the outer corona to be 10^2 km. Therefore, the lifetime of the plasma wave-packet is

$$\tau_1 \cong 0.1 \text{ s}$$

On the other hand, the plasma density of the filament may decrease with height along the filament. The effective height range, from h to h + Δh, to emit the plasma waves of a given frequency ω is given by the relation (2) and the gradient of plasma density along the filament; that is, Δh corresponds to $\Delta\omega_p \cong 0.03\,\omega_p$. The time interval $\tau_2 = \Delta h/u$ in which the fast electron pass through Δh is about 1 second at the layer for 5 MHz and 4 seconds at 1 MHz.

Therefore, both τ_1 and τ_2 are much shorter than the observed decay time of the type III bursts at such low frequencies.

TIME PROFILE OF TYPE III BURST

Assume that a group of electrons is impulsively ejected at t = 0 from the base of the corona radially outwards having an initial radial velocity distribution $f_0(u)$, and that the velocity does not change during the travel through the corona. Due to the velocity dispersion, the length of the electron cloud increases with time and with height, and the electrons arrive at a given height successively in order of the speed. The flux F_e of electrons passing though a height h is given by

$$F_e(h, t) = f_0(u) \left| \frac{du}{dt} \right| \tag{4}$$

where $u = h/t$. If we use a normalized time

$$\xi = t/t_0 \quad (= u_0/u)$$

where $t_0 = h/u_0$ and u_0 indicates the electron speed which gives a maximum of F_e in Equation (4), we have

$$F_e (h, \xi) = \left(\frac{u_0}{\xi}\right)^2 f_0 \left(u = \frac{u_0}{\xi}\right) /h \tag{5}$$

Therefore, if the amplitude is normalized, $F_e(\xi)$ is independent of h. Accordingly, if the present hypothesis is valid, the time profiles of a single type III burst observed at different point frequencies may be the same if we plot the normalized radio flux against ξ, provided that the radio flux $F_R (\xi)$ is given by

$$F_R (\xi) \sim F_e^\alpha (\xi) g (u) \tag{6}$$

where α is an arbitrary constant and g(u) indicates an arbitrary function of $u = u_0/\xi$.

This has been tested by the use of type III bursts observed at 8 and 5 MHz with the Japanese satellite Shinsei. Figures 1 and 2 show the comparison of time profiles at the two frequencies. The solid curves show the time profile at 8 MHz, and crosses indicate 5 MHz (the peak flux of 5 MHz is fitted to 8 MHz). The burst shown in Figure 2 seems to be composed of 4 type III's if we refer to the observation in 60 to 20 MHz range at the Clark Lake Observatory, so that only the increasing phase of the second burst and decaying phase of the fourth burst are used in the present comparison. The fitting seems to be satisfactory.

If the present hypothesis is valid, the comparison of F_R with F_e which can be observed directly with the spacecraft would give α and g(u) as given by (6).
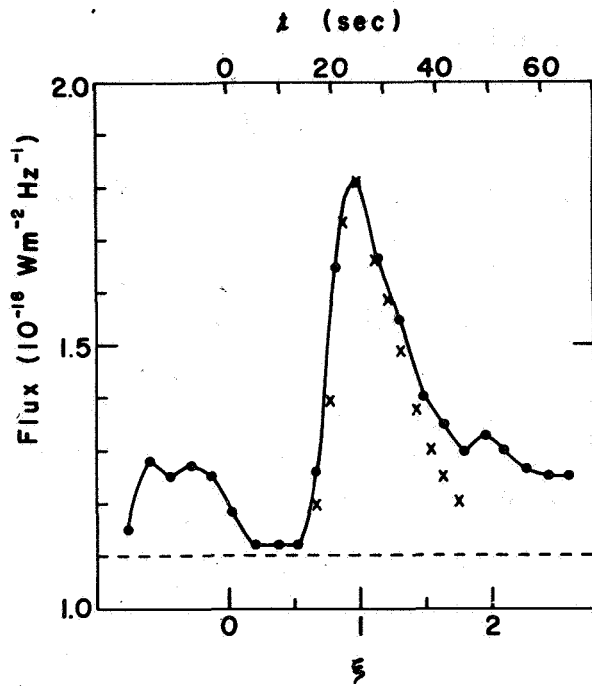
Figure 1. Time profile of the type III burst at 8 MHz (solid curve and dots) on Nov 13, 1971, $10^h09^m11^s$ UT ($\xi = t = 0$). The profile of 5 MHz plotted against ξ is indicated by crosses, whose peak is fitted to the peak of 8 MHz.

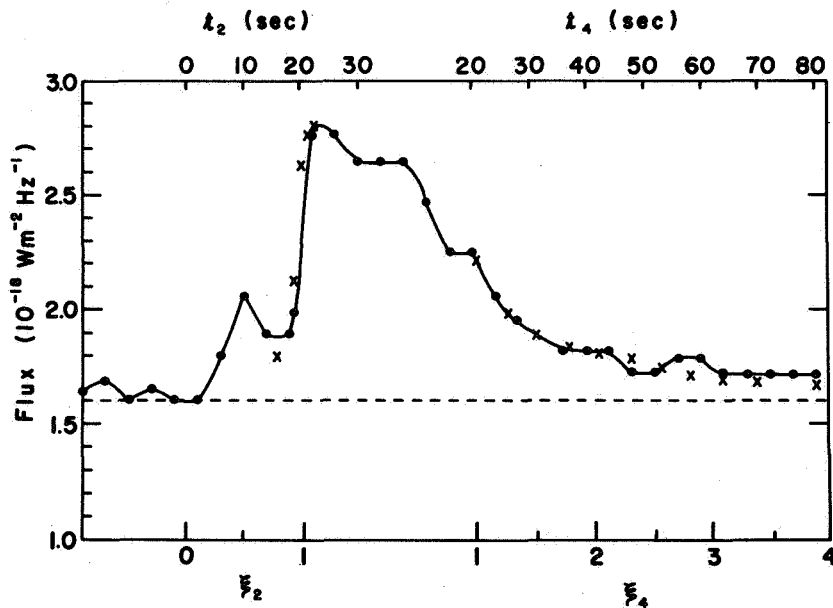Figure 2. Oct 20, 1971, $17^h12^m49^s$ UT ($\xi_2 = t_2 = 0$) and $17^h13^m19^s$ UT ($\xi_4 = t_4 = 0$). See caption of Figure 1 for further explanation.

FLARE-INDUCED MHD DISTURBANCES IN THE CORONA—
MORETON WAVES AND TYPE II SHOCKS

Yutaka Uchida

Tokyo Astronomical Observatory
University of Tokyo
and
High Altitude Observatory
National Center for Atmospheric Research (Boulder, Colorado)

ABSTRACT

The propagation in the corona of the magnetohydrodynamic (MHD) disturbance possibly emitted at the explosive stage in the initial phase of a flare is considered. The behavior of the MHD fast-mode wavefront, whose source is located at the flare, is calculated by using eiconal-characteristic method in the High Altitude Observatory (HAO) realistic models of coronal magnetic field and density for the days of some particular flare events. It is shown as the result that the peculiar behavior of Moreton's surface wave and the peculiar appearance in the shape and position of the type II burst sources can be consistently understood by considering the refraction, focussing, and formation of shocks of MHD fast-mode disturbance in the actual distribution of Alfven velocity in the corona. Moreton waves seem to appear only when the flare explosion happens to occur at the edge of an active region and faces a low-Alfven-velocity region lying on the surface. The wave, which is initially emitted isotropically, is refracted into a direction in which the condition for down-refraction holds to allow chromospheric reentrance of disturbance.

When low-Alfven-velocity regions exist high up in the corona (or extending from below in a streamerlike shape), it is shown that the wavefront is refracted into such structures, and the shock strength, which is weak otherwise, is markedly enhanced as the wavefront proceeds into such structures. Based on some comparison of the positions of low-Alfven-velocity regions in the corona with observed positions of type II burst sources, it is proposed that the type II burst sources may be identified with such low-Alfven-velocity regions "illuminated" by thus enhanced shocks.

INTRODUCTION

It has long been suggested that a type II solar radio burst may be the manifestation of a coronal MHD fast-mode shockwave exciting plasma waves on its passage (Uchida, 1960; Wild et al., 1963; Weiss, 1965). However, the accumulation of the observation, mainly by Culgoora radioheliograph, revealed the complexity of the appearances of type II burst sources (Kai, 1969; Stewart and Sheridan, 1970; Smerd, 1970; Dulk and Smerd, 1971;

Riddle and Sheridan, 1971). It required a consistent explanation for the fact that a certain flare produces sources at certain distant places in the corona, sometimes beyond its horizon, without brightening up other parts of the corresponding plasma level lying closer to the flare.

It is claimed more recently (Anderson, 1966; Meyer, 1968; Uchida, 1968; Wild, 1969) that another manifestation of the existence of coronal MHD disturbances may be the flare-associated solar chromospheric disturbance which is usually referred to as Moreton waves, after the name of the first reporter (Moreton, 1960). Fourteen events of this phenomenon, observed in the period of 1960 to 1968, are reported by Smith and Angle (1971), but again there seems to be a mysterious preference, both in the association with flares (even a powerful flare does not necessarily produce Moreton waves, while sometimes a subflare may produce them), and also in the direction of propagation in cases where the wave event takes place.

These peculiar aspects for both type II bursts and Moreton waves should, of course, be inherent to their mechanism, and the proper mechanism should be such that it explains these peculiarities by itself.

The intention of the present paper is to propose a unified explanation of these aspects, based on the behavior of MHD fast-mode wavefront calculated in HAO realistic models of coronal magnetic field and density. These models are essentially best-fitted spherical harmonic expansions of a) coronal magnetic field in current-free approximation (Altschuler and Newkirk, 1969) with the photospheric magnetic field distribution measured at Mount Wilson as the boundary condition, and b) coronal density (Perry and Altschuler, 1972) best fitted to the daily K-coronameter data obtained in HAO Coronal Station in Hawaii (Hansen et al., 1969).

MORETON'S WAVE PHENOMENON

The existence of a flare-associated propagation of down-up swing of chromospheric material, up to a distance of the order of 10^6 km along the solar surface, was first evidenced by Moreton and Ramsay in a movie taken at the shoulder part of $H\alpha$ line (Moreton, 1960), and later investigated by S. F. Smith and her colleagues at Lockheed Solar Observatory. It is characterized by the propagation velocity of several hundred to a few thousand kilometers per second, and by a certain sector angle of propagation of the order of 90°. It is shown later that this sectorial region for propagation clearly avoids the strong field regions (Uchida, Altschuler, and Newkirk, 1972).

Trials of interpretation by particle bombardment (Athay and Moreton, 1961), or by trapped waves in wave ducts whose upper and lower boundaries consist of low corona and the chromosphere respectively (Meyer, 1968), seem to have difficulties. One hopeful hypothesis, namely the sweeping skirt hypothesis by an expanding coronal MHD wavefront, has been developed by Uchida (1968, 1970) based on a suggestion by Anderson made in an

intuitive two-dimensional formulation by assuming sunspot magnetic field (Anderson, 1966).

Although, in general, a treatment of the propagation of (oblique) shockwave front in realistic magnetized atmosphere having no symmetry seems to be almost impossible, the particular situation of our problem, fortunately, allows us to treat the problem in a certain approximate way. Namely, since a) the material velocity involved in a flare explosion may be of the order of 10^2 km $\cdot$ s^{-1} and considerably smaller than the Alfven velocity in the surrounding medium, which is of the order of 10^3 km $\cdot$ s^{-1} up to 10^4 km $\cdot$ s^{-1} near sunspot, and b) the typical wavelength contained in the wavepacket seems to be considerably shorter than the typical scale length of the coronal structures, $\sim 5 \times 10^4$ km, the hydromagnetic version of eiconal-characteristic method may be applied (Uchida, 1970).

Instead of repeating the detail of the formulation and its physical significance, only one point will be made here: the distribution of Alfven velocity (when $V_A^2 >> A_o^2$ as in most part of the corona) is corresponding, in a very rough sense, to the potential distribution in classical particle dynamics, if we note the parallelism in behavior of our MHD wavepacket and classical particle (see Uchida, 1970); a high-(low) Alfven-velocity region repells (attracts) the wavepacket like a hill (dip) in potential in classical particle dynamics.

Through an examination of the distribution of Alfven velocity around the flare region, using HAO realistic models for magnetic field and density for the days of Moreton wave events, it was discovered that, as expected, a low-Alfven-velocity region is actually sitting on the surface in the direction of Moreton wave propagation, while Alfven-velocity-hills are surrounding in directions where no wave appeared (Figure 1). Actual calculation of wavefront
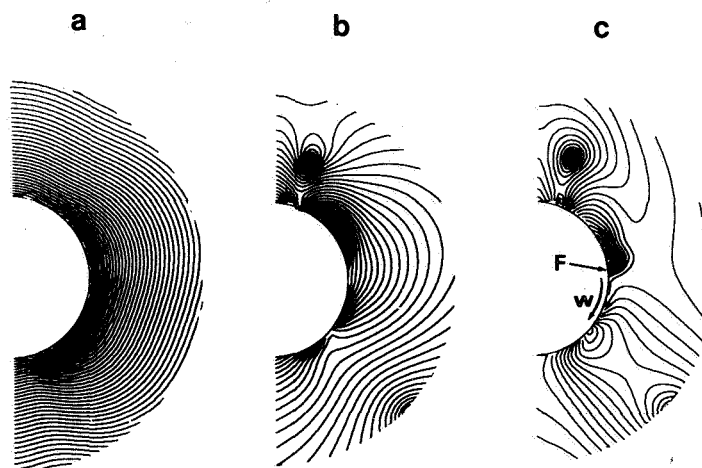

Figure 1. Contours of (a) equal density, (b) equal magnetic field strength, and (c) equal Alfven-velocity, in the meridional plane passing the flare of July 31, 1967, as an example.

behavior, for example for May 23, 1967, and July 31, 1967 events, reveals that the skirt of the wavefront is very much weakened and lifted up in the corona, and therefore does not sweep on the chromosphere in directions in which the disturbance in the chromosphere was not observed (Figures 2 and 3). The rays emitted initially isotropically tend to be refracted away from high-Alfven-velocity regions and focussed into low-Alfven-velocity regions lying in the low corona (Figure 4). The skirt of the wavefront sweeps on the chromosphere only in directions in which the chromospheric disturbance was actually observed (Uchida, Altschuler, and Newkirk, 1972) as shown in the conference by computer-produced movie.
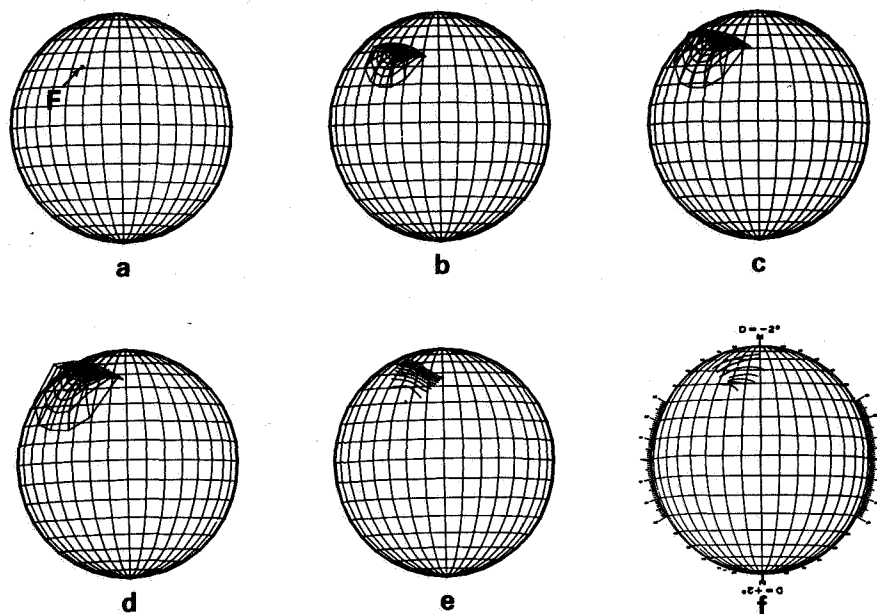

Figure 2. Time evolution of the calculated wave-surface (a ~ d) and its intersection with chromosphere proceeding in time (e), for the May 23, 1967 event. The observed Moreton wave is shown in (f). The responsible flare-flash is at $18^h37^m10^s$ UT, and the loci in (f) are, from the south, $18^h39^m00^s$, $18^h39^m30^s$, $18^h41^m30^s$, $18^h43^m15^s$, and $18^h45^m00^s$ UT, respectively. The wavefront calculation is performed in the corresponding timespan in similarity transformation.

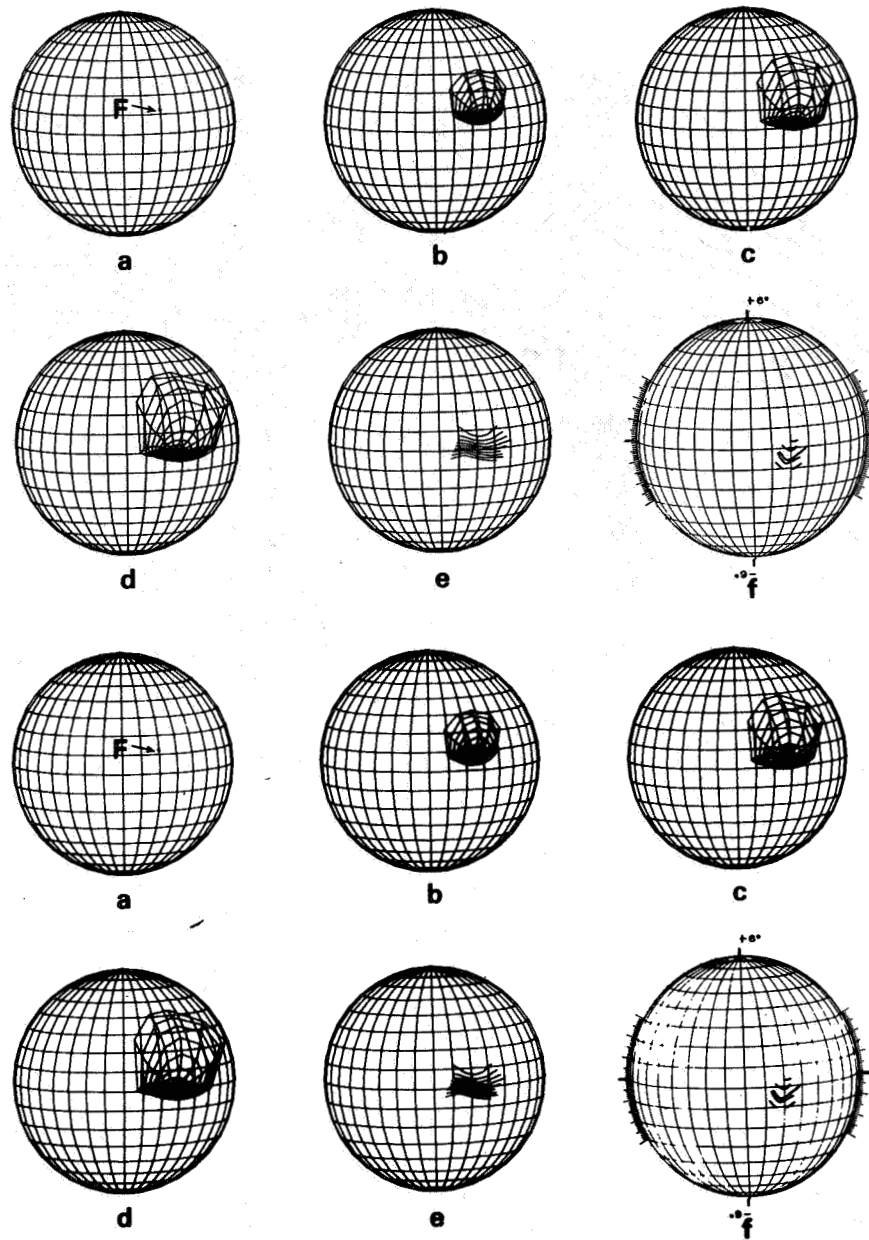Figure 3. Similar to Figure 2 for the July 31, 1967 event. The responsible flare flash occurred at $17^h21^m00^s$, and the loci in (f) are, from the north, $17^h22^m15^s$, $17^h24^m15^s$, $17^h24^m45^s$, $17^h25^m30^s$, and $17^h26^m30^s$ UT, respectively.
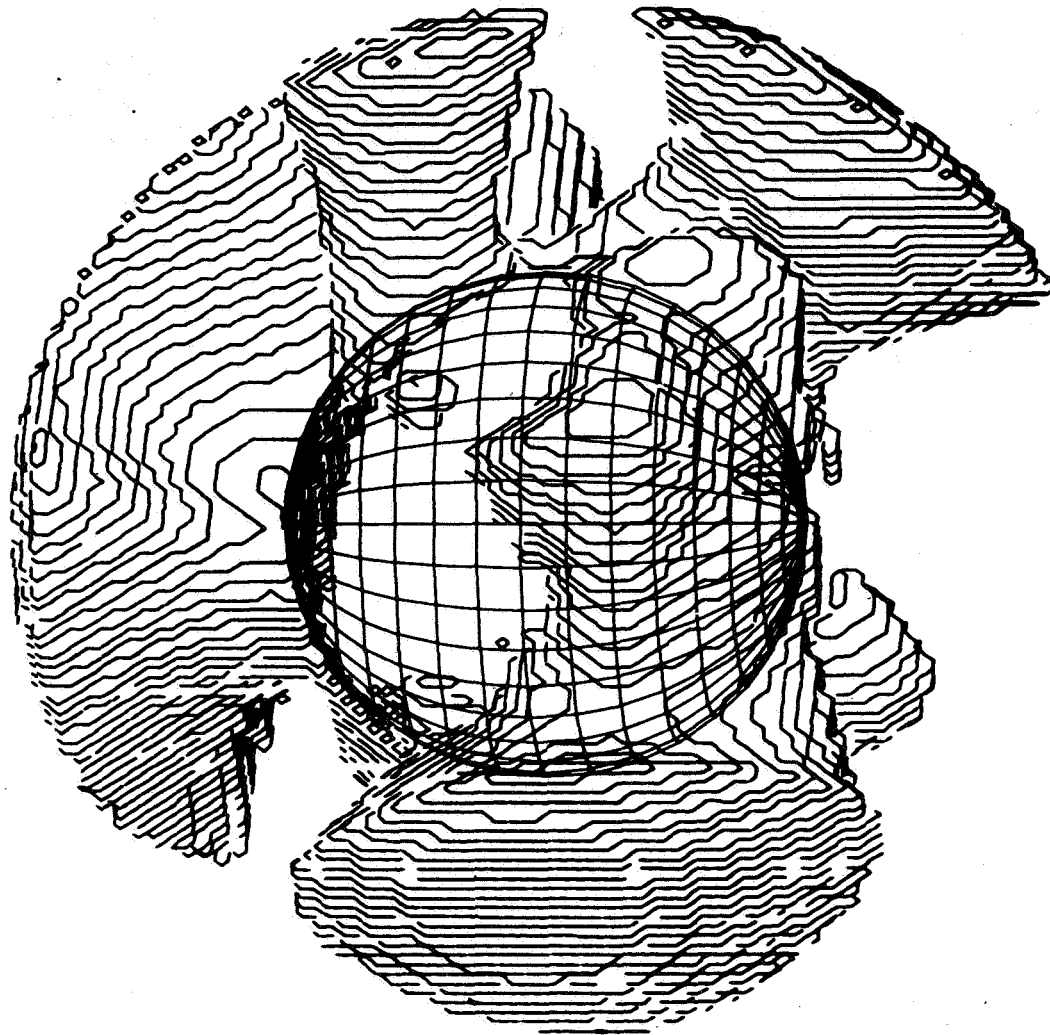
Figure 4. Three-dimensional representation of regions with Alfven-velocity higher than 5×10^2 $km \cdot s^{-1}$ in the July 31, 1967 corona. A solid body is visualized by an aggregate of thin plates whose normal is directed 45° to the east on the equator from the sun-earth direction. A comparison of this with the observed region of Moreton wave propagation in Figure 3 (f) shows clearly that the statement in the text is the case.

TYPE II SHOCKS

It naturally occurs that the irregular appearance of type II burst sources, which sometimes appear at unexpected places relative to the flare position, (sometimes beyond the horizon of the flare without brightening up parts of plasma level under consideration lying near-by (Smerd, 1970)), may also be due to a similar effect. The shock strength, otherwise considerably weak as mentioned earlier, builds up when the wavefront hits a low-Alfven-velocity region into which the wave energy tends to be focussed. The Mach number gets all

the more greater, since the propagation velocity of the disturbance is low in these regions. This situation is readily seen from the conservation of kinetic energy flux along the tube of ray-paths

$$\frac{1}{S} \frac{d}{ds} (\rho v^2 V_A S) = -D$$

where s is the distance along the ray, S is the cross-sectional area of tube of ray-paths, and D is the shock dissipation. In the region where D is small, or in other words, where the shock strength is still fairly small, one gets

$$M_A \equiv \frac{v}{V_A} \propto (\rho V^3{}_A S)^{-\frac{1}{2}}$$

This shows that the Mach number builds up where the rays are focussed into a small area and Alfven velocity is low, especially if ρ is smaller for given value of V_A. Actual calculation shows (Figure 5) that a remarkable strengthening of shocks takes place when the wavefront encounters a low-Alfven-velocity region in the corona, and sometimes the Mach number thus estimated exceeds unity by far*, starting from a reasonable estimate of initial value as small as 0.05 and using realistic model corona. Thus the candidate places, where some remarkable effects such as sudden particle acceleration (Smith, 1972), or plasma turbulence take place, are low-Alfven-velocity regions located not too far from the flare explosions. Outside of these low-Alfven-velocity regions, the disturbance stays fairly weak, and the only effect to be observed may occur in such low-Alfven-velocity regions.

Actually, the calculation of the behavior of the wavefront for the May 23, 1967 event, after the disappearance of Moreton waves, shows that the shock-strength enhancement takes place when the wavefront traverses a low-Alfven-velocity region extending high in the north-pole crown region, while the position of type II burst measured by Warwick and Swann (private communication, 1972) is in the same general region. We have compared the projected position on the plane of the sky of the three-dimensional configuration of low-Alfven-velocity regions on the 80 MHz plasma-frequency level (or 40 MHz for the case where the second harmonic is dealt with) in the corona (which has an appearance of broken shell), with the two dimensional position of type II-bursts observed by Culgoora radioheliograph. The above-mentioned hypothesis seems to be roughly the case (Figure 6) for at least one already examined event, that of October 13, 1969 (Dulk and Smerd, 1971). The fact that the closer source brightened later corresponds to a low-Alfven-velocity region located far from the flare, but with its projected position closer to it.

*In the case of down-refracted waves (Moreton waves), M_A is smaller through the factor of $\rho^{-\frac{1}{2}}$ for the same V_A and S values. The relation may also explain the phenomenon that the visibility of Moreton waves, corresponding to the magnitude of v, sometimes increases in the propagation. This may occur in our picture if the wave propagates into a region of decreasing V_A, which compensates the increase in S.
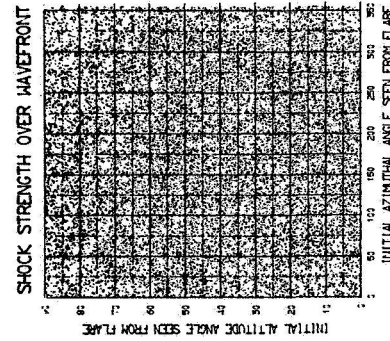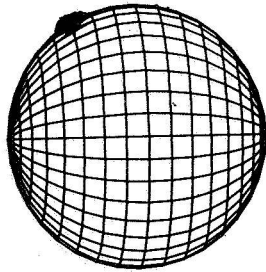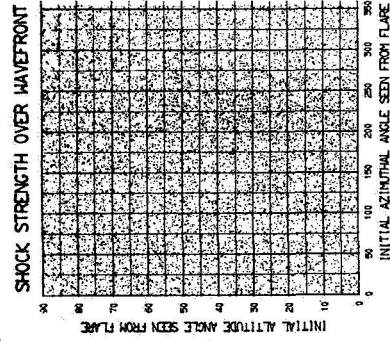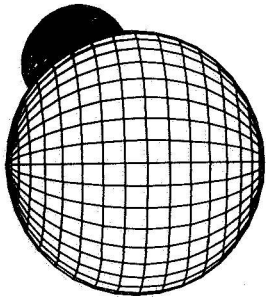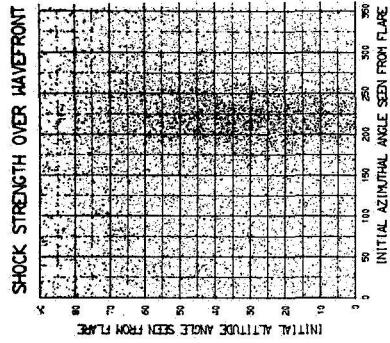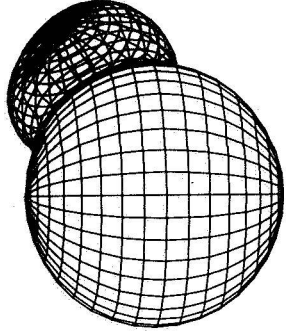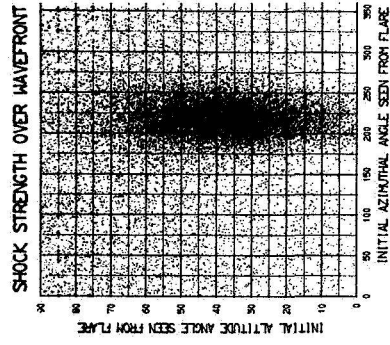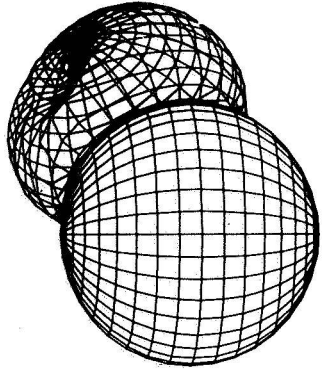
Figure 5. The wavefront evolution when a low-Alfven-velocity region in the corona is encountered (above), and the variation of Alfven-Mach-number on each part of the wavefront (lower). The probability of appearance of dark spots in the lower figures is set proportional to the normalized value of Mach number on the wavefront. The positioning of dark spots is assigned to the initial direction of each ray.

Figure 6. Three-dimensional representation of regions of $V_A < 1.5 \times 10^2$ km·s^{-1} on 40 MHz plasma level for October 13, 1969. This is to be compared with Dulk and Smerd's observation of source shape (with a correction of tilt in solar axis), since they measured the position of second harmonic radiation at 80 MHz. General trends of both coincide, and it may be that one of 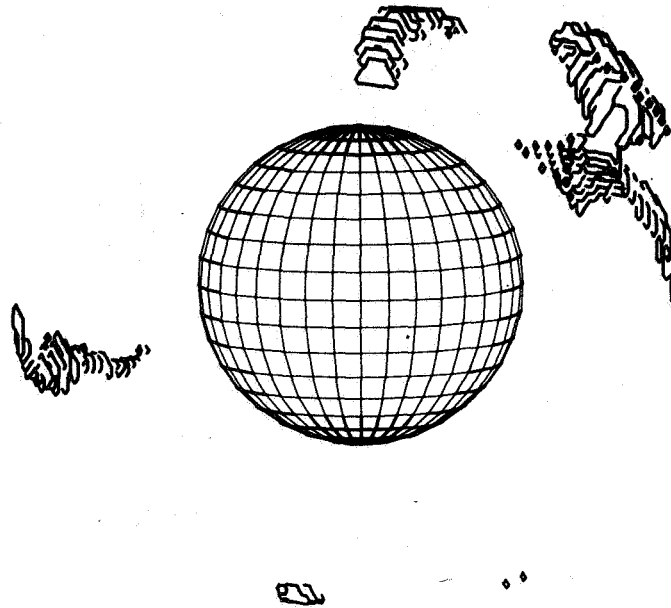the type II sources which came up closer at a later time is corresponding to one of the low-Alfven-velocity regions located far from the flare behind the limb, but with a small projected distance to the flare site.

PROPOSED UNIFIED EXPLANATION

From the discussion given above, it is readily concluded that, although the type II shock and Moreton waves may have not only similar interpretation but also a common source of disturbance, the chances of appearance of each are not necessarily equal, and are highly dependent on circumstantial physical conditions at the relevant places for each (Figures 7a, b). For example, if the flare explosion is completely surrounded by high magnetic field regions as in the August 1972 flare (Rust, private communication, 1972), the wavefront may be emitted only upward. Therefore little chance for Moreton wave appearance may be expected, while the chance for the occurrence of type II burst may be enhanced (Figure 7b). Moreton waves may occur only when the flare explosion faces open to an extended low-Alfven-velocity region sitting on the surface. This may explain the rareness of observed Moreton wave events compared with type II burst events. We also found that the velocity of propagation of Moreton waves does not depend much on the importance of the associated flares. This strongly suggests the circumstantial determination of the propagation velocity of Moreton waves, consistent with our working hypothesis.

(a) Type II and Moreton Wave
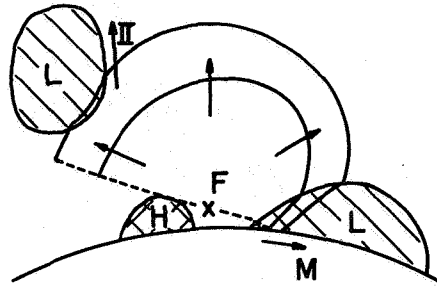
(b) Only Type II
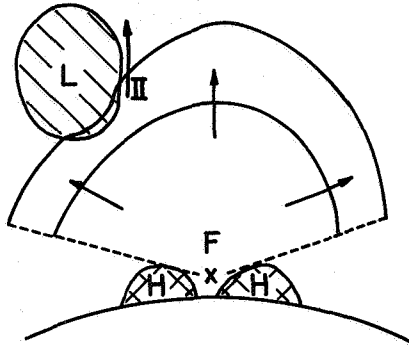
(c) Along Streamer
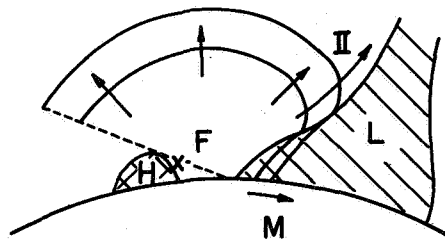
Figure 7. Possible cases for chances of Moreton wave and type II burst occurrence. (a) If a flare explosion takes place at the edge of a spot group facing open to a low-Alfven-velocity region, Moreton waves may occur. (b) If, on the other hand, it takes place in the middle of a complex spot group, Moreton waves may not occur. In any case, a type II may take place as long as low-Alfven-velocity regions exist in the corona within a reasonable distance. (c) A case with a streamer-type low-Alfven-velocity region. The region of shock strength enhancement sweeps along the structure roughly with the Alfven-velocity of surrounding medium.

586

Next, it is expected from the nature of our working hypothesis that the coronal streamer structure containing a magnetic neutral sheet may provide a site for type II bursts. This is because it provides a higher density and lower magnetic field region (Pneuman, 1970) into which our coronal MHD fast-mode wave tends to be refracted. The locus of wave entry points to the structure again sweeps along the structure with roughly the local Alfven velocity in the surrounding medium (Figure 7c). This may be consistent with the statement of Dulk et al. (Dulk, Altschuler, and Smerd, 1971). The behavior of the wave in such a region seems to provide a favorable condition for electron acceleration (Smith, 1972), and the strong focussing and strengthening of the shock at the neutral sheet itself may lead to some drastic release (Martin, 1972) of metastable prominence material. This would be due to the destruction of a delicate stabilizing condition by sudden heating or by causing plasma turbulence which may destroy the current system and cause the destabilization. This may be related to the type II - IV association (Steward and Sheridan, 1970), or the observed opening-up of coronal magnetic structure (Wagner, 1972).

ACKNOWLEDGEMENTS

REFERENCES

Altschuler, M. D. and Newkirk, G., 1969, *Solar Phys.* 9, 131.

Anderson, G. E., 1966, Ph.D. Thesis, Univ. of Colorado.

Athay, R. G., and Moreton, G. A., 1961, *Ap. J.* 133, 935.

Dulk, G. A., Altschuler, M. D., and Smerd, S. F., 1971, *Astrophys. Letter* 8, 235.

Dulk, G. A., and Smerd, S. F., 1971, *Austral. J. Phys.* 24, 177.

Hansen, R. T., Garcia, C. J., Hansen, S. F., and Loomis, H. G., 1969, *Solar Phys.* 7, 417.

Kai, K., 1969, *Solar Phys.* 10, 460.

Martin, S. F. (Smith), 1972, in *Proc. Symp. Coronal and Interplanetary Disturbances* (National Center for Atmospheric Research, Boulder).

Meyer, F., 1968, in *Structure and Development of Solar Active Regions,* ed. Kiepenheuer (D. Reidel, Dordrecht).

Moreton, G. A., 1960, *Ap. J.* **65**, 494.

Perry, M., and Altschuler, M. D., 1972, *Solar Phys.,* to appear.

Pneuman, G. W., 1968, *Solar Phys.* **4**, 578.

Riddle, A. C., and Sheridan, K. V., 1971, *Proc. Astron. Soc Austral.* **2**, 62.

Smerd, S. F., 1970, *Proc. Astron. Soc. Austral.* **1**, 305.

Smith, D. F., 1972, *Ap. J.* **174**, 643.

Smith, S. F., and Angle, K., 1971, in *Physics of Solar Corona* (D. Reidel, Dordrecht).

Stewart, R. T., Sheridan, K. V., and Kai, K., 1970, *Proc. Astron. Soc. Austral.* **1**, 229, 313.

Uchida, Y., 1960, *Publ. Astr. Soc. Japan* **12**, 376.

Uchida, Y., 1968, *Solar Phys.* **4**, 30.

Uchida, Y., 1970, *Publ. Astr. Soc. Japan* **22**, 341.

Uchida, Y., 1972, in *Proc. Symp. Coronal and Interplanetary Disturbances* (National Center for Atmospheric Research, Boulder).

Uchida, Y., Altschuler, M. D., and Newkirk, G., 1973, *Solar Phys.* **28**, 495.

Wagner, W. J., 1972, in *Proc. Symp. Coronal and Interplanetary Disturbances* (National Center for Atmospheric Research, Boulder).

Weiss, A. A., 1965, *Australian J. Phys.* **18**, 167.

Wild, J. P., 1969, *Proc. Astron. Soc. Australia* **1**, 181.

Wild, J. P., Smerd, S. F., and Weiss, A. A., 1963, *Ann. Rev. Astron. Astrophy.* **1**.

REGULAR PULSATIONS FROM THE SOLAR CORONA

J.P. Wild

Division of Radiophysics, CSIRO (Sydney)

We have already had from Dr. Alan Maxwell a talk on microwave pulsations from solar flares. I now wish to discuss another class of pulsating phenomenon, namely the meter-wave pulsations, which sometimes show extraordinary regularity.

Looking back through published records I find the first really convincing example of such pulsations to be that of Abrami (1970), recorded on January 13, 1968, in which groups of 5 to 20 regular pulses appeared on three occasions in the one event with periodicities of 3.1 s, 2.4 s, and 2.9 s. Examples of this phenomenon recorded at Culgoora are listed in Table 1 and three of special interest are shown in Figures 1(a) to 1(c). In case a (see McLean et al., 1971) some fifty sharp pulses appeared during a 2.5-minute interval with a period varying gradually from 2.5 s to 2.7 s. In case b, pulse trains with two or more periodicities occurred in superposition. In case c some 25 pulses occurred with a period of 4.25 s.

The properties of these and other pulsation events may be summarized as follows:

- Their dynamic spectrum shows that the pulses occur practically simultaneously over a frequency range typically of 2:1. Their centre frequency usually lies in the band 100 to 300 MHz.

- Individual pulse shapes are often spiky (Figure 1(a)) and sometimes (as noted by Abrami, 1972) of sawtooth shape with slow rise and fast fall (Figure 1(c)).

- The pulse train may begin as a series of emission peaks (Figures 1(b) and 1(c)) or may develop as an apparent modulation of an existing continuum. The pulse train may end abruptly and give way to continuous radiation at peak-pulse level (Figures 1(a) and 1(b)); or it may assume the form of a simple damped oscillation (Figure 1(c)).

  They occur as a feature of a small proportion of type IV bursts (Abrami, 1970).

  They characteristically occur during the late part of a type II burst (see Figure 2 and McLean et al., 1971) when the fundamental band has drifted down to a frequency of about 15 to 30 MHz.

  Their occurrence shows a suggestive correlation with proton flares (McLean et al., 1971). On the latest count, out of fourteen events recorded at Culgoora, eight were associated with proton flares (see Table 1). If the most easterly events are excluded, this correlation is improved to seven out of nine.
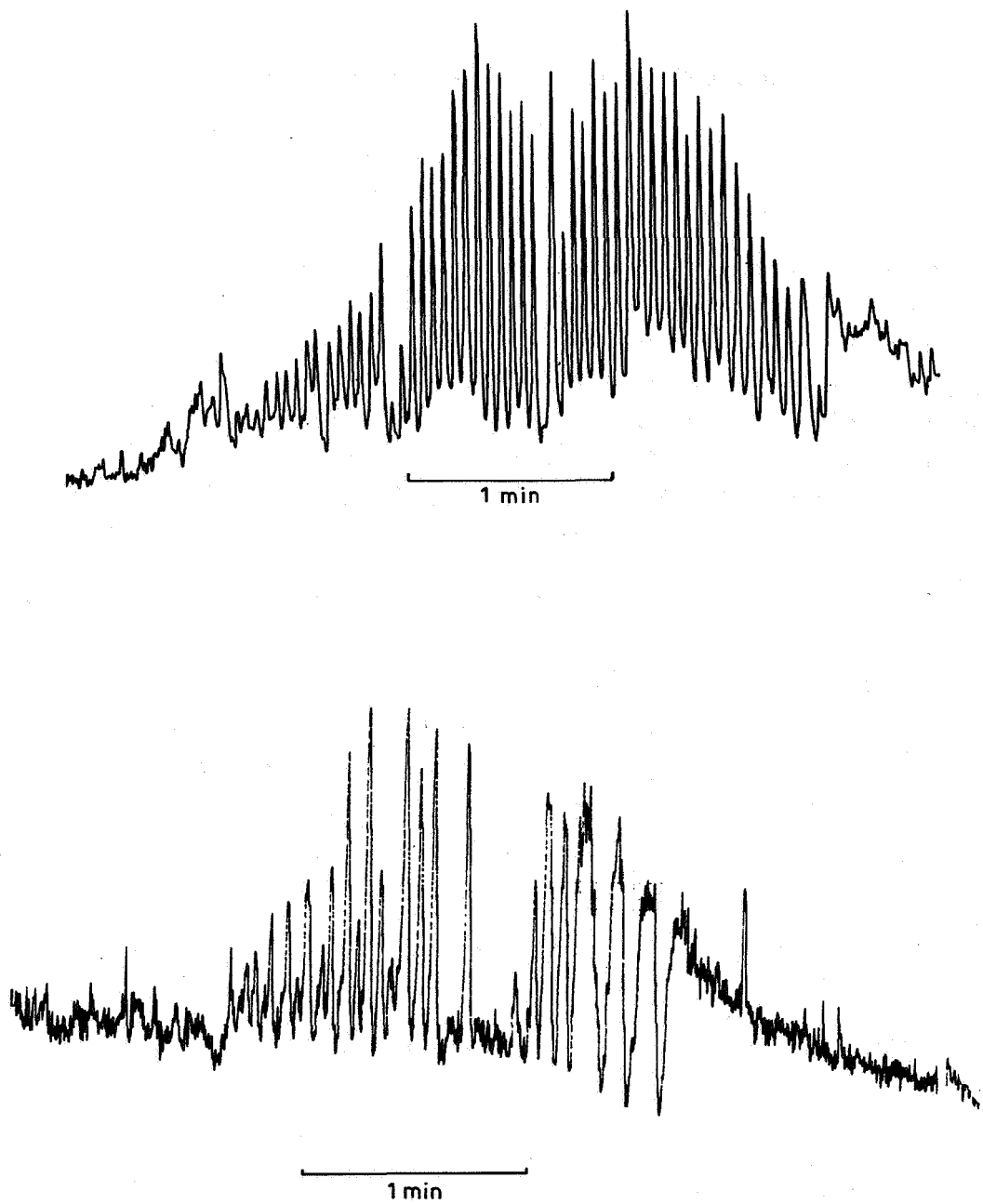
Figure 1.   Examples of coronal pulsations recorded at Culgoora.   The records are microphotometer tracings of spectral records: (a) September 27, 1969, 150 MHz; (b) November 5, 1970, 150 MHz.
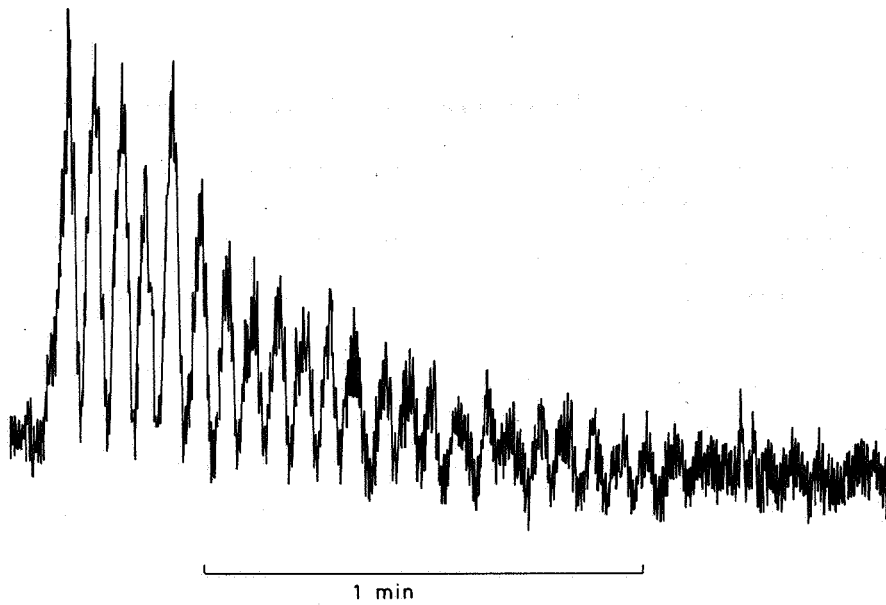
Figure 1. Examples of coronal pulsations recorded at Culgoora. The records are microphotometer tracings of spectral records: (c) May 16, 1972, 230 MHz.
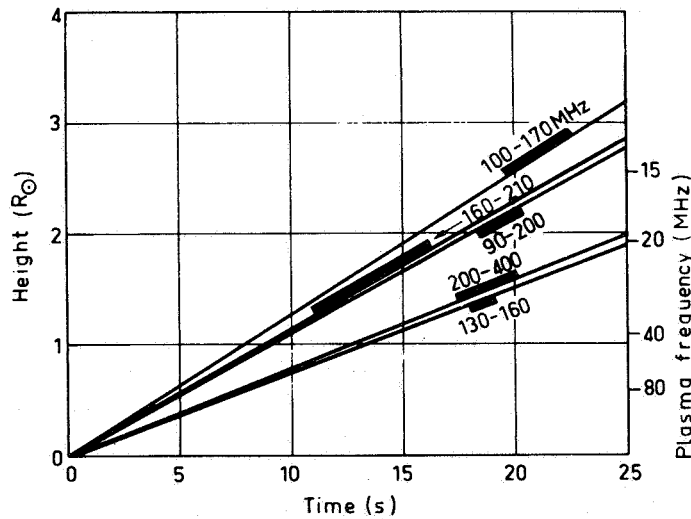
Top to bottom: 27.9.69; 23.11.71; 5.11.70; 16.5.72; 27.6.60

Figure 2. Diagram showing the relation between five pulsating events and type II bursts. The abscissa gives time measured from the flash phase of the flare. The ordinate gives height of the type II shock wave (derived from the fundamental plasma frequency, shown on the right). The radial lines are linear approximations to the height/time plots of the five type II sources. The thick parts of these lines correspond to periods of pulsations. The frequency range of each pulsation event is indicated in megahertz.

591

Table 1

Summary of Pulsation Events Recorded at Culgoora.

Event	Flare (Time of Max)	X-Ray Start 0.5-3A	II Start	Frequency Band (MHz)	Pulsation Times		Quality of Pulsations		Proton Event Detected
1960 June 27	3, S10, E33 (0010)	-	0005	130-160	0013-0014	0018-0021	strong, QP	weak, QP	No
1960 Oct. 11	2, S13, W35 (0601)	-	0532	130-160	0535-0538		weak, QP		No
1969 Feb. 24	2B, N12, W32 (2316)	?	?	100-200	2324-2326		weak		Yes
1969 Mar. 22	1B, N10, W20 (0646)	0643	0647	70-100	0650-0655		strong, QP		?
1969 Sept. 27	3B, N09, E02, (0412)	0350	0403	95-170	0412-0415	0419-0420	strong, P	weak, QP	Yes
1970 Mar. 29	2B, N13, W37 (0046)	0035	0039-0042	200-800	0037-0043		medium, irregular, show drifts		Yes
1970 Apr. 8	-N, N16, E55 (2337)	2325	2334	75-150	2354-2400		weak, QP (instrumental ?)		No
1970 June 13	-N, N18, E56 (0303)	0300 (weak)	0306	70-200 400-700	0302.5-0305.5	0312.5-0313.5	weak, P some drift	weak	No
1970 Nov. 5	3B, S12, E36 (0330)	0310	0324	90-200	0337-0339	0344-0347	strong, P	weak, QP	Yes
1970 Dec. 11	1N, N16, W02 (2241)	2215	2238	80-160	2251-2252.5		weak, QP		Yes
1971 Jan. 24	2B, N19, W49 (2320)	2310	2316	100-200 200-400	2324-2326	2327.5-2328.5	dubious	strong, QP	Yes
1971 June 29	-B, N17, W22 (2238)	? (weak)	2239	200-400	2301.5-2302.5		weak, QP		Yes
1971 Nov. 23	1B, S19, E60 (0604)	0545	0555	150-200	0550-0555	0555-0601	weak	strong, QP	probably
1972 May 16	-B, S06, W15		0310	200-400	∩314.5-0316.5		strong, P		No

The origin of the pulsations has been attributed by Rosenberg (1970) to synchrotron radiation from electrons trapped in a flux tube undergoing radial oscillations from standing mhd waves. Assuming this to be the case, McLean et al. (1971) proposed a unified model which attempted to explain the acceleration of the particles (electrons and protons), the pulsating phase, the declining continuum phase, and the correlation with type II bursts. The model depended on the interaction of a shock wave with an arch-shaped magnetic flux tube in the corona; the pulsations occur as the shock passes through the top of the arch which the type II evidence locates at a height of 1 to 3 $R_\odot$ above the photosphere. The model clearly predicts that the sources of these pulsations are located at these heights; no suitable positional measurements are yet available to check this prediction.

There remain a number of puzzling features not yet explained. No theory satisfactorily accounts for the abrupt finish of the pulsations (typified by Figure 1(b)) and for the continuity of the ensuing continuum with the envelope of the pulses. Nor has the

characteristic sawtooth waveform been explained. The explanation of this intriguing phenomenon may make a considerable contribution to the understanding of the acceleration process responsible for solar protons.

ACKNOWLEDGMENT

I wish to thank Ian Palmer for assembling the Culgoora data presented in Table 1 and Figure 2.

REFERENCES

Abrami, A., 1970, *Solar Phys.* 11, 104.

Abrami, A., 1972, *Nature* 238, 25.

McLean, D.J., Sheridan, K.V., Stewart, R.T., and Wild, J.P., 1971, *Nature* 234, 140.

Rosenberg, H., 1970, *Astr. Ap.* 9, 159.

THE POSITION AND SIZE OF RADIO SOURCES

ASSOCIATED WITH SOLAR ELECTRON EVENTS

I. D. Palmer

University of California, Los Alamos Scientific Laboratory
Los Alamos

R. P. Lin

Space Sciences Laboratory, University of California
Berkeley

ABSTRACT

The positions and sizes of the sources of type III bursts which are associated with inter-planetary electron events (> 45 keV) are observed by the 80-MHz Culgoora radioheliograph. The sizes of the responsible electron streams at 0.6 $R_\odot$ in the corona are much smaller than the cones of propagation of the electrons in interplanetary space. Many of the type III bursts are shown to be accompanied by a type V continuum, and it is argued that the observation of a type III to V radio burst implies an increased spreading of electrons at heights > 0.6 $R_\odot$, consistent with the extent of the propagation cone of the electrons in interplanetary space.

INTRODUCTION

The study of energetic particle events detected in interplanetary space provides insight into the generation and escape of the particles from the sun. The Culgoora radioheliograph has made it possible to investigate the positions and movements of energetic particles in the corona at heights $0.6 \rightarrow 1.0$ $R_\odot$ (Wild and Smerd, 1972). One current investigation, which we report on here, concerns the position and spatial size of the type III bursts which are associated with interplanetary electron events of energies > 45 keV. Alvarez et al. (1972) report essentially one to one correlation of kilometric wavelength type III bursts and electron events from flares in the western solar hemisphere. The current estimates of electron energy required to produce the observed drift rates of type III bursts are 10 to 100 keV, in good correspondence with the > 45 keV energies detected in interplanetary space. In this paper we assume that a type III radio burst which is closely associated in time with the onset of an interplanetary electron event (that is, occurring < 1 hour before) represents the escape of the electrons from the sun. We present the positions and sizes of type III radio bursts recorded at 80 MHz in several events, and consider their implications for the size of the escaping electron stream.

594

THE ELECTRON EVENTS AT 1 AU

The intensities of the electron events recorded at energies > 45 keV by IMP-5 (Earth-orbiting) during five days in 1970 are shown in Figure 1 (the University of California detectors are described in Anderson and Lin, 1970). The associated type III burst is designated by the black rectangle. The onset time, o, and the time of maximum, m, of each electron event are shown on an expanded time scale in Figure 2. Comparison with the times for direct transit across 1.3 AU for 100 keV and 200 keV electrons (see the bottom of the figure) implies that in all but the September 13, 1970 event, the first arriving electrons have traveled directly from the region of the type III burst to earth. That is, the onset and the time to maximum of the first five events of Figure 2 are essentially independent of the longitude of the flare source between W46 and W87 (the flare positions are given in Figure 2).
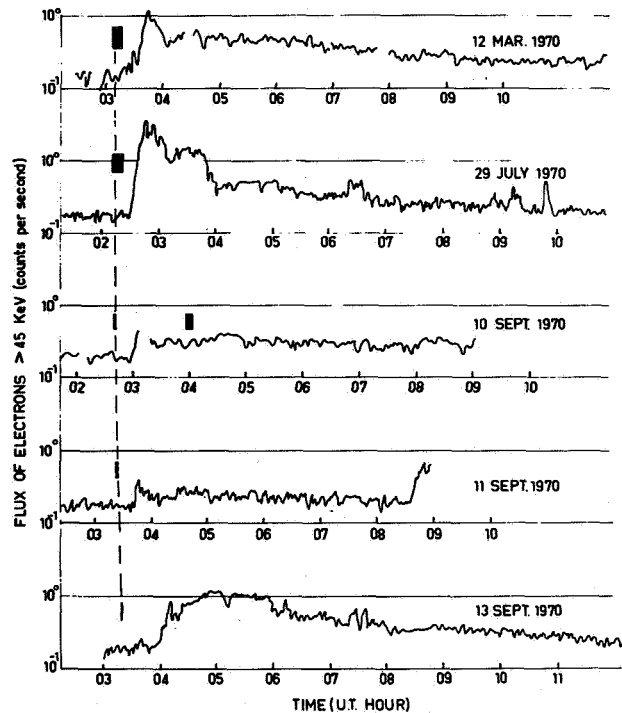

Figure 1. Time profiles of the intensity of > 45 keV electrons recorded at 1 AU by IMP-5 during 1970. The associated type III burst is designated by the black rectangle.

Type Three Burst   >45 keV Electrons
                    Onset (o)   Maximum (m)

12 Mar. 1970
2N, Sl4, W46   0306 U. T.

29 July 1970
IN, Nl3, W63   0212

10 Sept. 1970
--N, Nl4, W67   0241

10 Sept 1970₂
-N, Nl3, W7l   0400

11 Sept. 1970
--N, Nl4, W87   0321

13 Sept. 1970
? Wl00-ll0   0016 U. T.

Direct transit |————| 100 keV
Across 1.3 A. U. |————| 200 keV

0   20   40   60   80   100 Minutes
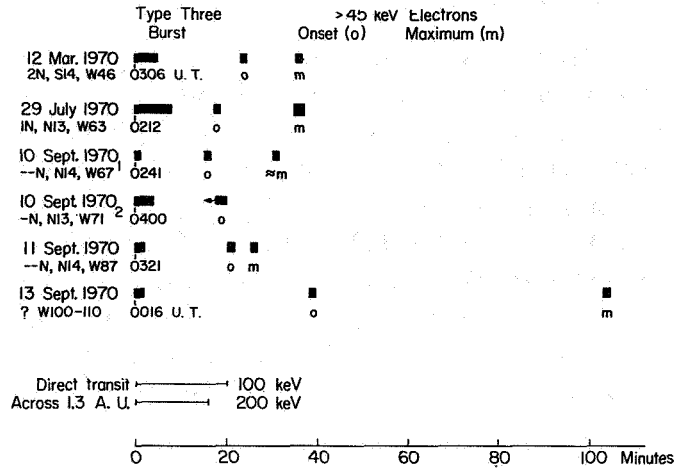
Figure 2. The onset time, o, and the time of maxi-
mum intensity, m, for each of the electron events of
Figure 1. These times are compared with the time for
direct transit of 100 keV and 200 keV electrons
across 1.3 AU.

These observations can be used to deduce the size of a "propagation cone" into which the electrons are injected from the sun and along which they have direct access to distances 0 (1 AU) in interplanetary space. If it is assumed that the foot of the nominal spiral field line through earth lay at W60 at the sun (the solar wind velocity was approximately 400 km/s^{-1} around the time of each of the events in Figure 1), the range of flare longitudes (W46 to W87) implies a propagation cone of width $\gtrsim 30°$ in longitude at 1 AU. This conclusion confirms the results of Lin (1970b) in which many scatter-free electron events (> 45 keV) from one particular active region gave a cone size of 70°, and the results of a comprehensive study of many prompt > 45 keV electron events recorded during 1967 and 1968 (Lin and Anderson, 1967).

THE TYPE III RADIO SOURCES

In Figure 3(a) is shown, corresponding to each electron event of Figure 1, a representative 1-second contour diagram of the associated type III radio source at 80 MHz (1/2 and 1/4 power contours are drawn). Each source is superimposed on a Stoneyhurst disk which is 1.6 times larger than the sun's photosphere to enable the projected position of the source on the photosphere to be read off directly. We make the usual assumption that the radio emission came from the 80-MHz plasma level at a height of 0.6 $R_\odot$ above the photosphere (fundamental and harmonic sources are observed to come from almost the same position, Stewart, 1972). This procedure yields good agreement between the projected source position and the solar flare position in the first event of Figure 3(a), while in the others the radio source appeared to come from slightly higher than 0.6 $R_\odot$. Figure 3(b) shows

596

12 MAR. 1970
2N,S14,W46

29 JUL. 1970
1N,N13,W63

10 SEPT. 1970₁
--N,N14,W67

10 SEPT. 1970₂
-N,N13,W71

11 SEPT. 1970
--N,N14,W87

13 SEPT. 1970
? W100-W110

Figure 3(a). Representative 1-second contour diagrams of the 80 MHz type III radio sources associated with the > 45 keV electron events of Figure 1. The contours are 1/2 and 1/4 power levels. The positions of the associated solar flares are also given. The Stoneyhurst disks are drawn 1.6 times larger than the photosphere, thereby projecting the radio source onto the photosphere (the radio emission is assumed to come from a height of 0.6 $R_\odot$).

11 Sept. 1968
?

31 Oct. 1968
3B, S14, W37

25 Nov. 1968
-N, S11, E01

26 Feb. 1969
2B, N13, W46

29 May 1969
1B, N11, W64

13 Oct. 1969
-N, S13, W37
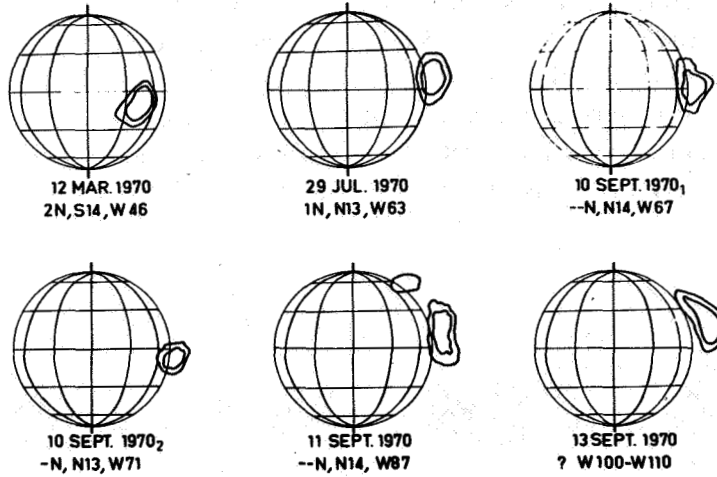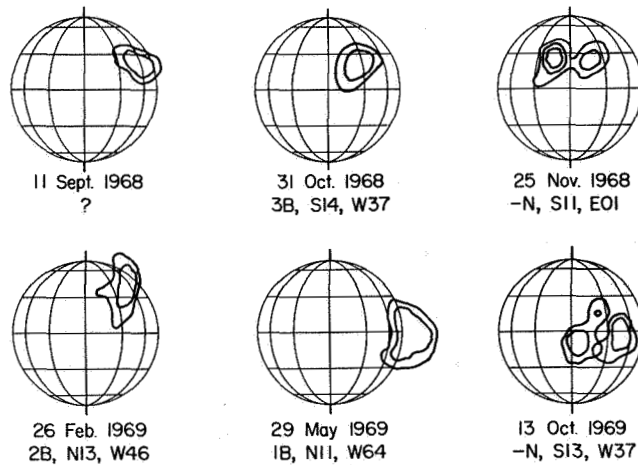
Figure 3(b). Representative 1-second contour diagrams of 80 MHz type III radio sources associated with > 45 keV electron events which were detected by AIMP-2 and IMP-5 in 1968 and 1969.

597

representative 1-second contours for another six type III radio bursts associated with electron events recorded in 1968 and 1969. (Note the northward displacement of the radio sources from the flare positions in the October 31, 1968, and the November 25, 1968 events; these may represent magnetic guiding of the responsible electrons.) Figure 4 shows the Culgoora dynamic spectrum at the times of three of these type III events. As can be seen, a type III group may consist of a varying number of individual bursts.
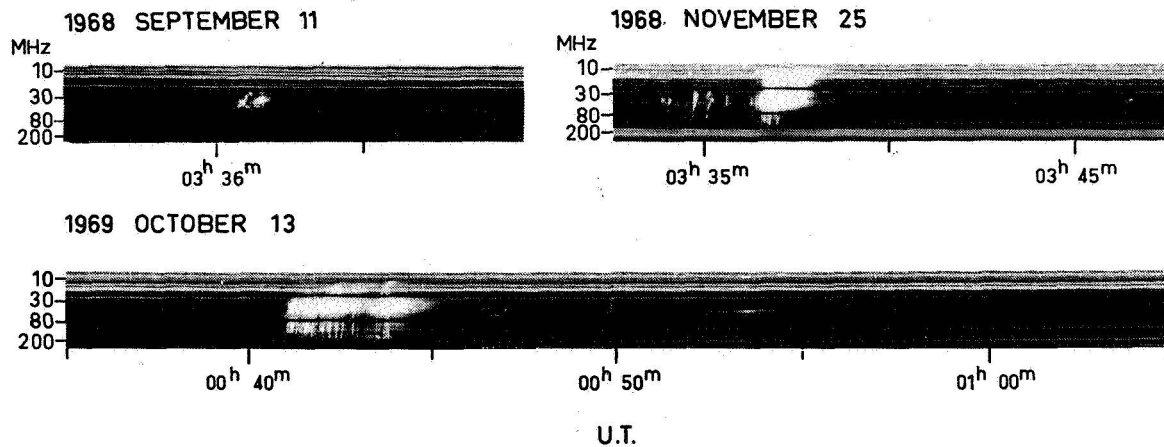
Figure 4. The Culgoora dynamic spectra of three of the type III radio bursts in Figure 3(b). The vertical scale is frequency in MHz. Note the type V continuum which appears as an extension of the type III bursts on November 25, 1968 (0337 to 0338 UT), and October 13, 1969 (0344 to 0345 UT).

The average size of all the radio sources in Figures 3(a) and (b) is 6 arcmin as seen from earth. However, before this dimension can be converted to a longitude at the sun, the effect of scattering by coronal inhomogeneities, which increases the size of a radio source, must be taken into account. Riddle (1972) and private communication, 1972, has been able to predict observations of source sizes and positions by numerically modeling ray transport from a point source through a scattering corona. His conclusion is that an apparent source size of 6 arcmin should be almost entirely due to scattering of radiation from a true source size of $\lesssim$ 1 arcmin. (Note that if the smallest source size — 4 arcmin — was regarded as the amount of broadening due to scattering in all cases, the true source size deduced in this way would average 1.8 arc minutes.) Thus the true dimension of the type III radio sources would probably have been $\lesssim$ 4° in longitude at W60 on the sun. If we assume that the radio source is indicative of the electron stream size, then there exists a marked discrepancy between the longitudinal extent ($\lesssim$ 4°) of the electron stream at 0.6 $R_{\odot}$ and the cone of propagation ($\gtrsim$ 30°) of electrons in interplanetary space.

DISCUSSION

Evidence for divergence of the electron stream above 0.6 $R_\odot$ in the November 25, 1968 event is provided by the radioheliograph observations in Figure 3(b). Here the type III burst at 80 MHz first appeared as the source on the left, but was later followed by the source on the right. This second source is identified as type V and is seen clearly on the Culgoora dynamic spectrum, shown in Figure 4, as a continuum (between 10 and 80 MHz) extension of the type III burst, lasting about 1 minute at 30 MHz. For type V sources which can be identified on the spectrum at 80 MHz, radioheliograph observations usually show a displacement or an enlargement from the preceding type III source (the contours of October 13, 1969, and May 29, 1969 are more examples of this behavior). The current interpretation of the type V continuum is that it is radiation from electrons which have become trapped in magnetic loops adjacent to the field lines along which the type III-generating electrons escape (Weiss and Stewart, 1965; Wild and Smerd, 1972). Now ten out of twelve of the radio events considered here do exhibit either a displacement (6/12 events, including three out of the first five of the events in Figure 2), or an enlargement (4/12 events). Although the type V continuum cannot in all cases be clearly seen on the dynamic spectrum, a displacement in position (or an enlargement) may well be the signature for a type V in the more sensitive radioheliograph observations (Labrum, private communication, 1972).

Thus type III radio bursts that are accompanied by a type V continuum provide evidence for the increased spreading of the electron stream at heights > 0.6 $R_\odot$. Figure 5 illustrates the distribution of electrons in the magnetic field configuration invoked to explain the type III to V emission. Also shown are the regions of generation of the type III and type V radio bursts at 80 MHz. The divergence of the electron stream at heights above the 80 MHz level would result in a much-enlarged radio source as seen by, for example, a 20 MHz radioheliograph (see the figure). One prediction which arises as a consequence of this discussion is that interplanetary > 45 keV electron events should be associated with type III radio bursts which contain a more predominant type V component than in type III bursts not associated with electron events.

An alternative hypothesis, that electron cones remain small ($\lesssim 4°$) in interplanetary space but occur randomly over a larger $\gtrsim 30°$) cone associated with an active region, is rejected because the statistical correlation observed between > 20 keV X-ray bursts and electron events is too great during the times when the active regions discussed by Lin (1970b) are producing electrons detectable at earth.

In conclusion, electron streams which appear in interplanetary space are observed through their radio emission as they escape through the inner corona at heights of 0.6 $R_\odot$. The size of the electron streams responsible for the type III bursts is much smaller than the longitudinal cone in which the interplanetary electrons propagate. After finding that a type V component of emission accompanies the type III burst in many of the events analyzed, we have suggested that the coronal magnetic field configurations which are invoked to

explain these radio bursts imply the increased divergence of the electron stream at heights > 0.6 $R_\odot$. Hence the observations of type III to V radio sources with the 80-MHz radioheliograph are consistent with the cones of propagation of the electrons in interplanetary space.
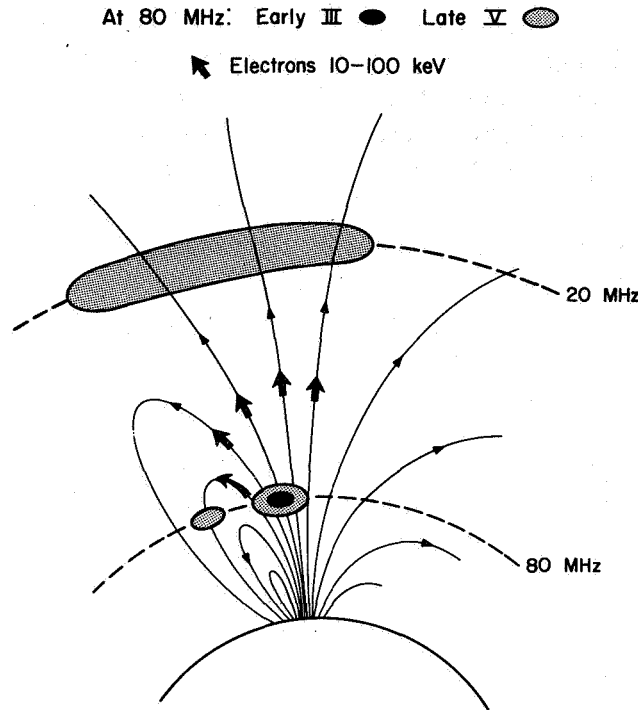
Figure 5. Illustrating the distribution of electrons in the coronal magnetic field configuration which is invoked to explain type III to V radio emission. Representative type III and type V source regions are shown at the 80 MHz plasma level. Considerable divergence of the electron stream occurs above this level.

ACKNOWLEDGMENT

REFERENCES

Alvarez, H., Haddock, F., and Lin, R.P., 1972, Preprint, Space Sciences Laboratory, Univ. California, Berkeley.

Anderson, K.A., and Lin, R.P., 1970, Preprint 89, Space Sciences Laboratory Series II, Univ. California, Berkeley.

Lin, R.P., and Anderson, K.A., 1967, *Sol. Phys.* **1**, 446.

Lin, R.P. 1970a, *Sol. Phys.* **12**, 266.

Lin, R.P. 1970b, *Sol. Phys.* **15**, 453.

Riddle, A.C., 1972, *Proc. Astron. Soc. Austral.* **2**, 98, and private communication.

Stewart, R.T., 1972, *Proc. Astron. Soc. Austral.* **2**, 100.

Weiss, A.A., and Stewart, R.T., 1965, *Austral. J. Phys.* **18**, 143.

Wild, J.P., and Smerd, S.F., 1972, *Ann. Rev. Astron. Astrophys.* **10**.

HIGH SENSITIVITY SPECTRAL OBSERVATIONS IN THE DECAMETRIC RANGE

Jérome de la Noë, André Boischot,
and Monique Aubier

Meudon Observatory (France)

INTRODUCTION

High resolution dynamic spectra of solar emissions are obtained in the range 80 to 20 MHz at the Nancay station of Meudon Observatory. The frequency resolution is 15 kHz; the time resolution is 20 ms. Simultaneously, three fixed-frequency receivers are used on 60, 36.9, and 29.3 MHz. For one month in Summer 1970 (Boischot et al., 1971), the equipment had been used with the 1,000 feet dish of Arecibo Observatory in order to obtain a much higher sensitivity. Only three major features of our observations will be described here.

DECAMETRIC CONTINUUMS OR DECAMETRIC STORMS

Decametric continuums have been described by Warwick (1965) as "broadband, smooth emission coupled with minor bursts but not in association with a major type II or type III burst." With better time resolution we observed that these continuums are accompanied by a lot of type III bursts and various kinds of bursts: type V bursts, drift pair bursts (de la Noë and Pedersen, 1971), split pair bursts, and so forth. Our observations presented in Figures 1 and 2 confirm the result derived previously from statistical studies (Boischot et al., 1970), namely that decametric storms are associated with metric noise storms mainly constituted by type I bursts superimposed on a broadband continuum. The high sensitivity observations allow us to study this association in more detail, and in particular to conclude that in the decametric range there are two classes of type III bursts:

- The first class regroups type III bursts which are generally intense, isolated, or in small groups, and correlates them with type III bursts in the metric range. These bursts occur at the time of flares of small as well as large importance.

- The second class concerns storm type III bursts observed during the decametric storms. They are only accompanied by type I bursts in the metric range. Some examples are shown in Figures 1 and 2. These storm type III bursts are not correlated with flares.

The main feature of storm type III bursts is their starting frequency located between 100 and 40 MHz, generally closed to the low frequency cutoff of the related type I noise storms. The transition between type I and type III storms corresponds to altitudes between 0.5 and 1.0 solar radius above the photosphere.
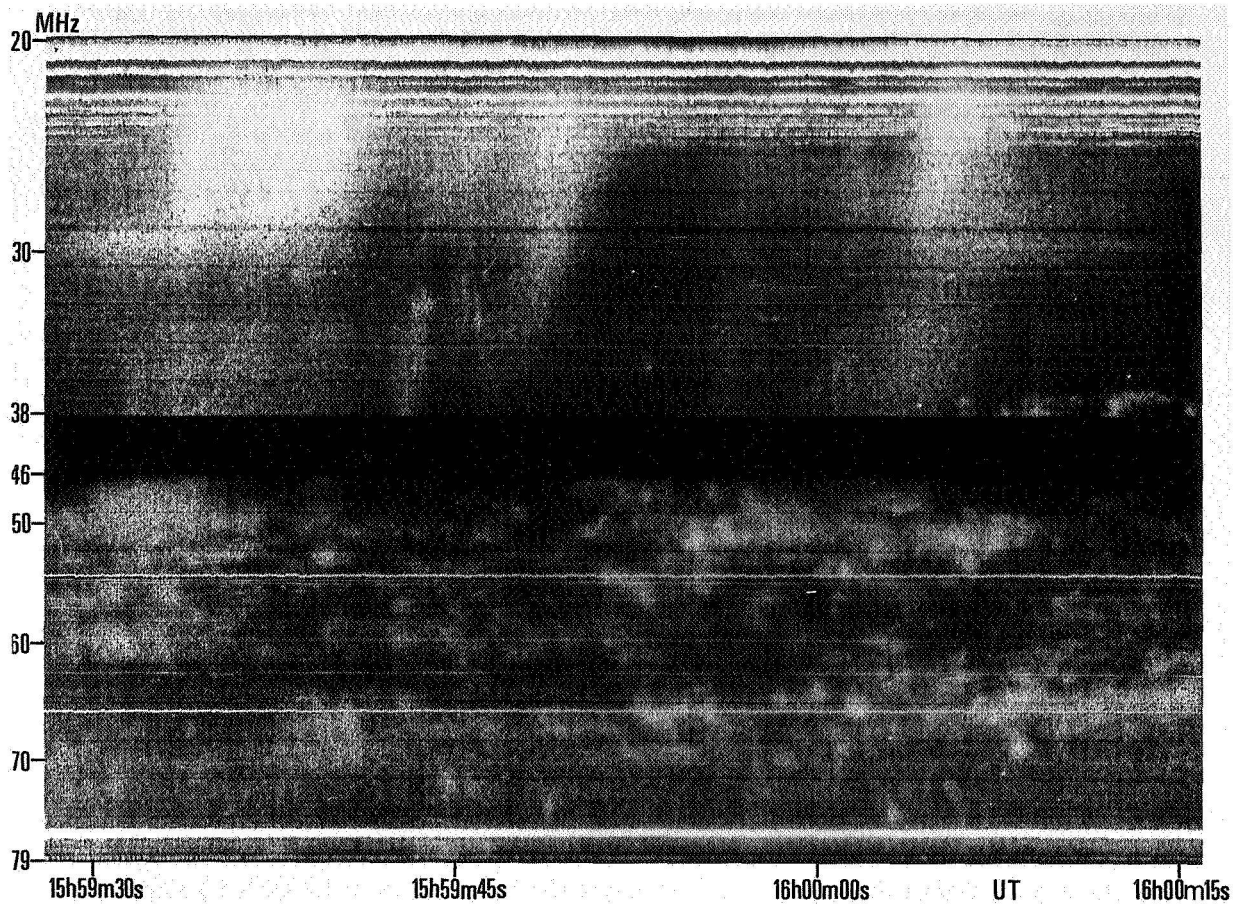
Figure 1. Storm type III bursts in the 20 to 40 MHz range correlated with only type I bursts in the 37 to 80 MHz range on July 23, 1970. White horizontal lines are interferences: local broadcasting and transmitters (TV at 77.5 MHz).

Up to now, only the low starting frequency and the average intensity seem to distinguish the storm type III bursts from the flare-associated type III bursts. Then we are led to take into consideration the possibility of particle acceleration in the upper corona proposed by Gordon (1970) to generate storm type III bursts. Another possibility would be a quasi-continuous leakage of high energy electrons in the upper corona.
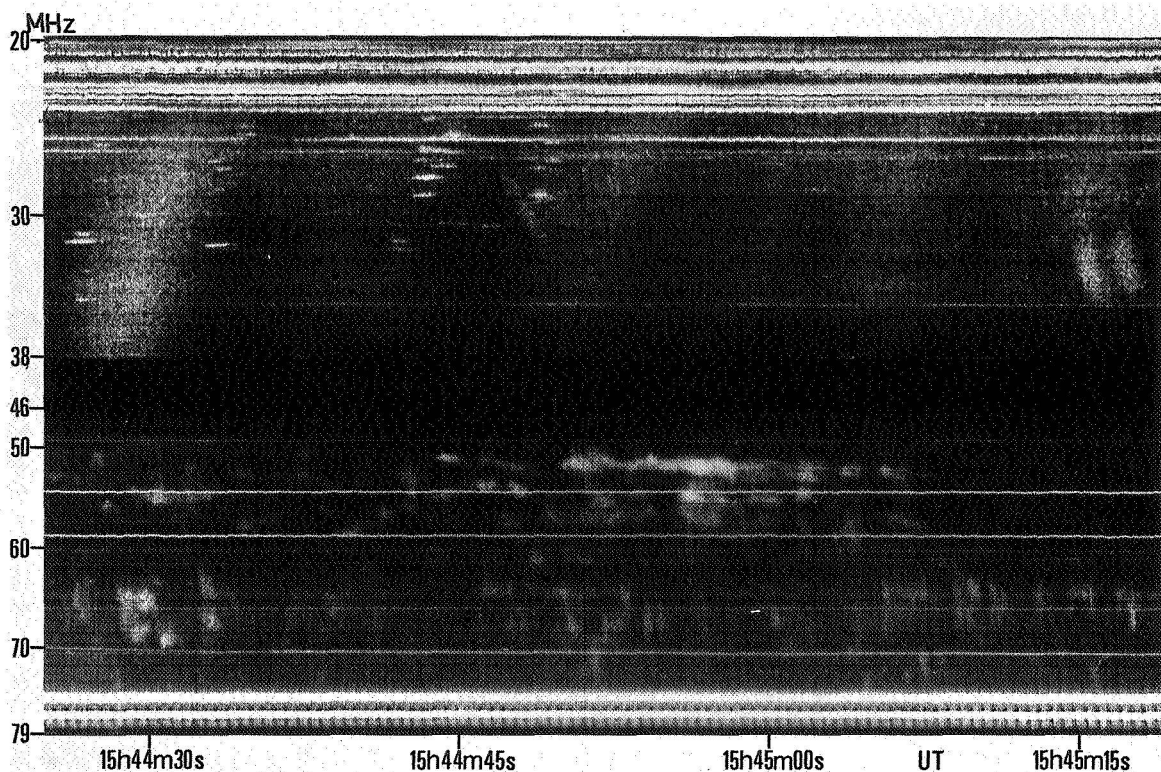
Figure 2. Various kinds of bursts during decametric storm on July 25, 1970, associated with type I noise storm: storm type III bursts (example: $15^h 44^m 30^s$), type IIIb bursts (example: $15^h 44^m 45^s$), single reverse drift burst ($15^h 44^m 50^s$), and reverse drift pair burst ($15^h 45^m 16^s$). Note the sharp low frequency cutoff of the type I storm.

TYPE IIIb BURSTS

Split pair bursts have been observed by Ellis several years ago (Ellis and McCulloch, 1966, 1967; Ellis, 1969). These bursts are made of two narrow-banded, short-lived, slowly drifting bursts. Their mean bandwidth is 100 kHz and their mean frequency splitting 120 kHz; their duration is about 1 second and their drift rates vary from 0 to -50 kHz·s^{-1}.

In our Arecibo observations we obtained several hundreds of these bursts in addition to a ten times greater number of similar single emissions that we called stria bursts. These elementary bursts are observed either randomly distributed in the frequency-time plane or grouped in chains which drift in frequency in the same way that the type III bursts drift (Figure 3). So we called these chains type IIIb bursts (de la Noë and Boischot, 1972). Their main characteristics are the following:

       ●   Type IIIb bursts occur in decametric storms (Figure 2) and are nearly as frequent as storm type III bursts.

604
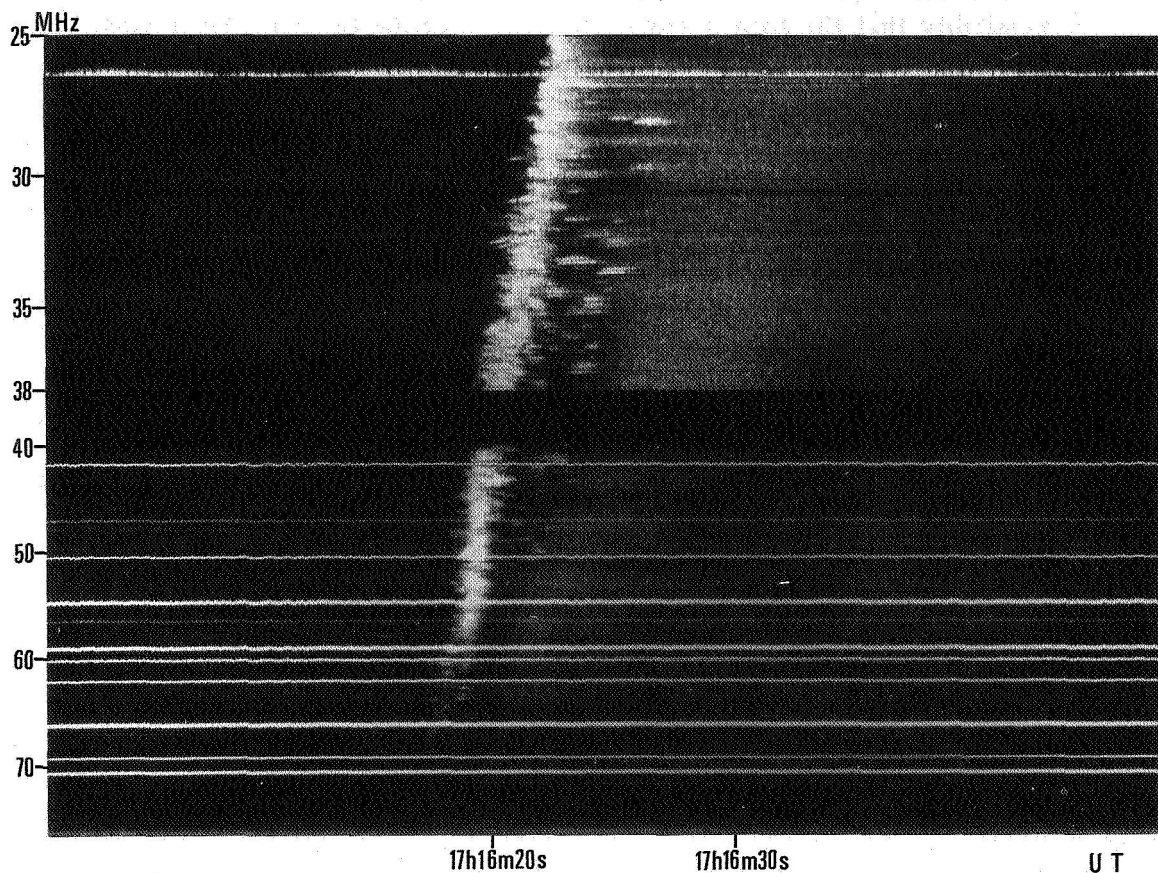
Figure 3. A type IIIb burst precursor of type III burst on August 8, 1970 from 75 to 25 MHz. Note the dispersion in time of striae and the large number of split pair bursts in the type IIIb burst.

- They occur at low frequencies, especially around 30 MHz.

- Their drift rates are of the same order as that of the type III bursts in the same frequency range.

- The number of elementary bursts in a type IIIb burst may be very large (up to 40 units in the 80 to 25 MHz range), but it is often of only a few units. At the limit an isolated stria or split-pair burst may be considered as a type IIIb burst reduced to a single element.

- Type IIIb bursts are much more circularly polarized than type III bursts with degrees of polarization reaching 100 percent.

- Thirty percent of type IIIb bursts are immediately followed by a type III burst as in Figure 3. A detailed analysis of the time delay and frequency ratio between the

605

two related type IIIb and type III bursts cannot completely exclude the possibility that the former burst corresponds to the fundamental emission, and the latter to the harmonic. But several characteristics suggest that type IIIb burst is more likely a precursor of the type III burst.

All these properties lead us to conclude that:

- The exciters of type IIIb and type III bursts are of the same nature, probably a stream of electrons moving upward in the corona with velocity of 0.3c.

- The fact that type IIIb bursts can be reduced to a single elementary burst suggests that some streams of particles can go up in the corona without giving rise to any emission. Then we can imagine that for decametric storms there is a quasi-continuous leakage of high energy electrons, the occurrence of type IIIb and type III bursts being observed only in suitable circumstances.

- The relation of type IIIb to type III bursts would be explained by a mechanism taking place in the front of the stream, due either to the fastest electrons or to a kind of wave of great amplitude accompanying the leading edge of the stream.

TIME PROFILE OF TYPE III BURSTS

The decay of type III bursts has generally been assumed to be due to collisional damping of the plasma waves which give rise to the radio emission. This theory leads to a very simple way to determine the electronic temperature in the corona.

In our fixed frequency records (60, 36.9, and 29.7 MHz) obtained in Arecibo, we selected a large number of perfectly well isolated bursts. The results of the analysis (Aubier and Boischot, 1972) are the following:

- Time profiles at high levels are always symmetrical around the peak of emission.

- For lower levels (inferior to 10 dB) the decay follows an exponential law.

- The decay time constants are scattered only within a factor of 2 or 3 for all the days of observation; the same is true for half peak durations at a given frequency.

- The duration of the burst and the decay constant are independent of the intensity of the burst (Figure 4).

- There is a clear relation between the duration of the burst and the decay constant: the larger the duration, the larger the decay constant. This important relation shows that even if the deduced temperatures are in agreement with the generally expected temperatures at each altitude in the corona, the theory of collisional damping is probably not right.

This conclusion is also drawn from Figure 5, which gives the coronal temperatures derived from type III bursts assuming a collisional damping. In the decimetric and metric ranges, it is difficult to conclude due to the inaccuracy of the determinations. In the decametric range

606
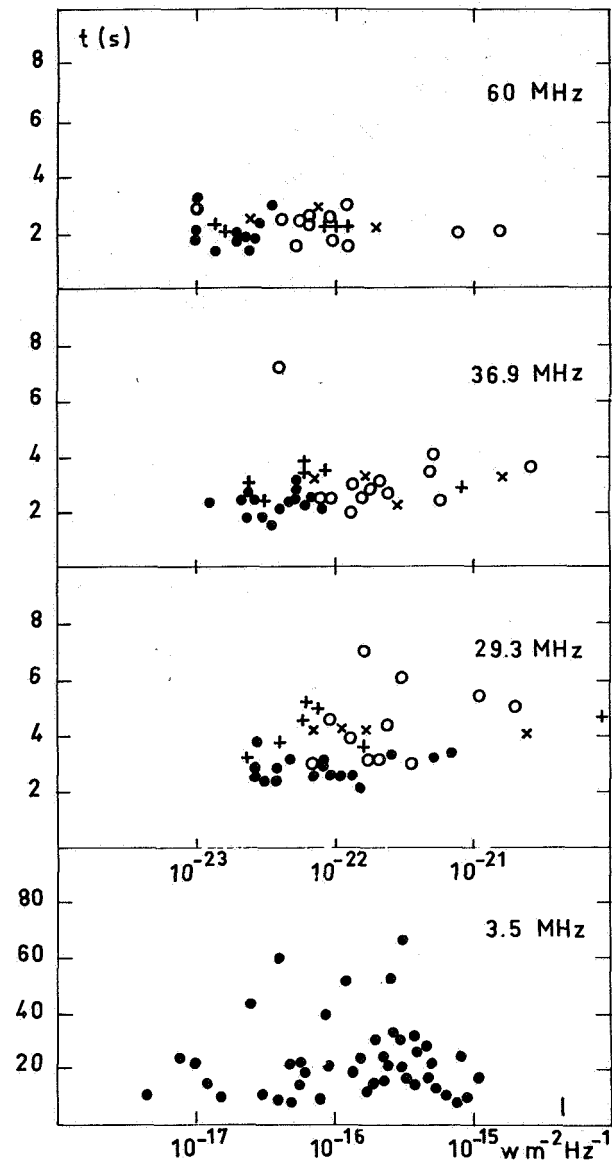
Figure 4. Half-peak intensity duration t of type III bursts versus intensity. Different symbols correspond to different days. The 3.5 MHz data shown for comparison are from Graedel (1969).
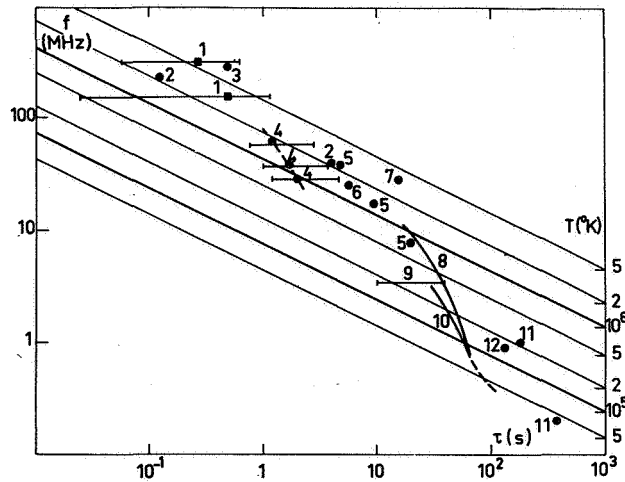
Figure 5. Observed decay time constant versus frequency. The straight lines correspond to constant temperatures. References: 1. Elgarøy (1961). 2. Elgarøy et al. (1963). 3. de Groot (1966). 4. Aubier et al. (1972). 5. Boischot (1967). 6. Malville (1962). 7. Riihimaa (1963). 8. Hartz (1969). 9. Graedel (1969). 10. Alexander et al. (1969). 11. Slysh (1967). 12. Slysh (1967).

the gradient of the electronic temperature is too large to easily fit the temperatures in the low corona and the temperatures measured at 1 AU. In the hectometric and kilometric ranges, values of the electronic temperature are derived which are much too low. Then we can conclude that at least in these ranges collisional damping theory does not apply.

Some new study of Landau damping is being made which could explain part of these results (Harvey and Aubier, 1973).

REFERENCES

Alexander, J.K., Malitson, H.H., Stone, R.G., 1969, *Solar Phys.* **8**, 388.

Aubier, M.G., Boischot, A., 1972, *Astron. Astrophys.* **19**, 343.

Boischot, A., 1967, *Ann. Astrophys.* **30**, 85.

Boischot, A., de la Noë, J., Møller-Pedersen, B., 1970, *Astron. Astrophys.* **4**, 159.

Boischot, A., de la Noë, J., du Chaffaut, M., Rosolen, C., 1971, *C.R. Acad. Sci. Paris,* Series B, **272**, 166.

608

de Groot, T., 1966, *Rech. Astr. Obs. Utrecht* **XVIII**, (1).

de la Noë, J., Boischot, A., 1972, *Astron. Astrophys.* **20**, 55.

de la Noë, J., Møller-Pedersen, B., 1971, *Astron. Astrophys.* **12**, 371.

Elgarøy, Ø., 1961, *Astrophys. Norvegica* **7**, 123.

Elgarøy, Ø., Rødberg, H., 1963, *Astrophys. Norvegica* **8**, 271.

Ellis, G.R.A., McCulloch, P.M., 1966, *Nature* **211**, 1070.

Ellis, G.R.A., McCulloch, P.M., 1967, *Austral. J. Phys.* **20**, 583.

Ellis, G.R.A., 1969, *Austral. J. Phys.* **22**, 177.

Gordon, I.M., 1970, *Astrophys. Letters* **5**, 251.

Graedel, T.E., 1969, Thesis, NASA Contract NA 5-2051.

Hartz, T.R., 1969, *Plan. Space Sci.* **17**, 267.

Harvey, C.C., Aubier, M.G., 1973, *Astron. Astrophys.* (in press).

Malville, J.M., 1962, *Ap. J.* **136**, 266.

Riihimaa, J.J., 1963, *Ann. Academia Scientiarum Fennicae* Series A' Physica, 131.

Slysh, V.I., 1967, *Soviet Astronomy—A.J.* **11**, 389.

Slysh, V.I., 1967, *Cosmic Res.* **5**, 759.

Warwick, J.W., 1965, *Solar System Radio Astronomy* (New York: Plenum Press), 131.

A HIGH RESOLUTION STUDY IN TIME, POSITION, INTENSITY, AND FREQUENCY OF A RADIO EVENT ON JANUARY 14, 1971

C. Caroubalos and M. Pick
Observatoire de Paris-Meudon

H. Rosenberg
Sterrewacht "Sonnenborgh", Utrecht

C. Slottje
Solar Radio Observatory,
Netherlands Foundation of Radio Astronomy

INTRODUCTION

High resolution position and spectrum measurements have been made of a complex solar radio activity on January 14, 1971, from 1120 to 1130 UT. Positions were measured with the 169 MHz Nancay E-W Radioheliograph, while dynamic spectra and polarization were observed with the 60-channel radiospectrograph of Nera.

The radio event consisted of two closely similar groups of type III bursts and type II- like details, and a stationary type IV continuum, including some very clear pulsating structures. The general aspect of this activity is seen in Figure 1.

THE PULSATING STRUCTURE

Very often, the spectrum of a stationary type IV burst seen at metric wavelengths shows a striated aspect, that is a sequence of short, broad band pulses superimposed on the continuum. In general, these pulses occur at typical intervals of 0.1 to 3 seconds. For some rare events, the pulsating structure modulates the intensity in a periodic manner (Rosenberg, 1970; Mc Lean et al., 1971; Abrami, 1972).

It was suggested that the continuum emission is caused by a synchrotron radiation mechanism, and that the fluctuation in the emission is due to the fluctuation of the local magnetic field strength. This is in turn due to magnetohydrodynamic (MHD) disturbances propagating perpendicularly to the magnetic field (Rosenberg, 1971). Up to now no radioheliographic observations have been available for testing the validity of this suggestion.

A short period of typical pulses on January 14, 1971, is presented in Figure 2. They occur at irregular intervals of 0.1 to 1 s. Both the pulses and the continuum were circularly polarized in the same sense. The most important result of the observations is that the measured angular size of the pulses is found to be 3.6 ± 0.3 arcmin, which is very close to

610
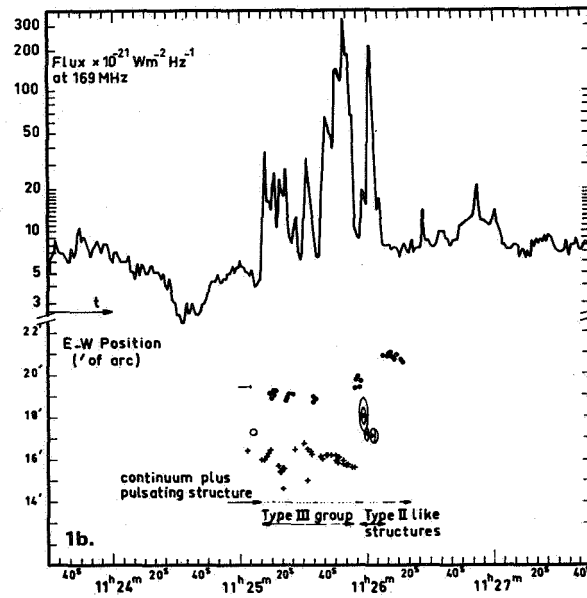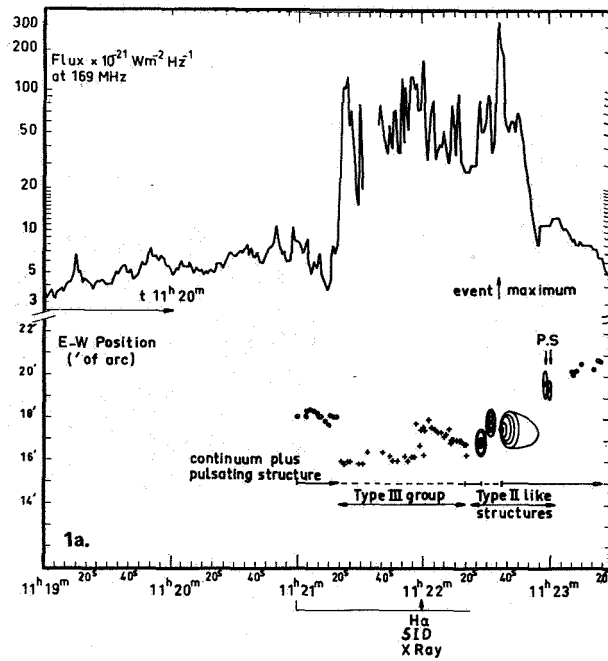
Figures 1(a), (b). General aspect of the activity at 169 MHz. Upper portion: flux density versus time; lower portion: positions versus time.

● Pulsating structure of continuum

⊙ ps: 2 intense pulses identifiable on the spectrum

+ type III bursts

◉ type II bursts.
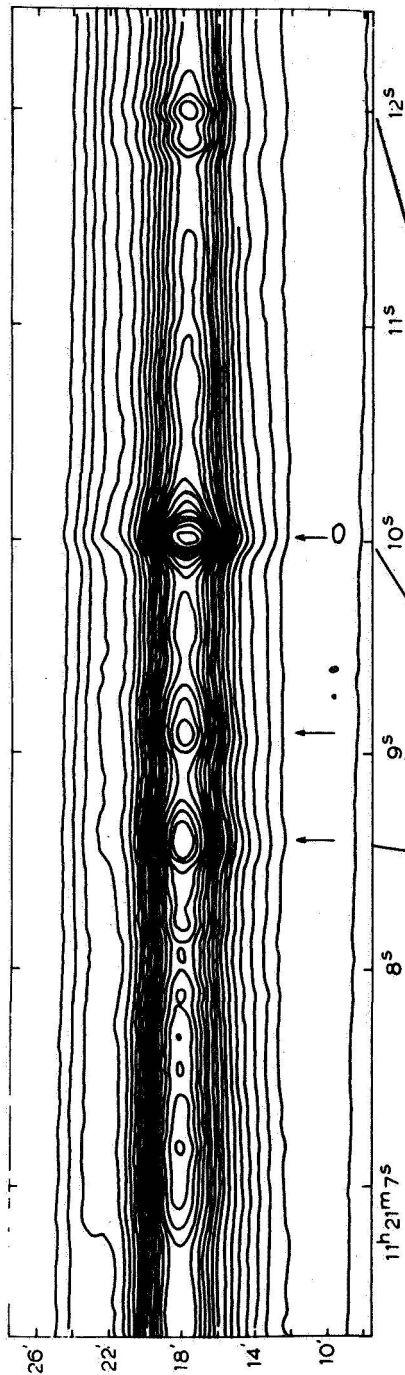
Fig. 2a

Fig. 2 b

Figure 2(a). Isophotes illustrating the E-W intensity distribution of the continuum and pulsating structure before the first part of the event. Ordinates: positions in arcmin west from the central meridian. Abscissae: UT time. Arrows indicate the pulsation maxima clearly visible on the spectrum. Figure 2(b). Radio spectrum of the first part of the event; the corresponding period of Figure 2A is clearly visible. The upper portion represents polarization (black regions: total right hand polarization; white regions: total left hand polarization).

the half-power beam width of the theoretical lobe of the instrument. We conclude that the real size of the pulsating structure would be much smaller than the continuum which is found to be 5.5 arcmin. The position of the pulses appears very stable well within the angular extent of the continuum. So we can argue that the pulsations of a stationary type IV source originate from a small part of this source. These results are in good agreement with the Rosenberg model.

TRANSIENT ACTIVITY CAUSING DISPLACEMENT OF THE STATIONARY TYPE IV SOURCE

Two parts of similar transient activity (11^h 21^m 00^s to 11^h 23^m 15^s and 11^h 25^m 00^s to 11^h 26^m 20^s UT) containing a series of fast, normal type III bursts followed by type II-like details were observed.

During both parts, the angular position of the stationary type IV source changed considerably close to the appearance of the type II-like bursts. In the first part it moved from 18 arcmin W to 20.5 arcmin W, which corresponds to an apparent speed of about 700 km·s^{-1} assuming the motion to be regular through the whole burst group, and about 2500 km·s^{-1} assuming the motion to take place during the interval of the type II-like structures.

In the second part, during the short time interval between the type III group and the type II-like structures, the intensity was so low that a few pulses were observable. These pulses, according to their spectral and size characteristics, were identical with the ones before the event, and had a position $19\overset{'}{.}5$ W, which is, within the accuracy of measurement, the same as before the type III group. This fact enabled us to certify that the subsequent apparent motion to $20\overset{'}{.}8$ W took place entirely during the interval of the type II-like structures, 11^h 26^m 00^s to 11^h 26^m 08^s UT, thus at an average speed of about 4000 km·s^{-1}. The continuum returned in the following 20's at an apparent speed of about 1200 km·s^{-1} and afterwards at 450 km·s^{-1}.

We can easily verify that the observed westward speeds are much faster than the Alfven speed, so they must be due to a shock wave. The continuum and pulsations do not show an appreciable change in spectrum, so the shock is most likely to be fast, but not energetic.

The energy necessary for the motion of the continuum can be estimated from the difference in magnetic energy content of a magnetic flux tube being budged by the shock. This energy is roughly 10^{29} ergs, which is one or two orders of magnitude below accepted values for flare energies.

The shockwave moving the continuum may be produced in the flare region. Another possibility is that the loop system is repelled by injection of fast particles. To account for the required energy we need approximately 6×10^{34} particles of 1 MeV.

Assuming the continuum radiation to be of synchrotron nature and assuming an average field strength of 1 Gauss, such an amount of electrons can account also for the observed flux values at 169 and 408 MHz. The returning motion may be due, in this model, to the redistribution of the injected electrons over the whole flux tube. A more detailed study will be presented in Solar Physics (1973).

REFERENCES

Abrami, A., 1972, *Nature—Phys. Sci.* **236**, 25-28.

McLean, D. J., Sheridan, K. V., Stewart, R. T., Wild, J. P., 1971, *Nature* **234**, 139-142.

Rosenberg, H., 1970, *Astron. Astrophys.* **9**, 159.

Rosenberg, H., 1971, *Solar Magnetic Fields*, Howard (ed.)., IAU Symp. 43.

THE CHROMOSPHERIC ASSOCIATION OF THE METRIC TYPE III BURSTS--IMPLICATIONS CONCERNING THE ACCELERATION OF SOLAR ELECTRONS AND THE ACTIVE STREAMERS

F. Axisa

Service d'Electronique Physique, Centre d'Etudes Nucléaires de Saclay

M. J. Martres, M. Pick, and I. Soru-Escaut

Observatoire de Meudon

ABSTRACT

In two recent papers we showed that the metric type III emission is closely related to a transient perturbation seen in absorption in the Hα line. In addition, this perturbation sometimes triggers a flare, sometimes not. This can explain why the type IIIs have a poor Hα flare correlation rate and still are a typical flash phase emission when flare-associated. Here we first summarize the characteristics of the new association proposed. We assume that 10 to 100 keV electrons are accelerated in connection with a particular kind of transient Hα absorbing feature. For as yet undetermined reasons, this process would often, but not always, result in a more efficient acceleration coincident with the early phase of the optical flare. The possibilities that this process could lead occasionally to long lasting subrelativistic particle emissive region are explored. On the other hand, the region where the acceleration takes place is certainly connected to a coronal streamer, at least when a type III emission is observed. Consequently our observations indicate that a coronal streamer also exists above $H_{/\!/} = 0$ lines which are not materialized by a stable filament.

INTRODUCTION

Former statistical analyses concerning the type III Hα flare association have led to a puzzling situation. Indeed the metric type III bursts are often observed in the absence of any visible flare (some 70 percent, after Malville, 1962). However, the study of those bursts which are flare-coincident strongly suggests that they are closely connected to the first acceleration process characteristic of the early phase of the Hα flare. Consequently most authors agree in considering the type III's as a typical flash phase emission (Wild et al., 1963; De Jager, 1968). During the last few years several investigations have reinforced this point of view. Today the electron stream theory initiated by Wild (1950) appears as the best candidate for interpreting the type III emission (Alvarez et al., 1972; Lin, 1970). At the same time the importance of accelerated particles in many solar flare processes has been abundantly emphasized. In particular, it has been shown that a population of 10 to 100 keV

electrons may be both the agent initiating the flare, and the early form of the flare energy which is afterward released in various thermal and nonthermal emissions (Lin, 1972; Hudson, 1972).

Recently we have reconsidered the problem of the chromospheric type III association in Martres et al. (1972) and in Axisa et al. (1972). We used a selection of 44 radio events for which the chromospheric situation, as observed in the Hα core and ± 0.75 Å away, was clear enough for association purposes. In this sample it happens that the type III groups which take place during the progress of a visible flare are as numerous as those occurring in their absence. Here our purpose is to summarize the main results obtained, and to discuss the observations in relation with the problems of the acceleration and the propagation of subrelativistic particles in the solar atmosphere.

THE CHROMOSPHERIC ASSOCIATION OF THE METRIC TYPE III BURSTS

In the absence of flares the type IIIs are emitted in relation with a particular Doppler-shifted Hα-absorbing feature which is transitory in nature:

- The feature is revealed by the transient appearance of a dense and cool gas which is probably similar to the filamentary material.

- A portion of the gas is observed streaming upward, the other downward. The radial velocities involved extend at least up to a few $10 \text{ km} \cdot \text{s}^{-1}$. Faster motions, if real, are not detectable with our Hα camera which is fitted with a 0.75 Å bandpass Lyot filter in the wings. By following the evolution of the feature, both in the red and the blue wing, it is possible to estimate the start, the paroxysm, and often the end of the motion. The time accuracy is limited to ± 1 minute by the cycle of the camera. In these conditions we find that the upward and the downward motions are frequently distinct also in time. The type IIIs are typically coincident within ± 1 minute with the paroxysm of the downward motion.

- The perturbation is located along an $H_{\parallel} = 0$ line which often is not materialized by a stable filament.

- The feature and its associated $H_{\parallel} = 0$ line takes place at the border of an active center (see Figure 1). A portion of it lies inside the facula between a well-developed spot and a parasitic polarity. The external part lies outside the facula; hence, in a region where the magnetic fields are weaker and more dispersed. These last two properties appear at this time as the most characteristic ones for distinguishing the type III associated absorbing features from many others which are otherwise optically similar on our records.

616
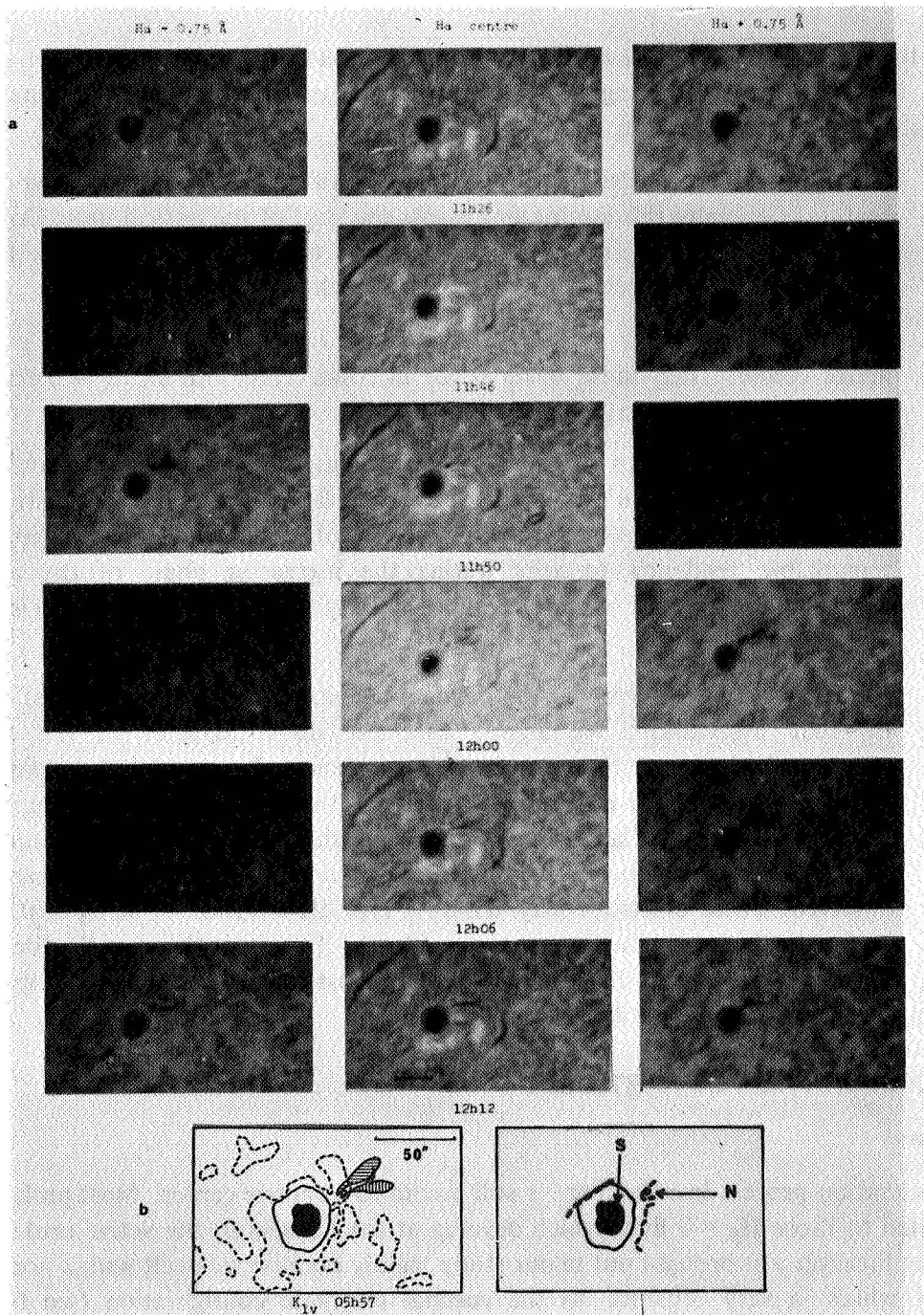
Figure 1. The transient Hα-absorbing feature associated with the type III group at 1208 UT on July 10, 1970. (a) Time sequence showing the evolution of the transient feature. (b) Location of the feature with respect to the active center: Left: Hatched lines identify the border of the K_{1v} facula. Right: Hatched lines identify the location of the magnetic inversion lines.

617

During the progress of a flare the study has been limited to those situations when only one specific Hα feature was evolving at the time of the type III group. Consequently our investigation refers mainly to tiny flares and subflares.

- The type IIIs are emitted within $\pm$ 1 minute of the sudden brightening of a flare feature. Generally this brightening marks the start of the optical flare. However, it also happens that distinct type III groups are emitted during the same flare. We find that they are all related to distinct Hα bright features.

- In our sample, all the type III related flares are located in the outer part of an active center. Then these flares occur in connection with an $H_{\parallel} = 0$ line of the same kind as that described previously.

- For most of the cases the type III coincident flaring features are related to a preceding transient Hα absorbing feature. The latter is of the same nature as those which are type III associated in the absence of flares. The flaring material has a remarkable tendency to arise during the increasing phase of the red wing absorbing component. A more detailed description of this relationship is given in Axisa et al. (1972).

In this paper we interpreted the results in relation with the problem of the type III flare association. We argued that the dual character of the type III chromospheric association may be a consequence of a causal link between three distinct phenomena, namely, a particular kind of Hα absorbing feature, the type IIIs, and the optical flare. As a working hypothesis we stated that an acceleration of subrelativistic electrons is acting in connection with the dynamic perturbation observed. These electrons may trigger a type III emission or an optical flare, or both of them at the same time. Clearly this hypothesis calls for further experimental checks. However, it is of interest to infer some of its implications from the observations available at this time.

THE ACCELERATION OF PARTICLES

Location

The acceleration process invoked here is still bound to an active center. Most probably it is not limited to those $H_{\parallel} = 0$ lines which develop at the borders of the active centers. This particular location was brought out in our study mainly because we dealt with a nonthermal emission which is very sensitive to the coronal magnetic configuration (see following section). We believe that transient Hα absorbing features, in motion along $H_{\parallel} = 0$ lines embedded well inside the active regions, also are a source of fast particles. In such cases the type III emission is significantly reduced because of the more closed and intricate magnetic field pattern.

618

Time Scale and Efficiency of the Process

According to its type III signature the acceleration would be an impulsive and repetitive mechanism. Many pulses of electrons are certainly produced during the whole chromospheric perturbation. Obviously the radio receivers are sensitive only to the most intense pulses which arise mainly in coincidence with the paroxysm of the downward motion. From our observations the optical flare would be a possible consequence of one or several particularly intense pulses accelerated in connection with the preexisting absorbing material. Often, for as yet unknown reasons, the pulses result in a type III group but fail to initiate a flare. This accounts for the dual type III chromospheric association. Whether the acceleration which is known to occur at the beginning of the flares is of the same nature or not, is still questionable. This is a tempting hypothesis. However, we have to recognize that the relation between a flare and a preceding Hα absorbing feature is not always evident. In addition, the electrons accelerated during a flare are obviously much more abundant than those involved in an individual pulse accelerated in the absence of flares. This is adequately proved by the high flare association rate of various nonthermal emissions like the hard X-ray bursts and the 40 keV solar electron events.

Another and important aspect of the problem is revealed by the optical data. We observed that in some active centers the relevant Hα absorbing activity is particularly abundant and lasts for several days. In such a situation the impulsive and rather moderate acceleration process could still supply a long lasting particle emissive region. The potential role of such a source is obvious for various nonthermal radiations. In particular, the characteristics outlined above would account for the long duration of the type I noise storm centers and at the same time for the impulsive nature of the individual type I bursts.

Nature and Energy of the Particles Emitted

As in the first step flare process, the particles would be accelerated only up to nonrelativistic velocities, and it is not known whether or not protons are accelerated together with the electrons. Protons of low energy (a few MeV), unlike 40 keV electrons, are often not clearly associated with specific flares. Occasionally they behave rather like a slowly varying component connected to an active region as a whole (Fan et al., 1968). In principle this is interpreted either in terms of an assumed coronal storage or in terms of a long-lasting acceleration region (Pick, 1970). Our observations provide a good argument for the latter.

TYPE III BURSTS AND CORONAL STREAMERS

In the electron stream theory the type IIIs are excited by electrons which escape from the source region through a coronal streamer. The particles have either a guiding center line motion along the open magnetic field lines of the streamer, or they are channeled in its neutral sheet. Various studies have shown that the coronal streamers develop above $H_{/\!/} = 0$ lines which are materialized by a stable filament. Optical investigations are mostly concerned with the large scale streamers which expand above the quiescent filaments. On

the limb photographs, several actually distinct streamers often appear as mixed together because of perspective and superposition effects. This largely precludes any specific filament streamer association, particularly above the active regions where several small filaments are often gathered in a close pattern. Disk observations of the streamers by means of their thermal radio emission have been initiated at 169 MHz by Axisa et al. (1971). These observations confirmed the configuration inferred by Sturrock and Smith (1968). The coronal streamers are closely related to a magnetic neutral sheet and their cross section at 169 MHz essentially reflects the configuration of the underlying filament. As disk observations are more systematic and less sensitive to superposition effects than the optical ones, it was also possible to recognize that most (if not all) of the filaments which last more than a few days support a coronal streamer. On several occasions coronal streamers have been unambiguously detected above a small plage filament. This is supported, in some favorable cases, by the limb photographs. Figure 2 shows the relative disposition of the coronal and the chromospheric features, which were present on September 22, 1968, near the eastern limb. The coronal features are drawn from an eclipse photograph in white light, kindly provided by Laffineur and Koutchmy. The chromospheric information is provided by K_{1v} and $H\alpha$ spectroheliograms from Meudon Observatory. Special interest has been focused on a rather thin and well localized streamer (dotted area on Figures 2-1 and 2-3). This streamer is apparently anchored in region A. Figure 2-2 displays the chromospheric situation in the relevant region as observed a few days later. This is used in Figure 2-3 for deriving the location of the chromospheric features both in front of and behind the limb on September 22, 1968. On this figure the association of the streamer with the plage filament (a'), which was at that time behind the limb, is clearly apparent. It is worthwhile noticing that the $H_{\parallel} = 0$ line corresponding to this filament is at a suitable location as far as the type III emission is concerned. From our observations it can be inferred that the basic streamer configuration is already present before the appearance of the stable filament, at least above the $H_{\parallel} = 0$ lines where the transient $H\alpha$ absorbing features give rise to a type III emission. Perhaps the perturbations we are observing have some connection with the formation of a stable filament and of a stable coronal streamer.

620
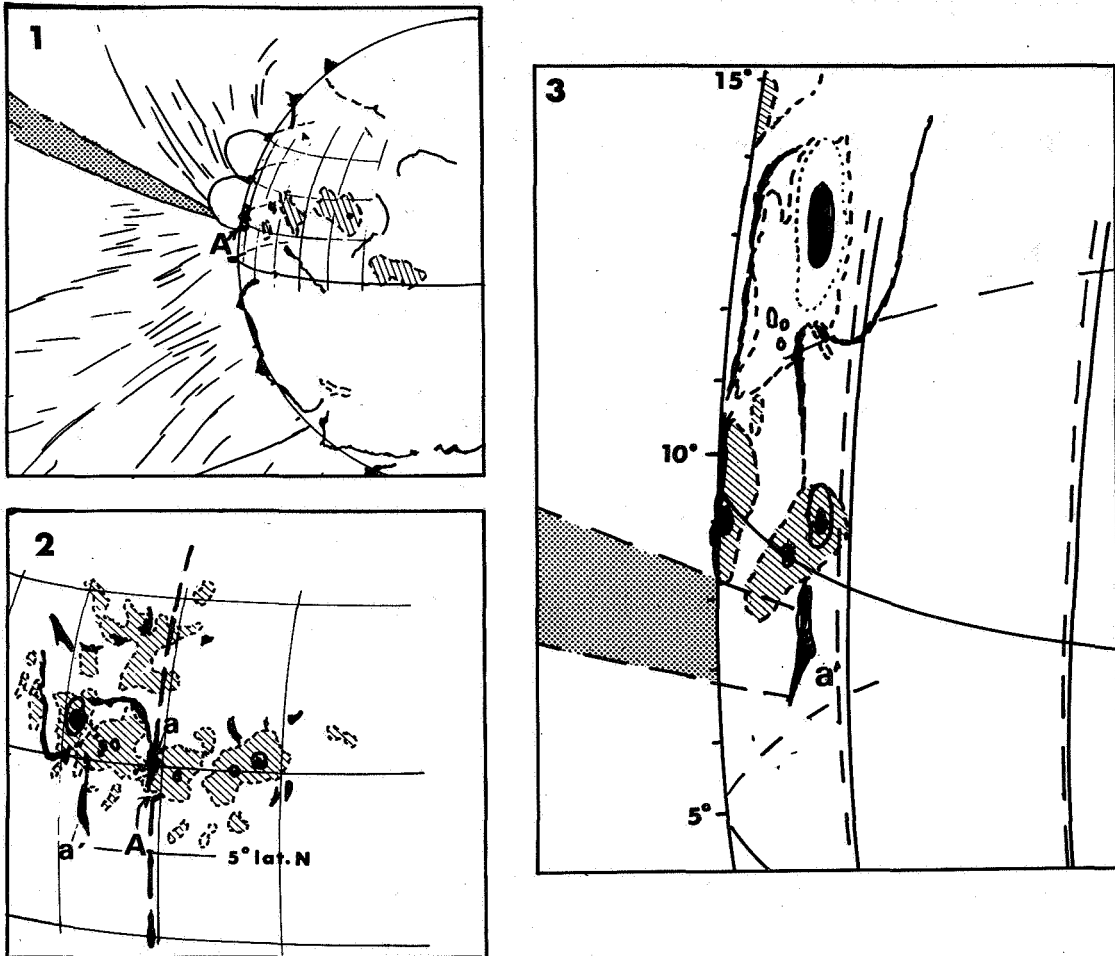
Figure 2. Association of an active streamer with a plage filament.

(2-1): Composite drawing of the coronal and chromospheric feature near the eastern limb on September 22, 1968. The thin active streamer is represented by the dotted area.

(2-2): Enlarged view at the chromospheric level of the region A. Heavy dashed line marks the limb position on September 22.

(2-3): Disposition of the streamer and the chromospheric features behind and in front of the limb on September 22. The streamer clearly corresponds to the plage filament (a') which is located behind the limb (cf 2-2).

REFERENCES

Alvarez, H., Haddock, F., and Lin, R. P., 1972, (preprint).

Axisa, F., Avignon, Y., Martres, M. J., Pick, M., and Simon, P., 1971, *Solar Phys.* **19**, 110.

Axisa, F., Martres, M. J., Pick, M., and Soru-Escaut, I., 1972, *Solar Phys.*

De Jager, C., 1969, *Solar Flares and Space Research,* Tokyo Symposium, 1968,
    North Holland Publ. Co.

Fan, C. Y., Pick, M., Pyle, R., Simpson, J. A., and Smith, D. R., 1968, *J.G.R.* **73**, 1555.

Hudson, H. S., 1972, *Seminar on the Generality of Particle Acceleration of Various
    Scales in Cosmos,* Leningrad, 1972.

Lin, R. P., 1970, *Solar Phys.* **12**, 266.

Lin, R. P., 1972, *Solar Terrestrial Conference,* Calgary, 1972.

Malville, J. M., 1962, *Ap. J.* **135**, 834.

Martres, J. M., Pick, M., Soru-Escaut, I., and Axisa, F., 1972, *Nature* **63**, 25.

Pick, M., 1972, *Solar Terrestrial Physics,* Leningrad, 1970, Reidel Publ. Co.

Sturrock, P. A., and Sheldon Smith, M., 1968, *Solar Phys.* **5**, 87.

Wild, J. P., 1950, *Australian J. Sci. Res.* A3, 541.

Wild, J. P., Smerd, S. F., and Weiss, A. A., 1963, *Ann. Rev. Astron. Astrophys.* **1**, 291.

IX: SUMMARY AND OUTLOOK

HIGH ENERGY PHENOMENA ON THE SUN SYMPOSIUM—
SUMMARY AND OUTLOOK

James W. Warwick

Department of Astro-Geophysics
University of Colorado

The evening before the last day of the conference I counted some 52 papers on the program. Solar physics is as broad a science as there is, so broad that without meetings such as this one, we can labor for years in isolation from one another. We heard discussions of optical and particle phenomenology, both in advanced stages of sophistication; of plasma turbulence; of nuclear energy level structure and transition probabilities; of radiative transfer; and of particle energy gains and losses in the chromosphere and the corona — with and without complications of anisotropy. Under the circumstances I can only apologize for a somewhat disorganized presentation. I am writing this document several weeks after the symposium, but will not depart far from the text I presented verbally. My talk responded principally to my own prejudices and prior interests, and is undoubtedly disorganized owing to the short timescale in which I had to prepare. But so be it.

Elliot and Sturrock presented discussions of flare models. It is not obvious to me that $B^2/8\pi$ is the ultimate energy of flares, at least not magnetic energy in the chromosphere or corona. I think Elliot's ideas are perhaps oversimplified in many ways, and yet in others a good deal more than simply charmingly useful. Science, particularly solar physics, often works on intuition as much as on multiple, independent demonstrations. My own intuition is that the stability and predictability of solar magnetic fields must be an important ingredient in physics of the solar atmosphere. Not withstanding, I am impressed by the rare dynamic events, such as March 30, 1969 (now that event is in my talk). In 1963, at the Goddard Flare Symposium, I estimated that the ratio of escaping protons to trapped protons was very small. Does Elliot want a total of 10^{32} ergs in particles including the trapped population, or does he count his 10^{32} ergs as energetic particles that are observed in interplanetary space? In that case (which I submit is closer to the truth) his (or my) trapping factor leads to as much as 10^{35} ergs in total energetic particle production. This low a trapping ratio is, however, one or two orders of magnitude less than Newkirk's values based on pretty good estimates of what the lines of force really are like. At that high energy what Elliot said about efficiency of the acceleration mechanisms becomes even more compelling.

I am also worried, as are many others, about how all these energetic protons get accelerated on the sun. Sturrock didn't help us with that, and neither did Sonnerup, although he showed how reconnection could begin the process through a modified Petschek mechanism. Perhaps Sturrock expects that Fermi acceleration comes into play after the Petschek-Sonnerup process gets protons up to MeV.

I don't feel as cynical as all that may sound. We've heard many individual discussions that provide essential clues to what coronal dynamics is all about. The corona is in fact an apparently stable structure for days on end; dynamic optical events are rare at heights above, say, 50,000 km. This creates obvious difficulties for radical field annihilation theories, a point already made by Elliot and many others. Many speakers, optical and radio, told us about solitary waves and shock waves, and Fisk, Sonnerup, and others who didn't speak about them clearly implied them. The interaction of these waves with particles needs to be studied.

What about type II theories? Since Tidman have we learned more? Paul Wild told us about the Moreton wave of 1963 that proved to him that shocks produce type II's. I restate my own demonstration of II-associated prominences, not surges as had previously been claimed for type II bursts, starting with an especially spectacular case that occurred in 1960. Unlike Moreton waves, this disturbance lay in the middle corona but surely had the configuration of a moving current sheet. At risk again of undue personal emphasis, I stress the difficulty in regarding a single expanding magnetic arch (even if that can be actually demonstrated) as a useful trapping structure. And I don't think that radio data, even the beautiful Culgoora data, or other radio data, imply in any case an expanding magnetic arch, or in the case of Westward Ho, a self-contained plasmoid at many solar radii above the disk. The point is that traveling discontinuities in field are of themselves quite probably adequate sources of transport for energetic particles across the sun, as well as likely regions to look toward for particle acceleration. I think that a major theoretical problem lies not so much in discovering piston or driver gases for shocks in the corona as it does in studying the loading by hydrogen of a blast wave made obvious through Hα emission. We know almost everything about the wave: shape, speed, neutral density, point of origin, but not magnetic field jump or flux density in the front. Lin charmed us with detailed correlations between interplanetary electrons and type III bursts, and also the still somewhat tentative but obviously emerging connections between hard X-ray bursts and type IIIs. In this circumstance I should reemphasize the type III burst storm and its connection with type I noise storm. Type III storms typically occur at low frequencies, below 50 MHz, and are almost always associated with type I storms at 60 MHz and higher. They appear to be excellent evidence against Simnet's demonstrations of electron-trapping based on Nancay 169 MHz noise storms.

We heard extensive discussions of the hard photon spectrum of flares, from X-rays to gamma rays. There is a live hope that one can extract from these data information on energetic electrons created during flares at the low end of the range, and on incipient nuclear reactions at the high, which indicate the presence of acceleration of protons directly at the sun, into the range near or above 1 MeV. This of course is a very exciting possibility and underlines the importance of Chupp's report on gamma ray lines in the range from 1/2 MeV to 6 MeV. The question in one's mind remains as to how model-dependent are these results? The density and lifetime of energetic particles within the gamma ray production region is the really crucial datum, rather than the characteristics of the region itself, however

626

interesting that is in its own right. X-rays seem to provide important diagnostics on the characteristics of energetic electrons, but there again the region in which the X-rays are formed mixes its properties with the properties of the energetic electrons, although these are the ultimate objective. The report on microwave bursts by Enome is very important in this context. He reported continuously changing polarization across regions of production of microwave emission during a burst; particles thus appear in several contrasting magnetic field regions.

Noyes, in discussing EUV spectra, puzzled me with his analogy between the transition region, that is, the chromospheric coronal interface, and solar flare spectra. And I was intrigued by Doscheck's discussion of X-ray diagonistics of the nonthermal regime in flares, hopeful that further progress can be made, and doubtful of how to achieve it. Will results from the Apollo Telescope Mount help, or are there better ways?

By the way, Croom's discussion of total millimeter wave energetics in comparison to X-ray energetics needs to be mentioned. The major energy in solar radio emission may well be contained in this spectral region, but is this a very significant point? Radio emissions in general are diagnostic of plasma and plasma thermodynamics in the sun. The actual energies, as long as they lead to recordable radiations in our equipment on the earth, are in any case unimportant; the processes they represent are enormously energetic, a conclusion valid throughout the radio spectrum.

Zirin's lovely $H\alpha$ pictures intrigued, not to say confused, us. The pictures are too rich in details for my easy understanding, particularly in explicit terms such as *magnetic reconnection*. Joan Vorpahl's discussion of heights also intrigued me; insofar as they show an impulsive event, I am delighted, but not surprised. Extrapolating these events up into the solar atmosphere appears to give heights of only a few thousand kilometers. At one time I thought I knew that flare heights on the disk were considerably higher, say in the range 10 to 20,000 km. A friend of mine showed that this distribution is consistent with the heights of limb flares, and furthermore that ionospheric disturbances are correlated with the heights of associated limb flares. Finally there are rare but distinctly flarelike structures far above the limb on occasions. May 8, 1951 was such an event which appeared in situ at several tens of thousands of km within 30 seconds of time, and afterwards was followed by a spray prominence.

The question of isotopic abundances in interplanetary space arose. In the post-shock interplanetary gas, α to proton ratios are high, but apparently are low in solar particle events. My impression as an interested bystander in this work is that much will be learned about flare energy and particle density from these studies. Their importance is in relation to the physics of flares, the time development of energetic particles during the flare, their spatial history, and the kind of material they traverse. As an outsider, I am tempted to wait for the moment when data are consistent among many observers before attempting on my own to unfold the energetic particle spectrum and density out of the abundance of determinations.

McDonald summarized many particle events seen at the earth over recent years and with great detail in flux, spectrum, time variations, and so forth. This material remains to be sorted through, at least by me, but two especially important statements were made by McDonald: he plans to publish these details of individual events, for many different observations made through the years; and, he has concluded that long-term solar trapping (for example, more than one day) is not the explanation for what is seen. Newkirk, of course, showed us how difficult that is in any event.

Roelof's neutral line discussion was difficult for me to follow, first because I wasn't so sure I saw what he pointed out on his graphs, and second because I was semantically side-tracked by neutral line identified as filament. This is not semantically very useful, since most people will assume neutral line refers to zero longitudinal field and really means a point at the top of a line of force, where quiescent prominences are supported a la Kippenhahn-Schluter. In that case neutral line may mean base of a helmet structure which really means open coronal ray structure extending into interplanetary space and whose relation to the magnetic structure of interplanetary space isn't at all obvious. If I have accurately understood what he said, it is that the ray structures in the outer corona are the geometrical locus along which move the low-energy energetic particles. I like his rejection of long term trapping.

Radio data were discussed in extenso during the conference. Many of these data had been reported at earlier times, especially the absolutely stunning Australian heliograph data from Culgoora. I should like to underline one caveat in those data: they do not identify the topology of the magnetic lines of force. There is a distinction, therefore, between one possible reconstruction of the magnetic field which may be present during such an event, and the uniqueness of that magnetic configuration. This critique is particularly important for the more dramatic and dynamic events of the heliograph records.

De la Noe described the beautiful high resolution HF and VHF radio spectra of type III bursts seen in France and at Arecibo. Owing to the extraordinary fine structure in these bursts on these time scales, the French have been led to a group of important phenomenological conclusions on the source of radio excitation. Streams of particles can move up through the corona without the appearance of radio emission; the emission mechanisms lie at the leading edge of the excitor. Towards low frequencies the duration of type III bursts gets longer and longer, to the extent that collision damping theory must be incorrect. The temperature gradient becomes too steep, collision damping appears to be too simple, and new studies of Landau damping are in progress.

Stone described Radio Astronomy Explorer-1 (RAE-1) and Interplanetary Monitoring Platform-6 (IMP-6) low-frequency observations of type III and type II bursts. The most intriguing aspect of these data for me has yet to be fully explored. At the lowest observational frequencies, the spacecraft actually lies within the burst source. Presumably therefore, it should be possible to infer the details of plasma physical theories required to explain the bursts. Lin reemphasized the need for correlating type III's at decametric frequencies with interplanetary electron events, and his data may provide the other side of plasma physical

628

question, that is, the flux in the burst excitor. Finally, we heard from Dean Smith who is puzzled by the absence of adequate numbers of protons in space needed to create the neutral plasma stream excitation he has required for the burst sources near the sun. In space near the earth, stabilization of these electrons isn't a problem, although the situation is serious at the sun. Whatever else may be true, near the sun the initial electron distribution doesn't look like a beam. Smith also reviewed type II theory which, with the observation of a slow-drift burst at hectometric wavelengths, may be evolving towards the second generation.

OUTLOOK

Solar physics, especially flare physics, is dramatically improved over its status as recently as one dozen years ago. This is especially true of energetic photons and charged particles, but is also true of solar atmospheric dynamics in relation to high energy phenomena.

This healthy situation is signalized by the relatively less well-developed theory of energetic phenomena at the sun, which is nevertheless far better off than it was in 1960. Critical tests of the plasma-physical theory of solar radio emission are easier now, with essentially in situ simultaneous EM and energetic particles measures. There will be no stronger stimulus for improvements in the theory.

The flare itself remains an enigma for which answers reside in as-yet unmeasured phenomena. Radio data at long wavelengths are too complex to help and may not be close enough to the parent flare to provide insight. At microwaves the situation is, in principle, improved, but data with the necessary high spatial and temporal resolution are lacking. The detailed correspondence between short microwave impulsive bursts and hard X-rays argues powerfully that we can learn a lot about energetic processes in flares by looking at these short wavelength radio emissions. The equipment necessary to do this job is large and expensive, on the scale by which ground-based astronomy is done, but cheap on the scale of space physics.

Observations of magnetic field changes are critically important to many theories of flares, and are notably difficult to make. This is particularly true at levels of the chromosphere and low corona where flares are known to occur. Both theory of optical line formation and polarization and clever experimentation are required.

In reviewing the last decade of observational techniques in the visible range, I am impressed at how profitable the very few off-band films of solar activity have been. At 50 kilometers per second per angstrom, large wavelength displacements, tens of angstroms or more, are required to add, to our library of limb photos of active flares, their disk equivalents. Synoptic observations are required to catch these fleeting events and good luck besides!

The outlook for energetic particle observations is extremely promising with many measurements, such as isotopic abundances, particle spectra to low energies, and electron fluxes now possible, even though still mostly not unified into the rest of the flare data. The process of

diffusion by energetic particles across complex coronal magnetic field structures is better understood phenomenologically now, although still lacking a firm theoretical explanation. There appears to be emergent the beginnings of a consensus on the role of particle storage versus continuous production in the vicinity of the sun. And the discovery of gamma rays from the sun offers rich new possibilities for modeling of the regions of origin and propagation of solar energetic particles.

From a general astrophysical point of view we are making major steps towards solutions of problems of wide-ranging application. Aside from mechanisms of plasma instabilities associated with radio burst production, or of the origin and slow variation of solar magnetic fields, solar phenomena offer a prototype case of energetic particle production in the universe. It is notable that at the sun, as elsewhere, the energetics leave little room to doubt that high efficiency in particle production is the name of the game. But the sun offers hope that we can solve these problems in basic ways not depending quite so completely on ad hoc models as, for example, in the case of extragalactic radio models. There are frequently independent checks on solar theories, which have in consequence a shorter life expectancy than do theories in other areas of astrophysics.

But, about the sun, as an astronomer I ought to make this negative comment: unlike the classical objects of astronomy outside the solar system, the sun can be virtually touched by our space apparatus. This is not good, astronomically speaking! Most of the astronomical world regards an object which is within its grasp as too close for comfort; the rules of this game are: if you can touch it, it's off limits. I vigorously disagree of course. The sun represents a critical object for astronomical, geophysical, and space physical investigations. The question it raises, and may answer, are questions valid throughout the universe, and its unpopularity among academicians is more a question of academic style than logic.

APPENDIX A
SYMPOSIUM PROGRAM

APPENDIX A

SYMPOSIUM PROGRAM

September 28, 9:00 A.M. - 12:30 P.M.

Chairman: T. Chubb

P. Sturrock	A Model for Solar Flares
H. Zirin	Observations of Magnetic Field Reconnection in Flares
C. Hyder	Optical Flare Observations and Theory
S. Kane	Hard X-ray Observations
K. Frost*	Hard X-ray Observations
D. Gruber	MeV Gamma-ray Observations
L. Peterson	Thermal and Nonthermal X-ray Bursts
H. Hudson	Interpretation of X-ray Emission
R. Wolff	High Energy X-ray Polarimetry

September 28, 2:00 P.M. - 5:30 P.M.

Chairman: F. Haddock

S. Enome	Structure of Microwave Bursts
D. Guidice	Spectral Characteristics of Microwave Bursts
A. Maxwell*	Microwave Pulsations
J. Hagen*	Generation of Microwave Bursts
D. Croom	Millimeter Observations
M. Kundu	Millimeter Observations
H. Ko	Gyrosynchrotron Radiation Formulae
R. Ramaty	Theory of Microwave Emission
J. Vorpahl	Optical X-ray and Microwave Emission
T. Takakura	Theory of X-ray and Microwave Emissions

September 29, 9:00 A.M. - 11:30 A.M.

Chairman: D. Wentzel

B. Sonnerup	Particle Acceleration and Field Reconnection
F. McDonald	Charged Particle Observations
E. Stone	Charged Particle Observations
L. Lanzerotti	Solar Flare Alpha Particles
L. Fisk	Modulation of Solar Particles
D. Reames*	Composition of Solar Particles
B. Price	Composition and Spectra of Heavy Nuclei
B. Cartwright	Preferential Acceleration of Heavy Nuclei

* Presented at the Symposium, but not printed in these Proceedings.

September 29, 1:00 P.M. - 3:30 P.M.

Chairman: J. Lockwood

E. Chupp	Gamma Ray and Neutron Observations
R. Lingenfelter	Nuclear Interactions on the Sun
J. Simpson	Flare Accelerated Isotopes of H and He
G. Simnett	Energetic Particle Storage on the Sun
H. Elliot	Energetic Particles as a Source of Flare Energy
I. Palmer	The Position and Size of Radio Sources
P. Wild*	Solar Radio Emission: General Goddard Colloquium

September 30, 9:00 A.M. - 12:30 P.M.

Chairman: T. Takakura

R. Noyes	Ultraviolet Observations and Their Interpretation
G. Doschek	Soft X-ray Observations
K. Phillips	Low energy (<10 keV) Nonthermal X-ray Events
T. Takakura	Time Profile of Type III Bursts
G. Newkirk	Solar Magnetism
S. Smerd*	Theory of Solar Radio Emission
Y. Uchida	MHD Disturbances and Type II Bursts
H. Alvarez	Decay Time of Type III Bursts

September 30, 2:00 P.M. - 5:30 P.M.

Chairman: A. Maxwell

J. Wild	Regular Pulsations from the Solar Corona
J. de la Noë	Decametric Observations
M. Pick	Results from the 169 MHz Radioheliograph
T. Kuiper	Type III Bursts at Meter Wavelengths
E. Roelof	Coronal Propagation of Charged Particles
R. Stone	Radio Observations from Space
R. Lin	Solar Electron Observations at 1 A.U.
D. Smith	Theory of Type II and Type III Bursts
R. Donnelly	Ground-based Observations
S. Kahler	Low Energy Nonthermal X-ray Events
M. Pick	Chromospheric Associations
S. Krimigis	Coronal Particle Storage
E. Howard	Observations of Type III Bursts
J. Warwick	Summary and Outlook

* Presented at the Symposium, but not printed in these Proceedings.

634

APPENDIX B
LIST OF ATTENDEES

APPENDIX B

LIST OF ATTENDEES
SYMPOSIUM ON HIGH ENERGY PHENOMENA ON THE SUN

J. Aarons	Air Force Cambridge Research Laboratory, Bedford, Massachusetts
I. Adler	Goddard Space Flight Center, Greenbelt, Maryland
J. Alexander	Goddard Space Flight Center, Greenbelt, Maryland
M. D. Altschuler	High Altitude Observatory, Boulder, Colorado
H. Alvarez	University of Michigan, Ann Arbor, Michigan
S. Amar	University of New Hampshire, Durham, New Hampshire
T. P. Armstrong	Applied Physics Laboratory, Johns Hopkins University, Silver Spring, Maryland
G. Ascher	Goddard Space Flight Center, Greenbelt, Maryland
R. G. Athay	High Altitude Observatory, Boulder, Colorado
W. Barron	Air Force Cambridge Research Laboratory, Bedford, Massachusetts
S. Basu	Air Force Cambridge Research Laboratory, Bedford, Massachusetts
C. Baugher	Marshall Space Flight Center, Huntsville, Alabama
R. Becker	University of Maryland, College Park, Maryland
W. Behring	Goddard Space Flight Center, Greenbelt, Maryland
S. Berstein	Hunter College, New York, New York
D. Bertsch	Goddard Space Flight Center, Greenbelt, Maryland
S. Biswas	Goddard Space Flight Center, Greenbelt, Maryland
J. Blake	Aerospace Corporation, Los Angeles, California
R. L. Blake	University of Chicago, Chicago, Illinois
R. Bleach	Naval Research Laboratory, Washington, D. C.
J. D. Bohlin	Naval Research Laboratory, Washington, D. C.
C. Bostrom	Applied Physics Laboratory, Johns Hopkins University, Silver Spring, Maryland
G. Borner	Goddard Space Flight Center, Greenbelt, Maryland
R. Braunstein	Goddard Space Flight Center, Greenbelt, Maryland
G. E. Bruckner	Naval Research Laboratory, Washington, D. C.
E. C. Bruner, Jr.	University of Colorado, Boulder, Colorado
L. Burlaga	Goddard Space Flight Center, Greenbelt, Maryland
B. Cartwright	University of Chicago, Chicago, Illinois
H. Caulk	Goddard Space Flight Center, Greenbelt, Maryland
J. Chao	Goddard Space Flight Center, Greenbelt, Maryland
C. C. Cheng	Goddard Space Flight Center, Greenbelt, Maryland
T. A. Chubb	Naval Research Laboratory, Washington, D. C.
E. Chupp	University of New Hampshire, Durham, New Hampshire
T. Cline	Goddard Space Flight Center, Greenbelt, Maryland
A. E. Covington	National Research Council of Canada, Ottawa, Canada

D. Croom	S.R.C. Radio and Space Research Station, Slough, England
D. Datlowe	University of California, San Diego, California
W. Decker	Pennsylvania State University, University Park, Pennsylvania
L. deFeiter	Space Research Laboratory, Utrecht, Holland
J. de la Noë	Meudon Observatory, Meudon, France
B. Dennis	Goddard Space Flight Center, Greenbelt, Maryland
K. Dere	Naval Research Laboratory, Washington, D. C.
U. Desai	Goddard Space Flight Center, Greenbelt, Maryland
J. C. Dodge	University of Colorado, Boulder, Colorado
R. F. Donnelly	NOAA, Boulder, Colorado
G. A. Doschek	Naval Research Laboratory, Washington, D. C.
H. Elliot	Imperial College, London, England
S. Enome	Nagoga University, Toyokawa, Japan
W. C. Erickson	University of Maryland, College Park, Maryland
L. Evans	Goddard Space Flight Center, Greenbelt, Maryland
J. Fainberg	Goddard Space Flight Center, Greenbelt, Maryland
L. A. Fisk	Goddard Space Flight Center, Greenbelt, Maryland
R. J. Fitzenreiter	Goddard Space Flight Center, Greenbelt, Maryland
D. Forrest	University of New Hampshire, Durham, New Hampshire
M. Frankel	Stanford University, Stanford, California
K. Frost	Goddard Space Flight Center, Greenbelt, Maryland
L. M. Garrison	Naval Research Laboratory, Washington, D. C.
T. Gergely	University of Maryland, College Park, Maryland
M. Goldstein	Goddard Space Flight Center, Greenbelt, Maryland
B. Gotwals	Applied Physics Laboratory, Johns Hopkins University, Silver Spring, Maryland
D. Gruber	University of California, San Diego, California
D. Guidice	Air Force Cambridge Research Laboratory, Bedford, Massachusetts
F. Haddock	University of Michigan, Ann Arbor, Michigan
J. Hagen	Pennsylvania State University, University Park, Pennsylvania
B. Hausler	Max Planck Institute, Munich, Germany
R. Hedeman	University of Michigan, Ann Arbor, Michigan
D. Hovestadt	Max Planck Institute, Munich, Germany
E. Howard	Martin Marietta, Denver, Colorado
R. Howard	Naval Research Laboratory, Washington, D. C.
H. Hudson	University of California, San Diego, California
C. Hyder	NASA, Albuquerque, New Mexico
F. Jones	Goddard Space Flight Center, Greenbelt, Maryland
S. Jordan	Goddard Space Flight Center, Greenbelt, Maryland
S. Kahler	American Science & Engineering, Cambridge, Massachusetts
M. Kaiser	Goddard Space Flight Center, Greenbelt, Maryland
S. Kane	University of California, Berkeley, California

S. Kastner	Goddard Space Flight Center, Greenbelt, Maryland
H. Kikuchi	New York University, New York, New York
J. King	Goddard Space Flight Center, Greenbelt, Maryland
H. Ko	Ohio State University, Columbus, Ohio
M. J. Koomen	Naval Research Laboratory, Washington, D. C.
S. M. Krimigis	Applied Physics Laboratory, Johns Hopkins University, Silver Spring, Maryland
A. Kritz	Hunter College, New York, New York
T. B. H. Kuiper	University of Maryland, College Park, Maryland
M. Kundu	University of Maryland, College Park, Maryland
N. Labrum	CSIRO, Epping, Australia
C. Lacombe	Meudon Observatory, Meudon, France
Nand Lal	Computer Sciences Corporation/Goddard Space Flight Center, Greenbelt, Maryland
P. Landecker	Columbia University, New York, New York
L. J. Lanzerotti	Bell Telephone Laboratories, Murray Hill, New Jersey
C. P. Leavitt	University of New Mexico, Albuquerque, New Mexico
R. Lin	University of California, Berkeley, California
J. A. Lockwood	University of New Hampshire, Durham, New Hampshire
D. S. Lund	NOAA, Boulder, Colorado
H. Mallitson	Goddard Space Flight Center, Greenbelt, Maryland
J. Mangus	Goddard Space Flight Center, Greenbelt, Maryland
S. P. Maran	Goddard Space Flight Center, Greenbelt, Maryland
G. E. Marandino	Goddard Space Flight Center, Greenbelt, Maryland
A. Maxwell	Harvard Radio Astronomy Station, Fort Davis, Texas
F. McDonald	Goddard Space Flight Center, Greenbelt, Maryland
R. McEntire	Applied Physics Laboratory, Johns Hopkins University, Silver Spring, Maryland
P. S. McIntosh	NOAA, Boulder, Colorado
R. B. McKibben	University of Chicago, Chicago, Illinois
L. H. Meredith	Goddard Space Flight Center, Greenbelt, Maryland
John Moore	University of Maryland, College Park, Maryland
S. Mosier	Goddard Space Flight Center, Greenbelt, Maryland
W. Neupert	Goddard Space Flight Center, Greenbelt, Maryland
G. Newkirk	High Altitude Observatory, Boulder, Colorado
T. G. Northrop	Goddard Space Flight Center, Greenbelt, Maryland
J. Novaco	Goddard Space Flight Center, Greenbelt, Maryland
R. Novick	Columbia University, New York, New York
R. Noyes	Smithsonian Astrophysical Laboratory, Cambridge, Massachusetts
G. K. Oertel	NASA Headquarters, Washington, D. C.
J. O'Gallagher	University of Maryland, College Park, Maryland
C. Opal	Naval Research Laboratory, Washington, D. C.

| A. Opp | NASA Headquarters, Washington, D. C. |
L. Orwig	Goddard Space Flight Center, Greenbelt, Maryland
I. Palmer	Los Alamos Scientific Laboratory, Los Alamos, New Mexico
F. Paul	Goddard Space Flight Center, Greenbelt, Maryland
G. Paulikas	Aerospace Corporation, Los Angeles, California
C. Pellerin	Goddard Space Flight Center, Greenbelt, Maryland
L. Peterson	University of California, San Diego, California
K. Phillips	Goddard Space Flight Center, Greenbelt, Maryland
M. Pick	Meudon Observatory, Meudon, France
G. Pieper	Goddard Space Flight Center, Greenbelt, Maryland
B. Price	University of California, Berkeley, California
H. D. Prince	University of Michigan, Ann Arbor, Michigan
R. Ramaty	Goddard Space Flight Center, Greenbelt, Maryland
D. Reames	Goddard Space Flight Center, Greenbelt, Maryland
G. Resch	Goddard Space Flight Center, Greenbelt, Maryland
E. Roelof	University of New Hampshire, Durham, New Hampshire
J. Saba	Computer Sciences Corporation/Goddard Space Flight Center, Greenbelt, Maryland
K. Sakurai	Goddard Space Flight Center, Greenbelt, Maryland
D. Sawyer	Goddard Space Flight Center, Greenbelt, Maryland
A. Schardt	NASA Headquarters, Washington, D. C.
A. Serlemitsos	Goddard Space Flight Center, Greenbelt, Maryland
F. I. Shimabukuro	Aerospace Corporation, Los Angeles, California
G. M. Simnett	University of California, Riverside, California
P. Simon	Meudon Observatory, Meudon, France
J. Simpson	University of Chicago, Chicago, Illinois
R. P. Sinha	University of Maryland, College Park, Maryland
S. Smerd	CSIRO, Epping, Australia
D. Smith	High Altitude Observatory, Boulder, Colorado
E. Smith	University of Maryland, College Park, Maryland
H. J. Smith	NASA Headquarters, Washington, D. C.
B. Sonnerup	Dartmouth College, Hanover, New Hampshire
F. Stecker	Goddard Space Flight Center, Greenbelt, Maryland
D. Stern	Goddard Space Flight Center, Greenbelt, Maryland
E. C. Stone	California Institute of Technology, Pasadena, California
R. G. Stone	Goddard Space Flight Center, Greenbelt, Maryland
R. M. Straka	Air Force Cambridge Research Laboratory, Bedford, Massachusetts
P. Sturrock	Stanford University
J. D. Sullivan	University of California, Berkeley, California
T. Takakura	University of Tokyo, Tokyo, Japan
R. Taylor	Naval Research Laboratory, Washington, D. C.
B. Teegarden	Goddard Space Flight Center, Greenbelt, Maryland

R. G. Teske	University of Michigan, Ann Arbor, Michigan
R. Thomas	Goddard Space Flight Center, Greenbelt, Maryland
J. R. Toraskar	Columbia University, New York, New York
J. Trainor	Goddard Space Flight Center, Greenbelt, Maryland
S. Tsuruta	University of Maryland, College Park, Maryland
H. Tung	Computer Sciences Corporation/Goddard Space Flight Center, Greenbelt, Maryland
Y. Uchida	High Altitude Observatory, Boulder, Colorado
M. Van Hollebeke	Goddard Space Flight Center, Greenbelt, Maryland
D. Venkatesan	University of Calgary, Calgary, Canada
J. Vesecky	Stanford University, Stanford, California
J. Vette	Goddard Space Flight Center, Greenbelt, Maryland
T. von Rosenvinge	Goddard Space Flight Center, Greenbelt, Maryland
J. Vorpahl	Sacramento State College, Sacramento, California
J. Warwick	University of Colorado, Boulder, Colorado
K. Watts	Computer Sciences Corporation/Goddard Space Flight Center, Greenbelt, Maryland
F. Wefer	Pennsylvania State University, University Park, Pennsylvania
C. Wende	Goddard Space Flight Center, Greenbelt, Maryland
D. Wentzel	University of Maryland, College Park, Maryland
K. G. Widing	Naval Research Laboratory, Washington, D. C.
P. Wild	CSIRO, Epping, Australia
D. J. Williams	NOAA, Boulder, Colorado
R. S. Wolff	Columbia University, New York, New York
C. Wu	University of Wisconsin, Madison, Wisconsin
J. Weldon	Goddard Space Flight Center, Greenbelt, Maryland
H. Zirin	California Institute of Technology, Pasadena, California
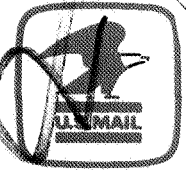
"*The aeronautical and space activities of the United States shall be conducted so as to contribute . . . to the expansion of human knowledge of phenomena in the atmosphere and space. The Administration shall provide for the widest practicable and appropriate dissemination of information concerning its activities and the results thereof.*"
—NATIONAL AERONAUTICS AND SPACE ACT OF 1958

NASA SCIENTIFIC AND TECHNICAL PUBLICATIONS

TECHNICAL REPORTS: Scientific and technical information considered important, complete, and a lasting contribution to existing knowledge.

TECHNICAL NOTES: Information less broad in scope but nevertheless of importance as a contribution to existing knowledge.

TECHNICAL MEMORANDUMS: Information receiving limited distribution because of preliminary data, security classification, or other reasons. Also includes conference proceedings with either limited or unlimited distribution.

CONTRACTOR REPORTS: Scientific and technical information generated under a NASA contract or grant and considered an important contribution to existing knowledge.

TECHNICAL TRANSLATIONS: Information published in a foreign language considered to merit NASA distribution in English.

SPECIAL PUBLICATIONS: Information derived from or of value to NASA activities. Publications include final reports of major projects, monographs, data compilations, handbooks, sourcebooks, and special bibliographies.

TECHNOLOGY UTILIZATION PUBLICATIONS: Information on technology used by NASA that may be of particular interest in commercial and other non-aerospace applications. Publications include Tech Briefs, Technology Utilization Reports and Technology Surveys.

Details on the availability of these publications may be obtained from:

SCIENTIFIC AND TECHNICAL INFORMATION OFFICE

NATIONAL AERONAUTICS AND SPACE ADMINISTRATION
Washington, D.C. 20546